

Lecture Notes on Multidisciplinary Industrial Engineering
Series Editor: J. Paulo Davim

M. S. Shunmugam
M. Kanthababu *Editors*


Advances in Additive Manufacturing and Joining

Proceedings of AIMTDR 2018

 Springer

Lecture Notes on Multidisciplinary Industrial Engineering

Series Editor

J. Paulo Davim , Department of Mechanical Engineering, University of Aveiro, Aveiro, Portugal

“Lecture Notes on Multidisciplinary Industrial Engineering” publishes special volumes of conferences, workshops and symposia in interdisciplinary topics of interest. Disciplines such as materials science, nanosciences, sustainability science, management sciences, computational sciences, mechanical engineering, industrial engineering, manufacturing, mechatronics, electrical engineering, environmental and civil engineering, chemical engineering, systems engineering and biomedical engineering are covered. Selected and peer-reviewed papers from events in these fields can be considered for publication in this series.

More information about this series at <http://www.springer.com/series/15734>

M. S. Shunmugam · M. Kanthababu
Editors

Advances in Additive Manufacturing and Joining

Proceedings of AIMTDR 2018

 Springer

Editors

M. S. Shunmugam
Manufacturing Engineering Section
Department of Mechanical Engineering
Indian Institute of Technology Madras
Chennai, Tamil Nadu, India

M. Kanthababu
Department of Manufacturing Engineering
College of Engineering, Guindy
Anna University
Chennai, Tamil Nadu, India

ISSN 2522-5022

ISSN 2522-5030 (electronic)

Lecture Notes on Multidisciplinary Industrial Engineering

ISBN 978-981-32-9432-5

ISBN 978-981-32-9433-2 (eBook)

<https://doi.org/10.1007/978-981-32-9433-2>

© Springer Nature Singapore Pte Ltd. 2020

This work is subject to copyright. All rights are reserved by the Publisher, whether the whole or part of the material is concerned, specifically the rights of translation, reprinting, reuse of illustrations, recitation, broadcasting, reproduction on microfilms or in any other physical way, and transmission or information storage and retrieval, electronic adaptation, computer software, or by similar or dissimilar methodology now known or hereafter developed.

The use of general descriptive names, registered names, trademarks, service marks, etc. in this publication does not imply, even in the absence of a specific statement, that such names are exempt from the relevant protective laws and regulations and therefore free for general use.

The publisher, the authors and the editors are safe to assume that the advice and information in this book are believed to be true and accurate at the date of publication. Neither the publisher nor the authors or the editors give a warranty, expressed or implied, with respect to the material contained herein or for any errors or omissions that may have been made. The publisher remains neutral with regard to jurisdictional claims in published maps and institutional affiliations.

This Springer imprint is published by the registered company Springer Nature Singapore Pte Ltd. The registered company address is: 152 Beach Road, #21-01/04 Gateway East, Singapore 189721, Singapore

AIMTDR 2018 Conference Core Organizing Committee

Patrons

Dr. M. K. Surappa, Vice-Chancellor, Anna University

Dr. J. Kumar, Registrar, Anna University

President (NAC-AIMTDR)

Mr. P. Kaniappan, Managing Director, WABCO India Ltd.

Vice-President (NAC-AIMTDR)

Dr. Uday Shanker Dixit, Professor, IIT Guwahati, India

Co-patrons

Dr. A. Rajadurai, Dean, MIT Campus, Anna University

Dr. T. V. Geetha, Dean, CEG Campus, Anna University

Dr. L. Karunamoorthy, Chairman, Faculty of Mechanical Engineering, Anna University

Dr. S. Rajendra Boopathy, Head, Department of Mechanical Engineering, Anna University

Chairman

Dr. S. Gowri, Honorary Professor, Department of Manufacturing Engineering, Anna University

Co-chairman

Dr. P. Hariharan, Professor, Department of Manufacturing Engineering, Anna University

Organizing Secretary

Dr. M. Kanthababu, Professor and Head, Department of Manufacturing Engineering, Anna University

Joint Organizing Secretaries

Dr. M. Pradeep Kumar, Professor, Department of Mechanical Engineering, Anna University

Dr. A. Siddharthan, Associate Professor, Department of Production Technology, Anna University

International Scientific Committee

Prof. Abhijit Chandra, Iowa State University, USA
Prof. Ajay P. Malshe, University of Arkansas, USA
Prof. Andrew Y. C. Nee, NUS, Singapore
Prof. Chandrasekar S., Purdue University, USA
Prof. Dean T. A., University of Birmingham, UK
Prof. Hong Hocheng, National Tsing Hua University, Taiwan
Prof. John Sutherland, Purdue University, USA
Prof. Kamlakar P. Rajurkar, University of Nebraska, USA
Prof. Kornel Ehmann, Northwestern University, USA
Prof. Liao Y. S., National Taiwan University, Taiwan
Prof. McGeough J. A., University of Edinburgh, UK
Prof. Mustafizur Rahman, NUS, Singapore
Prof. Philip Koshy, McMaster University, Canada
Prof. Rakesh Nagi, University at Buffalo, USA
Prof. Shiv Gopal Kapoor, University of Illinois, USA
Prof. Srihari Krishnasami, Binghamton University, USA
Prof. Tae Jo Ko, Yeungnam University, S. Korea
Prof. Tugrul Ozel, University of New Jersey, USA

National Advisory Committee

Prof. Ahuja B. B., Government College of Engineering, Pune
Prof. Amitabha Ghosh, BESU
Prof. Bijoy Bhattacharyya, Jadavpur University, Kolkata
Prof. Biswanath Doloi, Jadavpur University, Kolkata
Prof. Chattopadhyay A. K., IIT Kharagpur
Prof. Deshmukh S. G., IIT Gwalior
Shri. Dhand N. K., MD, ACE Micromatic, Bangalore
Prof. Dixit U. S., IIT Guwahati, Guwahati
Prof. Jain P. K., IIT Roorkee, Roorkee
Prof. Jain V. K., IIT Kanpur
Prof. Jose Mathew, NIT Calicut

Shri. Lakshminarayan M., WABCO India Pvt. Ltd.
Prof. Lal G. K., IIT Kanpur
Prof. Mehta N. K., IIT Roorkee
Prof. Mohanram P. V., PSG Institute of Technology and Applied Research
Shri. Mohanram P., IMTMA, Bangalore
Dr. Mukherjee T., TATA Steel Ltd., Jamshedpur
Shri. Muralidharan P., LUCAS—TVS Ltd., Vellore
Prof. Narayanan S., VIT University, Vellore
Mr. Niraj Sinha, Scientist 'G' PSA to GOI
Prof. Pande S. S., IIT Bombay, Mumbai
Dr. Prasad Raju D. R., MVGREC
Prof. Radhakrishnan P., PSG Institute of Advanced Studies, Coimbatore
Prof. Radhakrishnan V., IIST, Trivandrum
Prof. Ramaswamy N., Chennai
Prof. Ramesh Babu N., IIT Madras
Shri. Rangachar C. P., Yuken India Ltd., Bangalore
Prof. Rao P. V., IIT Delhi
Dr. Santhosh Kumar, IIT BHU
Dr. Sathyan B. R., CMTI, Bangalore
Prof. Satyanarayan B., Visakhapatnam
Prof. Selvaraj T., NIT Trichy
Prof. Shan H. S., Chandigarh
Prof. Shunmugam M. S., IIT Madras
Shri. Shirgurkar S. G., ACE Designers Ltd., Bangalore
Dr. Sumantran V., Celeris Technologies
Dr. Suri V. K., BARC, Mumbai
Shri. Venu Gopalan P., DRDL, Hyderabad
Prof. Vinod Yadav, Motilal Nehru National Institute of Technology, Allahabad

Foreword

It gives us immense pleasure to present the Advances in Manufacturing Technology and Design—Proceedings of All India Manufacturing Technology, Design and Research (AIMTDR) 2018 Conference.

We would like to express our deep gratitude to all the members of Organizing Committee of AIMTDR 2018 Conference and also to the authors, reviewers, sponsors, volunteers, etc., for their wholehearted support and active participation. Our special thanks to Mr. P. Kaniappan, Managing Director, WABCO India Ltd., Chennai, who kindly agreed to act as President of National Advisory Committee (NAC) of the AIMTDR 2018 Conference. We also express our sincere thanks to Chairman Dr. S. Gowri, Honorary Professor, and Co-chairman Dr. P. Hariharan, Professor, Department of Manufacturing Engineering, Anna University, Chennai, for their wholehearted support. We would like to express our sincere thanks to research scholars Mr. K. R. Sunilkumar, Mr. U. Goutham, Mr. V. Mohankumar, Mr. R. Prabhu and also UG/PG students of the Department of Manufacturing Engineering, Anna University, for their contributions to the preparation of this volume.

High-quality papers have been selected after peer review by technical experts. We hope you find the papers included in the Proceedings of AIMTDR 2018 Conference are interesting and thought-provoking.

We also like to express our gratitude for the support provided by WABCO India Ltd., Chennai; Kistler Instruments India Pvt. Ltd., Chennai; AMETEK Instruments India Pvt. Ltd., Bengaluru; Central Manufacturing Technology Institute, Government of India, Bengaluru; Defence Research and Development Organisation, Government of India, New Delhi; and Ceeyes Engineering Industries Pvt. Ltd., Trichy.

Finally, we would like to express our gratitude to National Advisory Committee (NAC) members of AIMTDR 2018 for providing the necessary guidance and support.

Guwahati, India

Uday S. Dixit
Vice-President, National Advisory
Committee, AIMTDR

Preface

All India Manufacturing Technology, Design and Research (AIMTDR) Conference is considered globally as one of the most prestigious conferences held once in two years. It was started in 1967 at a national level at Jadavpur University, Kolkata, India, and achieved the international status in 2006. It was organized by various prestigious institutions such as Jadavpur University, IIT Bombay, IIT Madras, CMTI Bangalore, PSG Tech, IIT Kanpur, CMERI, IIT Delhi, NIT Warangal, IIT Kharagpur, BITS Ranchi, VIT Vellore, IIT Roorkee, Andhra University, IIT Guwahati and College of Engineering, Pune.

The recent edition of the AIMTDR Conference, 7th International and 28th All India Manufacturing Technology, Design and Research (AIMTDR 2018) 2018 Conference, was jointly organized by the Departments of Manufacturing Engineering, Mechanical Engineering and Production Technology during 13–15 December 2018, at College of Engineering, Guindy, Anna University, Chennai, India, with the theme ‘Make in India—Global Vision’. A major focus was given on recent developments and innovations in the field of manufacturing technology and design through keynote lectures. About 550 participants registered for the conference. During the conference, researchers from academia and industries presented their findings and exchanged ideas related to manufacturing technology and design.

Of the 750 papers received initially, 330 papers were finally selected after rigorous reviews for publication in these proceedings. The proceedings volumes will be published in the Springer series Lecture Notes in Multidisciplinary Industrial Engineering in five volumes, namely **Volume 1**—Additive Manufacturing and Joining, **Volume 2**—Forming, Machining and Automation, **Volume 3**—Unconventional Machining and Composites, **Volume 4**—Micro & Nano Manufacturing and Surface Engineering and **Volume 5**—Simulation and Product Design & Development.

Chennai, India
May 2018

M. S. Shunmugam
M. Kanthababu

Contents

Part I Additive Manufacturing

1	Fabrication of Customized Ankle Foot Orthosis (AFO) by Reverse Engineering Using Fused Deposition Modelling	3
	Harlal Singh Mali and Shivendra Vasistha	
2	Friction Stir Welding of Three-Dimensional Printed Polymer Composites with Semi-consumable Tool	17
	Ranvijay Kumar, Rupinder Singh and Inderpreet Singh Ahuja	
3	Mechanical Characterization and Process Optimization of PolyJet 3D Printing Using Digital ABS with Different Part Geometries	31
	B. N. Sontakke and B. B. Ahuja	
4	Retrofitment of Laser Cladding System with CNC Machine for Hybrid Layer Manufacturing	47
	Seema Negi, Sajan Kapil, Arun Sharma, Priyanka Choudhary, Parag Bhargava and K. P. Karunakaran	
5	Influence of Various Tool Path Patterns on Hardness Used in Weld Deposition-Based Additive Manufacturing	61
	Panchagnula Kishore Kumar and Panchagnula Jayaprakash Sharma	
6	Design of Robot Gripper with Topology Optimization and Its Fabrication Using Additive Manufacturing	75
	M. Sugavaneswaran, N. Rajesh and N. Sathishkumar	
7	Fabrication of Gradient Density Components Through Extrusion-Based Additive Manufacturing	87
	Shashi Ranjan Mohan and Suryakumar Simhambhatla	
8	Tensile Strength of 3D Printed PLA Part	103
	Shilpesh R. Rajpurohit and Harshit K. Dave	

9	Study of Residual Stress in Nickel Micro Parts Made by Electrochemical Additive Manufacturing	115
	Anne Brant, Abishek Kamaraj and Murali Sundaram	
10	Laser Polishing of Wire Arc Additive Manufactured SS316L	127
	Vinod Singh Thakur, M. Manikandan, Shalini Singh, Shivam Mishra, Ankit Kaithwas, S. S. Mani Prabu and I. A. Palani	
11	Energy Consumption of Welding-Based Additively Manufactured Materials	137
	Nandhini Raju, G. Balaganesan and Gurunathan Saravana Kumar	
12	Manufacturing Standardization of Jaipur Foot by Additive Manufacturing	149
	Harlal Singh Mali and Aniket Singh	
13	Fused Deposition Modeling Using 6-Axis Industrial Robot	159
	Arigela Sri Harsha and Chintamreddy Vikram Kumar	
14	Characterization of Rapid Foam Castings Produced by Different Mold Making Processes	169
	Ranjeet Kumar Bhagchandani, Rohan Ghodke, R. Manivannan, Seema Negi, Sajan Kapil and K. P. Karunakaran	
15	Layer Separation Mechanisms in DLP 3D Printing	179
	Patil Yogesh, Patil Richa, N. S. Chandrashekhar and K. P. Karunakaran	
16	Topology and Build Path Optimization for Reducing Cost in FDM uPrint SE	189
	T. Ravi and Rajesh Ranganathan	
17	Tailored Support Structures for Additive Manufacturing	199
	Hemnath Anandan Kumar, Peter Francis Reginald Elvis, Madhanagopal Manoharan, Jayakrishnan Jayapal and Senthilkumaran Kumaraguru	
18	Redesigning ECMM Fixture with Part Consolidation and DfAM Principles	209
	R. Prithvirajan, K. Mohan kumar and G. Arumaikkannu	
19	Life Cycle Assessment of an Additive Manufactured Automotive Component	219
	Rohit Agrawal and S. Vinodh	
20	PLA-Based Material Design and Investigation of Its Properties by FDM	229
	M. Ramesh and K. Panneerselvam	

21 Numerical Analysis of Thermal Stresses in Selective Laser Melting 243
 Rahul Swarup Sharma and A. Kumar

22 Experimental Investigations of Printing Parameters of Fused Deposition Modeling-Based 3D Printers for Average Surface Roughness 253
 Apoorv Srivastava and Jitendra Bhaskar

23 Modeling of Linear Shrinkage in PLA Parts Fabricated by 3D Printing Using TOPSIS Method 267
 Jonty Mago, Rajat Kumar, Raj Agrawal, Anoop Singh and Vineet Srivastava

24 Investigation on Quality of In-house Fabricated PLA Filament for 3D Printing Application 277
 Ashish R. Prajapati, Harshit K. Dave and Shilpesh R. Rajpurohit

25 Investigation of Mechanical Behaviour and Surface Roughness Properties on Copper Electroplated FDM High Impact Polystyrene Parts 287
 N. Sathishkumar, N. Arunkumar, L. Balamurugan, L. Sabarish and A. Samuel Shapiro Joseph

26 Effect of Build Orientation on Mechanical Strength of FDM Printed PLA 301
 Naushil H. Patadiya, Harshit K. Dave and Shilpesh R. Rajpurohit

27 Intensifying Hands-on Learning and Experimentation of Fused Deposition Modeling Three-Dimensional Printers 309
 Pushpendra Yadav, Ishant Singhal, Bobby Tyagi, Ankit Sahai and Rahul Swarup Sharma

28 Simulation of Extrusion of Thermoplastic Binder in Additive Manufacturing Process 319
 Sunidhi Dayam, Satwik Priyadarshi and Puneet Tandon

29 Investigations on Synthesis of Porous NiTi Shape Memory Alloy Structures Using Selective Laser Melting Techniques 329
 A. Sahu, I. A. Palani, Sachin Bhirodkar, C. P. Paul and K. S. Bindra

30 Application of Low-Cost Natural Binders in Direct 3-D Printing of Sand Molds 337
 Madhvendra Tiwari, Devanshu Kathrecha, Kuldeep Meena, K. A. Desai and A. K. Plappally

31 Experimental and Numerical Investigation of the Flexural Behavior of Fused Deposition Modeling Parts 347
 Jothibabu Gokulakrishnan and Gurunathan Saravana Kumar

Part II Joining

- 32 Some Studies on Mechanical Properties of AISI 316L Austenitic Stainless Steel Weldments by Cold Metal Transfer Process** 359
A. Rajesh Kannan and N. Siva Shanmugam
- 33 Effect of Pre-weld Solution Treatment on Mechanical Properties and Microstructure of Micro-Plasma Arc Welded Inconel 718** 373
Ajit Kumar Sahu and Swarup Bag
- 34 Refilling of Pinhole in Friction Stir Spot Welding Using Waste Chips** 385
N. Bhardwaj, R. Ganesh Narayanan and U. S. Dixit
- 35 Dissimilar Friction Stir Welding of DH36 Shipbuilding Steel and Mild Steel** 397
Pardeep Pankaj, Avinish Tiwari, Saurav Suman, Abhishek Kumar, Rituraj Bhattacharjee, Subhashis Majumder and Pankaj Biswas
- 36 Multi-step Radiographic Segmentation of Weld Defect Images** 409
R. Sowmyalakshmi, M. R. Anantha Padmanaban, S. M. Girirajkumar, S. Benazir and A. Farzana
- 37 Thickness Evolution During End Forming Operations of Friction Stir Processed AA 6063-T6 Tubes at Different Tool Geometries** 421
Arvind K. Agrawal, R. Ganesh Narayanan and Satish V. Kailas
- 38 Geometric Model of the Weld Bead in DC and Square AC Submerged Arc Welding of 2.25 Cr-1 Mo Heat Resistant Steel** 433
Uttam Kumar Mohanty, Abhay Sharma, Yohei Abe, Takahiro Fujimoto, Mitsuyoshi Nakatani, Akikazu Kitagawa, Manabu Tanaka and Tetsuo Suga
- 39 Mechanical Characterization and Microstructural Investigation of MicroPlasma Arc Welded AISI 316L Thin Stainless Steel Sheets** 447
Srikant Prasad, K. Vigneshwaran, Dibakor Boruah and Pintu Thakur
- 40 Comparison of Single- and Multiple-Spot Resistance Welding of Sub-millimeter Thick SS304 and SS316 Sheets** 461
Dhanraj B. Waghmare and Partha Saha
- 41 Effect of Tool Pin Profiles Using Tungsten Carbide Tool on Microstructure and Tensile Properties of Friction Stir Welded AA 6082-T6 Thin Aluminium Alloy Joints** 475
M. D. Sameer and Anil Kumar Birru

42	Effect of Pin Diameter in Underwater Friction Stir Lap Welding of Dissimilar Materials: AA6061-T6 and AISI304	487
	Raju Prasad Mahto, Manan Kinjawadekar, Chaman Gupta and Surjya Kanta Pal	
43	Brazeability of Synthetic Diamond with Steel Substrate Using Two Different Active Filler Alloys	497
	Prithviraj Mukhopadhyay and Amitava Ghosh	
44	Friction Stir Welding of Al-Cu Alloy Metal Matrix Composites Reinforced with B₄C and Graphite Particle Fabricated by Stir Casting and Thixoforming Method	507
	K. Sekar and P. Vasanthakumar	
45	Comparative Study of Feed-Forward and Recurrent Neural Networks in Modeling of Electron Beam Welding	521
	Sanjib Jaypuria, Santosh Kumar Gupta and Dilip Kumar Pratihari	
46	Effect of Beam Offset on Dissimilar Laser Beam Welding of Ti6Al4V and Inconel 718 Superalloy	533
	Anitesh Kumar Singh, Kalinga Simant Bal, Suman Sharma, Aditya Harbajanka, Mukesh Prasad, Dipanjan Dey and Asimava Roy Choudhury	
47	Study on the Dissimilar Joining of Martensitic Stainless Steel and Carbon Steel Using TIG Welding	545
	S. Karthi, S. P. Kumares Babu, S. Shanmugham and V. P. Balaji	
48	Influence of Tool Probe Offset and Traverse Speed on Microstructure and Mechanical Properties of Friction Stir Weld Dissimilar Joints of AA2024-T351 and AA7075-T651	555
	K. S. Anil Kumar, S. M. Murigendrappa and Hemantha Kumar	
49	Joining of Different Thickness Dissimilar Materials SS 316L/SS 310 By μ-PAW Process	569
	Swagat Dwibedi, Swarup Bag, Deepak Kumar Lodhi and Arindam Kalita	
50	Modification of Aluminium Alloy Surface Composite Reinforced with ZrO₂ Particles Fabricated Through Friction Stir Processing	579
	Surendra Kumar Patel, Virendra Pratap Singh and Basil Kuriachen	
51	Investigation of General Welding Defects Found During Friction-Stir Welding (FSW) of Aluminium and Its Alloys	587
	Virendra Pratap Singh, Surendra Kumar Patel, Basil Kuriachen and Saurav Suman	

52	Study of Heat Treatment Effect on Microstructure of PTA Weld Deposited Surface of SS 316L Steel	597
	H. V. Naik, D. D. Deshmukh and V. D. Kalyankar	
53	Modelling of Welding Sequences for Minimization of Weld-Induced Distortions and Residual Stresses	609
	Saurav Suman, Avinish Tiwari, Pradeep Pankaj, Pankaj Biswas, Basil Kuriachen and Abhijit Sinha	
54	Effect of Different Activated Fluxes on Mechanical Properties of DSS 2205 in Pulsed Tungsten Inert Gas Welding	619
	Dhananjay S. Satelkar, Bhagwan F. Jogi and Shrikant B. Thorat	
55	Effect of Pre- and Post-welding Processes on the Distortion Pattern in a SAW-Welded Butt Joint of P91 Steel Plate	631
	Saurav Suman, Pradeep Pankaj, Avinish Tiwari, Pankaj Biswas, Basil Kuriachen and Abhijit Sinha	
56	Effect of Welding Parameters on Tensile Strength of AA7075-T₆ Friction Stir Welded Joints	641
	Mallapuram Bala Chennaiah, Podaralla Nanda Kumar and Karanam Prahlada Rao	
57	Effect of Tool Plunge Depth on the Mechanical Performance of Joints Fabricated by Dieless Friction Stir Form Joining of Dissimilar Grade Aluminum Alloys	651
	Tinu P. Saju and R. Ganesh Narayanan	
58	Influence of Perturbations on Actuation Characteristics of Friction Stir Welded Shape Memory Alloy	661
	S. S. Mani Prabu, R. Mithun, Suhel Khan, S. Jayachandran, M. Manikandan, Yeshwanth Sai, M. Anbarasu and I. A. Palani	
59	Ultrasonic Welding of Molybdenum Using Aluminium Interlayer	669
	Sanjay Kumar Patel, Harshit K. Dave and Himanshu V. Patel	
60	Experimental Investigation and Mechanical Characterization of Double-Sided Submerged Arc Welding of AISI 304 Austenitic Stainless Steel	679
	P. V. S. S. Sridhar, Shailesh Kumar, Kaushik Pal, Bhaskar Kumar Chakraborty, Rituraj Bhattacharjee, Subhashis Majumder, Pankaj Biswas and Pinakeswar Mahanta	
61	A Study on Hardness of CRNO Electrical Sheets for Edge Joining Through TIG Welding	689
	Bhushan Y. Dharmik and Nitin K. Lautre	

62 Friction Stir Welding for Joining of Dissimilar Materials	699
Suryakanta Sahu, Omkar Mypati, Soumya Sangita Nayak, Pooja Sarkar, Surjya Kanta Pal and Shiv Brat Singh	
63 Effect of Process Parameters on Quality Characteristics of Al/Cu Dissimilar Friction Stir Welding Joint	711
A. Mandal, J. D. Barma and A. Bandyopadhyay	
64 Numerical Simulation to Predict Temperature Distribution and Weld Profile in Laser Beam Welding of Carbon Steel St37 and Mechanical Properties	719
Pramod Kumar and Amar Nath Sinha	
65 Influence of Friction Pressure/Time on Mechanical and Microstructural Characteristics of Rotary Friction Welded LM25/10% SiC Aluminium Matrix Composites	727
M. Abdul Ghani Khan, S. Rajakumar and T. Pragatheswaran	
66 Effect of Holding Time on Microstructural Characteristics and Mechanical Properties of Ti64 Diffusion Bonds	741
T. Pragatheswaran, S. Rajakumar, V. Balasubramanian, Vijay Petley and Shweta Verma	

About the Editors

M. S. Shunmugam is a Professor (Emeritus) in the Manufacturing Engineering Section in the Department of Mechanical Engineering, Indian Institute of Technology (IIT) Madras. After receiving his PhD in Mechanical Engineering from IIT Madras in 1976, he has worked in IIT Bombay (from 1977 to 1980) and in IIT Madras from 1980 onwards. He was a visiting faculty member at Michigan Technological University during 1989–1991 and was a member in the board of governors of IIT Madras during 2012–2013. Dr. Shanmugam’s research interests include metrology, machine tools, manufacturing, gears, micro-machining and computer applications in manufacturing. He has published about 130 peer-reviewed international journal papers, 15 peer-reviewed national journal papers, 75 international conferences and about 80 national conferences.

M. Kanthababu is a Professor in the Department of Manufacturing Engineering in Anna University, Chennai, India and the Director of the Centre for Intellectual Property Right and Trade Marks in Anna University. He has completed his MS in Mechanical engineering and PhD in Advanced Manufacturing Technology from IIT Madras. Prof Kanthababu’s research interests include manufacturing technology, composite materials and machining, and automation in manufacturing. He has published more than 30 peer reviewed international journal papers and 2 books, and holds one patent.

Part I
Additive Manufacturing

Chapter 1

Fabrication of Customized Ankle Foot Orthosis (AFO) by Reverse Engineering Using Fused Deposition Modelling



Harlal Singh Mali and Shivendra Vasistha

Abstract Ankle foot orthosis (AFO) is an assistive device used for support and correction of musculoskeletal structure. This research focuses on the development of a methodology to design and fabricate a patient-specific AFO for drop foot by redressing the geometrically 3D scanned data cloud of patient's lower limb. Unlike traditional plaster moulding technique, this technique has leverage of fast and precise AFO generation. It consists of acquisition of geometrical and anatomical data of patient's limb with the help of 3D scanning. Post-processing of data points is done to obtain refined limb geometry. Design of AFO from point cloud is done according to structural needs and requisite correction. An analysis based on the planter flexion and dorsiflexion movement of AFO and rotation about ankle in saggital plane are conducted on Fusion360™. Comparison of traditionally used polypropylene (PP) material is done with acrylonitrile butadiene styrene (ABS) and poly-lactic acid (PLA) based on the predefined tests. FEA enables to obtain result conforming to design aspect, and finally, fabrication of AFO using fused deposition modelling is done.

Keywords AFO · Drop foot · FDM

1.1 Introduction

Gait cycle is the sequence of movements which define the event of locomotion of homosapien. It consists of two different phases of foot movement, i.e., stance phase and swing phase. In swing phase of gait cycle of bipedal, it starts with initial contact of foot with the ground; then, the load of the body is shifted to reference foot in contact. It is followed by balancing of weight of body on reference foot, and in last step, toe of foot leaves the contact surface in order to engage in swing phase. Swing

H. S. Mali (✉) · S. Vasistha

Advanced Manufacturing & Mechatronics Lab, Department of Mechanical Engineering,
Malaviya National Institute of Technology, Jaipur 302017, India
e-mail: harlal.singh@gmail.com; 2016PPE5185@mnit.ac.in

© Springer Nature Singapore Pte Ltd. 2020

M. S. Shunmugam and M. Kanthababu (eds.), *Advances in Additive Manufacturing and Joining*, Lecture Notes on Multidisciplinary Industrial Engineering,
https://doi.org/10.1007/978-981-32-9433-2_1

phase is the movement in which the foot traces, while it is not in contact with the ground. Stance phase constitutes 60% of the entire gait cycle [1].

Parameters defining the gait cycle are step length, stride length, stride width, cadence and walking speed. Discrepancy in these parameters would cause abnormal gait cycle. Drop foot is the medical condition which has been considered for study. Foot drop in general is substantial weakness of ankle area and toe dorsiflexion movement. Patient suffering from drop foot opts to take stride with overstressed flexion in order to clear toes from striking the ground. Thus, it makes drop foot a high steppage gait and it also consumes more energy [2]. During the gait, the heel strike experiences direct reaction force and foot slaps the floor.

Causes behind drop foot range from muscular, neurological to anatomical. Peroneal and sciatic nerve structures the neural pathway in lower segment of human body. Peroneal nerve is more prone to injury and causes motor and sensory losses. Neurological causes for it are lumbosacral plexopathy, motor neuron disorder, cerebral palsy, lumbar radiculopathy, parasagittal cortical and spina bifida.

Orthotic devices thus find application in correction and support of functional and structural characteristics of skeletal and neuromuscular system [3]. Orthotics help in assisting the limb movement, controlling and guiding body segment, to constraint movements and aid rehabilitation. Ankle foot orthosis (AFO) constitutes the maximum portion of orthotic devices and is expected to grow to 7.3 million by 2020 [4]. Traditional fabrication techniques of fabrication of AFO are labour-intensive and time-consuming and require skilled labour. Rapid prototyping techniques are the future of orthotic field.

Motion analysis system also justifies the usage of orthotic device. It reduces the possibility of further deterioration of postural and walking stance of patient. It states the improvement in dynamic motion of limb when using orthosis. Orthotists are using thermo-plastic materials in manufacturing of upper limb and lower limb orthosis: polypropylene, co-polymer, polyethylene and others. Polypropylene is most commonly used amongst all due to good mechanical strength, fatigue strength and flexibility [5].

In India, traditional technique of thermoforming of plastic is used for production of ankle foot orthosis. This process involves preparation of negative mould of patient limb by experienced medical staff with the help of plaster of Paris in neutral position. From negative mould, a positive cast of the patient limb is produced. That positive cast is the replica of effected patient limb. Thermoforming of polypropylene at high temperature is done in order to produce ankle foot orthosis. By trimming and finishing, end product is developed. This entire process is dependent on the skills and experience of medical expert, and the level of customization is also at lower end.

In current scenario, multiple technologies are available for production of ankle foot orthosis and additive manufacturing is the most suitable amongst them as it provides high level of customization and easy to produce intricate shapes. Mavroidis et al. [6] has produced leaf spring-type AFO using stereo-lithography. Accura 40 resin and DSM Somos 9120 epoxy photopolymer are the materials used for fabrication, later one producing more flexible AFO. The weight of flexible AFO was observed to be lower by 21%. Yuan Jin et al. [7] has developed a wavy tool path to optimize the

deposition of material. It avoids any acceleration or deceleration during deposition unlike zig-zag path. Build time reduced significantly by 23%, and weight was also observed to lesser by 17%. Research in development of dynamic AFO by selective laser sintering has also been conducted. Rilson D80 had minimum dissipation of energy and was able to withstand large deformation [8]. Morshed Alam et al. [9] has conducted research on fabrication of custom articulated AFO with computer design. Sidebars and foot plate were manufactured from aluminium alloy using wire-cut EDM and calf band by PLA 3D printing. FDM process using Nylon AFO performs better than other devices in inertia test [10].

3D scanning technologies are useful in acquiring data points of geometry entitled to be used. Inspection of reflective surfaces is difficult due to undesirable specular reflection and causes outlier formation. It has been found that outliers are view-dependent only, while good points in scan are view independent. Data segmentation and processing of point cloud is essential to obtain homogeneous surface. Data available from physical model lack in parameters and constraints. Inspection of 3D parts using laser-plane sensors is adapted because of the accessibility limitation and slower scanning rate of coordinate measuring machine (CMM).

Post-processing of 3D point cloud is one of the major challenges, as it requires conforming data points to homogeneous set of points. Obtained points are a collection of discrete points in space, and it is necessary to assign reference to them. Irrelevant points are discarded, and residual points are projected as a refined data points. These points yet do not signify any solid structure as they encounter errors of incomplete mesh, critical points and overlapping points. Multiple iterations are necessitated to resolve these issues.

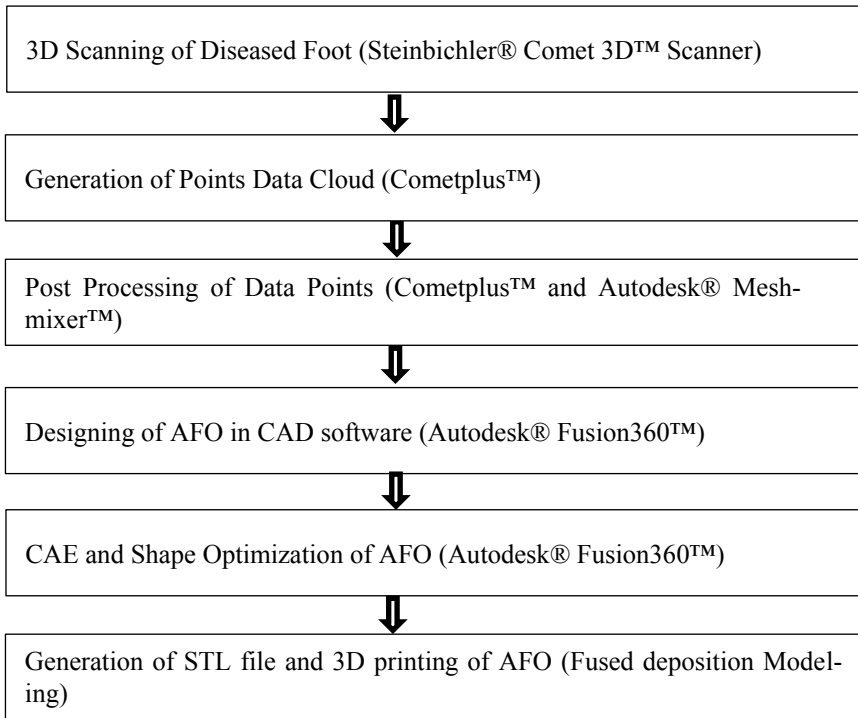
Ankle foot orthosis fitted to patient is subjected to forces, moments and reaction forces. Body weight of the human is balanced by reaction forces through ground. In case of patients suffering from drop foot, the distribution of load is uneven in gait cycle. Ankle foot orthosis assist individuals with weaker dorsiflexor muscle are unable to control ankle motion in loading and lifting properly the foot in swing phase of gait cycle. R. E. Major et al. have emphasized on computing the stiffness of AFO to resist the dorsiflexion [11]. Toshiki Kobayashi et al. performed both plantar and dorsiflexion angle test based on resistive torque acting on centre of rotation of AFO [12]. Sumiko Yamamoto et al. conducted study on flexibility of AFO with respect to velocity. Study revealed that in test at three different velocities, it did not alter the flexibility of ankle foot orthosis [13].

Computer-based designing (CAD) is the most suitable platform for producing model of ankle foot orthosis. This has an advantage of adding details to model that can be altered in timeline, and inputs to geometry can be assigned as per the model specification. Finite element analysis (FEA) of model prior to production would highlight the details in structure needed to be rectified. Considering the mechanical characteristics of AFO based on its rigidity and load-bearing capabilities, computer-aided engineering (CAE) of product could also be explored. CAE of ankle foot orthosis is supposed to highlight the high stress and deflection area which could be rectified by changing the design aspect of model. Thus, a durable ankle foot orthosis could be manufactured with the implication of CAD and CAE. Research focuses on

the cloud-based aspect of production of ankle foot orthosis with compatible geometry and functioning.

1.2 Schematic Flow Chart of Process

The fabrication process has been schematized in standard manner to produce rapid and accurate ankle foot orthosis. Flow chart represents the process with proprietary softwares utilized in the complete cycle. Most of these softwares are either supported with the equipments or are free for academic users.



With the due application these processes, customization and production of ankle foot orthosis with additive manufacturing has been proposed.

1.3 3D Scanning of Diseased Foot

1.3.1 Sample Foot Preparation

In order to evaluate geometry of foot, first step is to prepare the model for scanning. The scanning operation requires non-reflective surface for structured blue light scanner. Thus, the diseased foot needs to be covered in non-reflective coating of plaster of Paris. In current study, to avoid the needs of ethical approval, for preparing the foot geometry at this stage of the research work, no patient interaction was done. Based on available literature, the geometry is in conformance to the anatomical shape of human feet, as shown in Fig. 1.1.

1.3.2 Scanning Operation

Steinbichler Comet3D™ structured blue light scanner is utilized for scanning process. It scans the geometry on the principle of deformation of structure and distance to evaluate the shape. Multiple scan frames are stored in the software. Multiple scan frames are stitched together and aligned as per the scanning direction. Scanning procedure consisted aligning scanner head according to foot model, aligning laser guide to the model and perform scan. The scans from 3D scanner were obtained in manner as follows (Fig. 1.2).



Fig. 1.1 Sample foot

1.4 Point Data Cloud and Post-processing

1.4.1 Point Data Cloud

The scanning operation generated a large number of points in the space known as point cloud. Thus, geometry of foot obtained is a mere collection of point clouds. These point clouds are not sufficient to generate a closed body structure for modelling. Need for redressing of data is compulsory for homogeneous surface. These points refer to relative position of each other but are not referred to any origin (Fig. 1.3).

Point clouds can be converted to solid geometry with the help of embedded software of 3D scanner. Each scan data points lie in a plane. Software overlaps these

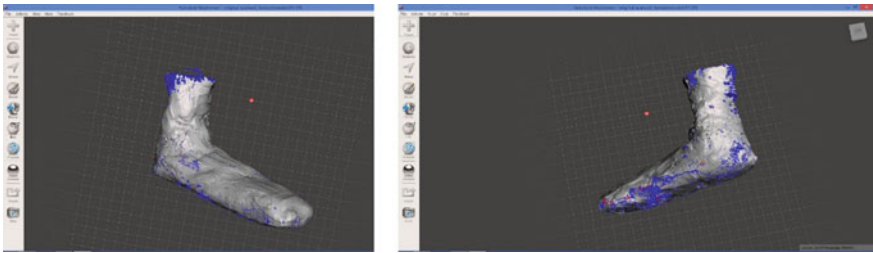


Fig. 1.2 Scanned model of foot

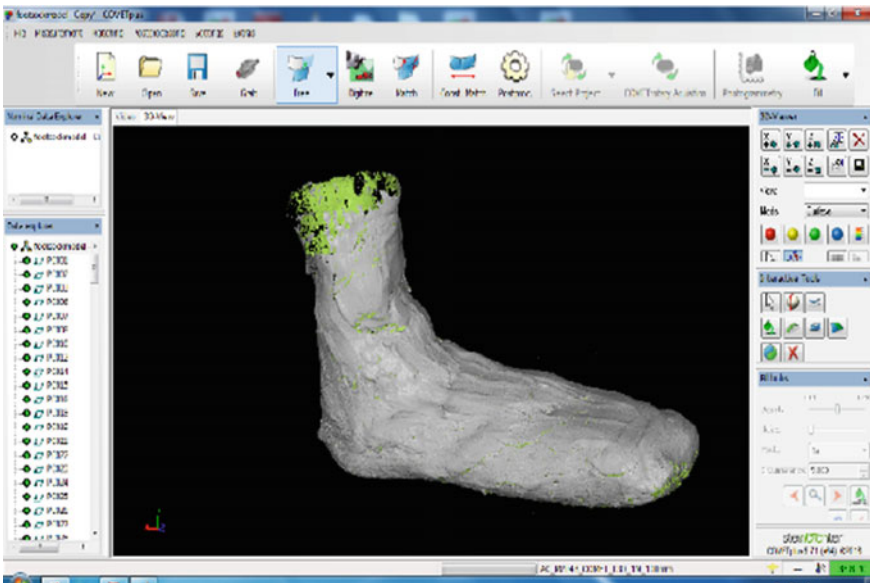


Fig. 1.3 Point cloud details of foot model

planes to form the structure of scanned model. Due to reflectivity, scanning direction, ambient condition and processing software, flaws are present in 3D model.

1.4.2 Post-processing

The geometry before post-processing is present with outliers, holes, overlapping surfaces and non-homogeneous surface. Outliers are insignificant points that are not part of the required geometry. In Cometplus™ software, these outliers were selected and discarded as whole. It is an iterative process which requires multiple operations to obtain the outlier free model. All point clouds do not combine to make a complete surface, thus resulting in a hole. Hole formation is primary due to non-conformity of scanning process of critical points. All the operations of designing require solid geometry, for that purpose, holes are filled with help of Cometplus™ and Autodesk® Meshmixer™.

Fixing the voids in model would eliminate the holes. Yet surfaces connected to sharp curvature or intermediate surfaces are not redressed. Solidification of geometry would result in overcoming all these challenges. In this particular manner, a complete model of foot is obtained (Fig. 1.4).

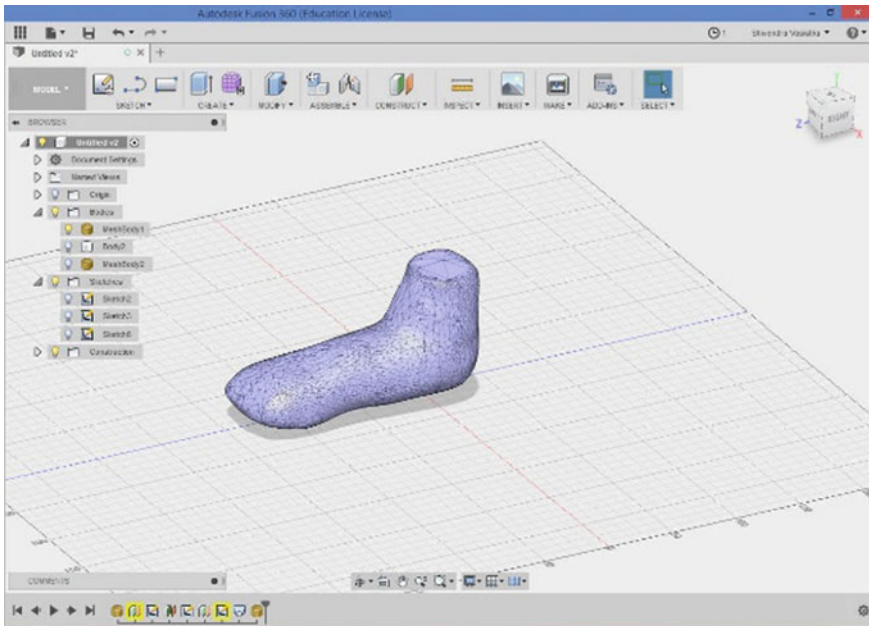


Fig. 1.4 Post-processed foot model

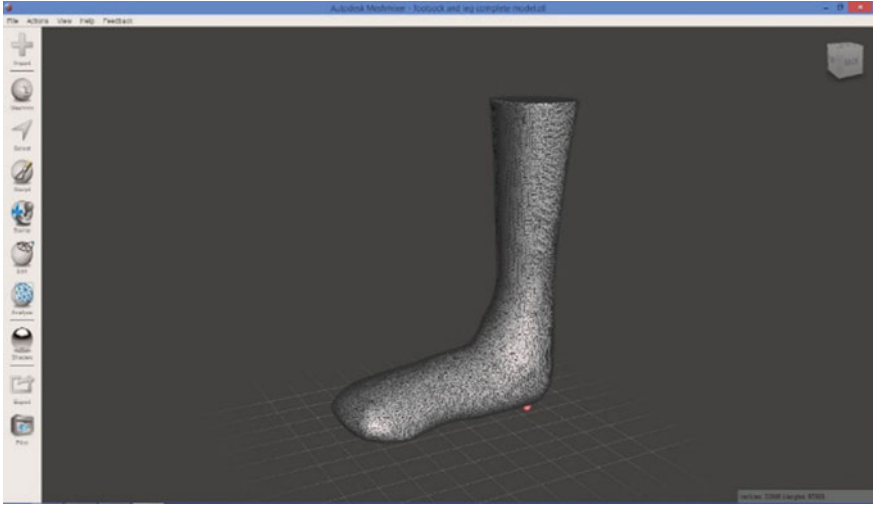


Fig. 1.5 Complete leg and foot model

Number of mesh triangles denotes the quality of scan. Suitable to the purpose, the details of mesh triangle are utilized. The final geometry is overdetailed with higher number of triangle mesh count. This hinders the process of designing operation due to large file size. 93969730 were the number of data points obtained from scan. The number of triangle counts in mesh was reduced to 10,000 to perform the design operation with ease.

1.5 Designing of Ankle Foot Orthosis

1.5.1 Geometry of Foot

As the geometry obtained was up to the ankle section, the anatomical structure of the ankle section was generated with the help of Autodesk Fusion360™ software with multiple cross sections to extrude the geometry. Both files were added using combine feature. Mesh sizes were not found to be uniform, and the re-meshing of complete file was performed to obtain homogeneous mesh size (Fig. 1.5).

1.5.2 Ankle Foot Orthosis Design

Solid ankle foot orthosis was designed for the scanned model of foot obtained. For designing purpose, Autodesk® Fusion360 software was utilized. In sculpt environ-

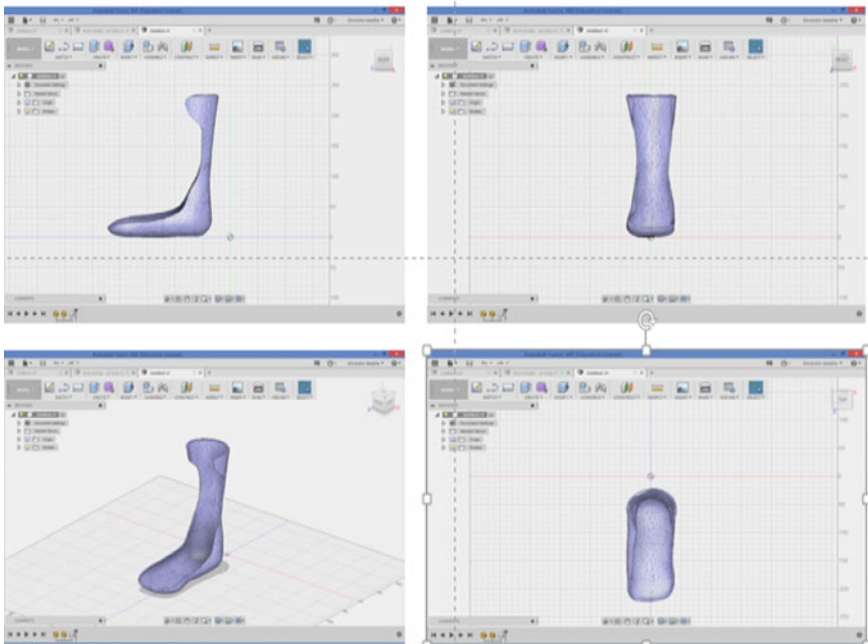


Fig. 1.6 Designed ankle foot orthosis

ment of the software, a geometry conforming to the structure of foot was developed. Model of ankle foot orthosis was then derived from sculpt model by using tools of the software. Different orientations of AFO are depicted below (Fig. 1.6).

1.6 CAE and Shape Optimization

The designed AFO is traditionally produced from polypropylene (PP). Two other materials used for testing are acrylonitrile butadiene styrene (ABS) and poly-lactic acid (PLA). The mechanical properties of these materials are used for the computer-aided engineering of ankle foot orthosis. The properties are shown in Table 1.1 as follows:

Table 1.1 Test material properties

Material	E (MPa)	μ	ρ (kg/mm ³)	UTS (MPa)	YS (MPa)
ABS	2240	0.38	1.06×10^{-6}	29.6	20
Polypropylene	1340	0.392	8.99×10^{-7}	36.5	30.3
Poly-lactic acid	3500	0.36	1.252×10^{-6}	73	70

Finite element analysis of the ankle foot orthosis is conducted on Autodesk Fusion360™. The analysis was conducted for two separate cases of static load and moment applied on AFO for three different materials namely ABS, PLA and PP. ABS and PP properties are imported from Fusion360™ material library. The static load analysis has boundary conditions of fixed posterior section of AFO, where calf bend is situated and load is applied on the third metatarsal. It accounts for the maximum load acting on AFO in entire gait cycle.

Maximum load applied = 4 kg
 Acceleration due to gravity = 9.81 m/s²
 Force = 4 × 9.81 = 39.24 N

Second analysis has boundary conditions of fixed ankle region, while the moment is applied in the plane containing metatarsal and phalanges of foot section. Moment about ankle could be taken as 1.58 times the body weight in Nm [14], taking average human body weight as 62 kg [15]. The maximum moment applied on three different materials was taken as 97.96 Nm.

Stress and displacement of different material AFOs were tested for static load and moment applied. CAE helped in finding the results, which are graphed as below.

Based on the above-mentioned loading conditions, shape optimization work of ankle foot orthosis has been conducted. Boundary conditions included constraint of posterior face. Load was distributed normally on the sole section. Conformity of shape after load application and rigidity were taken as the optimization parameters. Cloud-based analysis displayed the critical section and target value. Target value is the value up to which reduction in material would not cost significant strength of the product (Figs. 1.7, 1.8, 1.9, 1.10, 1.11 and 1.12).

Fig. 1.7 Stress in static loading

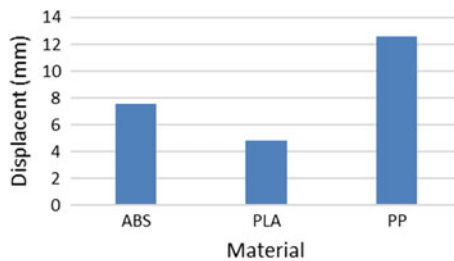
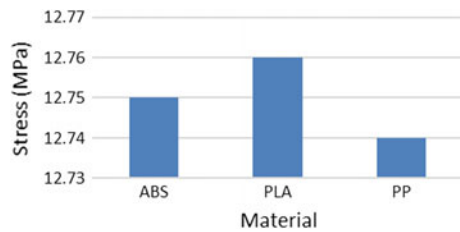


Fig. 1.8 Displacement in static loading

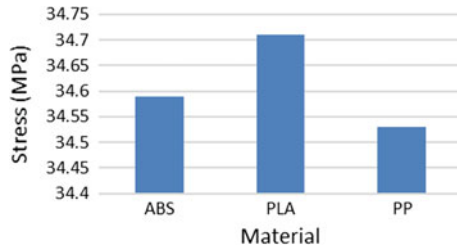


Fig. 1.9 Stress in moment loading

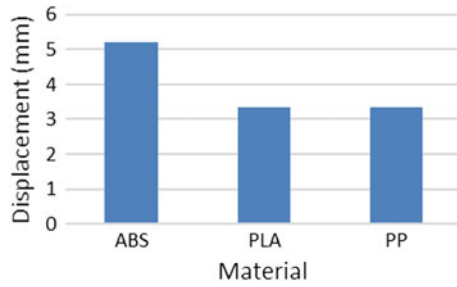


Fig. 1.10 Displacement in moment loading

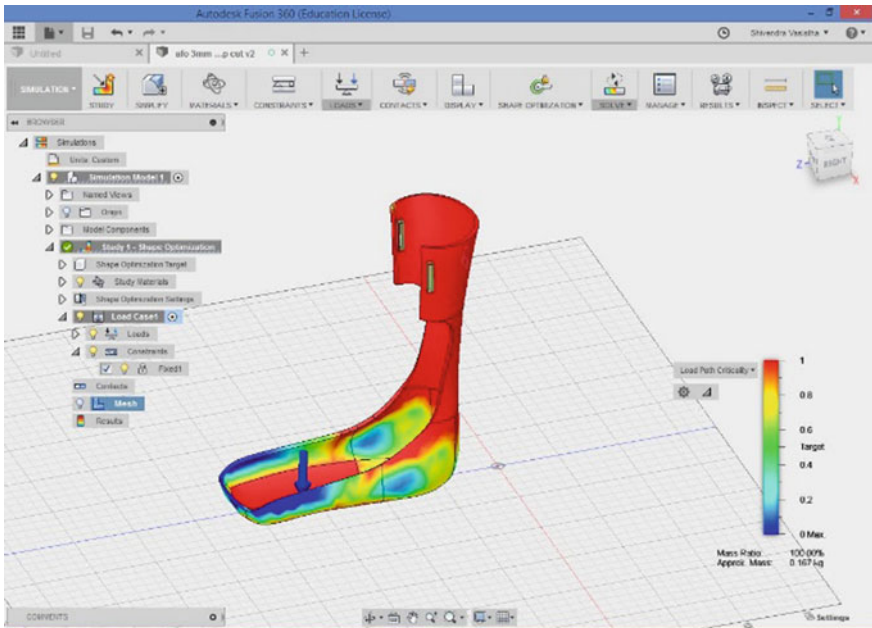


Fig. 1.11 Test results of shape optimization

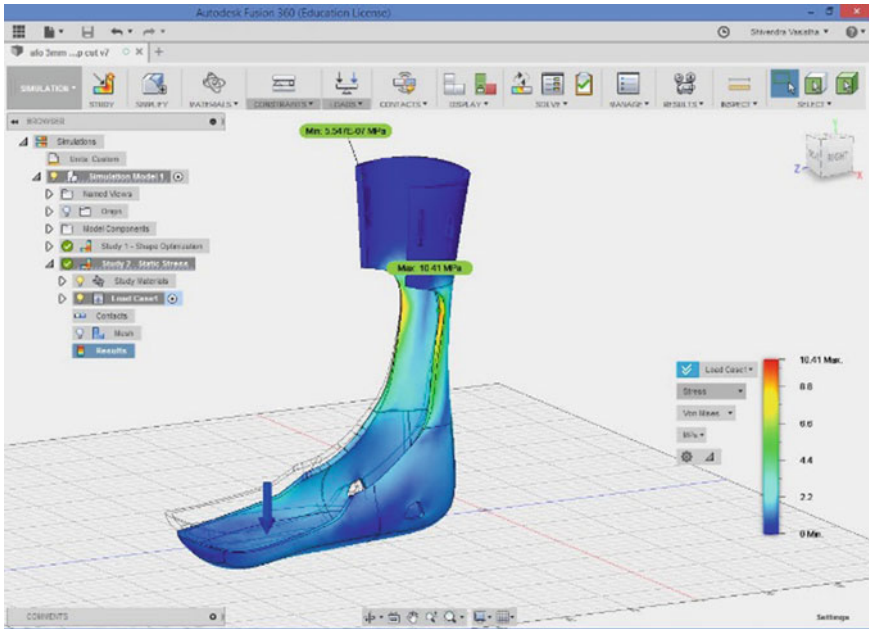


Fig. 1.12 Shape-optimized AFO

1.7 Results and Discussions

The stresses generated in AFOs of ABS, PLA and PP for static load were found to be approximately near to each other. In case of displacement, PP showed the highest value of 12.57 mm, while was found to show minimum displacement of 4.84 mm. It implies that PLA-based AFO shows lesser deflection when subjected to similar loading condition.

Stresses generated in AFOs for moment loading showed that the stresses produced in ABS, PLA and PP were similar as per the analysed results. ABS-based AFO was the most deflected one under moment loading condition with the value of 5.227. PLA- and PP-based AFO were approximately closed in displacement value. In this analysis, both ABS- and PP-based AFOs failed to the maximum moment of 97.96 Nm.

Shape optimization result displayed the critical area cross section of AFO. Optimization of AFO resulted in increase in safety factor, higher strength and lesser displacement when compared to non-optimized AFO.

Production of AFO with the help of fused deposition modelling can be performed for above-discussed model and materials. Clinical trial of physical prototype would help in concluding the entire cycle of AFO production.

Acknowledgements This part of work is financially supported by Autodesk India Pvt. Ltd.

References

1. Ayyappa, E.: Normal human locomotion. *J. Prosthet. Orthot.* **9**, 10–17 (1997)
2. Stout, J., Tervo, R., Gorton, G.S.: Comparison of skill difficulty for typically developing children and those with gait impairment using the Gillette Functional Assessment Questionnaire. *Dev. Med. Child Neurol.* **54**, 27–28 (2012)
3. Karimi, M.T., Mostamand, J., Fatoye, F.: The use of motion analysis system and orthosis in patients with neuro-musculoskeletal disorders. *J. Mech. Med. Biol.* **14**(02), 1450028 (2014)
4. ARCIndustry.: Global orthotic devices market analysis and forecast, p. 16 (2014)
5. Showers, D.C., Strunck, M.L.: Sheet plastics and their applications in orthotics and prosthetics. *Orthot. Prosthet.* **38**(4), 41–48 (1985)
6. Mavroidis, C., et al.: Patient specific ankle-foot orthoses using rapid prototyping. *J. Neuroeng. Rehabil.* **8**(1), 1 (2011)
7. Jin, Y., He, Y., Shih, A.: Process planning for the fuse deposition modeling of ankle-foot-orthoses. *Procedia CIRP* **42**, 760–765 (2016)
8. Faustini, M.C., Neptune, R.R., Crawford, R.H., Stanhope, S.J.: Manufacture of passive dynamic ankle-foot orthoses using selective laser sintering. *IEEE Trans. Biomed. Eng.* **55**(2), 784–790 (2008)
9. Alam, M., Choudhury, I.A., Mamat, A.B., Hussain, S.: Computer aided design and fabrication of a custom articulated ankle foot orthosis. *J. Mech. Med. Biol.* **15**(04), 1550058 (2015)
10. Shih, A., Park, D.W., Yang, Y.Y., Chisena, R., Wu, D.: Cloud-based design and additive manufacturing of custom orthoses. *Procedia CIRP* **63**, 156–160 (2017)
11. Major, R.E., Hewart, P.J., Macdonald, A.M.: A new structural concept in moulded. *Prosthet. Orthot. Int.* **28**, 44–48 (2004)
12. Kobayashi, T., Leung, A.K.L., Akazawa, Y., Naito, H., Tanaka, M., Hutchins, S.W.: Design of an automated device to measure sagittal plane stiffness of an articulated ankle-foot orthosis. *Prosthet. Orthot. Int.* **34**(4), 439–448 (2010)
13. Yamamoto, S., Ebina, M., Iwasaki, M., Kubo, S., Kawai, H., Hayashi, T.: Comparative study of mechanical characteristics of plastic AFO's. *JPO J. Prosthet. Orthot.* **5**(2), 59 (1993)
14. Farah, S., Anderson, D.G., Langer, R.: Physical and mechanical properties of PLA, and their functions in widespread applications—a comprehensive review. *Adv. Drug Deliv. Rev.* **107**, 367–392 (2016)
15. Walpole, S.C., Prieto-Merino, D., Edwards, P., Cleland, J., Stevens, G., Roberts, I.: The weight of nations: an estimation of adult human biomass. *BMC Public Health* **12**(1), 1 (2012)

Chapter 2

Friction Stir Welding of Three-Dimensional Printed Polymer Composites with Semi-consumable Tool



Ranjivay Kumar , Rupinder Singh  and Inderpreet Singh Ahuja 

Abstract For practical applicability of friction stir welding (FSW) in repair/assembly of thermoplastics, it is required to have compatibility between two dissimilar polymers (from mechanical, morphological, chemical, and thermal view point). This study highlights that reinforcement of 15% Al powder in ABS (as ABS-15Al) and 50% to PA6 (as PA6-50Al) resulted in similar melt flow index (MFI) range of 11.57 g/10 min and 11.97 g/10, which further confirmed the enhanced material compatibility with possibility of FSW. The processing of polymer composite on twin-screw extrusion (TSE) process followed by substrate preparation on fused deposition modeling (FDM) as digital manufacturing tool has been used in the present study (to prepare functional prototypes for FSW on milling setup). The output parameters such as grain size number on stirred zone, break load, break strength, and Young's modulus of welded joints have been investigated.

Keywords Digital manufacturing · Melt flow properties · Friction stir welding · Milling

2.1 Introduction

FSW is one of the advance techniques for joining/welding of thermoplastics and thermoplastic composite materials. Some studies have reported that FSW for sheets of same materials such as high-density polyethylene (HDPE), polypropylene (PP), acrylonitrile butadiene styrene (ABS), and nylon 6 was feasible and resulted in comparable mechanical strength to the parent materials, processed with conventional experimental setups [1–4]. But at the similar condition, FSW of two dissimilar thermoplastic materials such as ABS-HDPE, poly (methyl methacrylate)

R. Kumar · R. Singh (✉)

Department of Production Engineering, Guru Nanak Dev Engineering College, Ludhiana 141006, India

e-mail: rupindersingh78@yahoo.com

I. S. Ahuja

Department of Mechanical Engineering, Punjabi University, Patiala 147 002, India

© Springer Nature Singapore Pte Ltd. 2020

M. S. Shunmugam and M. Kanthababu (eds.), *Advances in Additive Manufacturing and Joining*, Lecture Notes on Multidisciplinary Industrial Engineering,

https://doi.org/10.1007/978-981-32-9433-2_2

(PMMA)-PMMA/silica, HDPE-Al alloy, ABS-PMMA, and HDPE-PP required the strong materials attentions such as material flow, heat generations, controlled melting during process, and optimum machining inputs [5–9]. Performing welding of two dissimilar polymeric materials requires special attentions because of differences in the material properties such as glass transition temperature, melting point, molecular weight, and carbon chain structure. Some studies suggested that silica nanocomposite reinforced PMMA sheets proposed elastic particle–particle interaction between the polymeric sheets when welded by friction spot welding [10]. The volumetric flow generally generates on thermo-mechanical heat affect zone which is the main criteria for determining final quality of the welds. Those pores can be controlled by controlling thermal degradation of the materials during processing phase [11]. Controlled heat generation mechanism can be achieved by shoulder design. It was observed in Al alloy sheet joining that heat produced on the top of the AA6082T6 sheets has soften the thermoplastic material which later provided the back-extrusion through the pre-drilled hole to assure the joining [12]. FSW for PMMA sheets has resulted in an interesting fact that during welding of metals, both shoulder and pin driven the material volume in thermo-mechanical heat-affected zone, whereas in case of polymers, only pin drives the material volume in thermo-mechanical heat-affected zone [13]. Heating the plastic material during the FSW process may be one of the alternative property improvement techniques which can make robust product. A 3-mm-thick polyethylene (PE) sample was driven by heated step pin tool, resulted in the improved welding product as prospect of mechanical strength [14]. Mechanical sustainability of the joints is highly dominated by the role of tool geometry and configuration. The FSW conducted for polypropylene and PE, the optimum pin geometry, resulted in the tensile strength 98% to the polyethylene as well as elongation and hardness greater than the base material [9]. Some researchers highlighted that mechanical, thermal, rheological, morphological, and thermo-chemical properties of the weld are largely affected by design of shoulder and pin, so for performing successful FSW operations, one should have proper design of shoulder and pin [15–18]. As most of the studies have been focused on similar material joining, but dissimilar material need to be made compatible for possible joining/welding application. Three-dimensional printers have revolutionized the digital manufacturing of functional as well as non-functional prototypes made up from polymer composites for high-precision, defect-less parts (which fits from mechanical, morphological, tribological, chemical, and thermal aspects) [4–7]. In the present study, processing of polymer composite on TSE followed by substrate preparation on FDM as digital manufacturing tool has been used (to prepare functional prototypes for FSW on milling setup). The output parameters such as grain size number (on stirred zone), break load, break strength, and Young's modulus of joint prepared have also been investigated.

2.2 Experimentation

Initially, pilot experiments were conducted for FSW (at 1200 rpm, 30 mm/min with pin diameter 7 mm) of 3D printed ABS and PA6 sheets result in weak joint (visual observations) which were failed by applying very small quantity of load. From this pilot test, it has been ascertained that ABS and PA6 are from two different class of polymers with poor welding/joining compatibility and needs some reinforcement (may be metallic/nonmetallic) material for successful welding/joining.

2.2.1 Materials and Methods

As per reported literature, ABS and PA6 have dissimilar material properties based upon their mechanical, chemical, metallurgical, and thermal behavior [6, 7]. These thermoplastic materials have significant difference in their MFI (g/10 min), specific heat capacity, chemical resistivity, melting point, and mechanical strength. The mechanical, rheological, and thermal properties of extruded filaments of virgin ABS and virgin PA6 polymers (selected for present study) are shown in Table 2.1.

FSW with the use of the semi-consumable tool (Al reinforced PA6) of shoulderless design has been selected for the present study to join sheets of substrate (Al reinforced ABS). The present method with the use of semi-consumable tool has numerous applications for repair/maintenance of cracks generated in the polymeric pipelines (see Fig. 2.1).

Table 2.1 Properties of virgin ABS and PA6 filament

Materials	MFI (g/10 min)	Melting point (°C)	Break load (N)	Break strength (MPa)	Young's modulus (MPa)
ABS	8.78	201.14	59.21	23.4	55.30
PA6	23.29	219.32	203.1	94.9	35.41

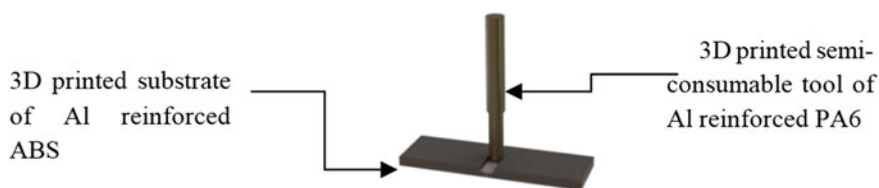


Fig. 2.1 Proposed FSW for joining 3D printed parts

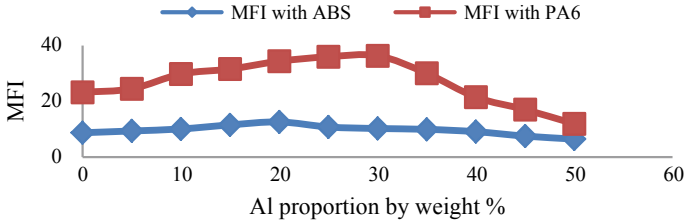


Fig. 2.2 MFI characterization of ABS and PA6 with Al powder

2.2.2 MFI

During pilot experimentation, it has been observed that joining of ABS and PA6 resulted in weak joints (may be because of dissimilar flow properties, as MFI of ABS is 8.78 g/10 min and PA6 having 23.29/10 min). Based upon those observations, a set of experiments have been conducted to evaluate the MFI of Al powder reinforced ABS and PA6. It was observed that ABS and PA6 matrix resulted in similar MFI as reinforcing 15% Al powder to ABS matrix (ABS-15Al) (11.57 g/10 min) and 50% Al powder to PA6 matrix (PA6-50AL) (11.97 g/10 min) (see Fig. 2.2).

2.2.3 DSC Analysis

The differential scanning calorimeter (DSC) under 50 mL/min N₂ gas flow with heating and cooling rate of 10 °C/min in two repeated cycles have been conducted for ABS, PA6, ABS-15Al and PA6-50Al. The first cycle of heating and cooling has been neglected with prospect of re-moving thermal history of samples, and second cycles have been considered to be the final results. It was observed that ABS-15Al and PA6-50Al came under the similar range of melting points as 201.12 and 219.35 °C, respectively (Fig. 2.3). It can be ascertained that by making MFI in a particular range, one can maintain similar melting range (as observed in the present case).

2.2.4 TSE

TSE process with the intermeshing with co-rotating twin screws has been used to prepare the feedstock filaments of 1.75 ± 0.05 mm diameter for FDM 3D printer. As per the dimensional accuracy achieved for feedstock filaments by pilot experimentation of Al reinforced polymers, the input process variables has been selected as rotational speed (rpm), applied load (Kg), and extrusion temperature (°C). For ABS-15Al, extrusion temperature of 220 °C, 30 rpm, and 20 kg load and, for PA6-50Al, extrusion temperature of 245 °C, 20 rpm, and 15 kg applied load have been selected.

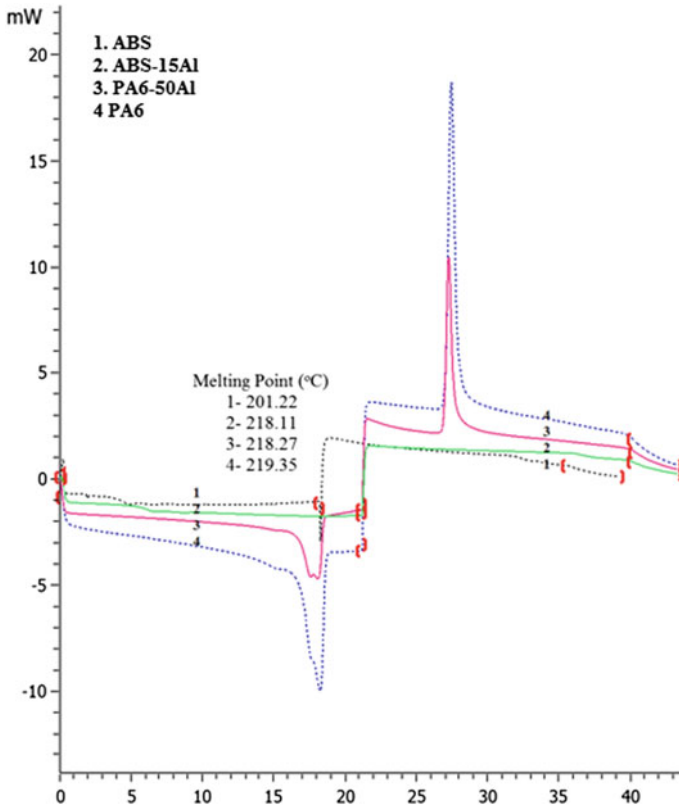


Fig. 2.3 DSC results of ABS, ABS-15Al, PA6, and PA6-50Al

2.2.5 FDM (3D Printing)

The .STL files of 3D geometry (dimensions: 50 × 30 × 3 mm) on the solid works were prepared and loaded to the processing unit of FDM for part printing. The settings of FDM printer were fixed as follows: infill density of 0.8, 06 number of perimeter, deposition angle of 60o, nozzle diameter of 0.3 mm, filament diameter of 1.75 mm, honeycomb fill pattern, perimeter speed of 30 mm/s, infill speed of 60 mm/s, travel speed of 130 mm/s, extruder temperature of 250 °C, and bed temperature of 55 °C. Rectangular sheets were prepared with ABS-15Al, whereas PA6-50Al was used to fabricate the pin profile under these same processing conditions (see Fig. 2.4).

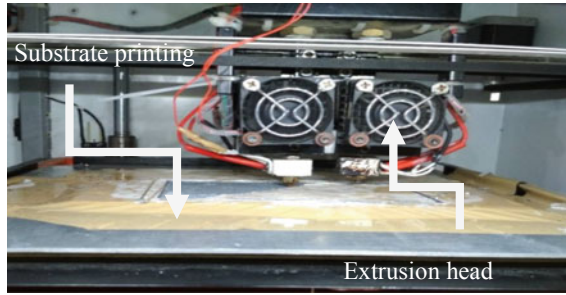


Fig. 2.4 3D printing of parts by FDM process

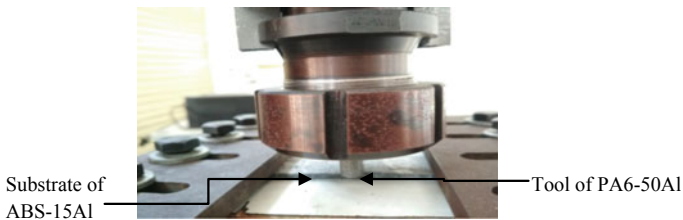


Fig. 2.5 Experimental view of FSW process

2.2.6 FSW Process

The FSW process with use of a 3D printed shoulder-less consumable pin of PA6-50Al was put to join the sheets of ABS-15Al. A vertical milling setup integrated with automated control of rotational speed and transverse speed has been selected. Figure 2.5 shows the 3D view of FSW setup.

Considering the design of experimentations based upon Taguchi L9 orthogonal array, a set of experimentation has been taken for final study of FSW as shown in Table 2.2 by considering the input process variables as rotational speed (rpm), transverse speed (mm/min), and pin diameter in mm.

2.3 Results and Discussion

It has been observed that FSW of ABS-15Al by using semi-consumable tool of PA6-50Al resulted in sound welding joints. Ultimate tensile machine (UTM) with ASTM D638 has been used to evaluate the joints' characteristics such as break load, break strength, and Young's modulus, whereas ASTM E2015-04 (2014) has been used to evaluate the microstructural grain size number at stirred zone. The evaluated properties of joints are shown in Table 2.3.

Table 2.2 Design matrix

S. No.	Rotational speed (rpm)	Transverse speed (mm/min)	Diameter of pin (mm)
1	1000	30	7
2	1000	40	8
3	1000	50	9
4	1200	30	8
5	1200	40	9
6	1200	50	7
7	1400	30	9
8	1400	40	7
9	1400	50	8

Table 2.3 Mechanical properties of the joints

Exp. No.	Break load (N)	Break strength (MPa)	Young's modulus (MPa)	Grain size number on stirred zone
1	3.07	2.55	3.79	3.50
2	6.82	5.71	6.93	3.75
3	2.26	1.88	2.45	3.50
4	9.31	7.59	19.74	1.50
5	11.17	9.31	20.01	1.75
6	8.17	6.81	18.77	3.00
7	4.49	3.65	9.27	1.25
8	7.33	6.11	10.39	1.75
9	3.90	3.18	6.32	1.75

Signal-to-noise ratio (SNR) determines the accuracy and effect of input variables of the process. SNR of the properties can be desired 'smaller is better' or 'larger is better' depending upon nature of the properties. For the properties desired 'larger is better,' SNR can be expressed as follows:

$$\eta = -10 \log \left[\frac{1}{n} \sum_{k=1}^n \frac{1}{y^2} \right]$$

For properties which desired 'smaller is better,' SN ratios can be calculated as follows:

$$\eta = -10 \log \left[\frac{1}{n} \sum_{k=1}^n y^2 \right]$$

where η is SN ratio, n is the number of experiment, and y is the material properties at experiment no. k . Based upon Table 2.3, SNR of break load, break strength, Young’s modulus (selected for larger is better case), and grain size number at stirred zone (selected for smaller is better case) have been calculated (see Table 2.4).

As per calculations made to evaluate SNR for different mechanical and metallurgical properties, the main effect plots for all the properties have been drawn with help of Minitab software to see contributing input variables. Figure 2.6a–d shows the linear model for SNR of different properties (a: break load, b: break strength, c: Young’s modulus, and d: grain size number on stirred zone). It has been observed that 1200 rpm, 40 mm/min transverse speed, and 8 mm pin diameter are the best settings for mechanical properties (break load, break strength, and grain size number at stirred zone), whereas 1400 rpm, 30 mm/min transverse speed, and 9 mm pin diameter are the best settings for change in grain size number at stirred zone (see Fig. 2.6). Further based upon Table 2.3, ANOVA was performed for all mechanical properties. For break load, ANOVA resulted in P value of 0.048 for input parameter as rotational speed. This means the rotational speed is the significant factor under 95% confidence limits. Transverse speed is the second most desired input parameter and pin diameter contributed least (see Table 2.5) for changes in SNR of break load. Based upon Table 2.5, response ranking has been made (see Table 2.6), which highlights that rotational speed was ranked 1, transverse speed was ranked 2, and pin diameter was ranked 3 for changes in the SNR of break load.

The optimum value of the break load can be predicted from the given Eq. (1). The optimum value can be predicted from combination of input variables suggested in Fig. 2.6 (for break load as 1200 rpm, 40 mm/min transverse speed, and 8 mm pin diameter).

$$\eta_{opt} = m + (mA2 - m) + (mB2 - m) + (mC2 - m) \tag{1}$$

Table 2.4 SNR of evaluated properties

Exp No.	SNR (break load)	SNR (break strength)	SNR (Young’s modulus)	SNR (grain size number on stirred zone)
1	9.74	8.13	11.57	−10.88
2	16.67	15.13	16.81	−11.48
3	7.08	5.48	7.78	−10.88
4	19.37	17.60	25.90	−3.52
5	20.96	19.37	26.02	−4.86
6	18.24	16.66	25.46	−9.54
7	13.04	11.24	19.34	−1.93
8	17.30	15.72	20.33	−4.86
9	11.82	10.04	16.01	−4.86

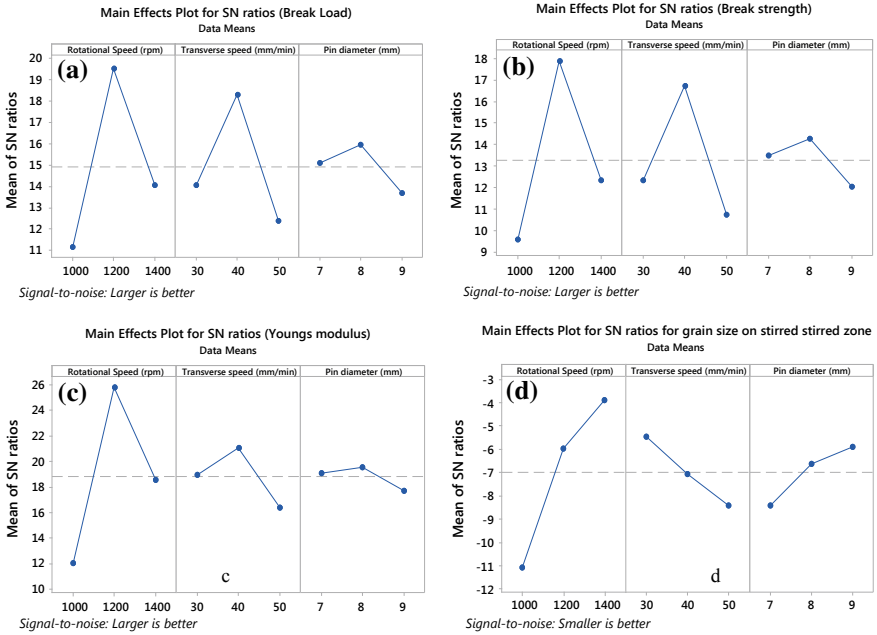


Fig. 2.6 Linear model of SNR for joints' properties

Table 2.5 ANOVA for SN ratios for break load

Source	DF	Seq SS	Adj SS	Adj MS	F	P
Rotational speed (rpm)	2	108.20	108.20	54.1	19.96	0.048
Transverse speed (mm/min)	2	56.09	56.09	28.04	10.35	0.088
Pin diameter (mm)	2	7.82	7.82	3.912	1.44	0.409
Residual error	2	5.42	5.42	2.71		
Total	8	177.53				

Table 2.6 Response table for signal-to-noise ratios (larger is better) for break load

Level	Rotational speed (rpm)	Transverse speed (mm/min)	Pin diameter (mm)
1	11.17	14.06	15.10
2	19.53	18.31	15.96
3	14.06	12.38	13.70
Delta	8.36	5.93	2.26
Rank	1	2	3

where ‘*m*’ is the overall mean of SN ratio, *mA2* is the mean of SN ratio for rotational speed at level 2 (1200 rpm), *mB2* is the mean of SN ratio for transverse speed at level 2 (40 mm/min), and *mC2* is the mean of SN data for pin diameter at level 2 (8 mm).

If the desired output properties are of ‘maximum is better’ nature (e.g., break load, break strength, young’s modulus), then

$$y_{opt2} = (1/10)\eta_{opt}/10 \tag{2}$$

If the desired output properties are of ‘minimum is better’ nature (e.g., porosity, grain size number, residual stress), then

$$y_{opt2} = (10)\eta_{opt}/10 \tag{3}$$

From here, calculations can be made as follows: Overall mean of SN ratio (*m*) is the average of the SNR provided in Table 2.4.

m = 14.92 dB (See Table 2.4). From the response (Table 2.5), it is given as *mA2* = 19.53, *mB2* = 18.31, *mC2* = 15.96. Considering the Eq. (2),

$$\eta_{opt} = 14.92 + (19.53 - 14.92) + (18.31 - 14.92) + (15.96 - 14.92) \eta_{opt} = 23.96 \text{ dB}$$

Inserting the value of η_{opt} in Eq. (3),

$$y_{opt2} = (10)\eta_{opt}/10$$

$$y_{opt2} = (10)24.90/10$$

$$y_{opt} = 15.77 \text{ N}$$

The predicted optimum value for break load = 15.77 N. It is predicted from here that by considering the parametric combination of 1200 rpm rotational speed, 40 mm/min transverse speed, and 8 mm pin diameter, the break load value will be 15.77 N. The confirmatory experimentation has been performed on the desired setting, and it resulted in break load of 15.56 N. Similarly, for break strength, Young’s modulus, and grain size number on stirred zone, the values at optimum setting have been evaluated and experimentation were performed to get actual values (see Table 2.7).

Here, it should be noted that maximum value of break load, break strength, and Young’s modulus is obtained at experiment no. 5 and minimum at experiment no. 3 (see Table 2.3). A set of load vs. deflection curves have been merged for all the nine experiments, and it is denoted that maximum values of load achieved for experiment no. 5 and minimum for experiment no. 3 (see Fig. 2.7).

Table 2.7 Predicted versus actual value of properties under suggested setup

Properties	Break load (N)	Break strength (MPa)	Young’s modulus (MPa)	Grain size number on stirred zone
Predicted/actual	15.77/15.56	13.09/13.21	27.67/27.25	1.15/1.0

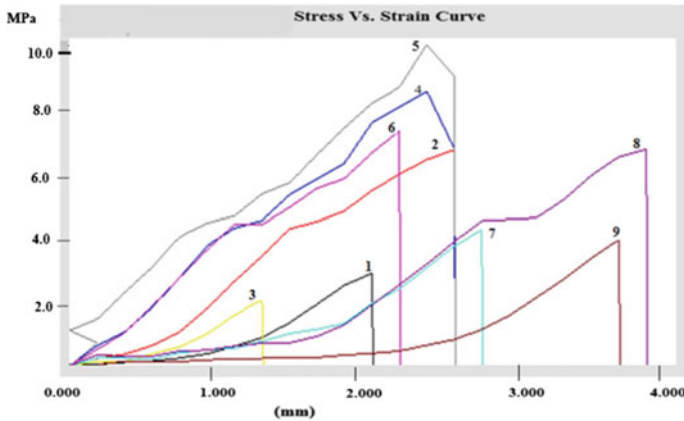


Fig. 2.7 Load versus deflection curves of welded pieces by tensile failure

The photomicrographs (under 100× magnification) obtained for experiment no. 5 and experiment no. 3 clearly show the mixing and distribution on stirred zones (see Fig. 2.8). The joints at experiment no. 3 observed as less stirred with more defective surface as compared to experiment no. 5. The proper mixing at experiment no. 5 in stirred zone strongly confirms the attainment of larger strength as compared to welded piece at experiment no. 3.

SNR for all output parameters as per Table 2.4 has been maximized for multifactor optimization. The main effect plot for SNR of combined properties suggested that 1200 rpm rotational speed; 40 mm/min transverse speed; and 8 mm pin diameter are the best settings to get the optimum properties (see Fig. 2.9).

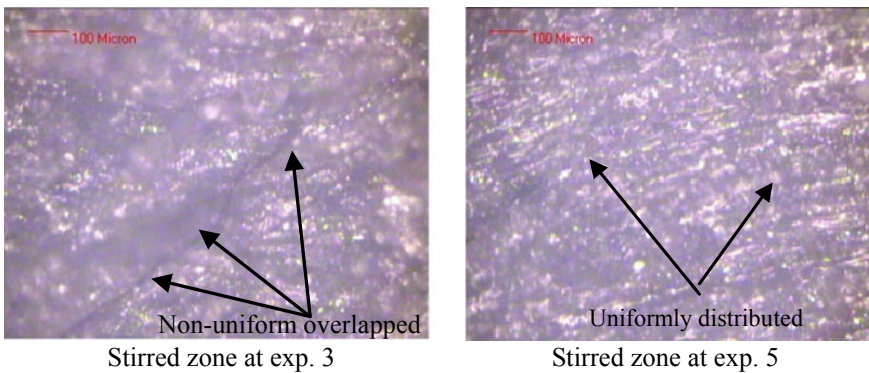


Fig. 2.8 Photomicrographs of welded joints on stirred region

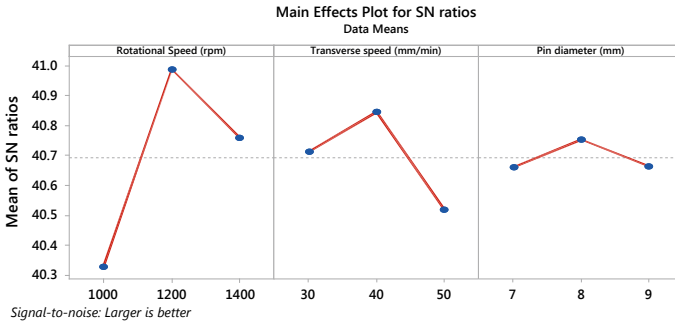


Fig. 2.9 Best settings of input parameters for multifactor optimization

2.4 Conclusions

The joining of 3D printed two virgin ABS sheets by using 3D printed virgin PA6 pin resulted in weak joints. Hence, it is strongly recommended to establish the similar properties (mechanical/thermal/rheological, etc.) of two dissimilar polymers for welding/joining applications. The deposition of PA6 material as filler was not observed.

Reinforcement of Al metal powder to ABS matrix at 15% by weight and 50% by weight in PA6 matrix resulted in the similar MFI of 11.57 g/10 min and 11.97 g/10 min. FSW performed on 3D printed parts of such polymeric composite (based upon similar MFI) resulted in the feasible welding and consumption of tool material (as filler) was observed.

Optimization of input process variable suggested that mechanical properties (break load, break strength, and Young's modulus) would be better at 1200 rpm, 40 mm/min transverse speed, and 8 mm pin diameter, whereas grain size number would be achieved minimum at 1400 rpm, 30 mm/min transverse speed, and 9 mm pin diameter.

At optimized setting of input variable, it was observed that joints sustained break strength of 56.45% to virgin ABS and 13.91% to virgin PA6. Young's modulus of joints observed 49.28% to ABS, whereas 77.21% to PA6.

Acknowledgements The authors are highly thankful to BRNS No: 34/14/10/2016-BRNS/34036 for providing financial assistance.

References

1. Panneerselvam, K., Lenin, K.: Joining of nylon 6 plate by friction stir welding process using threaded pin profile. *Mater. Des.* **53**, 302–307 (2014)
2. Azarsa, E., Mostafapour, A.: Experimental investigation on flexural behavior of friction stir welded high density polyethylene sheets. *J. Manuf. Process.* **16**(1), 149–155 (2014)

3. Sadeghian, N., Givi, M.K.B.: Experimental optimization of the mechanical properties of friction stir welded Acrylonitrile Butadiene Styrene sheets. *Mater. Des.* **67**, 145–153 (2015)
4. Kumar, R., Singh, R., Ahuja, I.P.S., Penna, R., Feo, L.: Weldability of thermoplastic materials for friction stir welding—a state of art review and future applications. *Compos. Part B: Eng.* **137**, 1–15 (2017)
5. Kumar, R., Singh, R., Ahuja, I.P.S., Amendola, A., Penna, R.: Friction welding for the manufacturing of PA6 and ABS structures reinforced with Fe particles. *Compos. B Eng.* **132**, 244–257 (2018)
6. Kumar, R., Singh, R., Ahuja, I.P.S.: Investigations of mechanical, thermal and morphological properties of FDM fabricated parts for friction welding applications. *Measurement* **120**, 11–20 (2018)
7. Singh, R., Kumar, R., Feo, L., Fraternali, F.: Friction welding of dissimilar plastic/polymer materials with metal powder reinforcement for engineering applications. *Compos. B Eng.* **101**, 77–86 (2016)
8. Liu, Z.Y., Xiao, B.L., Wang, W.G., Ma, Z.Y.: Singly dispersed carbon nanotube/aluminum composites fabricated by powder metallurgy combined with friction stir processing. *Carbon* **50**(5), 1843–1852 (2012)
9. Hajideh, M.R., Farahani, M., Alavi, S.A.D., Ramezani, N.M.: Investigation on the effects of tool geometry on the microstructure and the mechanical properties of dissimilar friction stir welded polyethylene and polypropylene sheets. *J. Manuf. Process.* **26**, 269–279 (2017)
10. Junior, W.S., Emmmler, T., Abetz, C., Handge, U.A., dos Santos, J.F., Amancio-Filho, S.T., Abetz, V.: Friction spot welding of PMMA with PMMA/silica and PMMA/silica-g-PMMA nanocomposites functionalized via ATRP. *Polymer* **55**(20), 5146–5159 (2014)
11. Abibe, A.B., Sônego, M., Dos Santos, J.F., Canto, L.B., Amancio-Filho, S.T.: On the feasibility of a friction-based staking joining method for polymer–metal hybrid structures. *Mater. Des.* **92**, 632–642 (2016)
12. Buffa, G., Baffari, D., Campanella, D., Fratini, L.: An innovative friction stir welding based technique to produce dissimilar light alloys to thermoplastic matrix composite joints. *Proced. Manuf.* **5**, 319–331 (2016)
13. Simões, F., Rodrigues, D.M.: Material flow and thermo-mechanical conditions during friction stir welding of polymers: literature review, experimental results and empirical analysis. *Mater. Des.* **59**, 344–351 (2014)
14. Squeo, E.A., Bruno, G., Guglielmotti, A., Quadrini, F.: Friction stir welding of polyethylene sheets. *Anna. Dunarea de Jos University of Galati, Technol. Mach. Build.* **5**, 241–246 (2009)
15. Arora, A., De, A., DebRoy, T.: Toward optimum friction stir welding tool shoulder diameter. *Scripta Mater.* **64**, 9–12 (2011)
16. Rai, R., De, A., Bhadeshia, H.K.D.H., DebRoy, T.: Friction stir welding tools. *Sci. Technol. Weld. Joining* **16**(4), 325–342 (2011)
17. Eslami, S., Ramos, T., Tavares, P.J., Moreira, P.M.G.P.: Shoulder design developments for FSW lap joints of dissimilar polymers. *J. Manuf. Process.* **20**, 15–23 (2015)
18. Mendes, N., Neto, P., Loureiro, A., Moreira, A.P.: Machines and control systems for friction stir welding: a review. *Mater. Des.* **90**, 256–265 (2016)

Chapter 3

Mechanical Characterization and Process Optimization of PolyJet 3D Printing Using Digital ABS with Different Part Geometries



B. N. Sontakke  and B. B. Ahuja 

Abstract Last few decades have seen a rapid growth in additive manufacturing (AM) owing to its adaptability to new manufacturing requirement and trends. In PolyJet technology, a popular method in AM, parts are manufactured by depositing layer upon layer and, simultaneously, each layer is cured using ultraviolet energy. This process exhibits the structured approach of layered manufacturing process which produces state-of-the-art products with superior quality. The process has shown promising technological development in the field of design and manufacturing. This work aims at improving the performance characteristic and process optimization through the application of design of experiment approach. The response parameters viz. the storage modulus, loss modulus, loss factor, glass transition temperature, and surface roughness have been individually assessed. The statistical technique has been used to study the effect of process parameters and their significance. Gray relation grade analysis has been used for process optimization.

Keywords Additive manufacturing · PolyJet · Design of experiment · Dynamic mechanical analyzer · Surface roughness

3.1 Introduction

The manufacturing sector is passing through a phase where technological innovations demand shorter product development and manufacturing time along with faster product availability to market. Subtractive manufacturing has limitations in terms of product size, complexity, material loss, and high cost. These limitations have given a new direction to additive manufacturing, which offers rapid R&D, high complexity, and versatility. AM process basically builds the product by joining layer upon layer of required material and suits regular as well as complex products equally. The physical appearance and mechanical properties of parts manufactured by an

B. N. Sontakke · B. B. Ahuja (✉)

Department of Production Engineering and Industrial Management, College of Engineering Pune, Pune 411005, India

e-mail: director@coep.ac.in

© Springer Nature Singapore Pte Ltd. 2020

M. S. Shunmugam and M. Kanthababu (eds.), *Advances in Additive Manufacturing and Joining*, Lecture Notes on Multidisciplinary Industrial Engineering,

https://doi.org/10.1007/978-981-32-9433-2_3

AM process are mainly characterized by machine parameters and material used. The mechanical properties of parts need to be investigated thoroughly in order to justify the inadvertent use of AM machines.

The past decade has shown a growing interest of researchers in AM processes which helps in significant improvement in mechanical properties, reliability, and repeatability of AM processes [1]. Make to order a customized product which will be the future market scenario can be easily fulfilled by AM processes [2]. Due to the short span between design and manufacturing, this process is also defined as rapid manufacturing [3]. AM machines are available in wide varieties are capable to process different materials and geometries. AM process is making progress to tackle current issues but needs substantial product improvements in terms of quality and cost including the production time [4]. Performance parameters of the AM process need to be competent which require processing simplification and standardization, which in turn attracts manufacturers and customers [5]. Today, industries such as aerospace, automotive, defense, and medical as well as consumer electronics which are producing quite regulated, demand-customized, geometrically, and mechanically stable components. Dimensional and surface topologies are two important aspects that have the substantial impact on the application of AM machines for production. These aspects are largely dependent on the part location of the geometry, on the build tray as well as the quality of the digital material. In-depth experimental investigations need to be carried out considering these aspects of the AM process which enable simplification and standardization [6–8]. Fused deposition modeling (FDM), selective laser sintering (SLS), stereolithography (SLA), and PolyJet technology are the most promising and innovative technological developments which will cater the growing demand for customized make to order situation prevalent in today's engineering market [9].

In this work, additive manufacturing (AM), using PolyJet process shown in Fig. 3.1, has been studied and an attempt has been made to investigate the influence of process parameters on product quality. The Taguchi method which is popular offline quality improvement method and needs a less number of experiments for a detailed analysis of the process has been used in this work. A single objective optimization of individual process parameters using the Taguchi method is proposed herewith for process selection. Process optimization considering all the responses has been carried out using gray relation grade analysis. This study aims at bridging the research gap in the application of AM machines for made to order situation prevalent in current industrial practice.

3.2 Experimental Details

3.2.1 CAD Model and STL File

The different internal structure geometries are shown in Fig. 3.2. CAD models of the

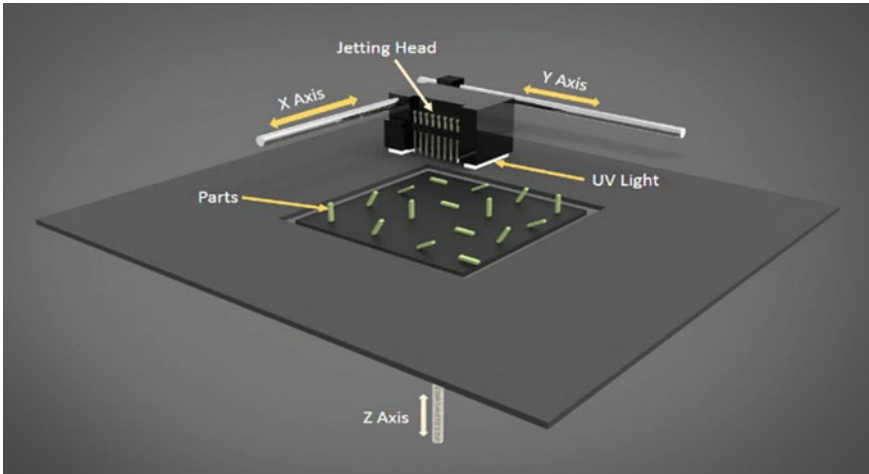


Fig. 3.1 Schematic representation of the PolyJet system

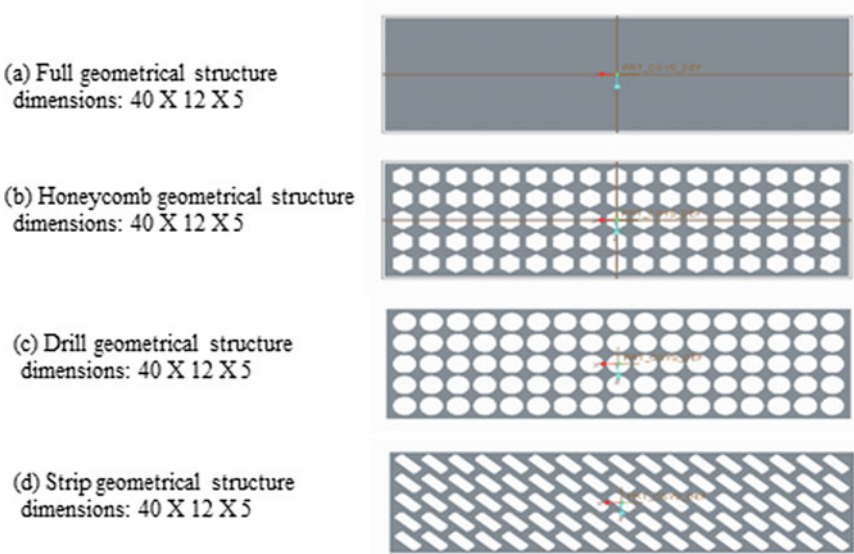


Fig. 3.2 Different internal structures, a full, b honeycomb, c drill, d strip

specimen are created using Creo Parametric 1.0, a popular CAD software (parametric technology corporation, USA). The CAD file is then exported as a standard tessellation language (STL) file. The standard parametric setting in the software (Creo) is used for STL file which are a coordinate system (default), format (ASCII with allowing negative values), and deviation control (chord height 0.1244 and angle control 0.5000).

3.2.2 *Material*

Objet ABS-like digital material (RGD5160-DM) [10] which is composed of Objet RGD515 and Objet RGD535 are used in this work as test material. This material is widely used in the industries as a model material due to its inherent mechanical and thermal properties. Digital ABS is produced inside the PolyJet machine by mixing two liquid resins in equal proportions or as required depending on the properties desired. The support material is required for supporting the model while making and stabilizing subsequent model sections. This material is removed after the completion of a product by pressurizing the water jet. Gel-like photopolymer FullCure 705 has been used in this work as a support material.

3.2.3 *Designs Build Tray Layout*

In PolyJet, AM machine parts are produced by depositing material layer upon layer on the built tray. The build tray area has been optimally designed to hold as many 16 specimens with orientations, different internal structure geometries, support structure, and surface finish. The tray is designed in such a way that the specimen length is oriented along the X -axis, the width along the Y -axis, and thickness parallel to the Z -axis. The tray design is shown in Fig. 3.3.

3.2.4 *Preparation of Test Specimen*

For this work, test specimen having different internal structures (full, honeycomb, drill, and strip) have been designed. The nominal thickness of 5 mm, width 12 mm, and length 40 mm have been used to 3D printed specimens by the PolyJet system according to ASTM specifications for dynamic mechanical properties evaluation as shown in Fig. 3.4. Four internal structures (full, honeycomb, drill, and strip) for test specimens have been used here for experimental investigation.

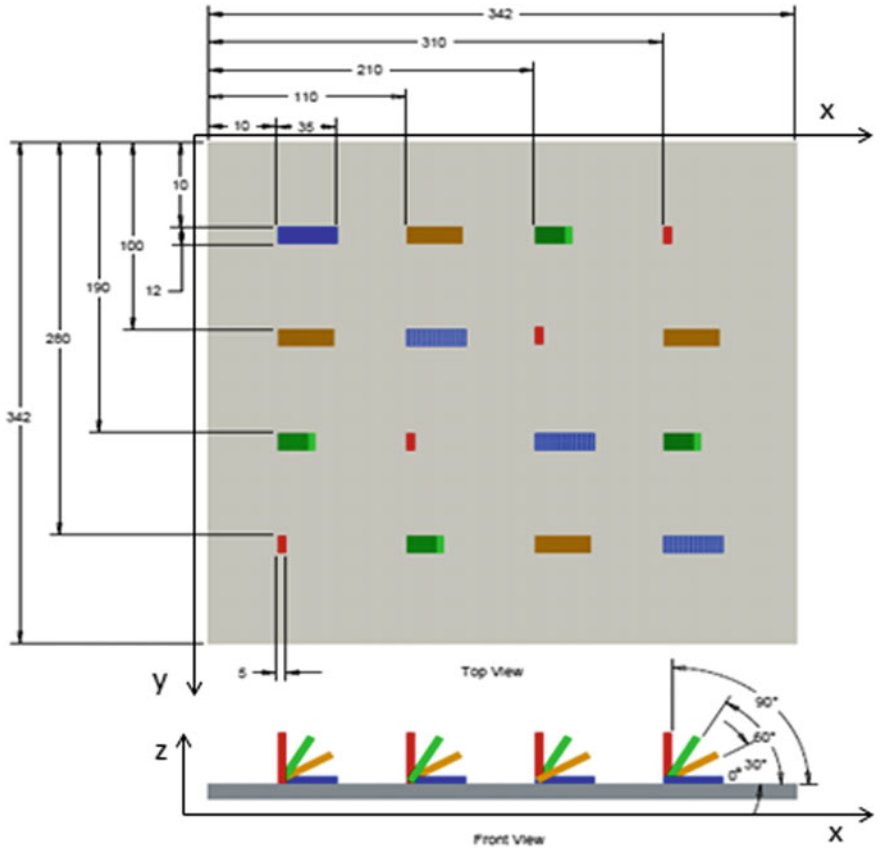


Fig. 3.3 Designs build tray layout

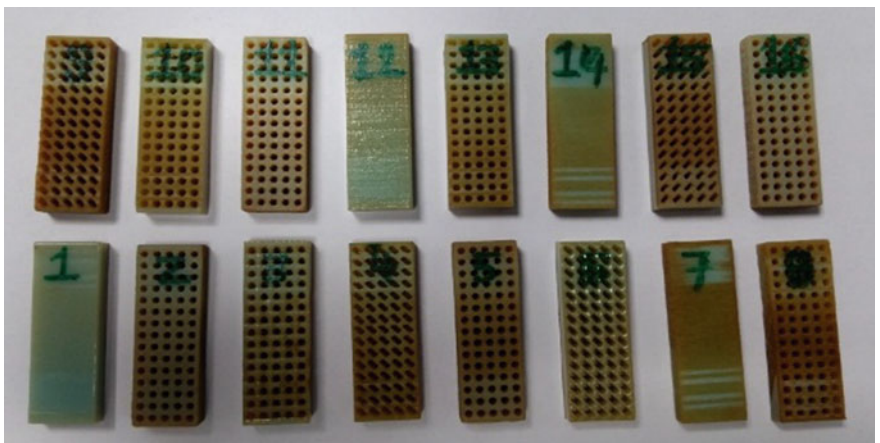


Fig. 3.4 3D printed specimens by the PolyJet system

3.2.5 Experimental Planning: Factors and Levels

Present work explores experimental investigation of PolyJet AM process using Connex 350 machine. Experiments have been carried out using L16 orthogonal mix array, comprising of 2-level arrays and 4-level arrays. The Taguchi method is useful in limiting the number of experiments and the optimal parameter setting. Six control factors have been varied in the present work in order to study their influence on response parameters. Control parameters and their levels are shown in Table 3.1 and explained in subsequent paragraphs. Experimental design and response parameters are shown in Table 3.2.

Part spacing along the X-axis (Δx): In PolyJet, AM process parts are produced by adding very thin layers over layers on the build tray and are a very time-consuming process. In order to utilize the machine effectively, it is recommended to produce multiple parts in a single build tray. The machine has the capability to produce multiple parts simultaneously and thus can be used efficiently, reducing the time consumption per parts considerably. Therefore, part placement on building tray is important to optimally utilize the build tray area to produce the maximum number of parts in a single build tray. The net built tray volume used for this work is $342 \times 342 \times 200$ mm. To select the proper part spacing, it is necessary to consider the size and dimension of parts, its orientation, and avoidance of superposing of the support material of two adjacent parts. Four levels of part spacing are considered for this experiment viz. 10, 110, 210, and 310 mm. With this spacing, four parts shall be manufactured along the X direction.

Part spacing along the Y-axis (Δy): Part spacing along the Y-axis shares the same minimum limit with X spacing. However, the maximum limit could have reached an 80 mm value, since the test part width allowed for a higher spacing than the

Table 3.1 Control parameters and their levels

Symbols	Control parameters	Unit	Levels			
			1	2	3	4
Δx	Part spacing along the X-axis	mm	10	100	190	280
Δy	Part spacing along the Y-axis	mm	10	110	210	310
θ	Orientation of the part within the tray	Degree	0	30	60	90
ISG	Internal structure geometry		Full	Honeycomb	Drill	Strips
SS	Support structure		Heavy	Lite		
SF	Surface finish		Glossy	Matte		

F full; *H* honeycomb; *S* strip; *D* drill; *H* heavy; *L* lite; *G* glossy; *M* matte

Δx part spacing along X-axis; Δy part spacing along Y-axis; θ° part orientation; *ISG* internal structure geometry; *SS* support structure; and *SF* surface finish

Table 3.2 Taguchi mixed level design L16 orthogonal array and measured output responses

Run	Factors					Responses					
	Δx	Δy	θ	ISG	SS	SF	Storage modulus MPa	Loss modulus MPa	Loss factor Tan δ	Glass transition temp. (T _g) °C	Surface roughness (Ra)
1	10	10	0°	F	H	G	634	14	0.0222	112.8	0.279
2	10	110	30°	H	H	M	272	18	0.0667	73.7	10.880
3	10	210	60°	D	L	G	345	17	0.0495	90.8	1.540
4	10	310	90°	S	L	M	188	9	0.0492	86	6.861
5	100	10	30°	D	L	M	254	16	0.0641	74.3	11.667
6	100	110	0°	S	L	G	404	12	0.03	98.5	0.392
7	100	210	90°	F	H	M	516	22	0.0423	93.8	13.700
8	100	310	60°	H	H	G	263	15	0.0583	78.2	3.255
9	190	10	60°	S	H	M	170	11	0.065	75.6	13.645
10	190	110	90°	D	H	G	279	14	0.0504	84.4	0.828
11	190	210	0°	H	L	M	312	17	0.0535	78.9	9.195
12	190	310	30°	F	L	G	610	20	0.0334	98.7	2.171
13	280	10	90°	H	L	G	317	14	0.0432	91.9	1.091
14	280	110	60°	F	L	M	528	24	0.046	97.1	14.098
15	280	210	30°	S	H	G	232	10	0.0446	85.8	1.023
16	280	310	0°	D	H	M	343	15	0.0451	86.8	5.669

previous factor. Nevertheless, the same limits and levels (10, 100, 190, and 280 mm) previously defined in the X direction spacing had been used for convenience.

The orientation of the part within the tray (θ): Due to symmetries involved, the orientation of the part within the tray can be limited for testing purposes between 0° and 90° . Test specimen already has 180° symmetry and, due to manufacturing strategy, possible differences in UV curing between zones of the same part are expected to be distributed in a specular pattern, in parts oriented symmetrically with respect to the YZ plane. According to this consideration, the test specimen rotated 90° is expected to present identical mechanical behavior. Internal structure geometry (ISG): Four types of internal structure geometry (full, honeycomb, drill and strip) are used for this experiment. According to this consideration, test specimens are expected to present different mechanical behavior. The support structure (SS): Three types of a grid are used as the support structure in PolyJet processed parts. The PolyJet technology offers three options for support structure: Standard, heavy, and lite can be related to the strength of the part.

Surface finishes (SF): Finally, the surface finish of PolyJet parts can be related to roughness profile but, in the particular case of flat surfaces parallel to the XY plane, differences in roughness shall be almost negligible. Nevertheless, the PolyJet technology offers two options for the surface finish: glossy and matte. Unsupported surfaces can be manufactured using either option since matte finishing can be obtained by applying a thin coating of support material over a glossy surface. On the other hand, supported surfaces are always matte, since contact between support and construction materials cannot be avoided. It is not clear how this additional coating should affect the mechanical properties of matte surfaces when compared to glossy ones.

3.3 Results and Discussion

3.3.1 Analysis of Storage Modulus

Storage modulus is the elastic property of polymer material. The main effects plot for the SN ratios of storage modulus is shown in Fig. 3.5. The storage modulus is mainly affected by part orientation and internal structure geometry. Storage modulus is found to be decreasing as part orientation varies from 0° to 90° . Storage modulus exhibits maximum value at 0° because of the orientation of part length along the X -axis. Storage modulus found to be on the higher side when the internal structural geometry is set at full structure, whereas storage modulus is least when the internal structural geometry is set at strips structure. ANOVA for storage modulus is carried out and the values obtained of R -sq = 98.36% and R -sq(adj) = 75.35%.

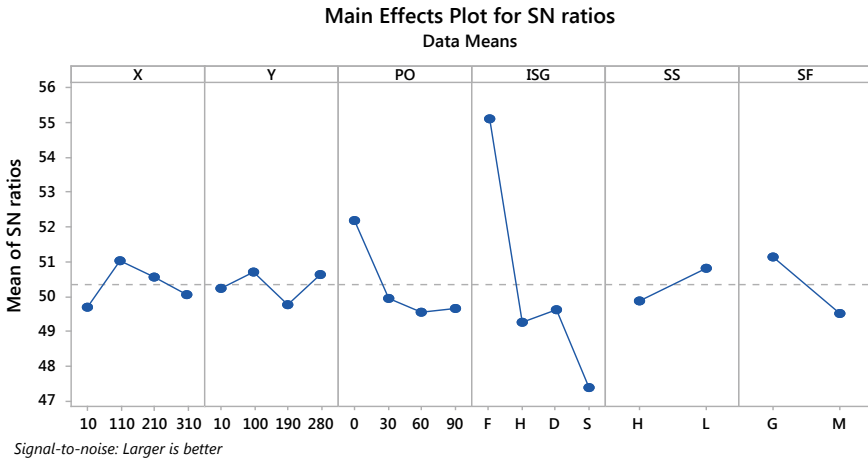


Fig. 3.5 S/N ratio plot for storage modulus

3.3.2 Analysis of Loss Modulus

Loss modulus defines the viscous property of the material. The main effects plot for the SN ratios of the loss modulus is shown in Fig. 3.6. Loss modulus found to be mainly affected by internal structure geometry. It is observed that loss modulus is minimum when the internal structural geometry is set at strips structure. Other variables are found to be the least significance. ANOVA for loss modulus is carried out and the values obtained of $R\text{-sq} = 97.83\%$ and $R\text{-sq(adj)} = 67.52\%$.

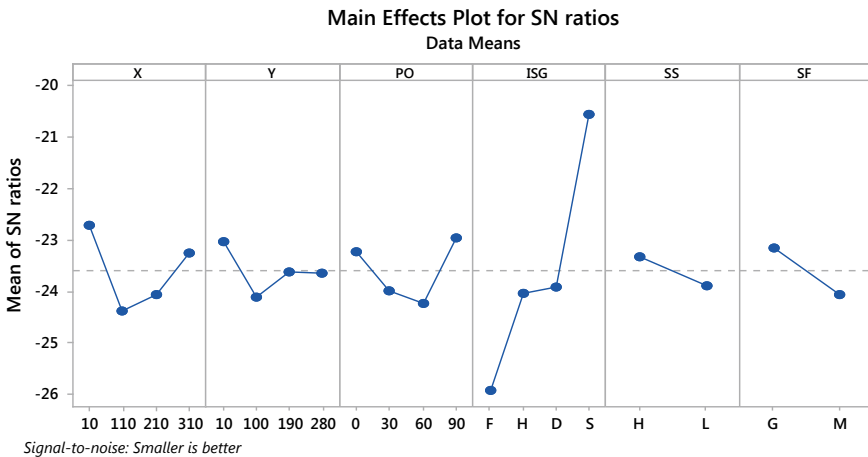


Fig. 3.6 S/N ratio plot for loss modulus

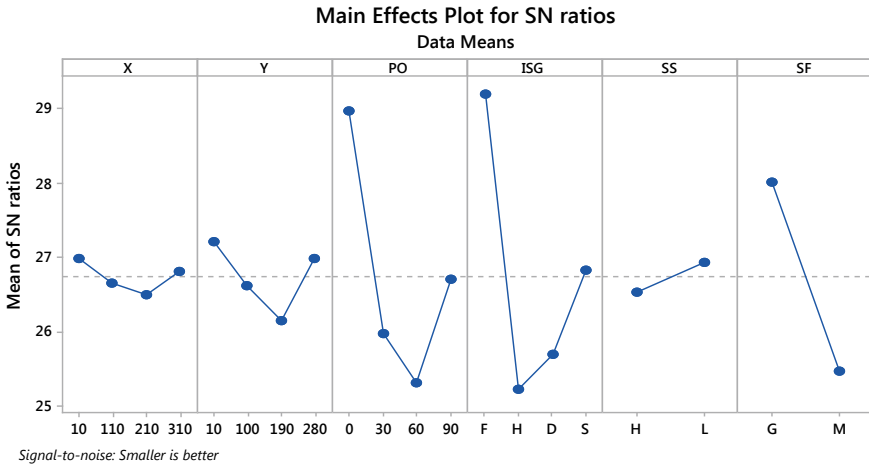


Fig. 3.7 S/N ratio plot for loss factor

3.3.3 Analysis of Loss Factor

Main effects plot for the SN ratios of loss factor is shown in Fig. 3.7. The loss factor is the ratio of the loss modulus to the storage modulus. The loss factor is found to be affected by partial orientation, internal structure geometry, and surface finish. Due to the orientation of part length along the X-axis, loss factor is minimum when part orientation set at 0°, internal structure geometry set at full structure, and surface finish is set on glossy. ANOVA for loss factor is carried out and the values obtained of $R\text{-sq} = 99.54\%$ and $R\text{-sq}(\text{adj}) = 93.08\%$.

3.3.4 Analysis of Glass Transition Temperature

Figure 3.8 shows the main effects plot for the SN ratio of glass transition temperature. The glass transition temperature is one of the most important properties of polymers and is the temperature region where the polymer transitions from a hard, glassy material to a soft, rubbery material. Glass transition temperature is found to be affected by part spacing along the Y-axis, part orientation, internal structure geometry, and surface finish. Part spacing along the Y-axis is an important factor in this study, due to layer deposition method of PolyJet technology. In PolyJet technology, the layer is deposited by nozzles in the raster scan method. Nozzles start depositing layer from origin and moves in X-direction. After completing one travel along the X-axis, it returns to start of deposition and increments in Y direction and deposits material in the same manner till full build tray is covered. It would require more deposition cycles per layer as a result for each layer available curing time is more.

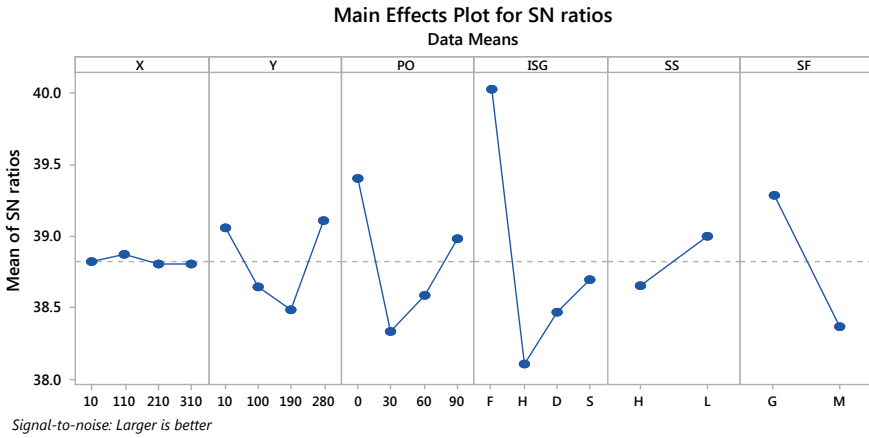


Fig. 3.8 S/N ratio plot for glass transition temperature

ANOVA for glass transition temperature is carried out and the values obtained of $R\text{-sq} = 99.45\%$ and $R\text{-sq(adj)} = 91.79\%$.

3.3.5 Analysis of Surface Roughness

Main effects plot for the SN ratios of surface roughness is shown in Fig. 3.9. Surface roughness is mainly affected by part orientation and surface finish. Surface roughness value of the prepared samples found to be less when a part is orientated at 0° With

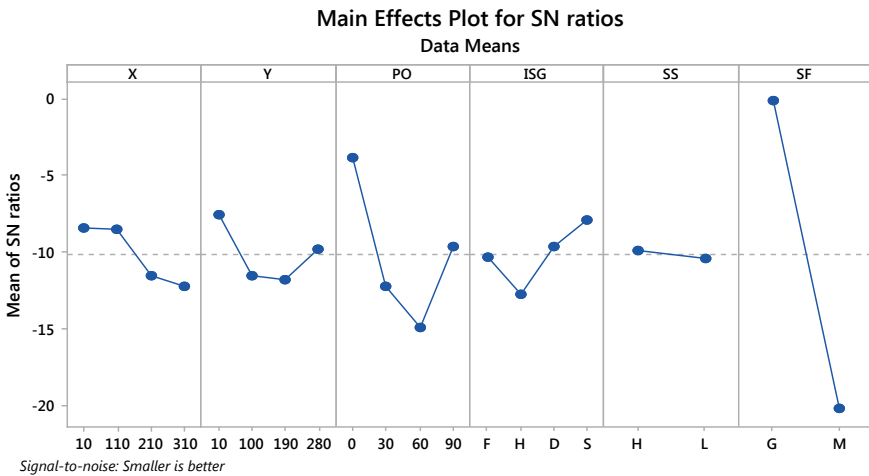


Fig. 3.9 S/N ratio plot for surface roughness

respect to Y -axis and surface finish is glossy. It is found that support material is deposited only in contact with bed lower surface of the sample, while parameters such as glossy mode are selected and the part length is oriented along the X -axis. ANOVA for surface roughness is carried out and the values obtained of R -sq = 99.95% and R -sq(adj) = 99.23%.

3.4 Optimization of Parameters Using GRG

Gray relation grade analysis is used to optimize the process parameters for the PolyJet process. GRG analysis is the most effective tool for multi-attribute decision-making, which converts the multiple responses into a single grade. The following steps are followed to calculate the GRG and multi-attribute decision-making:

- Step 1 Calculation of S/N ratio for giving observations. In the PolyJet process, the objective is to reduce the loss modulus, loss factor, and surface roughness. Hence, smaller the better criteria have been applied to loss modulus, loss factor, and surface roughness. To increase the storage modulus and glass transition temperature larger the better criteria have been applied.
- Step 2 Normalization of data.
- Step 3 Computation of Grey Relation co-efficient
- Step 4 Computation of Grey Relational Grade.
- Step 5 Taguchi analysis of GRG to get the optimal parameter setting.
- Step 6 Confirmatory experiments to validate the optimal settings of input parameters

The computed values of GRG are given in Table 3.3 and the main effects plot for SN ratios of GRG is shown in the Fig. 3.10. From the main effects plot it is observed that the optimal parameter setting in part spacing along the X axis at 0 mm, part spacing along the Y axis at 37.32 mm, the orientation of the part within the tray at 0° , internal structure geometry is full, the support structure is a lite, and matte surface finish is the optimal GRG. ANOVA for GRG is carried out and the values obtained of R -sq = 99.93% and R -sq(adj) = 98.91%. These optimal conditions are further validated by confirmatory experiments and found to be well within permitted variation.

Table 3.3 Grey relational grade (GRG)

Exp. No.	1	2	3	4	5	6	7	8	9	10	11	12	13	14	15	16
GRG	0.99	0.92	0.95	0.94	0.92	0.97	0.94	0.94	0.92	0.95	0.93	0.97	0.96	0.93	0.95	0.95

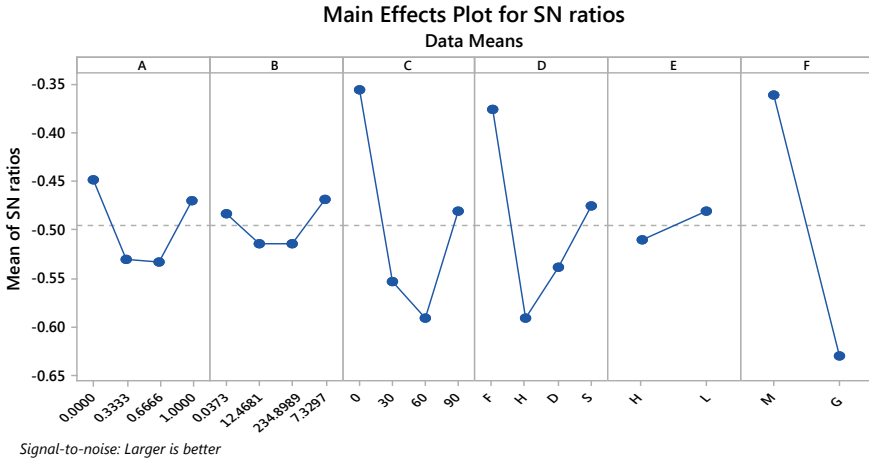


Fig. 3.10 Main effects plot for SN ratios of GRG

3.5 Conclusions

This research presented the analysis of the variability of mechanical properties in PolyJet-manufactured rectangular bars, regarding its pre-defined distribution pattern on the manufacturing tray. Rectangular bars have been used for testing purposes and later manufactured with a Stratasys Objet 350 machine. Subsequently, storage modulus, loss modulus, loss factor, Glass Transition Temperature, and surface roughness have been measured. Analyzed the following conclusions are drawn from this work:

- Storage modulus mainly affected by part orientation and internal structure geometry. Storage modulus is found to be decreasing as part orientation varies from 0° to 90°. Storage modulus exhibits maximum value at 0° because of the orientation of part length along the X-axis. Also, the storage modulus found to be on the higher side when the internal structural geometry is set at the full structure, whereas the storage modulus is least when the internal structural geometry is set at strips structure.
- Loss modulus found to be mainly affected by the internal structure geometry. It is observed that loss modulus is minimum when the internal structural geometry is set at Strips structure. Other variables are found to be the least significance.
- The loss factor is found to be affected by part orientation; internal structure geometry and surface finish. Due to the orientation of part length along the X-axis. The loss factor is minimum when the part orientation set at 0°, internal structure geometry set at full structure and surface finish is set on glossy.
- Glass transition temperature is found to be affected by part spacing along the Y axis, part orientation, internal structure geometry, and surface finish. Part spacing along the Y-axis, it would require more deposition cycles per layer as a result for

each layer available curing time is more. It is found that orientation of the part length along the X axis results in an increase in glass transition temperature.

- Surface roughnesses are mainly affected by part orientation and surface finish. Surface roughness value of the prepared samples found to be less when part orientated 0° and surface finish is glossy. This is found that the orientation of part length along the X -axis and selection of glossy mode deposits support material only in contact with the bed and lower surface of the sample.

From the GRG analysis, it is observed that optimal parameters setting for PolyJet 3D printing of ABS material are part spacing along the X axis at 0 mm, part spacing along the Y axis at 37.32 mm, the orientation of the part within the tray at 0° , internal structure geometry is full, the support structure is a lite, and matte surface finish.







References

1. Wohlers, T.: Wohlers Report—Annual Worldwide Progress Report—Additive Manufacturing and 3D Printing State of the Industry. Wohlers Associates (2014)
2. Santos, E.C., Shiomi, M., Osakadaa, K., Laoui, T.: Rapid manufacturing of metal components by laser forming. *Int. J. Mach. Tools Manuf.* **46**, 1459–1468 (2006)
3. Mellor, S., Hao, L., Zhang, D.: Additive manufacturing: a framework for implementation. *Int. J. Prod. Econ.* **149**, 194–201 (2014)
4. Clemon, L., Sudradjat, A., Jaquez, M., Krishna, A., Rammah, M., Dornfeld, D.: Precision and energy usage for additive manufacturing, volume 2A: advanced manufacturing. USA: ASME International Mechanical Engineering Congress and Exposition, San Diego, California(2013)
5. Gibson, I., Rosen, D. W., Stucker, B.: Additive manufacturing technologies—rapid prototyping to direct digital manufacturing. Springer (2010)
6. Dimitrov, D., van Wijck, W., Schreve, K., de Beer, N.: Investigating the achievable accuracy of three-dimensional printing. *Rapid Prototyp. J.* **12**(1), 42–52 (2006)
7. Brajlili, T., Valentan, B., Balic, J., Drstvensek, I.: Speed and accuracy evaluation of additive manufacturing machines. *Rapid Prototyp. J.* **17**(1), 64–75 (2010)
8. Anand, S., Ratnadeep, P.: Optimal part orientation in Rapid Manufacturing process for achieving geometric tolerances. *J. Manuf. Syst.* **30**, 214–222 (2011)
9. Pham, D., Gault, R.: A comparison of rapid prototyping technologies. *Int. J. Mach. Tools Manuf.* **38**, 1257–1287 (1998)
10. <http://www.stratasys.com/materials/material-safety-data-sheets/polyjet/digital-abs-materials>

Chapter 4

Retrofitment of Laser Cladding System with CNC Machine for Hybrid Layer Manufacturing



Seema Negi , Sajan Kapil , Arun Sharma , Priyanka Choudhary , Parag Bhargava  and K. P. Karunakaran 

Abstract MIG can deposit with a very high deposition rate but fails in realizing the fine features. The precise deposition of the laser cladding process makes it different from the others. Therefore, in future, MIG, TIG or laser cladding will be used as per the requirement. In this paper, retrofitment of an omnidirectional laser cladding system with a 4-axis CNC machine has been presented. This retrofitment is a challenging task as laser cladding system consists of several subsystems such as optical cladding head, laser power source, wire feeder, and external cooling unit. These subsystems need to be mechanically as well as electrically integrated with the CNC machine and its controller. Mechanical integration was achieved by mounting the cladding head on a retractable fixture, and electrical integration was achieved by providing extra relays in the CNC controller. The preliminary experiments were conducted to demonstrate the retrofitment and capability of the omnidirectional cladding.

Keywords Additive manufacturing · Hybrid layered manufacturing · Laser wire cladding · CNC · Rapid manufacturing

4.1 Introduction

Rapid prototyping is a well-known technology for more than 25 years, which was synchronized with the application of computer in manufacturing around 1988. RP which is also called layered manufacturing (LM) or additive manufacturing (AM) or 3D printing has been extensively exploited for its several capabilities such as complex

S. Negi (✉) · P. Bhargava
Metallurgical Engineering and Material Science, Indian Institute of Technology Bombay, Mumbai 400076, Maharashtra, India
e-mail: seema.negi@iitb.ac.in

S. Kapil · A. Sharma · K. P. Karunakaran
Mechanical Engineering, Indian Institute of Technology Bombay, Mumbai 400076, Maharashtra, India

P. Choudhary
National Institute of Technical Teachers Training and Research, Chandigarh 160019, India

© Springer Nature Singapore Pte Ltd. 2020
M. S. Shunmugam and M. Kanthababu (eds.), *Advances in Additive Manufacturing and Joining*, Lecture Notes on Multidisciplinary Industrial Engineering,
https://doi.org/10.1007/978-981-32-9433-2_4

geometry, lightweight, and fast production time. It makes part layer by layer through slicing 3D model into 2D tool path. Additive manufacturing (AM) is a new route of the manufacturing process which builds the part layer by layer and has been proved with several capabilities such as complex geometry and lightweight. Hybrid layered manufacturing (HLM) is a synergic integration of cladding (addition) and milling (subtraction) processes. HLM has been realized with metal inert gas (MIG) and tungsten inert gas (TIG) with CNC machine so far.

Hybrid manufacturing (HM) has been applied in several ways for manufacturing process to improve the part quality. However, in earlier stage of HM, it was used to improve the manufacturing process which was later concentrated to part quality. In LM, hybridization has been done on the basis of process or machines or energy source. A detailed knowledge on hybrid layered manufacturing (HLM) is well covered in [1]. In addition, HLM system has been developed by several groups [2, 3]. IIT Bombay has been working with Arc HLM which utilize arc cladding (MIG and TIG) for the deposition and milling for subtraction with CNC machine so far [4]. There are several advantages of Arc HLM such as high deposition rate, economical and high power efficiency [4, 5]. However, Arc HLM using with TIG raised the issue of omnidirectionality. As mass and energy sources are different, direction of the raw material during deposition on nonlinear path does not remain the same. Due to which non-uniform bead is deposited and can lead to geometric error. To avoid this, a coaxial wire-based laser cladding system has been utilized with HLM instead of Arc.

Laser in AM has been utilized with powder- and wire-based system due to its several advantages such as localized high energy deposition. Several commercialized processes such as LENS, DMLS, and DMD have been well developed. However, wire-based system is still in the research. The whole laser based AM processes can be classified in two categories: (1) powder bed based and (2) deposition based. In powder bed-based process, a layer of powder is spread and sintered or melt by the laser. Then, bed is lowered by the thickness of the layer in vertical direction and next layer is spread for sintering or melting. The same process is repeated till the whole part is build. While in deposition-based process, powder or wire is deposited in the melt pool generated by the laser on the substrate [6].

In this work, retrofitment of wire-based laser cladding system with CNC machine has been demonstrated, which is utilized for laser HLM.

4.2 Subsystems

To make laser HLM an automatic process, a laser cladding head is mounted on the CNC machine and controlled by Fanuc controller via NC programming. Schematics of all the subsystems are shown in the Fig. 4.1.

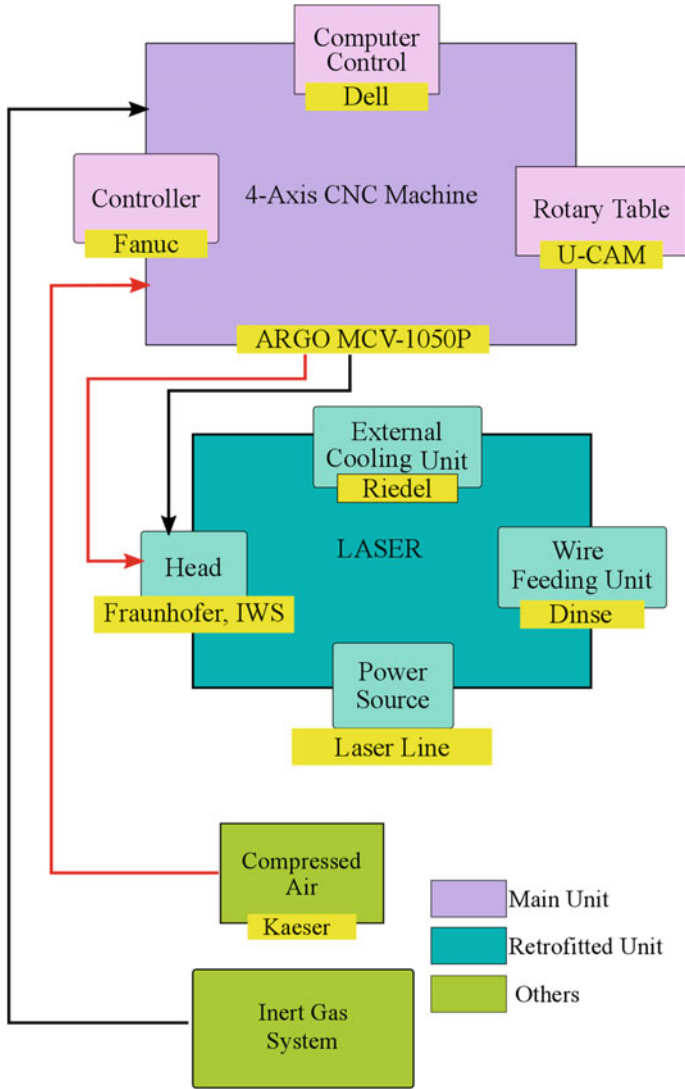


Fig. 4.1 Subsystems of laser HLM

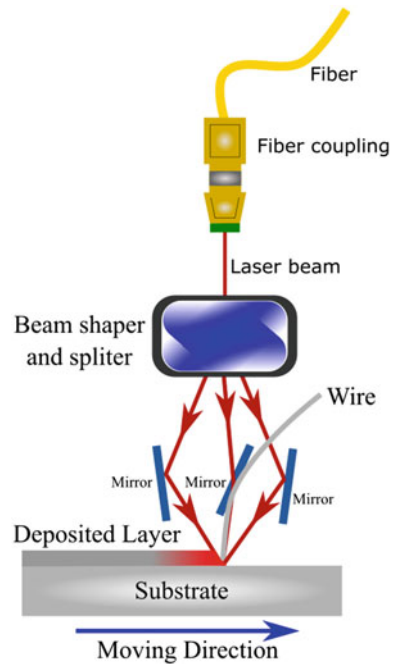
4.2.1 Laser Cladding System

Laser cladding system is integrated with 4-axis CNC machine. All other subsystems are used to transfer direct/indirect signal or mass to CNC machine and laser optic head. The entire laser cladding system is comprised of the following subsystems.

1. Laser power source
2. Laser optic head
3. Wire feeding system
4. External cooling unit
5. Compresses air
6. Shielding gas flow
7. Camera system
8. Computer system

It is a 4 KW diode laser coupled with an optical fiber. The wavelength of the diode laser is 1.020 nm, and the fiber core diameter is 600 μm. It is a multi-mode beam with top-head intensity distribution at the cross section. The diodes are pumped with a direct voltage applied. Each tiny diode generates an individual laser beam which is further bundled to generate a single beam. Collimation optics and other beam-forming components are used to rearrange the beam so that it can produce a focused beam at the end of fiber coupling. Power supply circuit is used to pump the diodes to perform the lasing action. The cooling module is connected with the external cooling unit to cool down the diode bars. After generating the laser from power source, the beam is delivered to the laser optics head through an optical fiber. Figure 4.2 shows the schematic diagram of the laser optics head. The laser head consists of an optics mechanism which trifurcates the beam to attack the coaxially fed raw stock from three directions. This head is developed by Fraunhofer IWS, Dresden, Germany,

Fig. 4.2 Schematic diagram of the laser optics head



which is also known as COAXwire, Pajukoski et al. [7] and IIT Bombay. Schematic of the laser head is shown in Fig. 4.2, and real head mounted on the CNC machine is shown in Fig. 4.3c.

Apart from this, a pull-type wire feeder from ‘Dinse’ has been integrated with laser optic head. It provides a pull-type wire feeding mechanism. A monitoring software has also been provided by ‘Dinse’ which provides the freedom of looking at the

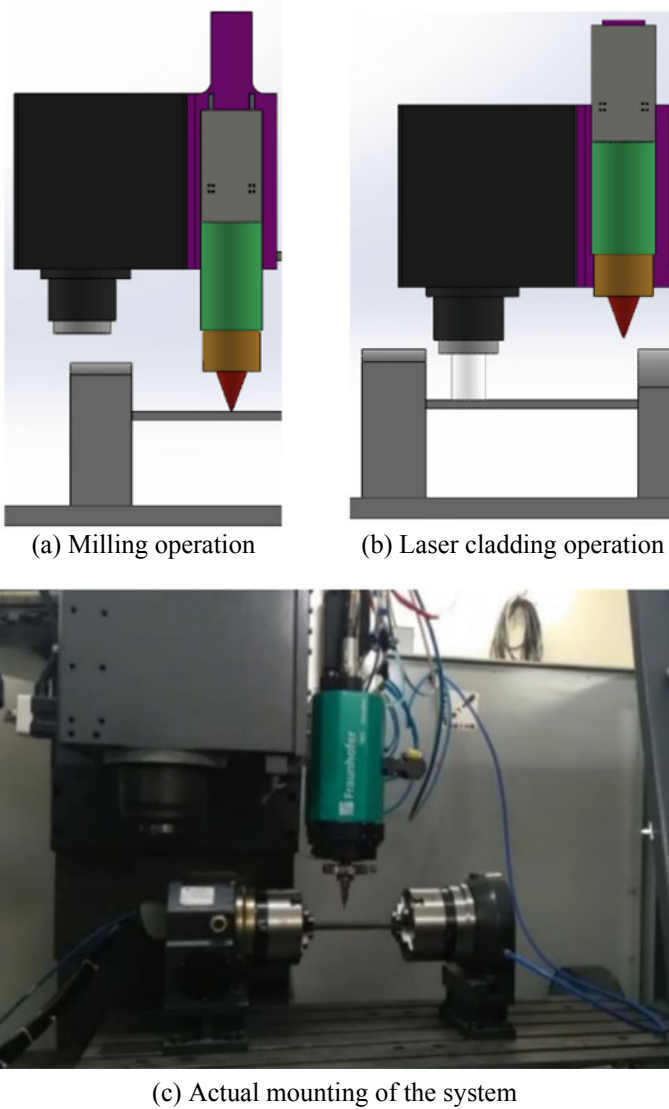


Fig. 4.3 Laser head mounted on CNC

variation in different parameters such as motor current, motor torque, and wire speed variation. Furthermore, as efficiency of the laser system is approximately only 40%, rest of the energy converts into heat. This unwanted heat has to be removed by using a cooling unit. In this system, a water-based external cooling unit is used. The chilled water is circulated into the laser power source to cool down the diode bars. Also, the optics inside the laser optics head also need to be cooled to work efficiently. Hence, a cooling circuit is provided into the laser optics head from the external cooling unit through the laser power source. Apart from this, compressed air is supplied to the laser power source and to the CNC machine. The air supply through CNC machine is further transferred to the laser optics and its pneumatic automatic tool changer (ATC). While for shielding gas, argon is used with 21 l/min. Shielding gas on/off is integrated with another relay (M code) of the CNC machine.

4.2.2 4-Axis CNC Machine

A 3-axis Argo VMC, 1050 CNC machine is upgraded to 4-axis (A-axis) by providing a rotary table. The diameter of rotary table is 170 mm with maximum rpm of 33.3. To hold the substrate from both the sides, a faceplate tailstock with 3 and 4 jaws chucks are also provided. It has pneumatic clamping system for which separate M code has been used.

4.3 Integration of Subsystems

Retrofitment of laser with CNC machine is a challenging task as several subsystems mentioned in Sects. 4.2.1 and 4.2.2 have to be well synchronized for final deposition. The entire integration was done in two parts: (1) mechanical integration and (2) electrical integration. The details on these integrations are provided in the subsequent subsections.

4.3.1 Mechanical Integration

Laser head is mechanically mounted on the CNC spindle. As in laser HLM, cladding and milling processes are done interchangeably at the same station for each layer, the chances of the collision between laser head and milling cutter can occur. To avoid this, retractable mechanism is used for laser head as shown in Fig. 4.3. For this, double acting cylinder with 5/2 solenoid pneumatic valve is used which provide smooth motion of the laser head.

4.3.2 Electrical Integration

To make the whole system automatic, extra relays have been provided for M code. To retract the laser cladding system, a relay has been used to control the 5/2 solenoid pneumatic valve of the cylinder. The wire feed and laser beam are two main parameters to be interface with the CNC machine using analog bus. In addition to that, compressed air for protecting the window glass and shielding gas to create the inert environment around the molten pool is also controlled via M codes. The list of M codes and action assigned to different M codes are listed in Table 4.1.

Figure 4.4 shows a schematic structure of implementing these M-codes for laser cladding process of single track. If the distance between nozzle tip and substrate is s , the velocity of wire feeder is v_w and speed of cladding head is v_l . Then, after switching on the wire feeder, the wire will hit the substrate after traveling a distance of $s \times \frac{v_l}{v_w}$. Hence there should be a delay = $\frac{s}{v_w}$, in switching the laser on so that both (wire and beam) can meet point 'a' (see Fig. 4.4).

Interfacing with the safety door. Generally, it has been found in such installation of laser, a separate contact-type mechanical switches are used. To install an additional component on the door, drilling is required. Hence, to avoid this additional

Table 4.1 List of M codes

S. No.	M code	Command
1	M80	Cladding head down
2	M81	Cladding head up
3	M20	Clamping of the rotary table
4	M21	Release of the rotary table
5	M60	Wire + Laser ready on
6	M61	Wire + Laser ready off
5	M62	Wire on
7	M63	Wire off
8	M64	Laser on
9	M65	Laser off
10	M66	Pilot laser on
11	M67	Pilot laser off
12	M72	Cladding head air on
13	M73	Cladding head air off
14	M74	Inert gas on
15	M75	Inert gas off

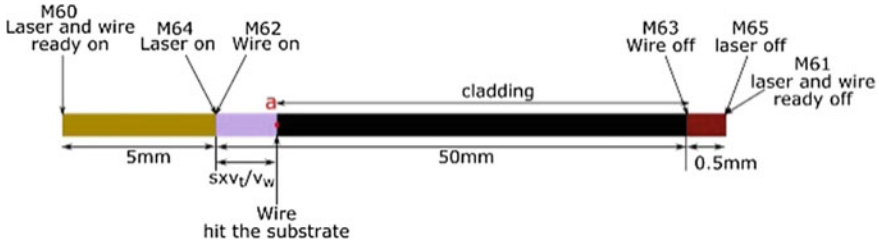


Fig. 4.4 Sample of M code for linear deposit

component, an integrated laser power safety shutdown relay with the circuit of door switch has been provided. If the door is open, the laser will not be switched on.

Interfacing for collision shut down. Laser optic head emergency stop loop has been integrated in the emergency stop circuit of the CNC machine. When the wire gets caught during the melting process (cold wire welding) on the substrate or the machine collide with the substrate or an object as shown in Fig. 4.5, then safety shutdown react and the complete machine gets switched off. Tolerance for the *XY* deflection is 7°, and the *Z* deflection is 3 mm.

4.4 Experimental Setup

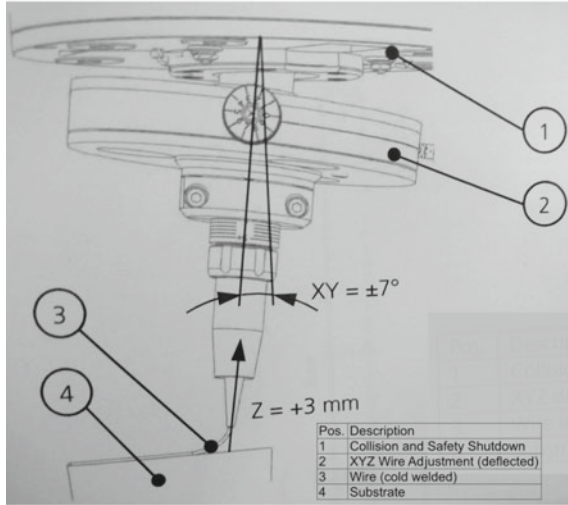
In this work, single circular and linear bead has been deposited to show the initial capability of the retrofitted system. The raw material used in this study is mild steel wire of diameter 1.2 mm supplied by ESAB group (ER70S-6). The deposition was done on the 20 mm mild steel substrate of mild steel in an open atmosphere. Argon gas (99.99%) was used as shielding gas for melt pool. The experimental setup is shown in Fig. 4.3c, and the real image during deposition is shown in Fig. 4.6.

4.5 Results and Discussion

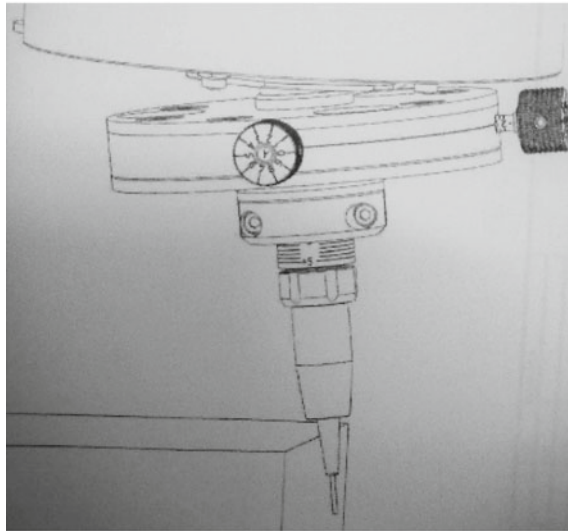
To get the parameters for deposition, following energy balance equation was used.

$$\eta P_c = \frac{\pi}{4} d_w^2 v_w \rho (C_p(T_m - T_0) + L) + \frac{\pi}{4} d_s d_p v_t \rho (C_p(T_m - T_0) + L) \quad (4.1)$$

Fig. 4.5 Safety shutdown



(a) Cold wire welding



(b) Collision

where P_c is the critical power (minimum required power), η is the efficiency, d_w is the wire diameter, v_w is velocity of wire, c_p is the specific heat, T_m is the melting temperature, T_0 is the initial temperature, L is the latent heat of melting, d_s is the diameter of spot on the substrate, d_p is the depth of penetration into the substrate, and v_l is the speed of cladding head. Using the parameters shown in Table 4.2 and Eq. 4.1, the obtained critical power P_c is 712 W. Hence, the minimum laser power should be

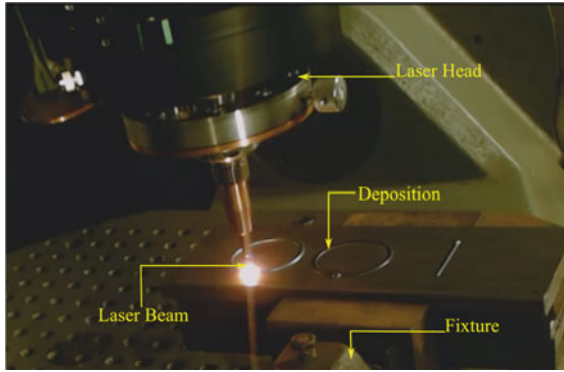


Fig. 4.6 Real image of deposition

Table 4.2 Process parameters

Symbol	Value
d_w	1.2 mm
v_w	25 mm/s
v_t	25 mm/s
d_p	0.5 mm
ρ	8000 kg/m ³
C_p	460 J/kg °C
T_m	1800 K
T_0	300 K
L	2.7×10^5 J/kg
η	70%
P_c	712 W
P_{used}	1500 W

712 W. For the preliminary experiment, a higher value of the power ($P_{used} = 1500$ W) was used.

Using these parameters, a single bead was deposited on both sides of the substrate. The sequence of instruction in the NC program is given in Fig. 4.7. The method of deposition on both sides of the substrate found an application in realizing the turbine blades, bulk head [8], etc. Following these instructions, good-quality deposition was obtained as shown in Fig. 4.8a. Using the same parameters, a circular bead was also deposited on the substrate as shown in Fig. 4.9a.

<pre> M81; (Cladding head Up) M21; (Unclamp rotary table) A0.0; M22; (Clamp rotary table) . M81; (Cladding Head Down) M72; (Cladding head air on) M74; (Inert gas on) M60; (Laser + wire ready on) A delay of 5 seconds M64; #Power=2000; (Laser on) M62; #Feed= 1500; (Wire on) . Toolpath for geometry . M63; (Wire off) M65; (Laser off) M61; (Laser + wire ready off) M73; (Cladding head air off) M75; (Inert gas off) M00 </pre>		<pre> M81; (Cladding head Up) M21; (Unclamp rotary table) A90.0; M22; (Clamp rotary table) . M81; (Cladding Head Down) M72; (Cladding head air on) M74; (Inert gas on) M60; (Laser + wire ready on) A delay of 5 seconds M64; #Power=2000; (Laser on) M62; #Feed= 1500; (Wire on) . Toolpath for geometry . M63; (Wire off) M65; (Laser off) M61; (Laser + wire ready off) M73; (Cladding head air off) M75; (Inert gas off) M00 M30 </pre>
--	--	---

Fig. 4.7 Sequence of instruction of NC program

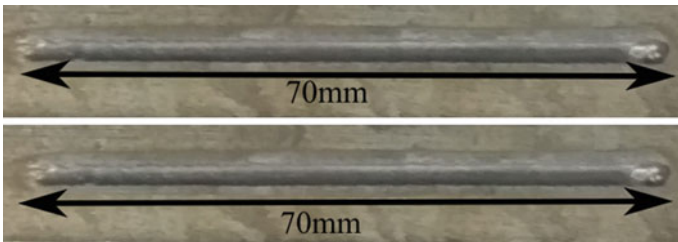


Fig. 4.8 Deposited single bead on both sides of the substrate

The bead parameters (height, width, and penetration) were characterized by tool-maker’s microscopy at two points A and B mentioned in Fig. 4.9a. From the experiments, it can be clearly observed that the deposited bead width, height, and dilution are consistent throughout the bead as shown in Fig. 4.9b. However, there is some extra material deposited at the end of the bead and need to be rectify in the future.

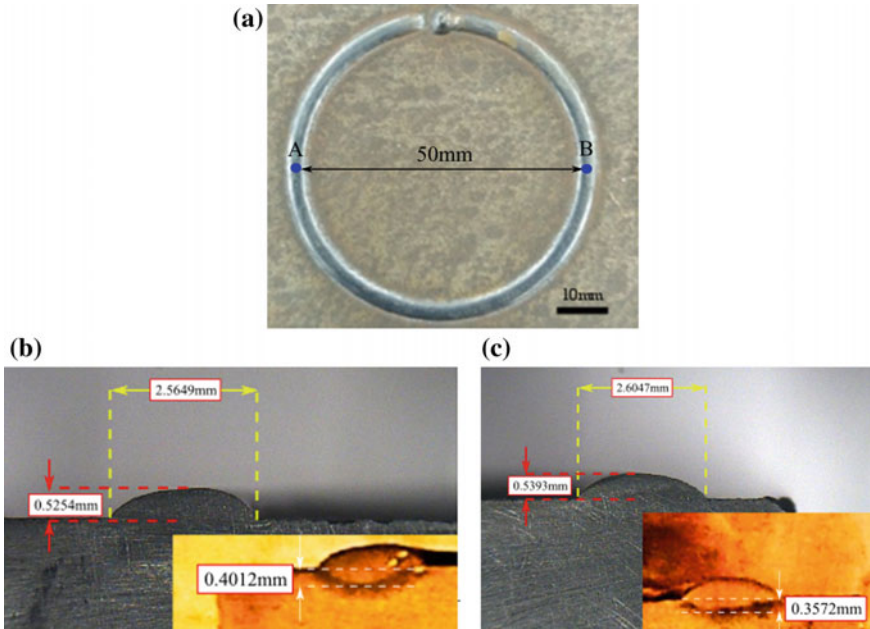


Fig. 4.9 Circular bead Image of the circular deposition (a) and bead height, width and penetration by tool maker's microscopy for A point (b) and for B point (c)

4.6 Conclusions

In this work, a unique wire-based laser cladding head has been successfully retrofitted with an existing 4-axis CNC machine. In this cladding head, the omnidirectionality is achieved by feeding the wire centrally into the molten pool surrounded by three laser beams. Several subsystems of the laser wire cladding system such as optical head, power source, wire feeder, air compressor, and inert gas supply are successfully interfaced with the controller of the CNC machine. The integration was carried out in such a way that the retrofitted CNC machine can efficiently work for additive and subtractive manufacturing. In order to test the retrofit and omnidirectionality of the cladding process, some preliminary depositions are performed along the linear and circular trajectories. The deposited single beads are found to be smooth and free from any waviness on the surface. The consistency in the width, height, and penetration at different location of the circular bead depicts its capability for omnidirectionality. In the future, this developed experimental setup will be used for realizing the objects through hybrid layered manufacturing (HLM) process. HLM finds several applications in the industries such as automobile, tooling, and aerospace.

Currently, the critical power for melting the wire and substrate was calculated using a simple energy balance equation. However, a detailed mathematical modeling

considering the temperature distribution in the moving molten pool and heat loss in conduction/convection/radiation will be done in the future.

With the developed experimental setup, three essential (single bead, multi-bead, and multi-layer) experiments for characterizing the object manufactured through HLM will be performed in the future.

References

1. Sealy, M.P., Madireddy, G., Williams, R.E., Rao, P., Toursangsaraki, M.: Hybrid processes in additive manufacturing. *J. Manuf. Sci. Eng.* **140**(6), 060801 (2018)
2. Song, Y.A., Park, S.: Experimental investigations into rapid prototyping of composites by novel hybrid deposition process. *J. Mater. Process. Technol.* **171**(1), 35–40 (2006)
3. Xiong, X., Zhang, H., Wang, G.: Metal direct prototyping by using hybrid plasma deposition and milling. *J. Mater. Process. Technol.* **209**(1), 124–130 (2009)
4. Karunakaran, K.P., Suryakumar, S., Pushpa, V., Akula, S.: Retrofitment of a CNC machine for hybrid layered manufacturing. *Int. J. Adv. Manuf. Technol.* **45**(7–8), 690–703 (2009)
5. Kapil, S., Legesse, F., Kulkarni, P., Joshi, P., Desai, A., Karunakaran, K.P.: Hybrid-layered manufacturing using tungsten inert gas cladding. *Prog. Addit. Manuf.* **1**(1–2), 79–91 (2016)
6. Frazier, W.E.: Metal additive manufacturing: a review. *J. Mater. Eng. Perform.* **23**(6), 1917–1928 (2014)
7. Pajukoski, H., Näkki, J., Thieme, S., Tuominen, J., Nowotny, S., Vuoristo, P.: High performance corrosion resistant coatings by novel coaxial cold-and hot-wire laser cladding methods. *J. Laser Appl.* **28**(1), 012011 (2016)
8. Kapil, S., Legesse, F., Kumar, R., Karunakaran, K.P.: Hybrid layered manufacturing of turbine blades. *Mater. Today Proc.* **4**(8), 8837–8847 (2017)

Chapter 5

Influence of Various Tool Path Patterns on Hardness Used in Weld Deposition-Based Additive Manufacturing



Panchagnula Kishore Kumar and Panchagnula Jayaprakash Sharma

Abstract Identification of optimal tool path is critical for successful fabrication of bulk metallic parts using weld deposition-based additive manufacturing (AM). The various features of tool path, i.e., the number of starts and stops, convolutions, and continuity, have a significant effect on the geometric as well as physical properties of manufactured parts. Ideally, an optimised tool path is a continuous path with no self-intersecting pattern, with a minimum of starts and stops and minimum convoluted patterns. The tool paths available in the literature are unable to achieve all the listed requirements. Further, there are no one-to-one comparisons of these tool paths in detail in the literature. The present work aims in comparing various tool path techniques based on flatness achievable by minimum material skinned out during face milling (thickness of the deposited layer) and the hardness achieved. Experiments are performed using the in-house developed weld-based metallic AM workstation (weld deposition torch is retrofitted with a CNC).

Keywords Weld deposition · Metallic additive manufacturing · Tool path generation · Hybrid layer manufacturing · Hardness

5.1 Introduction

To constantly concur with the rapid developments in the fields of aerospace, automobile and biomedical, there is a momentous need for manufacturing complex lightweight functional parts within a very short time span. These parts must also have minimum sub-parts for assembly and must incur minimum production costs. Currently, traditional manufacturing processes such as casting, forming (forging, extrusion) and material removal processes (turning, milling) and joining process (welding

P. Kishore Kumar

Department of Mechanical Engineering, Vignana Bharathi Institute of Technology, Aushapur, Hyderabad, India

P. Jayaprakash Sharma (✉)

Department of Mechanical Engineering, SRM University, Amaravati, Andhra Pradesh, India
e-mail: jayaprakash.p@srmmap.edu.in

© Springer Nature Singapore Pte Ltd. 2020

M. S. Shunmugam and M. Kanthababu (eds.), *Advances in Additive Manufacturing and Joining*, Lecture Notes on Multidisciplinary Industrial Engineering,
https://doi.org/10.1007/978-981-32-9433-2_5

or soldering) play a pivotal role in achieving this task. However, due to the inherent machine and process related limitations, traditional manufacturing processes are unable to achieve this task within the speculated time and with all design details faithfully reproduced. On the other hand, additive manufacturing (AM) commonly referred as 3D printing is the prospective technique that can achieve this task successfully. This technique is a layer-by-layer manufacturing approach which is only dependent on design and is not influenced by the machine limitations such as accessibility [1–4].

In AM, three-dimensional (3D) computer-aided design (CAD) model is used to build a component in layer-by-layer manner using a specific material. The stereolithography file (.stl) is the de facto file used to convey geometric data from the CAD file to AM machine. In this way, AM provides a high degree of design freedom.

Components made of several classes of materials such as plastic, metal, glass, ceramics and artificial biocompatible materials can be easily manufactured using AM. This technique in its infant stage was termed as rapid prototyping and was mainly used for developing prototypes for illustrative purposes. With dedicated research and development of customised machines, AM is now widely used to fabricate end-use products [1]. For both polymers and metals, the cost of commercially available rapid prototyping machines is relatively high. Since most of the functional parts are metallic, there is a need for developing economically viable machines for depositing complex metallic objects.

For fabrication of metallic components, AM using welding processes such as gas metal arc welding (GMAW) and gas tungsten arc welding (GTAW) is gaining popularity due to its high deposition rates, high material and power efficiency, lower investment costs, simpler setup and work environment requirements [2]. However, the surface finish of the final product fabricated by weld deposition-based AM is of inferior quality when compared to traditional machining. A process termed hybrid layered manufacturing (HLM) has been found to be suitable for producing complex metallic components [5]. This process is a combination of the traditional subtractive manufacturing process using CNC and the weld deposition-based AM, and both the processes are performed in a synchronous manner.

In HLM process, initially, the near net shape of the product is deposited using weld deposition (additive), and then, the final shape of the product is achieved by using finish machining operation [5]. In this study, the same has been used for weld-based AM or in other words an in-house weld-based metallic additive manufacturing machine is developed for depositing complex metallic objects.

Manufacture of thin-walled structures using arc-based deposition has been studied in detail by researchers [3]. These structures have also been presented to the aerospace industry for commercial application [6, 7]. However, for dense components manufactured using metallic AM, in spite of intense research done, there is a lacuna when it comes to identifying an optimised area filling technique. The most crucial task in weld-based AM for dense components is generation of optimised tool path which guides the welding torch to fill the sliced 2D layer that represents the cross section of a 3D model. These tool paths are generated by offsetting a defined

pattern in a sequential manner, and the offset distance is termed as road width or step-over value.

The step-over value is the distance between two consecutive weld beads. Approximating the weld bead geometry as a parabola, for smooth overlapping of weld beads, Suryakumar et al., had arrived at the optimal step over value to be two-thirds of the single bead width [8]. Based on Suryakumar et al.'s findings, throughout this work, the optimal step-over value is considered as two-thirds of the single bead width.

5.2 Tool Paths Used in Weld-Based AM Available in the Literature

The various tool paths available in the literature are tabulated in Table 5.1. Table 5.2 lists the merits and limitations of these commonly used tool paths. For uniform defect-free material deposition in weld-based AM, a continuous and self-intersection avoiding tool path with a minimum number of starts and stops is preferred [9].

There have been several attempts to arrive at a continuous tool path which is non-convoluted, non-self-intersecting, with a minimum number of starts and stops and easy to implement for complex geometries. Medial axis transformation along with other skeletonisation approaches has also been studied in detail to achieve an optimised area filling algorithm [10]. Conversely, none of the existing path planning algorithms has been able to achieve all the listed requirements at the same time. Further, details on one-to-one comparison of the techniques are not completely available in the literature. Information on how these tool paths affect the final properties of the part is also not available in the literature. Hence, a comparison on various tool path techniques based on flatness achievable, minimum material skinned out during face milling (thickness of the deposited layer), time taken to complete the deposition, and the final hardness achieved are done as a part of this preliminary study. Based on the observations, identification of an optimised generic area filling tool path algorithm is attempted.

5.3 Experimental Setup

The experimental setup for weld deposition-based AM is depicted in Fig. 5.1. This system is consisting of two major units,

1. GMAW weld deposition unit (additive) and
2. CNC milling system (subtractive).

A GMA welding unit is used for the weld deposition process in which a consumable electrode is surrounded by a gas mixture (82% argon + 18% CO₂). This gas mixture encapsulates the entire weld pool to avoid the oxidation during the deposition. In the present study, ER70S-6 is used as a filler wire, in other words, electrode.

Table 5.1 Commonly used tool paths for weld-based AM

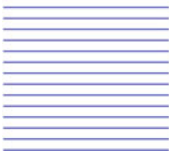



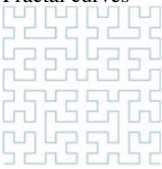
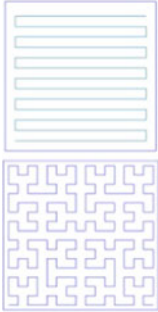
S. No.	Type of tool path	Description
1	<p>Raster/line</p> 	<p>The path described is a line</p>
2	<p>Zigzag</p> 	<p>The path fills the area in a zigzag fashion</p>
3	<p>Contour</p> 	<p>Path is generated by offsetting the outline of the part towards its interior, or from inside out with suitable step-over value</p>
4	<p>Spiral</p> 	<p>The path is generated by connecting the offsetted contours (either in to out or out to in)</p>
5	<p>Fractal curves</p> 	<p>Fractal curves such as Hilbert curve is used to cover an entire region</p>
6	<p>Hybrid</p> 	<p>The path is generated by combining more than one existing patterns to achieve a continuous and void free tool path</p>

Table 5.2 Merits and limitations of commonly used tool paths for weld-based AM

S. No.	Type of tool path	Merits	Limitations
1	Raster/line	<ul style="list-style-type: none"> (1) Very simple to implement (2) Suitable for any arbitrary geometry with multiple pockets and islands 	<ul style="list-style-type: none"> (1) Too many weld starts and stops leading to weld defects such as hump and crater at the start and end of the weld-bead respectively. (2) Maintenance of uniform weld bead height and layer thickness is difficult (3) Since it is unidirectional deposition, the part tends to have anisotropy in its material and physical properties (4) Does not capture the contour boundary accurately due to the discretisation errors at curvatures or edges that are neither parallel nor perpendicular to the deposition direction
2	Zigzag	<ul style="list-style-type: none"> (1) Simple to implement (2) Suitable for complex geometry with internal pockets and islands (3) Since the deposition happens alternately in two directions, the material and physical anisotropy of the part can be reduced (4) The path is continuous; hence, there is a significant reduction in the number of starts and stops (by dividing the complex entire region into sub-regions) 	<ul style="list-style-type: none"> (1) Similar to line pattern, it does not capture the contour boundary accurately due to the discretisation errors at curvatures or edges that are neither parallel nor perpendicular to the deposition direction
3	Contour	<ul style="list-style-type: none"> (1) Suitable for complex geometry with internal pockets and islands (2) Since the deposition is made in several directions, there is minimum material and physical anisotropy in the part (3) Captures outline profile of the slice accurately 	<ul style="list-style-type: none"> (1) The path has too many discontinuities (at the beginning and end of the contour), in turn too many starts and stop (2) Maintenance of uniform layer thickness is difficult

(continued)

Table 5.2 (continued)

S. No.	Type of tool path	Merits	Limitations
4	Spiral	<ol style="list-style-type: none"> (1) The path is continuous, which led to a minimum number of starts and stops (2) Similar to contour path, material and physical anisotropy of the part is minimum (3) Captures outline profile of the slice accurately 	<ol style="list-style-type: none"> (1) Tool path generation for arbitrary shapes and geometries with islands or pockets is difficult
5	Fractal curves	<ol style="list-style-type: none"> (1) The path is continuous with a minimum number of starts and stops (2) The material and physical properties of the parts tends to be almost isotropic 	<ol style="list-style-type: none"> (1) The path is highly convoluted (2) Arriving at an optimised order of curve and generation of tool path for complex geometries is laborious
6	Hybrid	<ol style="list-style-type: none"> (1) The path captures all the geometric details accurately (2) Suitable for complex geometries with multiple pockets and islands (3) Material and physical properties of the part tends to be almost isotropic 	<ol style="list-style-type: none"> (1) Arriving at an optimised path is difficult

ER70S-6 is a copper-coated mild steel (MS) wire. The general composition (percentage, %) of ER70S-6 is as follows: carbon 0.075, manganese 1.22, sulphur 0.014, silicon 0.67, phosphorus 0.01, and remaining is iron. Earlier studies on ER70S-6 reveals that it is suitable for fabricating fully dense components through weld deposition-based AM process [11]. For positioning the weld torch at a specified location with the required feed, the weld torch is retrofitted with the commercially available CNC milling centre. These two units are working on a single station in a synchronous manner without disturbing the actual purpose of the machine. The optimal process parameters to achieve continuous and uniform welds in weld deposition-based AM are voltage (V), current (I), touch speed (T_S), wire feed (W_F), and contact tip to work piece distance (CTWD).

5.4 Results and Conclusions

The optimal process parameters for weld deposition-based AM (continuous welds) were found to be 19 V, 135 A, 0.36 m/min as T_S , 4.5 m/min as W_F , and 10 mm as CTWD. The bead width and height obtained using the above-mentioned optimal

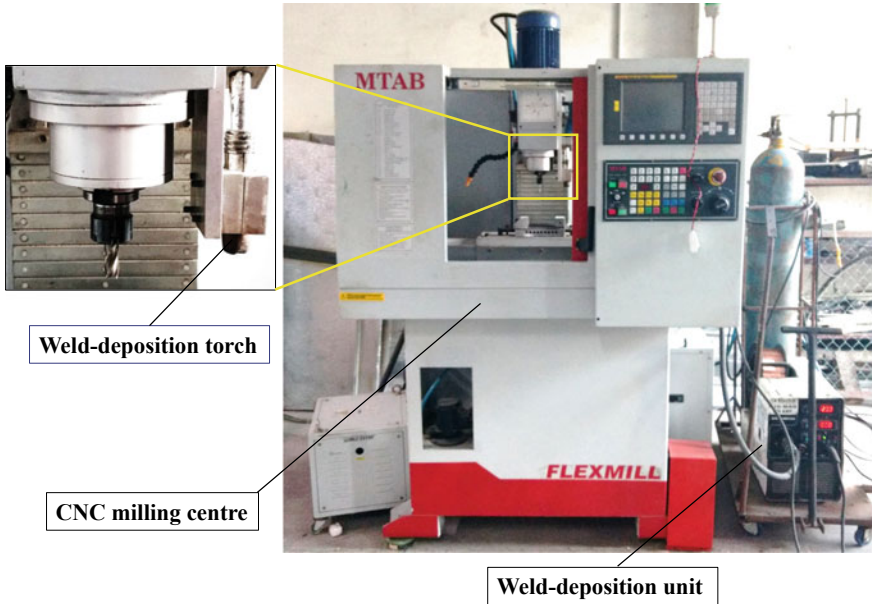


Fig. 5.1 Experimental setup

process parameters are 5.01 and 3.80 mm, respectively. The step-over value is taken as 3.30 mm (2/3rd of the bead width). For comparison of various tool paths planning listed in Table 5.1, a square geometry of 45 mm is considered for weld deposition. Figure 5.2 shows the various area filling paths considered for deposition and the final deposited layer.

After the layer deposition, face milling operation is performed to achieve the flat surface which is suitable for next deposition (Fig. 5.3). This face milling operation not only help in arriving at Z accuracy but also helps in removal of scales and oxides which are present on the top surface. Table 5.3 presents the comparison of various tool paths based on the weight of the deposited layer, the weight of the material skinned, the final layer thickness, and the hardness of layer deposited measured using Rockwell test (HRB, 100 kg load).

Fig. 5.2 Comparison of various tool paths used in weld-based AM

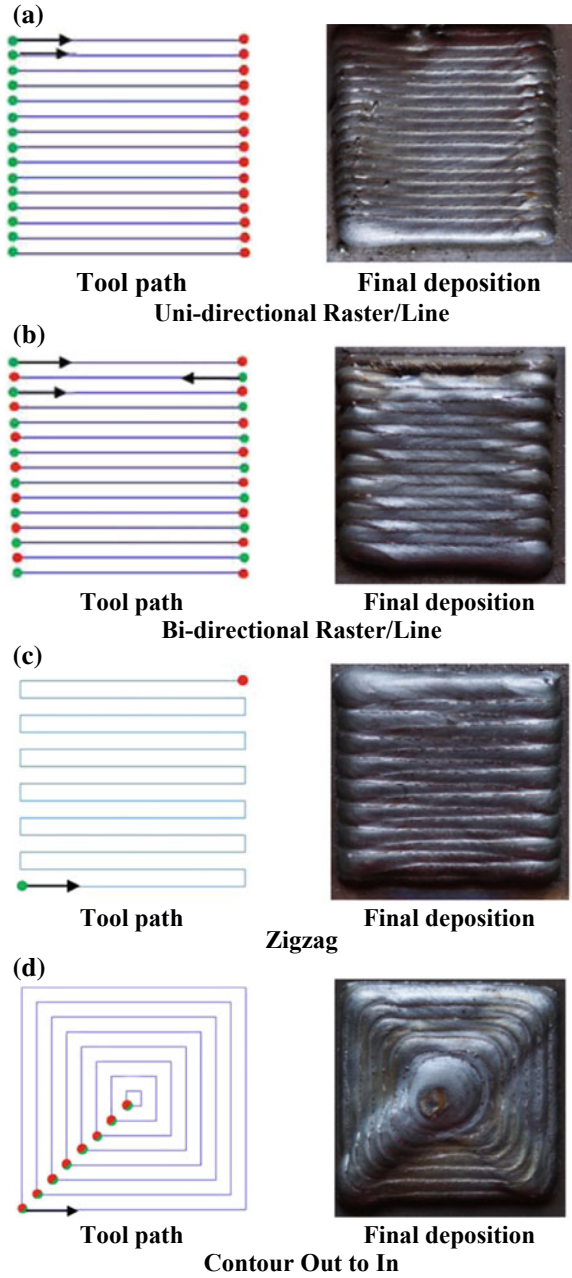


Fig. 5.2 (continued)

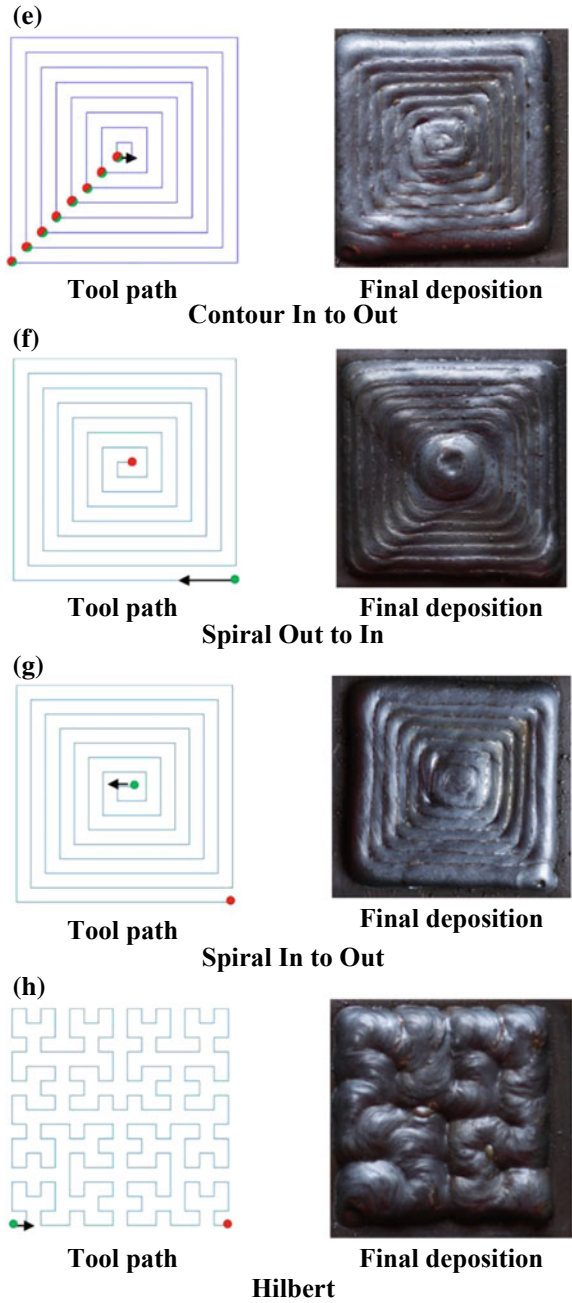
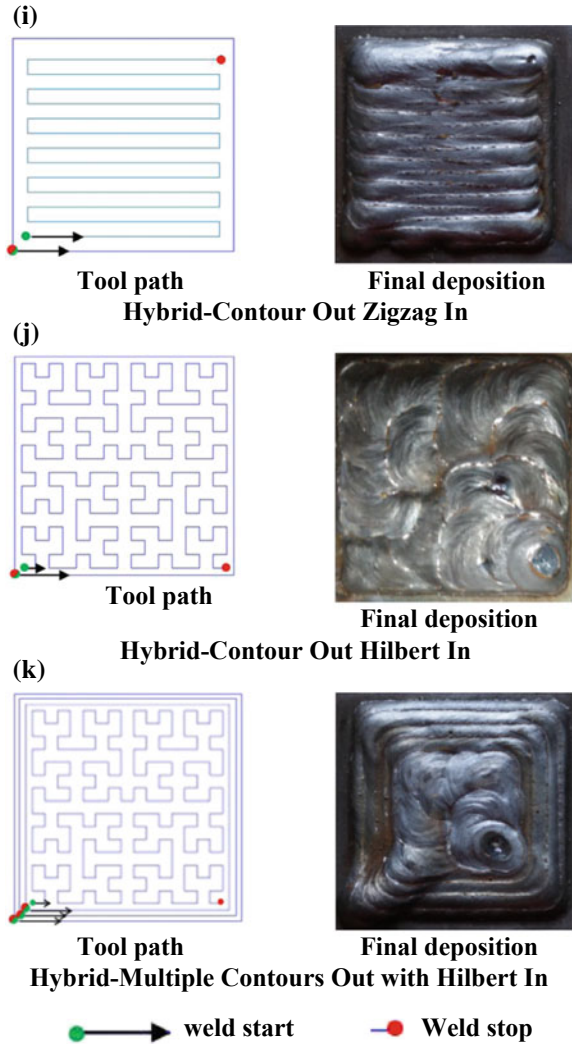


Fig. 5.2 (continued)



Based on the observations, following conclusions are drawn:

- The hybrid tool paths (layer height 3.00 mm for contour out and zigzag in, 3.04 mm and 3.02 for contour out and Hilbert in) provide maximum layer thickness and also capture the outer boundary accurately. Further, contours with Hilbert curves are densely packed and record the highest hardness values (HRB 87.00 only Hilbert, 88.00 one contour out and Hilbert in, and 88.60 three contours out and Hilbert in).
- Raster unidirectional and bidirectional (3.02 and 2.81 mm) also provides maximum layer thickness. However, the outer boundary is not completely captured. The hardness values are raster and zigzag are almost same.



Fig. 5.3 Final layer achieved after face milling operation

- Zigzag requires less material to be skinned (10 g), and the layer thickness is also comparable with hybrid tool path.
- In case of contour tool paths and spiral paths, the layer heights after face milling operation are varying only by 0.03 mm and the hardness is slightly less than zigzag and raster.
- Spiral in to out provides higher layer thickness than spiral out to in. However, the hardness values are lower.
- In case of Hilbert, as the path is fully convoluted, voids were present in the deposited layer; hence, more material had to be skinned. To avoid this, one has to either increase the order of Hilbert curve or decrease the step-over value suitably.

Based on the above observations, it can be concluded that, for bulk material deposition, even though the material skinned is high, the hybrid tool path is suitable as the layer thickness is high; the boundary is captured well, and the hardness values are higher.

Table 5.3 Summary of results obtained from analysing various tool paths used in weld-based AM

S. No.	Type of tool path	Substrate weight (g)	Substrate plus weld deposition weight (g)	Weight of the plate after face milling (g)	Weight of the material skinned (g)	Layer height (mm)	Hardness (HRB)
1.a	Raster—unidirectional	668	734	724	10	3.02	85.66
1.b	Raster—bidirectional	662	730	716	14	2.81	85.00
2	Zigzag	652	718	708	10	2.92	85.66
3	Contour out to in	660	726	716	10	2.71	86.00
4	Contour in to out	664	734	722	12	2.68	84.30
5	Spiral out to in	664	730	714	16	2.64	81.33
6	Spiral in to out	666	732	720	12	2.83	83.33
7	Hilbert	664	730	716	14	2.84	87.00
<i>Hybrid</i>							
8	Contour out + zigzag in	670	736	722	14	3.00	85.00
9	Contour out + Hilbert in	666	740	722	18	3.04	88.00
10	Three contours out to in + Hilbert in	660	740	720	20	3.02	88.60

Acknowledgements The authors would like to thank SRM University-AP, Amaravati for providing the necessary facilities to conduct the experiments. Also thank Dr. Venkata N Nori for his continuous encouragement and sharing his valuable thoughts for improving the quality of the work. One of the authors, Panchagnula Kishore Kumar, is a faculty member in Vignana Bharathi Institute of Technology (VBIT), Hyderabad, acknowledges VBIT management for their kind encouragement. Also acknowledges DST for providing computational facilities under its FIST Program at VBIT, where the computational work has been carried out.

References

1. Silva, R.J., Barbosa, G.F., Carvalho, J.: Additive manufacturing of metal parts by welding. *IFAC-PapersOnLine* **48**(3), 2318–2322 (2015)
2. Panchagnula, J.S., Simhambhatla, S.: Additive manufacturing of complex shapes through weld-deposition and feature based slicing. In: *ASME 2015 International Mechanical Engineering Congress and Exposition*, p. V02AT02A004 (2015)
3. Panchagnula, J.S., Simhambhatla, S.: Feature based weld-deposition for additive manufacturing of complex shapes. *J. Inst. Eng. India Ser. C* 1–8 (2016)
4. Panchagnula, J.S., Simhambhatla, S.: Inclined slicing and weld-deposition for additive manufacturing of metallic objects with large overhangs using higher order kinematics. *Virtual Phys. Prototyping* **11**(2), 99–108 (2016)
5. Kapil, S., et al.: Optimal space filling for additive manufacturing. *Rapid Prototyping J.* 660–675 (2016)
6. Ding, D., Pan, Z., Cuiuri, D., Li, H.: A practical path planning methodology for wire and arc additive manufacturing of thin-walled structures. *Robot. Comput. Integr. Manuf.* **34**, 8–19 (2015)
7. Ding, D., (Stephen) Pan, Z., Cuiuri, D., Li, H.: A tool-path generation strategy for wire and arc additive manufacturing. *Int. J. Adv. Manuf. Technol.* **73**, 173–183 (2014)
8. Suryakumar, S., Karunakaran, K.P., Bernard, A., Chandrasekhar, U., Raghavender, N., Sharma, D.: Weld bead modeling and process optimization in hybrid layered manufacturing. *Comput. Aided Des.* **43**(4), 331–344 (2011)
9. Zhang, Y., Chen, Y., Li, P., Male, A.T.: Weld deposition-based rapid prototyping: a preliminary study. *J. Mater. Process. Technol.* **135**, 347–357 (2003)
10. Jin, Y., He, Y., Xue, G., Fu, J.: A parallel-based path generation method for fused deposition modeling. *Int. J. Adv. Manuf. Technol.* **77**, 927–937 (2015)
11. Suryakumar, S., Karunakaran, K.P., Chandrasekhar, U., Somashekara, M.A.: A study of the mechanical properties of objects built through weld-deposition. *Proc. Inst. Mech. Eng. Part B J. Eng. Manuf.* **227**, 1138–1147 (2013)

Chapter 6

Design of Robot Gripper with Topology Optimization and Its Fabrication Using Additive Manufacturing



M. Sugavaneswaran , N. Rajesh  and N. Sathishkumar 

Abstract In industrial robot, the grippers are attached at its end and one of the most important components in it. Industrial robot for customized application results in need of gripper with unique design and limited volume in short span and least cost. FEA-assisted topology optimization has shown great potential in obtaining better design space for customized limited volume components. In this work, gripper of a mini-robot to lift the component of 100 g for palletizing operation is designed using topology optimization. However, there are limitations in terms of fabrication of complex optimized design using conventional manufacturing process. So in this work, optimized design is fabricated in ABS plastic using fused deposition modeling process which is an additive manufacturing technique. The fabricated optimized model along with existing design model is evaluated in the experimental setup for end applications.

Keywords Additive manufacturing · Topology optimization · Finite element analysis

6.1 Introduction

A robot gripper is the end effector of a robotic mechanism which is one of the major components in deciding the end use of robots. In this sense, it is akin to a human hand which allows one to pick and place any given object. Grippers attached to the robot are explored in areas which involve hazardous tasks such as high-temperature welding, defusing bombs in mines, space exploration, and handling radioactive materials [1]. In some case, design of robot gripper is complex in nature due to need of custom

M. Sugavaneswaran (✉) · N. Rajesh
Department of Design and Automation, School of Mechanical Engineering, Vellore Institute of Technology, Vellore 632014, India
e-mail: sugavaneswaran@gmail.com

N. Sathishkumar
Department of Mechanical Engineering, St. Joseph's College of Engineering, OMR, Chennai 600119, Tamil Nadu, India

shape for part specific and for applications such as micro-electronic structures and handling fragile parts [2]. Moreover, advancement in design of robot gripper has resulted in a complex mechanism employed as a gripper in robot end effector [3].

Topology optimization (TO) is a mathematical approach that optimizes material layout within a given design space, for a given set of loads and boundary conditions such that the resulting layout meets a prescribed set of performance targets with less volume of material [4]. Topology optimization with finite element analysis is used at the conceptual level of the design process to arrive at a conceptual design proposal that is then fine-tuned for performance and manufacturability [5]. The topology optimization of continuum structures corresponds to finding the connectedness, shape, and number of holes such that the objective functions are extremized/maximized. In Eq. (6.1), a density (ρ) function is defined on design domain (Ω) to describe the material distribution, which can take the value 0 (void) or 1 (solid). In finite element analysis (FEA) model, Eq. (6.1) is applied to decide whether the particular element or domain value is 0 or 1 based on volume constrains or strain energy value. FEA-assisted TO replaces time-consuming and costly design iterations, hence reduce new product development time and overall cost while improving design performance [6].

$$\rho(x) = 0 \text{ or } 1, \quad \forall x \in \Omega \quad (6.1)$$

Generally, TO results in complex shape which will have certain difficulties in terms of manufacturability using conventional manufacturing process [7]. However, an advance manufacturing process like additive manufacturing (AM) allows to build extremely complex objects without much constraints as faced in conventional process [8]. AM refers to the process of building part through layer-by-layer deposition of materials, which is contrast to material removal followed in the conventional manufacturing process [9]. As the design is built up through layering, AM process eradicates any issues that usually arise with other methods such as plastic injection molding, machining, or handcrafting [10]. The main advantages of AM over conventional manufacturing processes include the increased speed of part delivery from conception to market, the ability to produce objects with increased geometric complexity, and the decreased waste generation during fabrication [11, 12].

In this article, customized robot gripper is designed using TO approach, and then, it was fabricated using additive manufacturing, considering its advantages in terms of ability to deal with complex geometry and less lead time from concept to the final model.

6.2 Modeling and Analysis

6.2.1 CAD Modeling

Gripper for M-TAB modular tabletop 5-axis articulated mini-robot (see Fig. 6.1a) is

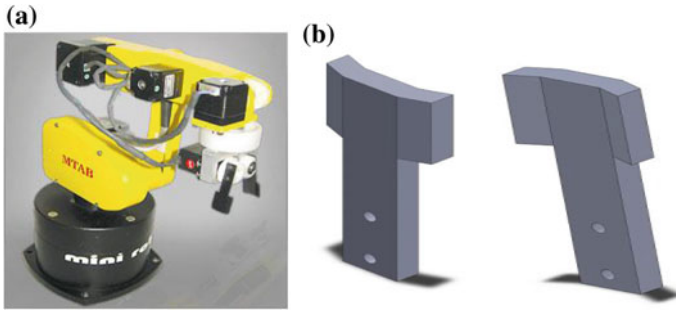


Fig. 6.1 a MTAB 5-axis articulated mini-robot and b CAD model of gripper pair

modeled using SOLIDWORKS software. Basic dimensions of gripper are finalized based upon the provision for end effector attachment in mini-robot. In this robot, gripper close and open movements are controlled using medium duty stepper motors. Mini-robot considered for this work is used for applications such as point-to-point operations such as palletizing, pilot study for new line in an assembly line, and laboratories in education institutes. CAD model of the left- and the right-hand gripper is shown in Fig. 6.1b.

6.2.2 FDM ABS Material Properties

Acrylonitrile butadiene styrene (ABS) thermoplastic, which is printable in fused deposition modeling (FDM) process, is used for robot gripper fabrication. Depending on the build orientation, material properties can and does make a difference in the strength, stiffness, and toughness of the part. So FDM material properties are heterogeneous in nature [13]. For finite element analysis, FDM-ABS material property under bending loading is measured as per ASTM D790 standard using the Instron-8322 testing machine. The test is conducted at ambient temperature with crosshead speed is set at 5 mm/min. Ultimate bending strength and elastic modulus are determined through machine associated software.

6.2.3 Finite Element Analysis

The robot gripper model is imported into the ABAQUS software, as a STEP format for FEA analysis and TO. As FDM printed ABS material is considered for gripper fabrication, material properties determined for FDM ABS through experimentation are assigned to the model. Imported model is meshed using the seed length of 1 mm. The meshed model is shown in Fig. 6.2a. The holes in the gripper which will attach

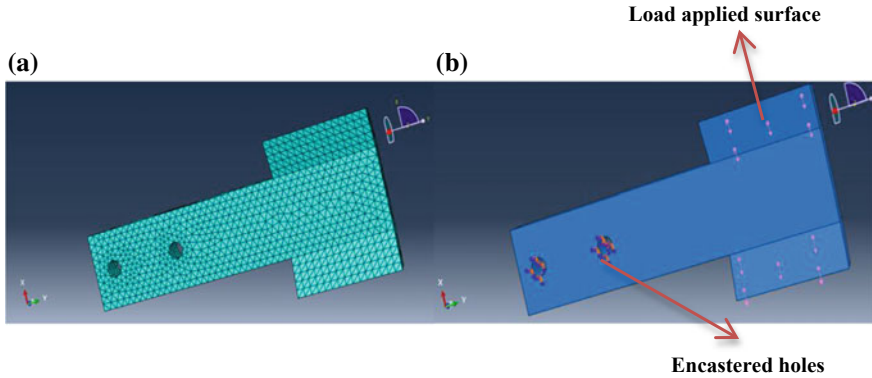


Fig. 6.2 **a** Mesh model of robot gripper and **b** gripper model with boundary conditions

to the robot through the screws are fixed; i.e., both the translational motion and rotational motion of the holes are restricted.

There are two types of force acting on the gripper: (i) Normal reaction: It is acting perpendicular to the surface. (ii) Friction force: It is acting parallel to the surface. So robotic gripper will have both bending and shear stress on the surface (where the load is acting), and the magnitude of these forces is calculated using Eqs. (6.2) and (6.3). Mini-robot is designed for a payload of 100 g.

$$F = mg/2 \quad (6.2)$$

$$2\mu F_1 = mg \quad (6.3)$$

where F = friction force (N), F_1 = normal force (N), m = payload (g), and μ = coefficient of friction. $F_1 = 1.4$ N is acting normal to the surface of gripper, and $F = 0.49$ N is acting parallel to the surface. Boundary conditions and applied forces on the robotic gripper are shown in Fig. 6.2b.

6.3 Topology Optimization

Topology optimization begins with an initial design, which is assumed to be the maximum physical extent of the component and then determines an optimal material distribution by changing the density and the stiffness of the elements in the initial design while continuing to satisfy the optimization constraints [14]. TO provides users with a choice of objective function terms and constraints, including optimization design responses: volume, mass, compliance, displacements, rotations, reaction forces, reaction moments, internal forces, natural frequencies, center of gravity, moments of inertia, results from frequency response analysis (amplitudes, phases,

velocities, and accelerations), and acoustic measures (surface velocities, sound pressure). Robot gripper considered for this work has been static structure, so optimization is done based on volume constraints. TO is performed with volume constraints of 25, 50, and 70% to achieve preliminary space volume for consider robot gripper boundary conditions. Design response for different volume constrains was measured in terms of minimum strain energy as objective function. Optimized model is shown in Sect. 6.5.3.

6.3.1 Surface Smoothing

Optimized model is generally results in rough surface, irregular features, and ergonomically poor. For this purpose, optimized model is redesigned based on manufacturing constraints. Though additive manufacturing does not have many constraints, model surface has to be smoothed for good surface finish. In this work, 3-matic module in MIMICS (Materialise's Interactive Medical Image Control System) software is used. It allows users to perform mesh and geometry manipulation in FEA model as well as to prepare 3D object (STL) files for additive manufacturing processes.

6.4 Part Fabrication

Optimized robotic gripper design is fabricated using the FDM TITAN machine. FDM is one among the additive manufacturing techniques which is working on the principle of laying down thermoplastic material in layer by layer from the bottom-up to produce a part [15]. Thermoplastic filament is extruded in nozzle wounded with heating coil in order to convert rigid filament into a semi-liquid state which is deposited in ultra-fine beads along the extrusion path.

The FDM-TITAN machine supports different types of thermoplastic, and ABS is widely used for fabrication of parts with high durability and fine feature detail. FDM printed ABS parts find applications in the range from prototype to production, which include concept modeling snap-fits, jigs and fixtures, end-use components for form, fit, and function. In addition, ABS is often chosen because it is easily machined, sanded, glued, and painted. Properties of FDM printed ABS part are almost similar to conventional processed material.

6.5 Results and Discussion

6.5.1 Flexural Properties

Load versus displacement graph for FDM-ABS material is shown in Fig. 6.3. It is observed that FDM-ABS fails at 10.19 kg load with a displacement of 6.4 mm. The stress–strain curve from the values obtained from the test is plotted, and flexural properties such as strength and modulus are 61.5 and 1687 MPa, respectively.

6.5.2 Stress Contour Plot

Von mises stress of FE analyzed robotic gripper is shown in Fig. 6.4. The maximum value of the stress analysis is found to be 10.6 MPa which is lower than the yield strength (61.5 MPa) of FDM-ABS obtained through experimentation. From stress contour plot, it is observed that stress is maximum near the hole which is provided to assemble gripper in mini-robot end effector. In more than 80% of gripper area, stress observed is less than 1.76 MPa. This observance provides sufficient freedom for further improvement in the component design using TO principle. Displacement plot of FE analysis on robot gripper is shown in Fig. 6.5. Maximum deformation of robot gripper for applied load is found to be 0.79 mm near the free edge.

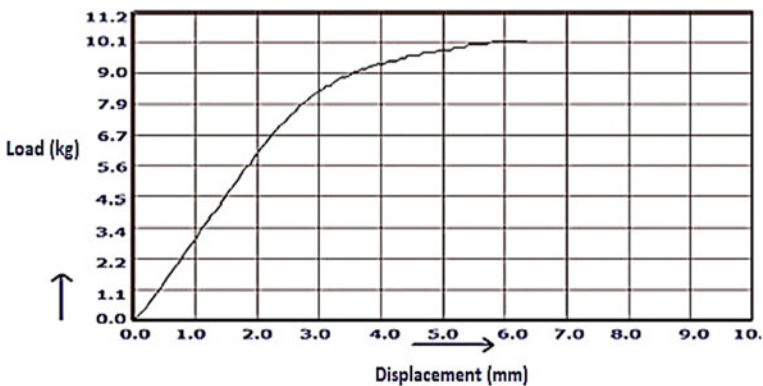


Fig. 6.3 Load versus displacement graph for FDM-ABS under bending load

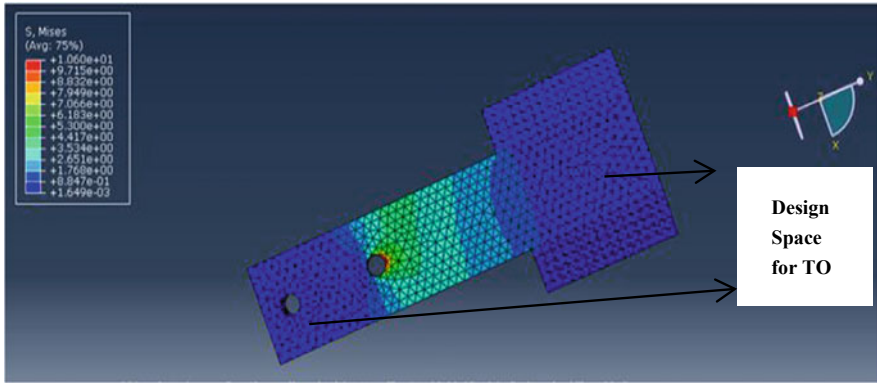


Fig. 6.4 Von mises stress contour plot of robot gripper

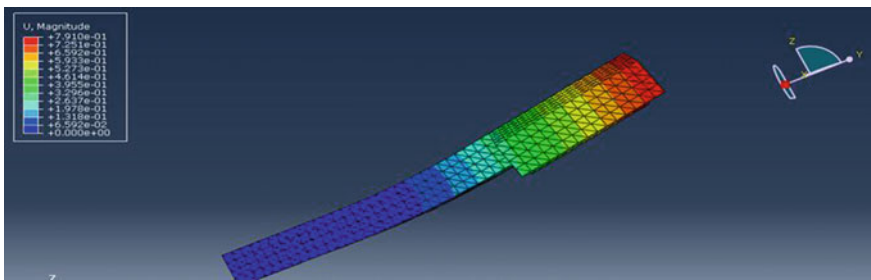


Fig. 6.5 Deformed contour plot of robot gripper

6.5.3 Optimized Contour Plot

A topology optimized gripper model for various volume percentage constrains is shown in Fig. 6.6. Table 6.1 summarizes the maximum stress developed in topology optimized model for each volume constraint. It is observed that there is an increase in stress as volume constrains percentage decreases. However, increases in stress are not significant and design is safe with factor of safety greater than 4 in all constraints. From Fig. 6.6, it is found that continuity did not appear for 25 and 50% volume constraints. The part continuity in the model is observed in topology optimization with 70% volume constraints.

The main objectives of TO are to achieve the design with least volume for the desired functionality. However, in terms of manufacturing using the FDM TITAN AM machine, minimum width printable is 1.2 mm [16]. In 25% volume constraint optimized model, there are features with less than 1.2 mm. So, an optimized model with 50% volume constraints is considered for further fabrication.

It is observed that the island of the part features in optimized model, however, in order to get the full benefit of AM process, part continuity is required for fabrication

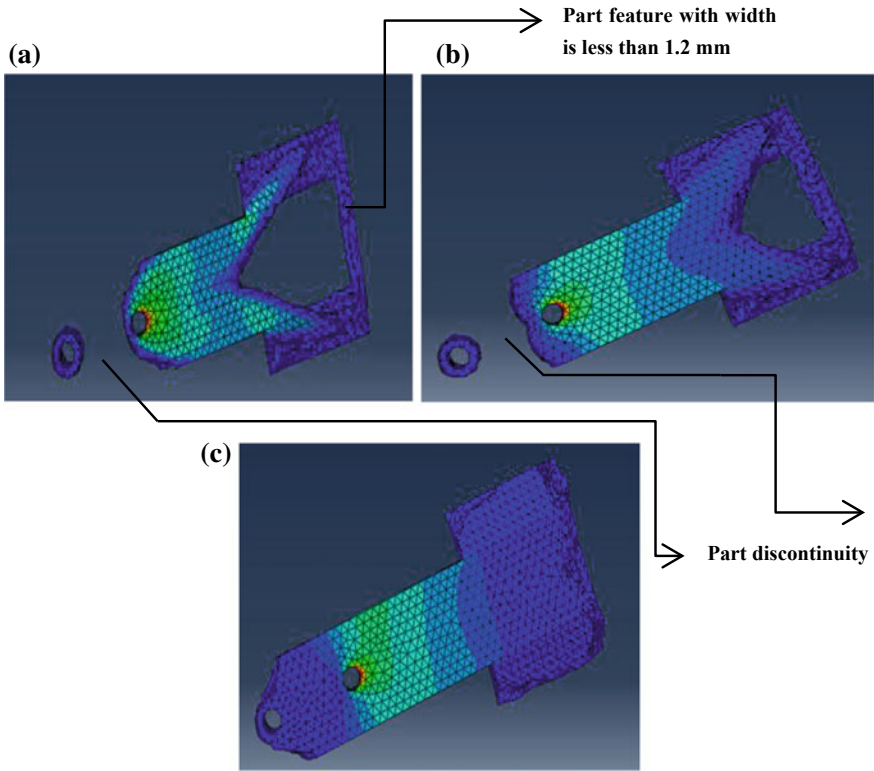


Fig. 6.6 Topology optimized structure of robot gripper with **a** 25, **b** 50, and **c** 70% volume constraint

Table 6.1 Maximum stress for topology optimized structure with different volume constraint

S. No.	Volume constraint (%)	Maximum stress (MPa)
1	25	14.14
2	50	11.87
3	70	10.67

of component in single built without assembly. In addition, design obtained after topology optimization has a rough surface topology, which has difficulty in terms of maintenance and ergonomics. Thereby, surface smoothing was necessary in the topology optimized design. Remodeling STL file to achieve part continuity and surface smoothing is done using the MIMICS software, and the final model is shown in Fig. 6.7.

Fig. 6.7 Surface smoothed model of optimized gripper with 50% volume constraint



6.5.4 Cost and Material Analysis

Additive manufactured gripper for original design and topology optimized design is shown in Fig. 6.8. The cost, time required, the volume of the material used to fabricate the gripper for both original design, and topology optimized are summarized in Table 6.2. It is observed that optimized model is advantageous in terms of cost, time, and material required for part fabrication. It is a well-known fact that cost of part fabrication in FDM process is directly proportional to material and time required for printing [17]. For validation, fabricated models (both original and topology opti-

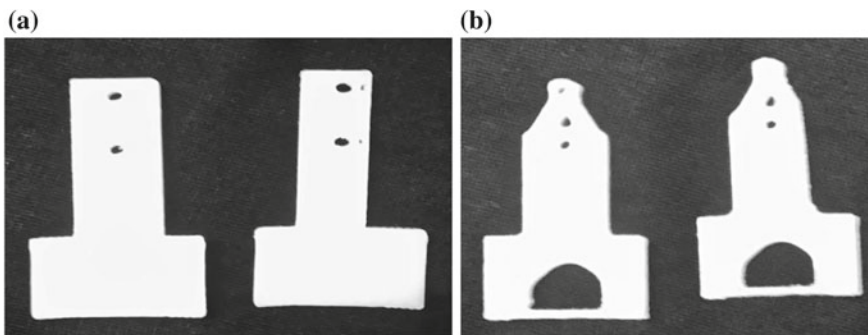


Fig. 6.8 Fabricated gripper with **a** original design and **b** topology optimized design

Table 6.2 Economic details of original and optimized gripper fabrication using the FDM machine

S. No.	Model type	Fabrication time (min)	Material consumption (cm ³)	Cost of printing (Rs.)
1	Original model	27	2.5	834
2	Optimized model	21	1.8	600

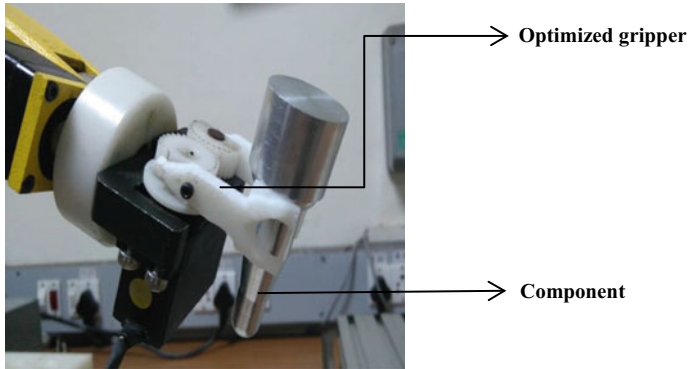


Fig. 6.9 Topology optimized grippers fixed in MTAB mini-robot are holding the component of weight 100 g

mized) are fixed with the MTAB (see Fig. 6.9) mini-robot for lifting a component of the 100 g weight.

6.6 Results and Discussion

Robot gripper for customized application is designed and fabricated with computer-assisted design and manufacturing techniques. In addition, in this work, advantage of integration of topology optimization with additive manufacturing is demonstrated. Proposed methodology results in weight reduction of 7 g and cost reduction of 39% is achieved. So, it is concluded that the framework reported in this work, reduces fabrication time, decrease volume of the material used and it is more cost effective. Therefore, the approach presented in this work can be seen as an alternative method for optimum design and fabrication of products for customized applications.

References

1. Raghav, V., Kumar, J., Senge, S.S.: Design and optimisation of robotic gripper: a review. In: Proceedings of the National Conference on Trends and Advances in Mechanical Engineering (2012)
2. Datta, R., Pradhan, S., Bhattacharya, B.: Analysis and design optimization of a robotic gripper using multiobjective genetic algorithm. *IEEE Trans. Syst. Man Cybern: Syst.* **46**(1), 16–26 (2016)
3. Saha, D.T., Sanfui, S., Kabiraj, R., Das, S.: Design and implementation of a 4-bar linkage gripper. *IOSR J. Mech. Civ. Eng.* **11**(5), 61–66
4. Bendse, M.P., Sigmund, O.: *Topology Optimization: Theory, Methods, and Applications*. Springer, Heidelberg (2003)

5. Andreassen, E., Lazarov, B., Sigmund, O.: Design of manufacturable 3D extremal elastic microstructure. *Mech. Mater.* **69**(1), 1–10 (2014)
6. Brackett, D., Ashcroft, I., Hague, R.: Topology optimization for additive manufacturing. In: Proceedings of the 22nd Annual International Solid Freeform Fabrication Symposium, Texas, US, pp. 348–362 (2011)
7. Smith, C., Todd, I., Gilbert, M.: Utilizing additive manufacturing techniques to fabricate weight optimized components designed using structural optimization methods. In: Proceedings of the 24th Annual International Solid Freeform Fabrication Symposium, Texas, US, pp. 879–894 (2013)
8. Jacobs, P.F.: *Rapid Prototyping & Manufacturing*. Society of Manufacturing Engineers, Dearborn, MI (1992)
9. Gibson, I., Rosen, D.W., Stucker, B.: *Additive Manufacturing Technologies: Rapid Prototyping to Direct Digital Manufacturing*. Springer, Heidelberg (2010)
10. Alam, S., Sugavanwaran, M., Arumaikkannu, G., Mukherjee, B.: An innovative method of ocular prosthesis fabrication by bio-CAD and rapid 3-D printing technology: a pilot study. *Int. J. Orbital Disord. Oculoplastic Lacrimal Surg.* **36**, 223–227 (2017)
11. Simhambhatla, S., Karunakaran, K.P.: Build strategies for rapid manufacturing of components of varying complexity. *Rapid Prototyp. J.* **21**(3), 340–350 (2015)
12. Gibson, I., Rosen, D.W., Stucker, B.: *Additive Manufacturing Technologies*, 2nd edn. Springer Publications, Heidelberg (2015)
13. Hernandez, R., Slaughter, D., Whaley, D., Tate, J., Asiabanpour, B.: Analyzing the tensile, compressive, and flexural properties of 3D printed ABS P430 plastic based on printing orientation using fused deposition modelling. In: Proceedings of the 26th Annual International Solid Freeform Fabrication Symposium, Texas, US, pp. 939–950 (2016)
14. Bankoti, S., Dhiman, A., Misra, A.: Comparative analysis of different topological optimization methods with ANSYS. *IOSR J. Mech. Civ. Eng.* **2**(4), 84–89 (2015)
15. Iyibilgin, O., Lieu, M.C., Chandrasekhar, K.: Investigation of sparse build rapid tooling by fused deposition modeling. *Int. Conf. Addit. Manuf.* **12**, 45–51 (2014)
16. Grimm, T.: *Fused Deposition Modeling: A Technology Evaluation*. T. A. Grimm & Associates, Inc., pp. 1–12 (2002)
17. Thrimurthulu, K., Pandey, P.M., Reddy, N.V.: Optimum part deposition orientation in fused deposition modelling. *Int. J. Mach. Tools Manuf.* **44**(6), 585–594 (2004)

Chapter 7

Fabrication of Gradient Density Components Through Extrusion-Based Additive Manufacturing



Shashi Ranjan Mohan  and Suryakumar Simhambhatla 

Abstract Due to its sequential and localized manner of material addition, additive manufacturing (AM) is very suitable to fabricate components with gradient density. This study attempts to generate components with gradient density through extrusion-based AM process using Hilbert area-filling curve. Four square samples having different infill density were fabricated by fused filament fabrication. A silicon membrane covering the various regions of the pattern was applied on one side of the surface, which helps in the experimental measurement when subjected to loading. Further, a demonstration case study of a shoe sole was taken to generate and fabricate with the gradient density based on the foot pressure data. Deflections of the membrane at different locations when subjected to uniform loading were measured. The behavior of the fabricated sample matched with the desired foot pressure data, thus validating the approach. This study can provide the basic framework to generate a gradient density component.

Keywords Additive manufacturing · Gradient material · Fused filament fabrication

7.1 Introduction

Additive manufacturing (AM) is a fabrication process in which three-dimensional (3D) parts are manufactured directly from the CAD model, by adding the material layer upon layer. The fabrication and modeling of the heterogeneous objects are getting more attention in the last few decades because AM is making it possible to fabricate such components. Fused filament fabrication (FFF) is an extrusion-based AM process in which thermoplastic filament is used to fabricate the 3D parts. It is a very popular and extensively used process due to its low initial cost, material cost, and operational cost [1]. The thermoplastic is used as raw material in the form of filament and fed to the nozzle through the roller, which is driven by the motor. These

S. R. Mohan (✉) · S. Simhambhatla
Department of Mechanical and Aerospace Engineering, Indian Institute of Technology
Hyderabad, Hyderabad 502285, Telangana, India
e-mail: me14resch11010@iith.ac.in

© Springer Nature Singapore Pte Ltd. 2020
M. S. Shunmugam and M. Kanthababu (eds.), *Advances in Additive Manufacturing and Joining*, Lecture Notes on Multidisciplinary Industrial Engineering,
https://doi.org/10.1007/978-981-32-9433-2_7

thermoplastic materials are extruded by heating through the nozzle in semi-molten form and joined layer upon layer to build the 3D component.

Heterogeneous object has better property where multifold functional applications are required. Multi-material objects, functional graded material object, micro-electro-mechanical system device, porous structures, and composites are some of the examples of heterogeneous objects [2]. A heterogeneous object can be produced either by mixing two or more different materials or by varying different density with the same material through additive manufacturing [3, 4]. These types of heterogeneous materials are used in various fields such as mechanical electrical thermal, optical, biomedical, and prosthetic [5–10]. The lightweight part having hard material outside and soft material inside is generally used in the medical application for prosthetics legs, feet, hands, etc.

Extrusion-based AM process fabricates the parts by using different infill density and patterns; hence, the heterogeneous or gradient density component can be fabricated by changing the infill density. The proposed approach attempts to generate the component with gradient infill density without boundary line at the interface by FFF process using Hilbert curve. Some square samples have been generated with different infill density to study their deflection behavior for the uniform load. Further, a case study of a shoe sole with gradient density based on foot pressure data has been taken to fabricate and the deflection at different points has been measured using uniform loading.

The current work is organized as follows: Sect. 7.2 describes methods to control the density in the FFF process and the basic experimental setup to fabricate the samples with ABS plastic filament. The technique to generate the uniform gradient density using the proposed method and the fabrication of the samples through FFF have been discussed in Sect. 7.3. Further, the deflections of the fabricated samples at different location were measured to validate the proposed methods in Sect. 7.4. The results obtained through the experiments have been discussed in Sect. 7.5. Finally, Sect. 7.6 summarizes the current work based on observed results.

7.2 Density Control Methods in FFF Process

7.2.1 Basic Experimental Setup

The parts are manufactured through FFF process by slicing the STL file with specified infill pattern and density. There are a number of softwares available, Slic3r, KiSSlicer, Cura, etc., for slicing and generating the tool path to fabricate the 3D parts through FFF process. The acrylonitrile butadiene styrene (ABS) plastic material is more commonly used to fabricate the samples through extrusion-based AM process due to its low price. The parameters affecting the mechanical property of fabricated parts through FFF are nozzle diameter, layer width, infill pattern, build orientation, and

Table 7.1 Input parameters for FFF process

Input parameter	Value
Nozzle diameter	0.5 mm
Filament diameter	1.75 mm
Extrusion width	0.3 mm
Layer height	0.3 mm
Extrusion temperature	230 °C
Bed temperature	100 °C

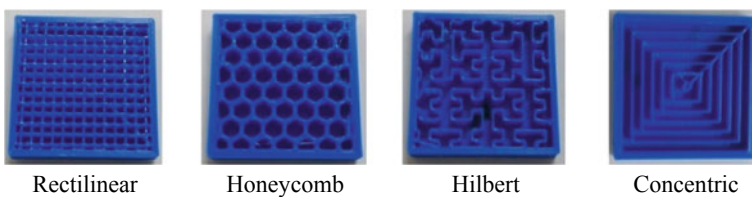
extrusion temperature [11–15]. The input parameters used to fabricate the samples of ABS plastic through FFF process in the current study are listed in Table 7.1.

7.2.2 Various Area Filling Patterns

There are various types of area infill pattern available on different slicing software. The most popular infill patterns are rectilinear, honeycomb, Hilbert, and concentric which are commonly used to fabricate the parts. The square component of ABS plastic fabricated with different infill patterns using FFF process is shown in Fig. 7.1 for illustration.

7.2.3 Combining Multiple STL Files with Different Fill Densities

The 3D component can be fabricated using FFF with single infill density in a given layer because an STL file can be sliced with one infill density through existing slicing software. Therefore, to fabricate the part with variable infill density, a CAD geometry is first splatted into multiple parts and sliced with different infill densities [16]. These sliced geometries are mixed together to create a component having different infill density. An illustrative example for generating a component C of two different infill

**Fig. 7.1** Different infill pattern and fabricated parts for illustration

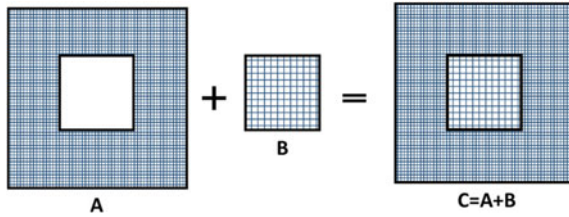


Fig. 7.2 Illustration of mixing two different sliced parts

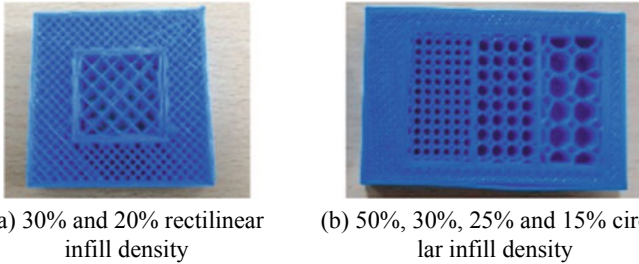


Fig. 7.3 Components with different infill density by mixing the different files

densities has been shown in Fig. 7.2. In this process, the component C is splatted into two parts (i.e., part A and part B) and then sliced with different infill density. The first sliced layer of part A and part B is mixed as shown in Fig. 7.2 and repeated till the last layer to obtain the component C of different infill density.

Few components were fabricated with different infill density by mixing two and three components with different infill density as shown in Fig. 7.3. The two parts were sliced with the rectilinear infill of 30 and 20% density and fabricated by mixing them through FFF as shown in Fig. 7.3a. Another component was prepared by mixing with four different infill density of 50, 30, 25, and 15% of circular infill as shown in Fig. 7.3b. However, the major drawback of this method is that the fabricated parts have boundary lines between two infill density interfaces. Hence, the component with continuous gradient density cannot be fabricated using this method.

7.3 Generation of Uniform Gradient Infill Density

7.3.1 Suitable Area Filling Approach for Gradient Infill Density

The various infill patterns such as rectilinear, honeycomb, concentric, and Hilbert have been analyzed for suitability of uniform gradient density through the FFF pro-

cess and discussed in Table 7.2. Rectilinear infill pattern cannot change the gap in the middle of the path as shown in Table 7.2. Therefore, discontinuity in the path will appear and, because of this, boundary or gap will be introduced at the interface of different density. Hence, continuous gradient density cannot be generated using a rectilinear pattern. The honeycomb infill pattern has also a similar problem, and it is very difficult to change the infill size in-between a single pass, and hence, gradient density will not be produced. The concentric infill pattern has no connectivity with the neighbor path, and hence, it will not hold the entire part together. Therefore, the stability and strength of the component will not be obtained. However, the Hilbert curve has a continuous path and its size can be changed easily without breaking the path. Therefore, among them, the Hilbert curve is more suitable to generate the component with gradient density.

Hilbert curve is a continuous space filling curve generated by traveling at each point of the square grid of size $2^n \times 2^n$ (i.e. 2×2 , 4×4 , 8×8 , 16×16 etc.) by duplicating the pattern itself which can be seen in Fig. 7.4. Here, n is representing the order of the Hilbert curve. The generation and fabrication of gradient density parts using the Hilbert curve as area infill pattern have been discussed in Sects. 7.3.2 and 7.3.3.

7.3.2 *Generation of Gradient Infill Density Using Hilbert Curve*

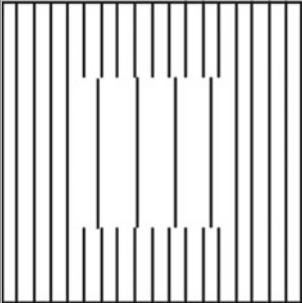
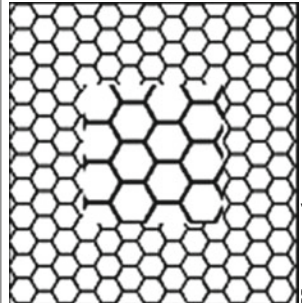
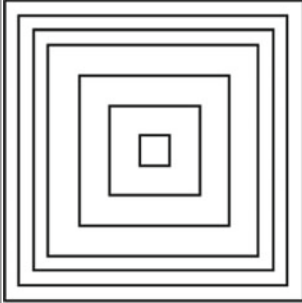
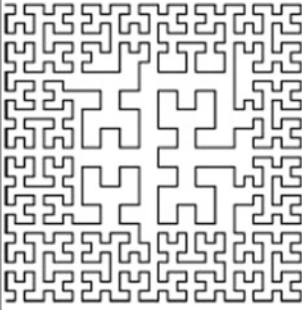
The gradient infill density using Hilbert curve area filling is possible because it has a continuous path that can change its size easily. To generate the gradient infill density, the input image was imported to image2hilbert software and converted into Hilbert area filling as .svg file. Image having white color is converted with low infill density, gray color with medium infill density (double of the white), and black image with high infill density (double of the gray). The gradient image can be used to generate the component with gradient infill density. These Hilbert infill curves are first converted from .svg to .dxf file using Inkscape, and then, the .dxf file to G code using dxf2gcode software. The filament feed length (E) should be assigned in the obtained G code for every movement of the nozzle in x - and y -direction. Hence, the E value can be calculated based on conservation of mass; i.e., the volume of filament feed will be equal to the volume of extruded material, which is formulated below,

$$(\pi/4)D^2E = (\pi/4)d^2l \quad (7.1)$$

So,

$$E = (d/D)^2l \quad (7.2)$$

Table 7.2 Suitability of infill patterns for gradient density

Infill pattern	 Rectilinear	 Honeycomb	 Concentric	 Hilbert
Suitability for gradient density	Not suitable	Not suitable	Not suitable	Suitable
Reason/description	Discontinuity in path and boundary/gap between variable densities	Difficult to change the infill size and boundary/gap between variable densities	No connection with neighbor path, hence no stable	It has continuous path and hence easy to change the size of Hilbert curve for gradient density

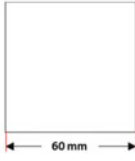

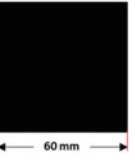
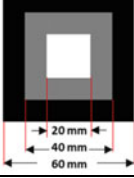
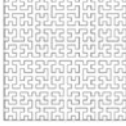


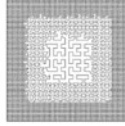
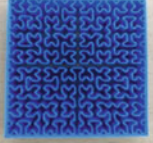
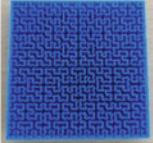


	Sample-A	Sample-B	Sample-C	Sample-D
Input image				
Area filling path				
Fabricated samples	 (a) 15% infill density	 (b) 30% infill density	 (c) 60% infill density	 (d) Gradient infill density

Fig. 7.4 Samples of various infill density

where D is the filament diameter, d is the extruded diameter, E is the filament feed length, and l is the length of extruded material. Therefore, the feed length for i th tool path movement (E_i) from point $i - 1$ to i can be calculated as follows:

$$E_i = (d/D)^2 [(x_i - x_{i-1})^2 + (y_i - y_{i-1})^2]^{1/2} \tag{7.3}$$

where x_i and y_i are the x - and y -coordinates of point i . The calculated E value has been assigned at the end of each line in the G code for uniform feeding of the filament material.

7.3.3 Fabrication Process

The continuous gradient density parts of ABS plastic material were fabricated on FFF machine using the input parameter as listed in Table 7.1. Four different samples were fabricated with the same dimensions of 60 mm length, 60 mm width, and 10 mm height using Hilbert area infill pattern. The first three samples (i.e., samples A, B, and C) have the uniform infill density, while the sample D has gradient infill density as shown in Fig. 7.4. White, gray, and black images were taken as input images and converted to Hilbert curve with area infill density of 15, 30, and 60% as shown in Fig. 7.4a–c, respectively. The sample D has gradient density of the combination of 60, 30, and 15% infill density, which had been generated by input image having

the combination of white, gray, and black colors as shown in Fig. 7.4d. First, the input images were converted into G code of Hilbert area infill curve as discussed in Sect. 7.3.2. Then, these samples were fabricated with blue color ABS plastic material on ProtoCentre-999 3D printer machine by adding the area infill path at each layer till 10 mm of height in the z-direction as shown in Fig. 7.4. Further, a thin layer of silicon (i.e., 1 mm thickness) was applied on one side of the surface to act as a membrane covering the various regions of the pattern as shown in Fig. 7.5. This membrane helps in the experimental measurement of the behavior of the various regions when subjected to loading.

A case study of shoe sole has been taken to demonstrate the proposed method by generating the gradient density sample, since the shape of foot varies from one person to other, and hence, the foot pressure generated on the sole has different values. A hypothetical shoe sole for such application based on the sample pressure map available in Wikipedia was used to create a simplified gradient foot sole for the same [17]. The high pressure, intermediate pressure, and low pressure are marked with red, green, and blue color, respectively, as shown in Fig. 7.6a. These pressure distributions are converted into white, gray, and black color (i.e., low, medium, and high density, respectively) as shown in Fig. 7.6b. The gradient infill density has been generated with infill density of 15, 30, and 60%, through the proposed method which has been shown in Fig. 7.6c. The shoe sole was fabricated with the dimension of 220 mm length and 86 mm width by adding layer till the 10 mm of the thickness using ABS plastic material through the FFF process as shown in Fig. 7.6d. The high pressure zone was considered as low infill density to get more deflection, whereas intermediate pressure zone was converted with medium density and less pressure zone with the high density. A thin layer of silicon was applied on one side of the surface, which will act as a membrane covering the various regions of the pattern. Subsequently, the sample was validated by applying the uniform load on the membrane at different locations.

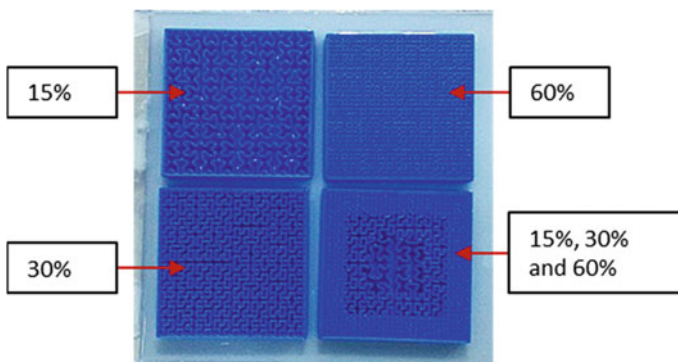


Fig. 7.5 Membrane created by silicon layering on the samples

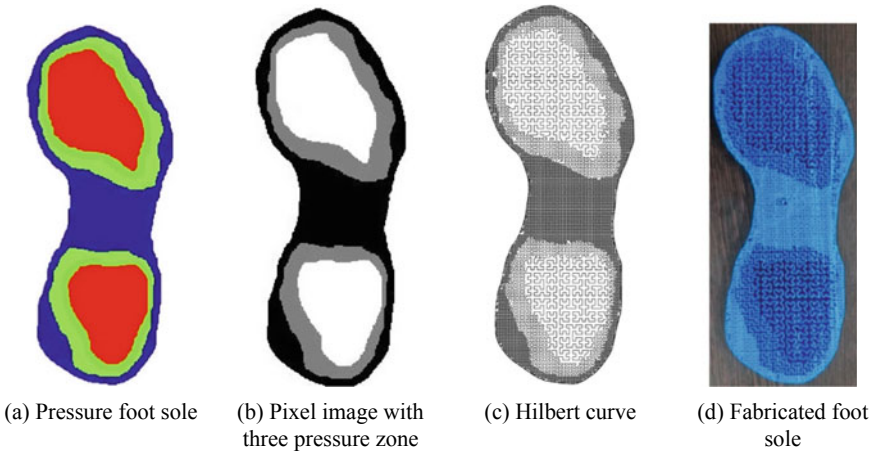


Fig. 7.6 Fabrication of gradient density shoe sole based on pressure distribution

7.4 Validation Setup

The generation of components with gradient infill density through the proposed method was validated by measuring the deflection of the membrane by applying the uniform loading at the different locations. The deflections of fabricated samples were tested by fixing all boundaries for a given load using CNC and dynamometer. The fixture was clamped on the dynamometer of Kistler Company, which was placed on the bed of CNC machine and a 4-mm ball-pointed tool was clamped on the head to apply the uniform load on the sample as shown in Fig. 7.7. The head was slowly moved in the negative z -direction (i.e., vertically downward), to observe the uniform load through dynamometer, and the corresponding deflection of tool head movement was recorded. The uniform square grid at 5 mm incremental distance in x - and y -direction was chosen to apply the uniform load of 1.3 N at every grid points on the

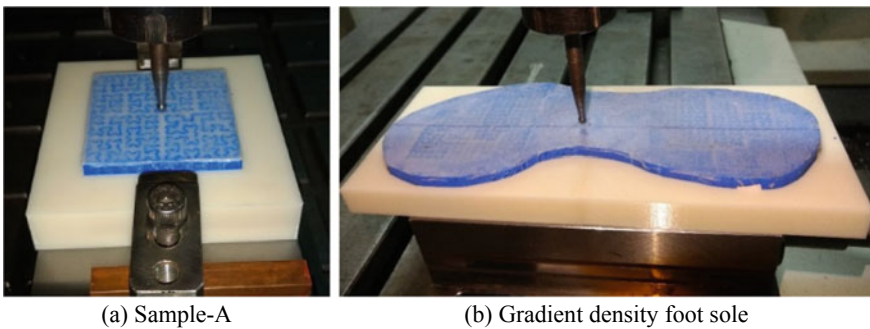


Fig. 7.7 Test setup for measuring the deflection

silicon membrane to measure the corresponding deflection. These experiments were performed for all four samples (i.e., samples A, B, C, and D), and the deflections were obtained under the same loading conditions. Similarly, the deflection at the different location of the gradient shoe sole was performed by fixing its outer boundary. The uniform load of 1.3 N was applied in the negative z-direction as shown in Fig. 7.7b by taking 10 mm of square grids in x- and y-direction.

7.5 Results and Discussion

The deflections at different locations of the samples were obtained by applying the uniform load. The deflection values obtained for samples A, B, C, and D are plotted with the 3D bar chart as shown in Fig. 7.8 to observe the deflection in the z-direction at different points. The green, blue, and red and color bars are shown in Fig. 7.8, which represents the deflection of the part containing 15, 30, and 60% infill density respectively. The maximum deflection in samples A, B, C, and D are 4.4, 2.2, 0.35,

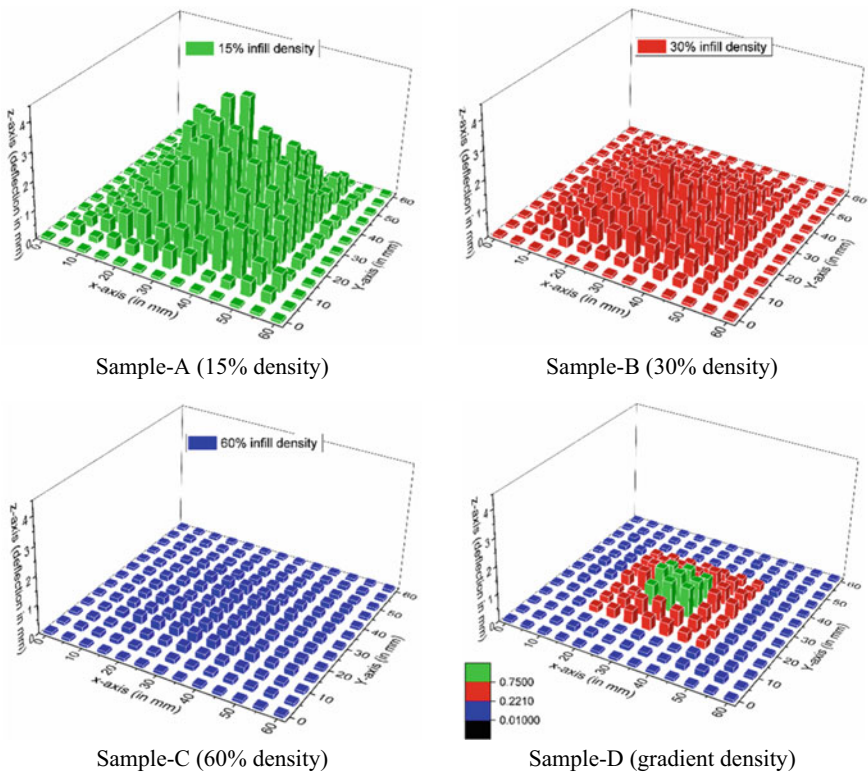


Fig. 7.8 Deflection of samples at various points for uniform load

and 1.1 mm, respectively, for uniform loading conditions. The deflection of samples is high where the infill density is less, and it increases when moves toward the center from boundaries. Thus, the deflection can be controlled by selecting the required infill density at the desired region.

Similarly, the deflections of the gradient shoe sole sample at different points are shown in Table 7.3 and the same data are plotted with 3D bar chart as shown in Fig. 7.9 for better visualization. The maximum deflection obtained in this sample is 4.5 mm in the z -axis, where the infill density is 15% (less) and the distance from the boundary is more. The bar chart having blue color represent the deflection less than 1.2 mm, red color represents deflection between 1.2 and 2.5 mm and green color represent deflection more than 2.5 mm. It can be clearly observed from Fig. 7.9 that the samples are gating more deflections where the pressure gradient was more and less where the pressure gradient was less value. This variable deflection is obtained by gradient infill density technique. The behavior of the fabricated sample matched with the desired foot pressure data, thus validating the approach. Due to these deflections, the pressure will be uniformly distributed throughout the foot. Hence, the localized pressure will be reduced which will provide more comfortable on the foot.

7.6 Conclusions

The component with gradient infill density has been generated without any boundary through the proposed approach using extrusion-based AM process. Since Hilbert curve has the ability to resize its pattern size easily, the gradient density part can be fabricated using the AM process. Four square samples of different infill density were generated using Hilbert area filling curve and fabricated on FFF machine, and subsequently, the deflection was measured by applying the uniform loads at different locations. A case study of shoe sole was taken to design and fabricate them using gradient infill density based on the foot pressure data to demonstrate the effectiveness of the proposed method. The conclusion of this study based on the observation of measured deflection at a uniform loading condition has been discussed as follows.

1. It has been observed that the deflections of the sole sample were more where the pressure gradient was high and less where the pressure gradient was low.
2. Thus, the behavior of the fabricated sample matches with the recommended foot pressure data, which will provide the uniform pressure distribution on the foot.
3. The current study gives the basic framework to generate the gradient density component, which can be used in various fields such as biomedical, prosthetic, and orthopedic.

In the future, the study can be extended to generate the samples of gradient density in two dimensions and three dimensions of the components using multiple infill patterns.

Table 7.3 Deflection of gradient shoe sole (in z-direction) in mm

Y (mm)	X (mm)											
	0	10	20	30	40	50	60	70	80	90	100	110
45	0	0	0	0	0	0	0.120	0.120	0	0	0	0
40	0	0	0	0	0	0.120	0.200	0.200	0.281	0	0	0
30	0	0	0	0.120	0.230	0.600	0.780	0.700	0.800	0.560	0.420	0.340
20	0	0	0.350	0.800	0.680	1.940	2.000	1.580	1.080	0.480	0.460	0.350
10	0	0.290	0.660	1.000	1.390	2.300	3.000	2.000	1.280	0.470	0.440	0.350
0	0.120	0.500	1.700	2.900	4.500	4.200	4.300	2.600	0.470	0.450	0.340	0.350
-10	0	0.600	0.590	3.700	4.200	3.700	2.900	1.900	0.460	0.340	0.300	0.340
-20	0	0.420	2.20	2.800	1.800	1.400	1.600	1.070	0.310	0.100	0	0
-30	0	0	0.400	0.490	0.600	0.750	0.650	0.500	0	0	0	0
-35	0	0	0	0	0.210	0.210	0.210	0	0	0	0	0
-40	0	0	0	0	0.120	0.120	0	0	0	0	0	0

(continued)

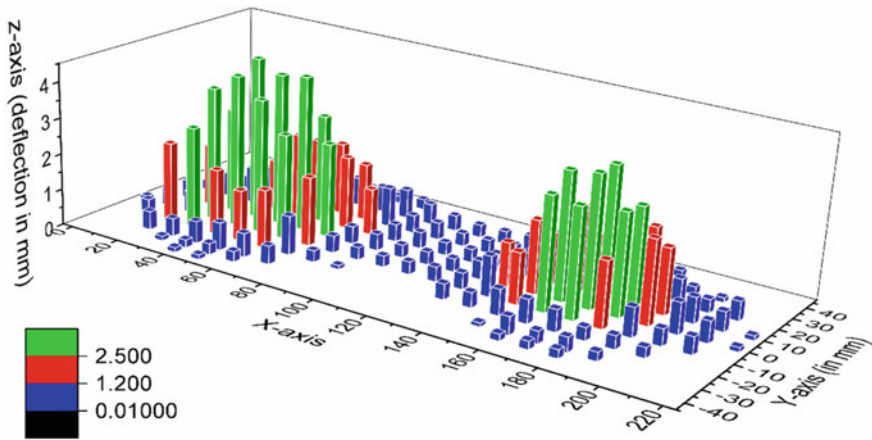


Fig. 7.9 Deflection of gradient shoe sole at various points for uniform load

References

1. Ning, F., Cong, W., Qiu, J., Wei, J., Wang, S.: Additive manufacturing of carbon fiber reinforced thermoplastic composites using fused deposition modeling. *Compos. Part B* **80**, 369–378 (2015). <https://doi.org/10.1016/j.compositesb.2015.06.013>
2. Kou, X.Y., Tan, S.T.: Heterogeneous object modeling: a review. *Comput. Aided Des.* **39**, 284–301 (2007). <https://doi.org/10.1016/j.cad.2006.12.007>
3. Wu, X., Liu, W., Wang, M.Y.: A CAD modeling system for heterogeneous object. *Adv. Eng. Softw.* **39**, 444–453 (2008). <https://doi.org/10.1016/j.advengsoft.2007.03.002>
4. Gupta, V., Kasana, K.S., Tandon, P.: Computer aided design modeling for heterogeneous objects. *Int. J. Comput. Sci. Issues* **7**(2) (2010)
5. Wang, M.Y., Wang, X.: A level-set based variational method for design and optimization of heterogeneous objects. *Comput. Aided Des.* **37**, 321–337 (2005). <https://doi.org/10.1016/j.cad.2004.03.007>
6. Qian, X., Dutta, D.: Feature-based design for heterogeneous objects. *Comput. Aided Des.* **36**, 1263–1278 (2004). <https://doi.org/10.1016/j.cad.2004.01.012>
7. Watari, F., Kondo, H., Matsuo, S., Miyao, R., Yokoyama, A., Omori, M., Hirai, T., Tamura, Y., Uo, M., Ohara, N., Kawasaki, T.: Development of functionally graded implant and dental post for bio-medical application. *Mater. Sci. Forum* **423–425**, 321–326 (2003). <https://doi.org/10.4028/www.scientific.net/MSF.423-425.321>
8. Mahamood, R.M., Akinlabi, E.T.: Functionally graded material: an overview, vol. III. In: *Proceedings of the World Congress on Engineering*, London, UK (2012)
9. Gupta, B.: Few studies on biomedical applications of functionally graded material. *Int. J. Eng. Technol. Sci. Res.* **4**(3), 2394–3386 (2017)
10. Sai, H.B.V.: Review on functionally gradient materials (FGMs) and their applications. *Int. J. Curr. Eng. Technol.* **8** (2018). <https://doi.org/10.14741/ijcet.v8i01.10894>
11. Abbas, T.F., Othman, F.M., Ali, H.B.: Effect of infill parameter on compression property in FDM process. *Int. J. Eng. Res. Appl.* **7**(10), 16–19 (2017). <https://doi.org/10.9790/9622-0710021619>
12. Baich, L., Manogharan, G.: Study of infill print parameters on mechanical strength and production cost-time of 3D printed ABS parts. *Int. J. Rapid Manuf.* **5** (2015). <https://doi.org/10.1504/ijrapidm.2015.074809>

13. Kumar, N., Shaikh, S., Jain, P.K., Tandon, P.: Effect of fractal curve based toolpath on part strength in fused deposition modelling. *Int. J. Rapid Manuf.* **5**(2) (2015). <https://doi.org/10.1504/ijrapidm.2015.073576>
14. Shaikh, S., Kumar, N., Jain, P.K., Tandon, P.: Hilbert curve based toolpath for FDM process. In: Mandal, D.K., Syan, C.S. (eds.) *CAD/CAM, Robotics and Factories of the Future*, pp. 751–759. Springer, New Delhi (2016). https://doi.org/10.1007/978-81-322-2740-3_72
15. Papacharalampopoulos, A., Bikas, H., Stavropoulos, P.: Path planning for the infill of 3D printed parts utilizing Hilbert curves. *Procedia Manuf.* **21**, 757–764 (2018). <https://doi.org/10.1016/j.promfg.2018.02.181>
16. Roger, F., Krawczak, P.: 3D-printing of thermoplastic structures by FDM using heterogeneous infill and multi-materials: an integrated design-advanced manufacturing approach for factories of the future. In *22nd Congrès Français de Mécanique Conference*, Lyon, France (2015)
17. Foot pressure distribution. <https://en.wikipedia.org/wiki/Pedobarography>. Accessed 15 May 2018

Chapter 8

Tensile Strength of 3D Printed PLA Part



Shilpesh R. Rajpurohit  and Harshit K. Dave 

Abstract Fused deposition modeling (FDM)-based 3D printing is one of the most widely used additive manufacturing (AM) techniques that can build a part with any complexity. FDM-processed parts have a wide range of applications in various fields such as aerospace, medical, automobile, and consumer part industries. However, its application may be restricted due to poor mechanical properties of parts because of the layer-by-layer forming of parts. Due to this, the application of FDM-processed part restricted as end-use functional parts. In the present investigation, an attempt has been made to study the effect of key process variables on the tensile strength of the printed part. Three process variables viz. raster angle, raster width, and layer height have been varied to study their influence on the tensile strength of the PLA part. Further, microscopic examination was carried out to understand the effect of process variables on the fractured surface.

Keywords Fused deposition modeling (FDM) · Polylactic acid (PLA) · Tensile strength · Raster angle · Raster width · Layer height

8.1 Introduction

The term additive manufacturing (AM) is defined by ASTM F42 committee as “Process of joining materials to make a 3D object from 3D model data, usually, layer upon layer as opposed to subtractive manufacturing method such as traditional machining” [1]. Fused Deposition modeling (FDM) is one of the widely used AM techniques due to its simplicity, low cost, and easy to operate. In FDM process, polymer filament is fed into a heated nozzle, and then, semi-liquid filament is extruded through the nozzle and deposited on the heated bed to form the object layer by layer as defined by CAD data [2, 3].

S. R. Rajpurohit (✉) · H. K. Dave
Department of Mechanical Engineering, Sardar Vallabhbhai National Institute of Technology,
Surat 395007, India
e-mail: shilpesh18@gmail.com

© Springer Nature Singapore Pte Ltd. 2020
M. S. Shunmugam and M. Kanthababu (eds.), *Advances in Additive Manufacturing and Joining*, Lecture Notes on Multidisciplinary Industrial Engineering,
https://doi.org/10.1007/978-981-32-9433-2_8

FDM printed parts have a wide range of application in the field of automobile, aerospace, biomedical and consumer part industries, and so on. However, the poor mechanical properties of the FDM printed part restrict the application of the 3D printed part. Mechanical performance of the 3D printed part may be enhanced by a proper selection of process variables. Recently, researchers have carried out some works in order to enhance the mechanical performance of the 3D printed component.

Dong et al. [4] examined the impact of infill density, layer thickness, and number of perimeters on mechanical properties of FDM printed PLA and PLA/wood fiber composite. They observed the higher mechanical strength of PLA samples than those of the samples printed using a composite filament. Rankouhi et al. [5] investigated the tensile properties of FDM-processed ABS material against layer thickness and orientation. Uddin et al. [6] examined the impact of layer height, build direction, and layer orientation on the tensile and compressive strength of FDM build part. Part printed in YZ plane with a smaller layer thickness displayed the better yield strength. Build orientation does not have any significance on compressive strength of build part. Li et al. [7] studied the bonding degree and tensile strength with respect to the layer thickness, print speed, and infill percentage. The bonding strength is significantly affected by layer height followed by print speed and infill percentage. Higher bonding strength helps to improve tensile strength. Aliheidari et al. [8] investigated the effect of nozzle temperature on the fracture resistance of the 3D printed ABS material. The surface intact ratio was increased to 53% with increment in nozzle temperature that improves the fracture resistance of the build part. Wang et al. [9] investigated the influence of bed temperature and layer height on impact strength of FDM build PLA part. Part built with 160 °C bed temperature and 0.2 mm layer height displayed a higher impact strength. Tymrak et al. [10] examined the tensile strength of printed components using the different open source 3D printer. Lederle et al. [11] printed the part in a nitrogen atmosphere. They observed a significant increase in tensile strength. Mohamed et al. [12] studied the influence of process parameters on the flexural creep stiffness of PC-ABS printed part. They observed that flexural creep stiffness could be improved with numbers of perimeters, lower layer height, and zero air gap. Ahn et al. [13] suggested a negative air gap improves the strength of the part. Compression strength of the FDM part is higher than that of tensile strength. Torrado et al. [14] reported that vertically build specimen has lower tensile strength than horizontally build specimen. Lanzotti et al. [15] examined the impact of layer height, infill angle, and numbers of shell perimeters on the mechanical strength of the PLA printed part. Tensile strength is observed to be decreased with increase in infill angle and increases with increment in shell perimeters. Huang et al. [16] reported that higher tensile strength can be obtained with 0° raster angle. Tanikella et al. [17] examined the tensile strength of the different commercially available feedstock filaments. They obtained the maximum tensile strength of 49 MPa with polycarbonate material.

Some work has been initiated to study the mechanical performance of the FDM printed part. However, research on the mechanical performance of FDM is still on the preliminary stage. Majority of the work has been carried out in order to understand the relationship between raster angle and build orientation on the mechanical properties of the printed part. Effect of raster width and layer height has not been much explored.

Layer height and raster width have been significantly affecting the building accuracy and build time. So, it is necessary to study their impact on the mechanical strength to build a stronger part within a reasonable time and accuracy. In the present study, an attempt has been made to investigate the effect of raster angle, raster width, and layer height on the tensile strength of the build part. The effect of process variables on the fracture pattern is also investigated.

8.2 Experimental Details

8.2.1 Material and Experimental Setup

PLA monofilament (esun3d Filament, China) having of 1.75 mm diameter has been used to fabricate the entire tensile specimen. OMEGA Dual extruder 3D printer (JAK Machinery, India) has been used in the present study. All the specimens printed with 100% infill density and rectilinear pattern. The PLA material is deposited at an extrusion temperature of 210 °C at the deposition speed of 50 mm/s, and the bed temperature is set at the 70 °C.

8.2.2 Tensile Testing

Tensile tests were performed on a Tinius Olsen H50KL universal testing machine, which is furnished with 50 kN load cell. FDM produced dog-bone tensile specimens (180 mm × 19 mm × 3.2 mm) were tested until the sample fractured at the straining rate of 5 mm/min according to ASTM D638 standard.

For the fractographic analysis, an SDM TRZ 5300 high precession measuring microscope (Sipcon Instrumental Industries) was used to analyze the fractured cross-sectional area of test specimens.

8.2.3 Process Parameters and Experimental Design

In this study, three build variables namely raster angle, layer height, and raster width have been varied as given in Table 8.1.

Three build variables have been varied at three levels, so according to full factorial experimental design, total 27 experimental runs have been performed as listed in Table 8.2. The entire set of experiments have been repeated twice to ensure the repeatability of the experiments.

Table 8.1 Process variable and their levels

Process variable	Level		
	1	2	3
Raster angle (°)	0	45	90
Layer height (µm)	100	200	300
Raster width (µm)	400	500	600

Table 8.2 The experimental result obtained through full factorial experimental design

S. No.	Raster angle (°)	Layer height (µm)	Raster width (µm)	Mean tensile strength (MPa)	S/N ratio
1	0	100	400	46.80	33.4049
2	0	100	500	44.50	32.9672
3	0	100	600	47.30	33.4972
4	0	200	400	41.20	32.2979
5	0	200	500	42.20	32.5062
6	0	200	600	45.70	33.1983
7	0	300	400	41.95	32.4546
8	0	300	500	46.65	33.3770
9	0	300	600	38.50	31.7092
10	45	100	400	44.15	32.8986
11	45	100	500	31.80	30.0485
12	45	100	600	45.15	33.0932
13	45	200	400	33.95	30.6168
14	45	200	500	32.95	30.3571
15	45	200	600	35.30	30.9555
16	45	300	400	38.80	31.7766
17	45	300	500	36.30	31.1981
18	45	300	600	37.65	31.5153
19	90	100	400	41.50	32.3610
20	90	100	500	23.80	27.5315
21	90	100	600	40.45	32.1384
22	90	200	400	29.25	29.3225
23	90	200	500	26.35	28.4156
24	90	200	600	35.00	30.8814
25	90	300	400	36.95	31.3523
26	90	300	500	34.10	30.6551
27	90	300	600	34.50	30.7564

8.3 Results and Discussion

In this experimental study, full factorial experiments were performed to determine the impact of build variables on the tensile strength of the FDM fabricated PLA part. The results were converted into the S/N ratio using “larger-the-better” characteristics, as it desired to have maximum tensile strength. The mean tensile strength and S/N ratio for the tensile strength are shown in Table 8.2.

Figure 8.1 shows the effect of the main plot of process variable on the S/N ratio of tensile strength. It can be seen that optimal condition to obtain higher tensile strength is raster angle at 0°, layer height at 100 μm, and raster width at 600 μm. It can also be observed that the raster angle has a strong influence on the tensile strength of the 3D printed part. The interaction effect of build variables on the tensile strength has been shown in Fig. 8.2. A significant interaction between layer height and raster width can be seen.

Further, analysis of variance (ANOVA) was carried out in order to identify the significant process variable on the tensile strength. ANOVA results for S/N data of tensile strength are listed in Table 8.3. From the ANOVA, it can be stated that raster angle, raster width, the interaction of layer height and raster width, and layer height is statistically significant.

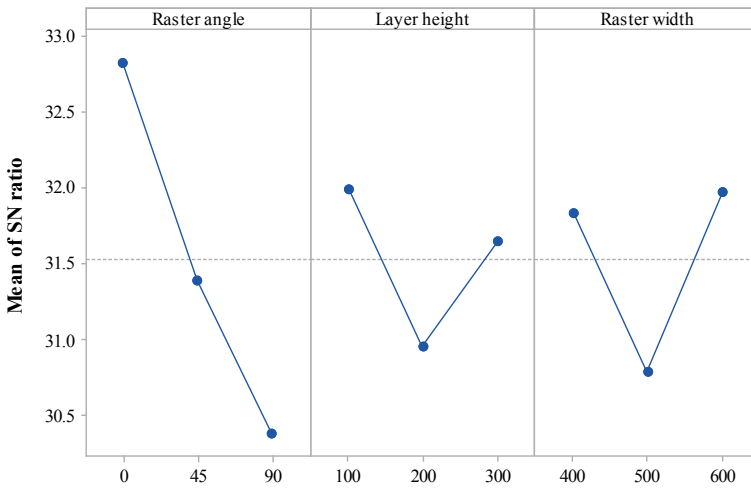


Fig. 8.1 Main effect plot of SN ratio for tensile strength

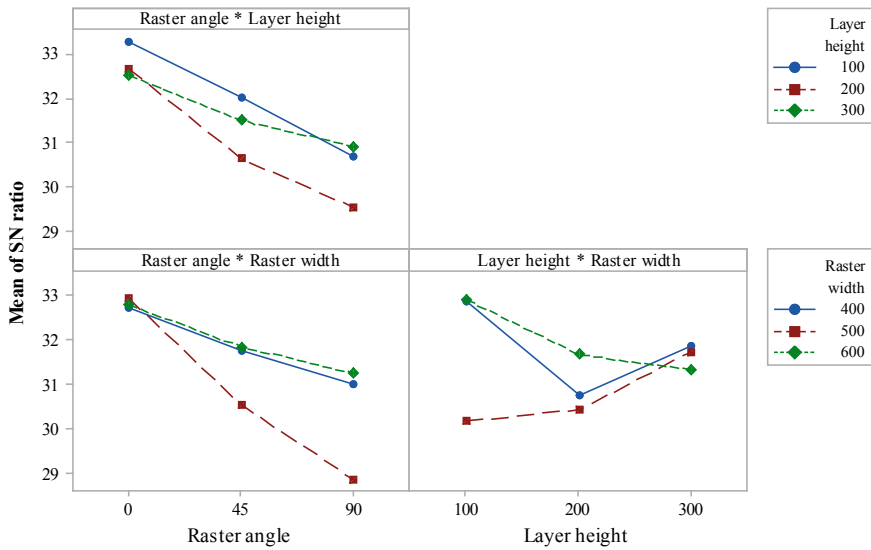


Fig. 8.2 Interaction effect plot of SN ratio for tensile strength

Table 8.3 Analysis of variance for tensile strength

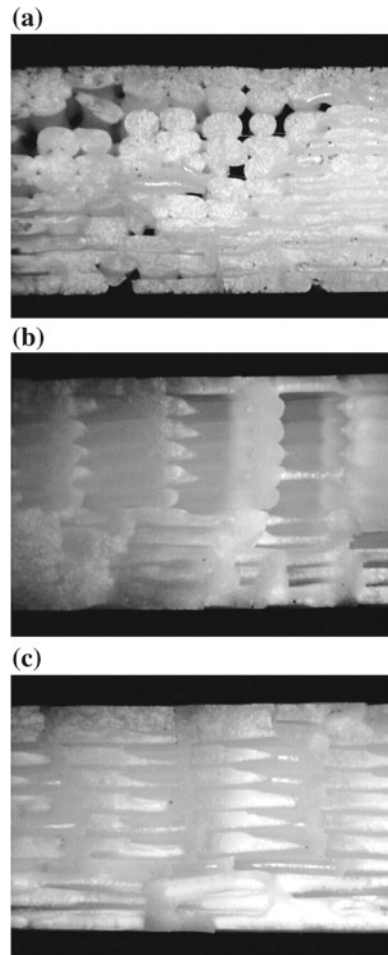
	DF	SS	MS	F-value	P-value
Raster angle	2	27.168	13.5481	43.34	0.000
Layer height	2	5.075	2.5376	8.10	0.012
Raster width	2	7.583	3.7913	12.10	0.004
Raster angle × Layer height	4	2.072	0.5181	1.65	0.252
Raster angle × Raster width	4	6.140	1.5350	4.90	0.027
Layer height × Raster width	4	10.189	2.5471	8.13	0.006
Error	8	2.508	0.3134		
Total	26	60.735			

8.3.1 Effect of Raster Angle

From Fig. 8.1, it is observed that tensile strength is found to be decreased with increment in raster angle. Higher tensile strength was obtained at 0° raster angle, while lower tensile strength was observed at 90° raster angle. Tensile strength at 45° raster angle mostly falls in between for 0° and 90°. At 0° raster angle, all the fibers are deposited parallel to the loading direction, which is capable to withstand more load as the effect of fiber bonding is minimized. The failure is taking place due

to pulling and breakage of the individual fiber, which has higher strength than the bonding between fibers. While during the 90° raster angle, all the fibers are deposited perpendicular to tensile loading. The failure is taking place due to breakage of fiber bonding that comparatively weakens than the monofilament that ultimately results in lower strength. In the case of 45° raster angle, fibers laid 45° to the tensile loading and failure take place due to shear between the fibers and breakage of the fibers. The tensile strength obtained at 45° raster angle mostly fall between the strength obtained with 0° and 90° raster angle. Figure 8.3 shows a microscopic image of a cross section of the fractured surface of the test specimen at various raster angle. It is observed that at 0° raster angle (shown in Fig. 8.3a), failure is taking place perpendicular to the loading direction. While during the 90° raster angle, failure is taking place through the bonding between the raster that creates plane surface known as planner fracture

Fig. 8.3 Microscopic image of a cross section of the fractured surface of the test specimen at **a** 0° raster angle, **b** 45° raster angle and **c** 90° raster angle at $300\ \mu\text{m}$ layer height and $600\ \mu\text{m}$ raster width



(Fig. 8.3c). Specimen printed with 45° raster angle, failure take place in line with the raster deposition direction (Fig. 8.3b).

8.3.2 Effect of Layer Height

Figure 8.1 shows that higher tensile strength is obtained at a smaller layer height. At the smaller layer height, a larger bonding area was observed with lesser voids that improve the performance of the test specimen. Higher extrusion pressure is required to deposit the molten bead at a smaller layer height. Higher extrusion pressure improves the contact area among the layers that results in stronger bonding between the layers, and tensile strength of the part has been enhanced. Smaller bonding area and a number of voids were observed for the specimen with a larger layer height that reduces the strength of the part. Figure 8.4 shows a microscopic image of a cross section of the fractured surface of the test sample at various layer height. At the higher layer height, the smaller bonding area between layers can be observed due to the presence of the voids that may be a reason to reduce the tensile strength of the FDM-processed part.

8.3.3 Effect of Raster Width

Influence of the raster width has been shown in Fig. 8.1. It is observed that higher tensile strength has been obtained with a higher value of the raster width. Larger raster width has more thermal mass, which allows it to cool slowly. Raster remains more time above the glass transition temperature as it takes more time to solidify. It improves the joining process among the rasters that results in a larger bonding area with the smaller amount of voids. Less void generation and larger bonding area are displayed the higher tensile performance of the part. Figure 8.5 shows a microscopic image of a cross section of the fractured surface of the test specimen at various raster width. At higher raster width, larger bonding can be seen (Fig. 8.5c) due to the high amount of heat possessed by raster, which reduces the generation voids between the layers. While a number of voids can be observed with lower raster width, which may act as a crack initiator and reduces the tensile strength.

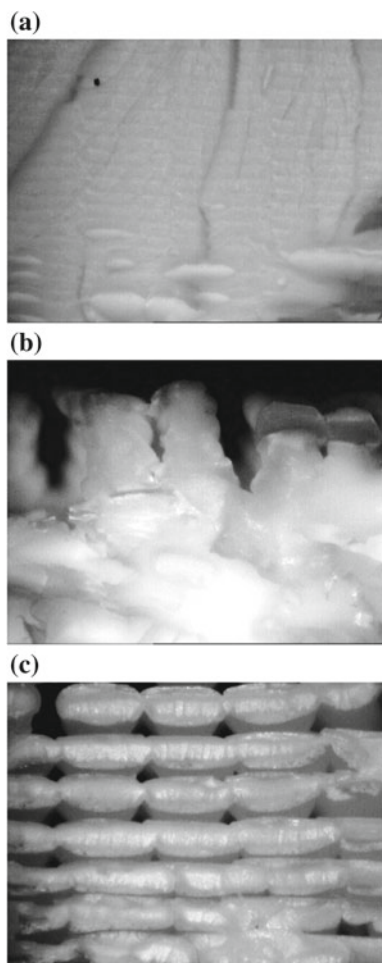


Fig. 8.4 Microscopic image of a cross section of the fractured surface of test specimen at **a** 100 μm layer height, **b** 200 μm layer height and **c** 300 μm layer height at 0° raster angle and 600 μm raster width

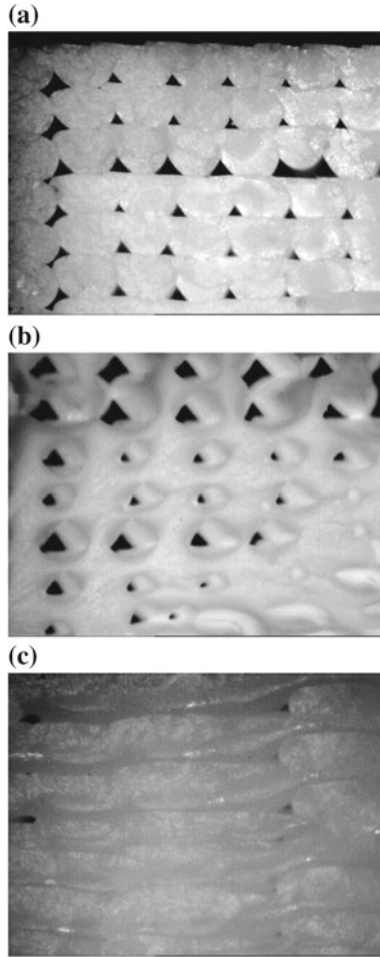


Fig. 8.5 Microscopic image of a cross section of the fractured surface of the test specimen at **a** 400 μm raster width, **b** 500 μm raster width and **c** 600 μm raster width at 0° raster angle and 300 μm layer height

8.4 Conclusions

The tensile strength of the 3D printed PLA samples was successfully studied in the present investigation. Effect of raster angle, layer height, and raster width were varied to identify their influence on the tensile performance of the part. S/N ratio and the ANOVA method have been employed to identify the significant process variables on the tensile strength of the printed part. Raster angle is found to be the most significant process parameter that affects the tensile strength. Individual fiber is capable to withstand a higher load than the bonding between the fibers that results in higher tensile strength. Furthermore, the cross section of the fractured surface of the part has been microscopically examined to understand the relation between the mode of failure and process variables. Fracture pattern is highly dependent on the angle of raster deposition. A number of voids have also appeared on the cross-sectional surface that leads to the brittle failure with low ductility.

References

1. ASTM: F2792-12 Standard Terminology for Additive Manufacturing Technologies. ASTM International, USA (2012)
2. Chua, C.K., Leong, K.F.: 3D Printing and Additive Manufacturing: Principles and Applications of Rapid Prototyping. World Scientific Publishing Co Inc., Singapore (2014)
3. Gibson, I., Rosen, D.W., Stucker, B.: Additive Manufacturing Technologies. Springer, New York (2010)
4. Dong, Y., Milentis, J., Pramanik, A.: Additive manufacturing of mechanical testing samples based on virgin poly (lactic acid)(PLA) and PLA/wood fibre composites. *Adv. Manuf.* **6**(1), 71–82 (2018). <https://doi.org/10.1007/s40436-018-0211-3>
5. Rankouhi, B., Javadpour, S., Delfanian, F., Letcher, T.: Failure analysis and mechanical characterization of 3D printed ABS with respect to layer thickness and orientation. *J. Fail. Anal. Prev.* **16**(3), 467–481 (2016). <https://doi.org/10.1007/s11668-016-0113-2>
6. Uddin, M.S., Sidek, M.F.R., Faizal, M.A., Ghomashchi, R., Pramanik, A.: Evaluating mechanical properties and failure mechanisms of fused deposition modeling acrylonitrile butadiene styrene parts. *J. Manuf. Sci. Eng.* **139**(8), 081018 (2017). <https://doi.org/10.1115/1.4036713>
7. Li, H., Wang, T., Sun, J., Yu, Z.: The effect of process parameters in fused deposition modelling on bonding degree and mechanical properties. *Rapid Prototyping J.* **24**(1), 80–92 (2018). <https://doi.org/10.1108/RPJ-06-2016-0090>
8. Aliheidari, N., Tripuraneni, R., Ameli, A., Nadimpalli, S.: Fracture resistance measurement of fused deposition modeling 3D printed polymers. *Polym. Test.* **60**, 94–101 (2017). <https://doi.org/10.1016/j.polymertesting.2017.03.016>
9. Wang, L., Gramlich, W.M., Gardner, D.J.: Improving the impact strength of poly (lactic acid)(PLA) in fused layer modeling (FLM). *Polymer* **114**, 242–248 (2017). <https://doi.org/10.1016/j.polymer.2017.03.011>
10. Tymrak, B.M., Kreiger, M., Pearce, J.M.: Mechanical properties of components fabricated with open-source 3-D printers under realistic environmental conditions. *Mater. Des.* **58**, 242–246 (2014). <https://doi.org/10.1016/j.matdes.2014.02.038>

11. Lederle, F., Meyer, F., Brunotte, G.P., Kaldun, C., Hübner, E.G.: Improved mechanical properties of 3D-printed parts by fused deposition modeling processed under the exclusion of oxygen. *Prog. Add. Manuf.* **1**(1–2), 3–7 (2016). <https://doi.org/10.1007/s40964-016-0010-y>
12. Mohamed, O.A., Masood, S.H., Bhowmik, J.L.: Investigation on the flexural creep stiffness behavior of PC–ABS material processed by fused deposition modeling using response surface definitive screening design. *JOM* **69**(3), 498–505 (2017). <https://doi.org/10.1007/s11837-016-2228-z>
13. Ahn, S.H., Montero, M., Odell, D., Roundy, S., Wright, P.K.: Anisotropic material properties of fused deposition modeling ABS. *Rapid Prototyping J.* **8**(4), 248–257 (2002). <https://doi.org/10.1108/13552540210441166>
14. Torrado, A.R., Roberson, D.A.: Failure analysis and anisotropy evaluation of 3D-printed tensile test specimens of different geometries and print raster patterns. *J. Fail. Anal. Prev.* **16**(1), 154–164 (2016). <https://doi.org/10.1007/s11668-016-0067-4>
15. Lanzotti, A., Grasso, M., Staiano, G., Martorelli, M.: The impact of process parameters on mechanical properties of parts fabricated in PLA with an open-source 3-D printer. *Rapid Prototyping J.* **21**(5), 604–617 (2015). <https://doi.org/10.1108/RPJ-09-2014-0135>
16. Huang, B., Singamneni, S.: Raster angle mechanics in fused deposition modelling. *J. Compos. Mater.* **49**(3), 363–383 (2015). <https://doi.org/10.1177/0021998313519153>
17. Tanikella, N.G., Wittbrodt, B., Pearce, J.M.: Tensile strength of commercial polymer materials for fused filament fabrication 3D printing. *Add. Manuf.* **15**, 40–47 (2017). <https://doi.org/10.1016/j.addma.2017.03.005>

Chapter 9

Study of Residual Stress in Nickel Micro Parts Made by Electrochemical Additive Manufacturing



Anne Brant, Abishek Kamaraj and Murali Sundaram

Abstract Electrochemical additive manufacturing (ECAM) is a novel process which uses localized electrochemical deposition as the material addition mechanism for additive manufacturing (AM) of metal parts at room temperature. While ECAM possesses highly controllable process parameters, complex electrochemical phenomena, such as nucleation patterns and hydrogen codeposition, may cause residual stresses in the output parts. To better predict this behavior for increased reliability and future commercial adoption of ECAM, localized deposits were studied under several controlled combinations of electrochemical process parameters under both constant-time and constant-height termination criteria. The residual stress was then measured using an atomic force microscopy (AFM) indentation procedure. Significant trends that were found include increased stress magnitude with increasing applied voltage, and the higher influence of voltage and then pulse period on the resulting stress, compared to the duty cycle. It was also seen that shorter deposition times led to compressive stresses and longer times led to tensile stresses.

Keywords Additive manufacturing · Electrodeposition · Residual stress

9.1 Introduction

Additive manufacturing (AM) methods are increasingly being used to manufacture functional parts. A significant amount of applications are present in the biomedical and aerospace industries, where highly customized parts are needed. However, the lack of industry confidence in the material properties of the parts curbs the widespread use of these processes. While some AM processes such as selective laser melting and electron beam melting are capable of producing parts on par with or even superior to conventionally machined ones, they suffer from very high residual stresses due to the complete melting of the material during manufacturing [1]. Also, traditional AM techniques have limitations such as choice of material, anisotropy, porosity, strength,

A. Brant · A. Kamaraj · M. Sundaram (✉)
University of Cincinnati, Cincinnati, OH 45221, USA
e-mail: murali.sundaram@uc.edu

© Springer Nature Singapore Pte Ltd. 2020
M. S. Shunmugam and M. Kanthababu (eds.), *Advances in Additive Manufacturing and Joining*, Lecture Notes on Multidisciplinary Industrial Engineering,
https://doi.org/10.1007/978-981-32-9433-2_9

scalability, support structure, thermal defects, and internal stresses. For example, high residual stresses (>200 MPa) are caused by the thermal gradient associated with sintering processes. Thus, even though AM processes are capable of producing any design, the residual stresses impart constraints on the wall thickness of the parts that are being produced.

Electrochemical additive manufacturing (ECAM) is a novel additive manufacturing process, which can manufacture 3D metal parts at room temperature directly from 3D model files. ECAM combines the principles of localized electrochemical deposition (LECD) with the layer-by-layer manufacturing procedure of additive manufacturing to create parts directly from 3D CAD models [2]. The ECAM process flow is illustrated as a schematic in Fig. 9.1.

LECD is capable of depositing most conductive materials, including metals, metal alloys, conducting polymers, and even some semiconductors [4]. It is a process of material addition that is electrochemical in nature (atom-by-atom); thus, the properties of the deposited materials can be modified as desired by varying the specific process parameters shown to yield the desired result. The residual stresses associated with the pulsed electrodeposition and electroforming processes are expected to be negligible as compared to those of sintering and melting processes. However, LECD is not totally a stress-free additive manufacturing process.

For example, electrochemical co-deposition of metal hydrides along with the metal is known to cause residual stresses during the electrodeposition process [5]. These stresses cause the deposited material to distort, which is especially pronounced in the case of micro components. Another cause for residual stresses in electrodeposits is from the mechanism of nucleation and growth of grains resulting in stresses

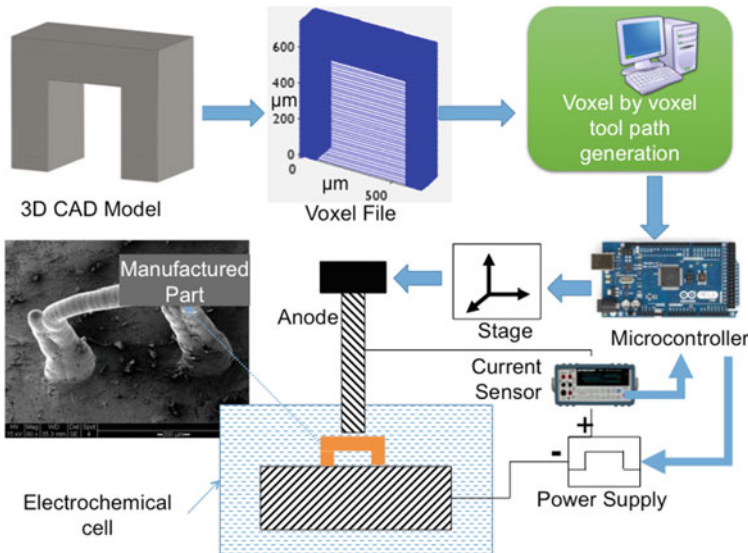


Fig. 9.1 Illustration of the steps involved in the electrochemical additive manufacturing [3]

both compressive and tensile. Both these mechanisms offer contradicting effects of current density on the internal stresses. While in some cases, higher current density increases the stresses [5], in others, the opposite effect is noticed [6].

Despite these considerations, ECAM still possesses advantages over related processes. For example, micro-electroformed parts are prone to local residual stress gradients. Prior work shows this can be mitigated by pre-setting a stress-release geometry [7]. However, this requires extra work and analysis that must be performed for each geometry, which would add to time, cost, and labor in manufacturing. Additionally, there could be a risk of damage and inconsistency in the part due to the stress release process. In contrast, ECAM allows for locally controllable electrochemical parameters that then give controllable residual stress at the local level for micro parts.

Compared to these other processes, the ECAM process has a significant versatility in local control of input and output parameters, including residual stress. It is therefore highly valuable to gain an understanding of the relationships between input and output parameters. Control of residual stress allows for its minimization, which results in better repeatability and reliability [8]. These are critical steps for ECAM to become a commercially viable additive manufacturing process.

In this work, the effects of varying deposition parameters using pulsed current were studied. Pulsed power during electrodeposition produces parts with higher strength when compared to parts made using DC power [9]. Input parameters included constant time versus height conditions, voltage, pulse period, and duty cycle.

9.2 Experimental Methods

9.2.1 Electrochemical Deposition

The experimental setup is given in Fig. 9.2. Watts bath was used as the electrolyte. A side-insulated platinum microelectrode and a highly polished brass metal plate were used as the anode and cathode, respectively. A pulsed power supply was used to provide square current pulses with varying levels of voltages, duty cycles, and pulse periods. Multiple trials of the deposits under each experimental condition were made to minimize the effect of experimental variations. One set of trials was performed under a constant gap condition, and another set of trials was performed at the same initial inter-electrode gap, but for constant-time conditions. All parameters are summarized in Table 9.1.

9.2.2 Residual Stress Measurement

Overview. An existing nanoindentation technique of measuring residual stresses [10] was adapted for use with the atomic force microscope (AFM) in this study.

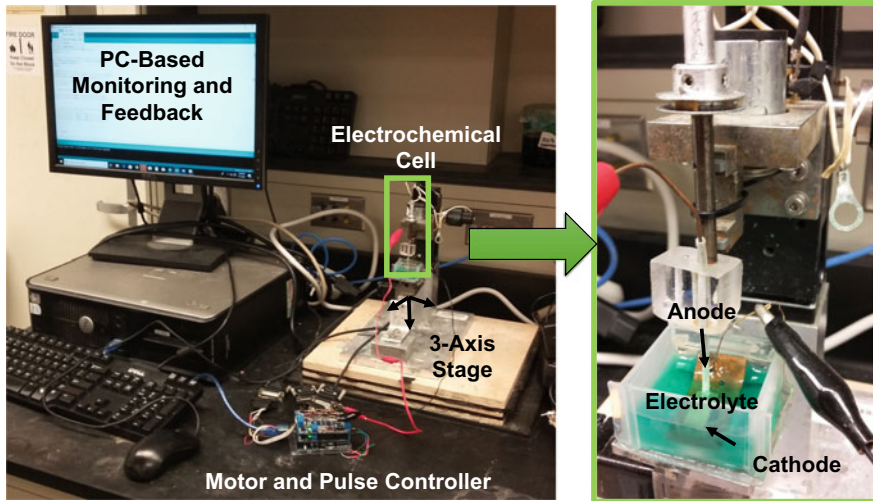


Fig. 9.2 ECAM experimental setup

Table 9.1 Levels of the experimental parameters used in this study

Process parameter	Levels
Voltage (V)	3, 4, 5
Pulse period (ns)	100, 200
Duty cycle (%)	50, 75
Initial inter-electrode gap (μm); all trials	10
Total deposition time (s); constant-time trials	30

This technique uses the retraction force-indentation curves from indentation into the parts to determine the magnitude and type (compressive or tensile) of residual stress. Figure 9.3 illustrates how the force P acts on the deposit and the indentation depth h physically observed during the AFM indentation process, and Fig. 9.3a illustrates the form of a typical force-indentation ($P-h$) curve for an AFM tip of angle 2γ . Only the retraction curve is necessary to calculate the residual stress, detailed in further equations.

Figure 9.3a also illustrates the phenomena that occur when an AFM tip of angle 2γ is indented into the sample. When the stress is tensile, as shown in Fig. 9.3b, the material is easier to indent, and the force-indentation curve is less steep than the curve of an unstressed sample of the same composition (referred to as the reference curve). When the stress is compressive, as shown in Fig. 9.3c, the material is not as easy to indent, and the force-indentation curve is steeper relative to the reference curve [10]. Furthermore, the illustrations show that the phenomena that occur at tensile and compressively stressed elements are not completely opposite. For the compressive element, the value of α corresponds to the angle between the tip of the

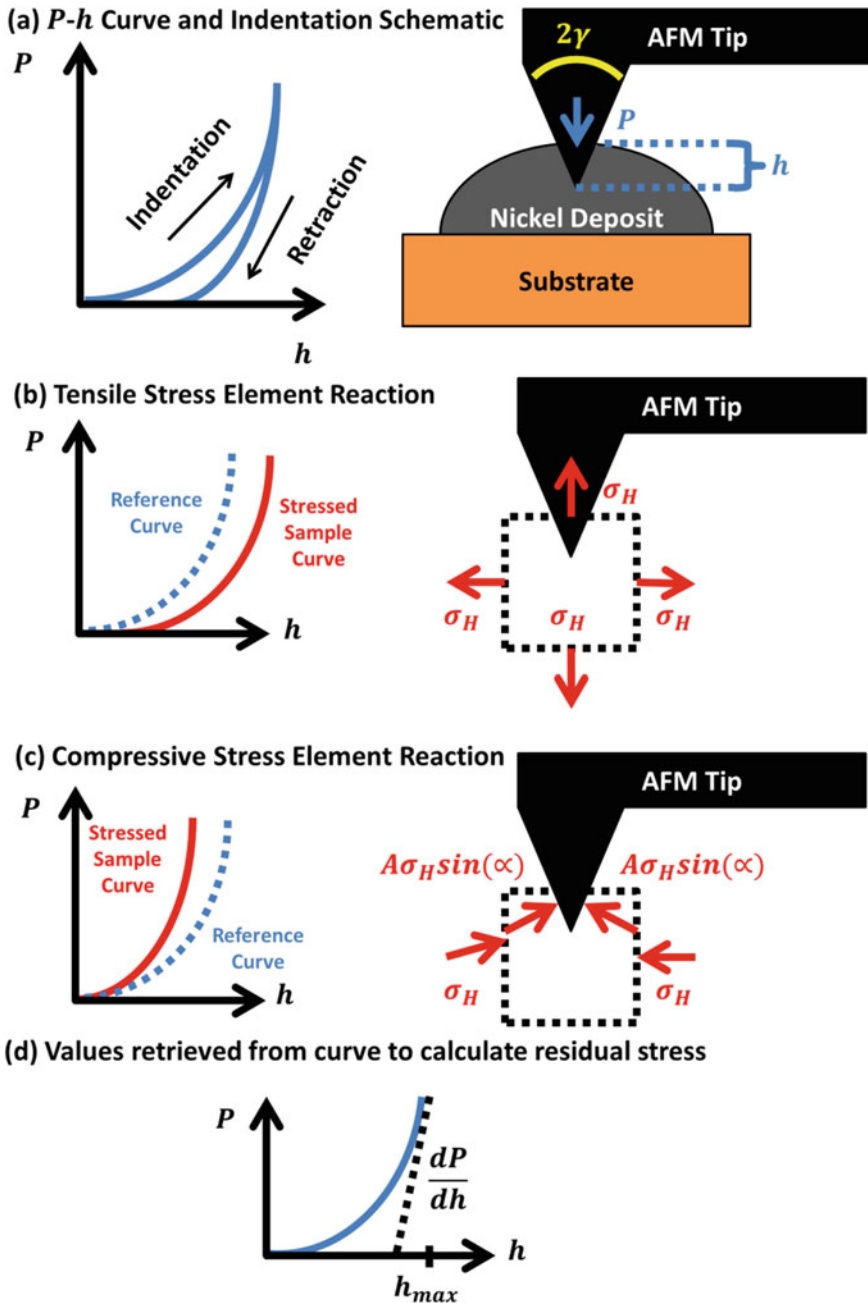


Fig. 9.3 *P-h* curve interpretation and AFM indentation mechanisms

AFM and the horizontal:

$$\alpha = \gamma - \frac{\pi}{2} \quad (9.1)$$

For small parts manufactured at the micro- and nanoscale, it is more advantageous to use the AFM instead of a conventional nanoindenter. A typical Berkovich indenter tip radius is in the range of 50–150 nm and imparts a force of the order of several mN [11], while the AFM tips used in this experiment have a tip radius between 8 and 35 nm and impart a force in a range of several μN . Because the smaller tip of the AFM imparts less force, there is less risk of damage to the small part. Also, since the electrodeposited parts are constructed atom by atom, a smaller tip gives a more accurate account of the material behavior of the part at the atomic scale.

Preparation. An AFM with contact mode and force curve plotting capability is used to measure the residual stress in the electrodeposited parts. An equivalent Young's modulus E^* is calculated from Young's modulus and Poisson's ratio for both the sample material and AFM probe [10]:

$$E^* = \left(\frac{1 - \nu^2}{E} + \frac{1 - \nu_{\text{in}}^2}{E_{\text{in}}} \right) \quad (9.2)$$

where

- ν Poisson's ratio of the substrate
- E Young's modulus of the substrate
- ν_{in} Poisson's ratio of the indenter
- E_{in} Young's modulus of the indenter

The following assumptions were used in the measurement process. They are a combination of assumptions used in experiments by Suresh and Giannakopoulos [10], as well as assumptions specific to the electrodeposition and AFM measurement.

1. The residual stress σ_{H} is equibiaxial across any given element on the surface of the measured part.
2. The stresses are uniform beneath to a depth of influence d_{R} , which is a function of A , the contact area between the indenter and the sample.
3. $d_{\text{R}} = 7\sqrt{A\pi}$ (9.3)
4. The sample is isotropic and permitted to undergo isotropic strain hardening.
5. The sample is pre-stressed from the electrodeposition process.
6. The indentation process is frictionless and quasi-static (infinitely slow thermodynamically).
7. In a nanoindentation procedure, the applied force P is proportional to the square of the indentation depth h , following Kick's Law: $P = Ch^2$ where C is a constant.
8. The AFM probe is assumed to be pyramidal, which corresponds to a C_{u} value of 1.167. This is a constant that will be used in the residual stress calculations.

Procedure

1. Each sample was indented with an AFM tip to a constant probe deflection of d_{\max} throughout all trials of the experiment. The data points for the retracting portion of the force curve were saved by the proprietary AFM software in a probe deflection versus sample height (d vs. Z) plot.
2. The d versus Z values at each point were converted into P and h values using the following relations. First, Hooke's law was applied to find the force between the probe and sample, using $k = 40 \text{ N/m}$ as the nominal spring constant of the AFM probe used in the experiment. This was also applied to convert d_{\max} into its equivalent force value P_{\max} .

$$\begin{aligned} P &= kd \\ P_{\max} &= kd_{\max} \end{aligned} \quad (9.4)$$

Then, the indentation height was found by computing the probe height Z_{probe} as the reverse of the sample height and compensating for probe deflection:

$$Z_{\text{probe}} = -Z; \quad h = Z - d$$

3. The portion of the retracting force curve at maximum measured force value $(P_{\max})_{\text{meas}}$ was located. If this was a point, the point's P and h values were saved. If this was a plateau with several values of h , then only the point with the minimum h value was maintained and all points with greater values of h were discarded.
4. The point with the P value closest to $(P_{\max})_{\text{meas}} - P_{\max}$ was located. Its height and force values were denoted $h_{\text{normalize}}$ and $P_{\text{normalize}}$, respectively.
5. The point found in step 4 was defined as the zero force and zero height point; the curve was normalized relative to the zero point by subtracting $h_{\text{normalize}}$ from every h value and $P_{\text{normalize}}$ from every P value. After normalization, any points with h and P values below zero were discarded.
6. The constant C for each curve was computed by fitting the curve to the 2nd degree polynomial $P = Ch^2$, in accordance with Kick's Law.
7. The following values were retrieved for each fitted curve at the P_{\max} point, as illustrated in 3d.
 - a. $\frac{dP}{dh}$, the initial unloading slope of the curve
 - b. h_{\max} , the height of the curve
8. The area of indentation A and average contact pressure p_{avg} for each stressed curve were calculated using the following relation. This step was not necessary for the unstressed curve [10].

$$A = \left(\frac{dp}{dh} \frac{1}{c_u E^*} \right)^2 \quad (9.5)$$

$$p_{\text{avg}} = \frac{P_{\text{max}}}{A} \quad (9.6)$$

9. Once all samples, including the unstressed sample, had undergone steps 1–7, the properties of each stressed sample curve were evaluated against the unstressed reference curve in each possible combination. In this experiment, each sample had five trials; therefore, five stressed curves evaluated against each of the five unstressed curves yielded a total of 25 analyses per sample.
 - a. First, the C polynomial coefficient of the stressed sample was compared to the corresponding C_o coefficient of the unstressed sample. If $C < C_o$, the residual stress was tensile. If $C > C_o$, the residual stress was compressive [10].
 - b. The tensile residual stress magnitude σ_H was calculated using the following relation [10]:

$$\left(\frac{h_{\text{max}}}{h_{\text{max}_o}} \right)^2 = \left(1 - \frac{\sigma_H}{p_{\text{avg}}} \right)^{-1} \quad (9.7)$$

The compressive residual stress magnitude σ_H was calculated using the following relation [10]:

$$\left(\frac{h_{\text{max}}}{h_{\text{max}_o}} \right)^2 = \left(1 + \frac{\sigma_H \sin \alpha}{p_{\text{avg}}} \right)^{-1} \quad (9.8)$$

In both relations, h_{max} corresponded to the stressed sample and h_{max_o} corresponded to the unstressed sample.

10. A positive sign is applied to the tensile residual stress values, and a negative sign to the compressive residual stress values.
11. All measured stress values were averaged for a given sample.

9.3 Results and Discussion

The constant-height trials are plotted in Fig. 9.4a, and the constant-time trials are plotted in Fig. 9.4b. The residual stress is plotted against the voltage, with separate lines for each duty cycle and pulse period combination, detailed in the legends.

For the constant-height trials, the residual stress was overall seen to increase with increasing applied voltage throughout the trials. For the constant-time trials, an overall decreasing trend was seen. The overall increasing trend for residual stress with respect to voltage for the constant-height trials suggests that higher residual stress is induced by higher current densities. The overall decreasing trend suggests

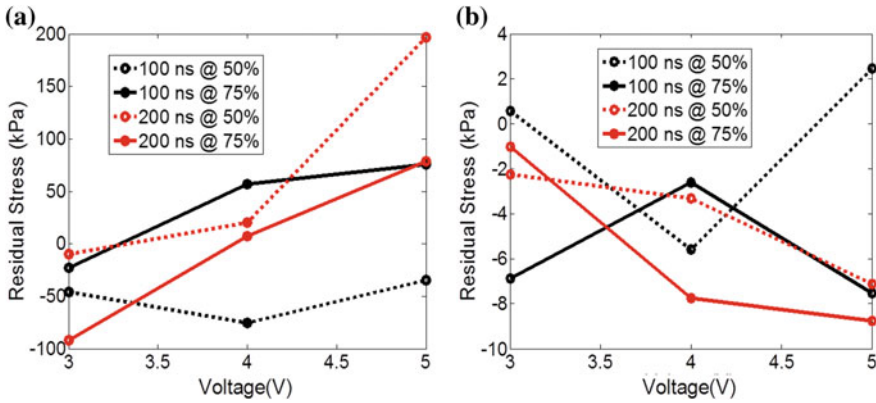


Fig. 9.4 Residual stress plots of **a** constant-height trials and **b** constant-time trials

that in the early stages of deposition at a higher voltage, a different mechanism occurs that increases the compressive stress in the part. The exceptions occurred when the pulse period was 100 ns and the duty cycle was 50% in the constant-height trials and both 50% duty cycle trials in the constant-time experiments.

Overall, for constant-height trials, which had a total deposition time of over a minute, the residual stress increase with voltage is lower in trials with a 100 ns pulse period, suggesting that it is optimal to lower the pulse period if parts need to be manufactured at higher voltages. For the constant-time trials, which lasted a shorter time, this trend did not exist. The stress ranges did not significantly vary among depositions of varying duty cycles and pulse periods. This suggests that the stresses did not develop to the full extent of the constant-height trials due to the shorter deposition time. Furthermore, lowering the duty cycle can cause the residual stress to decrease instead of increase, as seen in the data for the 100 ns pulse period 50% duty cycle trials for both constant-height and constant-time deposits, between 3 and 4 V. The opposite trend was seen for the 100 ns constant-time trial at 75% duty cycle, suggesting a different mechanism of deposition.

For the constant-height trials, increasing the applied duty cycle was seen to cause lower residual stress at a higher pulse period, while increasing the applied duty cycle was seen to cause higher residual stress at a lower pulse period. This indicates that the influence of the duty cycle on the residual stress of the deposit is dictated by the pulse period. At 4 V, for the constant-height trials, the resulting residual stress increased with increasing total pulse on time over an identical length of time. The data deviated from this relationship when 3 and 5 V were applied, suggesting a different mechanism of deposition at varying voltages.

9.4 Conclusions

According to literature, a lower current density yields a needle-like microstructure and a higher current density yields a coarser microstructure. This is correlated respectively with residual stress increasing from negative values to positive values. In the constant-height trials, this trend is clearly seen as a function of applied tool voltage, which is proportionally related to the resulting current density. As suggested in literature, this transition from negative to positive residual stress suggests that there is an optimal voltage and current density condition along this range that would yield zero residual stress [12].

The duty cycle has a different impact on the residual stress of the deposit, depending on the pulse period. At the lower pulse period, a higher duty cycle gave more positive residual stress in the deposit, suggesting a higher current density. At the higher pulse period, a higher duty cycle resulted in lower residual stress in the deposit, suggesting a lower current density. In electrochemistry, the current density always reaches a limiting value for a given set of parameters—the output residual stress may give a clue to the limiting current density occurring. Another explanation could be the fact that peak current density conditions give faster nucleation rates and a finer microstructure, which would lead to more negative residual stresses [13].

However, there is a significant deviation from any clear trends in the constant-time trials. This may be explained by the fact that higher current densities result in deposits of greater thickness variation, which then influences the resulting residual stress [12]. This would have been mitigated in the deposits that were grown to a consistent height, but not so in the constant-time deposits which could have grown to inconsistent heights. This suggests that a closed-loop control system may be preferable to an open-loop control system in order to ensure that the output ECAM parts are of a predictable residual stress.

Overall, the ECAM process holds advantages of traditional additive manufacturing, and other electroplating methods. Parts manufactured using the ECAM process exhibit residual stresses lower than traditional thermal-based additive manufacturing processes. The ECAM process also provides enhanced local control of the input parameters and therefore the output residual stress. Ideas for future work include the influence of additives in electrolyte [14], and the programmed control of plating current over time [15].

Acknowledgements Financial support provided by the National Science Foundation under Grant Nos. CMMI-1454181 and CMMI-1400800 is acknowledged.

References

1. Kruth, J.P., Froyen, L., Van Vaerenbergh, J., Mercelis, P., Rombouts, M., Lauwers, B.: Selective laser melting of iron-based powder. *J. Mater. Process. Technol.* **149**(1–3), 616–622 (2004)

2. Sundaram, M.M., Kamaraj, A.B., Kumar, V.S.: Mask-less electrochemical additive manufacturing: a feasibility study. *J. Manuf. Sci. Eng.* **137**(2), 021006 (2015)
3. Kamaraj, A.B., Sundaram, M.: A study on the effect of inter-electrode gap and pulse voltage on current density in electrochemical additive manufacturing. *J. Appl. Electrochem.* **48**(4), 463–469 (2018)
4. Bard, A.J., Huesser, O.E., Craston, D.H.: High resolution deposition and etching in polymer films. United States Patent No. 4,968,390 (1990)
5. Chan, K.C., Qu, N.S., Zhu, D.: Effect of reverse pulse current on the internal stress of electroformed nickel. *J. Mater. Process. Technol.* **63**(1–3), 819–822 (1997)
6. Basrou, S., Robert, L.: X-ray characterization of residual stresses in electroplated nickel used in LIGA technique. *Mater. Sci. Eng. A* **288**(2), 270–274 (2000)
7. Song, C., Du, L., Zhao, W., Zhu, H., Zhao, W., Wang, W.: Effectiveness of stress release geometries on reducing residual stress in electroforming metal microstructure. *J. Micromech. Microeng.* **28**(4), 045010 (2018)
8. Kume, T., Egawa, S., Yamaguchi, G., Mimura, H.: Influence of residual stress of electrodeposited layer on shape replication accuracy in Ni electroforming. *Procedia CIRP* **42**, 783–787 (2016)
9. Daryadel, S., Behroozfar, A., Morsali, S.R., Moreno, S., Baniyasi, M., Bykova, J., Bernal, R.A., Minary-Jolandan, M.: Localized pulsed electrodeposition process for three-dimensional printing of nanotwinned metallic nanostructures. *Nano Lett.* **18**(1), 208–214 (2018)
10. Suresh, S., Giannakopoulos, A.: A new method for estimating residual stresses by instrumented sharp indentation. *Acta Mater.* **46**(16), 5755–5767 (1998)
11. Li, X., Bhushan, B.: A review of nanoindentation continuous stiffness measurement technique and its applications. *Mater. Charact.* **48**(1), 11–36 (2002)
12. Kilinc, Y., Unal, U., Alaca, B.E.: Residual stress gradients in electroplated nickel thin films. *Microelectron. Eng.* **134**, 60–67 (2015)
13. Marro, J.B., Darroudi, T., Okoro, C.A., Obeng, Y.S., Richardson, K.C.: The influence of pulsed electroplating frequency and duty cycle on copper film microstructure and stress state. *Thin Solid Films* **621**, 91 (2017)
14. Lee, W., Lee, S., Kim, B., Kim, H.: Relief of residual stress of electrodeposited nickel by amine as additive in sulfamate electrolyte. *Mater. Lett.* **198**, 54–56 (2017)
15. Kao, L.C., Hsu, L.H., Brahma, S., Huang, B.C., Liu, C.C., Lo, K.Y.: Stabilized copper plating method by programmed electroplated current: accumulation of densely packed copper grains in the interconnect. *Appl. Surf. Sci.* **388**, 228–233 (2016)

Chapter 10

Laser Polishing of Wire Arc Additive Manufactured SS316L



Vinod Singh Thakur , M. Manikandan , Shalini Singh ,
Shivam Mishra , Ankit Kaithwas , S. S. Mani Prabu  and I. A. Palani 

Abstract This paper elucidates the surface analysis of laser polished SS316L samples fabricated using wire arc additive manufacturing (WAAM). The fabricated WAAM samples were polished using Nd: YAG laser source of wavelength 1064 nm at different power and the various number of passes such viz. 10 W, 10 W, and 25 W, and 8, 10, and 15, respectively. The roughness measurement was performed on before and after laser polishing by an optical profilometer and found that 40% of roughness was reduced after laser polishing. The crystal phase changes and hardness were also carried out and validated using XRD and hardness of the laser polished samples.

Keywords Laser polishing · Wire arc additive manufacturing · Surface roughness · Optical microscopy · SS316L

10.1 Introduction

The conventional manufacturing process is always consuming a huge amount of post-process such as machining, forming, welding, and heat treatment process for attaining final product. That post-processing also not enough to improve the mechanical properties and reduction of surface defects; hence, these processes are increasing the production cost of the product [1]. To overcome this, layer-by-layer material fabrication method is an aid to reduce the post-processing which process is termed as additive manufacturing (AM) method [3, 4]. There are different types of AM methods used as an alternative of conventional manufacturing such as powder bed-based, wire-based, thin layer addition process, bulk layer addition process, and non-metal layer-by-layer addition method. The thin layer additive manufacturing process takes

V. S. Thakur · M. Manikandan · S. Singh · S. Mishra · A. Kaithwas · I. A. Palani (✉)
Mechatronics Instrumentation Lab, Discipline of Mechanical Engineering, Indian Institute of
Technology Indore, Indore 452020, Madhya Pradesh, India
e-mail: palaniia@iiti.ac.in

S. S. Mani Prabu · I. A. Palani
Metallurgy Engineering and Materials Science, Indian Institute of Technology, Indore, Madhya
Pradesh, India

high production time as compared to bulk layer addition [2]. Wire arc-based additive manufacturing has attracted much attention as an encouraging 3D printing technique for metallic material and component as a consumable material in a recent year. That seems to contradict that the surface roughness of the additive manufactured structure and sample has been considered as a challenge to achieve high performance [7].

A wire arc additive manufacturing method is assisted to the fabrication of thin wall structure with high rate deposition [2], but this process also requires post-processing such as surface polishing and heat treatment for enhancing the properties [5]. Surface polishing is an important process for removing a thin layer of unwanted materials such as micro, macro, and nano size, which is reducing the peak and valleys of the surface [6]. This surface roughness is an important role to influence the mechanical or surface tribology properties, but the conventional polishing process consumes more time of production. So, there is various modern or unconventional polishing processes are suitable for attaining excellent surface finish [7], such as abrasive blasting, mechanical polishing, electrochemical polishing, and laser polishing. Among all these techniques, the laser polishing is a potential method to obtain superior surface finish with low roughness due to the surface melting of the substrate without any modifications in bulk properties [8].

In this research, an austenitic stainless steel 316L is used to fabricate the structures by using the WAAM method in which samples are assisted through laser polishing to attain superior surface roughness. The surface roughness will be evaluated through an optical profilometer, and crystalline structure, impurity content is evaluated by using X-ray diffraction. The mechanical property of the sample was measured by a microhardness instrument.

When laser radiation is used to polish metals, a thin surface layer of the workpiece is remelted and the surface smoothed due to interfacial tension. The innovation of laser polishing lies in its fundamentally different mode of action (remelting) compared to conventional grinding and polishing processes (ablation). For metallic materials, diode-pumped solid-state lasers are generally used. If the surfaces already have a low roughness, e.g., after grinding, pulsed lasers with pulse durations of several 100 ns can be used. If the surfaces are rougher, e.g., after milling or additive manufacturing, continuous lasers are used. The remelting depth is between a few 100 nm when pulsed lasers are used and up to 100 μm with continuous lasers. Laser polishing have so many features and advantages such as, once execute a program automated processing in 3D surfaces, Polishing result independent of the operator, High process speeds, especially when compared to manual polishing, High reproducibility, Selective polishing of selected areas, Low mechanical stress on the components, because of the non-contact process, No incorporation of grinding and polishing agents into the surfaces.

10.2 Materials and Methods

In order to aware about our study laser polishing of the wire arc additive manufactured SS316L, we optimized to use a parameter of the wire arc additive manufacturing (WAAM) machine and Yb Doped Fiber Laser, and the material, methods of the experimental process which are discussed below.

10.2.1 Material

WAAM-fabricated an austenitic stainless steel 316L samples were used for laser polishing process, chemical composition of which material is shown in Table 10.1. This material has unique properties such as good strength with high temperature and high corrosion resistance, which leads to food production and architectural applications [9].

10.2.2 Methods

WAAM. Wire arc additive manufacturing process also termed as additive manufacturing was performed using WAAM fabrication system by layer-by-layer deposition to obtain the desired part [11, 12]. Additive manufacturing (AM) is a technique where structures are produced by adding and depositing material in a layer upon layer manner. Wire and arc additive manufacturing (WAAM) is a technology which has been investigated in last 30 years, although the first patent dates from almost 100 years ago. It became interesting for scientists and manufacturers due to its ability to produce fully dense metal parts and large near-net-shape products. WAAM is mostly used in modern industries, like aerospace industry. It uses existing welding equipment, electric arc as the energy source, and welding wire as feedstock. Because of this, it is cheaper than other AM technologies, which usually need specific equipment and materials. The process consists of few steps (designing model in a repetier-host software by M code, G code, slicing into layers, tool path generating, choosing welding parameters, material deposition, and post-processing) [10]. The parts were constructed with an inert gas environment to attain defect-free parts, which parameter is shown in Table 10.2.

Laser Polishing. The laser material interaction principles were followed for laser polishing process. The word laser is an acronym for light amplification stimulation by stimulation emission of radiation. The laser is a device that amplifies or increase the intensity of light and produces highly directional light. The laser is not only amplified or increases the intensity of light but also generates the light. The laser emits light through a process called stimulated emission of radiation which amplifies or increases the intensity of light. Some lasers generate visible light, but others generate

Table 10.1 Chemical composition

Grade	C	Mn	Si	P	S	Cr	Mo	Ni	N
316L	-	-	-	-	-	16.0	2.00	10.0	-
	0.03	2.0	0.75	0.045	0.03	18.0	3.00	14.0	0.10

Table 10.2 WAAM parameters

Parameters	Wire feed rate (m/min)	Ar gas flow rate (Psi)	Volt (V)	Current (amp)	Dia. (mm)
Quantity rate	6	28	20	120	1.2

ultraviolet or infrared ray which is visible. In general, when an electron jumps from lower energy level to higher energy level, it emits light or photon. The energy of the emitted photon is equal to the energy difference between the energy levels. The loss of electron energy is attributed to the entire atom. Therefore, it can be thought that the atom is moving from a higher energy state to a lower energy state. Laser light is different from the conventional light. The laser has extraordinary properties which are not present in the ordinary light source like the sun and the incandescent lamp.

SCANTECH Yb-doped fiber laser source was assisted to polish the WAAM-fabricated samples with continuous wave laser interaction on the material at a constant wavelength and various powers with number of the pass which schematic diagram is shown in Fig. 10.1. The samples were mounted on the bed with a standoff distance at 30 cm with the wavelength of 1064 nm. Initially, started with low laser power and a number of passes further for governing the parameters, simultaneously increased the power as well as number of passes. The laser polishing process parameters are shown in Table 10.3.

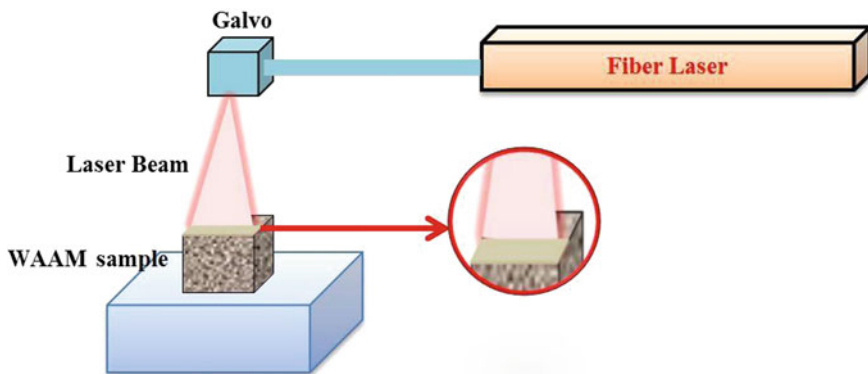


Fig. 10.1 Schematic of the laser polishing process

Table 10.3 Laser polishing parameters

Sample	Wavelength (nm)	Power (W)	No. of pass	Marking speed (mm/sec)
1	1064	10	8	20
2	1064	10	10	20
3	1064	25	15	20

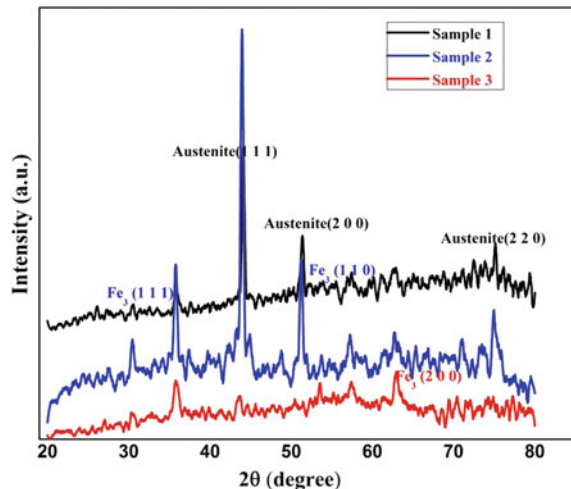
X-ray diffraction was used to determine crystallographic planes and structures of the sample using $\text{CuK}\alpha$ radiation ($\lambda = 0.1548 \text{ nm}$) at an angle of 20° to 90° . VHT machine was used to defining the hardness effect by laser polishing with 200 g load and holding time is 15 s. using Veeco optical profilometer were performed for measuring the surface roughness of before and after polished samples.

10.3 Result

10.3.1 X-Ray Diffraction

Rigaku X-ray diffraction was used to ascertaining the crystal phase changes and structures. The laser polishing process was aided to attain excellent surface finishing for WAAM-prepared samples. Two different laser parameters and three levels were considered for LP, for which XRD graphs are shown in Fig. 10.2. The sharp peak at 45° was describing an austenite phase of the lattice (111) in sample 1, also with the same sample at an angle of 35.8° and 51.2° peaks confirming that the ferrite structure with different crystal lattices such as $\text{Fe}_3(111)$ and $\text{Fe}_3(110)$. The higher laser power influenced sample 2 shows no sharp peak, so it has confirmed the amorphous structure. Sample 3 has used the lower number of laser scanning passes in which XRD peaks were shifted from 75° to 63.8° , respectively, as compared with sample 1. In this sample, all the sharp peaks were representing the austenite phase only but with different crystal lattice at (200) and (220).

Fig. 10.2 Different laser parameter influenced samples XRD graph



10.3.2 Roughness Measurement

An unconventional evaporation process is required to remove unwanted layers and micro- or nanoscale for attaining excellence surface finish. So laser polishing was assisted in removing a thin layer from the sample due to laser material interaction principles. Hence, it has attained a rough surface. The roughness of the samples was performed with Veeco optical profilometer. The average roughness was taken at three different places before and after laser polishing, and the values are shown in the table below. There was a 40% reduction in roughness value after doing the laser polishing (Table 10.4; Figs. 10.3 and 10.4).

Table 10.4 Laser polishing parameters

Sample	Pre-polishing Ra value (μm)	Post-polishing Ra value (μm)
S1	14.28	8.45
S2	14.80	9.01
S3	13.50	9.25

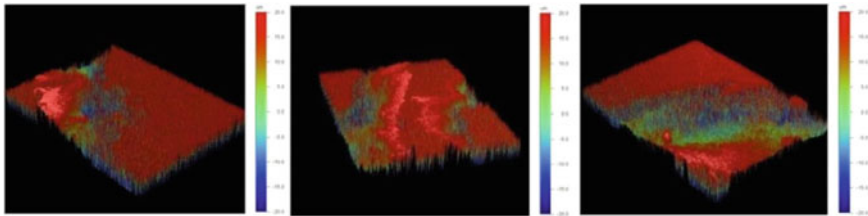


Fig. 10.3 Surface roughness images before laser polishing

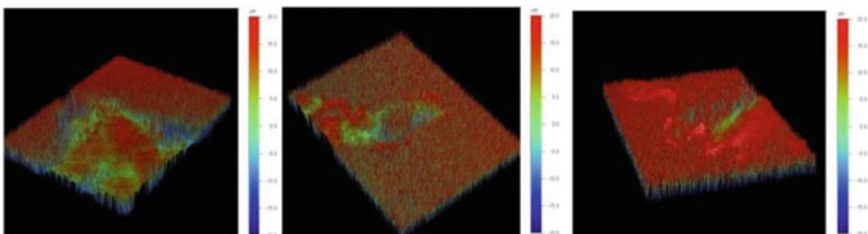
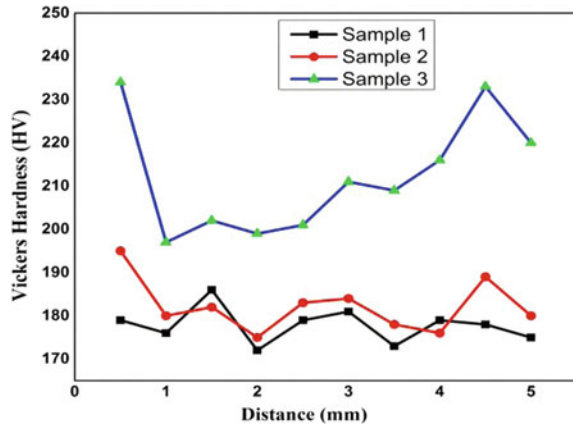


Fig. 10.4 Surface roughness images after laser polishing

Fig. 10.5 Vickers microhardness measurement of laser polished samples



10.3.3 Surface Hardness

UHL Vickers Micro Hardness Testing was used to measuring the microhardness of laser polished samples. In hardness measurement, the micro indenter load was maintained 200 g and a dwell time of 15 s also the crosshead speed of 0.025 mm/min. To reduce the measurement errors, the polished samples were used to measure in same cross section to attain the average value. LP sample microhardness profile was measured from top to bottom cross section with a distance of 0.5 mm. The microhardness was gradually reduced from top polished to bottom of the sample 1 and 2 at 198–178 but sample 3 has high microhardness value (235, 232 HV) at the distance of 0.5 and 4.5 mm as compared with other samples which are illustrated Fig. 10.5. During laser polishing the laser material interaction, the principle has assisted to remove a thin layer from the surface in which ablation has refining the surface grain structures and sizes. Hence, high laser power-influenced sample has achieved greater hardness rate as compared to other samples.

10.4 Conclusions

- Defect-free SS316L samples were fabricated using WAAM with argon environment.
- X-ray diffraction confirms the presence of austenite and ferrite phase before and after laser polishing.
- Laser polished samples have shown better surface finish as compared with untreated samples from 14.80 to 9.45 μm .
- High laser power has attained the higher microhardness of 235 HV than the low laser power.

References

1. Guo, N., Ming, C.: Additive manufacturing: technology, applications, and research needs. *Front. Mech. Eng.* **8**(3), 215–243 (2013)
2. Xiong, J.: Fabrication of inclined thin-walled parts in multi-layer single-pass GMAW-based additive manufacturing with flat position deposition. *J. Mater. Process. Technol.* **240**, 397–403 (2017)
3. Wang, T., Zhang, Y., Wu, Z., Shi, C.: Microstructure and properties of die steel fabricated by WAAM using H13 wire. *Vacuum* **149**, 185–189 (2018)
4. Xu, X.: Microstructural evolution and mechanical properties of maraging steel produced by wire + arc additive manufacture process. *Mater. Charact.* <https://doi.org/10.1016/j.matchar.2017.12.002> (2017)
5. Rosa, B., Mogno, P., Hascoët, J.-Y.: Laser polishing of additive laser manufacturing surfaces. *J. Laser Appl. Laser Inst. Am.* **27**, S2 (2015)
6. Bordatchev, E.V., Hafiz, A.M.K., Tutunea-Fatan, O.R.: Performance of laser polishing in finishing of metallic surfaces. *IJAMT* **73**, 35–52 (2014)
7. Ma, C.P., Guana, Y.C., Zhou, W.: Laser polishing of additive manufactured Ti alloys. *Opt. Lasers Eng.* **93**, 171–177 (2017)
8. Marimuthu, S.: Laser polishing of selective laser melted components. *Int. J. Mach. Tools Manuf.* **95**, 97–104 (2015)
9. Luo, K.Y., Jing, X., Sheng, J., Sun, G.F., Yan, Z., Lu, J.Z.: Characterization and analyses on microhardness, residual stress and microstructure in laser cladding coating of 316L stainless steel subjected to massive LSP treatment. *J. Alloys Compd.* <https://doi.org/10.1016/j.jallcom.2016.02.266> (2016)
10. Knezović, N., Topić, A.: *Wire and Arc Additive Manufacturing (WAAM)—A New Advance in Manufacturing*, University of Mostar, 88 000 Mostar, Bosnia and Herzegovina. *New Technologies, Development and Application*. NT: *Lecture Notes in Networks and Systems*, vol. 42. Springer, Cham (2018)
11. Colegrove, P.A., Martina, F., Roy, M.J., Szost, B.A., Terzi, S., Williams, S.W., Withers, P.J., Jarvis, D.: High pressure interpass rolling of wire + Arc additively manufactured titanium components
12. Martina, F., Mehnen, J., Williams, S.W., Colegrove, P., Wang, F.: Investigation of the benefits of plasma deposition for the additive layer manufacture of Ti-6Al-4V. *J. Mater. Process. Technol.* **212**, 1377–1386 (2012)
13. Bordatchev, E.V., Hafiz, A.M.K., Remus Tutunea-Fatan, O.: Performance of laser polishing in finishing of metallic surfaces. *Int. J. Adv. Manuf. Technol.* **73**:35–52 (2014)

Chapter 11

Energy Consumption of Welding-Based Additively Manufactured Materials



Nandhini Raju , G. Balaganesan  and Gurunathan Saravana Kumar 

Abstract The objective of this study is to determine a detailed energy model for Gas Metal Arc Welding (GMAW), Manual Metal Arc Welding (MMAW) processes and comparing energy consumptions of both techniques for additively manufactured rectangular blocks. Energy consumption as function of time and power calculated for Mild steel- MS-ER70, MS-E6013, stainless steel SS-ER347, SS-E308L-16, AISi-3 ER4043 rectangular solids manufactured by welding-based additive manufacturing. Qualitatively it is known that GMAW takes less energy comparing MMAW process. However, tools and dataset to quantitatively determine energy consumption of each step of GMAW, MMAW additively manufactured materials has been missing. Energy consumption is divided for pre-processing, WAAM process, post-processing. Even each of this process demanded energy input also traced. Comparisons of both energy values with carbon foot print and considerable parameters are discussed in detail.

Keywords Additive manufacturing · Welding · Wire arc additive manufacturing · Energy consumption

Nomenclature

AM	Additive Manufacturing
SLA	Stereolithography
FDM	Fused Deposition Modeling

N. Raju (✉)

Digital Manufacturing and Design, Singapore University of Technology and Design, Singapore 487372, Singapore

e-mail: nandhini_raju@sutd.edu.sg

G. Balaganesan

Department of Mechanical Engineering, Indian Institute of Technology Jammu, Jammu 181221, India

G. Saravana Kumar

Department of Engineering Design, Indian Institute of Technology Madras, Chennai 600036, India

© Springer Nature Singapore Pte Ltd. 2020

M. S. Shunmugam and M. Kanthababu (eds.), *Advances in Additive Manufacturing and Joining*, Lecture Notes on Multidisciplinary Industrial Engineering,

https://doi.org/10.1007/978-981-32-9433-2_11

EBM	Electron Beam Melting
DMLS	Direct Metal Laser Sintering
LENS	Laser Engineered Net Shaping
PBF	Powder Bed Fusion
DED	Direct Energy Deposition
WAAM	Wire Arc Additive Manufacturing
GTAW/TIG	Tungsten Inert Gas welding
MMAW	Manual Metal Arc Welding
GMAW/MIG	Gas Metal Arc Welding
TGMAW	Tandem Gas Metal Arc Welding
FSW	Friction Stir Welding

11.1 Introduction

Recently, manufacturing techniques rapidly developed and now called as Additive manufacturing. Automated fabrication, Freeform fabrication, layer-based manufacturing, stereolithography, 3D printing are same names called for additive manufacturing technologies. Initially, it is also called as rapid prototyping to mention its speed of process. It is not only about prototyping but also about improving accuracy, technology, and materials usage. So, ASTM standard [1] classified different names and different fabrication technology in the name of Additive Manufacturing. 75 different technologies also classified into 7 categories in AM technology. Those are VAT Photo-polymerization (SLA), sheet lamination, Binder jetting (3D printing), material jetting (poly jet), material extrusion (FDM), powder bed fusion (DMLS) and direct energy deposition (laser heat source with powder-LENS, EBM, electrical arc, spray). Polymeric materials, wax, metal, and paper laminates can be created by AM machines.

Development of AM is based on CNC machining because CNC is much helpful for subtraction of material. It is highly tough to make complex structures in CNC machines. So, AM technology developed and is having rapid growth in manufacturing technology. It will add material layer by layer in progressive way to build material. These manufacturing technologies are completely different from conventional manufacturing methods. The main advantage over conventional method of manufacturing technology is its time taken to produce a material. Time consumed by AM is less compared with conventional methods. So, industries benefited by increasing production within limited time frame and it is capable to improve economic growth of the business. Even it will encourage to make last-minute changes before production. In conventional manufacturing changes in last-minute will make huge loss to industry regarding mass production. Though it has so many advances over conventional manufacturing technologies, it has some drawbacks too. Some AM technology required high energy consumption. Example, in powder bed fusion technology, powder will be melted by laser. To operate the laser heat source, it requires

a lot of energy. High energy demand will require higher electricity for minimal material wastage. From pre-processing to post-processing there are lots of energy needed to nail the final product. Energy calculations are much needed to know the demand of energy for a product. To make it a sustainable technology process, energy requirement should be optimized. Low cost, affordable AM technologies are primary interest of this research. So, Wire Arc Additive Manufacturing technology followed the welding-based process to build material are discussed in detail.

Energy consumption is one of the main aspects for manufacturing domain which is decreased by 17% from 2002 to 2012 by just corrected its gross output only by 3% [2]. Manufacturing Energy Consumption Survey (MECS) reported glimpse of energy consumption over per unit gross output. Last two decades there is robust growth in manufacturing domain due to advanced manufacturing technologies. Especially, additive manufacturing technology is fast-growing area for manufacturing.

Margarita et al. work demonstrated SEC of recycled Al and improving stiffness of Additive manufacturing metals (Cladding) will have less energy [3] than conventional sheet metal forming. Reduction in energy also important when whole process considered with sustainability. WAAM is one of the cost-effective and affordable method to manufacture products. In industry and in research it has great development. Usage of WAAM started to weld the parts and now a day it is highly effective to produce large scale parts as rocket nozzle, large tubes with some machining process. Wire arc additive manufacturing can be done with EBM/Laser as well as electrical arc as heat source. Electrical arc is popular in use and easily available. But this electrical arc is significant as any EBM/Laser with post-processing. Electric arc/Welding is primary and most usable manufacturing process in the world. Electrical energy in welding processes is prime consideration for energy consumption to fabricate parts. Welding took a huge part in industry and consumes most of electrical resource. To optimize any welding energy, welding process and its parameters are needed to be considered into account. Bahrami et al. work showed how low carbon steel welding process is modeled by COMSOL Multiphysics®. Model helped to produce weld pool, velocity field in welded pool and heat transfer. Combination of power and translation speed of arc are investigated in detail. Finally concluded [4] that arc power with increment in travel speed lead to reduced energy consumption. Reduced energy will lead to high thermal efficiency. Usually, welding processes focus more on heat source improvement comparing parameter optimization. To optimize parameter for sustainable approach, Fitness Sharing Genetic Algorithm (FSGA) is proposed [5] results are compared with Generic Algorithms (GA). A case study used rail track joints by using sheet metal arc welding technique to validate the proposed technique. FSGA approach gives significant improvement regarding reduction of energy and improves the thermal efficiency.

As MMAW, GTAW process also used for additive manufactured materials. Different materials are used, and mechanical properties also tested. Some of the research [6, 7] showed GTAW produced less porosity and defects in manufactured materials. So many studies carried out about microstructure of GTAW based additive manufactured materials. Even parameter changes [8] are not only influencing microstructure and its mechanical properties but also has an effect on energy output.

GMAW process is widely used for its quality of welding. This can be done manually as well as automatically. Automatic one is simple which has CNC bed with it and torch, both are synchronized with computer. There are attempts made by attaching milling center and GMAW process for additive manufacturing and subtractive (post-processing) machining process. Jackson et al. [9] reported comparison of energy consumption of wire-based additive manufacturing and powder-based additive manufacturing technology with attachment of subtractive manufacturing methods for surface finishing of additive manufactured parts.

Energy consumption model also created and concluded that wire base additive manufacturing technology consumed less overall energy comparing powder-based additive manufacturing technology. To derive energy consumption, even modeling of GMAW process done and proved those models matched with experimental data. For example, Al GMAW process is modeled by Three-dimensional GMAW modeling [10] tool and energy flow, momentum and mass transfer are discussed. It proved that peak temperature will be in arc central axis. So, positioning arc near anode will improve less energy consumption. Modeling welding will give a great insight into process.

Though so many research works carried on WAAM and its energy consumption, but there is less study on energy model for whole process. This paper demonstrates energy model from pre-processing to post-machining, each process's energy input can be calculated. This can be used for any product manufactured by GMAW, MMAW process to understand the total carbon footprint of whole (cradle-to-grave) process.

11.2 Experimental Setup and Procedure

11.2.1 Wire Arc Additive Manufacturing

GMAW, MMAW are carried out in Central Workshop, Indian Institute of Technology, Madras. Welding is done with three different materials like Aluminum, Stainless steel, and Mild steel. Materials used as mild steel and stainless steel for both GMAW and MMAW processes are the same material with different grade. Base metals are cut by Shearing machine before welding-based additive manufacturing technique starts and power required for cutting plates are noted. All base metal plates are in dimension of 50 mm × 100 mm with thickness of 2 mm. MMAW process flux coated electrode is used and slug is repeatedly dispensed for next deposition of weld. Direction of weld is horizontal and varying voltage values are noted. Arc is created due to the presence of electrode and base plate and metal will be melted due to the higher energy. But in GMAW process solid wire is used as electrode and welding gun is set as oscillatory motion (perpendicular to this paper) on horizontal direction. Welding wire is melted by arc created between wire and base late. Both GMAW and MMAW processes are mentions in Fig. 11.1.

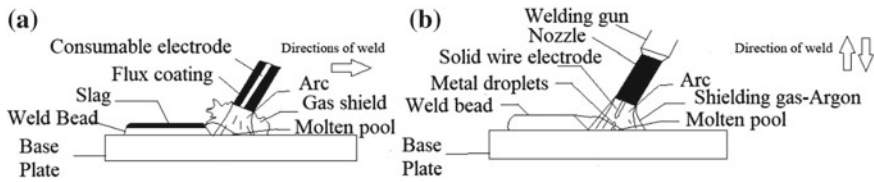


Fig. 11.1 a Schematic representation of Manual Metal Arc Welding (MMAW) b Schematic Representation of Gas Metal Arc Welding (GMAW)

Before processing for WAAM technique, Initial mass is measured. MMAW type welding is done on flat plate in horizontal position. MMAW is executed with multiple passes by help of standard power source. 3 mm diameter electrode is used. Welding process time, current and voltage are monitored for each welding to note power consumption. Welding length, thickness and final mass of base plate after welding also calculated to understand the deposition. After MMAW, post fabricate machining process started with milling machine. Energy consumption is noted for final calculation. Further machining can be used if it required. But including those energy values is recommended.

GMAW multi-pass welds used power source with its automatic robotic arm process. Welding is done by oscillating motion of torch over materials (Al, SS, MS). Control of torch can be operated by remote. Welding speed, wire speeds are pre-defined in machine, before GMAW process starts. To avoid up and down shape of welding bed, process parameters are optimized. Schematic diagrams of base metals with weld bead is mentioned in Fig. 11.2.

All GMAW, MMAW and GTAW process parameters are mentioned in Tables below. Pre-processing machine type and consumed energy of each material is given in Table 11.1. Base metals are same and dimensions are also maintained the same for MMAW and GMAW process.

Table 11.2 which is mentioned below gives a glimpse of parameters required for energy model. Voltage and current are fluctuating. Average values are mentioned

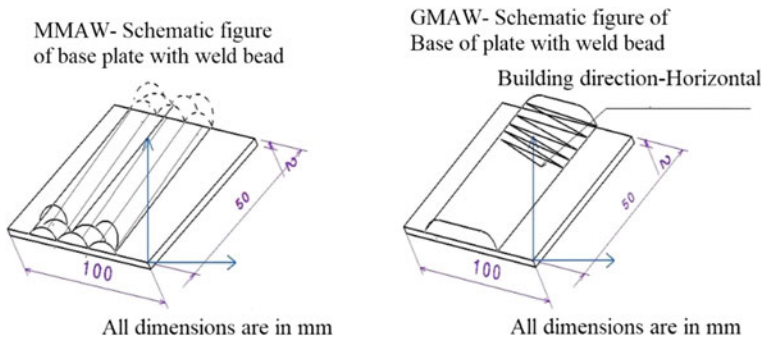


Fig. 11.2 Schematic diagram of base metal with weld bead

Table 11.1 Pre—processing (Cutting base metal)

Details of machine/base plate	Time/energy consumption
Machine: shearing machine; manufacturer: aristo engineers; model: PP818A; Job length: 1200 mm; Energy: 5.5 KW/hr	
Aluminum base metal plate (50 × 100 × 2)	Time: 34.6 s; Energy: 51.94 W
Stainless steel base metal plate (50 × 100 × 2)	Time: 23 s; Energy: 35.13 W
Mild steel base metal plate (50 × 100 × 2)	Time: 56 s; Energy: 85.6 W

Table 11.2 Parameters of MMAW based additive manufacturing

Details/material	Mild steel	Stainless steel
Machine type	ARC welding	ARC welding
Manufacturer	ESAB	ESAB
Model	RS-400	RS-400
Wire/electrode	MS-E6013	SS-E308L-16
Electrode dia	3 mm	3 mm
Welding process time	1118 s	1070 s
Current	124 A	113.33 A
Voltage	25.75 V	13.33 V
Weld Length	100 mm	100 mm
Weld thickness	8.5 mm	8.5 mm
Weld Width	30 mm	28 mm
Initial mass	85 g	89 g
Final mass	286 g	284 g
Deposition	201 g	195 g
Energy	3569.774 kJ	1616.437 kJ

SS Stainless steel; MS Mild steel

here. Time taken for MMAW is high due to the human factors included. This may give great influence in energy calculation. However, energy consumed by MMAW is always higher and the temperature maintained by MMAW is highly higher than the melting point of material. This cause higher energy demand.

Table 11.3 contains details of GMAW process parameters. Materials used for MMAW and GMAW are similar and changes in compositions are negligible. Comparing GMAW, MMAW had greater deposition. Here shielding gas is argon with flow rate of 12 L per minute is used. Aluminum is welded for GMAW process and energy values are calculated. Due to its weldability, melting temperature range it demands lesser energy comparing all other materials. It needs less deposition, 42 g to produce same dimension as stainless steel and mild steel rectangular blocks

Table 11.3 Parameters of GMAW based additive manufacturing

Details/material	Mild steel	Stainless steel	Aluminum
Machine type	CMT	CMT	CMT
Manufacturer	Fronius	Fronius	Fronius
Model	4000 CMT	4000 CMT	4000 CMT
Weld wire	MS-ER70s	SS-ER347	AISI-3 ER4043
Electrode dia	1.2 mm	1.2 mm	1.2 mm
Wire feed rate	2.9 m/min	4.2 m/min	3.8 m/min
Shielding gas	Argon	Argon	Argon
Shielding gas flow rate	12 lt/min	12 lt/min	12 lt/min
Weld speed	4 inch/min	4 inch/min	5 inch/min
Welding process time	363 s	316 s	246 s
Current	117.9 A	103 A	70.3 A
Voltage	9.95 V	12.2 V	11.43 V
Weld length	100 mm	100 mm	100 mm
Weld thickness	8.2 mm	8.3 mm	8.2 mm
Weld width	20 mm	20 mm	20 mm
Initial mass	81 g	83 g	30 g
Final mass	212 g	234 g	72 g
Deposition	131 g	151 g	42 g
Energy	425.837 kJ	397.085 kJ	197.668 kJ

SS Stainless steel, MS Mild steel, Al Aluminum

Most of research works related to energy audit did not involve energy of post-processing as machining or grinding. All those parameters mentioned in Table 11.4. Machining is done on overall faces of rectangular metal block. Each of machining and its duration, power also monitored. Notice that machining for stainless steel prepared by MMAW is higher comparing all other blocks of material.

Figures 11.3 and 11.4 are images of welded material on base plate and after machining parts of same materials. In MMAW heat-affected zones are visible and area affected by heat is large comparing GMAW process. There are lots of slugs are present in material manufactured by MMAW process.

In GMAW process, even materials are welded by automatic robotic arms, there is a presence of porosity on the surface. These spherical holes are due to oxygen presence during welding process because weld is exposed directly to environment. Noted parameters for GMAW, MMAW are processed for energy calculation and carbon foot print study.

Table 11.4 Parameters of post-processing—machining

Details of machine/base plate	Time/energy consumption
<i>Machine: Universal Tool milling machine; Manufacturer: Friedrich DeckelMunchen 25; Model: 1959-W2007; Power: 1.95 KW/hr; Volt: 380-3 Phase; Main motor: Siemens schkert-1.1/1.4 KW(700/1400 RPM); High speed motor: Siemens schkert-0.55 KW(2800 RPM)</i>	
MMAW-MS	RPM: 950; Time: 2761 s; Energy: 1495.52 J
MMAW-SS	RPM: 950; Time: 4399 s; Energy: 2382.7 J
GMAW-MS	RPM: 950; Time: 2448 s; Energy: 1325.98 J
GMAW-SS	RPM: 950; Time: 3184 s; Energy: 1724.64 J
GMAW-AL	RPM: 950; Time: 1823 s; Energy: 987.446 J

SS Stainless steel, MS Mild steel, Al Aluminum

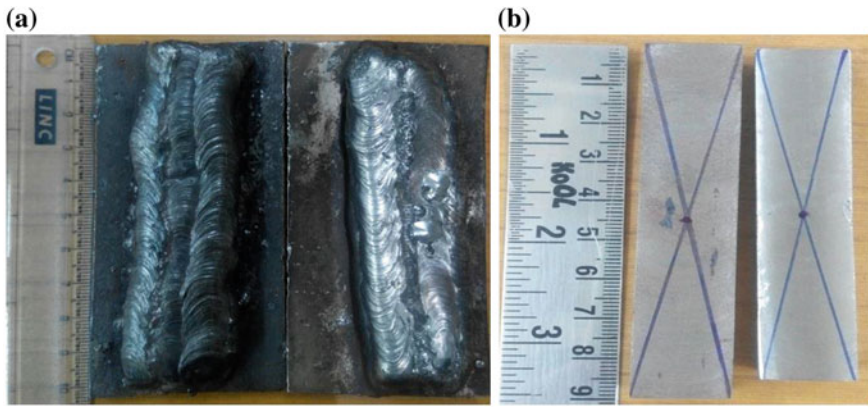


Fig. 11.3 Materials manufactured by MMAW process

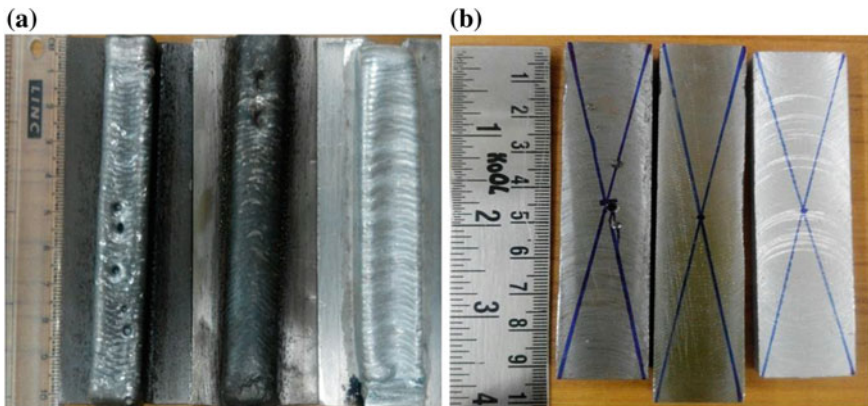


Fig. 11.4 Materials manufactured by GMAW process

11.3 Results and Discussion

Usually in conventional manufacturing like casting, to manufacture a product, it will deliver more than 60% of material as wastages in each step from casting to machining. For example, to manufacture same rectangular blocks by casting, furnace needs to be run for 8 h to just melt a material to use it for casting. Energy required for running this furnace is high. Same time it took most of material to deposit in runner and riser of mold. This is also huge waste of material. To modify to original required dimension, it needs some more energy with effect to deliver more wastage of material. This casting method is used for this research to understand the difference of energy required with WAAM especially GMAW, MMAW techniques. Results of energy and material wastage received from this can be controlled and even minimized more by AM technologies. Along with material wastage energy wastage also need to be monitored and controlled. MMAW and GMAW are discussed and parameters are presented in detail. Each process energy is calculated and tabulated below.

Table 11.5 showed results of energy for each process of MMAW and GMAW. In pre-processing stage, required base metal is cut down from same plates. So, this may not able to show any changes in energy values. To process weld deposition, stainless steel, mild steel and aluminum are used. To deposit stainless steel by MMAW process took more energy. Especially MMAW will have influence of time taken per bead and time between each bead. Deposition of mild steel also done and has high energy demand comparing energy values of other materials. GMAW is automatic and speed of deposition can be adjusted as we required. Here it is maintained as 4 inch/min and can fluctuate further to note down the influence in energy values. To deposit mild steel as product GMAW will be the best-comparing values of MMAW. GMAW considered only 11.96% energy of MMAW for Mild steel and 24.65% energy for stainless steel to be weld over bade metal

In post-processing stage, energy prices are high for MMAW process. Because deposits are not even to the surface. This needs to be removed to achieve required dimension. Milling is considered as post-processing process here. Heat affected zone are visible and comparatively large with metal manufactured by MMAW process. There is less uneven surface present in metals manufactured by GMAW process.

Table 11.5 Energy Consumption of each process

Welding type/material	Pre-processing-cutting base metal (J)	Additive manufacturing (KJ)	Post-processing-machining (J)	Total (KJ)
MMAW-MS	85.6	3569.774	1495.52	3571.355
MMAW-SS	35.13	1616.437	2382.7	1618.854
GMAW-MS	85.6	425.837	1325.98	427.248
GMAW-SS	35.13	397.085	1724.64	398.844
GMAW-AL	51.94	197.668	987.446	198.707

SS Stainless steel, MS Mild steel, Al Aluminum

Table 11.6 Specific energy consumption of each material

Type/material	Specific energy consumption (KJ/g)
MMAW-MS	17.76
MMAW-SS	8.289
GMAW-MS	3.25
GMAW-SS	2.629
GMAW-AL	4.706

SS Stainless steel, MS Mild steel, A/ Aluminum

Even it has even distribution of weld on surface, there is some porous are present. Machining for this metal parts needs lesser of energy comparing machining for MMAW process.

Table 11.6 showed specific energy values of each welded blocks. GMAW process needs less energy to deposit a gram material on base metal. Main reason is, machine parameters are optimized to the requirement of heat to melt a material. MMAW has no control over the heat generation. Even if it is controlled by changing current and voltage values, approximate heat value required to melt material unable to maintain. Time influenced for both process is directly proportional to energy price.

11.3.1 Carbon Foot Print

Approximately more than 40% of carbon emissions [11] come from electricity generation. This generation of more electrical power lead to produce heat, carbon dioxide, and green-house gases. Applying less energy technology to manufacture material by low-cost additive manufacturing will be highly helpful from small scale industry to large one. This affordable technology needs to be monitored and tailor the energy requirement. Reducing energy value will impact on reduction in carbon footprint. Though so many research included different computational tool to approximate the carbon footprint. This article used energy value as direct representative to understand the effect of carbon foot print.

Heat, emissions, and slugs are more present in MMAW process. GMAW did produce some emissions during welding but comparatively low and this reflects in energy values. Energy values presented in this study are representing carbon footprint. More electrical energy needs more electricity. By product, more electricity demands more greenhouse gases emission and hence it will have higher carbon footprint. Especially to manufacture mild steel product, MMAW will not be helpful to sustainable manufacturing. Material removed by MMAW during machining is high and demanded more energy for machining. GMAW process is optimized and so that it demands lesser energy to deposit material. Heat, current, values are monitored. Registered values of deposition meet specification of required dimension. Control over electrical power will proportionally reduce the carbon footprint of each process. This will reflect in reduction of carbon footprint of whole process of manufacturing.

11.4 Conclusions

The article presents a detailed approach to calculate energy value needed for MMAW and GMAW process. Energy flow diagram and process maps are in greater detail with involving each parameter's energy input. This proposed approach can be used to calculate energy values of materials manufactured by WAAM. This energy model can be extended to other welding techniques. Industries which demands sustainability in their objective, this energy model can be used.

Mild steel- MS-ER70, MS-E6013, stainless steel SS-ER347, SS-E308L-16, AlSi-3 ER4043 are used here to manufacture rectangular solid blocks by welding-based additive manufacturing techniques. Energy consumption dependent on power and time consumed for a process. MMAW is manual and energy values are influenced by human factors which has direct impact on time. This also produced more material wastage comparing GMAW process. Production of heat is more than required to melt material. Energy price to machine MMAW product is quite high due to its uneven surface presence. Wastage of material is low comparing MMAW products during machining. Though it has high drawback in cost of power. It has good deposition rate. GMAW process is automatic and energy values are controllable by changing parameters. Heat, Gases emitted by this process is comparatively low with MMAW. Aluminum also welded to understand its energy. GMAW requires less energy and it demands less carbon footprint from this technology. Detail quantitative model of each technique explained, and values are compared with concerns about sustainable manufacturing.

Acknowledgement Author would like to thank Senior Technician Mr. Muthurajan and his team, Mr. Rajesh for their timely support during experiments at Central workshop, Indian Institute of Technology Madras.

References

1. Gibson, I., Rosen, D.W., Stucker, B.: Additive Manufacturing Technologies Rapid Prototyping to Direct Digital Manufacturing. Springer, New York (2010)
2. EIA: Manufacturing Energy Consumption Survey (MECS)—Analysis & Projections. U.S Energy Information Administration (EIA) (2013)
3. Bambach, M.D., Bambach, M., Sviridov, A., Weiss, S.: New process chains involving additive manufacturing and metal forming—a chance for saving energy? In: International Conference on the Technology of Plasticity, Ambridge, UK (2017)
4. Bahrami, A., Valentine, A.D., Aidun, D.: Computational analysis of the effect of the welding parameters on energy consumption in GTA welding process. *Int. J. Mech. Sci.* 111–119 (2015)
5. Wei, Y., Zhang, H., Jiang, Z., Hon, K.K.B.: Multi-objective optimization of arc welding parameters—the trade offs between energy and thermal efficiency. *J. Cleaner Prod.* (2016)
6. Bai, J.Y., Yang, C.L., Lin, S.B., Dong, B.L., Fan, C.L.: Mechanical properties of 2219-Al components produced by additive manufacturing with TIG. *Int. J. Addit. Manuf. Technol.* (2015)

7. Wang, J.F., Sun, Q.J., Wang, H., Liu, J.P., Feng, J.C.: Effect of location on microstructure and mechanical properties of additive layer manufactured Inconel 625 using gas tungsten arc welding. *Mater. Sci. Eng.* 395–405 (2016)
8. Ayarkwa, K.F., Williams, S.W., Ding, J.: Assessing the effect of TIG alternating current time cycle on aluminum wire + arc additive manufacture. *Addit. Manuf.* 186–193 (2017)
9. Jackson, M.A., Van Asten, A., Morrow, J.D., Min, S., Pfefferkorn, F.E.: A comparison of energy consumption in wire-based and powder-based additive-subtractive manufacturing. In: 44th Proceedings of the North American Manufacturing (2015)
10. Lu, F., Wang, H.-P., Murphy, A.B., Carlson, B.E.: Analysis of energy flow in gas metal arc welding processes through self-consistent three dimensional process simulation. *Int. J. Heat Mass Transfer*, 215–223, (2014)
11. Abdallah, L., El-Shennawy, T.: Reducing carbon dioxide emissions from electricity sector using smart electric grid applications. *Jurnal of Eng.* 8 (2013)

Chapter 12

Manufacturing Standardization of Jaipur Foot by Additive Manufacturing



Harlal Singh Mali  and Aniket Singh 

Abstract In developing countries conventional prosthetic feet are preferred over the technologically advanced state of the art bionics, as these are made out of inexpensive materials by local vendors, bringing down the overall cost to a quite affordable price with extraordinary functionality, for amputees here. The work is focussed on standardising Jaipur foot fabrication by use of additive manufacturing. The goal is to obtain a reliable, light, interchangeable and robust product which could be produced with same accuracy in any facility with right set of equipment avoiding human-induced error. The compression strength test results provided a way higher modulus for additively manufactured thermoplastic polyurethane in comparison to microcellular rubber. The microcellular rubber comprises more than 60% of the foot by volume and weight, substitution of such a material with lighter and more reliable polymer brings about not just a comparable but also a better prosthetic foot on various fronts.

Keywords Additive manufacturing · Jaipur foot · Prosthetic foot · Fused deposition modelling · Computer-aided modelling

12.1 Introduction

Disability is a curse in any being's life as it restricts their degree of freedom in all aspects of life. The American Academy of Orthotics and Prosthetists projects that the number of persons using prosthesis is expected to increase from 1.6 million in 1995 to 2.4 million by 2020 [1]. Jaipur foot developed by Sethi et al. [2], shows that rehabilitation of the lower limb amputee can be done by use of various low-cost artificial limbs for those who cannot afford state of the art bionics consisting of sensory and actuation elements. Jaipur foot was designed which was more natural-looking and complied with the needs of Indian people where floor sitting culture is

H. S. Mali (✉) · A. Singh

Advanced Manufacturing & Mechatronics Lab, Department of Mechanical Engineering,
Malaviya National Institute of Technology Jaipur, Jaipur 302017, India
e-mail: harlal.singh@gmail.com

© Springer Nature Singapore Pte Ltd. 2020

M. S. Shunmugam and M. Kanthababu (eds.), *Advances in Additive Manufacturing and Joining*, Lecture Notes on Multidisciplinary Industrial Engineering,
https://doi.org/10.1007/978-981-32-9433-2_12

predominant. According to BMVSS, over 1.3 million amputees have been fitted with Jaipur foot/limb in India and in 26 other countries of Asia, Africa and Latin America [3].

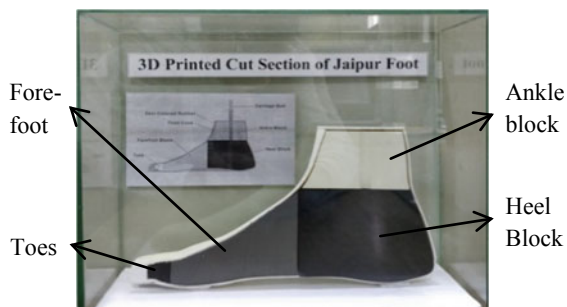
12.2 Design of Jaipur Foot

The essential features like better flexibility, inexpensive, durable and waterproof covering were employed. The amputees fitted with Jaipur foot were able to walk through rugged terrain with mud and water very comfortably, even without shoes. The foot was successful in both rural and urban cases. The foot's high conformance to requirements permits a considerable amount of dorsiflexion and transverse rotation which facilitates squatting and cross-legged sitting for an amputee. In order to increase the shock absorption at the heel, it was made of rubber block covered in a hard rubber shell which was basically made from a MCR (micro cellular rubber) sheet. The present design uses MCR for the whole meta-tarsal portion which disposes the initially used wooden block. The rubber used has high energy absorbing capacity which doesn't easily allow the ground reaction forces to get through, to the socket-stump interface. It displays a special property of slow controlled recovery after deformation. The various parts are (a) wooden ankle block with a carriage bolt, (b) MCR heel and forefoot block, (c) MCR toes, (d) Heat resistant cushion compound wrap, (e) Tyre cord with nylon fibres and (f) Skin-coloured rubber covering.

MCR used in the heel section is supposed to have a higher density in comparison to the forefoot part, therefore, a darker colour is used to display that part in Fig. 12.1. Natural rubber being the major component of the various rubbers used offers durability, resilience, and resistance to abrasion and tears which is not found in any other plastic or easily available basic materials.

The manufacturing process of the foot follows an artisan nature of work where all the MCR blocks are cut from a MCR sheet and then trimmed and grinded to the approximate shape of the real foot. The ankle block is cut from a wooden block of Cheed or Ardu and grinded to the appropriate shape. After obtaining the different parts they are glued together using a rubber compound and then wrapped with heat

Fig. 12.1 Cross-sectional view of Jaipur foot



resistant cushion compound tape and later with tyre cord to impart strength. The whole foot is now compressed using a die and then heated in an autoclave for vulcanisation at a pressure of 0.15 MPa and temperature 220 °C. Later the mould cools down with the help of atmospheric temperature for around 6–8 h. The process proficiency depends on the individual artisan which brings in the human error involved in this process.

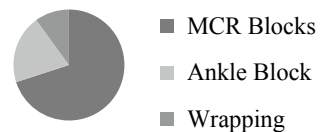
Computer-aided modelling has been used in various sectors to ease the manufacturing hurdles. Number of facilities is fabricating Foot and Ankle Foot orthosis with the use of 3D scanning and converting the obtained geometry into a CAD file [4]. The obtained file is later fabricated using CNC carving machine or Additive manufacturing. The idea is to use the similar process path and incorporate it into prosthesis such as Jaipur foot. Development of the CAD model for Jaipur foot could bring about the various possibilities of using it to fabricate the artisan-made foot in a standardised way. In present times the additive manufacturing using fused deposition modelling, stereolithography, and selective laser sintering has reached new horizons. The easy availability of FDM printers at low prices has made it affordable for all kind of users. The identification of the comparable material for Jaipur foot which could be additively printed is included under the scope of this study.

12.3 Modelling Standardised Parts

One of the studies reveals the performance and durability of Jaipur foot. The amputees fitted with the sample feet were followed for around 16 months on an average, with failure percentage around 27%. The failures were mostly related to skin fractures and fractures in the heel block. The data recorded from the foot's failures and its lifespan reveals the fact that the total span of a foot varies from 12 to 16 months [5]. After this period the foot is generally replaced or repaired (if possible) to continue its further use.

Another study done on the types of failures occurring in the Jaipur foot, point towards the MCR blocks. Most of the foot fails from either the conjunction of the two MCR blocks or the Heel block itself. The study concludes that the reason could be clearly owed to lack of standardization in materials and manufacturing processes [6]. Microcellular rubber sheets are developed with a stochastic cellular structure where the structure cannot be controlled microstructurally [7], making it difficult to predict the long term stability in structure and performance (Fig. 12.2).

Fig. 12.2 Volumetric distribution of traditional foot



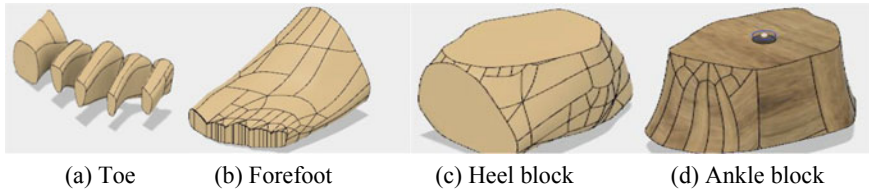


Fig. 12.3 CAD models designed to exact shape and size

The CAD model was developed to the exact shape and dimensions by the use of sculpt feature in Autodesk Fusion 360[®]. All the constituent parts were defined separately so that they could be further manufactured with one of the standardised manufacturing processes. The aim was to decrease the number of failures by identification of the failure-prone regions or parts. The MCR blocks constitute more than 60% of the foot by volume and more than 70% of its weight. The possibility of standardising the wrapping procedure was very restricted; therefore MCR blocks were made the centre of the study. The images in Fig. 12.3 are the constituent parts of Jaipur foot where the toes, forefoot and heel block are made from MCR. All these parts were assembled together to obtain a CAD model of complete foot by wrapping it with a covering imitating the actual prosthetic which consists a skin-coloured rubber wrapping.

12.4 Experimentations

12.4.1 Material Testing

Finding a material that possesses comparable properties to the existing materials was the main objective. The study was focussed on materials that could be additively manufactured or more precisely using fused deposition modelling. First of all the most easily available materials were considered such as ABS (Acrylonitrile, Butadiene, and Styrene) and PLA (Poly-lactic acid).

Prototypes of the parts were printed using both the materials. The complete foot was also fabricated, these showed excellent reduction in weight on the cost of flexibility. However, these feet were not good enough for static or dynamic loads. Walking is the second most complex activity done by our body where the forces applied on the foot are both compressive and shearing in nature at various points [8]. The toes and heel pad are the parts which bear maximum pressure, moreover, toes fabricated using such polymers possess negligible flexibility or resilience. A material with elastic properties which could be additively manufactured brought Thermoplastic polyurethane (TPU) into consideration.

The non-destructive testing of TPU was done by printing 10 samples of TPU material, with infill percentage varying from 10 to 100. The samples were printed

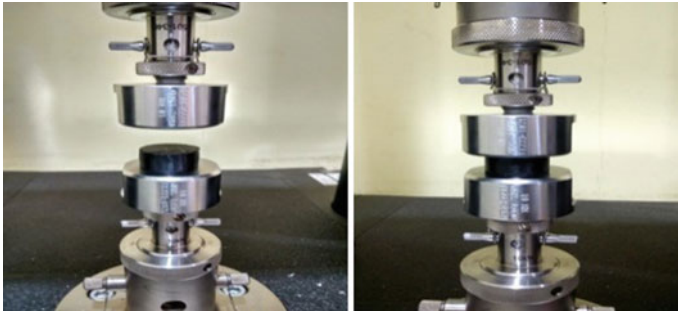


Fig. 12.4 UTM test rig used for testing TPU samples

in conformance to the ASTM Standard D143-14 with a diameter of 28.67 mm and height of 12.7 mm. All the samples tested for compression strength on uniaxial material tester-UTM (Instron model 5967, Instron Corporation, Canton, MA) with a 9 KN load cell (Instron model 2580-202, Instron Corporation, Canton, MA) with a strain rate of 15 mm/min.

Most of the rubbers used for prosthetic foots are tested for basically two properties which includes compression modulus and shore-A hardness. Similarly, the TPU samples were also tested for Shore-A hardness value of each sample using Shore-A hardness tester from Yuzuki with NABL accredited lab calibration. The test procedure was done according to the ASTM D2240 where each sample was placed on a horizontal surface and three readings were recorded for each sample by placing the tester vertically. The properties of the actual materials used in the Jaipur foot [9] were compared to the results obtained from the tests. Later two prototype foot were also fabricated using TPU which were tested for Heel compression to check whether its flexibility was in permissible limits (Fig. 12.4).

12.4.2 Additively Manufactured TPU Foot Testing

Prototypes for the foot were fabricated using fused deposition modelling and after a few number of unsuccessful attempts, they were printed successfully with excellent surface finish and structure as shown in Fig. 12.5. The infill for the prototypes was chosen to be 40 and 50%, later they were tested for permissible heel compression. For testing the printed foot, the back part of the foot was constrained and load was applied using a setup from below the heel as shown in Fig. 12.6. According to ISO 10328, the feet showing deformation more than 5 mm are considered failed [2].

Fig. 12.5 TPU-40 prototype

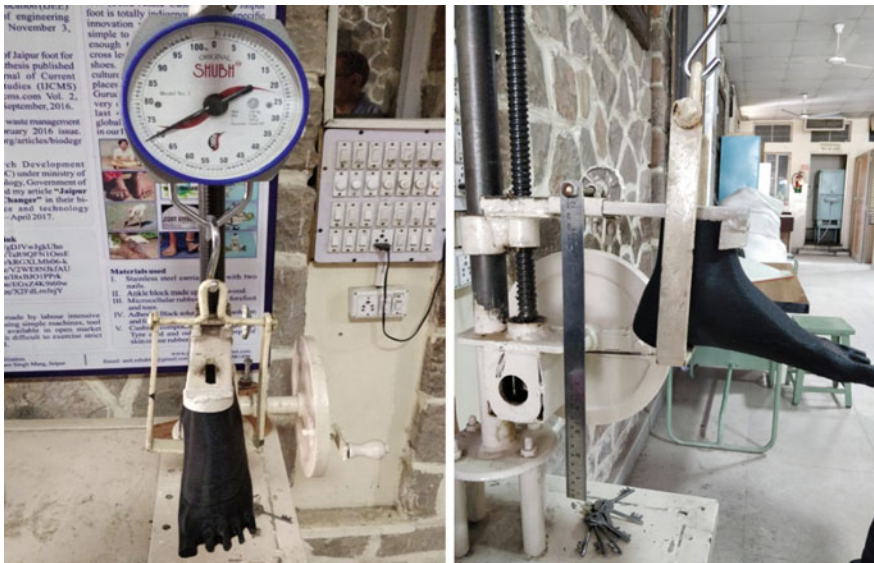


Fig. 12.6 Heel compression test equipment with TPU-50 prototype

12.5 Results and Discussion

The TPU samples are numbered according to their respective infill percentage where 10 represents 10 and 100 represents a completely solid specimen.

The compression strength as expected increased with the increasing infill. It can be easily observed in Table 12.1 that the increase is not much pronounced in the lower infill samples while it increases two folds after the 30% sample. The values are found to stand still at 14.7 MPa for infill above 70% due to the limitation of smaller load cell used in UTM while testing. None of the samples failed during the testing procedure. Similarly, Table 12.3 represents the properties for MCR (Table 12.2).

The average shore-A, hardness for all TPU samples was plotted against the respective infill percentage. The below plot clearly display an increase trend of surface hardness for respective samples.

The compression modulus indicates a better material, with the samples over 30% infill presenting way better load-bearing quality according to Table 12.2. Although an amputated foot bears more load in comparison to a normal one due to varying centre of gravity of the body using such a material which offers higher compression modulus could be really helpful. The TPU material with better homogenous infill structure could also promise a better life in comparison to the stochastic foam structure of the MCR. Shore-A hardness values for the samples are found to be higher than the MCR, but again finding a polymer with same shore-A hardness was not possible.

Table 12.1 Properties of ABS and PLA [10]

Material	Young's modulus (MPa)	Poisson's ratio	Ultimate tensile strength (MPa)	Yield strength (MPa)
ABS	2240	0.38	29.6	20
PLA	3500	0.36	73	70

Table 12.2 Compression strength of TPU samples

S. No.	Specimen	Compressive strength (MPa)	Maximum load (N)
1	TPU-10	2.1	1355.16
2	TPU-20	2.15	1374.81
3	TPU-30	2.17	1398.05
4	TPU-40	4.3	2776.53
5	TPU-50	6.41	4139.98
6	TPU-60	12.08	7783.97
7	TPU-70	14.7	9487.26
8	TPU-80	14.7	9496.41
9	TPU-90	14.7	9486.77
10	TPU-100	14.7	9493.83

Table 12.3 Properties of MCR specimens [9]

Samples	Shore-A hardness (average)	Compressive strength (MPa)
MCR grinded	47.8	2.17
MCR raw	53.5	2.17

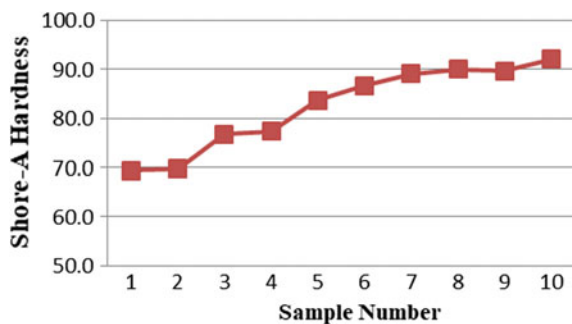
Table 12.4 Heel compression recorded for prototypes

S. No.	Applied load (kg)	Deflection (mm)	
		TPU-40	TPU-50
1	20	0	0
2	25	1	1
3	30	1	1
4	35	1	2
5	40	1	2
6	45	2	3
7	50	2	4

A better flexible and light prosthetic foot which could bear more loads at the cost of higher surface hardness is a good alternative. Moreover, a higher hardness could result in better life when used for barefoot purposes (which are common among Indian households) as it will be more resistant to abrasion. The values obtained from samples which are plotted in Fig. 12.7 shows an increasing trend with infill percentage where minimum shore-A hardness obtained is around 70. The prototypes fabricated possess a shore-A, hardness in the range of 75–80. Two different coloured filaments (white and black) were used for additively manufacturing the 40 and 50% infill foot respectively.

The prototypes were also weighed to compare it with the existing foot, the prototype fabricated using TPU-50 was found to be having a weight of 484 g while the other one fabricated using TPU-40 had a weight of 315 g. Heel Compression was found to be in permissible limits for both the prototypes according to Table 12.4. The foot with 40% infill (TPU-40) undergoes more compression in comparison to

Fig. 12.7 Plot of Shore-A hardness versus TPU samples



the foot with 50% infill. The load range was selected on the basis of average human weight from 60 to 80 kg with addition of factor of safety where single human foot bears half the load.

Based on the results, re-placement of MCR with PLA has been negated by the initial flexibility tests, however, the use of Thermoplastic polyurethane (TPU) in place of MCR has been successfully done, which is also additively manufactured with different fill percentage. These different fill percentages are equivalent to various grades of MCR from low to high densities.

12.6 Conclusions

The prototype foot fabricated with TPU produced excellent improvements over the previous foot which includes remarkable reduction of weight, polymer surface finish which is water-resistant and homogenous infill structure acting as a barrier to crack propagation. An additively manufactured foot with the use of a CAD model could be printed using a 3D printer anywhere in the world without any variation. Such a process will save the amputees from travelling exertion and expenditure. Number of amputees travel from other countries and states of India to Jaipur for the Jaipur foot. More number of tests could be performed on the prototypes to establish their legitimacy. The presence of a number of non-standardised sellers of TPU filaments makes it a bit complex to find the better quality product. The color of the filament being used is also restricted to fewer options; therefore a filament with skin color could produce a more conforming prosthetic foot as it will look more like a natural foot (as in the case of actual Jaipur foot). Moreover, constituent parts could be fabricated separately and a foot with wooden ankle and additively manufactured other parts could be manufactured. In doing so all the parts will be standardised in terms of shape and dimensions, taking out the human error presently incorporated.

Acknowledgements This part of the work is financially supported by Autodesk India Pvt. Ltd.

References

1. Nielsen, C., Affecting, I.: O & P trends & statistics. *Am. Acad. Orthot. Prosthet.* **39** (2010)
2. Sethi, P.K., Udawat, M.P., Kasliwal, S.C., Chandra, R.: Vulcanized rubber foot for lower limb amputees. *Prosthet. Orthot. Int.* **2**, 125–136 (1978)
3. Bhagwan Mahaveer Viklanga Sahayata Samiti: Jaipur foot [Online]. Available: <http://jaipurfoot.org/>. Accessed 20 Jan 2018
4. Jin, Y., Plott, J., Chen, R., Wensman, J., Shih, A.: Additive manufacturing of custom orthoses and prostheses—a review. In: *Procedia CIRP*, vol. 36, pp. 199–204 (2015)
5. Jensen, J.S., Raab, W.: Erratum: clinical field testing of vulcanized Jaipur rubber feet for trans-tibial amputees in low-income countries. *Prosthet. Orthot. Int.* **31**(1), 105–115 (2007)

6. Huber, I., Fischenich, K.M., Wolynski, J., Niese, B., Teater, R.H., Mali, H.S., Jain, A.K., Sorby, S.A., Abrams, L., Donahue, T.L.H.: Epidemiological study of failures of the Jaipur Foot. *Disabil. Rehabil. Assist. Technol.* **13**(8), 1–5 (2017)
7. Maiti, A., et al.: 3D printed cellular solid outperforms traditional stochastic foam in long-term mechanical response. *Sci. Rep.* **6**(1), 24871 (2016)
8. Cross, R.: Standing, walking, running, and jumping on a force plate. *Am. J. Phys.* **67**(4), 304–309 (1999)
9. Teater, R.H., Fischenich, K.M., Wheatley, B.B., Abrams, L., Sorby, S.A., Mali, H.S., Jain, A., Donahue, T.L.H.: Assessment of the compressive and tensile mechanical properties of materials used in the Jaipur Foot prosthesis. *Prosthet. Orthot. Int.* 1–7 (2018). <https://doi.org/10.1177/0309364618767143>
10. Farah, S., Anderson, D.G., Langer, R.: Physical and mechanical properties of PLA, and their functions in widespread applications—a comprehensive review. *Adv. Drug Deliv. Rev.* (2016). <https://doi.org/10.1016/j.addr.2016.06.012>

Chapter 13

Fused Deposition Modeling Using 6-Axis Industrial Robot



Arigela Sri Harsha and Chintamreddy Vikram Kumar

Abstract A conventional Fused Deposition Modeling (FDM) machine builds an object layer by layer on a horizontal platform from bottom to top fashion. The major drawback of the FDM machine is limited number of degree of freedom (only 3). Industrial robots with six degrees of freedom are capable to move its end effector in 3D space with high resolution and repeatability. A robot with an extruder as an end effector has the capability to print the objects on multiple planes. In this work, an attempt is made to simulate the FDM process with an industrial robot. Simulation of printing of a cube on horizontal and inclined planes is presented. Tool path for each sliced layer is developed using polygon-filling algorithm. The simulation of printing of 3D objects using 6-axis industrial robot is carried out using ABB RoboStudio simulation software.

Keywords Additive manufacturing · 3D printing · Fused deposition modeling

13.1 Introduction

Fused deposition modeling (FDM) is an additive manufacturing process where the material is deposited in horizontal layers one on another to create a three-dimensional object. The digital model, i.e., CAD model is the input for this process. Software, hardware, and materials work together to get the desired final product. Initially, this process is used for creating prototypes rather than end functional products. But due to the availability of newly developed materials and higher precise machines, objects are produced with very close or same mechanical and material properties of the end functional products. Nowadays, this technology has a very broad area of applications in almost every field [1, 2].

A. Sri Harsha

Department of Mechanical Engineering, JNTUA, Ananthapuramu 515002, Andhra Pradesh, India

C. Vikram Kumar (✉)

Department of Mechanical Engineering, N.B.K.R.I.S.T, Vidyannagar, Nellore Dt 524413, Andhra Pradesh, India

e-mail: cvikramkumar@gmail.com

© Springer Nature Singapore Pte Ltd. 2020

M. S. Shunmugam and M. Kanthababu (eds.), *Advances in Additive Manufacturing and Joining*, Lecture Notes on Multidisciplinary Industrial Engineering, https://doi.org/10.1007/978-981-32-9433-2_13

159

Manufacturing Industries aims to produce better quality products in the least time. The product quality is mainly dependent on the skill of the worker and the product cost is prohibitively high. In order to reduce the cost and increase the quality robot manipulators are introduced in the manufacturing industries. These robots can do repetitive tasks once they are accurately programmed. Reprogramming can also be done within less time. So these robots are so flexible systems to incorporate in manufacturing industries. High precision, speed, endurance, repeatability and having many numbers of degrees of freedom are the main advantages in the case of an industrial robot. Many numbers of end effectors were developed to meet the requirements in the industry. Autonomous robots are also being developed so that they can interact with the environment and take their own decisions based upon the situations [3].

Integrating robotic and 3D printing technologies will be so advantageous in the field of manufacturing. Because of the higher degrees of freedom, the robot arm can freely move in huge workspace compared to the conventional fused deposition modeling machines. Printing with the extruder in different orientations and over multiple planes is possible if the extruder acts as an end effector of the robot. Tse and Chen [4] explored the new application of robot in the subtractive manufacturing process. A milling tool was used to machine a prototype out of a material block using a CAD model. A number of complex surfaces were also produced using this method. Barnett and Gosselin [5] used a cable suspended robot having 6 degrees of freedom as a large scale 3D printer. In this work polyurethane foam was used as the object material and shaving foam as the supporting material.

The important factors needed to be considered in fusion deposition modeling using the industrial robot are categorized into two groups mainly process parameter and process planning parameters. Layer thickness, deposition speed, and flow rate are the important process parameters are needed to be chosen carefully to ensure good material deposition of layers. Orientation, support structure, slicing, and tool path generation are the process planning parameters that affect the overall product's surface quality and strength of the product [6]. Process parameters directly influence the dimensional accuracy of parts that are fabricated using the fused deposition modeling process. Orientation angle has an impact on repeatability and strength of parts [7]. Layer thickness and road width affect more on the surface quality and part accuracy, compared to raster angle. As well as the air gap has more impact over dimensional accuracy and has a low impact on surface quality [8]. In conventional FDM machines, while generating the tool path, it uses standard G and M codes for movement across the plane. For FDM with the robot, a translator is required to convert these instructions into standard robotic commands so that the robot can be moved accordingly [9].

In this paper, a new procedure is developed for combining additive manufacturing and robotics to print 3D objects. The industrial robot with extruder as end effector has more degrees of freedom than the conventional fused deposition modeling machine. The additional degrees of freedom help to print complex surfaces in multi-planes. The simulation of the 3D printing process with an industrial robot for a simple cube over the flat base and the inclined base is presented in this paper. The simulation work

is carried out in ABB RoboStudio simulation software. The methodology adopted and simulation results are presented in this paper.

13.2 Methodology

In this section, the procedure for printing 3D objects using the industrial robot is presented. Generally, in conventional fused deposition modeling machine, the STL format of a CAD model is taken and then processed to generate a number of slices and tool path for each slice. It depends on various input parameters like nozzle diameter, slice thickness, extruder speed, and feed rate. The tool path generates in terms of G and M codes and it is given to the machine to print the objects. The machine utilizes G and M codes for controlling the motion of the extruder and for the material deposition.

In this work ABB makes IRB 1600 industrial robot is used for 3D printing. ABB robots use rapid programming language to control the movement of the joints. The extruder with the nozzle of diameter 0.5 mm is used end effector for the robot to print the objects. In conventional fused deposition modeling machine, the extruder movement is constrained only in two directions, i.e., x and y . The z movement is provided by the heating bed, i.e., the base plate. Once this extruder is attached to the industrial robot it acts as an end effector and does contain six degrees of freedom. The flowchart indicating the procedure followed to print the objects with an industrial robot is shown in Fig. 13.1. First, the CAD model of the object to be printed is converted into the STL format. In STL format the outer surface of the CAD model is approximated with triangles. To determine boundary points a horizontal plane is used to intersect the triangles. All intersection points are connected to extract the boundary of the layer [10]. After generating the boundary of a layer the horizontal plane is taken with an increment of 0.5 mm and intersected again with the triangles to get the boundary points of the next layer. The same procedure is repeated for the entire height of the solid. For the first layer, the tool path is generated by scanning the boundary using horizontal line either in X or Y direction to determine coordinate

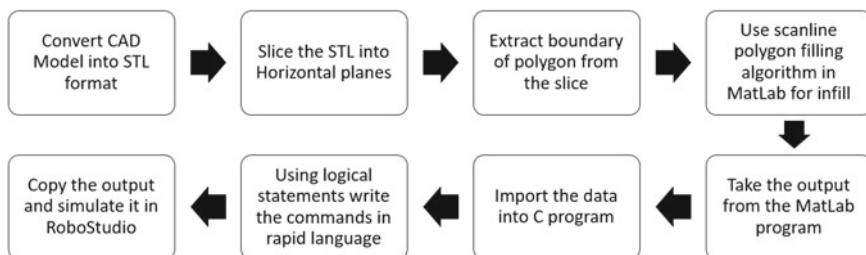


Fig. 13.1 Flowchart of the process

points on the boundary. The entire boundary is scanned by a horizontal line with the incremental movement of 0.5 mm which is equal to nozzle diameter.

All the coordinate points are connected by the zig-zag pattern to generate the tool path. Similarly, for the second layer, the tool path is generated by scanning the second layer using a horizontal line but perpendicular to the previous horizontal line. To create better bonding between the layers, the second horizontal scanning line is considered perpendicular to the previous scanning line, so that the strength of the overall component will increase. The same procedure is repeated to generate the tool path for the entire solid by considering alternative perpendicular scan lines for layer to layer. The extracted points on the boundary of the single slice are taken as input parameters for tool path generation. The tool path is generated in such a way that first tool (extruder) has to move along the boundary and then fill inside the boundary. After completing the first layer the same procedure adopted for the second layer. Like that, for the entire object (Cube in the present case) the tool path is generated. The program is developed in 'C' programming language to find a sequence of points that the extruder to move for each layer. The output of the program gives motion commands that are suitable for rapid language for ABB robot. These rapid commands are taken as the input for the RoboStudio simulation software. The simulation of 3D printing is executed in RoboStudio software. In this work, MatLab is used for slicing, C programming language for tool path generation and rapid programming languages for simulation are integrated to accomplish this procedure.

13.3 Simulation of 3D Printing of Cube

In this work, simulation of 3D printing cube of size 50 mm side using an industrial robot is carried out. For simulation, ABB makes IRB 1600 robot having 6 degrees of freedom, 1.45 m range, and 6 kg payload with IRC5 industrial robot controller is used. The position repeatability of this robot is 0.02 mm and the path repeatability is 0.19 mm. The working range of the robot is shown in Fig. 13.2.

First CAD model (as shown in Fig. 13.3) of a cube having 50 mm side is created and then it is converted into an STL file format (as shown in Fig. 13.4). In this format, the surface of the CAD model is approximated by triangles. Now this STL file is sliced using MatLab program and horizontal slices are obtained. The generated horizontal slices are shown in Fig. 13.5.

Now, from the sliced model each slice is extracted separately depending upon the z values. In this work, each slice of a thickness of 0.5 mm is taken along the z -axis. The cross-section of the slice is shown in Fig. 13.6.

For each layer polygon filling algorithm is implemented. The entire area is scanned with scan lines from left to right. For the first or base slice, the coordinate points are obtained by scanning horizontal lines as shown in Fig. 13.7. The intersection points between the boundary and horizontal lines are extracted for tool path generation. For the second slice, i.e., $z = 0.5$, the area is obtained and it is scanned with scan lines from front to back and intersections are obtained as shown in Fig. 13.8. The intersection points are highlighted with the red circles in both the figures.

Fig. 13.2 Working range of IRB 1600 robot

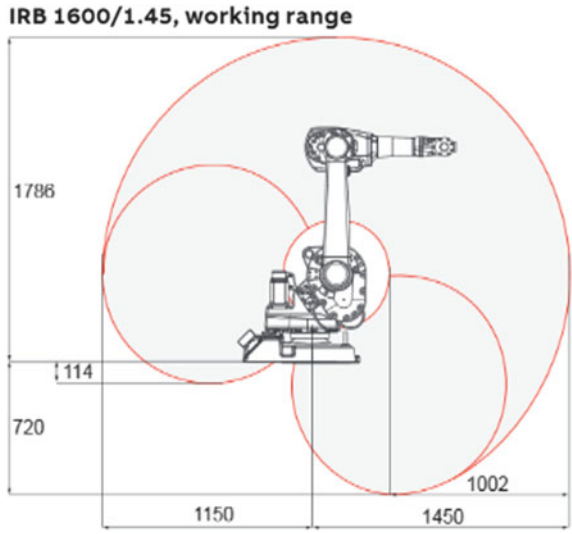


Fig. 13.3 CAD model of cube

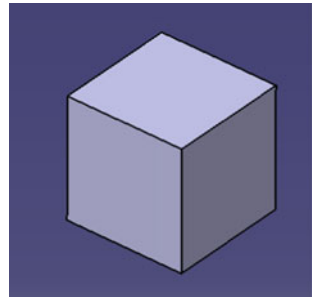


Fig. 13.4 STL form of cube

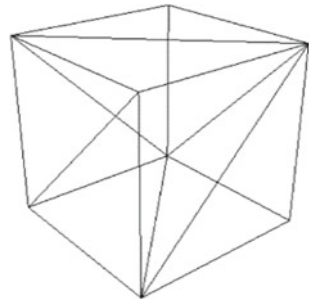


Fig. 13.5 Slices of the cube

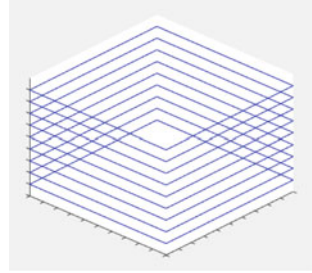


Fig. 13.6 The boundary of the slice

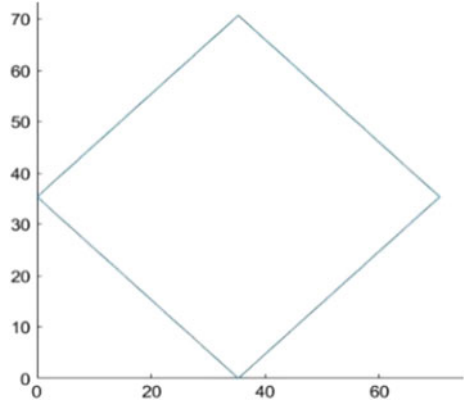


Fig. 13.7 Extracted coordinate point

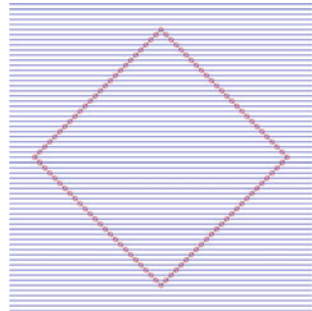
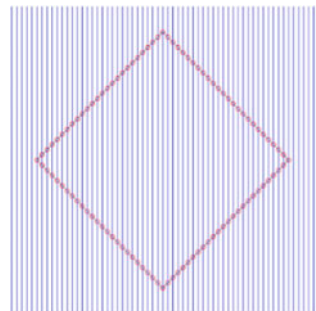


Fig. 13.8 Extracted coordinate points



For the third layer, i.e., $Z = 1$, the scanning is done again from left to right similar to the first slice as shown in Fig. 13.5. The same procedure is followed by scanning alternatively for the remaining layers. Alternative scanning provides better bonding between the layers. The incremental movement of each scan line is also taken as 0.5 mm in the present work.

These coordinate points are taken as input data and using these points tool path is generated in C programming for infill within the boundary. The logical statements convert these data points into tool paths and at the same time, these tool paths are converted into the motion commands in rapid programming language for the robot. Mainly these commands consist of MoveL (Move linear) statements. The tool path for one slice is shown in Fig. 13.9. Every slice is printed in such a way that, first the boundary is printed and then infill of the area is done.

Now the output of this C program, i.e., rapid commands are used to simulate the procedure in RoboStudio software. For printing a cube over the horizontal base, a work object is needed to be defined along the corner of the cube. The coordinate axes of the work object are in such a way that the Z-axis is aligned along with the height of the cube. The tool path is parallel to the XY plane of the work object. So deposition is carried out in the planes those are parallel to the XY plane and incremented through the Z-axis of the work object. So the orientation of the extruder (end effector of the robot) is perpendicular to the printing base and moves along the Z-axis for printing the layers.

If it is required to print the object over the inclined base, the work object is defined in the same way as the previous case. But in this case, the extruder is oriented with some angle of inclination to the global (or robot's base coordinate) Z-axis. The angle of inclination is equal to the inclination of the printing base. In this case, also the extruder is perpendicular to the printing base and it moves along the work object's Z-axis.

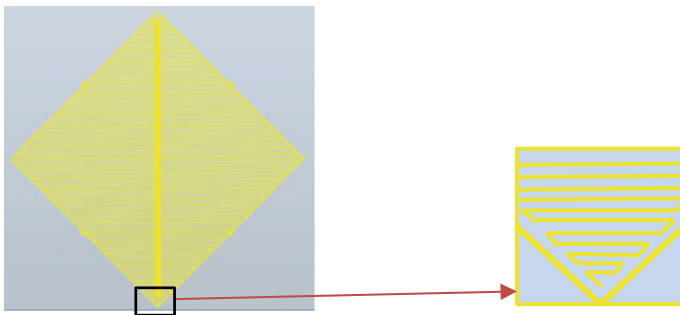


Fig. 13.9 Generated tool path

13.4 Results and Discussion

The simulation is done successfully and the end effectors tip, i.e., the extruder tip followed the path that is generated by this procedure. The simulation to print the object on horizontal base is shown in Fig. 13.10. The generated tool path is shown in Fig. 13.11. The simulation of the robot over the inclined base is shown in Fig. 13.12.

Conventional fused deposition modeling machine has the flat horizontal printing base. If an object is needed to be printed over a plane which is inclined, it is impossible, as the extruder can't move in an inclined path due to its restricted degrees of freedom. By using the extruder as the end effector of the robot it is possible to print over the inclined planes. Simultaneous printing over different planes is possible.

By using the extruder as an end effector of a six-axis industrial robot offers several advantages compared to the conventional fused deposition modeling machine. Having large workspace and more degrees of freedom, multi-plane printing is possible using the six-axis industrial robot. This eliminates the printing of support structures and saves material and time. The conventional fused deposition machine has the limitation of getting staircase effect while printing of curved surfaces. Curved tool paths

Fig. 13.10 Simulation of the printing process

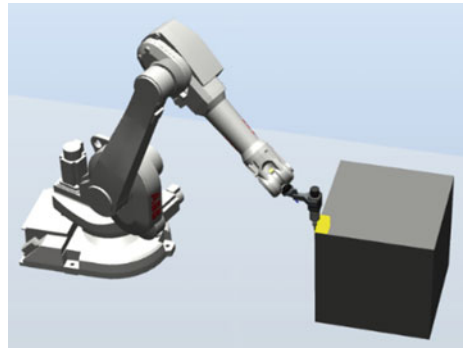


Fig. 13.11 Tool path of the cube

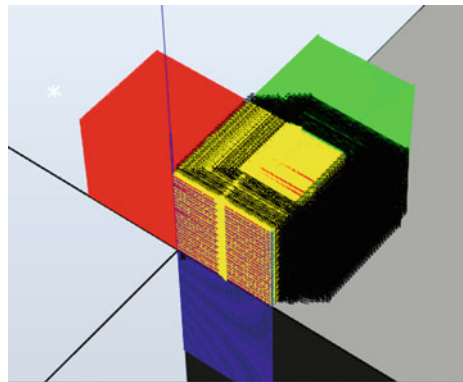
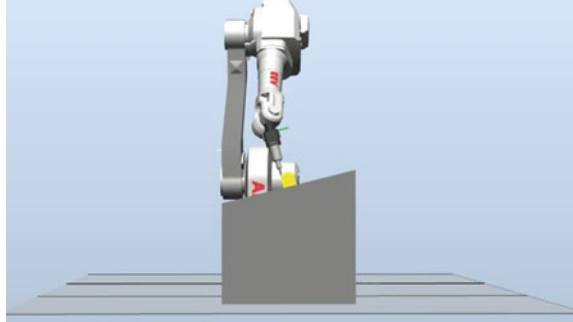


Fig. 13.12 Simulation of printing over an inclined plane



can minimize this staircase effect. These curved tool paths can be generated by the robot, which is impossible by the conventional fused deposition machine. Adaptive printing can be done using different nozzle diameters to minimize the printing time and power consumption. The material being used in this process is thermoplastic material. It will solidify quickly within a fraction of seconds when it is exposed to the atmosphere. So it will stick to the previous layer when depositing is done in either horizontal or inclined planes. The material won't drop if the correct parameters are chosen while printing over the inclined plane.

In conventional FDM machines, the horizontal base has to move in a vertically downward direction to build layer by layer and the base should possess high rigidity and strength while printing large-size components. Whereas printing with robot takes place by moving the extruder in vertically upward direction and no need to provide any robust support system and even sometimes robot can build the objects from the ground.

13.5 Conclusions

In this paper, a new procedure that combines both the additive manufacturing and robotics to print 3D objects is presented. A generalized procedure for 3D printing of objects using a robot is presented in this paper. The industrial robots having the capability to print the objects over entire workspace with high resolution and repeatability. Minimum support system for the printing base is required while printing with the industrial robots.

References

1. Gibson, I., Rosen, D.W., Stucker, B.: Additive Manufacturing Technologies. Springer (2010). ISBN: 978-1-4419-1119-3
2. Chee Kai, C., Kah Fai, L., Chu Sing, L.: Rapid Prototyping: Principles and Applications, 2nd edn. (2003). ISBN 981-238-117-1
3. Tsai, L.W.: Robot Analysis the Mechanics of Serial and Parallel Manipulators (1999)
4. Tse, W.C., Chen, Y.H.: A robotic system for rapid prototyping. In: Proceedings of the 1997 IEEE International Conference on Robotics and Automation, pp. 1815–1820 (1997)
5. Barnett, E., Gosselin, C.: Large-Scale 3D printing with a cable-suspended robot. Accepted manuscript Additive Manufacturing. Elsevier (2015)
6. Ishak, I., Larochele, P.: Robot arm platform for rapid prototyping: Concept. In: Proceedings in Florida Conference on Recent Advances in Robotics, (2015)
7. Górski, F., Kuczko, W., Wichniarek, R.: Influence of process parameters on dimensional accuracy of parts manufactured using fused deposition modeling technology. Adv. Sci. Technol. Res. J. **7**(19), 27–35 (2013)
8. Nancharaiah, T., Ranga Raju, D., Ramachandra Raju, V.: An experimental investigation on surface quality and dimensional accuracy of FDM component. Int. J. Emerg. Technol. **1**(2), 106–111 (2010)
9. Swanson, M., Spurgeon, W., Vass, T., Danielewicz, M.: 3D printing robotic arm. Project report, Worcester Polytechnic Institute (2016)
10. Eragubi, M.: Slicing 3D CAD model in STL format and laser path. Int. J. Innov. Manag. Technol. **4**(4) (2013)

Chapter 14

Characterization of Rapid Foam Castings Produced by Different Mold Making Processes



Ranjeet Kumar Bhagchandani , Rohan Ghodke , R. Manivannan , Seema Negi , Sajan Kapil  and K. P. Karunakaran 

Abstract Rapid casting gives the opportunity to develop a new casting in days, not in weeks or months. Evaporative Pattern Casting (EPC) process gives flexibility to produce complex geometries by integrating several parts in single casting. The lead-time and cost involved in designing and fabricating the metal tooling for Expanded Polystyrene (EPS) pattern making can be overcome by using the Segmented Object Manufacturing (SOM) machine. This hybrid system of pattern making is explored with all sub-systems and a complicated EPS pattern is produced by this Rapid Prototyping system. Conventional EPC process is more complicated due to coating development, vacuum assisted metal pouring and vibration system for filling the cavities by unbounded sand. In the present work, different mold-making processes are explored to avoid complications of conventional process. The Green sand, No-bake sand, and Plaster of Paris molds are prepared using Rapid Prototyped EPS pattern to produce the castings. The castings are characterized by comparing the surface roughness, dimensional accuracy, hardness, and surface morphology.

Keywords Segmented object manufacturing · Rapid foam casting · Evaporative pattern casting · Expanded polystyrene

14.1 Introduction

It is an exhaustive change in manufacturing, that the oldest metal manufacturing technique can be executed with the most advanced technology viz., Rapid Prototyping. It gives freedom to the designer to realize his ideas and manufacturer a way

R. K. Bhagchandani (✉) · R. Manivannan · S. Kapil · K. P. Karunakaran
Mechanical Engineering, Indian Institute of Technology Bombay, Mumbai 400076, India
e-mail: ranjeet.bhagchandani@gmail.com

R. Ghodke
Mechanical Engineering, National Institute of Technology, Surathkal 575025, Karnataka, India

S. Negi
Metallurgical Engineering and Material Science, Indian Institute of Technology Bombay, Mumbai 400076, India

to produce parts while considering designer's expectations. The demand for shorter lead-time is also accompanied by the need for quality assurance and cost reduction. Complicated castings can be realized in days instead of months. It expands the communication bandwidth between designer and manufacturer. Evaporative Pattern Casting (EPC) process gives the flexibility to produce complex geometries by integrating several parts in a single casting. The EPC process gives an opportunity to develop Bimetallic casting to fulfil the requirement of lightweight construction. Jiang et al. [1] have proved the capability of EPC process to develop compound casting and investigated on compound interface characteristics. The use of a polystyrene pattern increases dimensional accuracy, and gives improved casting quality, compared to conventional casting [2]. Complicated tooling is required in the form of dies and multiple parameters have to be controlled nicely to get acceptable quality patterns. The RP process gives an opportunity to explore the unconventional pattern-making processes.

Freeform Automated Sculpting Technology (FAST) is a system developed within the Department of Mechanical Engineering, University of Canterbury, New Zealand [3]. The system consists of Laser Scanner, CAD/CAM package, Six-axis Kuka KR6 industrial robot, and an electrically heated cutting tool. TruSurf is a layered manufacturing method developed by Hope et al. [4]. It uses a high-pressure, five-axis water-jet cutter to cut the model's cross-sections from layers of polystyrene and assembly of the layers is done manually. Model Angelo, another RP system was developed, which utilizes a combination of linear and rotational axis to cut foam with a heated cutting tool [5]. The block is held with the rotating fixture and its motion is synchronized with the cutting tool. Broek et al. [6] have developed Freeform thick-layered object manufacturing (FF-TLOM) system for EPS pattern making. This system is very much similar to the TurSurf, the only difference is that it has flexible cutting tool which changes shape to provide high order approximations of the desired surface. Chen et al. [7] discussed all existing methods of EPS pattern making which includes foaming, molding, manual cutting, CNC machining, and rapid prototyping. As all these machines utilize a taut hot wire cutting tool which greatly restricts the geometry which can be sculpted. The second most important drawback is that if the thickness of the sheet is more than 4 mm the temperature gradient will come in picture and affect the surface finish and quality of the product. These processes are capable of the first-order approximation of the surfaces only.

In this work, a new RP machine called Segmented Object Manufacturing is explained and an EPS pattern is produced by Visible Slicing process. The Rapid Prototyped patterns are then converted into castings by using different mold making processes. SOM machine is a hybrid system to produce EPS patterns of complicated geometries. The machine works on the principle of V-slicing, and converts a complicated object into multiple visible segments. The machine has three sub-systems: machining, hot wire slicing for subtraction and glue dispensing for assembly. Unlike most RP systems, which build parts using an additive, layer by layer process, SOM starts with a block and convert it into the desired shape by combination of slicing, machining and gluing.

The numbers of parameters which affect the EPC process are alloy composition, vibration amplitude, vacuum, pattern material, sand, and coatings. The coating is not required merely to prevent direct contact with the sand and metal, but its main task is to support the sand during the brief interval between the gasification and replacement of pattern by the molten metal. Kumar et al. [8] studied the influence of process parameters on the density of coating in EPC process. The molten metal filling rate increases with increasing coating permeability and thickness. The molten metal filling rates of cast iron and a copper alloy were measured for various coating permeability and thicknesses [9]. These parameters increase the complexity of the process. In resin-based sand molding process, there is no need of applying vacuum for removing the gases from the mold because the mold is porous and allows gases to escape after solidification. Modern foundries are using the no-bake sand molds because it provides good permeability, surface finish, and dimensional accuracy. The researchers are trying to explore different mold making processes to produce casting by EPS pattern. Emami et al. [10] have developed Al/Mg compound casting by using EPS pattern with Cold Box CO₂ mold process. Al ingot was machined to get a shape and placed inside the EPS pattern. The pattern with metal insert was buried into the Na₂SiO₃ mixed silica sand and CO₂ was passed into the mold box to create complicated mold. In the present work Green sand, No-bake sand, Cold box, and POP molding processes are explored to produce castings using Rapid Prototyped EPS pattern. Rapid Foam Casting is proposed and comparative study has been done to characterize the castings produced by different mold making processes. Figure 14.1a shows the inverted tree diagram of conventional EPC and Rapid Foam Casting process.

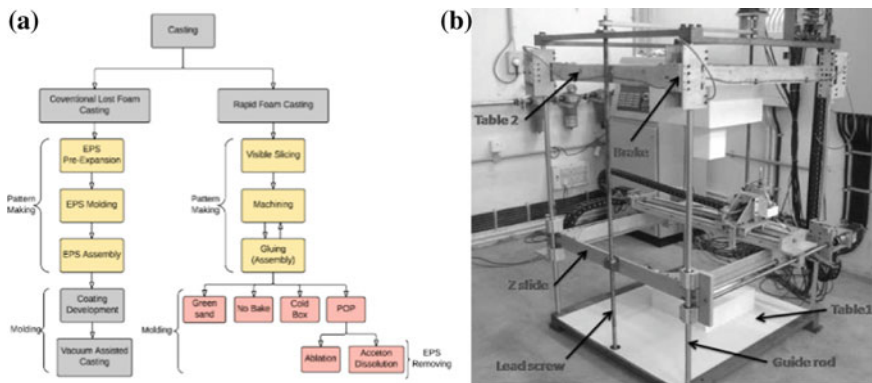


Fig. 14.1 a Inverted tree diagram of conventional EPC, rapid foam casting with different mold making processes, b developed SOM machine for pattern making [11]

14.2 Materials and Methods

The experimental procedure consists of the three major setups viz., (1) Rapid Prototyping of EPS patterns (2) Material Selection (3) Mold Making and Metal Pouring. Segmented Object Manufacturing machine as shown in Fig. 14.1b is a developed RP machine for making prototypes of EPS and finally achieve a metallic prototype or final component by using this EPS Prototype as a pattern in Evaporative Pattern Casting (EPC). The complicated pattern is converted into the visible segments. The SOM has automatic hot wire slicing, gluing and machining systems. Hotwire slicing cuts the object into segments and machining operation is performed by milling system. The tool path planning for machining and simulation are done with PowerMill software as shown in Fig. 14.2. After verifying the simulation, the code is generated for FANUC Oi-mate MC series controller. After machining the segments, assembly of the complete pattern is done by using automatic glue dispensing system. The assembly is also fully automatic.

The SOM machine has two tables one is at the top and other is at the bottom, and the top table can move up and down on four guide rods. The machining spindle is in between the top and bottom table and it has an indexing mechanism to change the orientation of the cutter from up to down. The glue dispensing system is used to apply the glue at a particular position. The internal feature of top segment and machined and assembled with the bottom segment. After final slicing the top contour is visible to the cutter, it is machined to get the final pattern. AlSi12 alloy can be cast into thinner and more intricate sections than any of the other types of Al casting alloys and is especially suitable for leak-tight castings. A typical temperature for sand and chill castings is 725 °C but in practice, it may range considerably above or below this value according to the dimensions of the casting.

The conventional method of shell creation around the EPS pattern is difficult and time-consuming. This also increases the cost of mold preparation and this directly affects the final cost of the casting. To overcome these problems different types of mold-making process are discussed and comparative study has been done to find out the best process for mold making for EPC.

In this part of research, oil urethane no-bake binder process is used to make molds. This is a three-part system comprising (a) alkyd oil urethane resin, (b) polymeric

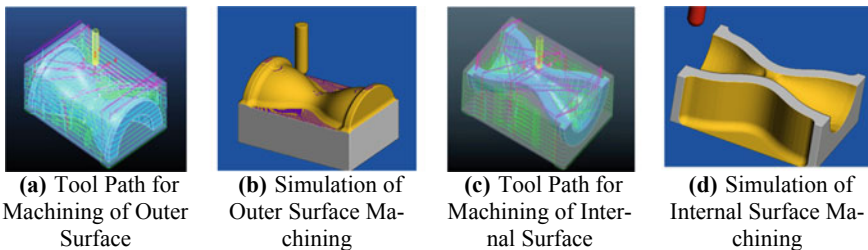


Fig. 14.2 Simulation of complete machining operation

crosslinking agent, and (c) liquid amine. The silica sand of 55 AFS GFN is supplied by the Gargi Foundry Chemical, Mumbai. The alkyd oil urethane resin and the liquid amine is mixed first, and added to sand. To the above premix, the crosslinking agent is mixed and the sand mixed with binders filled around the EPS pattern. The composition of the binder is: part a is 2.4 wt% of the sand and part b is 15 wt% of the resin and part c is 20 wt% of the part a. After some time, the mold becomes hard and can sustain the load applied during the metal pouring. The AlSi12 alloy is melted at 725 °C and poured into the mold. Figure 14.3a, b shows the mold making using the chemically bonded sand. The green sand mold is produced as shown in Fig. 14.3c. The additives for the green sand are bentonite, water, sea coal and dextrin. The composition of the green sand is 10% bentonite and 7% sea coal. The sand is blended in a muller, where the water and the additives are blended with the sand. The sand is then ready to be used to make a mold. The green sand mixture is compacted by hand around EPS pattern to create a mold. In POP molding process the CaSO₄ with talc and silica flour mixed with water gets clay-like consistency and is shaped around the EPS pattern. Since plaster has lower thermal conductivity, the casting cools slowly, and therefore has more uniform grain structure (i.e., less warpage, less residual stresses). The slow cooling rate allows the metal to fill thin cross-sections. The minimum possible cross-section is 0.6 mm. This results in a near-net shape casting. During pouring, if moisture is present, the casting will be defective. To avoid this, the POP mold is dried before pouring and the drying was done at two different temperatures in the oven. Figure 14.4 shows the POP mold heated at different temperatures with wax coated EPS patterns. At 500 °C the crack is noticed on to the mold surface.

Degasification is very difficult in EPC process and vacuum-assisted system is required to remove the gases from the cavity after metal pouring. The casting may have defects due to improper degasification. To avoid this problem, pattern is removed by filling acetone into the mold. The acetone easily dissolves the polystyrene, leaving very little residue. The Polystyrene becomes soft, releasing the air bubbles trapped in the foam, and the polystyrene ends up as a soft blob in the acetone and it is removed from the mold. Another method of pattern removing is also used, the mold is kept in the furnace at around 250–300 °C for couple of hours which completely evaporates

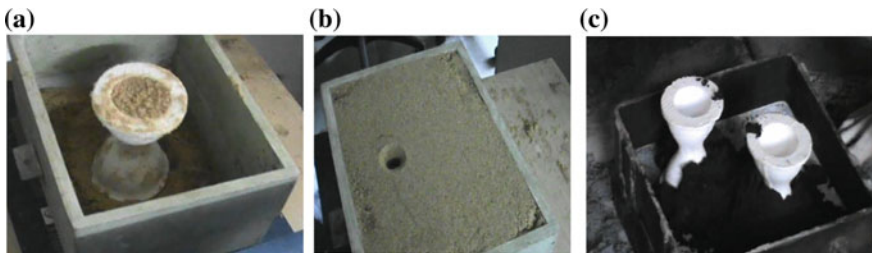


Fig. 14.3 a Beginning of no-bake sand mold preparation, b no-bake sand mold after curing, c green-sand mold making for EPC process

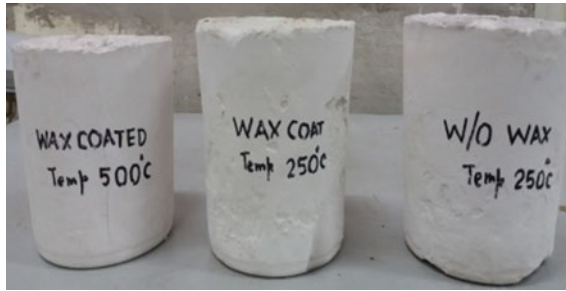


Fig. 14.4 Heated POP molds before metal pouring

the EPS pattern inside the mold. Thereafter the mold is taken out from furnace and kept in air to cool down. The molten metal is poured at 725 °C and allowed to cool down.

Sodium–silicate sand is prepared using silica sand and 1.5–6% of sodium silicate solution (also called as silica gel or water glass) which acts as a binder. The silica sand and binder are muller for 10 min and molds were prepared using the sand mixture. The molds are then hardened by passing CO₂ gas through them at a pressure of 1.5–2 kg/cm² for a few seconds.

14.3 Results and Discussion

Figure 14.5 shows the castings produced by different mold making processes. The surface roughness of casted parts was measured with the help of Zeta Microscope.

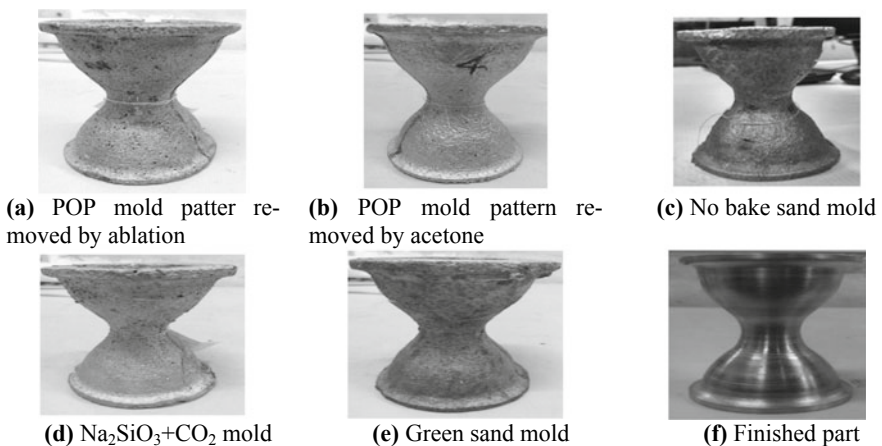


Fig. 14.5 Castings produced by different mold making processes

Table 14.1 Surface roughness of casted part with different mold making process

Casting	Sample no	R_a (μm)	
		Inner	Outer
No bake sand	1	35.3	34.0
POP and heating	2	22.8	21.4
POP acetone dissolution	3	25.0	21.26
$\text{Na}_2\text{SiO}_3 + \text{CO}_2$	4	27.5	29.3
Green sand	5	42.5	38.5

As the base of the sample should be flat, so the small samples of $5 \text{ mm} \times 5 \text{ mm} \times 3 \text{ mm}$ were cut from the collar area of castings, and roughness was measured. The surface roughness of different castings is shown in Table 14.1. Castings produced by POP mold give better finish as compared to the No-bake and Greensand molds. The EPS pattern may be distorted during ramming in case of green sand molding, so it is avoided and without ramming the flowability of the green sand is very poor as compared to No-bake and CO_2 molds. Fast internal cooling gives finer grains and better surface finish. The outer surface has better finish as compared to internal surface, because outer surface dissipates heat from the mold walls. Microstructure of each of the castings is determined by SEM analysis and elemental analysis is done by EDS. Following observations are made from the SEM analysis.

More carbon inclusion in the sand-based casting due to pyrolysis of the EPS foam which is evident from the composition as well as from the white spots in the images. But POP based mold with wax coated pattern and acetone dissolution of the pattern shows highest carbon content due to the fact that wax and acetone both are hydrocarbon and acetone got soaked in the POP mold when it is used to dissolve the EPS foam. Moreover, wax does not dissolve in the acetone so it remains inside the mold cavity which causes the high carbon content in the casting product.

Microstructures of the sand-based castings are more porous than that of POP based casting. This can be explained by the fact that in case of sand-based casting molten metal continuously replaces the EPS foam by pyrolysis and the gases have to regions of shrinkage porosity contain dendrite lobes, which existed as free surfaces within the cavities after solidification. The cavities could have been mainly caused by the pyrolysis of pattern materials, that is, molten metal feeding during pouring was obstructed by the gas pressure evolved by the pyrolysis of pattern materials.

The Vickers hardness test is performed to measure the hardness of the castings. The castings of pre-heated POP mold give higher hardness value as compared to the other mold-making processes as shown in Table 14.2. Pattern dissolved in acetone gives the least hardness. The pre-heating of POP mold to remove the EPS pattern before pouring is beneficial to achieve more hardness of the casting.

POP-based mold casting absolutely replicated the pattern. Among the two POP-based molds acetone dissolution process results in better dimensional accuracy. POP is in the powder form and after mixing with water the slurry becomes fluidic in nature which increases the flowability. POP slurry can easily fill the intricate areas. After hardening of the POP mold when it was heated EPS pattern vaporizes leaving

Table 14.2 Vickers Hardness test results of casted part with different mold making process

Casting	Sample no	Hardness (HV)
No bake sand	1	88.90
POP and heating	2	90.28
POP acetone dissolution	3	65.50
Na ₂ SiO ₄ + CO ₂	4	82.50
Green sand	5	82.80

behind the cavity inside the mold. With heating POP mold also subjected to thermal expansion resulting in the changes in the dimensions of the mold cavity. But in case of acetone dissolution of the EPS pattern, the mold does not subject to any thermal load. Which maintain the original dimension of the pattern and there is a negligible deviation in the dimensions of the casting compared to the EPS pattern.

14.4 Conclusions

Rapid Prototyped EPS patterns are produced by SOM machine. This hybrid system of pattern making is explored with all sub-systems of this machine. After pattern making four different mold-making processes are adopted for producing castings. Three methods are of sand-based mold making, whereas two are POP based mold making. Each of these are measured for their dimension, surface roughness, and microstructure. Dimensions of the castings are compared with the EPS pattern. However, in case of POP mold and acetone dissolution of the pattern method produces more accurate casting in terms of dimension. From the point of view of surface roughness POP mold with wax coated pattern and acetone dissolution of the pattern gives minimum surface roughness. This is because wax coating covers all the surface unevenness of the EPS foam pattern. POP mold directly comes in contact with wax surface which produces smooth surfaces. But POP mold with wax coating and acetone dissolution produces high carbon content in the casting. Although there was very less porosity but due to high carbon content it may become more brittle.

- POP mold with wax coating and acetone dissolution of pattern gives better dimensional accuracy and surface finish but carbon content is high.
- POP mold with wax coating and heating produces optimum dimensional accuracy. Moreover, POP mold with wax coating and heating gives less carbon content which reduces the brittleness of the casting.
- The maximum surface roughness is 42.5 μm in case of green sand mold sample and minimum value is 21.4 μm in the case of POP mold made of wax-coated sample.

References

1. Jiang, W., Li, G., Fan, Z., Wang, L., Liu, F.: Investigation on the interface characteristics of Al/Mg bimetallic castings processed by lost foam casting. *Metall. Mater. Trans. A* **47**(5), 2462–2470 (2016)
2. Monroe, R.M.: *Expendable patterns casting*. American Foundryman Society Inc., pp. 84 (1992)
3. Brooks, H., Aitchison, D.: A review of state-of-the-art large-sized foam cutting rapid prototyping and manufacturing technologies. *Rapid Prototyp. J.* **16**(5), 318–327 (2010)
4. Hope, R.L., Jacobs, P.A., Roth, R.N.: Rapid prototyping with sloping surfaces. *Rapid Prototyping Journal* **3**, 12–19 (1997)
5. Hamade, R.F., Zeineddine, F., Akle, B., Smaili, A.: Modelangelo: a subtractive 5-axis robotic arm for rapid prototyping. *Robot. Comput. Integr. Manuf.* **21**, 133–144 (2005)
6. Broek, J.J., Horvath, I., de Smit, B., Lennings, A.F., Rusak, Z., Vergeest, J.S.M.: Free-form thick layer object manufacturing technology for large-sized physical models. *Autom. Constr.* **11**, 335–47 (2002)
7. Chen, H.Z., Shan, Z.D., Dong, H.Z.: Research of foam pattern processing for lost foam casting. *Appl. Mech. Mater.* **331**, 600–603 (2013)
8. Kumar, S., Kumar, P., Shan, H.S.: Density optimization of slurry of coating material used in the EPC process through Taguchi's parameter design approach. *Mater. Manuf. Process.* **23**(7), 719–725 (2008)
9. Maruyama, T., Gou N., Mitsuyoshi T., Keisuke N.: Effect of coating thickness on the molten metal filling rate of cast iron in the evaporative pattern casting process. *Int. J. Metalcast.* **11**(1), 77–83 (2017)
10. Emami, S.M., Divandari, M., Hajjari, E., Arabi, H.: Comparison between conventional and lost foam compound casting of Al/Mg light metals. *Int. J. Cast Metals Res.* **26**(1), 43–50 (2013)
11. Bhagchandani R.K., Kapil S., Kamble P., Karunakaran K.P.: Investigation of ablation studies of EPS pattern produced by rapid prototyping. *Virtual Phys. Prototyp.* **13**(4), 311–324 (2018)

Chapter 15

Layer Separation Mechanisms in DLP 3D Printing



Patil Yogesh , Patil Richa , N. S. Chandrashekar 
and K. P. Karunakaran 

Abstract Additive Manufacturing (AM) also known as 3D printing, fabricates an object by addition of material layer by layer and well known for its ability to manufacture the complex objects and reduce material wastage, unlike the conventional manufacturing process. AM comprises a number of technologies, one of them is Digital Light Processing (DLP) which uses liquid photopolymer resin, cured with the help of ultra-violet (UV) light. There are two approaches, top-down and bottom-up. In the latter, the cured layer must stick to the build platform or previously cured layer. Instead, it sticks to the vat bottom, referred as vat sticking and it prevents the further printing process. In this paper, the reasons behind this issue and methods to overcome are reviewed. Anti-stick films have been used as a low-cost optimal solution and number of experiments were conducted.

Keywords Additive manufacturing · 3D printing · Digital light processing · Layer separation mechanism

15.1 Introduction

AM is a well-known process of building a three dimensional (3D) object, layer by layer directly from 3D CAD model. AM comprises a number of technologies viz. Stereolithography (SLA), Digital Light Processing (DLP), Fused Deposition Modeling (FDM), etc. In the DLP 3D printer [1], the 3D CAD model is sliced into the number of layers with layer thickness ranging from few microns to hundred microns, then the image of sliced layer and sliced data for Z-axis movement is fed to the machine to print a complete 3D object. While designing the DLP 3D printer, one

P. Yogesh (✉) · P. Richa · N. S. Chandrashekar
CAD/CAM& Robotics Section, Department of Mechanical Engineering, K J Somaiya College of
Engineering, Vidyavihar, Mumbai 400077, India
e-mail: patil.yogesh0808@gmail.com

K. P. Karunakaran
Manufacturing Engineering Section, Department of Mechanical Engineering, Indian Institute of
Technology, Mumbai 400076, India

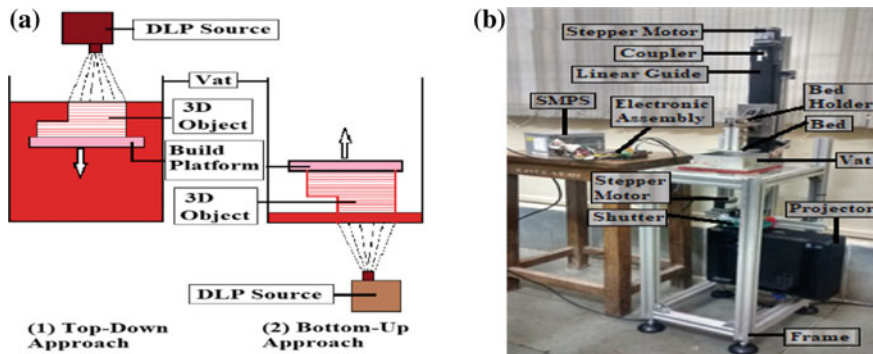


Fig. 15.1 a DLP 3D printing approaches; b Indigenously fabricated DLP 3D printing machine at KJ Somaiya College of Engineering, Vidyavihar, Mumbai, India

of the most critical considerations is the orientation in which the system projects the light on the build surface. It can be constructed in two different fashions [2, 3].

First, the top-down approach is also known as a free surface method, where the 2D cross-sectional image of the layer is projected on to the surface of the resin through projector which also emits the UV light, thus the resin falling in the projected area gets cured due to photo-polymerization reaction. Then the elevated platform lowers down by the distance equal to layer thickness followed by a recoater blade which swaps across resin surface for recoating it with the fresh material [4, 5] as shown in Fig. 15.1(a-1). The maximum height of the printable 3D object is limited by the depth of the vat. Top-down printer cures the top layer of the photopolymer resin. While printing an object, only the small amount of resin may be required but, the vat needs to be filled completely.

Second, the bottom-up approach also called as a fixed surface method where the light source is placed at the bottom of the system as shown in the Fig. 15.1(a-2). It projects a 2D cross-sectional image of the layer on the build platform through transparent vat surface. To get the final object, the first layer must stick to the build platform. After printing the first layer, the platform raises by a distance equal to the layer thickness and a 3D object is printed under the build platform [6]. An indigenously built bottom-up DLP 3D printer as shown in Fig. 15.1b is used for the experimental purpose. It consists of pure acrylic transparent vat base, Acer X1213P DLP Projector, and a stepper motors to drive axis and shutter. Experiments were conducted with and without layer separation mechanisms.

15.2 Vat Sticking Issue

Experiments with the apparatus shown in the Fig. 15.1b and MakerJuice SF resin was carried out without any mechanisms with layer thickness of 80 μm . It was found,

the cured layer sticks to the vat surface instead of build platform or previously cured layer. Thus, unable to print next layers. Table 15.1 shows the input parameters for these experiments.

Figure 15.2a shows the desired shape of an object and Fig. 15.2b shows results where the first layer of all experiments was attached to the vat surface.

The various reasons that can cause a layer to stick to the vat surface are as follows:

1. Insufficiently mixed resin: Using resin without mixing well causes pigments to settle down at the bottom of the resin bottle. This leads to no or partial curing when exposed the UV light. To avoid this, resin must be mixed well before using.
2. Insufficient bottom layer cure time: Due to insufficient bottom layer cure time, bottom layers may not get cured enough to hold against the build platform surface. Thus, the bottom layer irradiation time must be slightly more than the standard irradiation time provided by the material supplier.
3. Contaminated plate surface: Both vat and build surface must be cleaned with isopropyl alcohol (IPA) to remove any dirt particles, previously cured resin, etc.
4. Vacuum force: This is the major reason behind the vat sticking problem. After each layer of printing, the build platform is moved upward to peel off the layer from the vat surface. During this, the vacuum force generated causes layer to stick to the vat.

The first three reasons for the vat sticking can be easily resolved. The vacuum force generated between a build platform and vat surface plays vital role in vat sticking.

Table 15.1 Input parameters

Experiment number		1	2	3	4
Irradiation time (t) (sec)	Bottom layers	12	14	14	13
	Subsequent layers	8	9	8	9

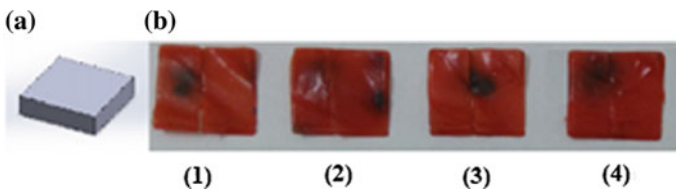


Fig. 15.2 Experiment without any layer separation mechanism

15.3 Layer Separation Mechanisms

To overcome the vat sticking problem, different mechanisms can be used known as layer separation mechanisms. It can be either done mechanically or by using special semi-solid solutions or both. Some of the mechanisms are explained below:

15.3.1 *Anti-stick Material*

Anti-stick material is one of the layer separation mechanism. It must be transparent in order to pass the UV light. Application of anti-stick material on the vat surface affirms that the cured layer does not stick to the vat surface but to the build platform or previously cured layer. The use of films/coating with minimum thickness gives a maximum UV output [7]. Different anti-stick materials are explained as follows:

A PDMS Layer on Solid Vat Floor. PDMS (Poly-Di-Methyl-Siloxane) also commercially known as Sylgard 184 (gel form) is transparent at frequencies 240–1100 nm. After applying its coating on the vat surface, absorbs oxygen and creates a thin lubricating film of non-polymerized resin. It gives the best result. But it swells by absorbing resin and gets damaged during use. It is consumable and degrades due to prolonged exposure. Major drawbacks include, expensive, cannot sustain at high temperature and gets consumed very easily during prints and has to be recoated after few prints [7, 8].

Anti-Stick Films. Using anti-stick films seems a very effective method because of easy availability, low cost, higher transmissivity to UV light, etc. In order to use the films as an anti-stick material, it must exhibit the following properties [8]:

- Anti-stick: Films used must have the anti-stick property so that cured layer will not stick to the film.
- Transparent: Films must be transparent enough to transmit UV light through it.
- Chemically inert: Films must be chemically inert and should not be affected by any chemical reaction with resin.
- Wrinkle-free: No wrinkles should be formed on the film surface otherwise it will affect surface quality.
- No elongation: Films should not get elongated during printing since it affects the dimensional accuracy of the printed objects.

15.3.2 *Active Peeling Mechanism*

Active peeling is the second most commonly used layer separation mechanism after anti-stick material. This mechanism alone does not give good results and hence it has been suggested to use it with PDMS layer. It uses shear forces to resolve the vat sticking. The different active peeling mechanisms are explained below [7, 8]:

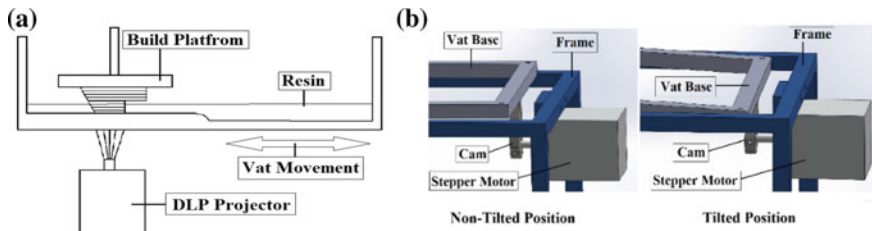


Fig. 15.3 a Gliding the printed object mechanism; b Active tilt system mechanism

Gliding The Printed Object. Gliding the printed object method uses the shear force to peel off the layer from a vat surface as the B9creator 3D printer does. The vat assembly moves in the horizontal plane to apply the shear force using a motor. The object slides horizontally into a deeper area in order to peel the object from the surface after a layer of resin is cured as shown in the Fig. 15.3a. It increases the complexity of the assembly, degrades the surface quality of the layer and affects the dimensional accuracy [5, 8].

Active Tilt System. The active tilt mechanism causes the vacuum to break with a smaller force when the product was pulled off in the normal direction to the floor. It is done by using servomotor/stepper motor with a cam that tilts the vat support downward. After tilting, the platform is moved a bit up and down to peel off the product as shown in the Fig. 15.3b. For this, the four-bar mechanism, eccentric cams, and spindles can be used. If this mechanism is used alone, it affects the surface quality and the dimensional accuracy, but at a lower extent as compared to the other active peeling mechanisms. Thus, it must be used together with the PDMS.

Rotating Vat or Build Platform. Another method of active peeling uses a stepper motor to rotate the vat (most preferably circular) along a vertical axis. So that a shearing force can be applied at every step. This method uses lesser linkages and uniform force can be applied. If there is no provision for the movement of the vat then the bed can be rotated with no change in projecting image, only if the part produced is circular in geometry. But if it is not, the projected images also have to be rotated in synchronization with the bed rotation. Thus, the whole assembly becomes heavily complicated because of both vertical and rotating motion, making it costlier.

15.3.3 Passive Peeling Mechanism

Passive peeling uses high stiffness springs instead of motors. Property of resisting the compression of spring helps to resolve the vat sticking problem. But it reduces precision [8]. Thus, passive peeling mechanism should be used only with PDMS, not with any films as the forces may tear apart the films.

15.3.4 *Inhibition by Oxygen*

Oxygen can inhibit free radical polymerization since it consumes free radicals [9]. For (meth) acrylates the oxygen concentration is approximately 10^{-3} mol/L, which is higher than the concentration that allows polymerization [10]. The influence of oxygen on the free radical reaction depends on the monomer selected. CLIP (Continuous Liquid Interphase Printing) technology by Carbon3D [6] uses oxygen as an inhibitor. It uses a membrane which is permeable to oxygen. Here, the bottommost layer is not cured, hence it doesn't stick to the vat surface. It allows continuous printing, by controlling speed of motor and rate of oxygen inhibition.

15.4 Experiments with Anti-stick Films

After a brief study of different mechanisms, their availability and costs associated. It was decided to use anti-stick films as a layer separation mechanism. Poly Tetra Fluoro Ethylene (PTFE) and Fluorinated Ethylene Propylene (FEP) were used as anti-stick films for experiment purpose. These films can be glued or clamped to the vat surface.

15.4.1 *PTFE Thin Film*

PTFE film is chemically inert to all the known chemicals and is available from a thickness of 25 μm to 3 mm. It is non-sticky and 25 μm film shows 70–80% transmissibility to the UV light. An experiment was carried out with MakerJuice SF photopolymer resin and a 25 μm PTFE film clamped to the vat surface. The layer thickness of 80 μm and exposure time of 4 seconds per layer was used for further experiments. The results of this experiment are shown in Fig. 15.4. Even though layers were peeled off quite well, the object was not properly cured. The prime reason being the air trapped between the film and the vat surface. Hence, to ensure smooth and complete separation of the object from the film, there should not be any air trapped. A small amount of air causes a large amount of film deformation. Figure 15.4(a-1) shows the desired object shape while Fig. 15.4(a-2) shows a final object printed with dimensional inaccuracy, film failure in Fig. 15.4(a-3) and excessive curing between films and vat surface in Fig. 15.4(a-4) which leads to permanent print failure. Thus great care must be taken before clamping the films. Figure 15.4(b) describes the deformation of the film due to insufficient clamping force.

Hence, the following care must be taken:

1. The film and the vat assembly must be leakage proof to avoid leakage of the resin.
2. No air should be trapped between the film and vat surface.

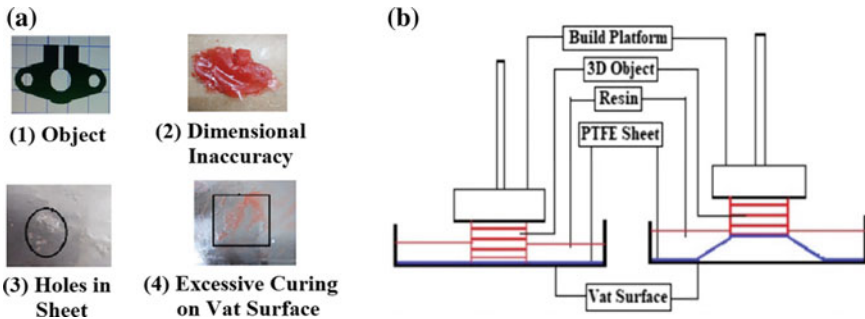


Fig. 15.4 **a** Experimental results: (1) 3D object, (2) Dimensional inaccuracy, (3) Film failure, (4) Unnecessary curing between film and the vat surface; **b** Deformation of sheet

3. Clamping must be sufficiently strong, it should not release the film during printing.

For further experiments, it was decided to glue the films to the transparent acrylic surface and then clamp it with aluminum the vat. First, the film was spread over the cleaned acrylic surface and glued at the edges using transparent cello tape, leaving no air bubbles. Then clamping the aluminum vat and acrylic base together with silicone rubber gaskets in between to ensure proper sealing. Table 15.2 shows the input parameters used for experiments with 80 μm layer thickness and 25 μm PTFE film.

Figure 15.5 shows the original object shape and final objects printed using PTFE film. Four experiments were carried out with PTFE film shows that increase in irradiation time causes excessive curing. The disadvantage with PTFE is that it starts to deteriorate at higher temperatures and easily gets distorted upon continuous usage.

Table 15.2 Input parameters for experiments with PTFE film

Experiment number		1	2	3	4
Irradiation time (t) (sec)	Bottom layers	14	16	17	18
	Subsequent layers	8	9	9	10

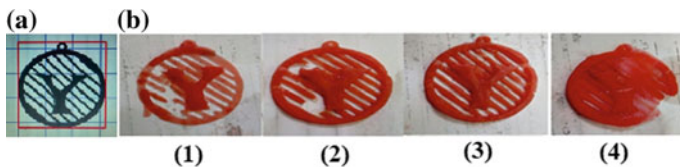


Fig. 15.5 Experimental results: **a** Desired object shape; **b** Final printed objects

Table 15.3 Input parameters for experiments with FEP film

Experiment number		1	2	3	4
Irradiation time (t) (sec)	Bottom layers	10	11	12	13
	Subsequent layers	5	6	7	8

**Fig. 15.6** Experimental results: **a** Desired object shape; **b** Final printed objects

15.4.2 FEP Thin Film

FEP films are non-sticky and highly transparent [7, 8], available in thickness from 25 μm to 3 mm. A 25 μm thick film shows 90–95% transmissivity to light, costing much less than that of any other layer separation mechanisms mentioned. The film was stretched and glued to the acrylic vat base then clamped as discussed earlier (Sect. 4.1). Satisfactory results were obtained using FEP. The advantage of FEP over PDMS/Sylgard 184 is that it is cheap and easy to use. Table 15.3 shows the input parameters used for experiments with 80 μm layer thickness and 25 μm FEP film.



Figure 15.6 shows the original object shape and final objects printed with FEP film. Four experiments were carried out with one FEP film shows better results compared to that of PTFE film.

It has been also found that the FEP films are wrinkle-free, deform by a very small amount, shows higher transmissivity to the UV light as compared to the PTFE films. So, based on the literature reviewed and experiments conducted, a comparison has been made in order to provide better visualization as shown in Table 15.4.

15.5 Conclusions

The possible reasons for the vat sticking issue include vacuum force generated between the build platform and the vat, contaminated plate surface, insufficient bottom layer cure time and insufficiently mixed resin. In order to overcome vat sticking issue number of layer separation mechanisms are available, active and passive peeling mechanisms are very popular but they alone do not provide good results. Hence, they must be used with PDMS to get satisfactory results which increase the cost further. Use of oxygen as an inhibitor is the best way to resolve this issue. But it is costly compared to any other method mentioned. Use of PTFE and FEP films which

Table 15.4 Comparative study of layer separation mechanisms

Layer separation mechanisms 	PDMS gel	Active and passive peeling	Inhibition by oxygen	Anti-stick film
Parameters ^a 				
Cost	**	**	*	****
Local availability	****	****	**	*****
UV transmission	****	—	*****	****
Solution to the problem	****	***	*****	****

^aParameters: Cost: Very expensive = *; Very cheap = *****; Local availability: Easily available = *****; Not available = *

UV transmission: ***** = $\geq 80\%$; * = $\leq 20\%$; Solution to problem: Very satisfactory = *****; Very unsatisfactory = *

costs very less compared to other mechanisms can alone provide good results. But, they must be applied on vat surface carefully. Using FEP film seems to be the best solution to the vat sticking issue due to its low cost, wrinkle-free nature, better UV transmissivity, less deformation, etc.

References

- Bertsch, A., Renaud, P.: Chapter 1.2 Microstereolithography, William Andrew applied Science Publishers, Lausanne, Switzerland. <https://doi.org/10.1016/b978-0-323-35321-2.00002-9> (2016)
- Takagi, T., Nakajima, N.: Photoforming applied to fine machining. In: Proceedings of the IEEE Micro Electro Mechanical Systems, 1-3, IEEE, FL USA. <https://doi.org/10.1109/memsys.1993.296927> (1993)
- Patil, R., Patil, Y.: Microstereolithography: concepts and methods. *Int. J. Mod. Trends Eng. Res. (IJMTER)* **3**(4), 1051–1057 (2016)
- Choi, Jae-Won, Kim, Ho-Chan, Wicker, Ryan: Multi-material stereolithography. *J. Mater. Process. Technol.* **211**(3), 318–328 (2011). <https://doi.org/10.1016/j.jmatprotec.2010.10.003>
- B9ceater DLP 3D Printer website. Last accessed 1 Apr 2016, 12.30PM IST
- Desimone, J.M., Ermoshkin, A., Ermoshkin, N., Samulski, E.T.: Continuous Liquid Interphase Printing, Patent No. WO2014126837A2, WO (2014)
- Build your own sla forum, anti-stick material, Last accessed 23 Dec 2015, 11AM IST
- Holtrup, R.: XZEED DLP—a multimaterial 3D printer using DLP technology. University of Twente, NL (2015)
- Batch, G.L., Macosko, C.W.: Oxygen inhibition in differential scanning calorimetry of free radical polymerization. *Thermochemica. Acta.* **166**, 185–198. [https://doi.org/10.1016/0040-6031\(90\)80180-7](https://doi.org/10.1016/0040-6031(90)80180-7) (1990)
- Chong, J.S.: Oxygen consumption during induction period of a photopolymerizing system. *Appl. Polym. Sci.* **13**(1), 241–247 (1969). <https://doi.org/10.1002/app.1969.070130123>

Chapter 16

Topology and Build Path Optimization for Reducing Cost in FDM uPrint SE



T. Ravi and Rajesh Ranganathan

Abstract The idea of generating a physical model straightly from the CAD data is largely documented as additive manufacturing (AM) or rapid prototyping (RP). This invention has facilitated in leftover minimization, reduced time to market, and flexibility for new product development as well as fast prototyping. Even after having all these benefits, the economic factors play a major role for any client to choose this manufacturing process for prototyping. Therefore, here an effort made primarily on the cost-saving strategies for parts built by FDM uPrint SE. This paper led at this juncture aims to manage the material consumption before and after a topology optimization and additionally to further reduce the cost and time of manufacture, build path analysis is also carried out to find the optimum build path for the AM machine FDM uPrint SE. Factors such as material consumption, build time, and post-processing time remain as the valid parameters for incurring the cost of AM parts. Lastly, this specific research will be suitable for the AM machines where the process parameters such as nozzle diameter, layer thickness, and temperature remain as an uncontrollable parameter.

Keywords Additive manufacturing · Topology optimization (TO) · Build path · Build orientation · Fused deposition modeling (FDM)

16.1 Introduction

Additive manufacturing (AM) technology was first familiarized in the year 1987 with the starter as stereolithography technology in which the liquid polymer layers tend to solidify by means of laser technology and subsequently a number of other AM technologies were brought in, such as: fused deposition modeling (FDM), selective laser sintering and laminated object manufacturing, solid ground curing, and poly-jet [1]. Among all the inventions, FDM technology-based 3D printer was first introduced in the year 1992, by Stratasys, which was having the capability to yield a physical

T. Ravi (✉) · R. Ranganathan
Coimbatore Institute of Technology, Coimbatore, Tamil Nadu, India
e-mail: travi.cit@gmail.com

© Springer Nature Singapore Pte Ltd. 2020
M. S. Shunmugam and M. Kanthababu (eds.), *Advances in Additive Manufacturing and Joining*, Lecture Notes on Multidisciplinary Industrial Engineering,
https://doi.org/10.1007/978-981-32-9433-2_16

prototype directly from CAD information without a tool or die [1]. This technology empowered in eliminating the monotonous and ordinary way of making prototypes which turned out to be a painless method for the designers to work and experiment with prototypes [2]. The layer-by-layer technology enabled the users to produce parts with intricate surfaces, topologies, and interior assemblies at ease with good accuracy, finishing, and greater structural stability with minimized weight at a nominal cost as compared to the traditional manufacturing processes, therefore numerous used this technology [2]. AM technology in spite of advantages offers several drawbacks such as: low production, low part quality, and low yield, and thus, these factors influence in carrying out research in design and development of AM processes to obtain the functional parts with decreased manufacturing time and cost [3].

16.1.1 Fused Deposition Modeling (FDM)

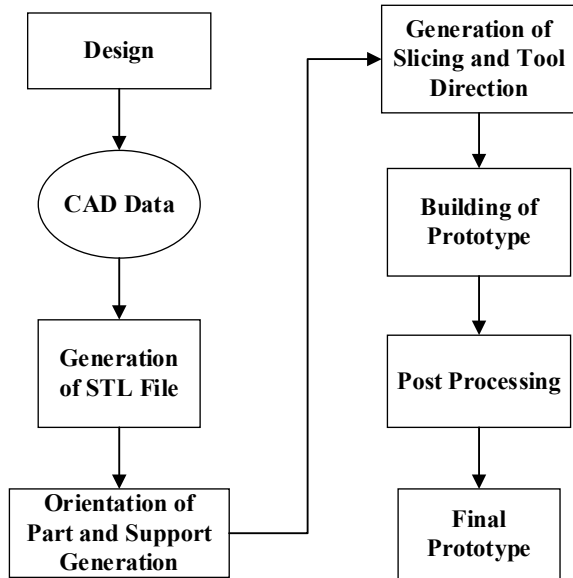
FDM is capable of building any part or geometry with simple or complex surfaces volumes by depositing material on the build tray in a sequential layer-by-layer manner [4]. The process uses a nozzle to extrude the heated thermoplastic filaments in semi-liquid state and allowed to deposit on the built tray (X - Y plane) in an arranged manner with identical slices and allows to solidify at compartment temperature [4]. The built quality or cost of the printed part purely depends on the process parameter set during the process, but in this paper, the AM machine used is FDM uPrint SE in which the process parameters remain uncontrollable. The main specifications of the FDM uPrint SE are, build volume of $8 \times 6 \times 6$ in., the layer thickness of 1.24 mm, ABS P430 filament with a diameter of 1.78 mm and Catalyst Ex being the interfacing software for this technology. The typical FDM uPrint SE build process is shown in Fig. 16.1.

16.2 Topology Optimization

In recent periods, topology optimization (TO) has turned out to be a power tool for the designers for constructing contour shapes and structures [5]. This enabled the designers to generate optimized parts by distributing required material only within a definite area (i.e., design domain) which was accomplished by decreasing or increasing the various properties of the structure based on the loading and boundary constraints [5]. Now, the finite elements of the design domain are used in a method where the material distribution occurs, i.e., allocating material to the required element and void to the non-required element [5].

Initial TO algorithms [6, 7] focused mainly on the issue of decreasing the structural elastic deformation based on the load constraints applied on the used volume of material to the design domains' entire volume. Over the ages for accepting different mechanical properties like natural frequencies [8] and yield stresses [9], objective

Fig. 16.1 FDM uPrint SE build process



and constraint functions were used [5]. Figure 16.2 shows the process, how a model of mass M_1 can be reduced to mass M_2 on optimizing through an appropriate optimizing software to save material with adequate strength and cost of the building.

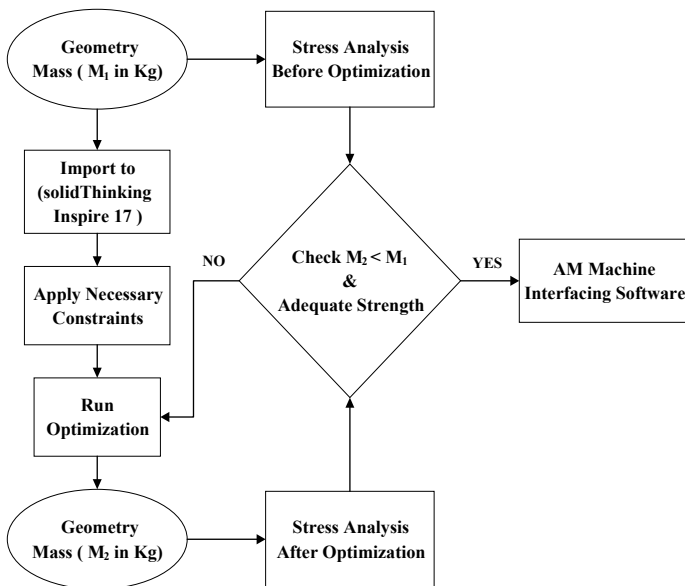


Fig. 16.2 Topology optimization process

16.2.1 Topology Optimization of Bracket

For this study of TO, a rear set bracket model has been chosen from the solidThinking Inspire 2017 database, and analysis has been carried out with the aim to reduce the volume of the material (mass). Initially, the mass of the bracket with steel as the material was weighing around $M_1 = 1.0643$ kg before optimization as shown in Fig. 16.3a. With the application of boundary conditions, loads and torques on the non-design space as shown in Fig. 16.3b, the weight of the optimized bracket (design space) with a factor of safety as 1.2, the mass reduction is about 56% ($M_2 = 0.5964$ kg) as shown in Fig. 16.3c. Further, the factor of safety-2 can be considered for a more stable structure. On comparing the volume of support structure generation before and after optimization, the latter tends to have a larger volume of support structure generation which leads to a time-consuming post-processing. In spite of this downside, the cost of the bracket before optimization will be high in comparison with bracket after optimization. Further to resolve high support structure generation of the bracket after optimization to an extent, build path analysis for finding the optimum orientation in FDM uPrint SE has been carried out in the later section of this chapter.

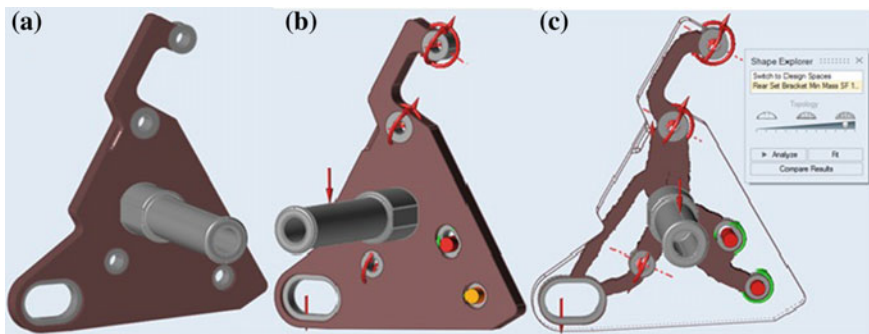


Fig. 16.3 **a** Model before topology optimization, **b** boundary constraints **c** model after topology optimization with a factor of safety as 2

Table 16.1 Comparison of quantities before and after topology optimization

S. No.	Quantities	Before optimization	After optimization
1	Mass (Kg)–steel	1.0643	0.59645
2	von Mises stress (Pa)	4.074×10^8	6.144×10^8
3	Displacement (m)	3.522×10^{-4}	9.117×10^{-4}

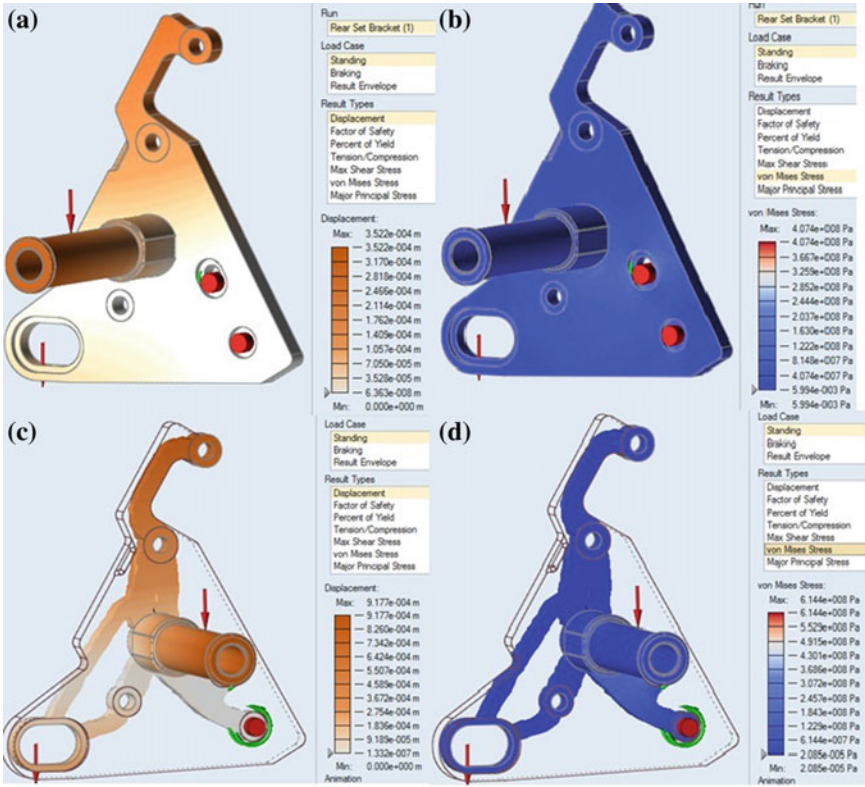


Fig. 16.4 **a** Displacement before topology optimization, **b** von Mises stress before topology optimization, **c** displacement after topology optimization, and **d** von Mises stress after topology optimization

Table 16.1 shows the evaluation of mass, displacement, and stresses before and after optimization. The use of combined topology and build path optimization as suggested in this paper can have a superior saving capability of material and time. Figure 16.4a and b shows the displacement values, and Fig. 16.4c and d shows the von Mises stress values of the bracket before and after optimization and values are under the safe limit.

16.3 Build Path Analysis

Parts produced through several AM processes need the presence of external and internal support structures for supporting the over-hanging parts during the construction. These support structures are removed once the part is built, and thus, they are mea-

sured as waste, and it requires a considerable amount of time, energy, and material which will have a direct impact on the manufacturing cost of the part and increase in the post-processing time as well [10]. One of the effective ways to lessen the quantity of support structure required is to find the optimum build path or build orientation where the support structure changes delicately based on the build orientation [10].

Figure 16.5 shows the process of finding the optimum build path where the best build path is being chosen based on the various degrees of rotation as shown in Table 16.2. The optimum build path for both bracket and the optimized bracket is found to be at $(0, 90, 0)$ with a material consumption as shown in Fig. 16.6.

Fig. 16.5 Build path optimization process

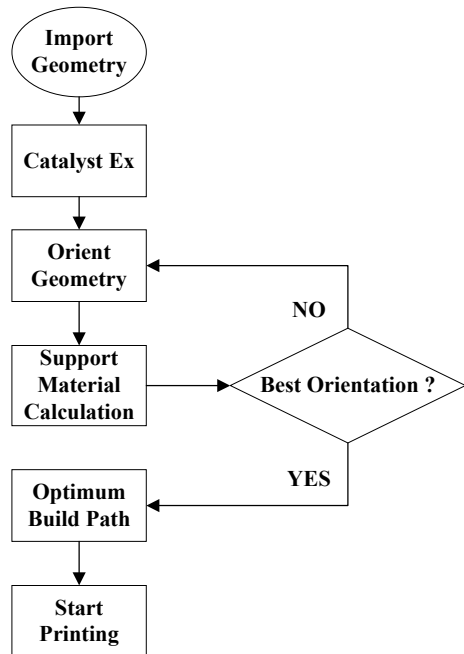


Table 16.2 Optimum build path analysis before and after topology optimization

Quantities	Before build path optimization				After build path optimization					
	Auto	30°	45°	90°	Best	Auto	30°	45°	90°	Best
		<i>Rotate (X-axis)</i>					<i>Rotate (X-axis)</i>			
Model material (in ³)	2.93	2.54	2.54	2.54	2.93	0.09	0.09	0.08	0.09	0.09
Support material (in ³)	0.54	1.66	1.76	1.69	0.54	0.05	0.24	0.233	0.20	0.05
Build time (h)	3:44	7:17	7:10	7:10	3:44	0:19	1:17	1:11	1:11	0:19
		<i>Rotate (Y-axis)</i>					<i>Rotate (Y-axis)</i>			
Model material (in ³)	2.93	2.46	2.50	2.47	2.47	0.09	0.09	0.09	0.09	0.09
Support material (in ³)	0.54	1.31	1.27	0.59	0.59	0.05	0.24	0.22	0.04	0.04
Build time (h)	3:44	6:46	5:57	3:42	3:42	0:19	1:12	1:09	0:19	0:19
		<i>Rotate (Z-axis)</i>					<i>Rotate (Z-axis)</i>			
Model material (in ³)	2.93	2.55	2.42	2.54	2.93	0.09	0.08	0.08	0.08	0.09
Support material (in ³)	0.54	1.39	1.34	1.34	0.54	0.05	0.18	0.18	0.18	0.05
Build time (h)	3:44	6:47	6:31	6:50	3:44	0:19	1:21	1:20	1:21	0:19

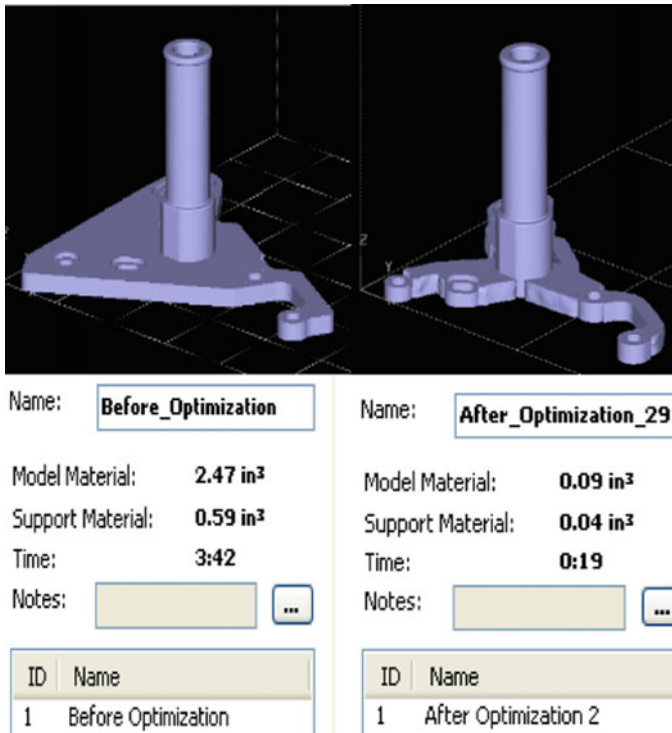


Fig. 16.6 Optimum build path and material consumption before and after topology optimization

16.4 Results and Discussions

The proposed case study on the idea of combining the TO and build path analysis has aided in reducing the materials consumption to a reasonable extent on comparing with earlier. The part before going for TO was weighing around 1.0643 kg and after doing TO, it was reduced to 0.59645 kg, thereby providing a potential saving of 56% material consumption as shown in below Fig. 16.7. Also, to further reduce the material consumption, the proposed concept of finding the optimum built path after TO has been implemented. From Fig. 16.7, it has been clearly seen that there is a major difference in the material consumption of the TO bracket before and after the build path analysis. The best build orientation of FDM uPrint SE for the optimized bracket was found to be at (0, 90, 0) in both cases and consumption of quantities are shown in Table 16.2 and Fig. 16.8.

Fig. 16.7 Mass before and after TO

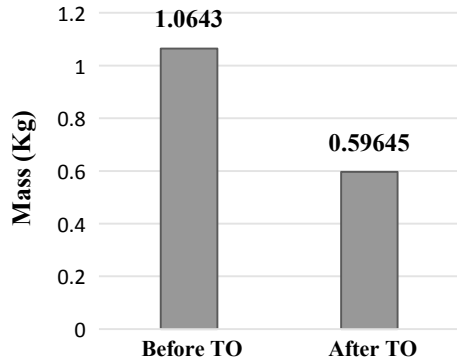
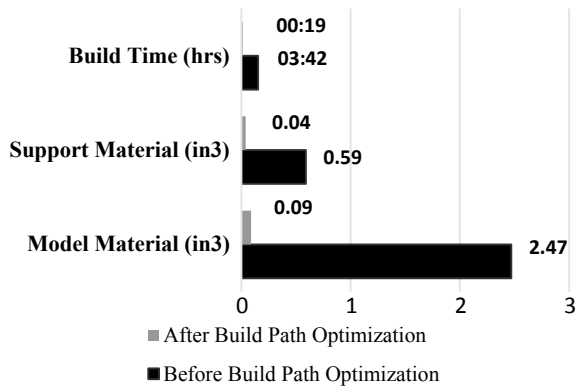


Fig. 16.8 Best build orientation before and after TO



16.5 Conclusions

The ultimate objective of this paper was to find a strategy for minimizing the cost in FDM uPrint SE or AM machines where the process parameters remain as constant and suggested a method to combine topology and build path optimization to decrease the cost of the part by reducing the build time and material consumption. The selected mass of the bracket has been reduced to 56% of the initial mass on doing topology TO with a factor of safety as 1.2 with objective set to be mass minimization in solidThinking Inspire 2017 and analysis of optimum build path suggested that (0, 90, 0) for the FDM uPrint SE have the much saving material potential in comparison with the auto-orientation of FDM interfacing software CatalySt Ex.

Acknowledgements We gratefully acknowledge the financial support for establishing the Centre of Excellence in Manufacturing Sciences at Coimbatore Institute of Technology, Coimbatore, India from Ministry of Human Resource Development (MHRD), and Government of India, where the sample/R&D work is being carried out.

References

1. Bual, G.S., Kumar, P.: Methods to improve surface finish of parts produced by fused deposition modeling. *Manuf. Sci. Technol.* **2**(3), 51–55 (2014)
2. Mendonsa, C., Naveen, K.V., Upadhyaya, P.: Characteristic study of rapid prototyped parts at different build orientation. **4**(3), 2013–2016 (2015)
3. Phatak, M., Pande, S.S.: Optimum part orientation in rapid prototyping using genetic algorithm. *J. Manuf. Syst.* **31**(4), 395–402 (2012)
4. Panda, S.K., Padhee, S., Sood, A.K., Mahapatra, S.S.: Optimization of fused deposition modelling (FDM) process parameters using bacterial foraging technique. *Intell. Inf. Manag.* **01**(02), 89–97 (2009)
5. Reddy, S.N.K., Ferguson, I., Frecker, M., Simpson, T.W., Dickman, C. J.: Topology optimization software for additive manufacturing: a review of current capabilities and a real-world example. In: 42nd Des. Autom. Conf. vol. 2A, p. V02AT03A029, (2016)
6. Bendsøe, M.P.: Optimal shape design as a material distribution problem. *Struct. Optim.* **1**(4), 193–202 (1989)
7. Bendsøe, M.P., Kikuchi, N.: Generating optimal topologies in structural design using a homogenization method. *Comput. Methods Appl. Mech. Eng.* **71**(2), 197–224 (1988)
8. Ma, Z.D., Kikuchi, N., Hagiwara, I.: Structural topology and shape optimization for a frequency response problem. *Comput. Mech.* **13**(3), 157–174 (1993)
9. Suresh, K., Takaloozadeh, M.: Stress-constrained topology optimization: a topological level-set approach. *Struct. Multidiscip. Optim.* **48**(2), 295–309 (2013)
10. Strano, G., Hao, L., Everson, R.M., Evans, K.E.: A new approach to the design and optimization of support structures in additive manufacturing. *Int. J. Adv. Manuf. Technol.* **66**(9–12), 1247–1254 (2013)

Chapter 17

Tailored Support Structures for Additive Manufacturing



Hemnath Anandan Kumar , Peter Francis Reginald Elvis ,
Madhanagopal Manoharan , Jayakrishnan Jayapal 
and Senthilkumaran Kumaraguru 

Abstract In some additive manufacturing processes, support structures are required while building parts, for structural stability as well as for some functional aspects. Support structure should be designed in a way that it should withstand the weight of the part especially overhanging features of the part to avoid distortion and mishap. This paper deals with design and fabrication of tailored support structures for some special cases. From the understanding obtained through various literature, initially, a broad classification of support structures is presented. Based on that, application-specific support structures were designed. Two different support structures were designed, analyzed and fabricated successfully. After fabrication, support structures were easily removed from the part manually.

Keywords Custom design · Additive manufacturing process · Process improvement

17.1 Introduction

Additive manufacturing (AM) is a class of manufacturing process in which parts are fabricated in a layer by layer manner. It is capable of fabricating complex features which are difficult to fabricate in conventional processes. Support structures are mainly required while fabricating parts with overhang features. In all AM processes, support structures are required to (i) keep the features in position during fabrication and prevent distortion/curling resulting from thermal stresses in the production of metal parts, (ii) anchor overhanging parts to the base plate when the critical inclination angle is reached for that part, (iii) help to remove heat away from the process in laser-based additive processes, (iv) separate parts from the platform easily, (v) provide a collision avoidance buffer and (vi) process improvement.

H. A. Kumar · P. F. Reginald Elvis · M. Manoharan · J. Jayapal · S. Kumaraguru (✉)
Department of Mechanical Engineering, Indian Institute of Information Technology, Design and
Manufacturing, Kancheepuram, Chennai 600127, India
e-mail: skumaran@iiitdm.ac.in

© Springer Nature Singapore Pte Ltd. 2020
M. S. Shunmugam and M. Kanthababu (eds.), *Advances in Additive Manufacturing
and Joining*, Lecture Notes on Multidisciplinary Industrial Engineering,
https://doi.org/10.1007/978-981-32-9433-2_17

Some important functions of the support structures are to avoid thermal deformations like warping and curling, control mechanical stress, provide a channel for flow of resins in SLA process and act as an effective thermal conductor for heat dissipation especially in metal AM processes, to separate parts from the substrate and to provide support for overhanging features and enhance its mechanical properties.

As the support structures play a vital role in AM part fabrication, those should be designed in a way such that its total weight is minimized without compromising its functions [1, 2]. The functional areas of support structures are sierras or needles, main support and separators. Other kinds of support structures include gussets, projected feature edges, a single web, webs, scaffolds, honeycomb, columns, zigzag and perimeter support.

The design for supports in AM processes has been studied for past three decades, but plenty of research groups in academia and industry are still working toward optimum support structure design and a correlation of support design with the original geometry for controlling the support material wastage. In general, support material properties are far different from the build material properties for the purpose of easy removal and good surface finish. A brief literature on the available supports for polymer and metal-based AM has been discussed in the following section.

17.2 Literature Review

This part of the paper reviews the previous work on support structures and is classified based on the different functions of supports as discussed in the previous section. Overhanging features or protruding features are areas where the designer has to take care in AM parts as they are the most concentrated area of stress. This, in turn, will result in warpage and curling and distorts the entire part which will result in poor build and deviate from the required geometry. Hence, support structures are features required in AM technology when there is an overhang feature present in the part. Some authors have pointed out that if rigid supports are used for overhang features, an enormous amount of residual stress will be generated than when the overhangs are without supports. So support structures should be in such a way that it is easily removable from the substrate, and the design should also be strong enough to withhold the stresses. The designer should also consider the capability of custom-designed support structures to support the structural overhangs and reduce thermal stresses generated during the part building process.

In this section, we discuss the importance of structural stability of the support structures. A design for manufacturability approach has been followed by Morgan et al. by varying design and process parameters such as laser power, scan speed and hatch spacing for better bead quality [3]. Along with that as a further scope, they suggested that by using a different material, the performance of support structures can be enhanced. Calignano suggested that overhanging features should be avoided while designing the parts. Under unavoidable circumstances, special support structures can be designed with less area of contact with the part. The author also found that the

downward sloping faces can be built without supports at angles up to 30° but all the faces had poor surface roughness. By this, it can be understood that there is a limitation in building features below certain angles without support structures which will result in failure of parts as well as the quality of the parts [4].

Bobbio et al. suggested that the morphology of the support structure geometries can be varied for effective structural strength, thereby minimizing the support volume and contact area with the build part [5]. An alternate methodology for minimizing the usage of support volume was developed by Cooper et al. using contact-free supports which minimize the distortions. Moreover, the authors have experimentally proved for various overhang geometries with different shapes and curves [6].

Another contact-free support structures were also developed by Tounsi and Vignat for overhang features in EBM process to reduce geometric defects as well as improve heat dissipation. In addition, authors also have proposed a methodology for optimizing contact-free support structures which will reduce geometric defects such as curling or warping, loss of thickness and side loss [7].

An innovative dissolvable support was proposed by Lefky et al. for stainless steel and was fabricated using PBF printer [8], and the same technology can be utilized for polymer material by varying the chemical composition of polymer supports. Apart from function-specific support structures, a research has been made by Strano et al. to produce optimized support structures considering the part built orientation with the cellular support structures. They confirmed that the topology described by the Schwartz equation enhanced a further 50% material saving with respect to the full dense support [9].

Wu et al. have proposed a novel methodology for generating application-specific infill structures with rhombic cells so that the resulting structures can automatically satisfy manufacturing requirements on overhang-angle and wall-thickness [10]. Figure 17.1 shows the various support structures used in AM.

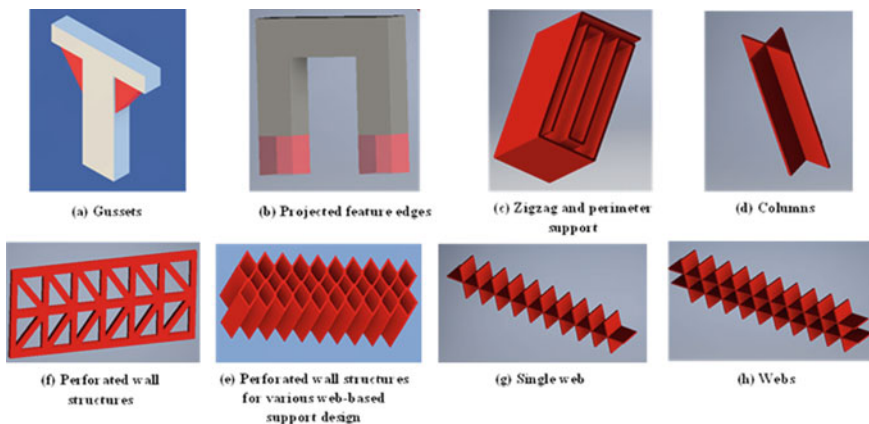


Fig. 17.1 Different types of support structures

17.3 Case Study

From the detailed literature survey about various types of support structures and the knowledge gained, two different tailored geometry were designed with the different type of support structures. In AM, removal of the support structure is essential which is considered as post-processing of parts. So in order to overcome the problem mentioned above, one of the options is a washable support structure, but constraint for such support structure build is the time consumption for removal. If customizable support structures are made without compromising the functional requirements and facilitating easy removal, it will be an added advantage for AM processes. Design of tailored support structures will also depend upon machine constraints. In this study, FORTUS 380MC machine was used for fabrication of parts. On using this machine, constraints faced were as follows: Any feature below 1 mm cannot be build and customized support structures were also unable to build using support structure material provided in the machine. Hence, part and support structures were built together with the same material.

In this paper, a special case has been taken for study, for which the customized structures were built. Here, support structures are designed to support manifolds which are horizontally oriented during the build and also for the manifolds of the same cross-section throughout its length as shown in Fig. 17.2. Support structures designed here are application specific and cannot be used for cylinders that are oriented in different directions apart from the horizontal. In this work, support structures were designed considering the aforementioned constraints. Two different types of support structures were designed by the authors using commercial CAD package and are shown in Fig. 17.3. The models shown in Fig. 17.4 were structures inspired from nature. In Fig. 17.4, design 1 (left) is designed based on bridge structure and design 2 (right) is based on inverted broccoli. The support structures are placed with some equal intervals such that it can withstand the load of the layers built above

Fig. 17.2 Parts having horizontally oriented cylinders [11]

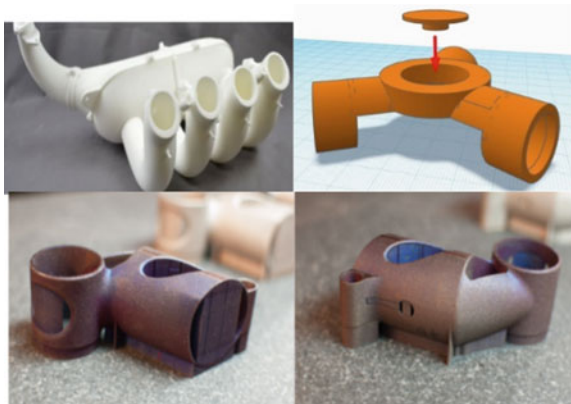


Fig. 17.3 Support structure design 1 (left) and design 2 (right) for horizontally oriented cylinder

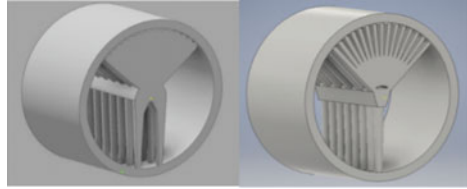


Fig. 17.4 Fabricated support structure design 1 (left) and design 2 (right) for horizontally oriented cylinder

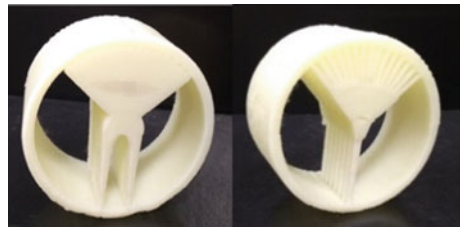
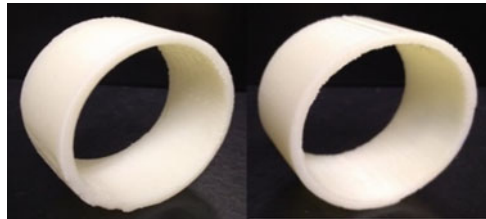


Fig. 17.5 Horizontally oriented cylindrical parts after the removal of support structures



them. Figure 17.5 shows the fabricated cylindrical parts after the removal of support structures manually.

17.4 Results and Discussion

Apart from fabrication and breakage of support structures, structural analysis was also carried out in FE commercial software to study about the load-bearing capacity of supports. The analysis was done on both designs by applying two different materials namely ABS (polymer) and SS316L (metal) and the results are shown in Figs. 17.6a–d. It was shown that for design 1, the deformation of support structures was at a higher magnitude than that of the design 2 while using ABS as a base material. While using SS316L as the base material, the same observations were found.

In this work, both parts, as well as support structures, were made out of the same material. Usually, it is not the procedure followed in the machines used for fabrication of FDM parts. While fabrication of customized support structures using the base material, the density of the support cannot be varied by the machine. Because of that, the support structures will have the same strength as that of the part. Then it will

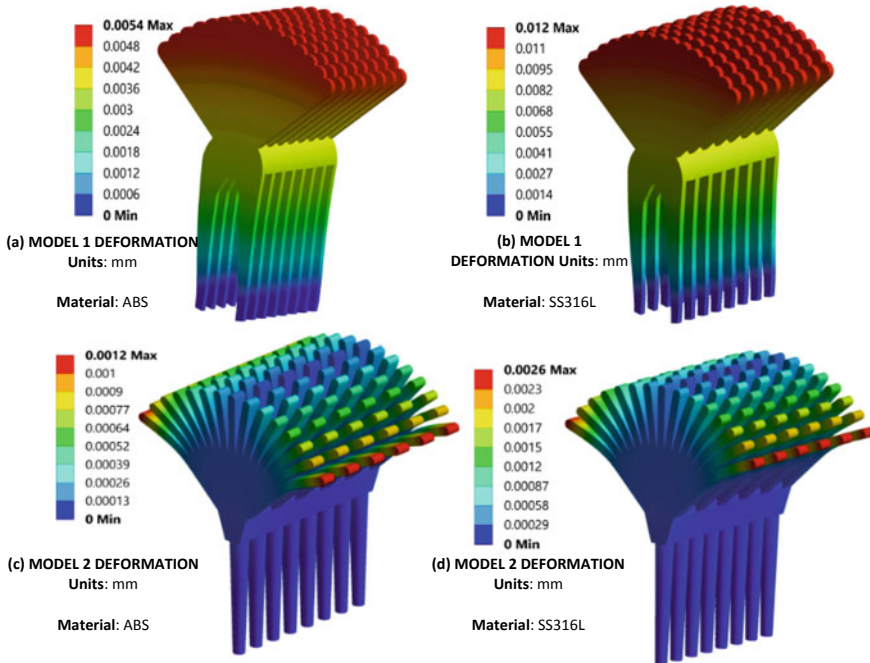


Fig. 17.6 Deformation of support structures for design 1 with **a** ABS and **b** SS316L and deformation of support structures for design 2 with **c** ABS and **d** SS316L

be difficult for post-processing to remove. Taking such constraint into consideration, many iterative designs were carried out for easy removal of support structures without compromising the functional requirements. For some designs, it was very difficult to remove the support structures as the point of contact of supports was fixed to inner surface of the cylinder. But after the removal of support structures, certain marks or residuals of support structure were found on the part's surface and were later removed by filing process. This spoiled the part quality and resulted in more post-processing.

After many iterations, two designs were finalized as shown in Fig. 17.4. These two designs were fabricated using FDM and processed for support structure removal. In comparison with the previous designs, it was found that this design support structures facilitated easy removal without the assistance of any tools.

From the experimental observation, it can be suggested that support structures can much easily be removed if it is made out of different material, by a reduction in density of the support structure material and also by using different lattice structures. Any variation in thickness of cylinder, support structures can be used by decreasing spacing in between them so that they can support the part rigidly without any distortion. Any variation in diameter of the cylinder, the support structure can suitably be scaled and used.

The analysis results were further studied to know more about the deformation pattern occurred in the designed supports. Both the design has 15 branches or 15

supportive features supported on a central shaft-like structure supported by leg(s). A study was carried out to depict the pattern of deformation on the support branches for a different angle of inclination with respect to the central branch. Figures 17.7 and 17.8 show the deformation pattern for a different angle of inclination. It depicts that the deformation is having a nearly same magnitude in both the models and slightly less in the magnitude when compared with the centrally located point. This

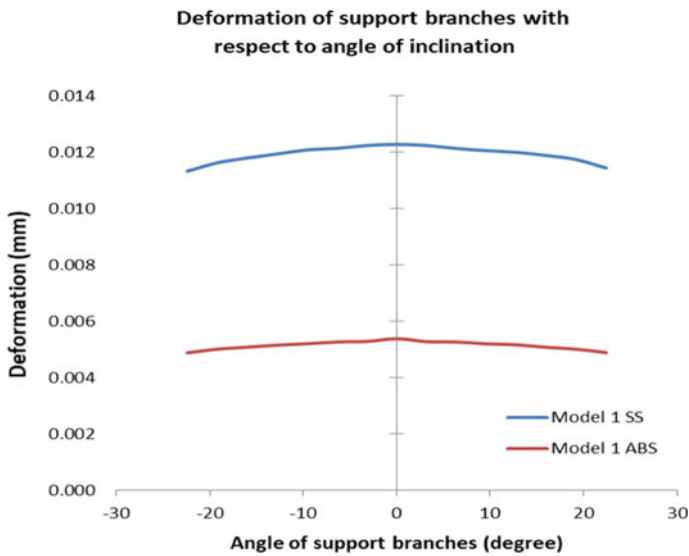


Fig. 17.7 Deformation of support branches with respect to the angle of inclination

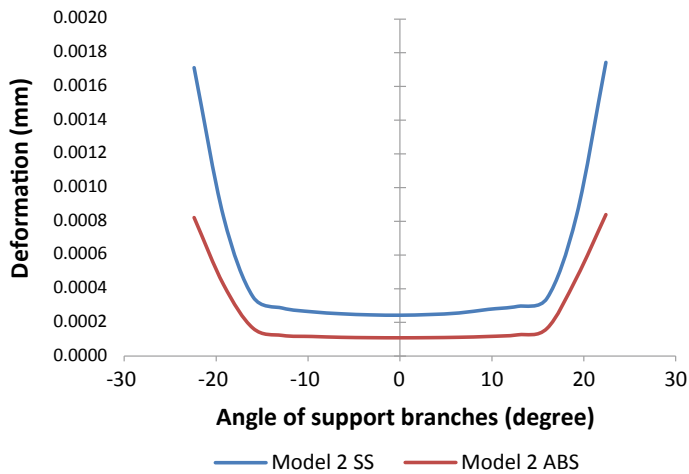


Fig. 17.8 Deformation of support branches with respect to the angle of inclination

occurs because the entire load is born on the top surface and additionally the design has no gaps or cleaves in between the branches to dissipate the force applied. The deformation pattern followed by the design was found to be the same for both the materials.

For design 2, the deformation pattern was quite different. In this design, the branches were distinctly separated from the neighboring branches. As a result of this, the load was distributed and carried away by the individual branches. It was found that the distortion was low at the centrally located one and increases as we move away from the center on either side. From the graph, it is to be noticed that there is a sudden increase in the magnitude of deformation at the extremes. This is due to the support branches at extremes are inclined with more degree, and hence it acts like a cantilever. On comparing the analysis and experimental results of both designs, it can be recommended to go with the design 2 which has less deformation, easy to remove in a single pass and has more load-bearing capacity than that of design 1. Further modifications in design can be carried out to enhance the reduction in deformation of support structures.

17.5 Conclusions

An overarching survey of literature related to the support structures was carried out in this paper. Based on the various information and knowledge gained, a broad classification of support structures based on different aspects was presented. This paper deals with support structures that can be used to support manifolds which are a horizontally oriented cylinder with the same cross-section throughout its length. Two different support structures were designed and successfully fabricated using FORTUS 380MC machine. Both part and support structures were build using the same material. After fabrication, support structures were easily removed manually without any tools. The support structures could have been removed much more easily by (i) using a different material, (ii) reducing density of support structure material and (iii) using different lattice structures. Still, a lot of scope is there for improving the design of support structure; here, in this work design is constrained by the machine. If it could possibly be addressed, then much more refined support structure can be tailored to different part geometries and can be built with a different material or with reduced density.

References




1. Gibson, I., Rosen, D., Stucker, B.: Additive Manufacturing Technologies: Rapid Prototyping to Direct Digital Manufacturing, 1st edn. Springer, New York, NY, USA (2010)
2. Venuvinod, P.K., Ma, W.: Rapid Prototyping, Laser-Based and Other Technologies (2004)
3. Morgan, D., Agba, E., Hill, C.: Support structure development and initial results for metal powder bed fusion additive manufacturing. *Proc. Manufact.* **10**, 819–830 (2017)

4. Calignano, F.: Design optimization of supports for overhanging structures in aluminum and titanium alloys by selective laser melting. *Mater. Des.* **64**, 203–213 (2014)
5. Bobbio, L.D., Qin, S., Dunbar, A., Michaleris, P., Beese, A.M.: Characterization of the strength of support structures used in powder bed fusion additive manufacturing of Ti-6Al-4V. *Addit. Manufact.* **14**, 60–68 (2017)
6. Cooper, K., Steele, P., Cheng, B., Chou, K.: Contact-free support structures for part overhangs in powder-bed metal additive manufacturing. *Inventions* **3**(1), 2 (2017)
7. Tounsi, R., Vignat, F.: New concept of support structures in electron beam melting manufacturing to reduce geometric defects. In: 15e Colloque National AIP-Priméca (2017)
8. Lefky, C.S., Zucker, B., Wright, D., Nassar, A.R., Simpson, T.W., Hildreth, O.J.: Dissolvable supports in powder bed fusion-printed stainless steel. *3D Print. Addit. Manufact.* **4**(1), 3–11 (2017)
9. Strano, G., Hao, L., Everson, R.M., Evans, K.E.: A new approach to the design and optimisation of support structures in additive manufacturing. *Int. J. Adv. Manufact. Technol.* **66**(9–12), 1247–1254 (2013)
10. Jun, W., Wang, C., Zhang, X., Westermann, R.: Self-supporting rhombic infill structures for additive manufacturing. *Comput. Aided Des.* **80**, 32–42 (2016)
11. Parts having horizontally oriented cylinders. <http://www.interiordesign.live/3d-printer-car-parts.html>, <https://medium.com/3d-printing-stories/3d-printing-titanium-the-bin-of-broken-dreams-40ab6a64dff5>

Chapter 18

Redesigning ECMM Fixture with Part Consolidation and DfAM Principles



R. Prithvirajan , K. Mohan kumar  and G. Arumaikkannu 

Abstract Fused Deposition Modeling (FDM) is one among the Additive Manufacturing (AM) technologies that is most widely available and cheaper technique due to the recent developments. This paper demonstrates the application of FDM to fabricate customized fixture for Electro Chemical Micro Machining (ECMM). Redesigning the fixture from conceptual design with part consolidation and Design for Additive Manufacturing (DfAM) principles enhanced its functionality and reduced fabrication time with the proposed methodology, ECMM fixture was consolidated to a single that part can be fabricated and delivered within the day.

Keywords Fused Deposition Modeling · Fixture · ECMM · DfAM · Part consolidation · Additive Manufacturing

18.1 Introduction

Additive Manufacturing (AM) refers to the group of technologies that creates components directly from the 3D models by adding material in layer-by-layer manner. FDM uses Acrylonitrile Butadiene Styrene (ABS), polylactic acid (PLA), etc., in filament form. These filaments were melted and deposited layer upon layer based on the tool path [1].

BMW an automobile manufacturer uses FDM to manufacture jigs and fixtures for the assembly of their production units. These jigs and fixtures are reported to be more ergonomic to handle because of their low weight, adapted complex organic shapes. They are produced in-house at a lesser cost and shorter time compared to conventional methods [2]. Further, additive manufactured parts were used as customized inspection fixtures for coordinate-measuring machine (CMM). AM fixtures are more suitable for a medium-size inspection volume [3] which provides better stability and measurement. Despite all these advantages, every AM technology has a

R. Prithvirajan · K. Mohan kumar · G. Arumaikkannu (✉)
Department of Manufacturing Engineering, College of Engineering Guindy, Anna University,
Chennai 600025, India
e-mail: arumai@annauniv.edu

© Springer Nature Singapore Pte Ltd. 2020
M. S. Shunmugam and M. Kanthababu (eds.), *Advances in Additive Manufacturing and Joining*, Lecture Notes on Multidisciplinary Industrial Engineering,
https://doi.org/10.1007/978-981-32-9433-2_18

different set of constraints. These new guidelines that were being developed through various researches were collectively referred as design for additive manufacturing (DfAM) [4, 5]. Products that are to be manufactured through AM have to be screened to ensure it adheres to these guidelines. New products that are being developed can take advantage of this guideline to improve its quality and functionality.

Though AM parts were used as the fixture or jig, the advantage of creating a customized fixture based on part consolidation and DfAM principles from the conceptual stage of design remains less explored. The objective of this work is to design a fixture for ECMM using these principles, fabricate with FDM, and explore its advantages. ECMM is an unconventional machining process in which electrically conductive materials were machined by anodic dissolution during an electrolysis process, and it is capable of producing features in 1–999 μm scale [6]. In the existing ECMM setup, the fixture is an assembly of different components that are subjected to corrosion. Hence, they are treated as a consumable item and replaced at regular intervals. Initially, the fixture was fabricated using ABS polymer through FDM technique to replace the corroded fixture. Later to reduce the number of components (eliminate the use of magnets), the fixture was redesigned by considering part consolidation, functional integration, and DfAM principles. The stages of design and advantage of redesigning with DfAM were documented.

18.1.1 ECMM Fixture

The workpiece, fixture, and tool in the ECMM setup are shown in Fig. 18.1a. The existing ECMM fixture was made of ferromagnetic material. Mostly, the workpiece will be a sheet metal of thickness ranging from 0.3 to 0.8 mm. The fixture was clamped to the acrylic tank, and the workpiece is secured over the fixture using magnets. Fixture is shown in Fig. 18.1b. The fixture and magnets were under electrolyte during machining, and it gets oxidized and corroded (Fig. 18.1c) over the period of use. Hence, both the fixture and magnets have to be replaced at regular intervals.

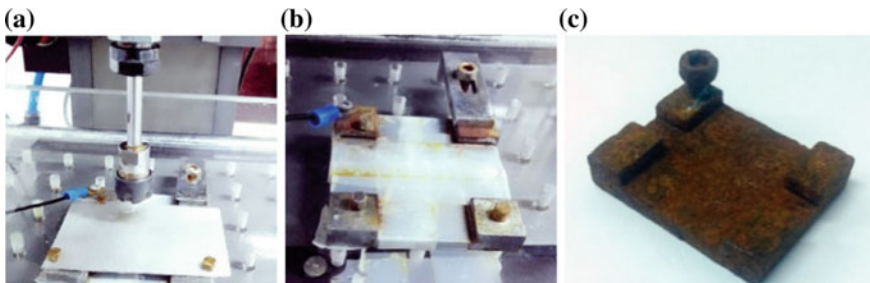


Fig. 18.1 a Tool and ECMM fixture arrangement. b ECMM fixture. c Corroded ECMM fixture after certain period of use

18.2 Fixture Design—Iteration 1

With an objective to replace the existing metal fixture with polymer (ABS), it was redesigned and fabricated using in-house FDM machine. ABS material was chosen as the temperature, and pressure exerted on the fixture was negligible. It was decided to carry over the same design concept as the existing fixture. However, holes are provided on the new design (iteration 1) to clamp the fixture with the bottom of the tank. Since ABS material does not possess magnetic property, a provision was given to attach four magnets permanently to the fixture using epoxy glue. The workpiece has to be directly connected to the power supply terminals as the ABS is an insulator.

18.2.1 Fabrication

The fixture was fabricated with the ABS material with 0.2 mm layer thickness and 100% infill density in Accucraft i250+ FDM machine (Fig. 18.2). The fixture was fabricated with nozzle extrusion temperature of 235 °C in the horizontal orientation (XY plane) without any support structure. After fabrication, magnets were attached to fixture permanently, with epoxy glue which takes around 24 h to cure. The magnets get exposed to the electrolyte on use that makes the magnets to get corroded rendering the fixture useless. Figure 18.3 highlights the corroded magnets that are attached to the fixture. To overcome these issues, the fixture has to be redesigned to eliminate the need for magnets which is explained in the next section.

Fig. 18.2 Fixture design iteration 1 fabricated with FDM

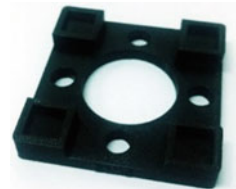


Fig. 18.3 Corroded magnets in the fixture after certain period of use



18.3 Redesigning the Fixture Using Part Consolidation

18.3.1 Iteration 2—Concept Model

The design iteration 1 is an assembly of one fixture, four magnets. The functionality of each part was evaluated using part consolidation principle. It was observed that fixture can be redesigned to a single part and eliminate the need of magnets.

A concept model was developed with the inspiration of snap joints. To secure the workpiece in position, a cantilever arm was incorporated to the fixture design. Workpiece clamping mechanism of the fixture design iteration 2 is shown in Fig. 18.4. The model consists of a slot to which the workpiece can be inserted when the load is applied at the free end of the lower jaw. The workpiece will get secured as the load at the lower jaw is released.

The conceptual design was further developed into a 3D model. Figure 18.5a and b shows the half front and top view of the fixture design iteration 2. There are two lower jaws attached to the cantilever arms that are placed in between three upper jaws to distribute the clamping force symmetrically.

18.3.2 Material Property

Since the material property data was not readily available and the mechanical properties strongly depend on the processing parameters [7, 8], tensile and flexural test were specimens were designed and fabricated with ASTM Standards. The tensile specimens were fabricated by orienting along the X -, Y -, and Z -axes of the machine with 100% infill. The X -axis and Y -axis specimens show the maximum stress of 26 and 31 MPa, respectively, with considerable yield. Tensile modulus was found to



Fig. 18.4 Schematic representation and work piece clamping mechanism of iteration 2 design

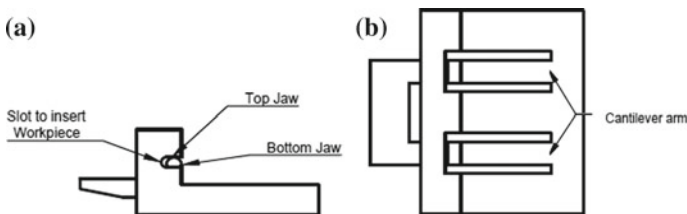


Fig. 18.5 Different views of fixture design iteration 2

be 2320 MPa. Z-axis specimen breaks abruptly at the maximum stress of 19 MPa. The flexural test done on the specimen fabricated with XZ plane shows the flexural strength of 66 MPa. These results conform to the anisotropic behavior of FDM components. Hence, the improper orientation of the part with respect to loading direction could cause catastrophic failure of fabricated parts.

18.3.3 Design Calculation

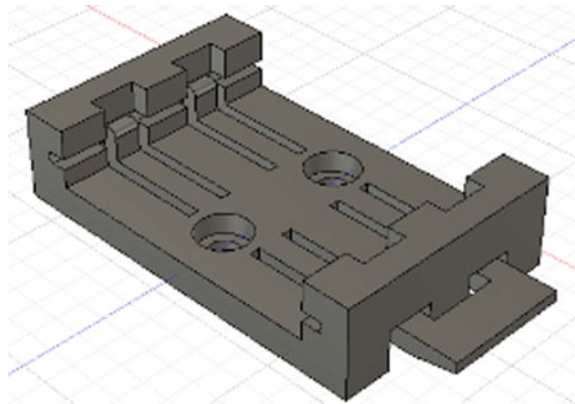
Based on the classical beam theory, the design calculations were made for the individual arm. Each arm is assumed to be a cantilever beam being fixed at one end, and load is applied at another end. The overall length of beam is 26 mm, and the distance of lower jaw from fixed end is 18 mm. The height of the slot to insert workpiece was assumed to be 2 mm, so the lower jaw should have a deflection of at least 2.5 mm to insert the workpiece. The width of each arm was assumed to be 5 mm, and the thickness (t) is calculated at maximum stress (σ) of 44 MPa which have a factor of safety at 1.65 with Eq. 18.1.

Thickness of the arm is given by Eq. 18.1

$$t = (2\sigma x^2(3l - x))/(6yEI) \quad (18.1)$$

The concept model was updated with the calculated thickness (t) of 2.3 mm (Fig. 18.6). 3D model is exported into STL file and fabrication time was evaluated for both horizontal and vertical orientations. Sky blue-, dark blue-, and gray-colored lines shown in Fig. 18.7 represent outer shell, infill, and support structure in the tool path, respectively. Horizontal and vertical orientations take 4 h 08 min and 5 h 03 min fabrication time, respectively.

Fig. 18.6 ECMM fixture design iteration 2



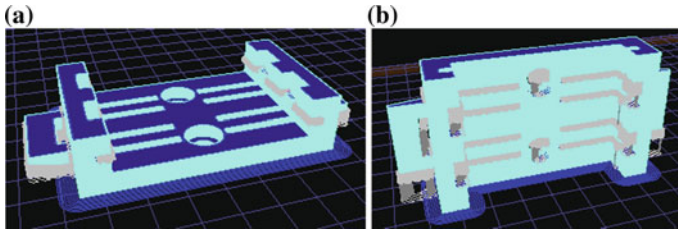


Fig. 18.7 Tool path for horizontal and vertical orientation of design iteration 2

18.4 Iteration 3—Redesigning for FDM Fabrication

When a component is to be fabricated with FDM, the minimum feature size, orientation, loading direction, and support removal play a vital role in the success of functional applications. Various DfAM literature shows redesigning the part to the selected AM technique which enables a better utilization of the process [9]. A pilot study was done on the machine to explore some of the design factors that affect the quality of the prints as they were mostly specific to print parameters and the machine. Minimum wall thickness, hole and pin size, and overhang that can be fabricated without support were found to be 0.8 mm, 3 mm, and 45° , respectively. Iteration 2 is evaluated with these parameters. There are few faces that are in right angle to the build orientation which requires support structures. All the other features satisfy the remaining parameters.

The orientation of the part during fabrication plays a vital role in fabrication time, strength, and support structure generation [5, 10]. Amount of support structures used in fabrication can be directly related to the increases in fabrication time, and the increase in z height will directly increase the fabrication time, whereas for a functional part orientation should be based on the loading direction. The part has to be studied to have a clear knowledge on the loading direction, type of load. So that best orientation can be selected irrespective of fabrication time and support structures [10]. For a feature subjected to a flexural load, best orientation was to keep the flexible member in a way that loading direction does not delaminate the layers. Though the most preferred orientation is to keep the Z height as low as possible and have a larger face at the base, orienting in the horizontal direction as Fig. 18.7a is not suitable as load acting on upper jaw tends to delaminate the layers. Hence, the fixture is oriented vertically in the context of the loading direction as shown in Fig. 18.7b.

Since the machine equipped with a single extruder breakaway type support is used. The support structure will be printed with the same material and it has to be removed manually through mechanical action. Design iteration 2 was evaluated for sufficient gaps that allow tools to remove the support structures generated during vertical orientation. As the vertical orientation of the fixture was selected based on loading conditions, support structures were generated in the gaps between each arm and the fixture base. To reduce support structure, the faces perpendicular to the build direction in the iteration 2 were redesigned with a 45° inclination in iteration 3 design.

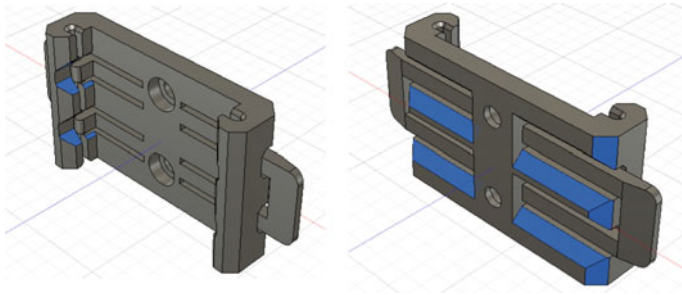


Fig. 18.8 Front and back view of the fixture design-iteration 3

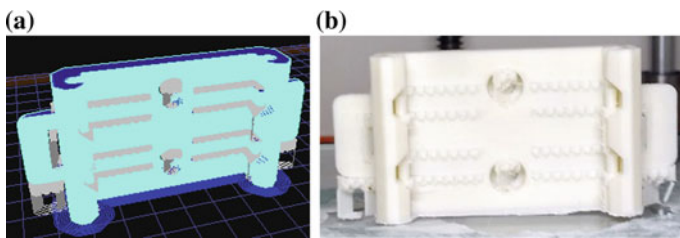


Fig. 18.9 **a** Tool path for iteration 3. **b** fabricated fixture-iteration 3

Figure 18.8 shows the front and back view of the iteration 3 design highlighted with the faces modified for overhang angle. The fabrication time of iteration 3 design is 4 h 31 min. Toolpath generated and fabricated fixture is shown in Fig. 18.9.

18.5 Results and Discussion

Design iteration 1 that incorporated the design concept of the existing metal fixture was an assembly of a fixture and 4 magnets using epoxy. However, the fabrication time of iteration 1 fixture is 2 h and 26 min assembling the magnets permanently with epoxy glue took 24 h to cure. Total lead time to get a finished fixture is at least 26 h 26 min. Further, corrosion of the magnets made it unusable after certain period of use.

Iteration 2 design was based on inspiration from snap joints, and the need for the magnets and the problem of corrosion were eliminated. To find the orientation having lesser fabrication time, both horizontal and vertical orientations were compared. The horizontal orientation takes 4 h 8 min while the vertical orientation takes 5 h 03 min to fabricate the same part. Even though the fabrication of vertical orientation is higher than the horizontal orientation, vertical orientation was selected based on loading direction. Total time to get a finished fixture is 5 h 30 min approximately including post-processing time.

Table 18.1 Comparison of total time to get finished fixture

S. No.	Iteration	Orientation	Fabrication time (Ft)	Total production time (Ft + post-processing + assembly time)
1	1	Horizontal	2 h 26 min	26 h 26 min
2	2	Horizontal	4 h 08 min	4 h 30 min
3	2	Vertical	5 h 03 min	5 h 30 min
4	3	Vertical	4 h 31 min	5 h

In the view of DfAM, design iteration 2 was redesigned based on limiting features of FDM. In the design iteration 3, overhanging faces were replaced to 45° inclined faces. That considerably reduced support structures and fabrication time. The total time to get the finished fixture is approximately 5 h including post-processing time which is the least time as iteration 3 eliminated the assembly process. The comparison of total time to produce the fixture is shown in Table 18.1.

18.6 Conclusions

The application of FDM made customized fixture for Electro Chemical Micro Machining (ECMM) was demonstrated in this work. A conceptual design was developed based on the part consolidation principles and classical beam theory. Further, the design for additive manufacturing principles (DfAM) was used to evaluate and improve the design to suit the FDM process.

Total production time of iteration 1 took 26 h 26 min including the assembly time of fixture and magnets using epoxy.

Iteration 2 takes 5 h 30 min as total production time that reduced the use of magnets. Redesigning the fixture with DfAM principles reduces the total production time to 5 h.

Though the fabrication of the iteration 1 design with in-house FDM machine reduced the cost and lead time, the application of part consolidation and DfAM principles made the total production of fixture (iteration 3) to further shorten the lead time.

Consideration should be given that the electrolyte does not chemically react with the ABS material.

This demonstrates the advantage of using part consolidation along with DfAM principles to get better economical advantage for the additive manufacturing processes to fabricate customized fixtures.

Acknowledgements Authors like to acknowledge support from CFR, Anna University, Chennai, under Anna Centenary Research Fellowship (ACRF).

References

1. Rosen, G.D., Stucker, B.: *Additive Manufacturing Technologies*, 2nd edn. Springer, New York, NY (2015)
2. Schmid, G., Eidenschink, U.: *Rapid Manufacturing with FDM in Jig and Fixture Construction*, vol. 1, no. 1, p. 8 (2014)
3. Minetola, P., Iuliano, L.: The reverse guillotine tribometer for evaluation of sliding wear of additive manufactured fixtures. *Rapid Prototyp. J.* **20**(2), 105–114 (2014)
4. Adam, G.A.O., Zimmer, D.: Design for additive manufacturing—element transitions and aggregated structures. *CIRP J. Manuf. Sci. Technol.* **7**(1), 20–28 (2014)
5. Leutenecker-Twelsiek, B., Klahn, C., Meboldt, M.: Considering part orientation in design for additive manufacturing. *Proc. CIRP* **50**, 408–413 (2016)
6. Rajurkar, K.P., Sundaram, M.M., Malshe, A.P.: Review of electrochemical and electrodischarge machining. *Proc. Soc. Behav. Sci.* **6**, 13–26 (2013)
7. Wittbrodt, B., Pearce, J.M.: The effects of PLA color on material properties of 3-D printed components. *Addit. Manuf.* **8**, 110–116 (2015)
8. Luzanin, O., Guduric, V., Ristic, I., Muhic, S.: Investigating impact of five build parameters on the maximum flexural force in FDM specimens—a definitive screening design approach. *Rapid Prototyp. J.* **23**(6), 1088–1098 (2017)
9. Meisel, N., Williams, C.: An investigation of key design for additive manufacturing constraints in multi material three-dimensional printing. *J. Mech. Des.* **137**(11), 111406 (2015)
10. Sells, E., Bowyer, A.: *Design for FDM Rapid Prototyping Manufacture (Basic)* (2007)

Chapter 19

Life Cycle Assessment of an Additive Manufactured Automotive Component



Rohit Agrawal  and S. Vinodh 

Abstract Additive manufacturing (AM) has a predominant role in enabling industries to move toward fourth-generation requirements. In order to enable AM process to be sustainable, environmental impacts need to be quantified. In this context, this article presents life-cycle assessment (LCA) of an industrial product. LCA facilitates the assessment of environmental impact across the life cycle phases. Eco-indicator 99 method is used for LCA. The impacts are determined in three categories. The practical implications are also being highlighted.

Keywords Additive manufacturing (AM) · LCA · Sustainability · Environmental impacts

19.1 Introduction

Automotive industries have realized the potential of AM processes over conventional processes. Among AM processes, FDM is widely used because it is cost efficient, less time consuming and ease of fabricating intricate shapes Gebler et al. [1]. Environmental impacts associated with AM processes need to be determined. In line with enabling AM process to be sustainable, life-cycle assessment has been used as potential sustainable manufacturing tools [2]. In this viewpoint, this article presents life-cycle assessment (LCA) of an automotive component (bevel gear) used in industrial applications. LCA is also known as cradle to grave analysis for determining environmental impacts across the life cycle phases [3]. The objective of the study reported in this article is to perform LCA to determine environmental impacts associated with an automotive component fabricated using AM process. Eco-indicator method is applied for impact assessment. Impacts are determined in three categories namely human health, ecosystem quality, and resources. The practical inferences are derived and presented.

R. Agrawal · S. Vinodh (✉)

Department of Production Engineering, National Institute of Technology, Tiruchirappalli 620015, India

e-mail: vinodh_sekar82@yahoo.com

© Springer Nature Singapore Pte Ltd. 2020

M. S. Shunmugam and M. Kanthababu (eds.), *Advances in Additive Manufacturing and Joining*, Lecture Notes on Multidisciplinary Industrial Engineering,

https://doi.org/10.1007/978-981-32-9433-2_19

19.2 Literature Review

Luo et al. [4] showed an approach for determining the environmental impact of solid freeform fabrication (SFF) process. They divided each phase into life phases. They then analyzed the environmental impact of all process phase by considering environmental data and resource management data. For environmental impact calculation, they considered raw material consumption, energy utilization, wastes and disposal action taken.

Kellens et al. [5] showed a parametric model for analyzing the environmental impacts of selective laser sintering (SLS) process. They consider resource consumption, energy consumption, and process emission for analysis. They analyzed the relationship between production time and product design features using multiple regression analysis. The presented model helps in analyzing the environmental impact of a product in the design stage itself.

Balogun et al. [6] aimed toward calculating the electrical energy required for building a model in STRATASYS DIMENSION STT FDM for determining environmental impact. They compared electrical energy consumption by varying volume and complexity of a part. They then calculated carbon footprint by converting energy consumed into CO₂ equivalent.

Faludi et al. [7] aimed toward the comparison of two different AM machine (FDM and an OBJET inkjet/polyjet) with CNC machine in environmental impact perspective. They selected IMPACT 2002+ and ReCiPe Endpoint H methods for cradle to grave analysis. They consider impacts due to cutting fluid, waste material generation, transportation, disposal action taken, and energy consumed in all stages, i.e., manufacturing stage, standby stage, and in idling stage. They found that sustainability of all machines mainly depends on the percentage utilization of machine.

Hapuwatte et al. [8] done the sustainability assessment of AM products. They determine the life-cycle sustainability of manufactured parts with AM and traditional manufacturing by using Product Sustainability Index (ProdSI) method. They showed that product sustainability for complex and intricate shaped product is more for AM as compared to traditional manufacturing.

Kafara et al. [9] done a comparison of AM and conventional manufacturing of mold core with respect to environmental impact. They performed LCA on four different processes for comparison. They found that for customized product and small-scale unit production, AM process consumes less time when compared with conventional manufacturing and with respect to cost-saving also, AM is more effective than conventional manufacturing.

19.3 Methodology

LCA is a tool to assess the environmental impact of a product or a process across its entire life cycle. It examines the product from extraction of raw material for manufacturing process, production phase, use phase, and the final disposal phase

including overall product system [10]. Comparison analysis can be made for different processes, material and services, using LCA in order to select the best alternative to minimize the overall environmental impact.

LCA consists of four phases, they are:

19.3.1 Goal and Scope Definition Phase

The LCA starts with a statement of goal and scope of the study. It is the requirements of ISO standards to clearly define the goal and scope of study. It includes the product description and system boundaries. The goal and scope also includes the technical details for further assessment. One of the important terms in goal and scope definition is overall product function. Overall product function needs to be clearly defined in order to specify the intended purpose of the product.

19.3.2 Inventory Analysis Phase

This is the most important phase of LCA also termed as data collection phase. Life cycle inventory analysis phase creates an inventory of all outflows and inflows for a product. It includes inputs of material consumption, energy consumptions, and other resources consumptions. It also includes emissions and releases to air water and land. A flow model is developed including all processes and activities involved in the product life cycle stage. The flow model consists of all inputs and outputs.

19.3.3 Impact Assessment Phase

The impact assessment is done after the inventory analysis phase. The impact assessment phase evaluates the significant environmental impact based on the inventory. For this stage, a method has to be selected for assessment among available methods based on the requirement and region. This phase consists of categorization, normalization, grouping, and weighting.

19.3.4 Interpretation Phase

Interpretation phase utilizes techniques to quantify, evaluate, and check the result from the life cycle inventory and life cycle impact assessment phase. The results from the impact assessment are summarized in this phase. In this phase, conclusions

are being drawn from the environmental impact assessment. And suggestions need to be given to reduce the environmental impact.

The first step of LCA is to define goal and set scope of the study. System boundaries have to be defined in this stage. In the second phase, i.e., inventory analysis step, all the data related to input and output of each process are collected and defined. Data include material consumption, energy consumption, etc. The third phase, i.e., the impact assessment phase calculates the environmental impact associated with the processes by using methods like eco-indicator 99, CML, ReCiPe, etc. The third phase is the base for the interpretation phase.

19.4 Case Study

Bevel gear has been taken for life-cycle assessment. Bevel gear is a conical shaped gear designed to transmit power between two intersection shafts. Bevel gears are used in lots of areas like automobiles, power plants, locomotives, marine applications, etc. the bevel gear has been modeled in Autodesk Inventor. The modeled bevel gear has been shown in Fig. 19.1.

19.4.1 FDM

Fused deposition modeling (FDM) is a 3D printing technology which uses thermo-plastic filaments for model printing. In FDM, the filament is heated to its melting temperature and then extruded for model fabrication. It prints model in a layer by layer manner. FDM uses two kinds of material, the first one is model material and the second one is support material. The model material makes the final product. And the support material helps in supporting the product in its printing stage. After printing the model from FDM technology, the support material can be easily removed as support material is soluble in water-based solution with the help of agitation tank.

Fig. 19.1 Modeled bevel gear

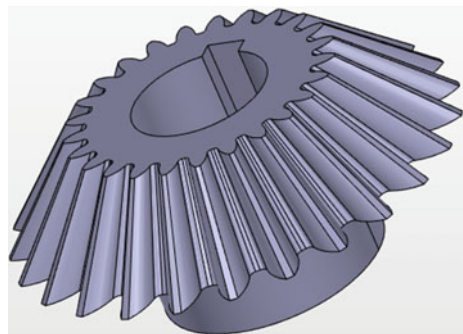


Fig. 19.2 Fabricated bevel gear



In this case study, bevel gear has been fabricated using FDM technology. STRATASYS UPRINT SE-PLUS 3D printer has been used for printing bevel gear. The STL File of bevel gear has been sent to GrabCad software. GrabCad sends the profile information to the 3D printer for printing. Acrylonitrile butadiene styrene (ABS) material has been used for printing bevel gear. The fabricated bevel gear has been shown in Fig. 19.2.

19.4.2 Life-Cycle Assessment

In this study, bevel gear has been taken as a case component for LCA. Life-cycle assessment of bevel gear has been done using software Simapro version 8.0.3.14.

Step-1

Goal and scope definition phase

Goal—life-cycle assessment of bevel gear

Scope (boundary condition)—LCA to be done only for fabrication process of bevel gear.

Step-2

Inventory analysis phase

The inventory analysis detail consists of input and output material details along with quantity. The input data are given below:

Input material: ABS P430

Input Quantity: 19.457 g

Processing sequence required: FDM extrusion followed by cleaning

Output from extrusion—unfinished bevel gear (17.69 g)

Output from cleaning process—finished bevel gear (16.68 g)

Step-3

Impact assessment phase

Eco-indicator 99 method has been applied for assessment as it is widely used LCA method. The eco-indicator approach divides environmental impact in three damage assessments. They are human health, eco-system quality, and resources. Human health category ensures that human being is not affected by environmentally trans-

mitted diseases. Eco-system quality ensures that non-human species should not be affected severely both in population as well as geographically. Resources category ensures that natural resources should sustain.

Eco-indicator (*I*) method is used in the present study. The weightages for damage categories in I method for human health, ecosystem quality, and resources are 55%, 25%, and 20%, respectively.

Step-4

Interpretation phase

The eco-indicator value is estimated as a sum of all three damage assessment values.

19.5 Result

Eco-indicator 99 method characterizes environmental impact in 10 categories. They are carcinogens, respiratory organics, respiratory inorganics, climate change, radiation, ozone layer, eco-toxicity, acidification/eutrophication, land use, and minerals. This module then normalizes and weights so as to evaluate single-point score also called as environmental impact point per job. For bevel gear, these categories are shown in Fig. 19.3.

The flowchart of bevel gear printing as well as its environmental impact at each step is shown in Fig. 19.4.

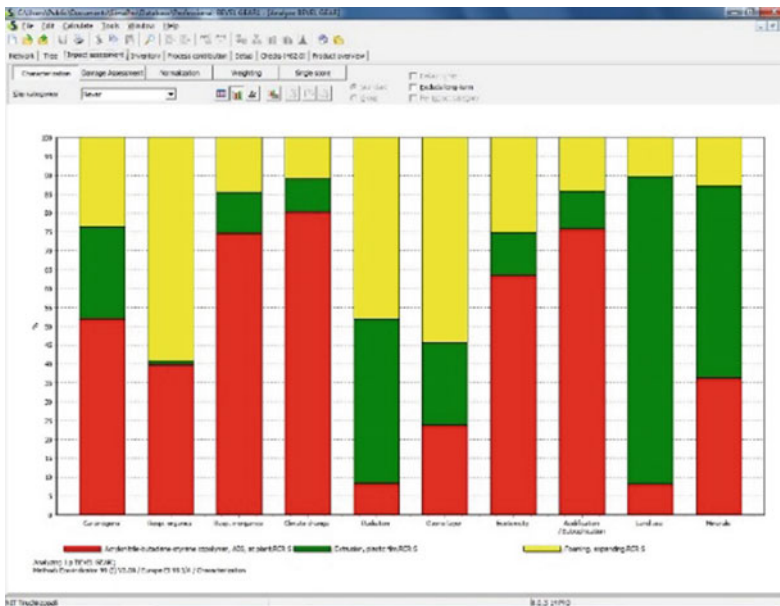


Fig. 19.3 Environmental characterization of impacts

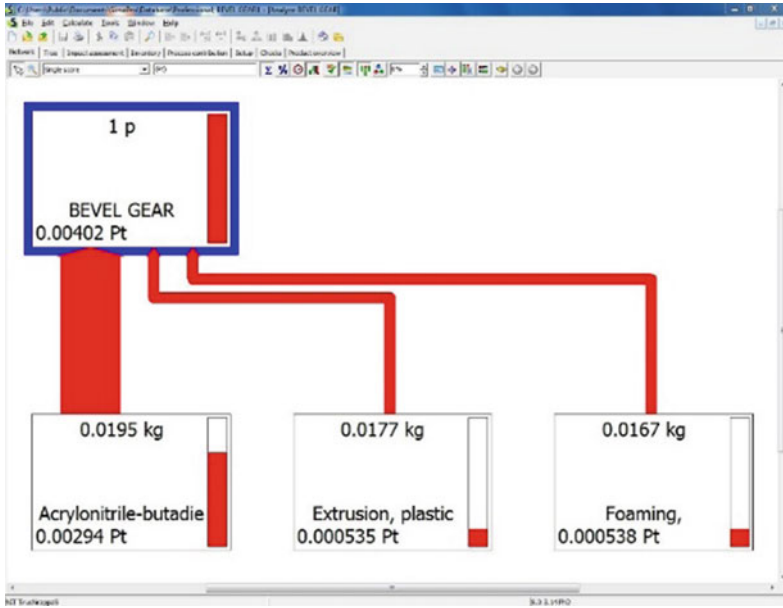


Fig. 19.4 Flowchart of bevel gear printing with environmental impacts

From Fig. 19.5, it can be concluded that human health can be affected mostly by ABS material, followed by cleaning process, and followed by extrusion.

Similarly, for ecosystem quality, ABS material affect mostly followed by extrusion process followed by the cleaning process (Table 19.1).

Resources are more affected by extrusion process followed by resources followed by the cleaning process.

The total environmental impact value of studied bevel gear is coming out to be 4.02 mpt as shown in Fig. 19.6.

Red color indicates effect on human health, and the environmental impact point for human health is 3.63 mpt. Green color indicates effect on ecosystem quality, and the environmental impact point for ecosystem quality is 0.13 mpt. Yellow color indicates effect on resources, and the environmental impact point for resources is 0.26 mpt.

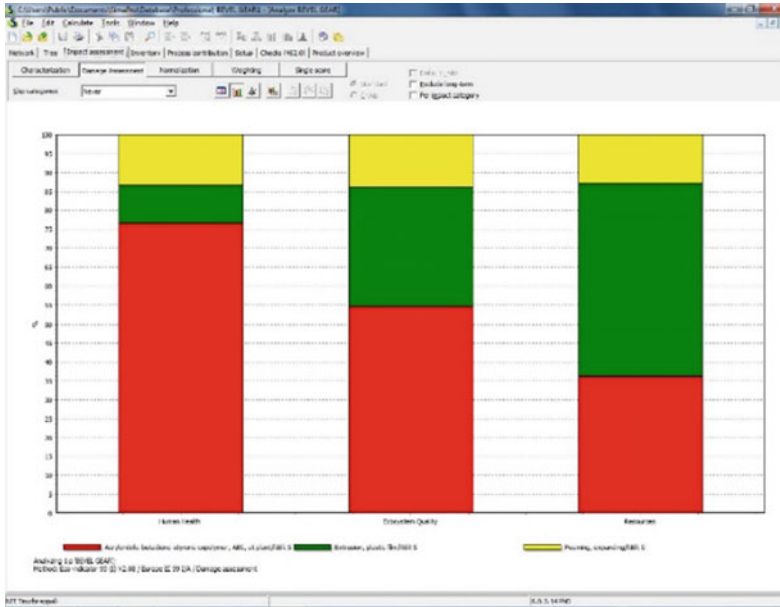


Fig. 19.5 Distribution of damage assessment in three categories

Table 19.1 Percentage impact of material and processes on environmental categories

Affect to environment	% affect by ABS material	% age affect by extrusion process	% age affect by cleaning process
Human health	77	10	13
Ecosystem quality	55	31	14
Resources	37	51	12

19.6 Conclusions

AM processes are gaining utmost importance in industrial applications. Also, AM processes are expected to be sustainable. This paper presents life-cycle assessment, a vital tool of sustainable manufacturing to determine environmental impacts associated with AM process. Bevel gear is taken as a candidate product. Four phases of LCA are being executed as per ISO 14044 standards and inferences are being derived. Impacts are determined in three end point categories. Total environmental impact based on eco-indicator 99 method is found to be 4.02 mpt. The determination of environmental impacts would enable opportunities for minimizing impacts and to make the product more sustainable. As automotive industries are more concerned with developing sustainable products, the conduct of the study facilitates industry practitioners to achieve the objective.

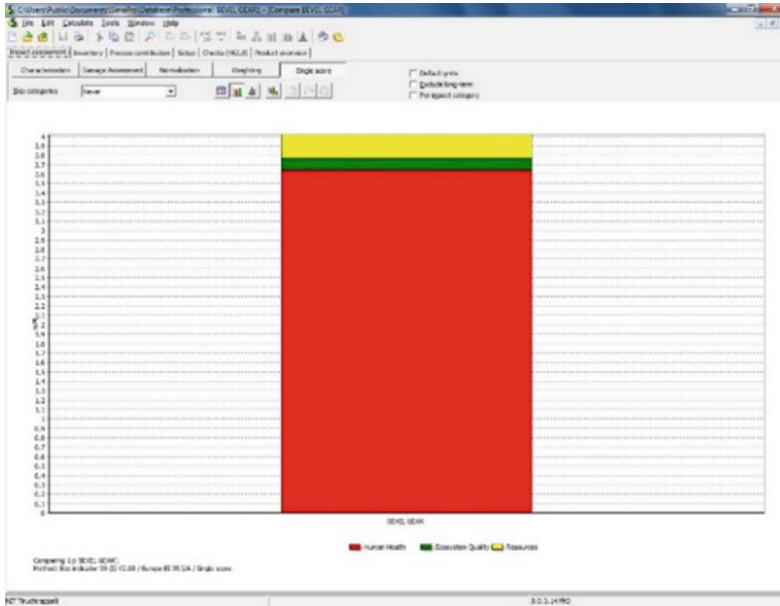


Fig. 19.6 Total environmental impact in single score

19.6.1 Limitations and Future Scope

In the present study, one automotive component bevel gear is being considered. In future, other industrial automotive product could be considered. Different design models of bevel gear could be considered to select best design which minimizes environmental impact. One of the important limitations of this study is it evaluates environmental impact for the processing stage itself. In future, other stages like material extraction, transportation, use phase, and end-of-life phase could be considered to evaluate overall environmental impact. Further research can be done on minimizing the environmental impact of product by considering DFAM and DFE guidelines in the design stage itself.

References

1. Gebler, M., Uiterkamp, A.J.S., Visser, C.: A global sustainability perspective on 3D printing technologies. *Energy Polic.* **74**, 158–167 (2014)
2. Ness, B., Urbel-Piirsalu, E., Anderberg, S., Olsson, L.: Categorising tools for sustainability assessment. *Ecol. Econ.* **60**(3), 498–508 (2007)
3. Jiménez-González, C., Curzons, A.D., Constable, D.J., Cunningham, V.L.: Cradle-to-gate life cycle inventory and assessment of pharmaceutical compounds. *Int. J. Life Cycle Assess* **9**(2), 114–121 (2004)

4. Luo, Y., Ji, Z., Leu, M.C., Caudill, R.: Environmental performance analysis of solid freedom fabrication processes. In: Proceedings of the 1999 IEEE International Symposium on Electronics and the Environment, 1999. ISEE-1999, pp. 1–6 (1999)
5. Kellens, K., Renaldi, R., Dewulf, W., Kruth, J.P., Duflou, J.R.: Environmental impact modeling of selective laser sintering processes. *Rapid Prototy. J.* **20**(6), 459–470 (2014)
6. Balogun, V.A., Kirkwood, N., Mativenga, P.T.: Energy consumption and carbon footprint analysis of fused deposition modelling: a case study of RP stratasys dimension SST FDM. *Int. J. Sci. Eng. Res.* **6**(8), 442–447 (2015)
7. Faludi, J., Bayley, C., Bhogal, S., Iribarne, M.: Comparing environmental impacts of additive manufacturing vs traditional machining via life-cycle assessment. *Rapid Prototyp. J.* **21**(1), 14–33 (2015)
8. Hapuwatte, B., Seevers, K.D., Badurdeen, F., Jawahir, I.S.: Total life cycle sustainability analysis of additively manufactured products. *Proc. CIRP* **48**, 376–381 (2016)
9. Kafara, M., Süchting, M., Kemnitzer, J., Westermann, H.H., Steinhilper, R.: Comparative life cycle assessment of conventional and additive manufacturing in mold core making for CFRP production. *Proc. Manufact.* **8**, 223–230 (2017)
10. Bribián, I.Z., Capilla, A.V., Usón, A.A.: Life cycle assessment of building materials: comparative analysis of energy and environmental impacts and evaluation of the eco-efficiency improvement potential. *Build. Environ.* **46**(5), 1133–1140 (2011)

Chapter 20

PLA-Based Material Design and Investigation of Its Properties by FDM



M. Ramesh  and K. Panneerselvam 

Abstract Fused deposition modelling (FDM) is a rapid prototyping method which can automatically construct models through software operated by computer-aided design data; the process is of layer-by-layer addition without the usage of external tooling. In this study, FDM is used as additive manufacturing processes in order to design and select optimal material structures with required properties. In this current research study, polylactic acid (PLA) material was explored for 3D printing. The parts were printed according to Taguchi's L9 orthogonal arrays with input parameters like print speed (PS), fill density (FD) and layer height (LH). The 3D-printed parts were tested for ultimate tensile strength, impact strength, flexural strength and shore D hardness according to ASTM standards. Analysis of variance (ANOVA) was employed to study the influence of output parameters with respect to input parameters. Optical microscopy was employed to study the fractured surfaces.

Keywords PLA · ANOVA · Tensile test · Fractography analysis

20.1 Introduction

Additive manufacturing is a process of creating objects through layer-by-layer manufacturing from the three-dimensional (3D) model data; it is an automation process, and it is quick and flexible. It also reduces half of the manufacturing lead time, even with high complex parts [1]. Rapid manufacturing processes are broadly classified into with laser usage and without laser usage; fused deposition modelling (FDM) is an emerging type which produces prototypes in aerospace application and rapid tooling of highest accuracy and ensures functional requirements without using laser. Stereolithography is a process which uses laser and needs high-level maintenance

M. Ramesh

Department of Production Engineering, National Institute of Technology, Trichy 620015, India

K. Panneerselvam (✉)

Department of Mechanical Engineering, K. Ramakrishnan College of Engineering, Trichy 621112, India

e-mail: kps@nitt.edu

© Springer Nature Singapore Pte Ltd. 2020

M. S. Shunmugam and M. Kanthababu (eds.), *Advances in Additive Manufacturing and Joining*, Lecture Notes on Multidisciplinary Industrial Engineering,

https://doi.org/10.1007/978-981-32-9433-2_20

and care than the FDM [2, 3]. The material is supplied to extrusion nozzle from a coil of plastic or metal wire filament which is unrolled. The nozzle is then used to heat the filament and melt it at respective temperatures. The nozzle can be moved in both vertical and horizontal directions by the numerically controlled mechanism, assisted by the software package. The beads are formed after the nozzle gets heated to form layers, and after the material gets extruded, it starts to harden immediately [4].

The influencing parameters to create high accuracy of FDM products depend on the layer thickness, print speed and fill density [5]. When improper factors are selected, there will be defects in the products produced. Anitha et al. [6] concluded that layer thickness is one of the influential factors during the FDM process. Sood et al. [7] studied the parameters like layer thickness, orientation, raster width, raster angle and air gap during the FDM process. Galantucci et al. [8] concluded that build direction has a little effect on 3D-printed parts.

Taguchi's design of experiments is used to reduce the number of parameters and to study the influencing factor during the experiments and their interactions. When the number of experiments is reduced, there is a reduction of cost while carrying out the experiments.

From the previous literature survey, it was found that there are only few works related to 3D printing of PLA using FD as factor. In the current research work, PLA filaments were used for producing test components by 3D printing process. The factors considered during the process were FH, LH and PS, and the experiments were designed according to L9 orthogonal array. The mechanical characterization and fractography study were carried out. ANOVA was used for studying the importance of input parameters.

The objective of the work performed in this paper is to explore the effect of parameters like print speed, layer thickness and fill density for the PLA material. The study of tensile, impact, hardness and flexural testing is done, and the optical microscopy is done to see the fracture of tensile specimens.

20.2 Experiment Details

20.2.1 FDM Machine

The FDM machine used in this work was supplied by M/s Julia dual by Fractal Works, India. The 3D printing machine has the ability to process with all the three chosen parameters. The samples have been manufactured by 3D printing process using polylactic acid (PLA) threads [9]. The parts to be produced were initially modelled using SOLIDWORKS. The 3D CAD model is then converted to tessellation STL file format using SOLIDWORKS. The Fractal works software assists to vary the build parameters and helps in generating the G-code, which controls the extrusion head

of the FDM machine [10]. The build plate was cleaned before each process, and it should be free from adhesives such that it should not affect the process.

20.2.2 Characterization of 3D-Printed PLA

The tensile test of the 3D-printed PLA was carried out according to ASTM D638 standards. The cross-head speed was maintained at 2 mm/min. Flexural tests of 3D printed were carried out according to ASTM D790-10 standards at a cross-head speed of 2 mm/min. The energy absorbed during the impact test of 3D-printed PLA was evaluated according to ASTM D256-10. The load applied was 6.5 J. The hardness of the 3D-printed PLA samples was assessed by shore D hardness according to ASTM D2240-05 standards. The microstructure of the fractured 3D-printed PLA samples was studied using optical microscope.

20.2.3 Parameters' Selection and Experiment Details

After the completion of several trial-and-error experiments, the parameters selected for the experiments are fill density, layer thickness and print speed. These three parameters were selected in three levels for 3D printing of components. The levels of the 3D-printed components are listed in Table 20.1. Experiments were carried out according to Taguchi's L9 experiments (Figs. 20.1, 20.2 and 20.3).

Table 20.1 Proposed levels of experiments

Factors	Level 1	Level 2		Level 3
Print speed (mm/s) PS	60	65		70
Layer height (mm) LH	0.1	0.2		0.3
Fill density (%) FD	50	75		100

Fig. 20.1 Fractured specimens after tensile test



Fig. 20.2 Fractured specimens after flexural test



Fig. 20.3 Fractured specimens after impact test



20.3 Results and Discussion

The 3D-printed PLA materials were characterized for mechanical characterization like tensile tests, flexural strength, impact strength, shore D hardness and fractured surfaces by optical microscopy. The results of the mechanical characterizations are listed in Tables 20.2 and 20.3.

Table 20.2 L9 orthogonal array of experiments using Taguchi’s method

Factors	Layer height (LH) (mm)	Fill density (FD) %	Print speed (PS) (mm/s)
1	0.1	50	60
2	0.1	75	65
3	0.1	100	70
4	0.2	50	65
5	0.2	75	70
6	0.2	100	60
7	0.3	50	70
8	0.3	75	60
9	0.3	100	65

Table 20.3 L9 orthogonal array of output response

S.no	Ultimate tensile strength (MPa)	Impact strength (J)	Shore D hardness	Flexural strength (MPa)
1	27.910	2.756	65.660	38.28
2	29.120	5.968	74.330	41.02
3	31.030	3.419	78.833	48.44
4	28.019	3.811	69.330	37.50
5	29.289	5.968	75.500	41.41
6	35.770	3.873	78.000	47.66
7	24.260	3.873	63.830	37.50
8	26.910	4.211	76.000	40.23
9	33.200	3.457	79.830	53.12

20.3.1 Tensile Strength of PLA Material

The main effect plots of tensile strength of 3D-printed PLA are shown in Fig. 20.4. The highest values of tensile strength were recorded at 0.2 LH, and the strength is below the mean between 0.1 and 0.3 LH. The ultimate tensile strength has increased with increase in fill content of PLA material. Meanwhile, the lowest value of tensile strength is 24.260 MPa when the PLA is at 50% fill. The tensile strength is higher at 60 mm/s and lowest at 70 mm/s; it might be due to the wrapping up of layers providing holes between layers which should have reduced the tensile strength of PLA material.

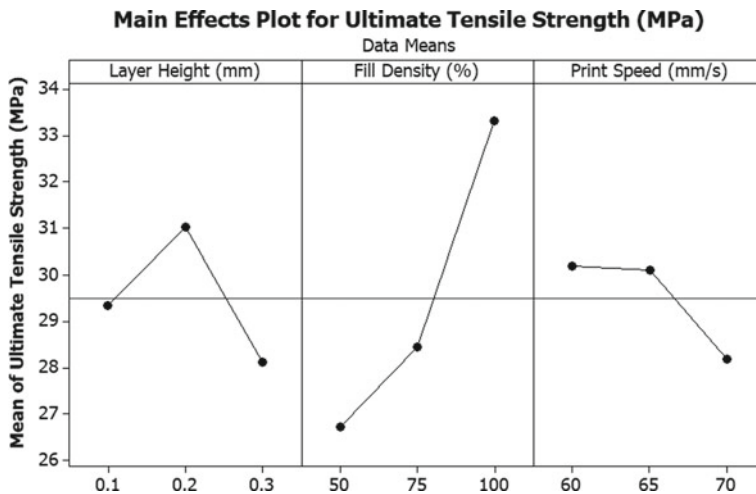


Fig. 20.4 Main effect plots for ultimate tensile strength

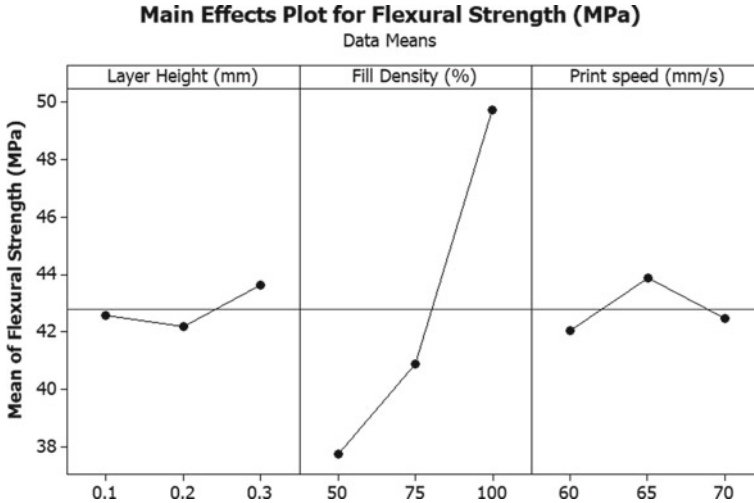


Fig. 20.5 Main effect plots for flexural strength

20.3.2 Flexural Strength of PLA Material

The main effect plots of flexural strength at 100% fill density had shown in Fig. 20.5, in which the highest value is 53.12 MPa and the lowest value is 37.5 MPa at 50% fill density. At 75% fill density, the flexural strength was better than the 50% fill density. The impact of layer height shows that the flexural strength has increased by increase in layer height but at 0.2 layer thickness, there is a small drop of strength as shown in graph. The flexural strength is high at 65 mm/s print speed but low at 60 mm/s. At 70 mm/s, there is a drop in flexural strength which might be due to wrapping effect caused between the layer-by-layer formations. Overall, the pattern shows an increase in flexural strength as the fill density concentration and layer thickness of PLA were increased.

20.3.3 Impact Strength of PLA Material

The main effect plot of impact strength is shown in Fig. 20.6. When LH was at 0.1, the impact strength was lower compared with 0.2 and better with respect to 0.3. The best strength is obtained at 0.2 LH. The lowest value of impact strength was recorded at 2.756 J when the percentage of PLA fill density is only at 50%. Meanwhile, the highest value of impact strength was recorded when the fill density of PLA is 75% when the impact strength is 5.968 J. But the strength is reduced to 100% fill due to the energy absorbed stress. The impact strength was maximum at 70 mm/s PS which is marginally higher when compared with 65 mm/s. The presence of low speed 60 mm/s

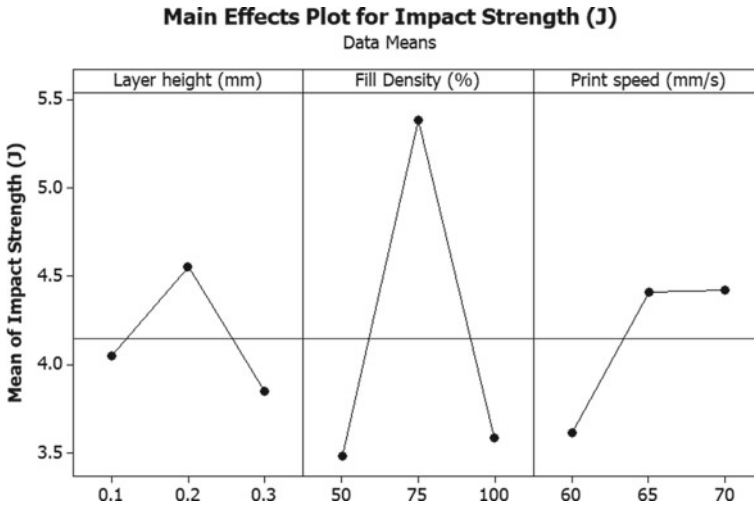


Fig. 20.6 Main effect plots for impact strength

had reduced the impact strength when the layer by layer is not formed uniformly with some voids.

20.3.4 Shore D Hardness of PLA

The main effect plot of shore D hardness is shown in Fig. 20.7.

When LH was at 0.1, the shore D hardness value was lowest, and it increased when the layer thickness was at 0.2. The formation of irregular structure when the LH was set at 0.3 resulted in decrease in shore D hardness. The value of shore D hardness increased when the FD was increased from 50 to 100%. The absence of pores when the FD was set at 100% resulted in better shore D hardness values. The value of shore D hardness was maximum when the PS was at 65 mm/s due to formation of uniform layer during the printing process. The formation of non-uniform layer and presence of pores resulted in decrease in shore D hardness value.

20.3.5 Fractography Studies

The nature of fracture of the thermoplastic component is ductile which is due to the stretching and reorientation of materials that result in deformation. The fracture surface of the 3D-printed PLA samples shows ductile type of fracture. The fracture surface was analysed using optimal microscope, and it is shown in Figure. From figure, it can be seen that there was a presence of large number of pores when FD

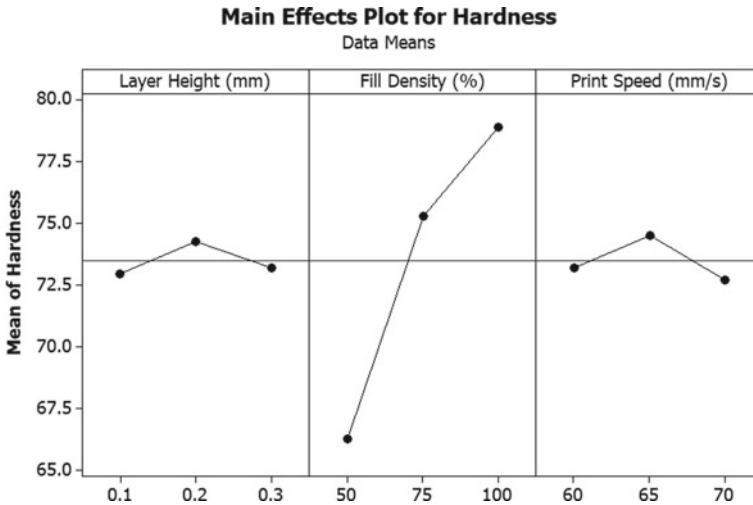


Fig. 20.7 Main effect plots for shore D hardness

was at 50% which resulted in poor strength. The fractured surface of 75% FD shows less number of pores when compared to 50% FD. This is mainly due to the presence of more amount of PLA material during 3D printing process. When the FD was at 100, the presence of pores was very meagre when compared to remaining two materials. The proper filling of material at 100% FD resulted in enhanced properties. Thus, the fill density must be selected properly for getting better characteristics. There was a good correlation between the optical microscopic studies and experimental data (Figs. 20.8, 20.9 and 20.10).

Fig. 20.8 Optical microscopy image of 50% FD

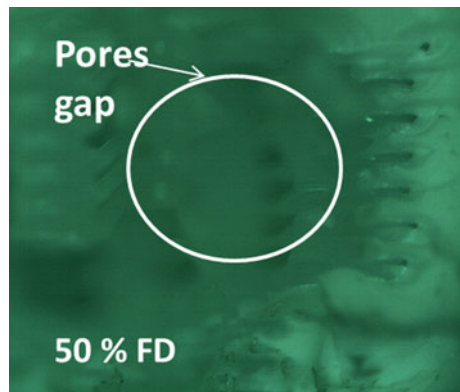


Fig. 20.9 Optical microscopy image of 75% FD

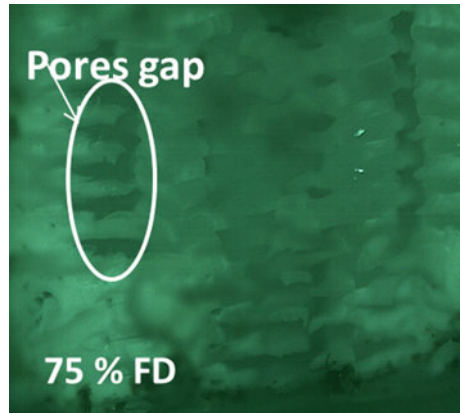
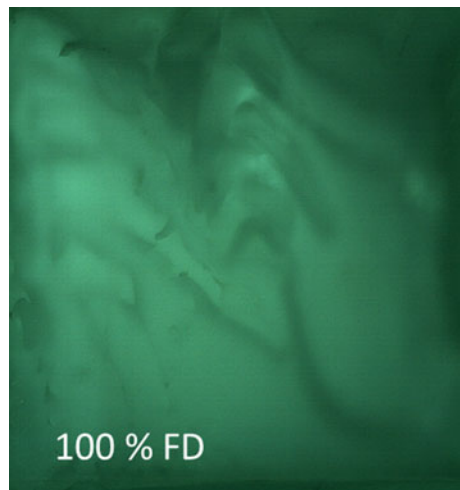


Fig. 20.10 Optical microscopy image of 100% FD



20.4 ANOVA

The ANOVA was employed for studying the effect of output parameters with respect to input parameters. The ANOVA table for tensile strength, flexural strength, impact strength and shore D hardness is shown in table. From table, it can be concluded that FD is one of the vital factors for determining the strength of 3D-printed PLA components (Table 20.4).

In the case of flexural strength, impact strength and shore D hardness, LH was the least dominant factor, while in the case of tensile strength, PS was the least one (Tables 20.5, 20.6 and 20.7).

Table 20.4 ANOVA for tensile strength

Source	DF	Seq SS	Adj MS	F_{cal}	% contribution
LH	2	12.736	6.368	3.64	13.49
FD	2	70.48	35.24	20.17	74.65
PS	2	7.708	3.854	2.21	8.16
Error	2	3.495	1.748	–	3.70
Total	8	94.42	–	–	–

Table 20.5 ANOVA for flexural strength

Source	DF	Seq SS	Adj MS	F_{cal}	% contribution
LH	2	3.262	1.489	0.28	1.30
FD	2	231.678	126.61	23.39	92.58
PS	2	5.524	2.516	0.46	2.21
Error	2	9.783	5.414	–	3.91
Total	8	250.247	–	–	100.00

Table 20.6 ANOVA for impact strength

Source	DF	Seq SS	Adj MS	F_{cal}	% contribution
LH	2	0.7884	0.3942	0.88	8.01
FD	2	6.8671	3.4335	7.66	69.79
PS	2	1.2886	0.6443	1.44	13.10
Error	2	0.896	0.448	–	9.11
Total	8	9.8402	–	–	–

Table 20.7 ANOVA for shore D hardness

Source	DF	Seq SS	Adj MS	F_{cal}	% contribution
LH	2	2.97	1.489	0.28	1.09
FD	2	253.22	126.6	23.3	93.08
PS	2	5.032	2.516	0.46	1.85
Error	2	10.82	5.414	–	3.98
Total	8	272.05	–	–	–

20.4.1 Predicted Mean

From the determination of the optimum values from the ANOVA table, the mean of the response (μ) at the optimum condition is predicted. From significant parameters, mean is calculated. The optimal value of the response characteristic is obtained from the significant parameters identified by ANOVA using Eq. 20.1.

$$\mu_{\text{Pred}} = \bar{A} + \bar{B} + \bar{C} - 2\bar{Y} \quad (20.1)$$

\bar{Y} Overall mean of the response;
 $\bar{A}, \bar{B}, \bar{C}$ Average values of response at levels of significant parameters.

20.4.2 Determination of Confidence Intervals

The estimate of the mean (μ) is only a point estimate based on the average of results obtained from the experiment. It is a statistical requirement that the value of a parameter should be predicted along with a range within which it is likely to fall for a given level of confidence. This range is called confidence interval (CI), and it is calculated by Eq. 20.2

$$CI_p = \sqrt{\frac{F_\alpha(v_1, v_2)MS_e}{\eta_{\text{eff}}}} \quad (20.2)$$

$F_\alpha(v_1, v_2)$ The F -ratio at the confidence level;
 v_1 The number of degree of freedom of the mean;
 v_2 Is the number of degree freedom of the error;
 N Total number of result;
 R Sample size for confirmation experiments;
 MS_e Error variance;
 η_{eff} Is the effective sample size.

$$\eta_{\text{eff}} = \frac{N}{1 + \text{DOF}_{\text{opt}}} \quad (20.3)$$

From the above, using Eqs. (20.1–20.3) and the significant parameters obtained from the ANOVA, the following predicted optimum and confidence interval of the predicted mean have been shown in Table 20.8 for tensile, flexural, impact and hardness tests.

20.4.3 Confidence Interval

The confidence interval (CI) is defined as an interval estimate of a parameter population, in which the significant parameter is indicated as the reliable estimate. The confidence level or confidence coefficient is used to determine the frequency of observed interval. The width depicts the confidence interval obtained which shows

Table 20.8 Predicted mean and confidence interval for various tests

Tests	Predicted optimum response	Confidence interval of predicted mean	
		Lower bound	Upper bound
Tensile	35.56	33.2986	37.0214
Flexural	51.84	48.727	54.953
Impact	6.056	5.114	6.998
Shore D hardness	80.71	77.434	83.986

how uncertain we are about the unknown parameter. A very wide interval may indicate that further data should be collected to narrow down to a very definite parameter.

20.5 Conclusions

The 3D printing of PLA components was carried out by FDM process, and it is tested by various characterization methods. From the results obtained from the varied parameters, viz. Print speed, layer height and fill density of PLA processed by 3D printing technology, the following conclusions are drawn.

The ultimate tensile strength, impact strength, shore D hardness and flexural strength were evaluated. The ultimate tensile strength, shore D hardness and flexural strength are maximum at 100% FD, and the impact strength is higher at 75% FD.

The fill density has the highest contribution factor which influences mechanical characteristics of the PLA material during the 3D printing process.

The LH of 0.2 mm has influenced the mechanical characteristics like tensile strength, impact and shore D hardness, but the flexural strength has been increased at 0.3 LH.

The chosen parameters of PS did not have a dominant factor that influences the mechanical characteristics, unless higher speed gives the defect of wrapping and low speed gives heat-affected zones.

From the 95% confidence interval, the optimized value of tensile strength was predicted to be 35.56 ± 1.86 MPa. The corresponding mean for the optimum conditions was found to be 35.77 MPa which is within the predicted range. Similarly, for the remaining flexural, impact and hardness tests, the values got from the optimum parameter were also within the predicted range.

Thus, this research gives some adequate knowledge of the 3D printing on PLA filament in popularizing digital manufacturing in Indian precision casting industries.

This work can be still further extended by adding fillers to PLA matrix, and the related properties can be evaluated and compared with pure PLA.

References

1. Chua, C.K., Leong, K.F.: *Rapid Prototyping: Principles and Applications in Manufacturing*. Wiley (1997)
2. Jain, P., Kuthe, A.M.: Feasibility study of manufacturing using rapid prototyping: FDM approach. *Proc. Eng.* **1**(63), 4–11 (2013)
3. Karapatis, N.P., Van Griethuysen, J.P.S., Glardon, R.: Direct rapid tooling: a review of current research. *Rapid Prototy. J.* **4**(2), 77–89 (1998)
4. Gregorian, A., Elliot, B., Navarro, R., Ochoa, F., Singh, H., Monge, E., Foyos, J., Noorani, R., Fritz, B., Jayanthi, S.: Accuracy improvement in rapid prototyping machine (FDM-1650). In: *Solid Freeform Fabrication Proceedings*, pp. 77–84 (2001)
5. Zhou, J., Herscovici, D., Chen, C.C.: Parametric process optimization to improve the accuracy of rapid prototyped stereolithography parts. *Int. J. Mach. Tools Manuf.* **40**, 363–379 (2000)
6. Anitha, R., Arunachalam, S., Radhakrishnan, P.: Critical parameters influencing the quality of prototypes in fused deposition modelling. *J. Mater. Process. Technol.* **118**, 385–388 (2001)
7. Sood, A.K., Chaturvedi, V., Datta, S., Mahapatra, S.S.: Optimization of process parameter infused deposition modelling using weighted principle component analysis. *J. Adv. Manuf. Sys.* **2**, 241–250 (2011)
8. Galantucci, L.M., Lavecchia, F., Percoco, G.: Experimental study aiming to enhance the surface finish of fused deposition modeled parts. *Manuf. Technol.* **58**, 189–192 (2009)
9. Marcos, M., Wendt, C., Fernandez-Vidal, S., Gomez-Parra, A., Batista, M.: *Adv. Mat. Sci. Eng.* (2016). Article ID 5780693. <http://dx.doi.org/10.1155/2016/5780693>
10. Groover, M.P.: *Modern Manufacturing*, 5th edn. Wiley (2013)

Chapter 21

Numerical Analysis of Thermal Stresses in Selective Laser Melting



Rahul Swarup Sharma  and A. Kumar 

Abstract The steep temperature gradient in the Selective Laser Melting additive manufacturing process due to localized heating of the powder layer will induce unwanted thermal stress in the component. They will remain in the material even after the component brought back to the ambient conditions and cause defects like cracking and deformation. In this study, a fully coupled thermo-mechanical model is developed to study the temperature field and resulting thermal stress by considering temperature-dependent properties and plastic behavior of the component. Tensile residual stress are found in the top layer of the scanned region and the balancing compressive zone is found underneath it to maintain the equilibrium. During the scanning process, the magnitude of stress increases the magnitude of the yield strength of the material due to which some permanent stress remain in the material as residual stress.

Keywords Selective laser melting · Additive manufacturing · Thermal stress · Thermo-mechanical model

21.1 Introduction

Additive manufacturing (AM) is modern manufacturing technique in which component is manufactured by using data from design software to deposit material in layer upon layer fashion. This technique is opposite of the conventional subtractive manufacturing technique in the way that the final component is manufactured by addition of material by this technique while in subtractive manufacturing final component is manufactured by removing the material. This technology has many advantages over the conventional manufacturing technique such as minimum or no material wastage, manufacturing of complex geometries and graded components and many more. Among the many additive manufacturing processes, Selective Laser Melting (SLM) is the most popular one as it has advantage of manufacturing the component

R. S. Sharma · A. Kumar (✉)

Department of Mechanical Engineering, Indian Institute of Technology Kanpur, Kanpur 208016, India

e-mail: arvindkr@iitk.ac.in

© Springer Nature Singapore Pte Ltd. 2020

M. S. Shunmugam and M. Kanthababu (eds.), *Advances in Additive Manufacturing and Joining*, Lecture Notes on Multidisciplinary Industrial Engineering,

https://doi.org/10.1007/978-981-32-9433-2_21

with very high density and minimum porosity. Despite of advantages, there are disadvantages also associated with this technique such as poor surface finish, delamination of the layers and residual stresses in the component due to high thermal gradient. Due to residual stresses, there will be crack formation in the component which is one of the major defects in the SLM manufactured component. Therefore, it is very important to perform qualitative and quantitative analysis of the thermal residual stresses for adoption of appropriate parameters and scanning technique to minimize the residual stress. Experimental study of temperature field and resulting thermal stresses are very difficult due to very rapid melting and solidification. In this case, development of computational model is very useful to save the experimental cost to study this manufacturing technique.

Many researchers investigated the temperature field and melt pool characteristics but only the few investigated the resulting thermal stresses by using the computational model. Mercelis and Kruth [1] developed the simple theoretical model to evaluate the stress distribution in powder layer laid over the substrate. After that by using an experimental approach, effect of number of layers, yield strength of the material and base plate height was studied. A zone of tensile stress in the upper layer followed by the compressive zone and then again, a tensile zone at the bottom was observed along the depth of the component. Shiomi et al. [2] developed similar type of stress profile along the depth of the material by establishing the theoretical model for selective laser melting process. The effect of heat treatment, substrate heating and re-scanning of the track on relieving the residual stress was studied. It was found that heat treatment for one hour to 600 °C, substrate heating to 160 °C and re-scanning of the track relieves 70, 40, and 55% stresses, respectively. Hussein et al. [3] developed a fully coupled thermo-mechanical analysis of the temperature field and stress distribution in 316L stainless steel layer made by SLM. The cooling rate was observed higher for scanning over a solid substrate than that on a powder bed. The temperature gradient is very high at the initial stage of scanning due to low thermal conductivity of the powder bed results in high von Mises stresses. Gu and He [4] developed a 3D transient model to analyze the stress distribution in parts produced by SLM using Ti–Ni powder. They found maximum residual stress at the end of the first track which is vulnerable to cracking. Therefore, it is recommended that the length of the scanning track should be less to avoid the cracks in the fabricated part. The effects of laser scan strategy on the development of residual stresses in additive manufacturing of Ti6Al4 V were studied by Parry et al. [5]. They found that the alternating scan strategy generates anisotropic stress field. The long scan vector length was advised to be avoided to produce uniform stress field.

This work aims to develop a fully coupled thermo-mechanical model in which thermal model incorporates melting, solidification, phase transition from powder to liquid to solid state, temperature-dependent material properties and mechanical model incorporates elasto-plastic behavior of the material to evaluate the thermal stresses. The temperature field obtained from the thermal study is used as initial condition for the mechanical model which in result gives the stress field in the whole domain. In this way, thermal model is fully coupled with the mechanical model.

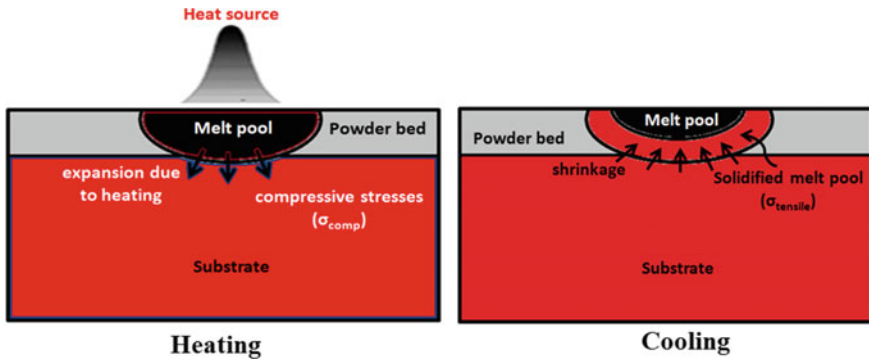


Fig. 21.1 Thermal stresses during heating and cooling

21.2 Origin of Thermal Stresses

Thermal stresses in the material originated basically from differential volumetric expansion or contraction at different location in the material. In SLM, there is steep temperature gradient which results in different temperature at different locations. Hence, there is different volumetric expansion or compression of the material as thermal expansion coefficient is function of the temperature. During heating, the solid substrate or previously deposited layer in heat affected region, experiences compressive stresses as material tries to expand by absorbing heat and this expansion is restricted by the remaining material away from the heat affected region. There is balancing tensile zone underneath the compressive stress zone to maintain equilibrium. During cooling period, the solidified melt pool experiences tensile stresses as it is restricted to shrink freely by the solid substrate material (Fig. 21.1). This time there will be balancing compressive zone underneath the tensile stress zone to maintain equilibrium.

21.3 Mathematical Model

A 3D finite element model is developed to study the temperature field and resulting thermal stress when a powder layer over the solid substrate is scanned by laser heat source. Figure 21.2 shows the schematic of the model used in this study where a Gaussian type laser heat source interacts with powder layer by adopting alternate laser scan strategy. There will be convective and radiative losses take place from the top boundary. Also, the material properties of the component such as yield strength and rigidity of the material varies considerably with the temperature, therefore, temperature-dependent material properties are considered for this analysis. The parameters and the material properties used in this study are tabulated in Tables 21.1 and 21.2, respectively. (Table 21.3).

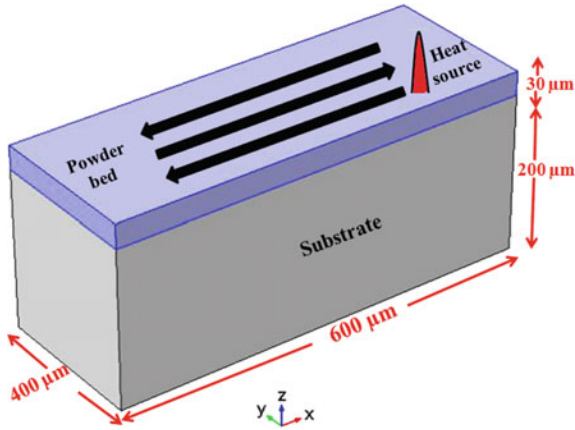


Fig. 21.2 Schematic of the computational domain

Table 21.1 Process parameters used in the study

Parameters	Value
Laser power	45 W
Laser spot radius	26 μm
Laser scanning speed	250 mm s ⁻¹
Hatch spacing	50 μm

Table 21.2 Thermo-physical material properties of Ti-6Al-4 V

Solidus temperature (K)	1877
Liquidus temperature (K)	1923
Density of bulk solid (kg m ⁻³)	4512
Density of the liquid (kg m ⁻³)	4122
Specific heat of bulk solid (J kg ⁻¹ K ⁻¹)	483.04 + (0.215 × T) T ≤ 1268
Specific heat of liquid (J kg ⁻¹ K ⁻¹)	412.7 + (0.1801 × T) 1268 < T ≤ 1923
Latent heat of fusion (kJ kg ⁻¹)	286
Thermal conductivity of bulk solid (W m ⁻¹ K ⁻¹)	1.2595 + (0.0157 × T) T ≤ 1268 -12.752 + (0.024 × T) 1268 < T ≤ 1923
Thermal conductivity of liquid (W m ⁻¹ K ⁻¹)	-12.752 + (0.024 × T)
Convective heat transfer coefficient (W m ⁻² K ⁻¹)	10

Table 21.3 Mechanical properties of Ti-6Al-4 V [5]

Temperature (°C)	Young's modulus (GPa)	Yield strength (MPa)	Plastic tangent modulus (GPa)
24	125	1000	0.7
94	110	630	2.2
205	100	630	2.2
317	100	525	2.2
428	80	500	1.9
539	74	446	1.9
650	55	300	1.9
761	27	45	2
872	20	25	2
1094	5	5	2
1650	0.1	0.1	0.1

21.3.1 Thermal Model

The governing equation for thermal model to evaluate the temperature field is energy conservation equation:

$$\frac{\partial(\rho C_p T)}{\partial t} + \vec{u} \cdot \nabla(\rho C_p T) = \nabla \cdot (k \nabla T) \quad (21.1)$$

The values of ρ , C_p and k in the powder bed were determined by the following equations:

$$\rho = (1 - \beta)\rho_{\text{phase1}} + \beta\rho_{\text{phase2}} \quad (21.2a)$$

$$\beta = \begin{cases} 0 & T < T_{\text{solidus}} \\ \frac{T - T_{\text{solidus}}}{T_{\text{liquidus}} - T_{\text{solidus}}} & T_{\text{solidus}} \leq T < T_{\text{liquidus}} \\ 1 & T \geq T_{\text{liquidus}} \end{cases} \quad (21.2b)$$

$$C_p = \frac{1}{\rho} ((1 - \beta)\rho_{\text{phase1}}C_{p, \text{phase1}} + \beta\rho_{\text{phase2}}C_{p, \text{phase2}}) + L \frac{\partial \alpha_m}{\partial T} \quad (21.2c)$$

$$\alpha_m = \frac{1}{2} \frac{\beta\rho_{\text{phase2}} - (1 - \beta)\rho_{\text{phase1}}}{(1 - \beta)\rho_{\text{phase1}} + \beta\rho_{\text{phase2}}} \quad (21.2d)$$

$$k = (1 - \beta)k_{\text{phase1}} + \beta k_{\text{phase2}} \quad (21.2e)$$

Here β is a linear function representing the fraction of liquid phase before transition, and α_m is the mass fraction.

A Gaussian type of laser heat source is used for scanning the powder bed and convective and radiative losses take place from the top boundary which is used as boundary condition for thermal model.

$$k \frac{\partial T}{\partial n} = q - q_{\text{conv}} - q_{\text{rad}} \quad (21.3)$$

21.3.2 Mechanical Model

The temperature field obtained from the thermal model analysis is used as initial conditions for the mechanical model at each time step. In this way, both the models are fully coupled. The governing equation for the mechanical model is:

$$\sigma_{ij} = C_{ijkl} \varepsilon_{ij}^{\sigma} \quad (21.4)$$

where

$$\varepsilon_{ij}^{\sigma} = \varepsilon_{ij}^{el} + \varepsilon_{ij}^{pl} \quad (21.5)$$

$$\varepsilon_{ij} = \varepsilon_{ij}^{\sigma} + \varepsilon_{ij}^{th} \quad (21.6)$$

$$\varepsilon_{ij}^{th} = \alpha(T - T_{\text{ref}}) \delta_{ij} \quad (21.7)$$

where α is the coefficient of thermal expansion of the solid and T_{ref} is the reference temperature (i.e. 293 K) at which the body is stress and strain-free. For boundary condition, the bottom surface of the material is taken as fixed boundary.

21.3.3 Properties of Powder Bed

The powder bed is considered as homogenous material with modified material properties. Following relations are considered to modify the material properties:

$$k_P = k_S \frac{(1 - \phi)}{(1 + 11\phi^2)} \quad (21.8)$$

$$\rho_P = \rho_S(1 - \phi) \quad (21.9)$$

where ϕ is the powder layer porosity taken as the typical value of 0.35.

21.4 Results and Discussion

A 40 W laser heat source of Gaussian profile is used to scan the powder bed. An alternate scan strategy of laser heat source is adopted in simulation. The laser heat source scans three tracks on the powder bed after which heat source is turned off and component is allowed to cool up to the time it reaches back to the ambient conditions. Figure 21.3 shows the temperature maps and the cross-sectional view during the scanning of powder bed by laser heat source. During the scanning of the powder bed by laser heat source some part of the solid substrate also gets melted to form the proper bonding between the first deposited layer and substrate (Fig. 21.3).

Figure 21.4a shows the map of longitudinal component of stress tensor at the end of the cooling stage when component comes back to the equilibrium condition.

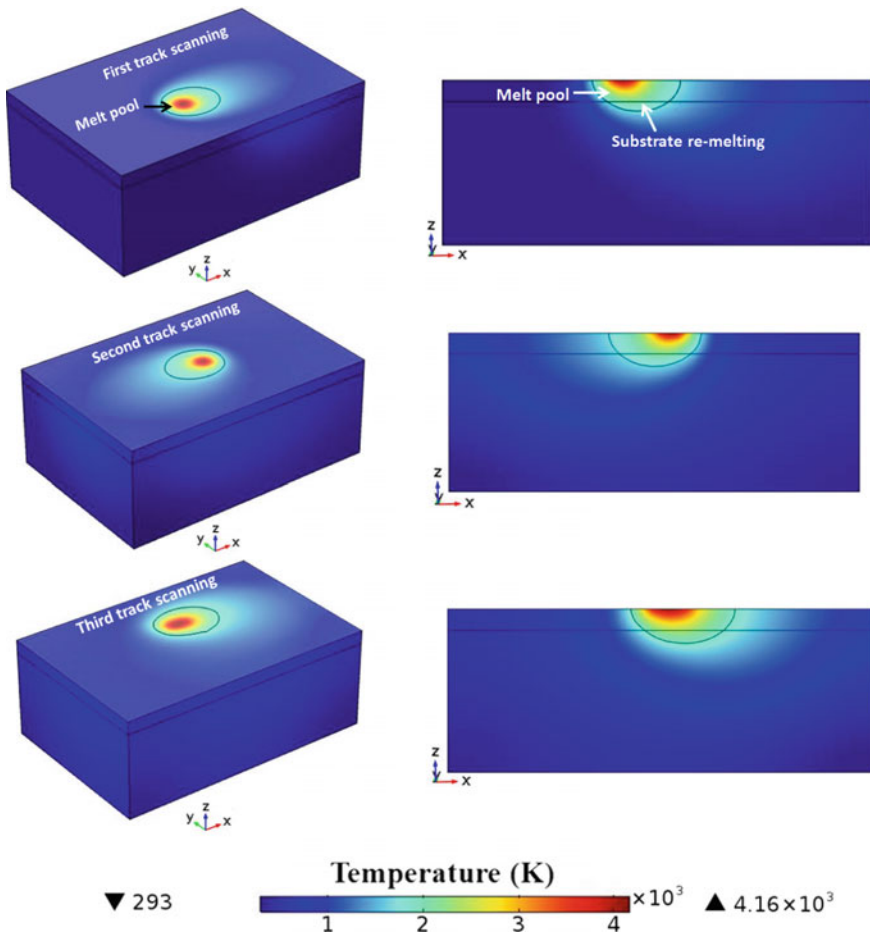


Fig. 21.3 Temperature maps and cross-sectional view along the scanning direction

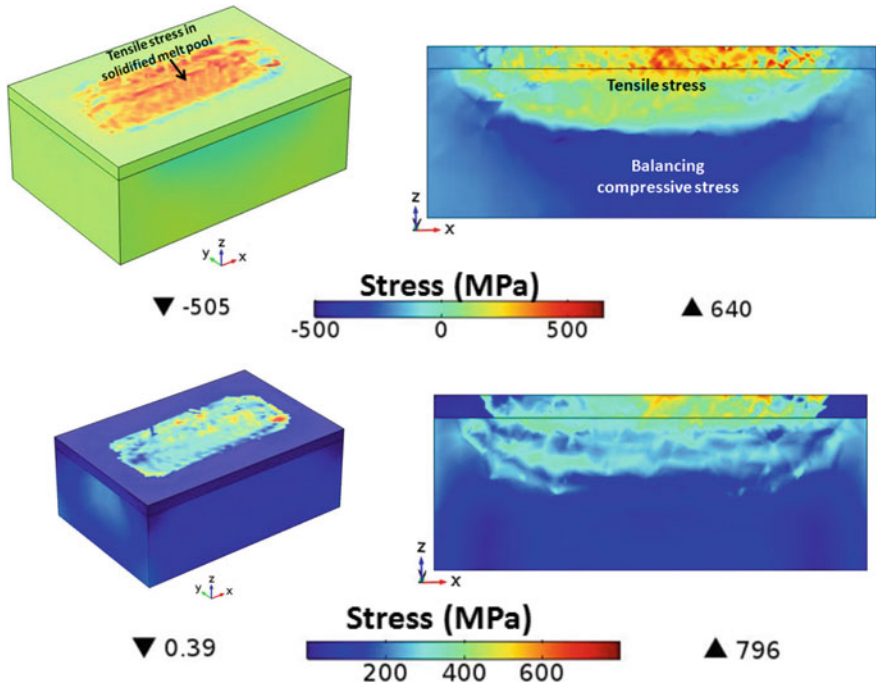


Fig. 21.4 **a** Longitudinal stress component and cross-sectional view, **b** von Mises stress and cross-sectional view along the scanning direction in second track

During the cooling stage, the top layer of the component tries to shrink but the remaining material of the component does not allow it to shrink freely. Therefore, a zone of tensile stress is developed at the top layer and balancing compressive stress developed underneath it to maintain equilibrium (Fig. 21.4a). Figure 21.4b shows the von Mises stress map at the end of the cooling stage. There are high von Mises stresses present in the solidified powder layer. During the scanning of the powder layer by laser heat source, the magnitude of the stresses exceed from the instantaneous yield strength of the material due to which hardening of the component takes place and permanent plastic stresses induce in the component which will remain as residual stresses in the component after complete cooling of the component (Fig. 21.4b).

21.5 Conclusions

In this work, a fully coupled thermo-mechanical model is developed to study the thermal field evolution and resulting thermal stresses. Thermal model incorporates melting, solidification; temperature-dependent material properties and phase change of the material whereas mechanical model incorporates temperature-dependent mate-

rial properties and plastic behavior of the material. Thermal model is fully coupled with the mechanical model and at each time step firstly the temperature field is calculated which is used as initial condition to evaluate the thermal stress field. Some important conclusions from this study are stresses in the SLM process originated due to high thermal gradient which causes uneven expansion and contraction of the material. Tensile residual stress will remain in the top layer of the component and there is balancing compressive stress zone underneath it to maintain equilibrium. The magnitude of the stresses will cross the instantaneous yield strength of the material due to which some hardening of the material takes place and permanent residual stress will locked-in the material.

References

1. Mercelis, P., Kruth, F.: Residual stresses in selective laser sintering and selective laser melting. *Rapid Prototyp. J.* **12**(5), 254–265 (2006)
2. Shiomi, M., Osakadal, K., Nakamural, K., Yamashital, T., Abe, F.: Residual stress within metallic model made by selective laser melting process. *CIRP Ann.* **53**, 195–198 (2006)
3. Hussein, A., Hao, L., Yan, C., Everson, R.: Finite element simulation of the temperature and stress fields in single layers built without-support in selective laser melting. *Mater. Des.* **52**, 638–647 (2013)
4. Gu, D., He, B.: Finite element simulation and experimental investigation of residual stresses in selective laser melted Ti–Ni shape memory alloy. *Comput. Mater. Sci.* **117**, 221–232 (2016)
5. Parry, L., Ashcroft, I.A., Wildman, R.D.: Understanding the effect of laser scan strategy on residual stress in selective laser melting through thermo-mechanical simulation. *Addit. Manuf.* **12**, 1–5 (2016)

Chapter 22

Experimental Investigations of Printing Parameters of Fused Deposition Modeling-Based 3D Printers for Average Surface Roughness



Apoorv Srivastava and Jitendra Bhaskar

Abstract The FDM technology-based 3D printers have become very popular for making models in the industry. Selection of printing parameters is the key issue in preparing models with good surface finish. An effort has been made to study the effect of printing parameters such as layer thickness, nozzle temperature and printing speed on the surface. Efforts were made to print test coupons using the FDM-based 3D printer, and surface roughness was measured using the stylus probe attached to surface tester to identify the role of printing parameters for surface roughness. ANOVA over L9 array of Taguchi for three variables has been used to study these parameters. Results by Taguchi method were validated by experiments and found reasonably well.

Keywords Fused deposition modeling · 3D printing · Surface roughness · Response surface methodology

22.1 Introduction

Rapid prototyping (RP) is an additive manufacturing process to fabricate 3D prototypes layer by layer directly from computer-aided design (CAD) data [1, 2]. Nowadays, various 3D printing technologies and 3D printers are available in the market. But fused deposition modeling (FDM)-based 3D printing is most commonly used and affordable technique since 1980. FDM was invented by Scott Crump, co-founder and chairman of Stratasys Ltd., a leading manufacturer of 3D printers. In this technique, heated thermoplastic filaments are extruded from a nozzle that moves in the x - y plane. The controlled extrusion head deposits very thin beads of material onto the heated platform to form the first layer [3–6]. Compared to other 3D printing methods, such as stereolithography (SLA) or selective laser sintering (SLS), FDM is a fairly slow process.

A. Srivastava · J. Bhaskar (✉)
Department of Mechanical Engineering, Harcourt Butler Technical University, Kanpur 208002,
India
e-mail: bhaskar48m@yahoo.com

© Springer Nature Singapore Pte Ltd. 2020
M. S. Shunmugam and M. Kanthababu (eds.), *Advances in Additive Manufacturing and Joining*, Lecture Notes on Multidisciplinary Industrial Engineering,
https://doi.org/10.1007/978-981-32-9433-2_22

Many researchers have been focusing on printing parameters to improve the quality of the product and same time reducing the printing time. Some of the researches such as Qattawia et al. [7] investigated the influence of FDM processing parameters on the final parts characteristics. The study investigated the effect of building directions, infill percentage, infill patterns, print speed, extrusion temperatures and layer height independently on mechanical properties and dimensional accuracy. Some more papers by Nor Aiman Sukinder et al. [8] studied five different parameters in FDM printing such as printing speed, raster angle, layer thickness, percentage infill and liquefier temperature and its influence on surface roughness. Nor Aiman measured the surface roughness with the surface profile-meter with stylus. It was concluded that percent infill does not have significant effect over surface roughness. Like one more investigation by Chaidas et al. [9] worked to observe the influence of nozzle temperature over the printed surface. It was observed that average surface roughness decreases while increasing the nozzle temperature. Surface finish is an important parameter for deciding the quality of the 3D model in terms of the functionality and aesthetics of finished parts. Taguchi method with L9 array of three variables has been used for reducing the number of experiments for finding suitable level of parameters for good surface finish.

In this paper, study of printing parameters such as nozzle temperature, layer size and print speed over roughness has been studied all together as these parameters are foremost printing parameters and effect of one over another. The objective was to find out which parameters affected the most among them using response surface methodology. In this paper, first pilot experiments were conducted to find the levels for three variables and then Taguchi L9 array was used for ANOVA to get the percentage contribution for each parameter.

22.2 Sample Preparation

The samples were designed by using solidworks and comprised a $25 \times 25 \times 0.4 \text{ mm}^3$ rectangular cuboid converted into standard triangular language (STL) format. Resulted .stl file is then imported to Ultimaker Cura for the g-codes conversion using the appropriate setting, and samples are printed at different parameters (Fig. 22.1).

22.3 Experiments

A custom built FDM-based 3D printer was used for experimentation for finding the level of parameters in view of achieving better surface finish of printed prototypes. Specifications of 3D printer are as following:

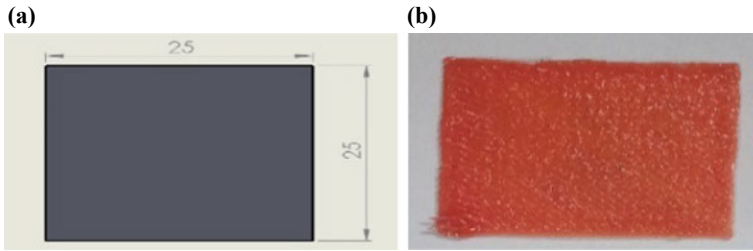


Fig. 22.1 a CAD file b Printed sample

Extruder Type: Direct with MK8 gearing, Type: Cartesian, Nozzle diameter: 0.4 mm

Parameters	Description
Nozzle diameter	0.4 mm
Shell thickness	1.0 mm
Bed temperature	45 °C
% Infill	20%
Raster angle	45 °C
Material	PLA (1.75 mm)

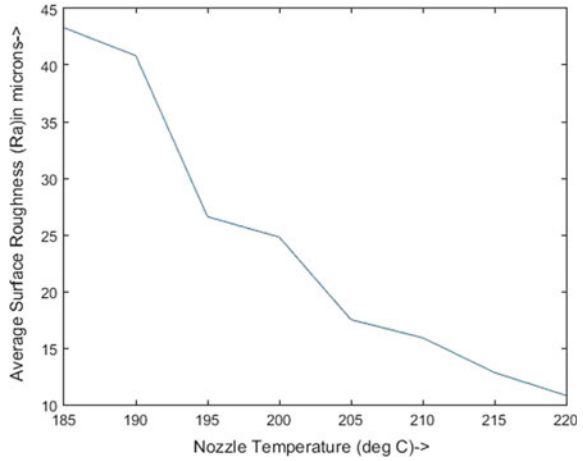
The theme of the work was to study the influence of one printing parameter over another and also to find the percent contribution of each over the average surface roughness. Firstly, the pilot experiments have been conducted to find the suitable range of parameters required for implementation of Taguchi L9 array scheme. Further, the results of Taguchi L9 array scheme were validated by experiments.

22.3.1 Pilot Experiments for the Effect of Nozzle Temperature on Surface Roughness (Ra)

Samples at different nozzle temperatures ranging from 185 to 220 °C at an interval of 5 °C were printed keeping all other parameters constant. Surface roughness was measured using the surface tester (Surtronic 3P). Surface tester used was working on the stylus probe method. Plots have been obtained using MATLAB to check influence of nozzle parameters on the average surface roughness parameter and also to find the safe range of parameters for further analysis (Fig. 22.2).

Here, this plot shows that the average roughness parameters are decreasing as we are increasing the nozzle temperature for printing keeping all other parameters same.

Fig. 22.2 Plot for nozzle temperature versus average surface roughness

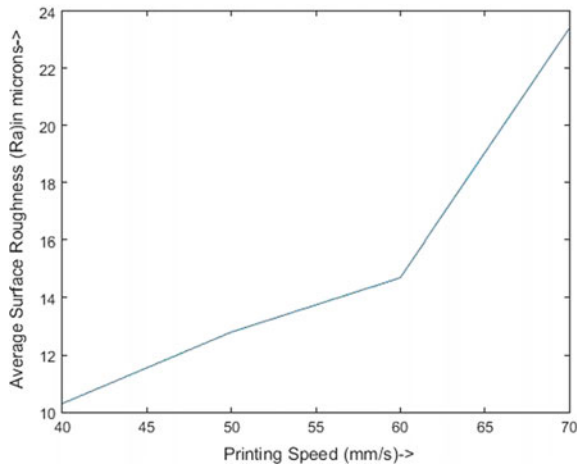


22.3.2 Pilot Experiments for the Effect of Printing Speed on Surface Roughness (Ra)

Samples of different printing speeds ranging from 40 to 70 mm/s at an interval of 10 were printed keeping all other printing parameters same to obtain the average surface roughness. These data were plotted to see how it affect the surface roughness parameter and will help in selecting the optimum parameter for further analysis.

Here, it shows that average surface roughness increases significantly while increasing the printing speed. Also it can be noted that there is steep increase after 70 mm/s print speed but slope at 40–60 mm/s does not vary much (Fig. 22.3).

Fig. 22.3 Plot for printing speed versus average surface roughness



22.3.3 Pilot Experiments for the Effect of Layer Size on Surface Roughness (R_a)

Samples are printed at different layer sizes from 0.10 to 0.40 mm keeping all other printing parameters same to obtain the average surface roughness parameter. Plotting these data in MATLAB, we got the straight line plot which shows the linear relationship between layer size and roughness (Fig. 22.4).

From the plot, it is clearly visible that on increasing layer size there is a linear increase in the average surface roughness parameter.

So out of these experiments safe levels for design of experiment are chosen as:

Layer size: 0.1, 0.2 and 0.3 mm

Print speed: 40, 50 and 60 mm/s

Nozzle temp: 215, 220 and 225 °C.

The range of parameters was selected at which there was a linear variation of roughness. After DOE for those selected levels, ANOVA is done to find the percent contribution and influence of each parameter to other using response surface methodology.

22.4 Design of Experiments

Taguchi L9 array is chosen as the DOE from the past research works and to plot the surface roughness vs print speed and nozzle temperature at various layer sizes from the model obtained after doing analysis of variance in Minitab software. Then after it ANOVA is used for further analysis (Table 22.1).

Fig. 22.4 Plot for layer size vs average surface roughness

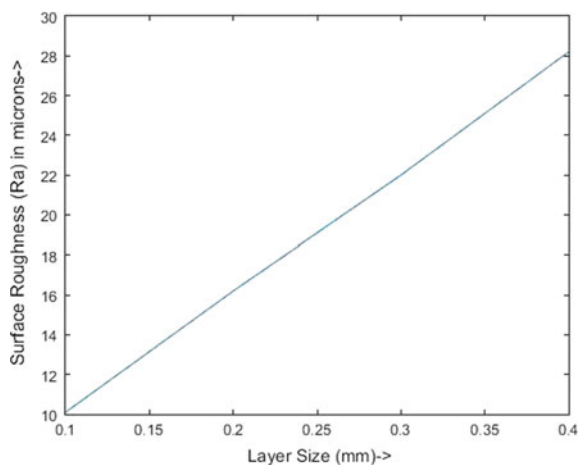


Table 22.1 Design of experiment (L9) [10]

Printing speed (mm/s)	Nozzle temp (°C)	Layer size (mm)	Roughness (μ)
40	215	0.1	7.5
40	220	0.2	9.5
40	225	0.3	11.4
50	215	0.2	10.9
50	220	0.3	11.7
50	225	0.1	7.9
60	215	0.3	15.9
60	220	0.1	9.9
60	225	0.2	10.8

22.5 Results and Discussions

After performing the pilot experiments and design of experiments, the model equation was developed for surface plots and percent contribution of the parameters.

22.5.1 Analysis for Variance

Ratio of Max/Min response = 2.12, so there is only little effect of power transformation. For that No Transform is used for further analysis.

Run	Sum of square	Mean square	F value
Mean	1013.361	1013.361	–
Linear	45.42833	15.14278	23.36448
2FI	2.545	0.848333	2.439297
Quadratic	0.695556	0.347778	–
Cubic	0	–	–
Residual	0	–	–
Total	1062.03	118.0033	–

From the sum of squares of error table, it is very much clear that linear, 2FI models need to be used for further analysis or modified quadratic model can also be used as others are giving the aliased model for the same.

Table 22.2 Analysis of variance table

	Sum of squares	DF	Mean square	<i>F</i> value	Prob > <i>F</i>	
Model	48.52008	7	6.93144	46.57928	0.1124	Significant
A	11.20667	1	11.20667	75.3088	0.0730	
B	2.94	1	2.94	19.7568	0.1409	
C	31.28167	1	31.28167	210.2128	0.0438	
A2	0.888889	1	0.888889	5.973333	0.2472	
AB	1.849	1	1.849	12.42528	0.1760	
AC	0.35219	1	0.35219	2.36672	0.3669	
BC	0.001667	1	0.001667	0.0112	0.9329	
Residual	0.14881	1	0.14881			
Cor total	48.66889	8				

Response: Roughness

ANOVA for Response Surface Reduced Quadratic Model

The “Model *F*-value” of 46.58 implies the model is not significant relative to the noise. There is a 11.24% chance that a “Model *F*-value” this large could occur due to noise (Table 22.2).

In this case, *C* is only the significant model term. “Adequate Precision” measures the signal to noise ratio. A ratio greater than four is desirable. Ratio of 22.933 indicates an adequate signal. This model can be used to navigate the design space.

Factor	Standard estimated	95% CI error
Intercept	−126.399	485.8706
A-Printing speed	4.465786	2.624723
B-Nozzle temp	0.668476	2.052435
C-Layer size	21.62381	223.0904
A2	0.006917	0.003608
AB	−0.01981	0.008248
AC	0.37619	0.412393
BC	−0.1	0.944911

Final Equation in Terms of Actual Factors:

$$\begin{aligned}
 \text{Roughness} = & -178.86190 + 3.72536 * \text{Printing Speed} + 0.90810 * \text{Nozzle Temp} \\
 & + 21.07143 * \text{Layer Size} + 6.91667E - 003 * \text{Printing Speed}^2 \\
 & - 0.019810 * \text{Printing Speed} * \text{Nozzle Temp} + 0.37619 * \text{Printing Speed} * \text{Layer Size} \\
 & - 0.100000 * \text{Nozzle Temp} * \text{Layer Size}.
 \end{aligned}$$

Actual value	Predicted value	Residual	Leverage
7.5	7.56	-0.06	0.976
11.7	11.94	-0.24	0.619
9.5	9.5	0	1
15.9	15.9	0	1
10.8	10.68	0.12	0.905
9.9	10.02	-0.12	0.905
7.9	7.9	0	1
11.4	11.34	0.06	0.976
10.9	10.66	0.24	0.619

22.5.2 Study of Model Equation

This surface plot was generated in MATLAB at the constant layer size of 0.1 mm from the obtained model above (Fig. 22.5).

Fig. 22.5 Surface plot at layer size 0.1 mm

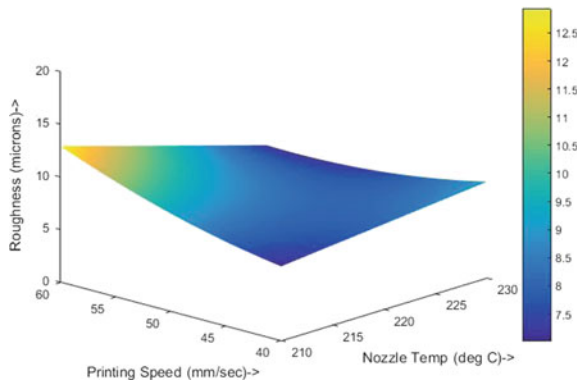
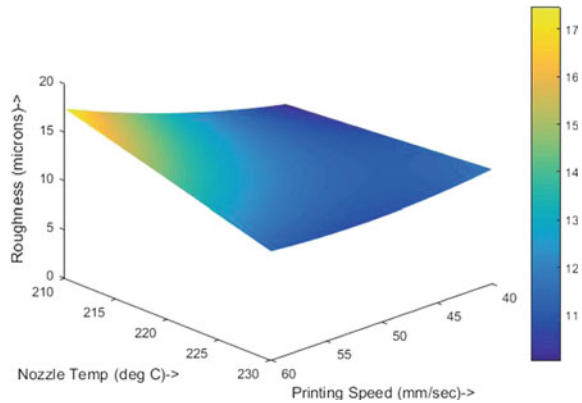


Fig. 22.6 Surface plot at layer size 0.2 mm



With this plot it can be seen that lower average surface roughness can be obtained by printing at lower speed and higher nozzle temperature. As the curve goes quite steep while going toward the higher printing speed which shows printing speed affects more than the nozzle temperature if both are varied together. While increasing printing speed from 40 to 60 mm/s, there is a change of around 5μ at constant nozzle temperature of $210 \text{ }^\circ\text{C}$, and negligible change is there when nozzle temperature is increased to $230 \text{ }^\circ\text{C}$. So effect of printing speed is much more when temperature is lower, i.e., $210 \text{ }^\circ\text{C}$ (Fig. 22.6).

This surface plot is obtained at constant layer size of 0.2 mm, and it shows that at constant nozzle temperature of $210 \text{ }^\circ\text{C}$ while increasing the print speed from 40 to 60 mm/s there is an increase of around 7μ while at constant printing speed of 40 mm/s there is not much effect of changing nozzle temperature. We checked it at 60 mm/s speed, there is a change of $2\text{--}3 \mu$ that can be interpreted as at higher print speed change of nozzle temperature can be noticed while at lower print speed its indistinguishable.

Now with change of layer size to 0.3 mm, it can be seen that the average surface roughness has increased a lot when compared from 0.2 and 0.1 mm. At a constant nozzle temperature of $210 \text{ }^\circ\text{C}$, change of more than 10μ average surface roughness can be seen while increasing the print speed. Here, it shows that at higher layer size, the impact of factors such as nozzle temperature and print speed increases significantly. At 60 mm/s speed and $210 \text{ }^\circ\text{C}$ the highest surface roughness can be observed, while these effects can easily be noticed from the 2D surface plot made in MATLAB by plotting the equation obtained from Minitab (Fig. 22.7).

Here, all the three surface plots at different surface layers are obtained on the same plot to compare the effects at different layer sizes. It can be seen that at increasing layer size the slope of the curve gets increasing while increasing the print speed as well the nozzle temperature. Highest roughness can be seen at the 0.3 mm layer, 60 mm/s print speed and $210 \text{ }^\circ\text{C}$ nozzle temperature as predicted from the pilot experiments. The highest effect is of the layer size while print speed have the effect when printing at nozzle temperature of $210\text{--}215 \text{ }^\circ\text{C}$ while doesn't have

Fig. 22.7 Surface plot at layer size 0.3 mm

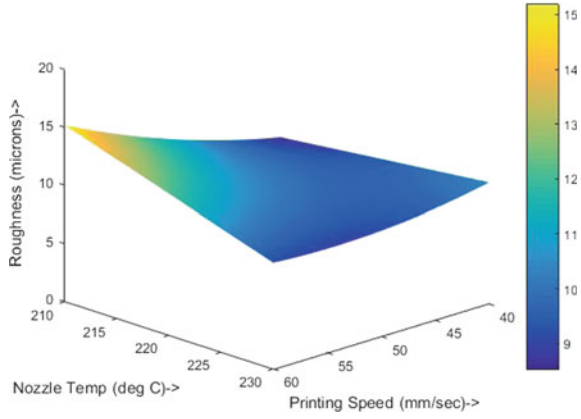
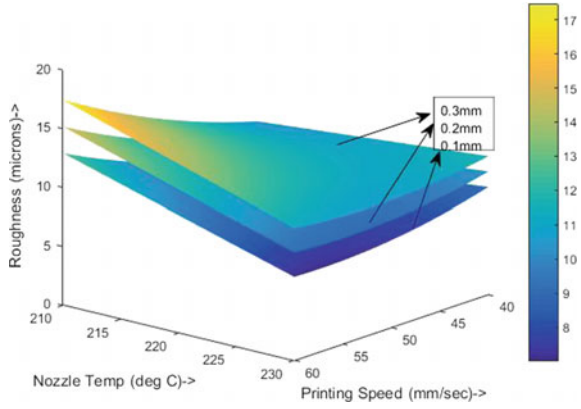


Fig. 22.8 Combined surface plot at all three layer sizes



much significant effect on the average surface roughness and nozzle temperature have significant effect at higher layer size but at lower layer size its effect seems to get reduced from checking at the response surfaces at constant layer sizes (Fig. 22.8).

22.5.3 Effect of Single Variable

Following observation has been made:

- Average surface roughness increases while increasing the printing speed (nonlinearly).
- Average surface roughness decreases while increasing the nozzle temperature (nonlinearly).

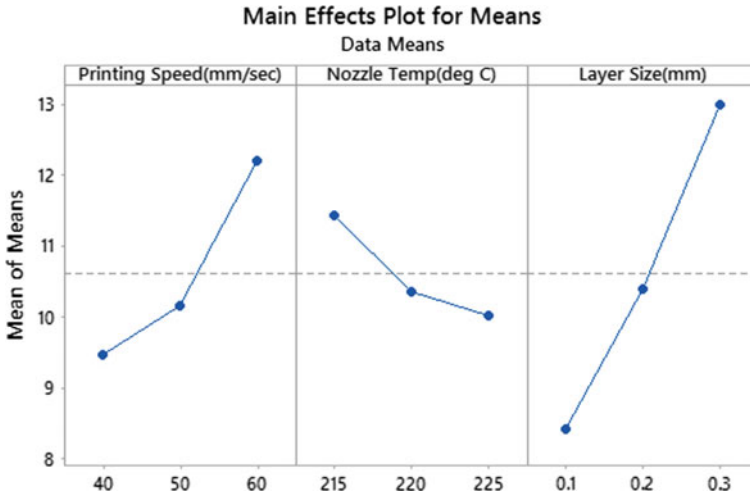


Fig. 22.9 Single main effects plot

- Average surface roughness increases while increasing the layer size (linearly) (Fig. 22.9).

These results are comparable to the results obtained in the pilot experiments performed before which proves it to be correct. Also these results are comparable to the results obtained in previous researches [11, 12].

22.5.4 Validation of Predicted Results

Three different samples are printed at data which is not in the DOE table

Sample	Layer size (mm)	Nozzle temp (°C)	Print speed (mm/s)	Actual roughness (μ)	Predicted roughness (μ)	Residual	Error (%)
1	0.25	217	45	9.7	10.4737	0.7737	7.976
2	0.17	222	55	10.8	9.994	0.8060	7.462
3	0.15	213	48	9.1	9.4535	0.3535	3.884

Obtained model is predicting the average surface roughness with the acceptable error range of less than 10%.

22.6 Conclusions

Impact of printing parameters such as printing speed, nozzle temperature and layer size is studied, and DOE-L9 is used for analysis of variance and to obtain a model have been between the printing parameters. Obtained model is predicting the average surface roughness parameter with the acceptable error while the percentage contribution, if we consider only three parameters, is highest for layer size, i.e., 68.6%, while for print speed and nozzle temperature is 24.8 and 6.6%.

Now, using response surface methodology, layer size found to be effects the most to the average surface roughness among the all three printing parameters that were studied. As the layer size increases, it linearly tends to increase the average surface roughness.

Printing speed effects are higher when layer size tends to increase. Otherwise its effect is not much significant. While increasing the printing speed, roughness parameter tends to increase and nozzle temperature have significant effect on roughness when printing in range of 180 to 215 °C else after that it tends to get stable and does not have significant effect on roughness parameter. Though at higher layer size (0.3 mm) its effect is quite visible.

References

1. Vaezi, M., Chua, C.K: Effects of layer thickness and binder saturation level parameters on 3D printing process. *Int. J. Adv. Manuf. Technol.* **53**, 275–284 (2011). <https://doi.org/10.1007/s00170-010-2821-1>
2. Jaya Christiyana, K.G., Chandrasekhar, U., Venkateswarlu, K.: A study on the influence of process parameters on the Mechanical Properties of 3D printed ABS composite. *IOP Conf. Ser. Mater. Sci. Eng.* **114**, 012109 (2016)
3. Shofner, M.L., Lozano, K., Rodriguez-Macias, F.J., Barrera, E.V.: Nanofiber-reinforced polymers prepared by fused deposition modeling. *J. Appl. Polym. Sci.* **89**(11), 3081–3090 (2003)
4. Shofner, M.L., Rodriguez-Macias, F.J., Vaidyanathan, R., Barrera, E.V.: Single wall nanotube and vapor grown carbon fiber reinforced polymers processed by extrusion freeform fabrication. *Composites* **34**(12), 1207–1217 (2003)
5. Shah, V.: *Handbook of Plastic Testing Technology*, Second edn. New York (1998)
6. Es Said, O.S., Foyos, J., Noorani, R., Mandelson, M., Marloth, R., Pregger, B.A.: Effect of layer orientation on mechanical properties of rapid prototyped samples. *Mater. Manuf. Process* **15**(1), 107–122 (2000)
7. Alafaghania, A., Qattawia, A., Alrawia, B., Guzman, A.: Experimental Optimization of Fused Deposition Modelling Processing Parameters: A Design-for-Manufacturing Approach, pp. 791–803 (2017)
8. Sukindar, N.A. et al.: Optimization of the parameters for surface quality of the open-source 3D printing. *J. Mech. Eng.* **3**(1), 33–43 (2017)
9. Chaidas, D., Kitsakis, K. et al.: The impact of temperature changing on surface roughness of FFF process. *IOP Conf. Ser. Mater. Sci. Eng.* **161**, 012033 (2016)
10. Mendonsa, C., Naveen, K.V., Upadhyaya, P., Shenoy, V.D.: Influence of FDM process parameters on build time using Taguchi and ANOVA approach. *Int. J. Sci. Res.* **4**(2), 2013–2016 (2015)

11. Akande, S.O.: Dimensional Accuracy and Surface Finish Optimization of Fused Deposition Modelling Parts using Desirability Function Analysis, vol. 4(4), pp. 196–202 (2015)
12. Kaji, F., Barari, A.: Evaluation of the surface roughness of additive manufacturing parts based on the modelling of cusp geometry. *IFAC-PapersOnLine* **48**(3), 658–663 (2015)

Chapter 23

Modeling of Linear Shrinkage in PLA Parts Fabricated by 3D Printing Using TOPSIS Method



Jonty Mago , Rajat Kumar , Raj Agrawal , Anoop Singh 
and Vineet Srivastava 

Abstract 3D printing is one of the most preferred rapid prototyping (RP) methods used for prototyping. However, for the functional use product, the part must be highly accurate and have good strength. The biggest constraint in the functional use of RP parts is the dimensional inaccuracies. These dimensional defects mostly happen due to the irregular surface profile and shrinkage of the part. The part fabrication process in RP is governed by many process parameters. In this study, selection of the process parameters which affect the shrinkage of PLA parts is determined by using TOPSIS. Part length (PL), layer thickness (LT) and printing speed (PS) were selected by applying TOPSIS method. Response surface methodology (RSM) has been used for the design of the experiment. ANOVA has been used to identify the significant parameters followed by regression to correlate the response with process parameters. A statistical model is developed for the shrinkage in PLA parts. It has been observed that shrinkage tends to increase with increment in PL and reduces with increment in LT and PS.

Keywords 3D printing · Shrinkage · PLA · TOPSIS · RSM

23.1 Introduction

The requirements of the current market are for higher quality and greater efficiency products with reduction in cost, faster product development and reduced time to market. Rapid prototyping (RP) has emerged as a key enabling technology with its ability to shorten product design and development time [1]. The RP process chain consists of construction of geometric model, tessellation and determination of suitable deposition orientation, slicing, generation of material deposition paths, part deposition and post processing operations. A major problem faced in RP is the dimensional inaccuracy of the parts. This lack of accuracy is primarily due to

J. Mago · R. Kumar · R. Agrawal · A. Singh · V. Srivastava (✉)
Mechanical Engineering Department, Thapar Institute of Engineering & Technology, Patiala,
Punjab 147004, India
e-mail: vineet.srivastava@thapar.edu

© Springer Nature Singapore Pte Ltd. 2020
M. S. Shunmugam and M. Kanthababu (eds.), *Advances in Additive Manufacturing and Joining*, Lecture Notes on Multidisciplinary Industrial Engineering,
https://doi.org/10.1007/978-981-32-9433-2_23

deteriorated surface quality and shrinkage of fabricated parts. The parts fabricated by RP process display shrinkage because they undergo phase transformation. The first transformation occurs when the temperature of the material decreases from solid to glass transition temperature and then when it changes to solid state [2]. This leads to the decline in the magnitude of the part as compared to the CAD model.

There are several attempts made to develop a model for dimensional accuracy of RP parts fabricated by different processes. Wang et al. [3] used neural network model to study the effect of layer thickness, laser power, hatch spacing, scanning speed, scanning mode, interval time and temperature of working environment on shrinkage of parts made by SLS process. It was found that shrinkage has a direct relationship with scanning speed and hatch spacing albeit in a definite range and an inverse relationship with layer thickness, laser power, interval time and temperature of working environment. Schmutzler et al. [4] studied the various defects produced in parts fabricated by 3D printing like curling, shrinkage, shape deformation, etc. They developed a mathematical model in order to compensate these defects based on the data collected. Finally, they proposed to change the shape and size of the part while slicing to reduce post-fabrication defects. Raghunath and Pandey [5] developed an empirical model to predict shrinkage along X , Y and Z directions for SLS process by using Taguchi method. The results generated from the model were found in good conformity with experiments. They also presented a case study of bench marking part to show that the parts developed by the model were more accurate. Boschetto and Bottini [6] developed a geometric model to predict the dimensional deviations of ABS parts fabricated by FDM process. It was observed that the dimensional deviations increased almost symmetrically as the deposition angle varied from 90° on both sides. A case study was also performed to validate the developed model. Literature review presented above shows that most of the previous work is concentrated toward FDM, SLS and SL processes. Therefore, in this study, selection of the process parameters which affect the shrinkage of PLA parts is determined by using TOPSIS. As solidified PLA has high strength, is strong and durable, biodegradable, safe for human exposure and less likely to warp, therefore, it has been selected as the work material in this study. Part length (PL), layer thickness (LT) and printing speed (PS) were selected by applying TOPSIS method. Response surface methodology (RSM) has been used for the design of the experiment. ANOVA has been used to identify the significant parameters followed by regression to correlate the response with process parameters. A statistical model is developed for the shrinkage in PLA parts. It has been observed that shrinkage increases with increment in PL and reduces with increment in LT and PS. The details of the research work performed have been given below.

23.2 Experimentation

23.2.1 Selection of Process Parameters for Experimentation by TOPSIS

Technique for order preference by similarity to ideal solution (TOPSIS) is a very famous method when the problem is related to multi-criteria decision. It includes a simple mathematical model which uses a multifaceted approach. Our criterion parametric values are given in Table 23.1.

It is required to create a decision matrix as given in Table 23.2. Then a weighted decision matrix (V) is created using Eq. (23.1).

$$V = V_{ij} = W_j \times R_{ij} \tag{23.1}$$

Table 23.1 Criterion parametric values

Attributes		Alternatives			
Input parameters	Output parameters	Strength (MPa)	Dimensional accuracy	Surface finish (Ra)	Build time (min)
Layer thickness (μm)		100	100	100	300
Part length (mm)		Moderate	Minimum	Moderate	Minimum
Infill pattern		Rectilinear	Wiggle	Concentric	Rectilinear
Infill percentage		Maximum or moderate	Moderate	Moderate	Minimum
Bed temperature ($^{\circ}\text{C}$)		50	50	52	50
Printing speed (mm/min)		Low	High	Low	High

Table 23.2 Components associated to decision matrix

Alternatives	Criteria's						
		Layer thickness	Part length	Infill pattern	Infill percentage	Bed temperature	Printing speed
Strength		3	5	8	8	5	6
Dimensional accuracy		5	6	8	8	7	5
Surface finish		3	4	3	5	5	3
Build time		8	2	5	6	2	10
Weights		0.25	0.25	0.08	0.08	0.14	0.20

Identify negative (related to cost criterion) and positive (related to advantage criterion) ideal solutions. Both the negative ideal (A^-) and the positive ideal (A^+) solutions are specified following the weighted decision matrix.

$$A^+ = \{0.3025, 0.2225, 0.0648, 0.00576, 0.028, 0.2\}$$

$$A^- = \{0.075, 0.575, 0.0192, 0.0312, 0.133, 0.048\}$$

Then compute separation from the positive ideal solution. Now repeat the above step for the negative ideal solution. After adding all the criteria values for an alternative we get,

$$S^+ = \{0.2974, 0.2652, 0.338, 0.167923\}$$

$$S^- = \{0.13826, 0.18982, 0.083995, 0.228164\}$$

Following that, compute the comparative closeness to the ideal solution with the help of Eq. (23.2):

$$C^* = \frac{S_i^-}{S_i^+ + S_i^-} \quad (23.2)$$

After evaluation, we obtain the competitive alternative with the relative closeness. The values for strength is 0.32, dimensional accuracy is 0.42, surface finish is 0.24 and build time is 0.57. From the relative closeness, we find that best alternative for the parameter selection is built time, but it does not guarantee the good responses. So, we have selected parameters according to the second best alternative that is dimensional accuracy. Layer thickness, part length and printing speed are selected as the variables for the study.

23.2.2 Design of Experiments

As it is evident that the variables that affect the shrinkage are quite large, it has been assumed that the response will be a minimum second-degree polynomial. This has been done because it is quite accurate for a relatively smaller domain [7]. To develop a relationship between input variables namely layer thickness, part length and printing speed and shrinkage along length, width and height of the specimen, it is essential to decide a set of variables. Further, these parameters can be controlled by the machine used for fabrication of specimens. The range of process parameters has been defined as per the specification of machine (FLASHFORGE CREATERPRO) given in the machine manual. The range of layer thickness is selected from 100 to 300 μm with a step of 50 μm , part length varies from 10 to 50 mm with a step of 10 mm and printing speed varies from 2500 to 3000 mm/min with a step of 125 mm/min. Filament of PLA with a diameter of 1.75 mm has been used in this study. The infill percentage was set at 80%, wiggly is the infill and external fill pattern; the extruder temperature and bed temperature have been set at 230 and 50 $^{\circ}\text{C}$. Digital vernier caliper by MitutoyoTM has been used to measure the linear measurement of the model. Linear shrinkage is measured by subtracting the measured prototype dimension from the original

Table 23.3 Measured responses corresponding to each trial

S. No.	LT	PL	PS	Change in length (ΔL) (mm)	Change in width (ΔW) (mm)	Change in thickness (ΔT) (mm)
1	200	30	2750	0.110	0.050	0.05
2	200	30	2750	0.090	0.040	0.09
3	150	20	2875	0.045	0.030	0.08
4	250	20	2625	0.105	0.040	0.03
5	250	40	2625	0.122	0.050	0.05
6	200	50	2750	0.122	0.050	0.08
7	100	30	2750	0.118	0.060	0.18
8	200	30	3000	0.070	0.020	0.05
9	200	30	2750	0.080	0.045	0.05
10	200	30	2750	0.102	0.040	0.04
11	200	30	2750	0.100	0.040	0.08
12	250	20	2875	0.020	0.040	0.02
13	150	20	2625	0.163	0.030	0.14
14	150	40	2625	0.125	0.090	0.11
15	150	40	2875	0.100	0.040	0.08
16	200	10	2750	0.020	0.020	0.06
17	200	30	2500	0.201	0.060	0.11
18	300	30	2750	0.090	0.020	0.02
19	200	30	2750	0.085	0.040	0.06
20	250	40	2875	0.130	0.010	0.06

dimension. The outcome is given as Eq. 23.3. The measured response corresponding each trial is given in Table 23.3.

$$\Delta L \text{ or } \Delta W \text{ or } \Delta H = \text{Dimension of CAD model} - \text{Measured Dimension} \quad (23.3)$$

23.3 Results and Discussion

23.3.1 Statistical Modeling of Shrinkage Along the Length

A statistical model for the change in length was developed, based on analysis of the data presented in Table 23.3 and is given below as Eq. (23.4).

$$\begin{aligned} \Delta L = & 7.81 - (0.00459 \times LT) - (0.05064 \times PL) - (0.004492 \times PS) \\ & - (0.0000648 \times PL^2) + (0.000001 \times PS^2) + (0.000028 \times LT \times PL) \\ & + (0.000001 \times LT \times PS) + (0.000019 \times PL \times PS) \end{aligned} \quad (23.4)$$

Based on the model developed, it is necessary to analyze the significance of the regression model, entity model coefficients and lack of fit. An ANOVA table is frequently used for the tests. This analysis was carried out for a level of confidence of 99%. The value of correlation is 88.7% which is desirable. The calculated value of *F* is greater than the tabular value of *F*, and hence the second order response function developed is quiet adequate. The value of *p* for lack of fit is more than 0.05 which indicates that the lack of fit is insignificant.

It was observed from Fig. 23.1a that print speed and part length are the most influential parameters affecting shrinkage along the length having a contribution of 43 and 23%. Figure 23.1b shows the main effects plots for shrinkage along the length. The shrinkage decreases with increase in layer thickness. Further, the shrinkage increases with increase in part length. Shrinkage showed a decrease with print speed. Printing Speed has come out to be the main factor that is governing the shrinkage along the length. At slow printing speed, the nozzle at particular location deposits more material but simultaneously the layer deposition rate is less which means the material at one extreme location get solidifies when the nozzle is depositing material at other extreme location. If part has larger length and high printing speed then the concept of thermal contraction and expansion come into play. When the heat is supplied to the workpiece and direction of heat flow governed is along length that will be the direction in which elongation will take place. PLA is plastic material, during solidification process, molecular reordering takes place. PLA has a high coefficient of thermal expansion which makes the material more brittle. This produces higher shrinkage which is also evident from the SEM images shown in Fig. 23.2.

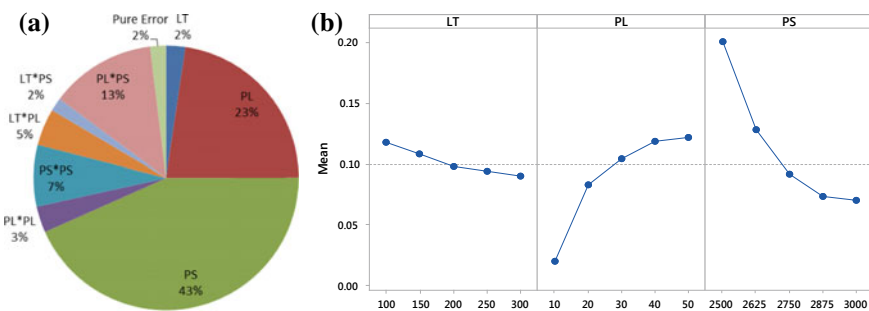


Fig. 23.1 Percentage contribution of the factors and main effects for Shrinkage along length

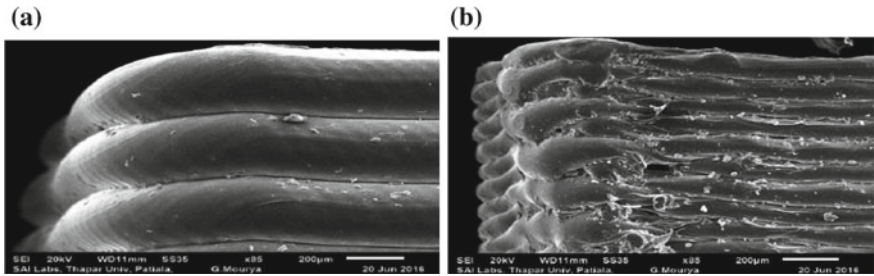


Fig. 23.2 SEM images at a 300 μm layer thickness b 100 μm layer thickness [8]

23.3.2 Statistical Modeling of Shrinkage Along the Width

A statistical model for the change in width was developed, based on analysis of the data presented in Table 23.3 and is given below as Eq. (23.5).

$$\Delta W = -0.6038 + (0.000513 \times LT) + (0.03086 \times PL) + (0.000185 \times PS) - (0.000015 \times PL^2) + (0.0000238 \times LT \times PL) - (0.000009 \times PL \times PS) \tag{23.5}$$

An ANOVA table is frequently used for the testing the significance of the regression model, entity model coefficients and lack-of-fit. This analysis was carried out for a level of confidence of 99%. The value of correlation is 90.5% which is desirable. The calculated value of F is greater than the tabular value of F and hence the second order response function developed is quiet adequate. The value of p for lack of fit is more than 0.05 which indicates that the lack of fit is insignificant.

It can be observed from Fig. 23.3a that the print speed has the highest significance in shrinkage with contribution of 32% which is followed by layer thickness with a contribution of 18% and part length with 13%. Figure 23.3b shows the main effects plots for shrinkage along the width. The five points shown in the plot are obtained

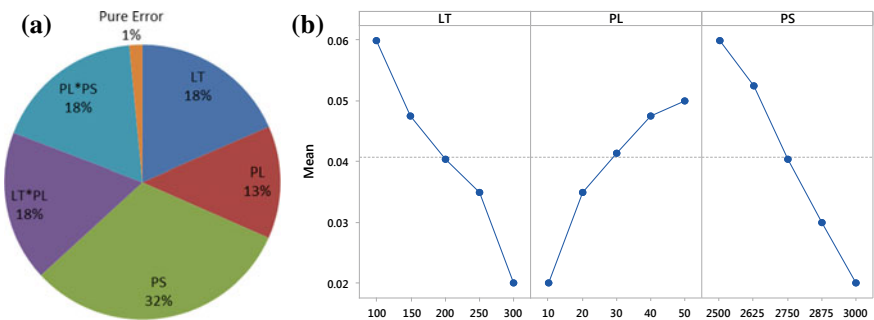


Fig. 23.3 Percentage contribution of the factors and main effects for Shrinkage along width

from the experimental data. Shrinkage decreases with increase in layer thickness and printing speed. Shrinkage increases with increase in part length. On analyzing the layer thickness, it was observed that there was filleting effect which tended to reduce the shrinkage. Further as the layer thickness increases, the stress accumulation also increases. At low layer thickness, increasing the nozzle diameter reduces the accumulation of the stress, thereby reducing shrinkage. The increase in shrinkage with increase in part length can be attributed to development of more internal stresses with increase in length, resulting from the contraction of depositing fibers. It has been reported that the deposited thermoplastic fiber is subjected to contraction when cooled from extrusion temperature to glass transition temperature [2]. At low printing speed, more material is deposited by the nozzle which allows the build material to settle down easily thereby increasing shrinkage. At high printing speed, there is lesser time for resolidification resulting in lesser shrinkage.

23.3.3 Statistical Modeling of Shrinkage Along the Height

A statistical model for the change in height was developed, based on analysis of the data presented in Table 23.3 and is given below as Eq. (23.6).

$$\begin{aligned} \Delta H = & 1.737 - (0.00762 \times LT) - (0.00468 \times PL) - (0.000465 \times PS) \\ & + (0.00003 \times LT^2) + (0.000023 \times LT \times PL) + (0.000002 \times LT \times PS) \end{aligned} \quad (23.6)$$

An ANOVA table is frequently used for the testing the significance of the regression model, entity model coefficients and lack-of-fit. This analysis was carried out for a level of confidence of 99%. The value of correlation is 70.1% which is desirable. The calculated value of F is greater than the tabular value of F and hence the second order response function developed is quiet adequate. The value of p for lack of fit is more than 0.05 which indicates that the lack of fit is insignificant.

It can be observed from Fig. 23.4a that the layer thickness has the principal considerable influence on shrinkage with contribution of 76% which is followed by print speed with contribution of 10%. Figure 23.4b shows the main effects plots for shrinkage along the length. The five points shown in the plot are obtained from the experimental data. Shrinkage decreases with increase in layer thickness. Further, shrinkage increases with increase in part length. Shrinkage showed a decrease with print speed.

Shrinkage decreases with increase of layer thickness. With increase in layer thickness, the component requires fewer layers thereby reducing the heating and the cooling cycles working alternatively during deposition. Further, the nozzle speed becomes non-uniform as it approaches the edges of the component, this result in requirement of more time for deposition of single layer. This phenomenon keeps the already deposited materials above the desired temperature and does not allow it to

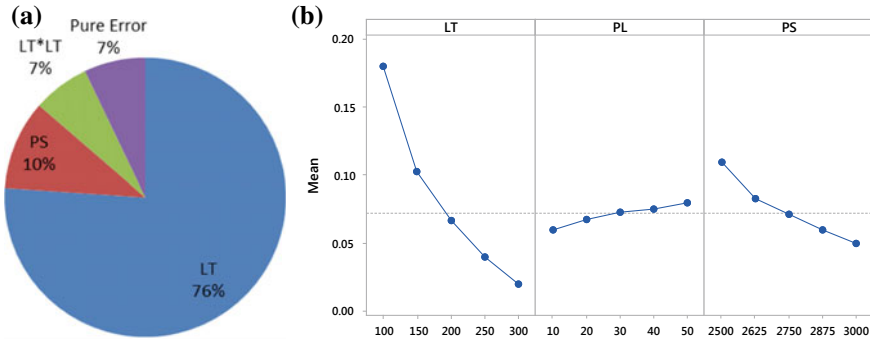


Fig. 23.4 Percentage contribution of the factors and main effects for Shrinkage along height

regain its original shape. In the meantime, another layer will be deposited which will not allow the contraction of previous layer. This complete process highlights that the increase in layer thickness decreases the shrinkage along the height.

23.4 Conclusions

In the present work, the PLA part was successfully manufactured by using FDM-based 3D printer. Selection of the process parameters which affect the shrinkage of PLA parts is determined by using TOPSIS, and part length, layer thickness and printing speed were selected. Statistical models have been developed for predicting shrinkage along the length, width and height for *x* direction laying. The results show that second-order models developed for shrinkage along the length, width and height of a component in *x* direction laying of work piece is statistically significant. It has been observed that shrinkage along the length, print speed and part length significantly affects the shrinkage. It can be seen that shrinkage decreases with increase in layer thickness and print speed. It is also observed that shrinkage increases with increase in part length. Further, shrinkage along the width, printing speed, layer thickness and part length are significant parameters. It can be seen that shrinkage decreases with increase in layer thickness and printing speed. It is also observed that shrinkage increases with increase in part length. Shrinkage along the height, layer thickness and printing speed are the most significant parameters. It can be seen that shrinkage decreases with increase in layer thickness and print speed. It is also observed that shrinkage increases with increase in part length.

References

1. Pandey, P.M.: Rapid Prototyping Technologies, Applications and Part Deposition Planning (2010)
2. Singh, S.K.: Effect of Process Parameters on Dimensional Inaccuracy of Solidified Polylactic Acid Parts Fabricated by 3-Dimensional Printing Process. *M.E. Thesis*, Thapar Institute of Engineering and Technology, Patiala, Punjab, India (2017)
3. Wang, R.J., Wang, L., Zhao, L., Liu, Z.: Influence of process parameters on part shrinkage in SLS. *Int. J. Adv. Manufact. Technol.* **33**, 498–504 (2007). <https://doi.org/10.1007/s00170-006-0490-x>
4. Schmutzler, C., Zimmermann, A., Zaeh, M.F.: Compensating warpage of 3D printed parts using free-form deformation. *Procedia CIRP* **41**, 1017–1022 (2016). <https://doi.org/10.1016/j.procir.2015.12.078>
5. Raghunath, N., Pandey, P.M.: Improving accuracy through shrinkage modelling by using Taguchi method in selective laser sintering. *Int. J. Mach. Tool Manufact.* **47**(6), 985–995 (2007)
6. Boschetto, A., Bottini, L.: Accuracy prediction in fused deposition modeling. *Int. J. Adv. Manufact. Technol.* **73**, 913–928 (2014). <https://doi.org/10.1007/s00170-014-5886-4>
7. Montgomery, D.C.: *Design and Analysis of Experiments*. Wiley (2010)
8. Saini, S.: *Statistical Modeling and Optimization of Dimensional Accuracy for Solidified Polylactic Acid Parts Fabricated by Fused Filament Modeling Process*. M.E. thesis, Thapar Institute of Engineering and Technology, Patiala, Punjab, India (2016)

Chapter 24

Investigation on Quality of In-house Fabricated PLA Filament for 3D Printing Application



Ashish R. Prajapati , Harshit K. Dave  and Shilpesh R. Rajpurohit 

Abstract Fused deposition modelling (FDM) is an additive manufacturing process in which successive layers of material are deposited to create a three-dimensional object. It is the most widely used additive manufacturing technology because of its ability to make specimens having a difficult geometrical shape in the reasonable time period and without any tooling requirement. In the present research work, the entire filament production chain is evaluated, starting with the polymer granules, filament production by an extrusion process and test samples printing. Polylactic acid (PLA) is easier to print than acrylonitrile butadiene styrene (ABS) and it is also a biodegradable material, therefore in present research work, PLA granules are used to fabricate the FDM feedstock filament. Various filament properties like melt flow index (MFI), thermal gravimetric analysis (TGA) and tensile strength have been investigated. After testing this filament, it is used in FDM to make tensile specimens. Specimens have been printed at different raster angles from both the PLA filaments (commercially available as well as in-house fabricated) and tensile properties have been compared. It is observed that mechanical and physical properties of in-house fabricated PLA filaments are in close agreement with those of the commercially available PLA filament and parts printed from in-house fabricated filament obtained higher tensile strength as compared to the commercially available filament.

Keywords Fused deposition modelling · Single-screw extruder · Polylactic acid (PLA) · In-house fabricated filament · Tensile strength

24.1 Introduction

Fused deposition modelling is the most commonly used additive manufacturing method. Many specimens of polymer material like PE (Polyethylene), PLA and ABS can be manufactured by this method. Even though FDM is generally used effective

A. R. Prajapati · H. K. Dave · S. R. Rajpurohit (✉)
Department of Mechanical Engineering, Sardar Vallabhbhai National Institute of Technology,
Surat 395007, Gujarat, India
e-mail: shilpesh18@gmail.com

© Springer Nature Singapore Pte Ltd. 2020
M. S. Shunmugam and M. Kanthababu (eds.), *Advances in Additive Manufacturing and Joining*, Lecture Notes on Multidisciplinary Industrial Engineering,
https://doi.org/10.1007/978-981-32-9433-2_24

277

process, it still has restricted applications due to its compatibility with recommended materials. This restriction can be vanquished by developing a new material that is compatible with the technology and has characteristics superior to the commercial qualities of a polymer material that is used in FDM [1].

One of the major concerns for the development of FDM filament is cost. Generally, the single-screw extruder is used to make the feedstock filament for FDM [2]. Nowadays, ABS and PLA are mainly used polymer in FDM. However, the problem associated with printing ABS using open-source 3D printer is that its high melting point makes it harder to liquefy and leads to warpage, while PLA is easier to print [3].

Singh et al. [2] developed ABS polymer filament using single-screw extruder. They have found that MFI of ABS-EG was in the similar range of the MFI of ABS P400 range. Carneiro et al. [4] fabricated filament of PP (Polypropylene) using single-screw extruder. By printing at different raster angles (0° , 45° and 90°) in FDM they have found that 0° angle gave the highest tensile strength as compared to other angles. Nikzad et al. [5] have investigated thermal and mechanical properties of ABS composites filled with metal particles for applications in FDM. Tensile strength dropped considerably as an effect of the addition of 10% volume per cent of iron. Perez et al. [6] fabricated ABS filament reinforced with TiO_2 and studied its mechanical properties. They have observed that the tensile strength of the composite was higher than pure ABS. Kalita et al. [7] developed biocompatible polymer-ceramic composites by homogeneous mixing of TCP (Tricalcium phosphate) in PP using single-screw extruder, and they observed that the stiffness of the composite increases with the presence of ceramic with no significant effect towards the tensile properties. Zhu et al. [8] made different blends of the polymer by mixing ABS and SAN (Styrene acrylonitrile) at various composition. Their results indicated that the flow properties and tensile strength of ABS could be improved by the addition of SAN, which helps its uses in FDM. Garg et al. [9] investigated the effect of raster angle on the mechanical properties. It was observed that 0° raster angle gave the highest tensile strength while at 90° raster angle tensile strength was lowest. Wu et al. [10] have studied the influence of raster angle on the mechanical properties of FDM printed parts, and they have observed that $0^\circ/90^\circ$ raster angle gave the highest mechanical strengths.

It was observed that number of research was carried out to develop an alternative FDM filament using different types of materials. However, the study of the critical requirements of the current FDM system, starting from fabricating the filament to the printing of parts in FDM using that filament is very less. In this work, attempts have been made to develop a new feedstock filament of FDM using granules of virgin PLA.

24.2 Experimentation

24.2.1 Material Selection

PLA (Ingeo™ 3D850) granules were used in present research work to fabricate the wire filament. PLA is one of the most used polymers in FDM due to its easier printability in FDM. Several applications of PLA are in the pharmaceutical, food, chemical and textile industries. It is an organic acid that can be obtained by various methods of chemical synthesis. The properties of the PLA material are good compared to many other bio-based materials.

24.2.2 Filament Fabrication

Single-screw extruder is used to fabricate the wire filaments from pallets of the polymer. The screw transports the material forward, which contributes to the heating and melting, mixes the melt and releases the melt to the die. The heaters and barrel help to heat and melt the polymer by controlling the temperature in several zones, thus preventing overheating and degradation of the material. The screw, in combination with the barrel delivers the polymer to the die. The various specifications of the single-screw extruder used in present research work are shown in Table 24.1.

The process parameters of the single-screw extruder which affects the wire dimensions such as diameter and ovality are barrel temperature, die temperature, screw speed and take-up speed. The proper temperature range of these parameters which fabricate the filament was found out from trial and error method and previous experience. Prior to extrusion, PLA granules were preheated in the oven at 80 °C for 4 h to remove moisture content. The working range of temperature at which filament has been drawn successfully is shown in Table 24.2.

Table 24.1 Specifications of the single-screw extruder

Screw diameter (mm)	L/D ratio	Number of heaters installed		Screw speed (rpm)	Take-up speed (rpm)
		Barrel	Die		
50	36:1	3	2	0–29	0–100

Table 24.2 Optimum parameters for fabrication of PLA filament

Barrel temperature (°C)			Die temperature (°C)	
Zone 1 (feed)	Zone 2 (transition)	Zone 3 (metering)	Zone 1	Zone 2
205	210	215	185	180

Die zone temperatures are 20–30 °C lower than barrel temperatures. The main function of die zone is to minimize the circular motion of material and to give proper round shape to the filament. It has been observed that if the temperature range is similar to barrel zone than material started to liquefy. Therefore, after some trial and error, the temperature range of die zone was set. Figure 24.1a shows the melting of the PLA when both die zone temperatures were 210 °C, and Fig. 24.1b shows the proper round shape filament extrudate from the die at a lower temperature. Figure 24.2 shows the in-house fabricated and commercially available PLA filament.

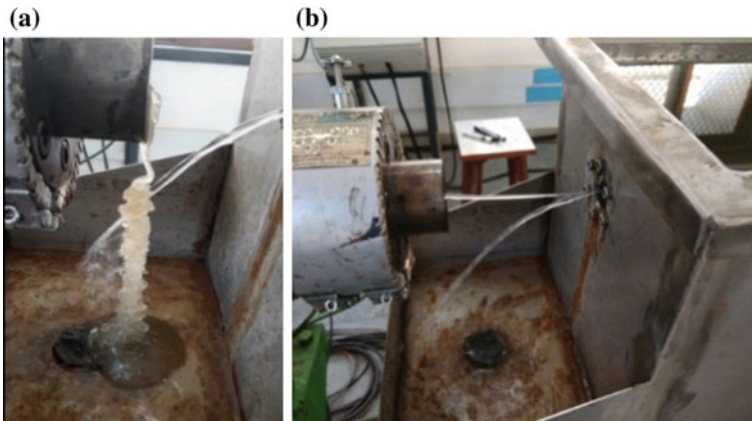
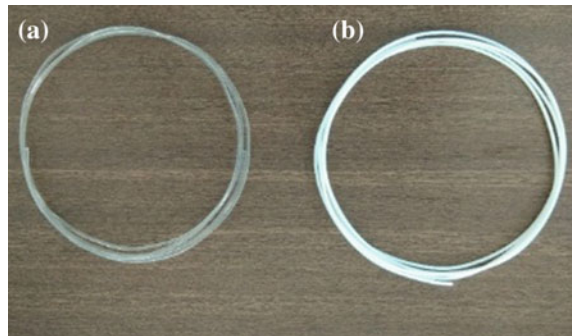


Fig. 24.1 Extrudate material from the die at **a** Initial stage of the process and **b** After setting proper temperature range

Fig. 24.2 **a** In-house fabricated and **b** Commercially available PLA filament



24.2.3 Filament Testing

The wire filament fabricated from the extruder is further tested for its physical and mechanical properties. MFI and TGA and tensile testing have been done on both PLA filaments. The material will be tested according to ASTM-D-1238 standard on MFI tester (Model: AE-MFI-B-FC and Make: Advance Equipments, Thane). As the viscosity of the resin decreases, the flow increases per unit of time. Lower melt flow rate or a fewer gram passing through the die in 10 min refers to the higher viscosity. TGA analysis was carried out to check the thermal stability of the fabricated filament. This analysis was done using a TA Module Q 600. TGA involves heating a sample at a constant rate, while simultaneously measuring the mass of the sample throughout the entirety of the test. The tensile testing was performed by a Tinius Olsen H50KL universal testing machine. Three specimens for each fabricated and readymade filament were tested according to ASTM-D-638 standard. The tests were conducted under controlled displacement at a constant crosshead speed of 5 mm/min. The machine has a load cell of 50 kN and built-in the horizon and the software allows to control, monitor and record measurement data.

24.2.4 3D Printing and Testing

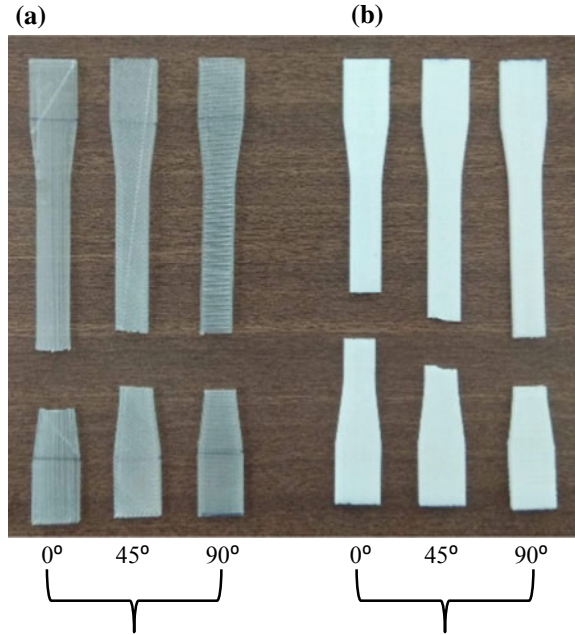
After testing thermal and mechanical properties of both the PLA filaments (in-house fabricated as well as commercially available), they were used to make the tensile specimen on FDM printer. Open-source FDM machine 3D Jet is used in this research work to print the specimens. Tensile specimens have been made according to standard ASTM-D-638.

The tensile specimens were printed at the three different levels of the raster angle (0° , 45° and 90°). Layer thickness and raster width are constant at 100 and 500 μm , respectively. All the specimens are printed twice. Figure 24.3 shows the tensile specimens after testing printed from both the filaments.

24.3 Results and Discussion

PLA filaments (commercially available and in-house fabricated) were tested for physical and mechanical properties. Results of MFI, TGA and tensile strength of both the filaments are discussed below. Apart from that tensile strength of printed specimens at different raster angles also discussed.

Fig. 24.3 FDM printed parts at different raster angle from **a** In-house fabricated PLA filament and **b** Commercially available PLA filament



24.3.1 Melt Flow Index

Melt flow index (MFI) defines the comfort with which a thermoplastic polymer can flow. MFI About 5 g of the chopped filament was tested according to standard ASTM-D-1238 at a temperature of 210 °C with an applied load of 2.16 kg after the preheat and compact time of about 360 s. In-house fabricated PLA filament, as well as a commercially available filament, was tested at the same condition. The average value of three observations was recorded for each filament.

Figure 24.4 shows the graphical representation of the MFI values of both the PLA filaments. The MFI value of fabricated material should be adequate with the MFI

Fig. 24.4 MFI of PLA filaments

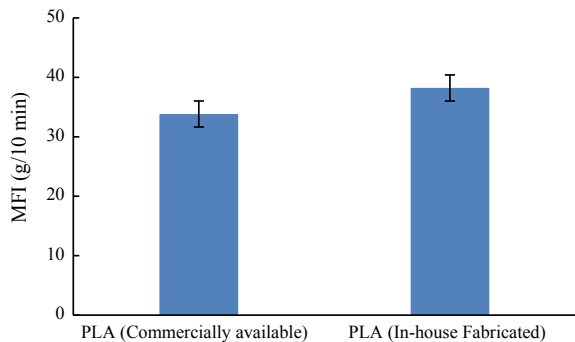
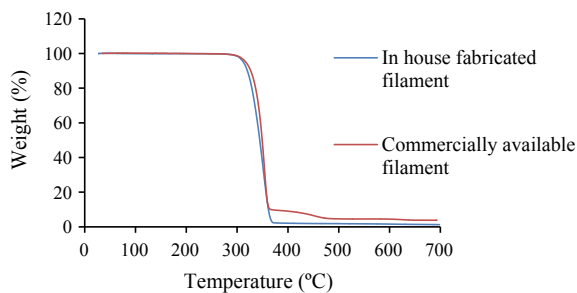


Fig. 24.5 TGA curves for PLA filament



value of commercially available PLA filament so that it can be used in FDM printer. It was observed that the MFI of both the filaments is nearly in the same range. So, it indicates that this fabricated filament can be used as a feedstock filament for FDM.

24.3.2 Thermal Gravimetric Analysis (TGA)

Thermal stability of in-house fabricated PLA filament was inspected by using thermal gravimetric analysis (TGA). The samples had a mass of approximately 10 mg and were tested in an airflow of 15 ml/min from 30 to 700 °C at a rate of 10 °C/min.

Figure 24.5 shows the experimental curves recorded for the thermal degradation of commercially available PLA and in-house fabricated PLA, under a nominal linear heating rate. The TG curves of both PLA are sigmoidal and represent a continuous decomposition profile. Therefore, the thermal decomposition of these two materials will have a unique value of the activation energy throughout the conversion range. The maximum mass loss rate is less for fabricated PLA as for commercially PLA it is around 3.75%, while for fabricated PLA it is around 2.5%. It was observed that both the TGA graphs exhibited similar behaviour.

24.3.3 Tensile Strength of the Filament

Ultimate tensile strength values of in-house fabricated, as well as commercially available PLA filament are shown in Fig. 24.6. It was observed that fabricated PLA is as good as a commercially available filament. In-house fabricated PLA filament has an average tensile strength of 23.13 MPa, while another filament is having the strength of 21.83 MPa. It was observed that there is no need for any modification or to add any filler material to increase the tensile strength as the result of fabricated filament is slightly superior than commercially available filament.

Fig. 24.6 Tensile strength of PLA filaments

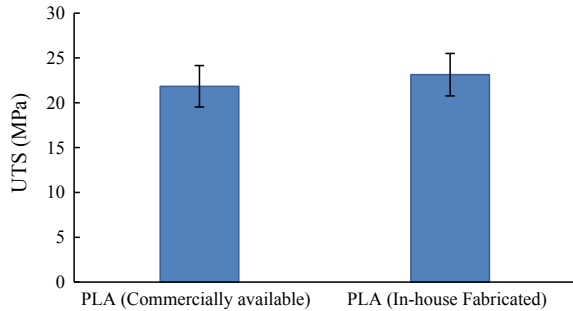
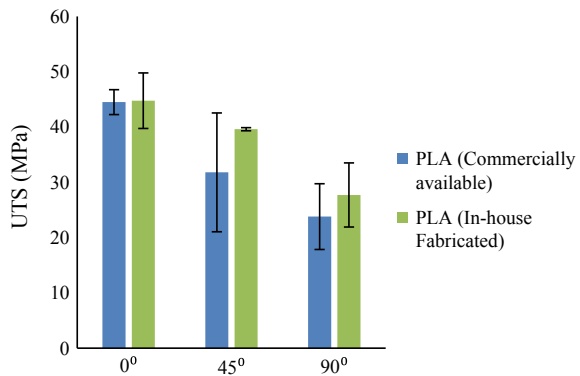


Fig. 24.7 Tensile strength of printed parts



24.3.4 Tensile Strength of Printed Specimens

Figure 24.7 shows the mean value of ultimate tensile strength and standard deviation for each raster angle for both the PLA filaments. Parts printed from in-house fabricated filament obtained higher tensile strength as compared to the commercially available filament. It was observed from the graph that 0° raster angle gave maximum strength and 90° raster angle gave minimum tensile strength for both the filaments. For the specimens built with 0° raster angle, the layers are deposited along the length of the specimen and are aligned in the direction parallel to the applied load. Therefore, acting load yields higher resistance to tensile failure and gave the maximum strength.

24.4 Conclusions

The outcomes of the work presented here show the possibility of fabrication of the FDM filament and its capability to produce parts on open-source FDM printer. The selection of temperature range of single-screw extruder is a very challenging

process as in present work barrel, and die zone temperatures are selected by some trial and error method. The results of MFI and TGA show that both the PLA filaments (commercially available as well as in-house fabricated) exhibited similar behaviour. The tensile strength of in-house fabricated filament is higher than the commercially available filament of PLA. Results of 3D printed part show that parts printed from in-house fabricated PLA filament have higher tensile strength. Apart from that, parts made from 0° raster angle obtained higher tensile strength and then after tensile strength decreases as raster angle increases from 0° to 90°.

References

1. Rocha, C.R., Perez, A.R.T., Roberson, D.A., Shemelya, C.M., MacDonald, E., Wicker, R.B.: Novel ABS-based binary and ternary polymer blends for material extrusion 3D printing. *J. Mater. Res.* **29**(17), 1859–1866 (2014). <https://doi.org/10.1557/jmr.2014.158>
2. Singh, R., Singh, S., Mankotia, K.: Development of ABS based wire as feedstock filament of FDM for industrial applications. *Rapid Prototyping J.* **22**(2), 300–310 (2016). <https://doi.org/10.1108/RPJ-07-2014-0086>
3. Hamod, H.: Suitability of recycled HDPE for 3D printing filament. 18–29 (2015)
4. Carneiro, O.S., Silva, A.F., Gomes, R.: Fused deposition modeling with polypropylene. *Mater. Des.* **83**, 768–776 (2015). <https://doi.org/10.1016/j.matdes.2015.06.053>
5. Nikzad, M., Masood, S.H., Sbarski, I.: Thermo-mechanical properties of a highly filled polymeric composites for fused deposition modeling. *Mater. Des.* **32**(6), 3448–3456 (2011). <https://doi.org/10.1016/j.matdes.2011.01.056>
6. Perez, A.R.T., Roberson, D.A., Wicker, R.B.: Fracture surface analysis of 3D-printed tensile specimens of novel ABS-based materials. *J. Fail. Anal. Prev.* **14**(3), 343–353 (2014). <https://doi.org/10.1007/s11668-014-9844-0>
7. Kalita, S.J., Bose, S., Hosick, H.L., Bandyopadhyay, A.: Development of controlled porosity polymer-ceramic composite scaffolds via fused deposition modeling. *Mater. Sci. Eng., C* **23**(5), 611–620 (2003). [https://doi.org/10.1016/S0928-4931\(03\)00052-3](https://doi.org/10.1016/S0928-4931(03)00052-3)
8. Zhu, J., Hu, Y., Tang, Y., Wang, B.: Effects of styrene–acrylonitrile contents on the properties of ABS/SAN blends for fused deposition modeling. *J. Appl. Polym. Sci.* **134**(7), 44477-1-5 (2017). <https://doi.org/10.1002/app.44477>
9. Garg, H.K., Singh, R.: Investigations for obtaining desired strength of Nylon6 and Fe powder-based composite wire for FDM feedstock filament. *Prog. Addit. Manufact.* **2**(1–2), 73–83 (2017). <https://doi.org/10.1007/s40964-017-0022-2>
10. Wu, W., Geng, P., Li, G., Zhao, D., Zhang, H., Zhao, J.: Influence of layer thickness and raster angle on the mechanical properties of 3D-printed PEEK and a comparative mechanical study between PEEK and ABS. *Materials* **8**(9), 5834–5846 (2015). <https://doi.org/10.3390/ma8095271>

Chapter 25

Investigation of Mechanical Behaviour and Surface Roughness Properties on Copper Electroplated FDM High Impact Polystyrene Parts



N. Sathishkumar , N. Arunkumar , L. Balamurugan , L. Sabarish 
and A. Samuel Shapiro Joseph 

Abstract Additive manufacturing is an advanced production technique which builds up complex-shaped parts layer by layer, as opposed to subtractive manufacturing methodologies by using the .stl file as input data. The mechanical strength and surface roughness properties of polymer-based additive manufacturing components need to be improved for its efficient use in functional end tooling applications. Many research methodologies were proposed to improve the mechanical strength and surface properties of additive manufacturing components but post-processing characterization is a kind of method, which is highly concentrated in recent years by various organizations. The various coating techniques like D.C sputtering, electroforming, electroless forming and electroplating were selected in this study, and a pilot study was conducted to choose a best technique that provides better adherence of source material over target in different build orientations of 3D-printing process. Among the various techniques in pilot study, the electroplating process was selected for this study because of its better coating properties, simple procedure, low-cost and good surface finish than other technique. In this study, the tensile and flexural test specimens were fabricated with high impact polystyrene material by using fused deposition modelling technique in five different build orientations (0° , 30° , 45° , 60° and 90°). The fabricated parts were electroplated with copper of thickness $250\ \mu$ by using sulphuric acid (H_2SO_4) and copper sulphate ($CuSO_4$) as electrolyte solution. The electroplated and non-electroplated parts were tested for its tensile and flexural properties as per ASTM standards at room temperature to analyze the effect of electroplating over HIPS parts. The portable surface roughness tester was used to analyze the improvement in roughness properties of electroplated parts. The results between electroplated and non-electroplated parts fabricated in five different orientations were compared and validated for its application in functional end tooling applications. The results are showing that electroplating process over 3D-printed HIPS parts significantly

N. Sathishkumar (✉) · N. Arunkumar · L. Balamurugan · L. Sabarish · A. Samuel Shapiro Joseph
Department of Mechanical Engineering, St. Joseph's College of Engineering, Old Mamallapuram
Road, Chennai 600119, Tamil Nadu, India
e-mail: sathishnsk2912@gmail.com

© Springer Nature Singapore Pte Ltd. 2020
M. S. Shunmugam and M. Kanthababu (eds.), *Advances in Additive Manufacturing and Joining*, Lecture Notes on Multidisciplinary Industrial Engineering,
https://doi.org/10.1007/978-981-32-9433-2_25

improved its tensile, flexural and surface roughness properties when comparing to non-electroplated parts.

Keywords High impact polystyrene · Fused deposition modelling · Copper electroplating · Anisotropic behaviour

25.1 Introduction

Additive manufacturing is an unconventional production technique which creates any complex-shaped geometrical parts at a stretch without in need of any additional experimental set-up. The additive manufacturing can be classified based on its nature of raw material usage like powder-based, liquid-based and filament-based technique [1]. The applications of additive manufacturing were expanded beyond the expectations and the limitations of conventional manufacturing are almost replaced by this technique [2]. Additive manufacturing in tooling is highly preferred than conventional tooling methods like CNC machining in terms of speed, difficulty and quality [3]. Post-processing characterization experimentations are performed to improve mechanical strength and surface roughness properties for development of additive manufacturing tooling in sand casting, investment casting and plastic moulding applications [4]. Electroplating has been practiced for many years in industries such as electronics and jewellery manufacturing. The electroplating process contains an anode and cathode in an electrolytic solution which together kept in an electrolytic bath. When potential difference is applied between the anode and cathode the ions from the anode got discharged and bonded to the cathode. This process is repeated till the cathode is completely electroplated by the metal from anode [5]. The cathode must be a conductive material, so the polymer parts must be coated with conductive ink preferably silver paint in most cases for making it conductive [6]. The nickel deposition over the polymer prototypes produced by fused deposition modelling technique showed a significant increase in ultimate tensile strength, young's modulus and impact strength which highly influenced overall strength and stiffness behaviour [7]. The electroplating process carried out with a thickness of 60 μm over the ABS parts showed lower ductility, while 70 and 80 μm samples showed considerable ductility improvement [8]. The electroplating of copper and nickel samples from stereolithography and laser sintering process showed that the samples with higher coating thickness provided more UTS and impact energy but had a poor effect on the ductility of parts [9]. The reaction between butadiene synthetic elastomer and (5–14%) styrene containing crystal polymer creates high impact polystyrene [10]. HIPS material provides very good mechanical resistance comparing to other polymers, which also facilitates excellent machinability as well as dimensional stability. The excellent aesthetic quality along with easy to glue and paint property in low-cost makes it ideal material for various applications like prototypes, covers and tooling in food industries, low strength mould applications, etc. [11].

25.2 Objective of the Study

The objective of this work is to study the mechanical behaviour and surface roughness properties of 250 μ copper electroplated and non-electroplated high impact polystyrene specimens fabricated by using fused deposition modelling process in five different build orientations (0°, 30°, 45°, 60° and 90°). The specimens manufactured as per ASTM standards were tested for tensile, flexural strength and the surface roughness also measured. The results were compared between electroplated and non-electroplated specimens for all the five orientations and based on findings an optimized orientation is suggested for further applications.

25.3 Methodology of the Study

The methodology used in this study is shown in Fig. 25.1 as follows:

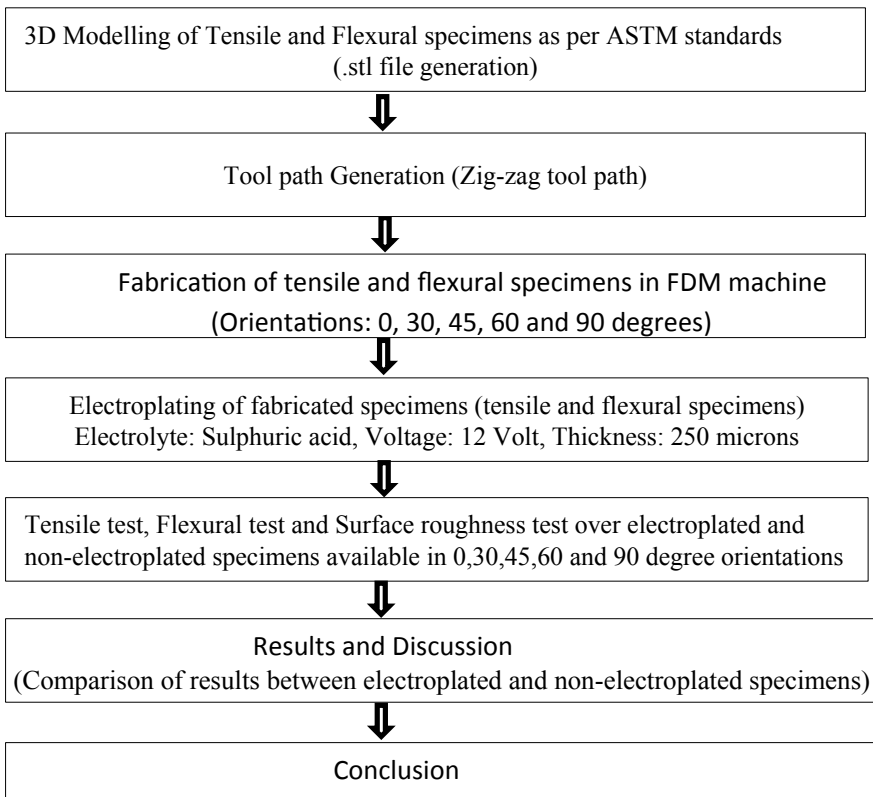


Fig. 25.1 Methodology of the study

25.4 Experimentation

25.4.1 3D Modelling

The material consumption and build time is an important parameter to be considered at the time of selecting standards for printing specimens, so here ASTM standards were accordingly selected to minimize the material consumption and build time as much as possible [12]. The tensile and flexural test specimens were modelled in CATIA software as per ASTM D638 and ASTM D6272 standards. The surface geometry of generated models was encoded by STL file format. The encoded STL file format was checked against standard file generation rules like vertex rule, orientation rule, all positive octant rule, and triangle sorting rule by using ASCII programming module. The ASTM standards and generated 3D models of tensile test specimen and flexural test specimen were shown in Figs. 25.2 and 25.3, respectively.

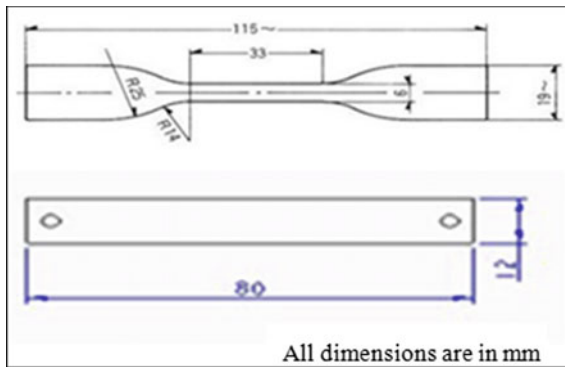


Fig. 25.2 ASTM standards of tensile and flexural specimens

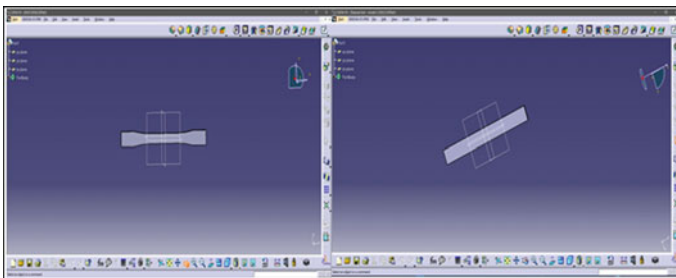


Fig. 25.3 3D models of tensile and flexural specimens

25.4.2 Fabrication

The Flash Forge 3D-printer machine was used for the fabrication of tensile and flexural test specimens. The tensile and flexural test specimens were fabricated in five different orientations (0° , 30° , 45° , 60° and 90°). Figures 25.4 and 25.5 show the different orientations of fabricated specimens. The specimens were fabricated by high impact polystyrene material based on the zig-zag tool path. The support structures were removed after fabrication by immersing in solution. The specifications of Flash Forge FDM machine and HIPS material are shown in Tables 25.1 and 25.2 as follows.

Fig. 25.4 Fabricated tensile specimens

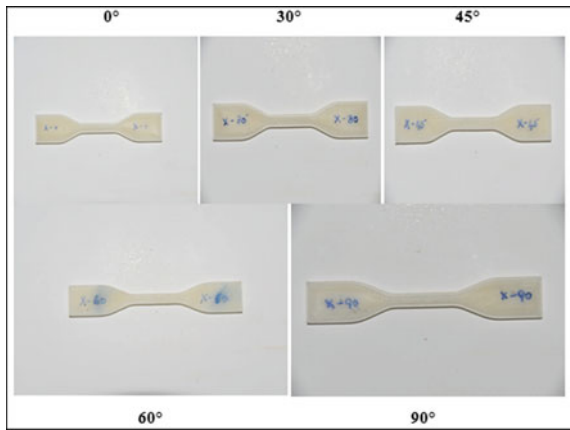


Fig. 25.5 Fabricated flexural specimens

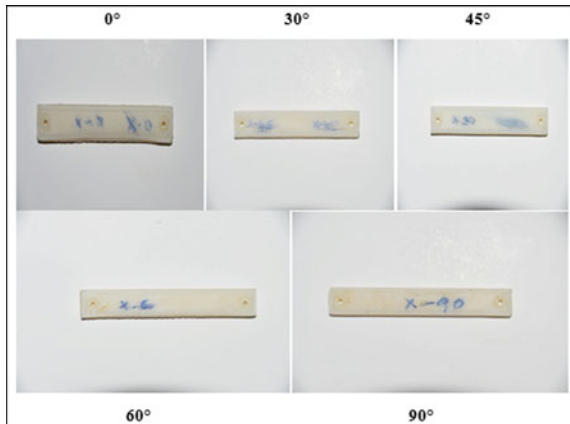


Table 25.1 Specifications of flash forge FDM machine

Model material	High impact polystyrene
Support material	SR 30 soluble
Build size (mm)	203 × 152 × 152
Layer thickness (mm)	0.254
Operating system compatibility	Windows XP/7
Network connectivity	Ethernet TCP/IP 10/100 baseT
Size (mm)	635 × 660 × 787
Weight (kg)	76
Power (VA)	100–127

Table 25.2 Specifications of HIPS material

Commercial name in FDM	HIPS
Glass transition temperature (T_g)	105 °C
Coefficient of thermal expansion	8.82×10^{-05} mm/mm/°C
Extrusion temperature	240 °C

25.4.3 Electroplating

The cleaning of specimens was done after fabrication and the specimens were prepared for electroplating process. The copper ink is painted over tensile and flexural specimens to make it conductive. In the electrolytic bath tank, the source copper material was attached to anode and the copper conductive ink coated specimens were attached to cathode. Sulphuric acid (H_2SO_4) was used as an electrolyte because of its well-known electrical conductivity and a better throwing power. The ability of the electrolyte to get uniform depositions in areas with different current densities is called as throwing power. From the pilot study, it was observed that the addition of more sulphuric acid provided increased throwing power. Based on the theoretical calculations the appropriate voltage and time were chosen. The pilot experiments were conducted based on theoretical calculations in a trial and error basis, which shows that maximum current of 4.5 A/in^2 provides better adherence and the experiments exceeding this value resulted in melting and collapsing of specimens. In electroplating process, the thickness of coating is directly proportional to voltage so in this study voltage was taken as a constant value of 12 V to perform the electroplating of specimens. The average time taken by each specimen of different orientation was 10 min approximately and the thickness of 250μ was achieved over each specimen. Figure 25.6 shows the steps followed in electroplating of specimens.

Fig. 25.6 Electroplating of 3D-printed HIPS specimens



25.4.4 Tensile and Flexural Testing

The electroplating process was followed by testing of electroplated and non-electroplated tensile and flexural specimens of all five different orientations. The tensile and flexural tests were carried out as per ASTM D638 and D690 standards at normal room temperature. The loads were gradually increased in steps and the corresponding stress versus strain graph was recorded for all the orientations. The ultimate tensile and flexural strength of all specimens in different orientations were calculated separately. Figure 25.7 shows the electroplated and non-electroplated specimens of

Fig. 25.7 Electroplated and non-electroplated specimens



Fig. 25.8 Experimental set-up of flexural test



Fig. 25.9 Experimental set-up of tensile test



different orientations used for tensile and flexural testing. The experimental set-up of tensile and flexural tests was shown in Figs. 25.8 and 25.9.

25.4.5 Surface Roughness Measurement

The surface roughness plays a significant role in determining the quality of the material printed in 3D-printing. Since from its introduction, the surface roughness oriented problems like stair-stepping effect in edges would be a major concern in various 3D-printing technologies. Even though this roughness oriented problems are greatly reduced by methods like adaptive slicing, customized tool path generation, etc. but the need for studying the surface roughness behaviour in this kind of electroplated specimens is highly recommended to verify the influence of coating thickness, bond-

Fig. 25.10 Portable surface roughness tester



ing nature between metal and plastics over the surface roughness properties so that for determining the anisotropic behaviour in each orientation. In this study, the surface roughness test was performed over electroplated and non-electroplated specimens by using portable roughness tester. The surface roughness (R_a) was calculated along the two adjacent lateral directions say x -direction (length) and z -direction (width). Figure 25.10 represents the portable surface roughness tester used for this study.

25.5 Results and Discussion

25.5.1 Tensile Test

The tensile test was conducted for the electroplated and non-electroplated specimens in all five orientations at room temperature. The results of tensile test experiment show a great improvement in ultimate tensile strength and ultimate load-bearing capacity of electroplated specimens over non-electroplated specimens. The ultimate tensile strength and ultimate load-bearing capacity of electroplated specimens exhibit a 55.63% and 61.42%, respectively. The % of elongation is very high for electroplated specimens in all orientations, which confirm the establishment of transition between brittle to ductile nature over the surface of non-electroplated high impact polystyrene specimens. This increase in elongation also confirms the perfect bonding of copper molecules over HIPS surface structure for the mentioned experimental conditions used in this study, and this increased percentage of elongation in electroplated specimens provided a great resistance against tensile loading in all directions. Even though the tensile nature is improved greatly for electroplated specimens, the 45° orientation built specimen showed a minimum percentage of improvement comparing other orientations against tensile loading because of its poor anisotropic nature as resulted from weak interfacial bonding between adjacent layers. The 90° built orientation provided a significant improvement in tensile properties because of its strong interface between adjacent layers facilitated by the good adhesion of copper molecules at the time of electroplating. Tables 25.3, 25.4 and 25.5 shows the maximum load-bearing capac-

Table 25.3 Maximum load-bearing capacity of tensile specimens

S. No	Orientation (°)	Ultimate tensile strength (MPa)	
		Non-electroplated	Electroplated
1	0	18.11	62.90
2	30	18.64	41.88
3	45	19.16	29.76
4	60	18.89	31.79
5	90	13.04	52.80

Table 25.4 Ultimate tensile strength of tensile specimens

S. No	Orientation (°)	Ultimate tensile load (KN)	
		Non-electroplated	Electroplated
1	0	0.41	1.52
2	30	0.44	0.85
3	45	0.46	0.76
4	60	0.44	0.85
5	90	0.31	1.52

Table 25.5 Elongation percentage of tensile specimens

S. No	Orientation (°)	% of Elongation	
		Non-electroplated	Electroplated
1	0	2.51	12.56
2	30	2.08	9.96
3	45	0.60	3.12
4	60	3.12	3.40
5	90	0.72	2.52

ity, ultimate tensile strength and percentage of elongation between electroplated and non-electroplated specimens in all orientations. Figures 25.11, 25.12 and 25.13 show the comparison graphs of ultimate tensile strength, maximum load-bearing capacity and % of elongation between electroplated and non-electroplated specimens for all the five different orientations, respectively.

25.5.2 Flexural Test

The three-point bending test was used to test flexural strength of the electroplated and non-electroplated specimens at room temperature. Since the specimen shape, loading geometry and strain rate plays a major role in determining the flexural strength of the material utmost care was taken to establish gradual loading condition over the specimens. Table 25.6 shows the results of flexural test in different orientations. The

Fig. 25.11 Ultimate tensile strength versus orientation

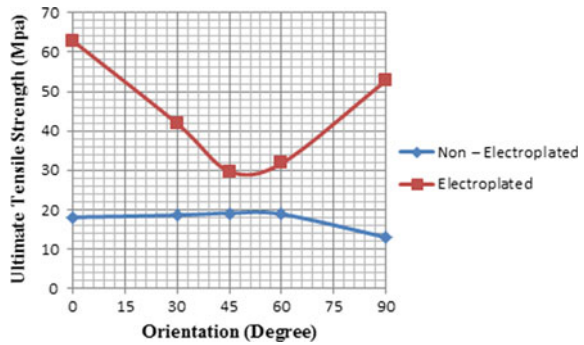


Fig. 25.12 Ultimate tensile load versus orientation

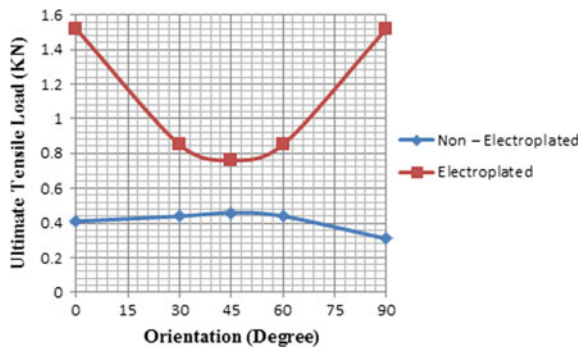


Fig. 25.13 Percentage of Elongation versus orientation

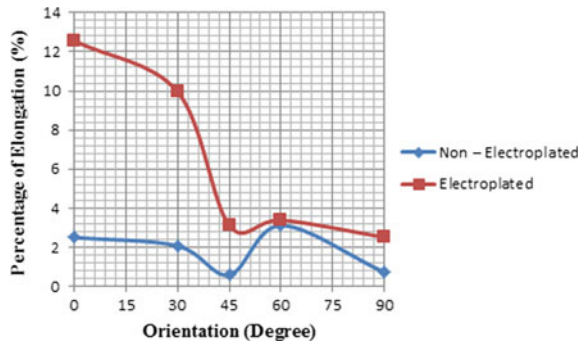
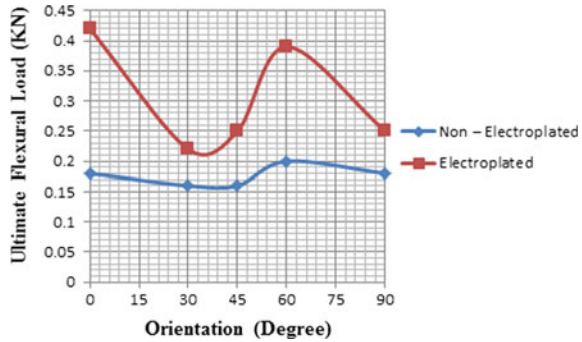


Table 25.6 Ultimate flexural load-bearing capacity of specimens

S. No	Orientation (°)	Ultimate flexural load (KN)	
		Non-electroplated	Electroplated
1	0	0.18	0.42
2	30	0.16	0.22
3	45	0.16	0.25
4	60	0.20	0.39
5	90	0.18	0.25

Fig. 25.14 Ultimate flexural load versus orientation



results are similar to tensile test as the electroplated specimens provided more flexural strength on the average of 39.41% than non-electroplated specimens. The electroplated specimen with 0° orientation provided maximum flexural strength because of its flat horizontal exposure of zig-zag tool path perpendicular to the direction of loading as shown in standard loading conditions. The electroplated specimen with 90° orientation shows minimum flexural strength over non-electroplated specimen because of its vertical exposure of zig-zag tool path perpendicular to the direction of loading. Figure 25.14 shows the comparison graph of specimens against respective orientations.

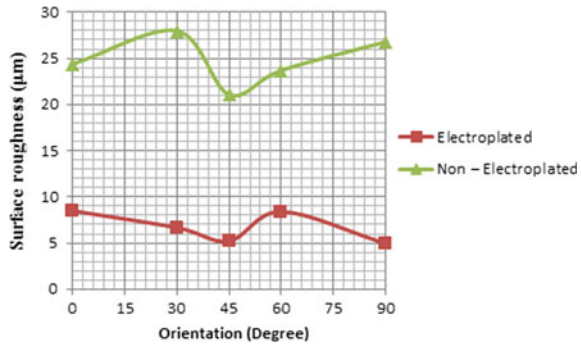
25.5.3 Surface Roughness Test

The high frequency, short wavelength component of a measured surface is called surface roughness. The surface roughness is a component of surface texture, which is quantified by the deviations in the direction of the normal vector of a real surface from its ideal form. The roughness is very high if deviations are large and surface is smooth if deviations are small. The surface roughness of electroplated and non-electroplated specimens was measured using portable roughness tester and the results indicated an average reduction of 72% surface roughness in electroplated parts comparing to non-electroplated parts because of the uniformed distribution of copper molecules over HIPS surface parts. The surface roughness is reduced about 60% in all orientations. Table 25.7 shows the surface roughness values of electroplated and non-electroplated parts. Figure 25.15 depicts the comparison of surface roughness between electroplated and non-electroplated parts.

Table 25.7 Surface roughness test results

S. No	Orientation (°)	Surface roughness (µm)	
		Non-electroplated	Electroplated
1	0	24.37	8.50
2	30	27.97	6.67
3	45	21.08	5.22
4	60	23.71	8.41
5	90	26.79	4.94

Fig. 25.15 Comparison of surface roughness



25.6 Conclusion

The study on electroplating of 3D-printed HIPS parts in five different orientations is novel and unique in this study. From the obtained results it is clearly understood that the electroplating of a 3D-printing HIPS material has significant impact over mechanical and surface properties of non-electroplated specimens. The results from this study can be further utilized for other materials in 3D-printing. Among the five orientations tested in this study, the each and every build orientation has its unique anisotropic property because of its complex tool path nature for material deposition over different spatial coordinate positions. The 90° orientation provided good tensile properties, while 0° orientation provided better flexural properties and regarding surface roughness the electroplating imparted high smoothness over surface by levelling deviations in all orientations but in electroplated specimens there is also a smaller amount of noise level deviation in frequency at lateral direction (z-direction) because of its stair-stepping phenomenon which shows that stair-stepping phenomenon is not fully compromised with this technique. The results of this study will help to meet the requirements for using 3D-printing technique in real end functional production of parts. The study also promises the improvement of aesthetics in 3D-printed complex-shaped parts which can be utilized in ornamental industry for creating customized designs.

References

1. Gibson, I., Rosen, D.W., Stucker, B.: Introduction and Basic Principles, Additive Manufacturing Technologies, pp. 20–35. Springer, US (2010)
2. Balamurugan, L., Sathishkumar, N., Arunkumar, N., Aravind, G.: Investigation of mechanical behaviour and surface roughness properties on electroplated FDM ABS parts. *Int. J. Eng. Res. Mech. Civ. Eng.* **02**, 60–67 (2017)
3. Noble, J., Walczak, K., Dornfeld, D.: Rapid tooling injection molded prototypes: a case study in artificial photosynthesis technology. In: 6th CIRP International Conference on High Performance Cutting, vol. 14, pp. 251–256 (2014)
4. Sahebrao Ingole, D., Madhusudan Kuthe, A., Thakare, S.B., Talankar, A.S.: Rapid prototyping—a technology transfer approach for development of rapid tooling. *Rapid Prototyping J.* **15**, 280–290 (2009)
5. Angel, Kristin, Tsang, Harvey H., Bedair, Sarah S., Smith, Gabriel L., Lazarus, Nathan: Selective electroplating of 3D printed parts. *Addit. Manufact.* **20**, 164–172 (2018)
6. Arthur, Alan: Phillip Michael Dickens, Richard Charles Cobb, Using rapid prototyping to produce electrical discharge machining electrodes. *Rapid Prototyping J.* **2**, 4–12 (1996)
7. Kumar, T.V.N., Kulkarni, M.V., Ravuri, M., Elangovan, K., Kannan, S.: Effects of electroplating on the mechanical properties of FDM-PLA parts. *J. Future Eng. Technol.* **10**(3), 29–37 (2015)
8. Kannan, S., Senthilkumaran, D.: Investigating the influence of electroplating layer thickness on the tensile strength for fused deposition processed ABS thermoplastics. *Int. J. Eng. Technol.* **6**(2), 1047–1052 (2014)
9. Saleh, N., Hopkinson, N., Hague, R.J.M., Wise, S.: Effects of electroplating on the mechanical properties of stereolithography and laser sintered parts. *Rapid Prototyping J.* **10**, 305–315 (2004)
10. Yilmaz, T., Sahin, T., Sinmazcelik, T.: Fracture characteristics of high impact polystyrene under impact fatigue loadings. *J. Mater. Sci.* **44**, 4308 (2009)
11. Rovere, J., Correa, C.A., Grassi, V.G.: Role of the rubber particle and polybutadiene cis content on the toughness of high impact polystyrene. *J. Mater. Sci.* **43**, 952 (2008)
12. Sathishkumar, N., Sugavaneswaran, M., Arumaikkannu, G.: Investigation of sparse mode build style on material consumption, build time and compressive behaviour of additive manufactured cellular structures. In: 6th International & 27th All India Manufacturing Technology, Design and Research Conference (AIMTDR-2016) (2016)

Chapter 26

Effect of Build Orientation on Mechanical Strength of FDM Printed PLA



Naushil H. Patadiya, Harshit K. Dave and Shilpesh R. Rajpurohit

Abstract Fused Deposition Modeling is one of the widely used extrusion-based additive manufacturing technique. FDM is widely used to create prototypes with any complexity. The application of FDM can also be extended for the rapid manufacturing application. The application of FDM may be restricted due to anisotropy in mechanical properties of the printed part. The mechanical performance of the FDM printed part is influenced by several process parameters. In the present investigation effect of the build orientations on the mechanical properties of the printed part have been investigated. Three build orientations X (Flat), Y (on edge) and Z (upright) have been considered to measure their influence on the mechanical strength of the printed PLA part. Analysis of result revealed that part printed in X direction has higher tensile and impact strength over the part printed in Y and Z direction. Further, it is also observed that the fracture pattern is also significantly affected by the build orientation. Inter-layer failure mode has been observed with x and y orientated specimen while trans-layer failure mode has been observed for z-orientated specimen.

Keywords Additive manufacturing (AM) · Fused deposition modeling (FDM) · Polylactic acid (PLA) · Build orientation · Tensile strength · Impact strength

26.1 Introduction

Additive manufacturing (AM) is defined as “a process of joining materials to create three-dimensional objects (3D) model data, usually layer by layer, opposite to subtracting production methodologies”. This technology has drawn much attention because of his capability to build functional components with any complex geometries without any specific tooling requirement. FDM is one of the most adapted AM technologies due to its low cost and simplicity. In the FDM process, polymer filament is fed into the heated nozzle wherein gets heated above the glass transition

N. H. Patadiya (✉) · H. K. Dave · S. R. Rajpurohit
Department of Mechanical Engineering, Sardar Vallabhbhai National Institute of Technology,
Surat 395007, Gujarat, India
e-mail: patadiyanaushil99@gmail.com

© Springer Nature Singapore Pte Ltd. 2020
M. S. Shunmugam and M. Kanthababu (eds.), *Advances in Additive Manufacturing and Joining*, Lecture Notes on Multidisciplinary Industrial Engineering,
https://doi.org/10.1007/978-981-32-9433-2_26

301

temperature. The polymer material is deposited on the heated bed as defined by the CAD geometry and the bed moves downward. These processes are repeating until the completion of the part [1, 2]. The mechanical strength of the FDM printed part is largely influenced by the selection of the printing parameters. The mechanical properties of the printed part can be improved with the careful selection of the build parameters. In this regard, recently some work has been initiated, to understand the relation between the mechanical strength and process variables for FDM printed part.

Durgun and Ertan [3] examined the influence raster angles and orientations on tensile strength and flexural strength of ABS printed part. They have observed that specimen printed with smaller raster angle displayed better mechanical properties. Qattawi et al. [4] observed that higher extrusion temperature and larger layer height improves the mechanical properties. Dawoud et al. [5] examined the influence of raster orientation and air gap on mechanical properties of FDM printed ABS component. They reported higher tensile strength with a negative air gap and $\pm 45^\circ$ raster angle. Uddin et al. [6] examined the mechanical properties and failure mechanism of the FDM processed ABS parts. They observed that smaller layer height help to improve the tensile properties. Song et al. [7] observed that 3D-printed part results into higher toughness than injection molded part. Wang et al. [8] observed that lower layer height and higher printing temperature help to improve the impact strength of the FDM printed part. Garg et al. [9] examined the effect of build orientation and raster angle on the surface roughness of ABS test specimens. Lanzotti et al. [10] studied the influence of build variables on the tensile properties of 3D printed part using open-source 3D printer. They observed that tensile is decreasing with increment in raster angle for PLA material.

The literature shows that mechanical strength is dependent on the many build parameter of the printed part. The aim of this work is to study the effect of build orientation on the mechanical strength of the FDM processed PLA part by performing tensile and impact test. Three build orientations X, Y and Z have been selected to study their influence on strength of specimen.

26.2 Experimental Details

26.2.1 Fabrication of Test Specimen

The purpose of this study, to study the influence of build orientation on the mechanical strength of printed part. In order to do so mechanical test in form of tensile and impact test has been performed on 3D printed part that has been fabricated using open-source FDM based 3D printer. PLA is one of the commonly used materials for 3D printing process. Polylactic acid (PLA) is a biodegradable polymer derived from renewable sources, such as corn starch, potato chips or starch or sugar cane, etc. Main advantages of the PLA are eco-friendly, high mechanical strength, good fold retention, resistance to grease and oil and excellent barrier properties to the aroma,

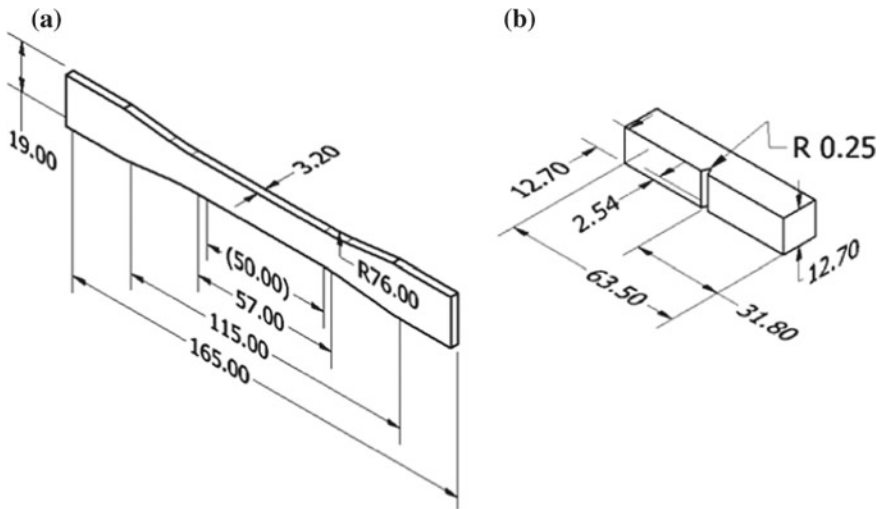


Fig. 26.1 Test specimens **a** tensile specimen as per ASTM D638 and **b** impact specimen as per ASTM D256 (all dimensions are in mm)

cheap, tougher than ABS and dimensionally stable and ideal for open source printer. PLA filament with 1.75 mm diameter was used to fabricate the test specimens.

The specimens used in this study to examine the mechanical strength are prepared based on ASTM D638 type I standards for tensile testing and ASTM D256 for impact testing. Figure 26.1 depicts the dimensions and geometry of the test samples. The tensile test and impact test specimens were first created in Autodesk Inventor, exported in the STL file format and then 3D printer slicing software has been used to create the G-code file using the STL file, which has been transferred to 3D printer to print the test samples.

The test specimens were printed at the three different build orientation namely X (Flat), Y (on edge) and Z (upright) as shown in Fig. 26.2. All the specimen printed at 100% infill density. The PLA material is extruded at the 210 °C at the deposition speed of 50 mm/s and the bed is kept at the 70 °C. After the printing, all the sample were measured to check whether the geometry and features have been created as per the respected standard. All the specimen has been printed twice to ensure the repeatability of the test. The other printing process parameter kept constant while printing the test specimen. The remaining fixed process parameters are summarized in Table 26.1.

26.2.2 Mechanical Testing

The tensile test of the fabricated samples was performed in accordance with ASTM D638 using a Kudale PC2000 electronic tension tester. The UTM is furnished with

Fig. 26.2 Build part orientation about X, Y, and Z

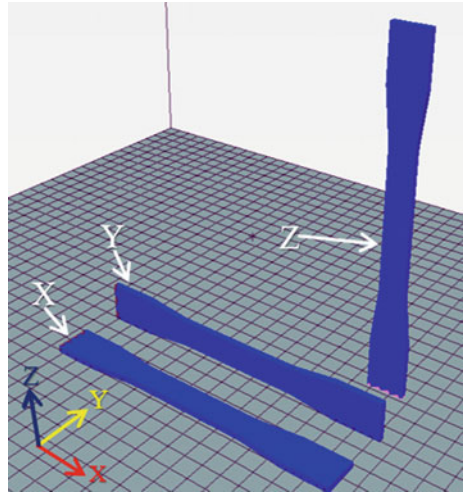


Table 26.1 FDM process printing parameter

Parameter	Value
Infill pattern	Rectilinear
Layer thickness	0.1 mm
Raster width	0.4 mm
Raster angle	0°
Perimeter	1
Solid top bottom layer	1

20 kN loadcell and inbuilt software allow to control, record, and monitor the measure. The test was conducted at room temperature and with a deformation speed of 5 mm/min.

The Izod impact test performed on the impact testing machine that is used to determine the impact resistance of the sample in accordance with ASTM D256. During the impact test, the sample is subjected to a rapid and intense blow from a hammer pendulum that hits the sample with a speed of 3.8 m/s. Impact resistance is calculated by dividing impact energy J based on the thickness of the sample.

26.3 Results and Discussion

In the present investigation, the impact of part orientation on the mechanical strength of the FDM processed PLA part has been carried out. Three build orientations have been varied to study their impact on tensile strength and impact strength of the FDM fabricated PLA parts.

26.3.1 Effect on Tensile Strength

In the present investigation, the influence of the build orientation on the ultimate tensile strength has been investigated. The experimental results of the ultimate tensile strength are shown in Table 26.2.

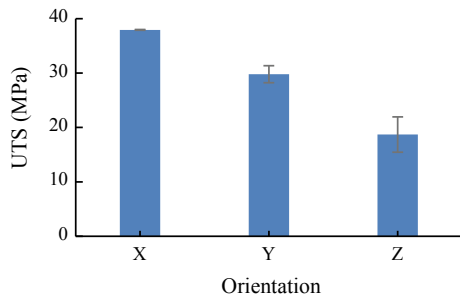
Figure 26.3 shows the ultimate tensile strength at different build orientation. From Fig. 26.3, it is clear that the orientation of the build has significantly influenced the tensile properties and, in particular, the behavior of ductility and failure. Experimental results have shown that specimens with X orientation generally have higher tensile strength than the Y and Z orientation build parts. Therefore, FDM parts manufactured in a different orientation exhibit anisotropic tensile strength properties.

It may be because the layers in the X and Y orientation are deposited parallel to loading direction during the tensile test. In contrast, the layers in the Z orientation will be stacked one on the other. In the case of the X and Y orientations, the load was applied parallel to deposition direction. Because of that, fibers were pulled in the loading direction that results in trans-layer failure. Most of the load withstand by the individual fiber and fiber breakage was observed. For the Z orientation, the load was applied perpendicular to fibers that result into inter-layer fusion bond failure. In this case, the adhesion of the layer or fiber to the fibers significantly affected tensile strength since the bond between the superposed layers between the adjacent layers or the fiber have supported most of the applied load and not its fibers. It was observed to have a lower tensile strength than individual fibers.

Table 26.2 Tensile strength of 3D printed part as a function of building orientation

S. No.	Orientation	Mean UTS (MPa)	SD
1	X	37.95	0.07
2	Y	29.80	1.56
3	Z	18.70	3.25

Fig. 26.3 Effect of build orientation on Izod impact strength



26.3.2 Effect on Impact Strength

Similarly, the influence of build orientation on the impact strength has been also investigated. The experimental results of the impact strength have been shown in Table 26.3.

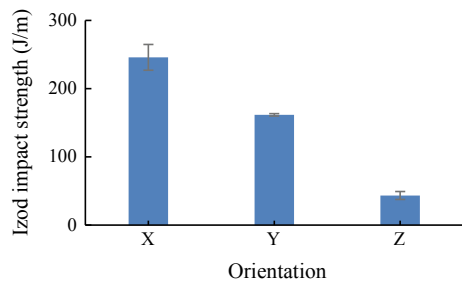
The influence of the build orientation on the impact strength of the 3D printed PLA is shown in Fig. 26.4. From Fig. 26.4, it can be clearly seen that specimen printed in X orientation generally have higher impact strength in comparison to that Y and Z orientation build specimens. The trend of the results is the same as that obtained with the tensile test.

It may be due to that the perpendicular deposition of layers in the X and Y orientation to withstand the load during the impact test. In contrast, the layers are stacked in the Z orientation relative to each other. For X and Y orientations, fibers were plastically deformed perpendicular to the direction of load, causing raster failure. In this case, the individual fibers are withstand impacted load and breakage of the fibers occurs. For the Z orientation, the load was also applied parallel to fibers, resulted into layer fusion bond failure. The adhesion of the layer or fiber to the fibers significantly affected the impact strength, since the fusion seam between the adjacent layers or fibers had borne most of the applied load and not the fiber itself. Therefore, samples made in Z orientation cannot be suggested for applications where the tensile strength is predominant.

Table 26.3 Impact strength of 3D printed part as a function of building orientation

S. No.	Orientation	Mean impact strength (J/m)	SD
1	X	245.93	18.81
2	Y	161.48	01.80
3	Z	43.48	05.80

Fig. 26.4 Effect of build orientation on ultimate tensile strength



26.4 Conclusions

In the present study, experimental investigation has been carried out to study the effect of build orientation on the mechanical strength viz. tensile strength and impact strength of FDM printed PLA part. An open-source FDM based 3D printer has been used to fabricate the standard test sample to evaluate the tensile and impact strength with respect to build orientation. The results show the mechanical strength of FDM printed part is greatly influenced by the selection of the build orientation. The results show that higher tensile strength and impact strength has been obtained with specimen printed along x-direction is 37.95 ± 0.07 MPa and 245.93 ± 18.81 J/m, respectively. In general, it can be stated, part printed along with x-direction have better mechanical properties than with those with printed in y-direction and z-direction. In the case of tensile test, part printed along with y-direction exhibits higher ductility over the part printed along with x-direction. The fractured pattern reveals that part printed along x and y direction displayed ductile failure while part build along z-direction shows the brittle failure. In the case of impact test, parts printed along with x and y-direction failure take place due to the breakage of individual bead, while failure takes place due to layer separation in the z-direction printed samples. In general, parts printed in x and y direction display the inter-layer failure while part printed in z-direction shows the trans-layer failure.

References

1. Chua, C.K., Leong, K.F. 3D Printing and Additive Manufacturing: Principles and Applications of Rapid Prototyping. World Scientific Publishing Co Inc. (2014)
2. Gibson, I., Rosen, D.W., Stucker, B.: Additive Manufacturing Technologies. Springer, New York (2010)
3. Durgun, I., Ertan, R.: Experimental investigation of FDM process for improvement of mechanical properties and production cost. *Rapid Prototyping J.* **20**(3), 228–235 (2014)
4. Qattawi, A., Alrawi, B., Guzman, A.: Experimental optimization of fused deposition modelling processing parameters: a design-for-manufacturing approach. *Procedia Manuf.* **10**, 791–803 (2017)
5. Dawoud, M., Taha, I., Ebeid, S.J.: Mechanical behaviour of ABS: an experimental study using FDM and injection moulding techniques. *J. Manuf. Processes* **21**, 39–45 (2016)
6. Uddin, M.S., Sidek, M.F.R., Faizal, M.A., Ghomashchi, R., Pramanik, A.: Evaluating mechanical properties and failure mechanisms of fused deposition modeling acrylonitrile butadiene styrene parts. *J. Manuf. Sci. Eng.* **139**(8), 081018 (2017)
7. Song, Y., Li, Y., Song, W., Yee, K., Lee, K.Y., Tagarielli, V.L.: Measurements of the mechanical response of unidirectional 3D-printed PLA. *Mater. Des.* **123**, 154–164 (2017)
8. Wang, L., Gramlich, W.M., Gardner, D.J.: Improving the impact strength of Poly (lactic acid) (PLA) in fused layer modeling (FLM). *Polymer* **114**, 242–248 (2017)
9. Garg, A., Bhattacharya, A., Batish, A.: Chemical vapor treatment of ABS parts built by FDM: analysis of surface finish and mechanical strength. *Int. J. Adv. Manuf. Technol.* **89**(5–8), 2175–2191 (2017)
10. Lanzotti, A., Grasso, M., Staiano, G., Martorelli, M.: The impact of process parameters on mechanical properties of parts fabricated in PLA with an open-source 3-D printer. *Rapid Prototyping J.* **21**(5), 604–617 (2015)

Chapter 27

Intensifying Hands-on Learning and Experimentation of Fused Deposition Modeling Three-Dimensional Printers



Pushpendra Yadav, Ishant Singhal, Bobby Tyagi, Ankit Sahai and Rahul Swarup Sharma

Abstract Additive Manufacturing (AM) is rapidly gaining popularity as a manufacturing process due to its ability to create unique geometries with unique material compositions across a different range of length scales from single microns to multiple meters. The 3D printers are able to create any complex object with improved cost and performance compared to subtractive manufacturing which is among the most accessible and versatile machines in the manufacturing industry. The present work focuses on the hands-on learning approach for students to identify and learn working on 3D printers so that they understand the product, system and software and process parameters in a better way. Students print 3D models for subject learning and also performed tensile testing and fractography for different infill densities ranging from 20 to 100%. It is observed that PLA printed specimen in XY Plane exhibits the maximum tensile stress of 45.09 MPa and elongation as 14.68%. Also, the fractured surface for XY orientation displayed an intermediate brittle-ductile fracture behavior with fracture morphology depicting difference in failure for different infill densities.

Keywords 3D printer · Additive manufacturing · Hands-on training · Tensile testing

27.1 Introduction

3D printing is considered as the future of the manufacturing technology in the world with a potential to revolutionize industries, factories and mass production in the coming years. 3D printing can reduce the cycle time as well as the cost of product development [1]. The development of 3D printing leads to generation of a large number of processes that allow the use of variety of materials and methods [2, 3]. Among these technologies, one of the most commonly used is fused deposition modeling (FDM), a layer-by-layer additive manufacturing technique, based on material

P. Yadav · I. Singhal · B. Tyagi · A. Sahai (✉) · R. S. Sharma
Department of Mechanical Engineering, Faculty of Engineering, Dayalbagh Educational Institute
Dayalbagh, Agra 282005, India
e-mail: sahaiankit13@gmail.com

© Springer Nature Singapore Pte Ltd. 2020
M. S. Shunmugam and M. Kanthababu (eds.), *Advances in Additive Manufacturing and Joining*, Lecture Notes on Multidisciplinary Industrial Engineering,
https://doi.org/10.1007/978-981-32-9433-2_27

extrusion technology. The advantages of this technology are low maintenance costs, easy material change, compact size, supervision-free operation, and low working temperature.

3D printers are a valuable addition to almost any learning space, with students ranging from the very young minds to adults and can inspire learners to explore, brainstorm, and experiment with many different ideas [4]. In 2012, an article in *The Economist* declared 3D printing “the third industrial revolution”. Barack Obama Ex-President, USA, in his State of the Union address lauded 3D printing saying, “A once shuttered warehouse is now a state-of-the-art lab where new workers are mastering the 3D printing that has the potential to revolutionize the way we make almost everything,” [5]. In China, 3D printer manufacturer Tier time estimates that “90 percent of its domestic market share comes from school laboratories, which need desktop 3D printers so students can learn, experience and design”, (China taps 3D printing consumer market, 2015). In Michigan, US, a group of 22 educators from across the state gathered for a 3½ day workshop to learn how open-source 3D printing can be implemented in and improve the curriculum and also at Dayalbagh Educational Institute, India students are learning and innovating through 3d printing in the areas of science, engineering, technology, and math, [6]. At a high school in North Carolina, US a STEM program has students who are using 3D printers to design and print pieces for biology and engineering experiments, “design and print microscope adapters for cell phone cameras”, design and print robotics and elements for rockets, and more, [7]. Eighth-grade students at a Middle School in Virginia were able to design and 3D print bases and cones for speakers as part of a lesson on electricity, [8].

The only limitation of the evolving technology is our ‘Imagination’. Sometimes young kids are the biggest experts and they should be encouraged to keep thinking and learning, and keep advancing their knowledge. So, a lot of efforts are being made to make 3D printing popular at school and college levels. The researchers and scientists are also trying to find different ways and exploring new applications related to 3D printing by critically analyzing its process parameters. Dizon et al. [9] discussed the review of work done to evaluate the mechanical properties of 3D printed parts related to tensile, bending, fatigue and various others. Antonio et al. [10] also extended it to understand the creep behavior of polycarbonate parts under the influence of certain process parameters. Now, understanding these properties is important for industrial applications and therefore it is also required to investigate how infill density affects these mechanical properties with deeper insights into the behavior of fractured surface under different loading conditions. This work proposes hands-on learning and experimentation for PLA printed specimens on FDM based 3D printers and analyses mechanical properties based on different infill densities on XY build orientation.

27.2 Hands-on Learning for Students on 3D Printers

Rapid Prototyping lab at Dayalbagh Educational Institute (DEI) provides the students a significantly deeper insight into the functioning of 3D-printing with the introduction of a new approach in the course in which an open-ended challenge is given to the students for embracing the design freedom of AM. We first ignite the mind of 3rd Year B.Tech. students during the summer term and motivating them to learn about AM (3D printing) while we simultaneous target students at 4th Year by introducing course as part of their curriculum. Courses for skill development (MEM-728, MEM-729—additive manufacturing for 3D printing) have been designed for undergraduates, which is open to student in all fields because it requires the skill and knowledge of multiple disciplines. It encompasses Mechanical Engineering (CAD, structural Design, etc.), Computer Science (Firmware development and Arduino programming), Electronics (IC's design and calibration) and Material Science (research on material properties), thus bringing students from different programs together to work on the same project inculcating in students the indispensable traits of critical thinking, communication skills, time management and self-organization and project management. This would bring a radical shift in engineering pedagogy and would also produce more 'efficient' engineers. The content was structured to train students in 'Design and Manufacture' with low cost indigenous 3D printer. To implement above objective, we have combined the lecture sessions with a sequence of workshop activities, and hands-on assignments. First module covered in the first five weeks of the class presents an overview of the AM industry and technology landscape and provides a deep understanding of the AM technologies through the use of a functional classification framework. This enables the students to realize the capabilities and limitations of current AM technology early in the semester, and foster appreciation for emerging topics addressed in later lectures. Second and Third modules are devoted to teaching the fundamentals of additive manufacturing by focusing on the cornerstone AM processes: fused deposition modeling (FDM), Stereo lithography (SLA), and selective laser sintering/melting (SLS/SLM) and covers around 38% of the overall course content. Each process is addressed in a two-lecture sequence, beginning with the fundamental mechanism of operation, main applications, and history of the technology. Occupying 30% of the course content, "Design for AM" class topics are focused on a structure similar to systematic engineering design methodologies in contemporary world. Through these efforts, we have achieved a group of undergraduate students with deep insights about AM each year. These skilled professionals not only increases the acceptance rate both among industries (whether small scale or large scale) and users for the AM technology but also can open new avenues of possibilities which have never been possible before. We asked the students to work in teams (18 students per team) to design and construct a small lowcost 3D printer having capability to print complex and flexible design at maximum accuracy, Fig. 27.1. Students acquire hands-on experience with mechatronics and process design of the 3D Printer. Research on mechanical components by attaining skills for screwing assembly, belts, shafts, rods, test of tension straps, threaded spindles, and



Design and Developed 3d printer

Fig. 27.1 3D printer evolved as part of projects developed by students

various structural design options are experimented with made of various materials (acrylic, aluminum, etc.). This enables the students to gain a better understanding of the functionality and configuration of additive manufacturing (3D printers). Some of the student groups also try to 3D print parts for testing mechanical properties under different combination of process parameters. So, this way the students also learn to optimize which combination of parameters will fetch best results related to tensile strength or compressive strength, etc. This helps in making pathways for learning while working with own hands and also understanding certain design concepts related to printed models.

The students use 3D printers constructed by them to produce parts for their fellow classmates. This results in greater depth of knowledge about working and operation of 3D Printers.

27.3 Experimentation Details

The most popular and used material extrusion technology is fused deposition modeling. FDM technology consists of equipment, which feeds a plastic filament wire into a liquefier chamber, Fig. 27.2. The molten filament which is extruded through a designed nozzle is deposited onto the platform or already extruded surface by layers where it cools into room temperature and bonding with the base material. The height of the extruded layer depends on the G-code generated by the slicing software while the width of the layer depends on the diameter of the extrusion nozzle. In present work, infill density is varied from 20 to 100% for XY orientation and mechanical properties like tensile strength, yield strength are calculated. The tensile test specimens were prepared based on ASTM D638 and standard dimensions are used corresponding to Type-1 Specimen in Fig. 27.3 and consisting of 5 specimens. The geometry of the 3D printed specimens was modeled using SolidWorks software exported as an STL file and imported to the 3D printing software. A 50 KN universal testing machine was used for tensile testing with speed of 5 mm/min and fractography was performed using scanning electron microscope (SEM). Before performing fractography tensile tested samples were cut and silver coating was done for obtaining better image analysis.

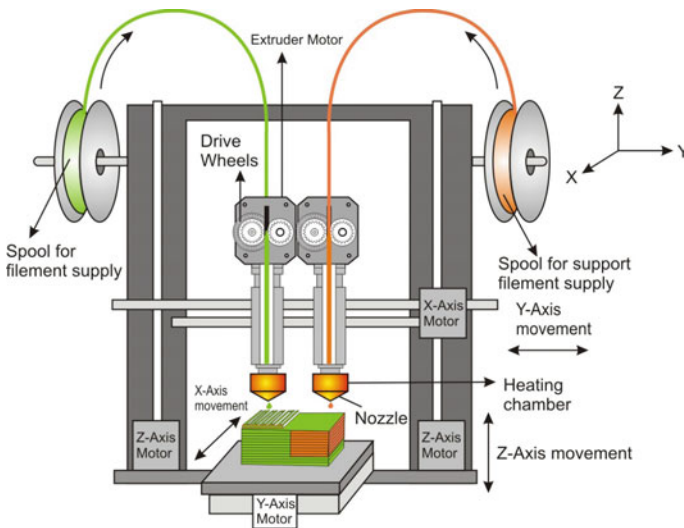


Fig. 27.2 Complete process FDM machine setup

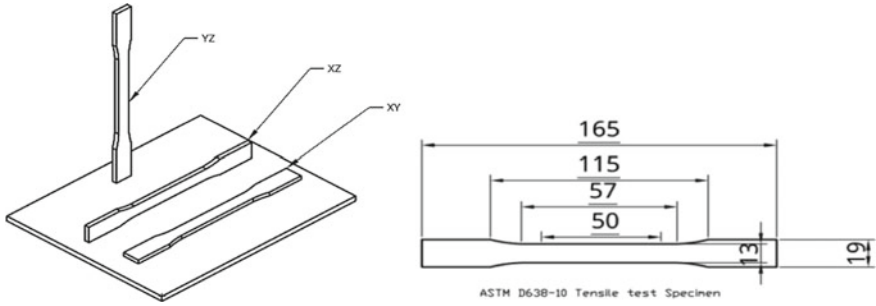


Fig. 27.3 Different build orientations XY, XZ, YZ, and ASTM D638-10 tensile test specimen

27.4 Results and Discussion

The PLA polymers have a strong correlation between infill densities and its tensile strength. These polymers find widespread applications in structural engineering where strength plays a major role. Hence, scientists and researchers are inventing new ways to increase the strength of these polymers which can then be used in various

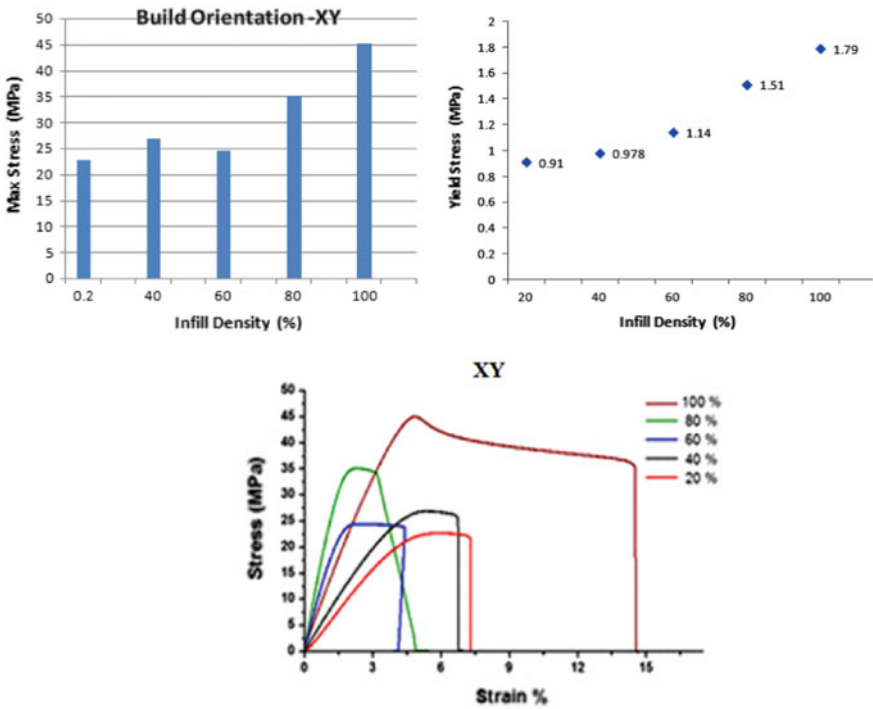


Fig. 27.4 Maximum stress and yield stress for different infill density and stress-strain curve

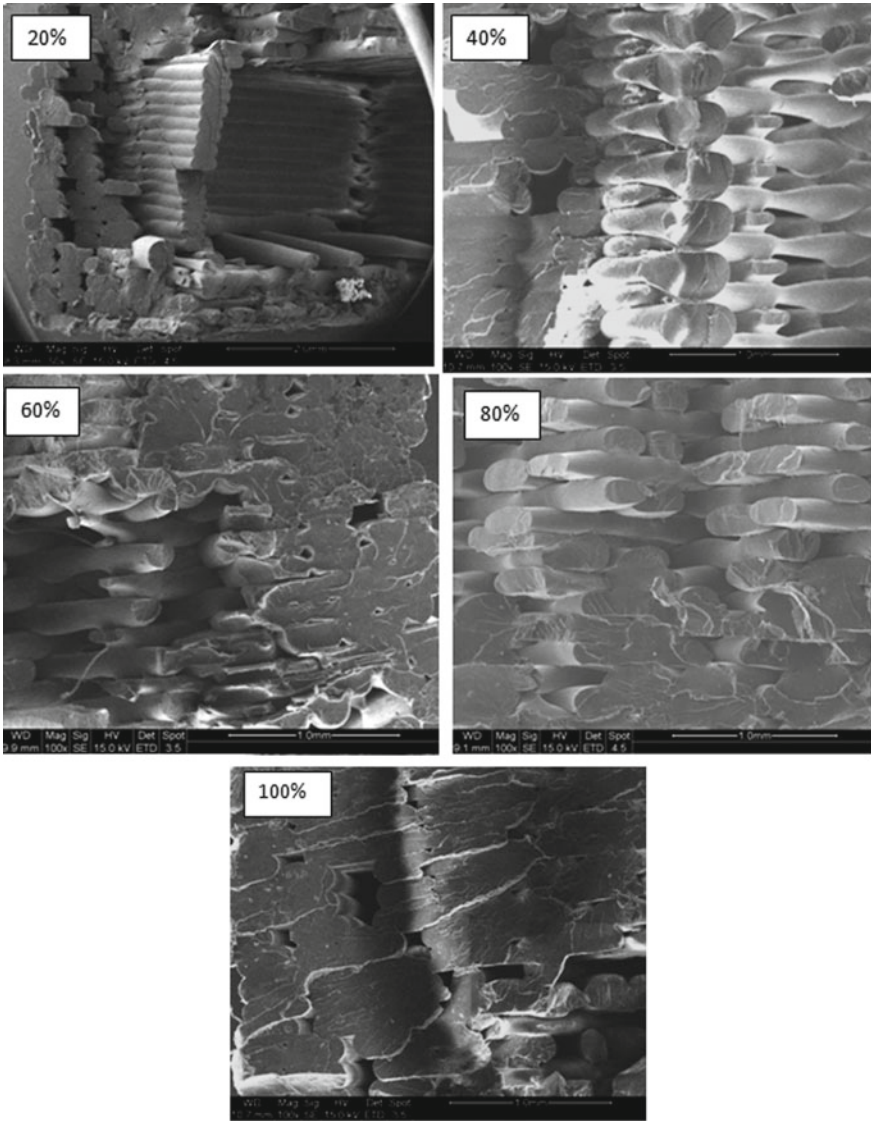


Fig. 27.5 SEM image of fractured surface for XY build orientation and different infill density

industrial applications. This work has been done to analyze the variation of tensile strength, yield strength with respect to the changes in infill densities in XY orientation. The maximum stress and yield stress in XY build orientation for different infill density is depicted in Fig. 27.4. The maximum value of stress is 45 MPa and yield stress is 1.79 MPa for 100% infill density. At 100% infill density, XY has 14.60% elongation (increase of 96%) as compared to 7.435% at 20% infill density. It is also observed that stress increases from 23 MPa at 20% infill density to 45 MPa at 100% (an increase of 95.6%). Therefore, on increasing infill density, the strength increases by a significant amount and with an added advantage of high % elongation (96%).

Understanding the fracture morphology of tensile tested specimens is important as it guides us to know the mode of failures in 3D printed specimens. Figure 27.5 shows the SEM images of the fractured surface of PLA material for different infill density. Fracture morphologies clearly indicate the difference in failure modes with respect to different infill densities in XY orientation. At 20% infill density, it is observed that the specimen is subjected to lot of rupturing of fibers which can be attributed to its low density. This pulling and rupturing slow down with increase of infill density. Also, fracture surface depicts hairline and major cracks because of large variation in infill densities. Hence, these polymers must be used in controlled or optimized parameters for obtaining maximum strength with lesser crack formation.

27.5 Conclusion

The research work outlines the following outcomes:

1. In 3D printing, at a beginner's level, students get familiar with the different parts of the printer and functioning. At the advance level, they are able to assemble a complete printer from identified components and perform experimentation.
2. The maximum value of stress is 45 MPa and yield stress is 1.79 MPa for 100% infill density.
3. The stress increases from 23 MPa at 20% infill density to 45 MPa at 100% (an increase of 95.6%). Also, the % elongation has increased from 7.435% at 20% infill density to 14.60% at 100% infill density (increase of 96%).
4. Fracture morphologies clearly indicate the difference in failure modes with respect to different infill densities in XY orientation. The microscopic view revealed the repeated failure of individual fibres by pulling and rupturing in ductile manner.

Acknowledgements The authors acknowledge the help from ACMS, IIT Kanpur for fractography analysis. Support from TEQIP-III, Faculty of Engineering, DEI is highly appreciated.

References

1. ASTM International. ASTM F2792-12a: standard terminology for additive manufacturing technologies. <http://web.mit.edu/2.810/www/files/readings/AdditiveManufacturingTerminology.pdf>. Last accessed 11 Aug 2018
2. Wohlers, T.T., Campbell, I., Diegel, O., Kowen, J.: Wohlers Report 2018, 344-page publication. Wohlers Associates, Inc., March 2018
3. Ahn, S., Montero, M., Odell, D., Roundy, S., Wright, P.K.: Anisotropic material properties off fused deposition modeling ABS. *Rapid Prototyping J.* **8**, 248–257 (2003)
4. Upcraft, S., Fletcher, R.: The rapid prototyping technologies. *Rapid Prototyping J.* **23**, 318–330 (2003)
5. Chacon, J.M., Caminero, M.A., Garcia-Plaza, E., Nunez, P.J.: Additive manufacturing of PLA structures using fused deposition modelling: effect of process parameters on mechanical properties and their optimal selection. *Mater. Des.* **124**, 143–157 (2017)
6. Sharma, R.S., Singhal, I., Gupta, S.: Innovative training framework for additive manufacturing ecosystem to accelerate adoption of three-dimensional printing technologies. *3D Printing Addit. Manuf.* **5**(2), 170–179 (2018)
7. Schelly, C., Anzalone, G., Wijnen, B., Pearce, J.: Open-source 3-D printing technologies for education: bringing additive manufacturing to the classroom. *J. Visual Lang. Comput.* **28**, 226–237 (2015)
8. Hathcock, L.: A look inside a high school MakerSpace lab. Available from <http://go.galegroup.com/ps/i.do?id=GALE%7CA392304104&v=2.1&u=gain40375&it=r&p=&sw=w&asid=690302ac6ee8dab1187a4946d1f876bb> (2014)
9. Dizon, J.R.C., Espera Jr., A.H., Chen, Q., Advincula, R.C.: Mechanical characterization of 3D printed polymers. *Addit. Manuf.* **20**, 44–67 (2018)
10. Salazar-Martin, A.G., Perez, M.A., Granada, A.A.G., Reyes, G., Puigoriol-Forcada, J.M.: A study of creep in polycarbonate fused deposition modelling parts. *Mater. Des.* **141**, 414–425 (2018)

Chapter 28

Simulation of Extrusion of Thermoplastic Binder in Additive Manufacturing Process



Sunidhi Dayam , Satwik Priyadarshi  and Puneet Tandon 

Abstract In the present work, extrusion of a thermoplastic binder through the nozzle in the Fused Deposition Modelling (FDM) process is simulated with Finite Element Analysis. In the literature, a discussion on HDPE as a thermoplastic binder is rarely found. Therefore, a study on extrusion of HDPE is required. As part of the study, extrusion of HDPE as a thermoplastic binder through a nozzle and heat-break assembly was simulated in this paper. A Multiphysics Modelling of the extrusion process was set up with the heat transfer and laminar flow solvers. It was observed that the binder reaches its melting point in 600 s. The study also establishes a relationship between different process parameters like temperature, pressure and extrusion velocity.

Keywords Additive manufacturing · Thermoplastic · Heat transfer · Fluid flow

28.1 Introduction

This paper discusses numerical simulation of polymer extrusion in Fused Deposition Modelling (FDM) process which is a type of additive manufacturing process (also known as 3D printing). In FDM process, the deposition of material by extrusion plays a major role in deciding the efficacy of the process. Extrusion of either polymers or metals is primarily governed by their thermo-fluid characteristics. Therefore, the present work covers the numerical prediction of the behaviour of thermoplastic binder while getting extruded through the nozzle through Multiphysics modelling of its thermo-fluid characteristics. Thermal residency and relationship between the pressure difference in the nozzle and fluid flow while extruding molten polymer is investigated along with analysis of the evolution of thermal gradient at the heat-break.

S. Dayam · S. Priyadarshi · P. Tandon (✉)
PDPM Indian Institute of Information Technology, Design and Manufacturing, Jabalpur, Madhya Pradesh, India
e-mail: ptandon@iiitdmj.ac.in

© Springer Nature Singapore Pte Ltd. 2020
M. S. Shunmugam and M. Kanthababu (eds.), *Advances in Additive Manufacturing and Joining*, Lecture Notes on Multidisciplinary Industrial Engineering,
https://doi.org/10.1007/978-981-32-9433-2_28

Here, the extrusion of High-Density Polyethylene (HDPE) powder, used as a binder is simulated in order to assess its suitability as a thermoplastic binder in the FDM process.

28.2 Background

Metal Additive Manufacturing (MAM) is a computer-automated process to produce metal objects from three-dimensional (3D) model data, basically, layer by layer, by joining the layers to make objects. MAM has many advantages over traditional manufacturing processes. Metal Additive Manufacturing (MAM) is expanding in many areas, such as in the automobile, aviation, and biomedical fields. Aerospace parts have complex geometries and are made from metals, such as aluminum alloys, titanium alloys, nickel alloys, which are costly, difficult and time-consuming to manufacture using conventional processes [1].

Different types of materials can be used for Additive Manufacturing (AM). Photopolymer resins are used in Selective Laser Melting (SLM), ceramic components are manufactured using Fused Deposition Modelling (FDM). Selective Laser Sintering (SLS) is commonly used to manufacture metal parts [2]. Bellini et al. [3] determined the mechanical properties of the part produced by FDM using composite filament containing ceramic and ABS. They also discussed the mechanical properties of the parts based on the orientation and path, when FDM technology is used to fabricate components for end-use. Dudek [4] developed ceramic-polymer composite material containing polyamide powder and hydroxyapatite in 1:1 and nylon polymer. The flexible filament of this new material has been successfully produced and processed using FDM process to produce sample parts. FDM method allows the use of a variety of thermoplastic materials by combining them with ceramics or metallic powders. Nikzad et al. [5] studied the melt flow analysis of an ABS-iron composite in Fused Deposition Modelling (FDM) process. A new composite material with 10% iron particles is mixed in ABS polymer matrix. The flexible filaments of the new material have been successfully produced. This filament is used to fabricate sample parts. Experiments have been done to characterize the mechanical and thermal properties. Wang et al. [6] reviewed the use of 3D printing to produce components with complex geometries. Due to limited mechanical properties of printed polymer parts, a need was felt to develop new printable materials, having high precision, and cost-effective. In spite of these developments, MAM would not replace conventional manufacturing in high-volume production; however, MAM would bring advances to the manufacturing sector by integrating with conventional manufacturing technologies. MAM techniques have progressed greatly in the recent years, but many challenges remain to be addressed, such as limited materials are available for use in MAM processes, machines use for MAM processes are costly and time-consuming. Materials research and development is required to increase the availability of materials for the selection of suitable materials for the parts to be manufactured by MAM. Very few materials

are available, which can be used in MAM processes for part fabrication, to provide the desired mechanical properties, such as mechanical strength, surface hardness, and fatigue strength.

28.3 Methodologies

The proposed process (shown in Fig. 28.1) comprises, fused deposition of metal-polymer matrix on a traditional Fused Deposition Modelling (FDM) based printer as green part, followed by sintering in a Muffle Furnace. The polymer in the matrix acts as a binder and imparts desired shape to the green part which mostly contains metal powder. After sintering, the green part becomes a pure metal part as the binder burns out while the metal powder particles fuse together as one. In order to efficiently design the process, it is essential to select a proper binder. In order to confirm selection of any polymer as binder, it is required to analyse its physical behaviour while being extruded.

High-Density Poly Ethylene (HDPE) powder was selected as the thermoplastic binder in the process being developed. HDPE being a high strength polymer imparts rigidity to the green part even when in sparse quantity. However, HDPE is rarely used in conventionally FDM process. Therefore, any substantial discussion on HDPE as a material for 3D Printing is difficult to find in literature. Therefore, scientific investigations are needed in order to assess the suitability of HDPE as a thermoplastic binder in the proposed process. As part of the aforementioned investigations, the

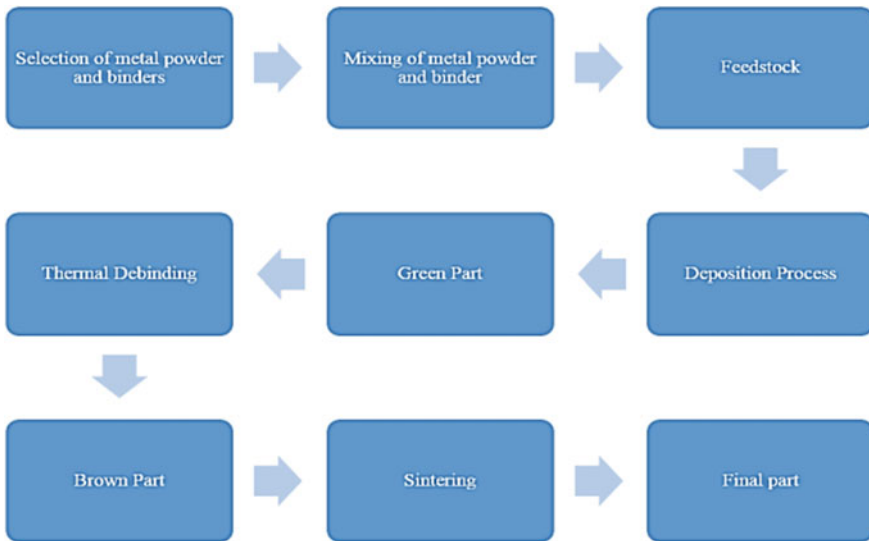


Fig. 28.1 Proposed process

present investigation aims to determine the amount of thermal residency required and the relationship between the pressure difference in the nozzle and fluid flow while extruding molten HDPE polymer.

During extrusion, heat transfer through conduction and convection and laminar fluid flow are two physical phenomena dictating the behaviour of binder being extruded. Thus, in order to simulate the physics of conjugate heat transfer and laminar fluid flow physics, a Multiphysics model was setup with the help of COMSOL, a popular Multiphysics simulation tool. Heat transfer module was used to simulate conjugate heat transfer and laminar fluid flow phenomena occurring during the extrusion process. The setup includes a brass nozzle and stainless steel (SS) heat-break, as shown in Fig. 28.2. The modelling process is described in Fig. 28.3.

As discussed, with the aforementioned materials and assembly, a Multiphysics model was developed. The model basically models two physical phenomena, (1) Conjugate Heat Transfer and (2) Laminar Fluid Flow. Modelling of both phenomena is discussed below. For defining the material properties of nozzle and heat-break, properties defined in the COMSOL Multiphysics material database was taken. The same is given in Table 28.1.

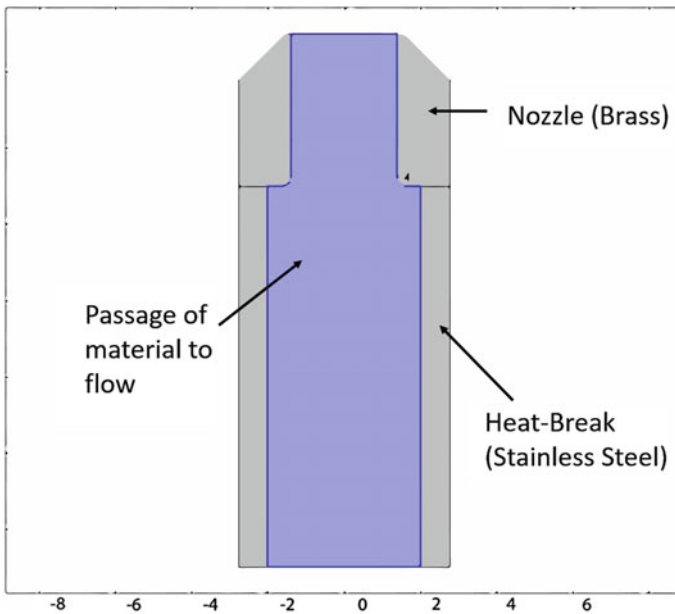


Fig. 28.2 2D geometry of the nozzle assembly

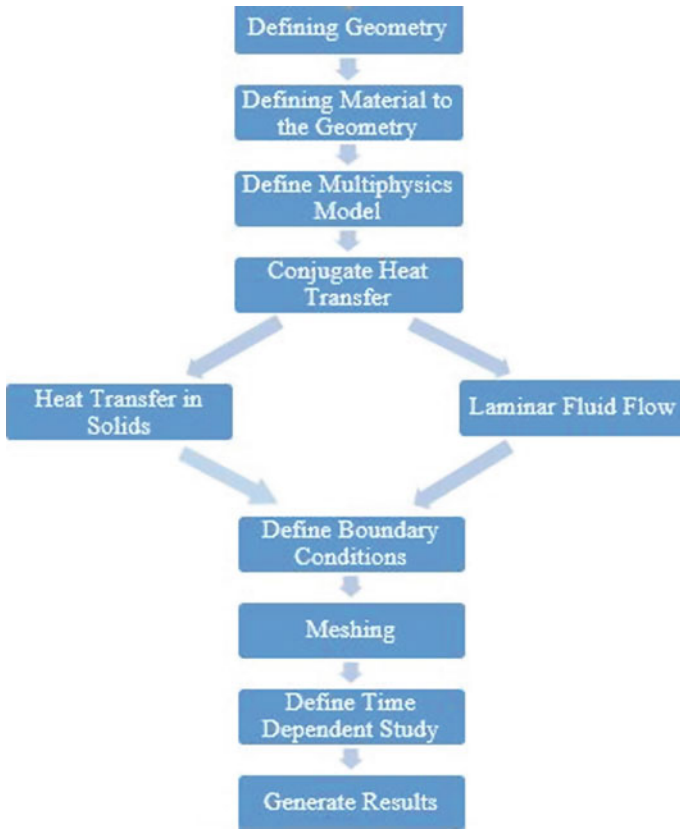


Fig. 28.3 Modelling process

Table 28.1 Material properties

	Stainless steel	Brass	HDPE
Density (kg/m ³)	7850	8525	970
Thermal conductivity (W/(mK))	44.5	109	0.51
Heat capacity (J/(kgK))	475	377	1900

28.3.1 Modelling of Conjugate Heat Transfer

In Multiphysics FEA models, heat transfer in solids and fluids are governed by the heat transfer equation

$$\rho C_p u * \nabla T = \nabla * (k \nabla T) + Q \tag{28.1}$$

where ρ is the density (kg/m^3), C_p is the specific heat capacity of the material (J/kgK), T is the temperature (K), u is fluid velocity field (m/s), and Q is heat source (W). Heating is done by an electric heating device of 25 W. The heating power is completely turned on when the nozzle heats up from room temperature. Environment temperature or room temperature was assumed as 20 °C. To reach printing temperature for HDPE of 162 °C, heating of 15 W gives stationary temperature at the nozzle tip. The complete heating power is turned on during the heating up the nozzle from room temperature.

28.3.2 Modelling of Laminar Fluid Flow

Laminar flow in the model is governed by the Navier–Stokes equation

$$\rho(u \cdot \nabla)u = \nabla \cdot \left[-pI + \eta(\nabla u + (\nabla u)^T) - \frac{2}{3}\eta(\nabla \cdot u)I \right] + F \quad (28.2)$$

$$\nabla \cdot (\rho u) = 0, \text{ continuity equation for a compressible fluid} \quad (28.3)$$

where, ρ is the density, u is the flow velocity, ∇ is the divergence, p is the pressure, I is the identity matrix, and η is the dynamic viscosity of the fluid. In the extruder, HDPE starts to flow as soon as the melting point is reached in the heat-break just before entering the nozzle. From this point, simulation of the fluid flow is started. Some key assumptions were taken while defining the model. The assumptions allow simplifying the modelling process without compromising with the accuracy of the simulation. They are listed as follows:

- (a) The flow is assumed to be incompressible and laminar within the nozzle.
- (b) A constant overall heat transfer coefficient of 15 $\text{W}/(\text{m}^2\text{K})$ is assumed based on the data from the engineering toolbox.
- (c) Environment temperature was assumed as 20 °C.
- (d) The flow of HDPE starts as soon as the temperature of heat-break reaches the melting point of HDPE, i.e., 162 °C.

28.4 Results

28.4.1 Heat Distribution

It was observed that the temperature of nozzle achieved the steady-state within 600 s of heating. The 2 dimensional (2D) study of conjugate heat transfer predicted the temperature distribution at the nozzle and heat-break. The prediction ranged from

20 °C at 0 s to 172.68 °C after 600 s of heating. Figure 28.4a, b show the temperature distribution at 0 and 600 s respectively. The temperature distribution curve for at 0 s is shown in Fig. 28.4c and the same for 600 s is shown in Fig. 28.4d. In parallel to 2D study a 3 dimensional (3D) study was also performed. The 3D study predicted that the temperature distribution at the nozzle and heat-break. The prediction ranged from 20 °C at 0 s to 199.17 °C after 600 s of heating. Same is shown in Fig. 28.5a, b respectively. Figure 28.6a, b show the curves obtained from the 3D study of temperature distribution in the nozzle and the heat-break at 0 s and at 600 s respectively. From 2D and 3D studies discussed above, it can be observed that the temperature increases gradually from 20 to 199.17 °C in 600 s. This leads to the conclusion that the thermal residency for HDPE in the given process is 600 s.

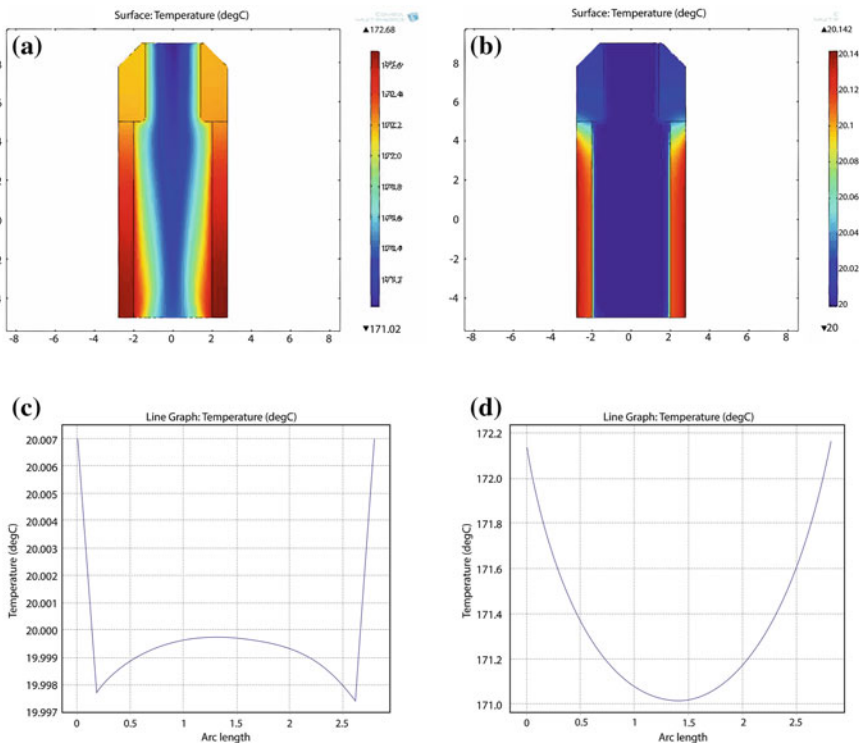


Fig. 28.4 a 2D study predicts the temperature distribution at the nozzle at zero second, b 2D study predicts the temperature distribution at the nozzle at 600 s, c 2D study of temperature distribution at zero sec, d 2D study of temperature distribution at zero sec

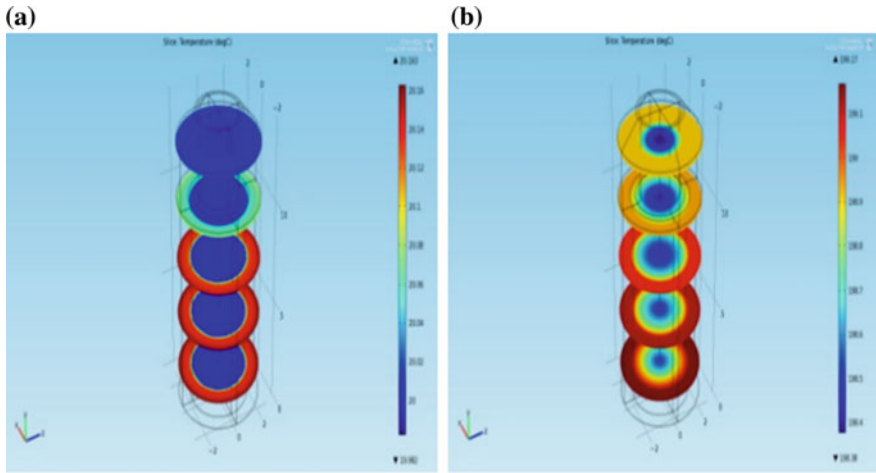


Fig. 28.5 a 3D study predicts the temperature distribution at the nozzle at zero second, b 3D study predicts the temperature distribution at the nozzle at 600 s

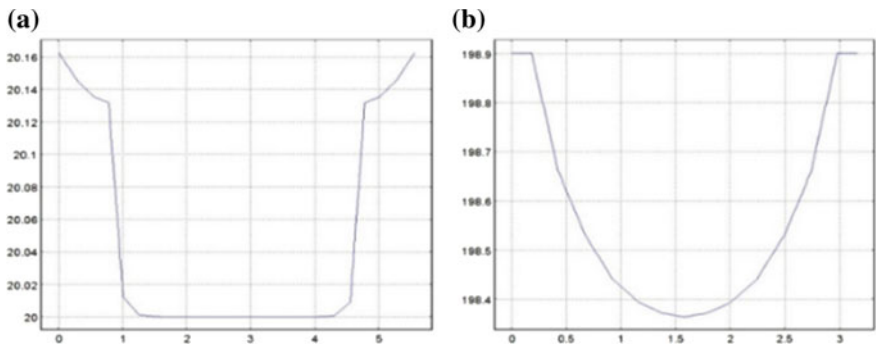


Fig. 28.6 a 3D study of temperature distribution at zero sec, b 3D study of temperature distribution at 600 s

28.4.2 Fluid Flow

The flow velocity of the material at the tip of the nozzle is predicted as 5.1206 and 6.5421 mm/s by 2D study and 3D study respectively. The predictions are visually elucidated in Fig. 28.7a, b respectively. The curves of the velocity distributions of the HDPE in the nozzle, obtained via 2D and 3D studies, are shown in Fig. 28.7c, d respectively. It can be concluded from aforementioned studies that the velocity of HDPE is maximum at the tip of the nozzle and minimum near the edges. The graph of fluid velocity towards the nozzle tip generates a parabolic curve. When the pressure at the nozzle inlet and nozzle outlet is changed from 3 to 10 atm, a change in velocity distribution is also observed. This leads to the conclusion that the flow

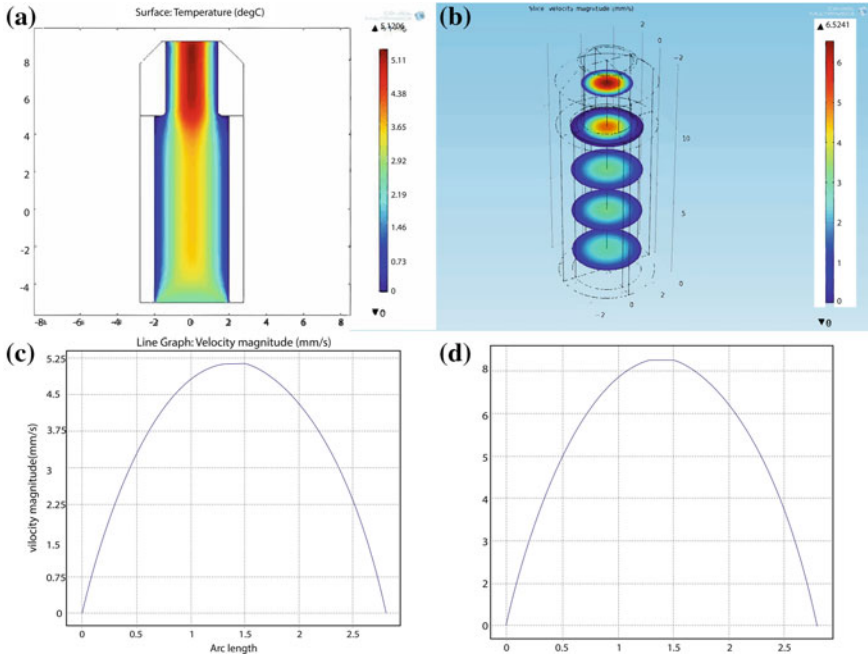


Fig. 28.7 **a** 2D study predicts the velocity of the fluid at the tip of the nozzle, **b** 3D study predicts the velocity of the fluid at the tip of the nozzle, **c** 2D study of velocity distribution of the HDPE in the nozzle, **d** 3D study of velocity distribution of the HDPE in the nozzle

velocity depends on the applied pressure. Therefore, it can be said that in order to control the velocity flow of the HDPE, pressure at the inlet of the nozzle should be controlled. This further means that the fluid flow is controlled by a pressure difference between the inlet and outlet causing a characteristic parabolic velocity distributions shown in Fig. 28.7c, d as would be supposed by the law of fluid dynamics.

28.5 Conclusions

Simulation results give valuable insight into the physical behaviour of the binder while being extruded. It also allows predicting relationships between process parameters like extrusion velocity, temperature and pressure. Both 2D and 3D studies show that after 600 s, the temperature at the nozzle reaches approximately 200 °C, which is above the melting point of the thermoplastic HDPE. Thus, it infers that after 600 s of heating, the material starts flowing from the nozzle. The temperature gradient changes greatly at the heat-break, causing the HDPE to melt easily and prevent any thermal degradation. From the simulations, it was observed that the velocity of the flow is directly proportional to the pressure applied for extrusion. Therefore, it can

be said that by manipulating pressure difference between inlet and outlet, the fluid flow can be controlled.

References

1. Huang, Y., Leu, M.C., Mazumder, J., Donmez, A.: Additive manufacturing: current state, future potential, gaps and needs, and recommendations. *J. Manuf. Sci. Eng.* **137**(1), 014001 (2015)
2. Cao, W., Miyamoto, Y.: Freeform fabrication of aluminum parts by direct deposition of molten aluminum. *J. Mater. Process. Technol.* **173**(2), 209–212 (2006)
3. Bellini, A., Güçeri, S.: Mechanical characterization of parts fabricated using fused deposition modeling. *Rapid Prototyping J.* **9**(4), 252–264 (2003)
4. Dudek, P.: FDM 3D printing technology in manufacturing composite elements. *Arch. Metall. Mater.* **58**(4), 1415–1418 (2013)
5. Mostafa, N., et al.: A study of melt flow analysis of an ABS-Iron composite in fused deposition modelling process. *Tsinghua Sci. Technol.* **14**, 29–37 (2009)
6. Wang, X., Jiang, M., Zhou, Z., Gou, J., Hui, D.: 3D printing of polymer matrix composites: a review and prospective. *Compos. B Eng.* **110**, 442–458 (2017)

Chapter 29

Investigations on Synthesis of Porous NiTi Shape Memory Alloy Structures Using Selective Laser Melting Techniques



A. Sahu , I. A. Palani , Sachin Bhirodkar , C. P. Paul 
and K. S. Bindra 

Abstract Additive manufacturing is an attractive and promising manufacturing technology in fabricating nitinol (NiTi) structures. NiTi physical mixture was synthesized from elemental powder mixture of nickel and titanium by selective laser melting process. The NiTi physical mixture was used to fabricate porous nitinol structure. The composition of intermetallic phases obtained in SLM-synthesized samples has been studied using X-ray diffraction (XRD) technique and the microstructure of the deposited samples is probed through scanning electron microscopy (SEM). It has been observed that the physical mixture NiTi-5P (5 laser scans) exhibits superior textural properties (97% enhancement in porosity) as compared to NiTi-3P (3 laser scans).

Keywords NiTi · Selective laser melting

29.1 Introduction

Nickel-titanium (NiTi) shape memory alloys (SMA) developed from additive manufacturing (AM) processes are gaining significant interest recently. Due to its unique properties like superelasticity, shape memory effect, high strength, excellent ductility, high damping capability, wear resistance and corrosion resistance, NiTi is a promising structural material for the fabrication of active smart structures for various functional applications [1]. It is well known that processing and machining NiTi

A. Sahu · I. A. Palani (✉) · S. Bhirodkar
Department of Mechanical Engineering, Indian Institute of Technology Indore, Indore 452020,
Madhya Pradesh, India
e-mail: palaniia@iiti.ac.in

A. Sahu
e-mail: ankitasahu100@gmail.com

C. P. Paul · K. S. Bindra
Laser Development and Industrial Applications Division, Raja Ramanna Centre for Advanced
Technology, Indore 452013, India

Homi Bhabha National Institute, Anushakti Nagar, Mumbai 400078, India

© Springer Nature Singapore Pte Ltd. 2020
M. S. Shunmugam and M. Kanthababu (eds.), *Advances in Additive Manufacturing
and Joining*, Lecture Notes on Multidisciplinary Industrial Engineering,
https://doi.org/10.1007/978-981-32-9433-2_29

to generate complex geometries is a difficult task [2]. Further, the distinct properties of NiTi alloy such as high ductility and superelasticity are highly sensitive to its phase transformation temperatures, makes its machining difficult through conventional manufacturing techniques [3, 4]. In this aspect, selective laser melting (SLM) is a laser-based additive manufacturing process considered to be a novel manufacturing technology towards creating porous NiTi structures [5, 6]. Krishna et al. observed from the microstructure of NiTi structures fabricated through laser engineered net shaping (LENS) that the pore diameter varied from 60 to 800 μm [7]. It is reported in Haberland et al. that low energy inputs (50 J/mm^3) result in large pore size, 500 μm , in SLM fabricated NiTi samples [5]. Significant pores and balling effect were observed on certain SLM NiTi structures fabricated using repetitive laser scanning by Khoo et al. [6]. However, detailed analysis on porosity measurement and pore formation was not revealed from the literature. AM material has prospective for tailoring the SMA behaviour by controlling the microstructure which is not possible through conventional NiTi fabrication methods [8]. It is worth noticing that, AM makes the fabrication of highly complex parts simple and easy due to its facile process designing. Especially, truss-like structures, hollow parts, and porous structures can be fabricated within an hour. Therefore, this process offers the potential to design and develop porous NiTi parts for various manufacturing applications. The present paper primarily aims at synthesizing porous NiTi structures for smart actuating applications from elemental nickel and titanium powders using SLM technique. The investigation has been done with three and five laser scans or passes over the NiTi powder bed.

29.2 Experimental Details

For the experiments, titanium plate with dimension of $100 \times 100 \times 10 \text{ mm}^3$ was used as a substrate material. The nickel and titanium powders used in the experiment had good fluidity with particle size of 74 μm . The experiments were carried out using a Ytterbium fibre laser system (Scantech—Pro-Mark F50-150) that could supply power between 0 and 50 Watts at 1064 nm wavelength. The pictorial view of the SLM system used in experiment was shown in Fig. 29.1. Equal amounts of nickel and titanium powders were taken and mixed in a 3D powder blender (Hexagon-Alphaie-3). Initially, nickel and titanium powders were separately put on the substrate and the desired pattern was drawn on the computer screen. The laser scans the pattern on the powder layer. Similar procedure was adopted for the Ni-Ti powder mixture on the titanium plate. The synthesized NiTi physical mixture was designated as NiTi-3P, NiTi-5P (as per the number of laser scans) throughout the manuscript. Figure 29.2 shows the deposited Ni powder, Ti powder and NiTi physical mixture on Ti substrate. The layer thickness was 1 mm. Table 29.1 shows the various process parameters that were used during this experiment. The phase composition of the deposited samples was studied by X-ray diffraction on a Rigaku X-Ray diffractometer using Cu-K α radiation and microstructural characterization was conducted using the Zeiss Supra55 scanning

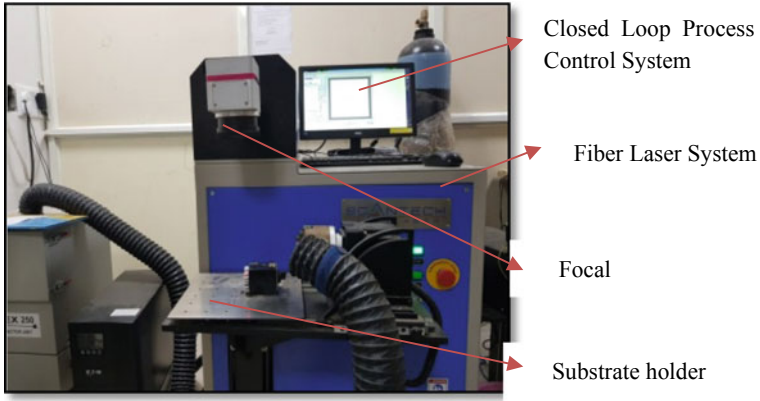


Fig. 29.1 Pictorial view of Selective Laser Melting System

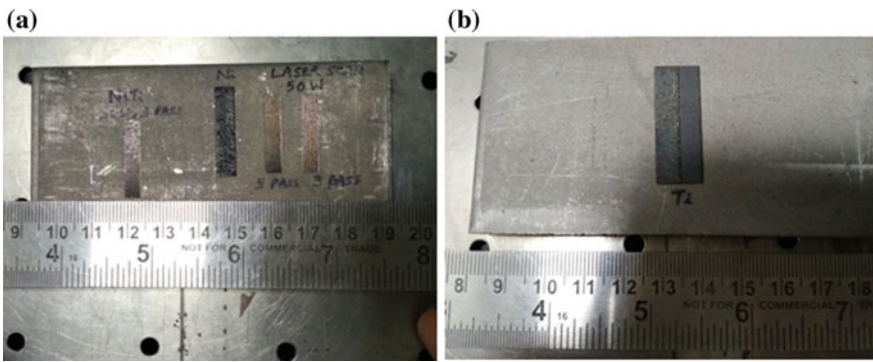


Fig. 29.2 Pictorial view of **a** Ni powder and NiTi physical mixture, **b** Ti powder, deposited on Ti plate

Table 29.1 Process parameters for deposition of Ni, Ti and Ni–Ti powders on Ti

Parameters	Unit	Range
Laser Power	W	50
Scan speed	bits/ms	50
Number of passes	–	3 and 5
Powder layer thickness	mm	1

electron microscope (SEM). The textural properties (surface area, pore volume, pore size) of the studied powders were determined using a Quantachrome Autosorb IQ2 TPX automated gas sorption system.

29.3 Results and Discussion

29.3.1 Surface Morphological Analysis

The microstructure of laser-scanned nickel and titanium powders are shown in Fig. 29.3a, b respectively. It can be clearly seen that nickel deposited sample exhibits more number of pores as compared to titanium one presumably due to the higher electron affinity of nickel towards oxygen. The stronger affinity towards oxygen, results in formation of nickel oxides. Figure 29.3c, d shows the FESEM image of NiTi physical mixture in as-deposited state. It should be noted that there is a variation in grain size across the sample section, which is due to variation in cooling rates during powder melting. Laser processes are characterized by high cooling rates. The formation of fine grain structure at some regions is attributed to the rapid cooling rates due to complete melting of powder at those regions. The light and dark shaded regions may be corresponding to NiTi and NiTi₂ phases respectively as evidenced from literature [2]. The bright features might be Ni₄Ti₃, Ni₃Ti, and Ni_{2.67}Ti_{1.33} metastable intermetallic phases which indicate the presence of some Ni-rich undesirable phase in the sample. However, NiTi-3P and NiTi-5P exhibit coarse mud like morphology with heterogeneous pores clearly observed in Fig. 29.3e, f. The creation of pores is independent of laser scan speed and power.

29.3.2 Structural Analysis

Figure 29.4a, b and c shows the XRD plot for nickel powder, titanium powder, and nickel-titanium physical mixture respectively. Processing conditions were kept the same for all the three samples. It is observed that some nickel oxide and titanium oxide peaks are formed which is probably due to the deposition carried out in an open atmosphere. In nickel XRD plot, cubic lattice is observed throughout the entire scan range, while for titanium we got hexagonal, cubic and tetragonal lattice for Ti, TiO and TiO₂ peaks respectively. Nitinol XRD plot shows that it has a large amount of intermetallic phases such as Ni₃Ti, Ni₄Ti₃ and Ni_{2.67}Ti_{1.33} which have been shown in literature [2, 9]. An additional metastable intermetallic phase NiTi₂ is present [2]. Nitinol is represented by its martensite phase with a monoclinic lattice (110 and 111 reflections) that appears due to laser remelting. Since the SLM process is not carried out in a purged environment, it leads to the formation of these precipitates.

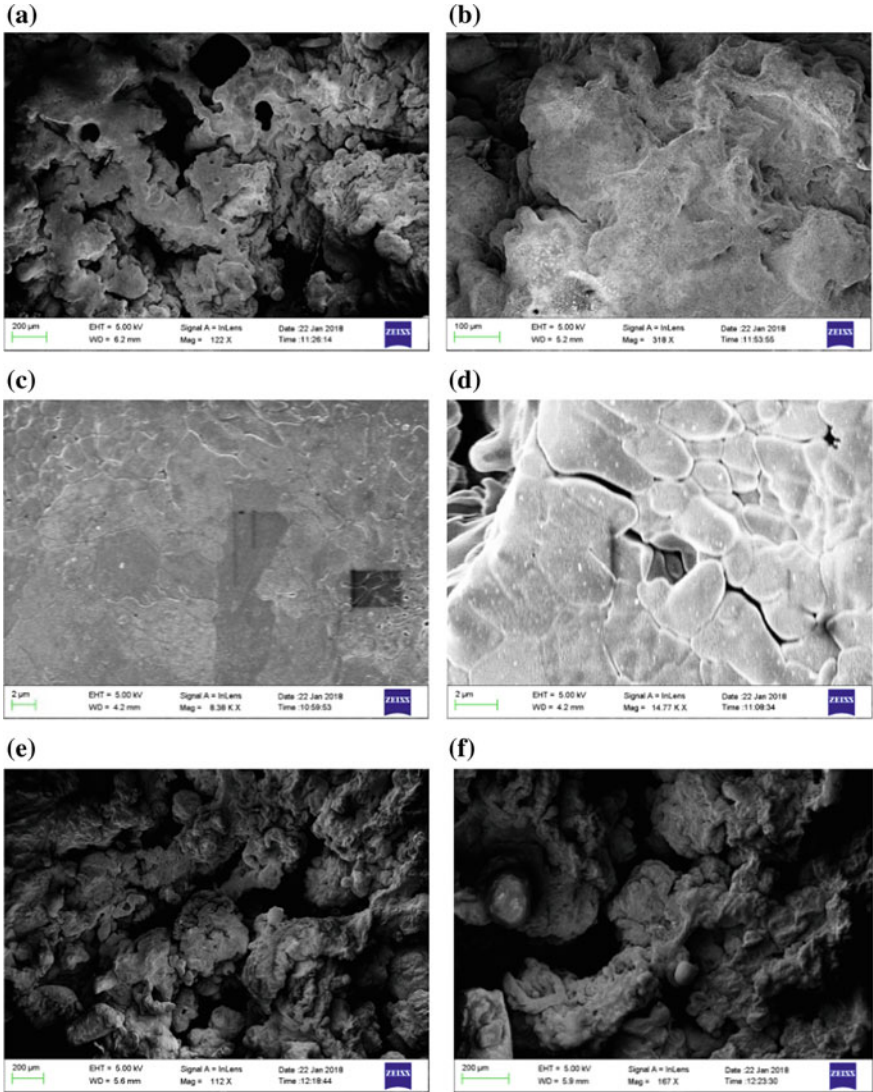


Fig. 29.3 FESEM micrographs of various metals deposited on Ti plate **a** Ni, **b** Ti, **c**, **d** NiTi physical mixture, **e** NiTi-3P and **f** NiTi-5P

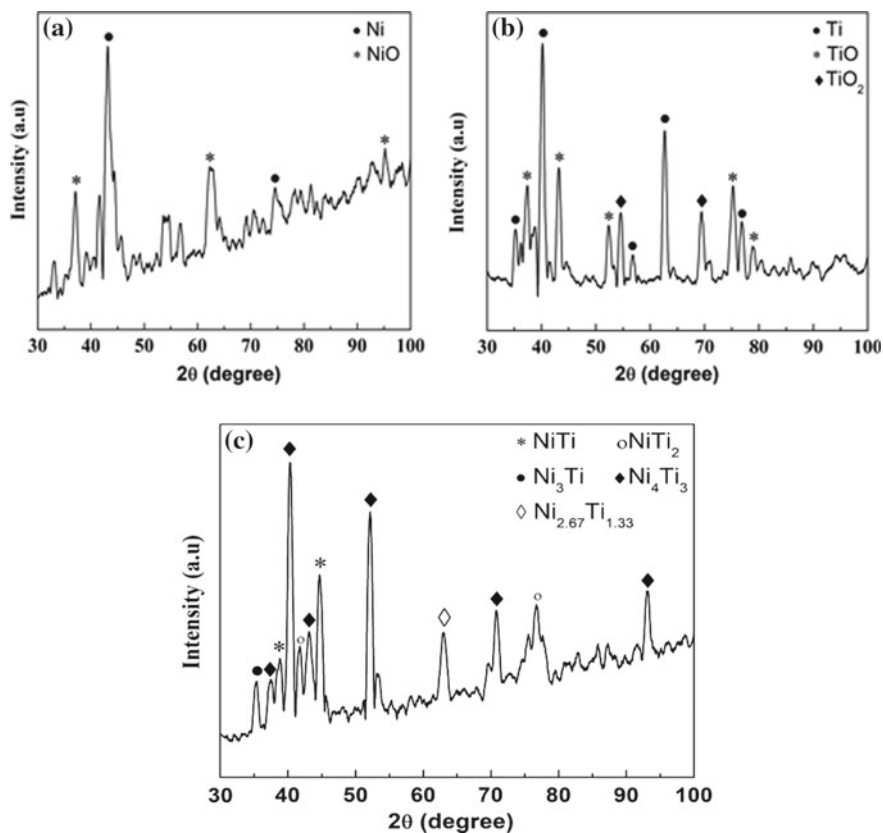


Fig. 29.4 a–c XRD patterns of various metallic powder deposited on Ti plate **a** Ni, **b** Ti and **c** NiTi physical mixture

29.3.3 Physicochemical and Textural Properties

Table 29.2 listed the physicochemical and textural characteristics of NiTi-3P and NiTi-5P derived from N_2 adsorption isotherm at 77 K. Brunauer-Emmett-Teller (BET) surface area was calculated using data obtained from N_2 adsorption isotherms at 77 K in a relative pressure (P/P_0) ranging from 0.05 to 0.30. In addition to the above, total pore volume was calculated from the amount of adsorbed N_2 at P/P_0

Table 29.2 Physicochemical and textural properties of NiTi-3P and NiTi-5P

Sample	BET Surface area (m ² /g)	Total pore volume (cc/g)	Average pore diameter (nm)	Porosity (%)
NiTi-3P	1.68	0.0065	15	7.27
NiTi-5P	8.90	0.0128	5.7	14.32

= 0.99 using single point adsorption method. Similarly, the average pore diameter (APD) was calculated from BET model considering both adsorption and desorption isotherm. Before the experiment, the studied materials were degassed at 150 °C for 6 h. From the Table 29.2, it can be observed that NiTi-5P exhibits superior textural properties (surface area, porosity) as compared to NiTi-3P suggesting that, with increasing laser scan pass, the physicochemical properties have enhanced.

29.4 Conclusions

- NiTi physical mixture was synthesized from elemental powder mixture of nickel and titanium by selective laser melting process.
- From the XRD plots, it was revealed that the sample that was deposited had a high amount of secondary phases. Depositions carried out in an open environment in the presence of oxygen attributes to the formation of these precipitates.
- The synthesized NiTi-5P attributed high physicochemical and textural properties as compared to NiTi-3P.
- Attempts are being carried out to do the experiments in a closed chamber with purged argon to prevent the oxygen contamination, which will be the future scope of the current experiment.

Acknowledgements The authors gratefully acknowledge the characterization facilities provided by the Sophisticated Instrumentation Centre (SIC), Indian Institute of Technology Indore for this study. The authors are grateful to Mr. Debashis Panda for his technical support in BET analysis. Ankita Sahu's sincere thanks to MHRD, Government of India, for providing her with financial support.

References

1. Shishkovsky, I.V., Yadroitsev, I.A., Smurov, IYu.: Manufacturing three-dimensional nickel titanium articles using layer-by-layer laser-melting technology. *Tech. Phys. Lett.* **39**(12), 1081–1084 (2013). <https://doi.org/10.1134/S1063785013120250>
2. Halani, P.R., Shin, Y.C.: In situ synthesis and characterization of shape memory alloy nitinol by laser direct deposition. *Metall. Mater. Trans. A* **43A**, 650–657 (2012). <https://doi.org/10.1007/s11661-011-0890-x>
3. Weinert, K., Petzoldt, V., Kotter, D., Buschka, M.: Drilling of NiTi shape memory alloys. *Mater. Sci. Eng. Technol. A* **35**(5), 338–341 (2004). <https://doi.org/10.1002/mawe.200400752>
4. Hassan, M.R., Mehrpouya, M., Dawood, S.: Review of the machining difficulties of nickel titanium based shape memory alloys. *Appl. Mech. Mater.* **564**, 533–537 (2014). <https://doi.org/10.4028/www.scientific.net/AMM.564.533>
5. Haberland, C., Elahinia, M., Walker, J.M., Meier Hand Frenzel, J.: On the development of high quality NiTi shape memory and pseudoelastic parts by additive manufacturing. *Smart Mater. Struct.* **23**, 1–13 (2014). <https://doi.org/10.1088/0964-1726/23/10/104002>

6. Khoo ZX, Liu Y, Low ZH, An J, Chua CK and Leong KF (2018) Fabrication of SLM NiTi shape memory alloy via repetitive laser scanning. *Shape Mem. Superelasticity*. <https://doi.org/10.1007/s40830-017-0139-7>
7. Krishna, B.V., Bose, S., Bandyopadhyay, A.: Fabrication of porous NiTi shape memory alloy structures using laser engineered net shaping. *J. Biomed. Mater. Res. B Appl. Biomater.* **89**, 481–490 (2009). <https://doi.org/10.1002/jbm.b.31238>
8. Hamilton, R.F., Bimber, B.A., Palmer, T.A.: Correlating microstructure and superelasticity of directed energy deposition additive manufactured Ni-rich NiTi alloys. *J. Alloy. Compd.* **739**, 712–722 (2018). <https://doi.org/10.1016/j.jallcom.2017.12.270>
9. Shishkovsky, I., Yadroitsev, I., Smurov, I.: Direct selective laser melting of nitinol powder. *Physics Procedia* **39**, 447–454 (2012). <https://doi.org/10.1016/j.phpro.2012.10.060>

Chapter 30

Application of Low-Cost Natural Binders in Direct 3-D Printing of Sand Molds



Madhvendra Tiwari, Devanshu Kathrecha, Kuldeep Meena, K. A. Desai and A. K. Plappally

Abstract Layered Manufacturing enabled the direct production of sand molds and cores by selective injection of binding agents into sand layer. These binding agents are chemically reactive and have significantly higher cost in comparison to Bentonite clay used in routine foundry work. These binders also need special mechanism for printing and storage which result into increased equipment cost. The present study explores feasibility of using low-cost natural binding agent, orange peel powder as an alternative to chemical binders. A preliminary framework for layered manufacturing of standard sand testing samples employing natural binders is developed. Some of the important mold properties such as mold hardness, mold permeability and green compressive and shear strength are evaluated. The results are compared with standard sand testing specimen prepared using conventional binding agents. It has been observed that the mold hardness and strength properties of layered mold using orange peel powder are significantly better. The outcomes of this preliminary study are quite encouraging and further work will focus on investigating reasons for improved sand mold properties and development of low cost layered manufacturing equipment for direct printing of sand molds.

Keywords Sand casting · Layered manufacturing · Binding agent · Mold hardness

30.1 Introduction

Sand Casting is one of the most economical processes employed for manufacturing of metallic objects since ancient era. The process is versatile and it can handle great variety of metals, sizes and complexity in manufactured components. Sand Casting process uses sand along with Bentonite clay and moisture as a mold material. A pattern matching the final product is required to make the cavity in two or more flasks known as molding boxes. These boxes are then joined together to form a hollow

M. Tiwari · D. Kathrecha · K. Meena · K. A. Desai (✉) · A. K. Plappally
Department of Mechanical Engineering, Indian Institute of Technology Jodhpur, Karwad, Jodhpur 342037, India
e-mail: kadesai@iitj.ac.in

© Springer Nature Singapore Pte Ltd. 2020
M. S. Shunmugam and M. Kanthababu (eds.), *Advances in Additive Manufacturing and Joining*, Lecture Notes on Multidisciplinary Industrial Engineering,
https://doi.org/10.1007/978-981-32-9433-2_30

337

cavity and molten metal is poured into it. The metal then solidifies and the mold is broken to get the final product. The intricate design requirement in the final product cannot be made by patterns and additional components, e.g., core will be necessary. Sand Casting consumes significant amount of time in preparatory stages, e.g., pattern making, mold making, core production, curing, etc. The complexity of manufactured components and need to produce in small batches add further challenges related to time and cost optimization for sand casting industries.

3-D printing or Layered Manufacturing technologies emerged as a new manufacturing method in late twentieth century and its applications were explored by various researchers to solve challenges of casting industries. Layered Manufacturing fabricate components using layer-by-layer deposition and it has been successfully employed in fabrication of molds, cores, and patterns which were otherwise impossible to fabricate. The application of Layered Manufacturing in casting industry provided ease of fabricating complex geometries, improved dimensional accuracy and increased freedom in the design of delivery components such as gating system and riser [1]. One of the most popular commercial solution is developed by ExOne for Layered Manufacturing of 3-D molds which uses Binder Jetting Technology. The process uses a chemical binder (mainly No-Bake FURAN) which is selectively deposited using a nozzle. No-Bake FURAN is one of the most commonly used binder which is colorless volatile liquid with planar unsaturated five-membered ring in its molecule. Studies were made on the final product manufactured using mold produced by this process and it has been observed that these components exhibit better properties in terms of tensile strength, surface roughness and AFS Grain Fineness number (GFN) [2]. Cold Hardening Phenol was also thought as an alternate binder for this process which exhibited various advantages over No-Bake FURAN [3]. These binders are chemically reactive and have significantly higher cost in comparison to Bentonite clay used in normal sand casting operation. These binders also require special mechanism for printing and storage which result into increase in the machine cost. The molds manufactured using this process does not have sufficient strength for heavyweight alloys like cast iron [4].

A similar process which uses plaster or starch-based powdered material during printing of mold or mold inserts was also proposed and it was termed as Z-cast process [5]. The process was employed as an alternate to investment casting and molds were manufactured for lightweight alloys such as Aluminum A356 and Zinc ZA-12. It has been observed that investment cast components exhibit better surface finish but Z-cast process can be used to make a molds with very thin walls [6]. Layered Manufacturing technique using Selective Laser Sintering was also used to cure the sand and printing of the molds [7]. The mold properties were investigated using statistical design of experiment and mathematical model was developed to optimize the strength and permeability of mold as a function of curing rate and temperature. It has been observed that the surface roughness of mold produced using this approach is not good for sand casting application and post-processing operations are necessary. Another study suggested the use of dual coating process to improve mold strength and hardness [8]. The process uses coating of multiple layers of polyvinyl alcohol on

the walls of 3-D printed molds. It results in increase of surface hardness and shows fine grain structure of cast components.

Based on review of previous studies exploring application of Layered Manufacturing technique in manufacturing of sand molds, it has been realized that majority of these solutions are costly due to expensive and unstable binders used in the process. It is also observed in few studies that the properties of these binders are not suitable and economical for sand casting. The present study aims at exploring the application of low-cost binders which can be used in direct 3-D printing of sand molds. Some studies are reported in the literature regarding use of chemical bonding agent in green sand molds [9]. It has been shown that the mechanical properties of chemically bonded molds are superior in comparison to conventional green sand molds made with bentonite clay as binding agent. Based on preliminary study of various binding properties, some of the popular organic sorbents were explored for its application as binder in sand casting process. It has been realized that various organic sorbents such as Xanthate, Zeolite, Bentonite clay, Peat Moss, Orange peel, etc. exist in nature and have high absorption capacity.

The present study explores application of Orange peel powder as a low-cost organic binder which can be extracted directly from the waste of orange fruits [10]. The orange peel can act as a sorbent which can be helpful in developing bond between different layers of sand. Orange peel is used as a preparation of high dietary fiber powder in food industry. It is also used in medical industries for making facial products. It is organic and not-reactive in comparison to other binding agents. It is chemically less reactive and its usage is not harmful for health [11]. Orange peel composites were studied in literature and their interfacial behavior is well explained [12]. The composites made of orange peel powder reinforced epoxy exhibited maximum strength at 20% mass fraction of orange peel in composite while its hardness was maximum at 30% mass fraction of orange peel. The flexural strength for orange peel reinforced epoxy composites was also studied and SEM image of loaded part showed good bonding between fiber and matrix [12]. Henceforth, the chapter is organized as follows; Sect. 30.2 discusses details of experimental work along with test set up proposed for manufacturing of layered molds. Section 30.3 presents comparison of mold properties for conventional green sand molds and layered molds along with results of image analysis used in determining particle size distribution. The chapter ends with summary of conclusions from the present study in Sect. 30.4.

30.2 Experimental Investigations

A series of experiments have been carried out to investigate the effect of using orange peel powder as binding and activating agent on mold properties such as green compression strength, green shear strength, mold hardness, and mold permeability. In order to assess the effectiveness of orange peel powder in improving properties, two combinations of mold are compared; conventional green sand mold and orange peel activated 3-D printed sand mold. This section presents details of experimental

set developed for fabrication of 3-D printed sand molds followed by experimental results related to determination of mold properties for both variants.

30.2.1 Experimental Set Up

An experimental setup has been designed for layered manufacturing of sand molds. The setup is capable of depositing uniform sand layer throughout the cross-section with control of layer thickness by generating compressive pressure using screw-nut mechanism. The binder can be selectively applied depending on the areas that are to be fused. The aim of present study is to prepare standard mold samples to evaluate various mold properties therefore, the binder is applied uniformly throughout the mold cross-section area. A molding box of 50 mm diameter circular cross-section with suitable thickness has been chosen in the study to produce sand molds using layered manufacturing. A metallic platform of 50 mm diameter and 10 mm thickness was attached at the end of threaded bar to apply uniform compressive force on the sand layer. The screw-nut mechanism achieves definite linear movement for generating required layer thickness.

Few trial experiments were carried out using this set up for normal green sand sample with Bentonite clay as binder and moisture as binding agent. It has been realized that determination of mass in each layer is crucial in deciding compressive force and thereby bonding strength. The thickness of single-layer was fixed at 2.5 mm and mass to be deposited in each layer was varied to achieve required density with compaction. A simple mathematical relationship is established to determine density at given compaction for known mass and layer thickness. Based on this relationship, required mass to be deposited in the molding box and movement of platform to generate required compaction can be determined. The process repeats in a similar manner to generate layered mold of required height i.e. 50 mm.

30.2.2 Specimen Preparation for Conventional Green Sand Mold

Using standard experimental setup consisting of sand rammer and other associated equipment, conventional green molds were made using silica sand, Bentonite clay, and water. The samples were tested for various mold properties such as green compression strength, green shear strength, mold hardness and mold permeability as per standard testing procedure. It is well established that varied content of clay and water affects these properties significantly therefore, various combinations were tried to determine the ideal composition for comparison. The amount of Bentonite clay was varied at the levels of 5, 10, and 15% by mass fraction. The amount of water content was varied at levels of 5, 7, 10 and 15% of mass fraction. The GFN of silica sand

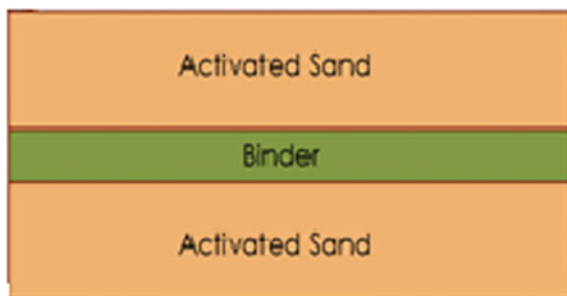
is maintained constant at 60 during all experiments which are commonly used in casting industries. Based on comparison of various mold properties, the ideal mold composition was found to have Silica sand (80% by Mass), Water (7% by Mass), Bentonite Clay (13% by Mass) and it is used for comparison with layered mold subsequently.

30.2.3 Specimen Preparation for Orange Peel Activated Molds

The second set of experiments were conducted by preparing mold samples using experimental set up proposed in Sect. 30.2.1. The set up uses activated sand mixture in one layer and binder paste in the subsequent layer. Figure 30.1 shows conceptual diagram of the proposed arrangement for manufacturing of layered molds. The density of activated sand composition was calculated corresponding to the case discussed in Sect. 30.2.2. The thickness of a layer was chosen as 2.5 mm and appropriate mass was determined for each layer. The activated sand mixture (sand, bentonite clay and water) of determined mass was deposited inside the mold and compacted to form a flat layer. The semi-solid binder agent (mixture of bentonite, water and orange peel) was spread uniformly across the entire cross-section. The density of binder has been calculated by measuring mass of the mixture and 2.5 mm thickness binder layer has been applied over the sand layer and compacted similarly. The layered sand molds were prepared with base layer and top layer comprising of activated sand. The dimensions of the mold were similar to the conventional mold of 50 mm diameter and 50 mm height. The cylindrical specimen was taken out from the mold and testing for mold properties was done similar to that of conventional mold testing.

Few trials were carried out with various combinations of mold constituents to determine the ideal combination for comparison with conventional sand molds. Based on comparison of various mold properties, the ideal mold composition for activated sand layer was found to have Silica sand (80% by Mass), Water (8% by Mass), Bentonite Clay (12% by Mass). Similarly, the composition for binder layer was chosen as Bentonite (30% by mass), Water (40% by mass) and Orange Peel

Fig. 30.1 Schematic of layered manufacturing for sand mold



(30% by mass). The above combinations of activated sand composition and binder were used further in the study for comparison with conventional molds. It has been observed that the presence of orange peel has significant effect on green shear and compression strength of molds. The excessive orange peel content in the binding layer was resulting into lower shear and compressive strength of the mold. It will be interesting to investigate this aspect further as future work. The further work focuses on determining optimal constituents for 3-D printing of sand molds along with sophisticated design of layered manufacturing equipment.

30.3 Results and Discussion

This section presents comparison of results corresponding to mold properties for conventional green sand mold and orange peel activated molds manufactured using layered manufacturing. Figure 30.2 shows comparison of mold hardness 30.2a, green compressive strength 30.2b, green shear strength 30.2c and mold permeability 30.2d for both cases. It can be seen that all mold properties except permeability are significantly improved in case of orange peel activated layer manufacturing mold. It can be seen that the orange peel activated molds manufactured using layered manufacturing technique exhibits better mold properties in comparison to conventional green sand molds. It is also realized that the orange peel powder shows great promise as a binding agent in layered manufacturing of sand molds.

In order to understand the improvement of mold properties in the presence of orange peel powder, microscopic analysis was carried out further to determine particle size distribution for both molds. Figure 30.3a, b shows microscopic images of both molds recorded using high magnification digital microscope. It can be seen that the particles are loosely bonded and attached to each other in case of conventional

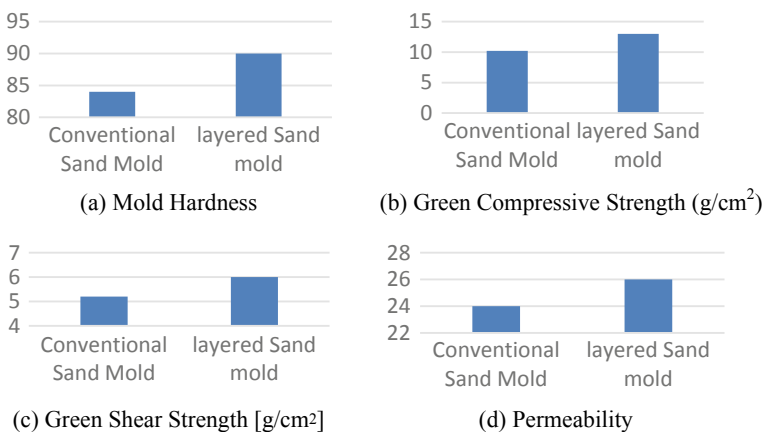
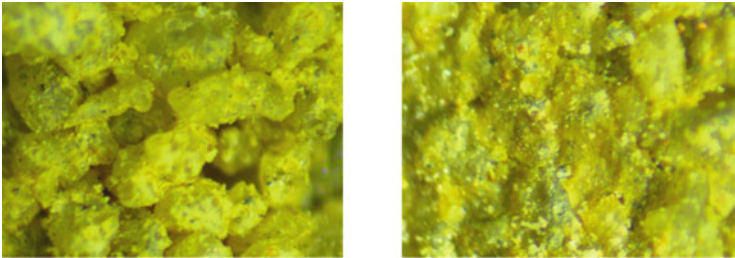


Fig. 30.2 Comparison of Mold Properties



(a) Conventional Green Sand Mold (b) Orange Peel Activated Mold

Fig. 30.3 Microscopic images of sand mold

sand molds meanwhile improved bonding is seen in the case of orange peel activated molds. The improvement in inter-particle bonding is one of the primary reason for improved mold hardness and strength properties for these molds.

In order to analyze this aspect further, these images were further analyzed using image processing based computer program, ImageJ. The images were converted to 8-bit monochrome to determine particle distribution and band-pass filter was applied for color separation. The grayscale threshold was then determined individually for both images and results are summarized in Fig. 30.4. Figure 30.5 shows comparison of particle size distribution in case of conventional and orange peel activated layered sand molds. It can be seen that the majority of particles are in the range of 60–75 nm size for the conventional mold. The fusion of between particles is quite good in case of orange peel activated layered molds and particles are not easily distinguishable. This results into distribution of particles towards smaller particle size (20 nm). This attributes towards good quality of binding between particles and better mold properties in case of orange peel activated layered molds.



(a) Conventional Sand Mold (b) Orange Peel Activated Layered Mold

Fig. 30.4 Processes images for determination of particle size

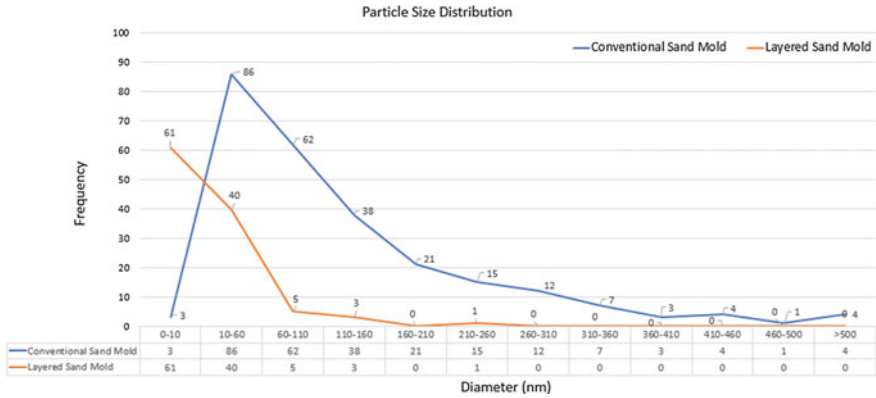


Fig. 30.5 Particle size comparison for molds

30.4 Conclusion

Sand casting is one of the most economical processes involving significant time and effort in preparation of molds and cores. A time-efficient alternative for the same is direct 3-D printing of sand molds and cores but it involves significantly higher cost and risks. One of the primary reason for the same is expensive and unstable binders used in the process. The present study explores feasibility of using natural binding agent such as orange peel powder as an alternative to costly and proprietary chemical binding agents. A preliminary mechanism for layered manufacturing of sand molds is proposed in the study. The comparison of mold properties such as mold hardness, green compressive strength, green shear strength, and mold permeability has been made for sand molds prepared using layered manufacturing technique and conventional green sand molds. It has been observed that the mold hardness and strength properties of layered manufactured molds is significantly improved due to addition of orange peel powder. The improved properties of the orange peel activated sand molds are further substantiated by conducting image analysis at microlevel to determine particle size distribution. The outcomes of the present study show that the addition of natural binder such as orange peel powder can reduce the cost of binding agent for direct 3-D printing of sand molds. The further work will focus on investigating optimal binding mixtures, reasons for improved sand mold properties and development of low cost layered manufacturing equipment for direct printing of sand molds.

References

1. Bassoli, E., Gatto, A., Iuliano, L., Violante, M.G.: 3D printing technique applied to rapid casting. *Rapid Prototyp. J.* **13**(3), 148–155 (2007)

2. Hackney, P.M., Wooldridge, R.: Characterization of direct 3-D sand printing process for the production of sand cast mould tools. *Rapid Prototyp. J.* **23**(1), 7–15 (2017)
3. Bednarz, M.: Cold hardening phenol: the new all-rounder among binder systems. Exone web resource (2018). <https://www.exone.com/Resources/Binders>. Accessed 29 Mar 2017
4. Upadhyay, M., Sivarupan, T., Mansori.: 3-D printing for rapid sand casting—a review. *J. Manuf. Process.* **29**, 211–220 (2017)
5. Clay, T., Krouth, T.: Direct metal casting. *Adv. Mater. Process. (ASM Int.)* **161**, 43–44 (2003)
6. Gill, S.S., Kaplas, M.: Efficacy of powder-based three-dimensional printing (3DP) technologies for rapid casting of light alloys. *Int. J. Adv. Manuf. Technol.* **52**, 52–53 (2011)
7. McKenna, N., Singamneni, S., Diegel, O., Singh, D., Neitzert, T., George, J., Roy Choudhury, A., Yarlagadda, P.: Direct metal casting through 3D printing: a critical analysis of the mould characteristics. In: 9th Global Congress on Manufacturing and Management, pp. 1–5. Gold Coast, Australia (2008). 12–14 Nov 2008
8. Choi, H.H., Kim, E.H., Park, H.Y., Cho, G.H., Jung, Y.G., Zhang, J.: Application of dual coating process and 3D printing technology in sand mold fabrication. *Surf. Coat. Technol.* **332**, 522–526 (2017)
9. Khandelwal, H., Ravi, B.: Effect of molding parameters on chemically bonded sand mold properties. *J. Manuf. Process.* **22**, 127–133 (2016)
10. Bailey, S.E., Olin, T.J., Bricka, R.M., Adrien, D.D.: A review of potentially low-cost sorbents for heavy metals. *Water Res.* **33**(11), 2469–2479 (1999)
11. Larrauri, J.A.: New approaches in the preparation of high dietary fibre powders from fruit by-products. *Trends Food Sci. Technol.* **10**, 3–8 (1999)
12. Anoopisan, Barath, I., Nagakalyan, S.: Interfacial behaviour of composites of polymer and orange peel particulates. *Int. J. Theor. Appl. Res. Mech. Eng.* **4**(4), 27–33 (2015)

Chapter 31

Experimental and Numerical Investigation of the Flexural Behavior of Fused Deposition Modeling Parts



Jothibabu Gokulakrishnan and Gurunathan Saravana Kumar

Abstract In this paper, fused deposition modeling (FDM) parts are characterized for flexural behavior using an experimental and numerical investigation. Flexural test was conducted using ASTM D790 standard to find the flexural strength and modulus. Tensile test and compression test were conducted using ASTM D638 and ASTM D695, respectively, to evaluate the mechanical properties. Finite element (FE) model using classical laminate theory was developed by considering a few build parameters of FDM. Flexural test condition was simulated using the elastic properties obtained from experiments based on CLT approach with orthotropic and isotropic material model. The results showed that the computational model built using classical laminate theory was well correlated with the experiments as compared to that of isotropic model for the same loading condition.

Keywords Additive manufacturing · FDM · Mechanical testing · FEM · Constitutive modeling

31.1 Introduction

Additive manufacturing (AM) is a technology that can produce parts of complex geometry for prototyping or functional requirements from 3D CAD data using layer by layer fabrication approach [1]. AM process provides flexibility to design part with complex geometries. The mechanical properties of parts printed using AM differ from bulk material properties of the material used, because of microstructural evolution that happens due to layering and process parameters used for printing. FDM is one such widely used AM process where the object is produced by extruding polymeric filament to deposit material based on the sliced part contours on the build platform. Several such layers are stacked in the build direction based on geom-

J. Gokulakrishnan · G. Saravana Kumar (✉)
Indian Institute of Technology Madras, Chennai 600036, India
e-mail: gsaravana@iitm.ac.in

J. Gokulakrishnan
e-mail: jgokul.krishnan28@gmail.com

© Springer Nature Singapore Pte Ltd. 2020
M. S. Shunmugam and M. Kanthababu (eds.), *Advances in Additive Manufacturing and Joining*, Lecture Notes on Multidisciplinary Industrial Engineering,
https://doi.org/10.1007/978-981-32-9433-2_31

etry to get the final part. FDM parts, when used for load-bearing application, need design evaluation before fabrication. Bellini et al. presented a methodology for FDM parts to characterize its mechanical strength using orthotropic material assumption, and the computational model was developed using those elastic constants to predict the behavior [2]. Alaimo et al. investigate the effect of raster angle on tensile strength of FDM printed ABS parts. The author has evaluated the elastic properties of FDM parts at a macro scale using classical laminate theory (CLT) by modifying the process parameters [3]. Casavola et al. conducted an experiment on FDM parts by describing its behavior using CLT and compared with theoretical results. A study showed CLT has the capability to predict the elastic properties of ABS parts that are built through the FDM process [4]. Somireddy et al. performed a linear finite element simulation by considering the mesostructure of FDM parts using CLT to find the elastic moduli values and compared with experimental work [5]. Dawoud et al. conducted tensile, impact and flexural experiments on FDM parts by using virgin acrylonitrile butadiene styrene (ABS) material by changing air gap and raster angle [6]. The results showed rasters parallel to loading direction can withstand more load, and it has a significant effect on dynamic behavior. Velivela et al. correlated FDM part's tensile response from experiments with FE simulation using CLT assumption for different infill density and raster angles [7]. Gokulakrishnan et al. conducted tensile experiments to find the influence of layer thickness on the FDM part's tensile strength using ABS material and found strength decreased as layer thickness increased for 0° raster angle [8]. Jothibabu et al. used surrogate-based approach to study the sensitivity of process parameters such as infill density, layer thickness and raster angle for FDM using Sobol sensitivity analysis method and found that infill density has more effect on tensile strength followed by raster angle and layer thickness [9]. In the current study, FDM parts were built using ABS, and it was characterized to find the elastic properties based on CLT using experiments. Elastic properties thus obtained were used in the finite element model, and FDM build parameters were considered to predict the flexural behavior, and it was compared with simulation.

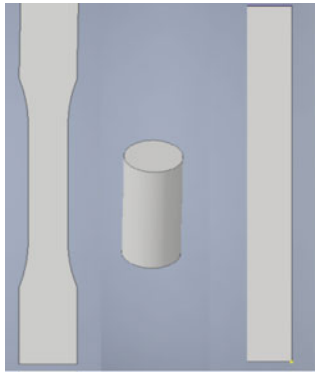
31.2 Methodology

31.2.1 Model Fabrication

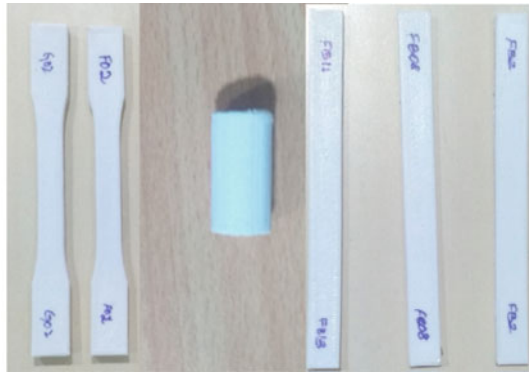
A low-cost FDM printer, S300DH™ (UV Bot®, India), was used to fabricate the specimen to evaluate the mechanical properties. The specimens were built from ABS filament using FDM printer. ASTM D638-14, Type I standard was used to build the tensile samples with 5 mm thickness, and ASTM D695-15 standard was used to fabricate the compression samples. The flexural samples were built as per ASTM D790 standard with a dimension of 127 mm × 12.7 mm × 3.2 mm. Auto desk Inventor® software was used to generate a CAD model, and it is converted to Standard Tessellation Language (STL) file format. Slic3r®, an open-source slicing software,

Table 31.1 FDM process parameters

S. No.	Process parameters	Values
1	Infill pattern	Rectilinear
2	Infill density (%)	100
3	Infill speed (mm/s)	80
4	Bed temperature (°C)	65
5	Nozzle temperature (°C)	225



(a) Virtual model



(b) Fabricated specimens for experiments

Fig. 31.1 Tensile, compression and flexure test samples

was used to slice the STL file. Each slice will have the contour and infill information of the part to be produced, and slicing software will generate the G-codes. It provides instructions for extrusion head movement to deposit the material. Table 31.1 shows the process parameter’s values used to build the samples. Specimens were built in the XY orientation on the build platform (ASTM F2971-13). The virtual model and fabricated samples are shown in Fig. 31.1.

31.2.2 Mechanical Testing

In this study, experiments were performed by changing the raster angle (measured counter-clockwise from x-axis of build platform) at 0°, 45° and 90° with a layer thickness of 0.25 mm to evaluate the mechanical properties required for creating the FE model based on CLT. Uniaxial testing machine (BiSS Nano-25™) with force capacity of 15 kN and minimum speed of 0.001 mm/min accuracy was used to perform tension, compression and flexural test. The flexural test was conducted on the specimen with 45° raster angle across all the layers with a support span of 52 mm using support pins and loading nose of 6.5 mm diameter. The test setup used for the

Fig. 31.2 Flexural test setup



experiments is shown in Fig. 31.2. For each level of the experiment, three specimens were used, stress–strain data for tensile and compression test and load–deflection data for the flexural test were recorded. The average mechanical properties obtained from tension and compression experiments were used in the FE simulation.

31.2.3 *Mathematical Formulation and Computational Model*

FE model was built by considering each layer as lamina with unidirectional reinforced fibers to replicate the behavior of FDM parts. In each layer, rasters printed by FDM process was considered as fibers, and it was assumed to exhibit orthotropic property. The constitutive model was defined using CLT that relates stress–strains under linear elastic conditions. The stress–strain relationship for the orthotropic material is given by Eq. (31.1)

$$\begin{bmatrix} \sigma_{11} \\ \sigma_{22} \\ \sigma_{33} \\ \tau_{23} \\ \tau_{31} \\ \tau_{12} \end{bmatrix} = \begin{bmatrix} K_{11} & K_{12} & K_{13} & 0 & 0 & 0 \\ K_{12} & K_{22} & K_{23} & 0 & 0 & 0 \\ K_{13} & K_{23} & K_{33} & 0 & 0 & 0 \\ 0 & 0 & 0 & K_{44} & 0 & 0 \\ 0 & 0 & 0 & 0 & K_{55} & 0 \\ 0 & 0 & 0 & 0 & 0 & K_{66} \end{bmatrix} \begin{bmatrix} \varepsilon_{11} \\ \varepsilon_{22} \\ \varepsilon_{33} \\ \gamma_{23} \\ \gamma_{31} \\ \gamma_{12} \end{bmatrix} \tag{31.1}$$

where σ_{ij} —normal stress (MPa); ε_{ij} —normal strains; τ_{ij} —shear stress (MPa) and γ_{ij} —shear strain. Each layer is thin while stacking the material in the build direction, it can be treated as plane stress condition ($\sigma_{33} = \tau_{31} = \tau_{23} = 0$) [10]. So, the stiffness matrix reduces to Eq. (31.2), and it can be defined with four independent elastic constants as given in Eqs. (31.3–31.6) [10].

$$\begin{bmatrix} \sigma_{11} \\ \sigma_{22} \\ \tau_{12} \end{bmatrix} = \begin{bmatrix} K_{11} & K_{12} & 0 \\ K_{12} & K_{22} & 0 \\ 0 & 0 & K_{66} \end{bmatrix} \begin{bmatrix} \varepsilon_{11} \\ \varepsilon_{12} \\ \gamma_{12} \end{bmatrix} \quad (31.2)$$

$$K_{11} = \frac{E_1}{(1 - \nu_{12}\nu_{21})} \quad (31.3)$$

$$K_{12} = \frac{\nu_{12}E_2}{(1 - \nu_{12}\nu_{21})} = \frac{\nu_{21}E_1}{(1 - \nu_{12}\nu_{21})} \quad (31.4)$$

$$K_{22} = \frac{E_2}{(1 - \nu_{12}\nu_{21})} \quad (31.5)$$

$$K_{66} = G_{12} \quad (31.6)$$

Based on material constants obtained from the tension test, the shear modulus was approximately calculated using Huber's equation as given in (31.7).

$$G_{ij} = \frac{\sqrt{E_{ii}E_{jj}}}{2(1 + \sqrt{\nu_{ij}\nu_{ji}})} \quad (31.7)$$

In the FDM process, the nature of bonding between the interlayer and intralayer rasters was assumed to be the same; So, E_2 , that was characterized across the rasters will be equal to that of E_3 . So the value of $G_{13} = G_{12}$ [10]. Here, G_{ij} —shear modulus; E_1 —Young's modulus along longitudinal direction (MPa); E_2 —Young's modulus along transverse direction (MPa); E_x —Young's modulus along 45° raster direction (MPa); E_3 —Young's modulus in Z-direction (MPa); ν_{ij} —Poisson's ratio. These elastic constants were obtained by conducting a tensile test as mentioned in Sect. 31.2.2.

$$S_{12} = \frac{1}{\sqrt{\left[\frac{4}{S_x^2} - \frac{1}{S_z^2} \right]}} \quad (31.8)$$

S_{12} —shear strength in 1–2 plane (MPa) [3]; S_2 —Tensile strength along 90° raster direction (MPa) and S_x —Tensile strength along 45° raster direction (MPa).

Two computational models were created using Abaqus™. The first model was built using CLT assumption by considering the build parameters of the FDM process. The raster angle and layer thickness were considered to replicate the flexural behavior using S4R type composite shell with 0.2 mm element size as shown in Fig. 31.3a. Based on the tension and compression test results, material properties were assigned to each layer. Finite element model with 0.25 mm layer thickness and 45° raster angle is depicted in Fig. 31.3b. The second model was built using isotropic material assumption without considering the build parameters. Both the models were simulated to compare with load from physical experiments.

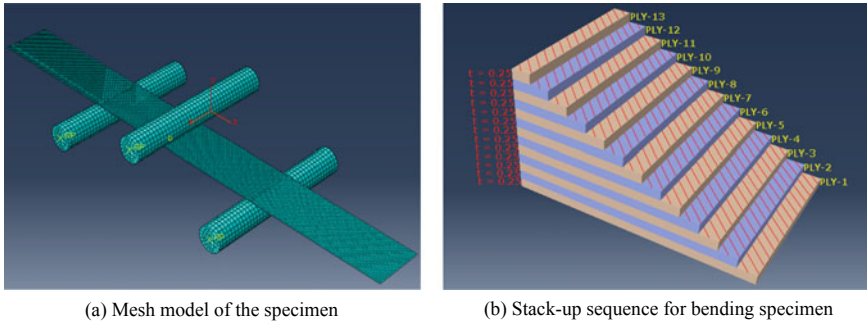


Fig. 31.3 Finite element model of flexural test specimen

31.3 Results and Discussion

31.3.1 Experimental Results

The average elastic properties and strength values were obtained by performing uniaxial tension and compression test on the FDM parts, and it is given in Table 31.2. Young’s modulus values E_1 , E_2 and E_x were obtained by printing specimens with raster angle of 0° , 90° and 45° , respectively, in XY orientation. The result of the tensile test shows that the tensile specimen with rasters (0°) printed along the direction of the load has higher tensile strength and specimen printed with rasters (90°) perpendicular to loading direction has least strength. The results of compressive strength show the same trend of maximum load-bearing capacity for the specimens printed with rasters along the loading direction. Shear modulus (G_{ij}) and shear strength (S_{ij}) were calculated using an analytical relation as given by Eqs. (31.7–31.8). The results of the flexural test performed over the specimen with 45° raster angle is given in Table 31.3. Flexural modulus and strength were calculated based on ASTM D790 standard. The specimen failed at the maximum load of 91 N with the flexural strength of 47.5 MPa and showed a maximum displacement of 7.2 mm. The failure was mainly because of intralayer raster breakage followed by interlayer de-bonding.

Table 31.2 Tension and compression test results (average value)

Layer thickness (mm)	E_1 (MPa)	E_2 (MPa)	E_x (MPa)	ν_{12}	S_1 (MPa)	S_2 (MPa)	S_x (MPa)	S_{c1} (MPa)	S_{c2} (MPa)
0.25	796	673	711	0.39	29	19	22	46	40.5

where S_1 —tensile strength along 0° raster direction; S_{c1} —compressive strength along 0° raster direction; S_{c2} —compressive strength along 90° raster direction

Table 31.3 Flexural test results (average value)

S. No.	Raster angle (°)	Max load (N)	Max displacement (mm)	Flexural modulus (MPa)	Flexural strength (MPa)
1	45	91	7.2	1502	47.5

31.3.2 Simulation Results

Flexural test was simulated using FE model in Abaqus™, 45° raster angle and 0.25 mm layer thickness was assigned for each layer with an orthotropic material assumption based on CLT, using the elastic properties ($E_1, E_2, G_{12}, \nu_{12}$) obtained from a tensile test. The second model was assigned with isotropic material property, using elastic property (E_x) of tensile specimen printed with 45° raster angle and Poisson’s ratio (ν_{12}), without considering FDM build parameters. Load and boundary conditions are defined similar as that of experiments. Figure 31.4 describes the simulation results of the flexural test. The force–displacement curves of experiments and simulation were obtained and analyzed. There was a difference in values obtained from experiments and simulation done based on CLT and isotropic model as shown in Table 31.4. The difference was around 12% for CLT model and 22% for the isotropic model. From the simulation results, it was evident that the model built based on CLT assumption has better prediction than model based on isotropic assumption. In order to predict the FDM part’s mechanical response by simulations, build parameters need to be considered in the computational model. The variation between experiment and CLT model can be attributed to the fact that the computational model considers bonding across the layers to be perfect and assuming Young’s modulus in Z-direction to be same as that of transverse direction for calculating the shear modulus. For achieving

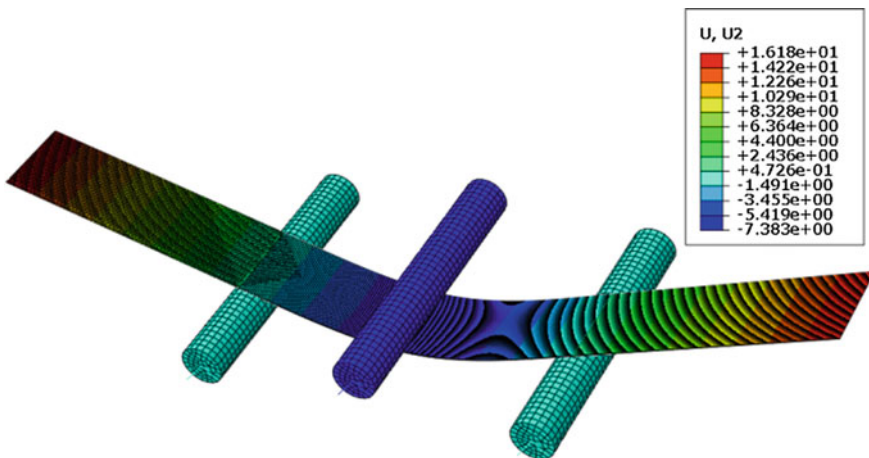


Fig. 31.4 Flexural test simulation result for 45° raster angle

Table 31.4 Comparison between experimental values and simulations

S. No.	Raster angle (°)	Max load from experiment (N)	Max load from simulation using CLT model (N)	Max load from simulation using isotropic model (N)	Difference (%)	
					CLT model	Isotropic model
1	45	89	78.3	69	12	22

better correlation, interlayer bonding can be considered in the FE model and further experiments can be conducted to find the interlayer bond strength and Young's modulus in Z- direction.

31.4 Conclusion

In this study, the FDM part was modeled as unidirectional fiber laminate, and mechanical properties were computed using orthotropic material assumption based on CLT. The flexural test was conducted with 45° raster angle, and flexural properties were calculated. The finite element model based on CLT and the isotropic assumption were used to replicate the behavior of FDM parts. It was found that the CLT model with orthotropic assumption has a better prediction, and it was compared with flexural experiment results. There was 88% correlation between flexural test experiment and simulation. Further studies can be done to find shear modulus, interlayer strength using experiments and model the interlayer bonding in FE simulation to improve the correlation of simulation with experimental results.

References

1. Saravana Kumar, G., Kalra, P.K., Dhande, S.G.: Direct layered manufacturing of point sampled objects. *Int. J. Manuf. Technol. Manag* **6**(6), 534–549 (2004)
2. Bellini, A., Güçeri, S.: Mechanical characterization of parts fabricated using fused deposition modeling. *Rapid Prototyp. J.* **9**(4), 252–264 (2003)
3. Alaimo, G., Marconi, S., Costato, L., Auricchio, F.: Influence of meso-structure and chemical composition on FDM 3D-printed parts. *Compos. B Eng.* **113**, 371–380 (2017)
4. Casavola, C., Cazzato, A., Moramarco, V., Pappaletta, C.: Orthotropic mechanical properties of fused deposition modelling parts described by classical laminate theory. *Mater. Des.* **90**, 453–458 (2016)
5. Somireddy, M., Czekanski, A.: Mechanical characterization of additively manufactured parts by FE modeling of mesostructure. *J. Manuf. Mater. Process.* **1**(2), 18 (2017)
6. Dawoud, M., Taha, I., Ebeid, S.J.: Mechanical behaviour of ABS: an experimental study using FDM and injection moulding techniques. *J. Manuf. Process.* **21**, 39–45 (2016)

7. Velivela, V., Saravana Kumar, G.: A finite element model to predict the part strength of fused deposition modeling printed parts. In: International Mechanical Engineering Congress and Exposition, ASME, Phoenix, USA (2016)
8. Gokulakrishnan, J., Saravana Kumar, G.: Optimum adaptive slicing considering the layer strength of fused deposition modelling parts. In: International Conference on Engineering Optimization, pp. 442–452. Springer, Cham, Lisbon, Portugal (2018)
9. Jothibabu, G., Saravana Kumar, G.: Surrogate based sensitivity analysis of part strength due to process parameters in fused deposition modelling. *Proced. Comput. Sci* **133**, 772–778 (2018)
10. Jones, R.M.: *Mechanics of composite materials*, 2nd edn. CRC Press, USA (1999)

Part II

Joining

Chapter 32

Some Studies on Mechanical Properties of AISI 316L Austenitic Stainless Steel Weldments by Cold Metal Transfer Process



A. Rajesh Kannan  and N. Siva Shanmugam 

Abstract Cold metal transfer (CMT) process widely employed in automobile industry offers better results in achieving distortion-free joints due to low heat input produced in comparison with the conventional GMAW process. The focus of this research is to explore the impact of CMT process on the microstructural changes and mechanical behavior, i.e., tensile strength, hardness, and elongation percentage of AISI 316L weldments. It was observed that microstructure of HAZ was similar to the base metal, and weldment microstructure is the main factor for the efficiency of joints. The uniaxial tension results revealed that the CMT joints exhibited higher tensile strength (UTS) of 571 MPa compared to base metal strength of 536 MPa. The results of mechanical testing showed an increase in hardness and a decrease in ductility is attributed to the existence of high delta ferrite content in the austenite matrix after welding. Ductile mode of failure was observed in the fracture surface with microvoids and dimple structure.

Keywords AISI 316L · CMT · Welding · Mechanical characterization · GMAW · Microstructure

32.1 Introduction

AISI 316L stainless steel weldments are mostly employed in gas and oil industries, structural applications, and automobile industry due to their outstanding impedance to stress corrosion cracking (SCC) and localized pitting, particularly in many eroding environments with acidic nature [1, 2]. The resistance to tarnish and oxide formation is due to the presence of chromium in stainless steels. The austenitic stainless steel (ASS) grades like 316L, 304L, and alloys having nitrogen are extensively used in numerous industrial applications where high-temperature operation is required. The molybdenum addition improves overall resistance to corrosion and pitting resis-

A. Rajesh Kannan · N. S. Shanmugam (✉)
Department of Mechanical Engineering, National Institute of Technology, Tiruchirappalli 620015,
India
e-mail: nsiva@nitt.edu

© Springer Nature Singapore Pte Ltd. 2020
M. S. Shunmugam and M. Kanthababu (eds.), *Advances in Additive Manufacturing and Joining*, Lecture Notes on Multidisciplinary Industrial Engineering,
https://doi.org/10.1007/978-981-32-9433-2_32

359

tance to chlorides. ASS can be joined with a variety of joining processes such as GMAW—gas metal arc welding, GTAW—gas tungsten arc welding, LBW—laser beam welding, EBW—electron beam welding, and PAW—plasma arc welding. The quality of the joined components depends mainly on the physical appearance of the weld bead, the metallurgical-mechanical features of the weld, and various aspects of the welding chemistry. Also, it is observed that these characteristics were the effect of various process parameters like welding current, voltage, a stick-out distance of the electrode, rate of movement of shielding gas, preparation of edges, welding speed, welding position, and various parameters in GMAW process. Liao et al. [3] studied the weldment properties depending on the supply of shielding gas to a large extent, as it controls the metal transfer mode. Thus, the preparation of an acceptable quality weldment looks to be interesting work. Welding researchers have always been looking for better welding quality on sheet metals. The joining of stainless steels, in specific, can be reviewed among the most extensive research areas where it can give its contribution, in important means to the joining process control specifically for improved and satisfactory welds.

Amударasan et al. [4] explored the 3-mm-thick AISI 316L ASS by GTAW, and the results of mechanical properties were superior to the base metal. Zumelzu et al. [5] reported the effect of microstructural changes on the features of mechanical behavior of AISI 316L steel weldments using GMAW. During the investigation of the literature, the impact of the joining parameters on weld bead profile and solidification structure of the weldments was analyzed by LBW [6], GTAW [7], and GMAW [8]. CMT process is relatively modern welding technique mainly distinctive by its controlled heat input, higher metal deposition amount, and low spatter during the short circuit of the filler metal to the base metal [9]. It is established by transmitting a short circuit in which the filler material is transferred to the area of weld pool by the filler wire that comes into contact with it. Schierl [10] reported that the decrease in a spattering of CMT process is due to the droplet detachment mode which works without the support of electrical and magnetic forces when compared to traditional MIG welding. From the joining point of view, “cold” is a relatively new concept. In the CMT process, the workpieces to be joined remain considerably “colder” than in the conventional GMAW process.

The studies of Subodh Kumar et al. [11] shows that the GTAW weldments made with a process of lower heat input revealed a higher tensile strength than the other welds joined with high heat input in AISI 304 grade steel. It was considered important that the realization of this study would be helpful to understand the mechanical behavior and metallurgical characteristics that influence the performance of weld prepared by different combinations of heat input. It is inferred that most of the researches reported on the CMT process are focused on aluminum alloys, magnesium alloys, and their development and durability aspects. As far as the authors are aware, a very few comprehensive investigations are carried out on the influence of low heat input on the mechanical and microstructural features of CMT welding of ASS is existing in the established literature. Hence, in this present study, we aim to find the optimal joining parameters for 1.6-mm-thick AISI 316L sheets, specifically welding current and speed. Afterward, the effect of joining parameters on the microstructural

Table 32.1 Composition of chemical elements (wt%) in AISI 316L

Name of the element	C	Mn	Si	P	S
Composition in %	0.03	2.0	0.75	0.45	0.03
Name of the element	Cr	Mo	Ni	N	Fe
Composition in %	18.0	3.0	11.0	0.10	Bal.

Table 32.2 Composition of chemical elements (wt%) in ER 308L

Name of the element	C	Mn	Si	P	S
Composition in %	0.03	1.75	0.48	0.03	0.03
Name of the element	Cr	Mo	Ni	Cu	Fe
Composition in %	19.6	0.3	10.0	0.75	Bal.

changes and mechanical behavior of AISI 316L sheets has been explored. Optimal process parameters to join the sheets with high quality for various applications in the automotive industry, food industry, and medical applications are established.

32.2 Material and Welding Procedure

32.2.1 Samples for Experimental Work

In this study, annealed sheets of AISI 316L austenitic grade of 1.6 mm thickness in is used as the base material. In Tables 32.1 and 32.2, the chemical composition of the base metal and filler metal is specified.

32.2.2 Welding Process

Cold metal transfer (CMT) process is employed to join the sheet metals. The square butt joint welding trials are carried out with ER308L filler wire of 1.2-mm dia. CMT welding of AISI 316L material is conducted using a Fronius Trans Pulse Synergic 4000 CMT machine with VR 7000 CMT wire feeder unit as shown in Fig. 32.1. The base plate is cut to small sections of 50 mm × 100 mm × 1.6 mm before joining.

All the specimens are scrubbed with steel brush and acetone to eliminate the effects of the oxide layer and other impurities in the surface of the specimens to be welded. After cleaning, the specimens are clamped and the mixture of shielding gas (argon 98% and carbon dioxide 2%) is supplied at a constant level of 20 L/min and is switched on 3 s before the arc is struck. During and after joining, the weldments are visually examined for the weld quality, and it is confirmed that all welds are

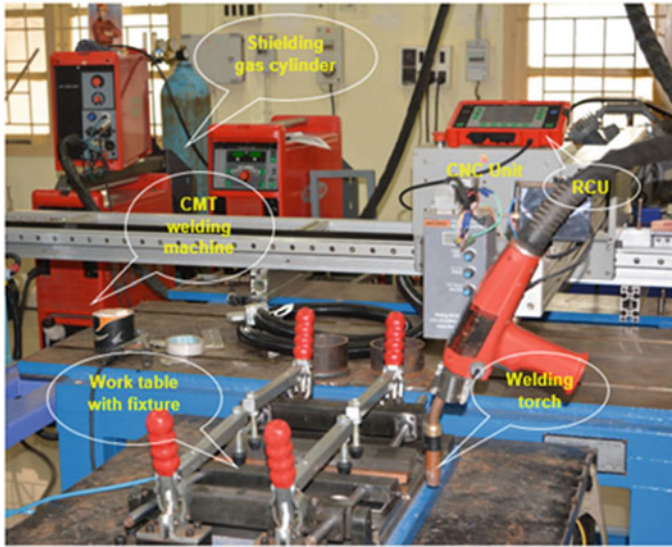


Fig. 32.1 Experimental set-up

free of visible defects like surface porosity, blowholes, etc., and finally obtain good geometric consistency. To avoid distortion, samples are held rigidly using fixtures.

The torch is set for an angle of 10° from the perpendicular axis during welding. Based on the bead on plate trials, an L9 orthogonal array of welding input parameters was selected by different heat inputs to the base metal and is provided in Table 32.3. The welding heat input is the comparative measure of transferred energy to the weld per unit length. It is a major characteristic as it has an effect on the solidification time and rate of cooling. Thus, in turn, it has an influence on the microstructure of weld metal (WM) and heat-affected zone (HAZ), as a result of the mechanical behavior

Table 32.3 Welding input parameters for AISI 316L 1.6-mm joint

Joint No.	Welding current (A)	Welding voltage (V)	Welding speed (mm/min)	Heat input (kJ/mm)
1	95	11.4	400	0.146
2	95	11.4	375	0.156
3	95	11.4	350	0.167
4	90	11.0	400	0.134
5	90	11.0	375	0.143
6	90	11.0	350	0.153
7	85	10.9	400	0.125
8	85	10.9	375	0.133
9	85	10.9	350	0.148

of the WM. The heat input (J) is calculated by using the equation:

$$\text{Heat input, } \eta = \frac{60 \times VI}{v} \tag{32.1}$$

where V —welding voltage, I —welding current, v —welding speed, and η —factor of efficiency.

32.2.3 Preparation of Samples—Tensile and Hardness Test

To examine the mechanical behavior, a portion of the WM is sliced by $50 \text{ mm} \times 8 \text{ mm} \times 1.6 \text{ mm}$ for tensile test following the ASTM E8/E8 M-16a standard. Since the sheet metal thickness is lesser, sub-sized samples were made for tensile test perpendicular to traverse direction. Using wire-cut EDM, the weldments are cut to the required size as shown in Fig. 32.2.

The specimen for the microhardness (Vickers Hardness) test is prepared with a size of $30 \text{ mm} \times 15 \text{ mm} \times 1.6 \text{ mm}$ covering the entire Fusion Zone (FZ), HAZ and BM following the ASTM E92-17 standard test method. The samples were prepared for testing in the as-joined conditions.

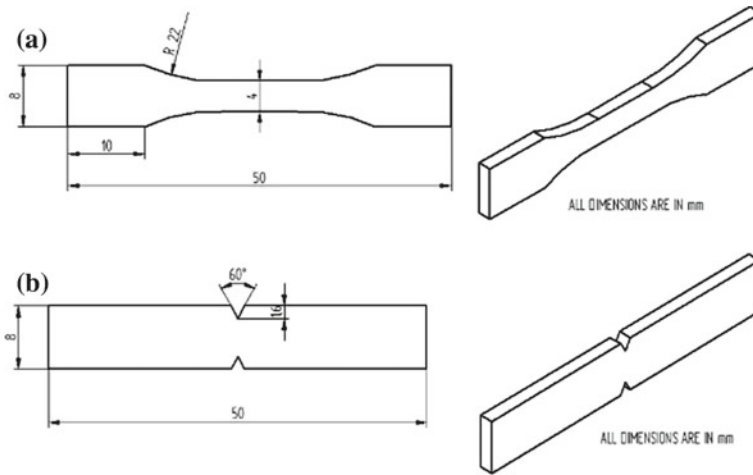


Fig. 32.2 Schematic drawing of tensile specimens, **a** tensile specimen without notch and **b** tensile specimen with notch

32.2.4 Metallography

The microstructural studies are carried out with the Leica DM2500 M model material analysis microscope incorporated with a software image analyzer. The base and weld metal samples for metallurgical evaluation were sliced to the required size and polished with various emery sheets. Samples are prepared with etching with 30 mL of distilled water, 20 mL of HCl and 15 mL of HNO₃ applying for few seconds. The surface of the fractured samples subjected to tensile test are investigated using a scanning electron microscope (TESCAN Vega 3) at magnification higher than 1000× to reveal the nature of fracture morphology.

32.3 Results and Discussion

32.3.1 Tensile Properties

The properties like tensile Strength (UTS), % of elongation, and NSR–notch strength ratio of the CMT weldments are examined. The weldment with full depth of penetration and having no defect is subjected to tensile test. Two BM and three WM specimens are tested, and results are presented in Table 32.4. Figure 32.3 shows the plot between UTS and % of elongation for the tensile samples. Three joints were prepared, and 15 samples were tested. The results were identical and the best results are plotted.

CMT Welds with equiaxed grains and columnar dendrites in the FZ have a comparatively high UTS and decrease in ductility. In addition, it was observed that all tensile specimens were fractured in the HAZ, which indicates that the WM throughout the joint had higher tensile strength than the BM and in turn achieved a joint efficiency of 106%. The tensile properties (UTS, Notch Strength Ratio (NSR) and percentage of elongation) of CMT weldments are superior compared to the BM. The notch strength of BM and WM are 697 MPa and 721 MPa, respectively. NSR is 1.30 for BM and 1.26 for WM. This reveals that the welds are unsusceptible to notches and falls under the notch ductile materials category [12].

Table 32.4 Results of tensile test for 1.6-mm BM and WM

Type of the specimen	UTS, MPa	Elongation (%)	NSR
Base metal (BM)	536	51.30	1.30
BM with V-notch	697	23.10	
WM (transverse)	571	34.80	1.26
WM with V-notch	721	19.59	
WM (longitudinal)	716	38.40	–

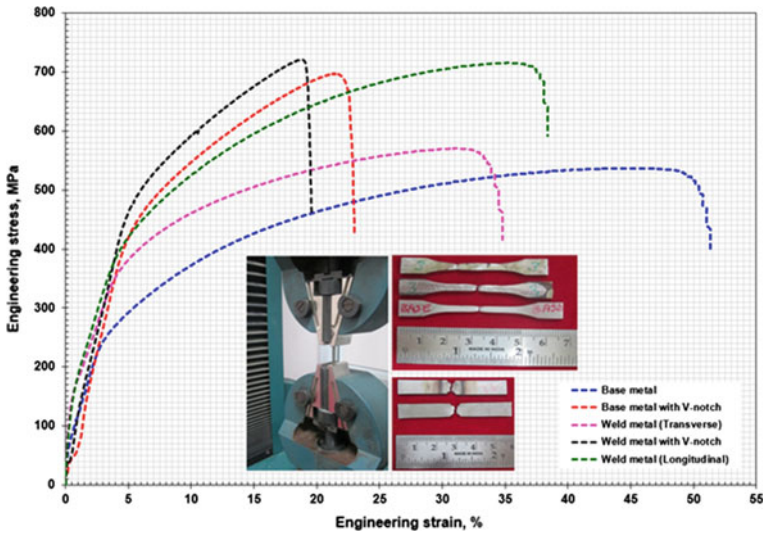


Fig. 32.3 Stress versus Strain plot for various samples and the corresponding fractured samples for 1.6 mm

32.3.2 Microhardness Properties

The Vickers microhardness values of weldment with full depth of penetration are evaluated, and they are plotted in Fig. 32.4. The average hardness for the 1.6-mm joint is 170.91HV. The fusion zone has the highest hardness, and the base metal

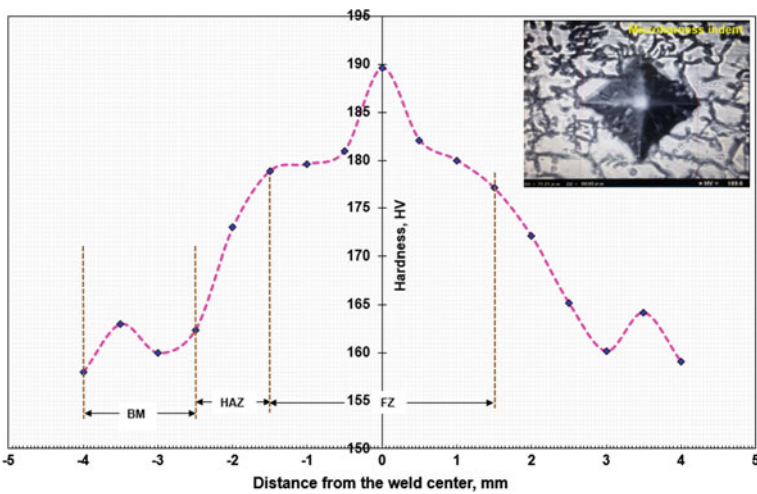


Fig. 32.4 Microhardness measurement of CMT tailor welded blanks

has the lowest. It is evident from the graph that the HAZ has a hardness greater than the base metal, but less than the fusion zone. The increase in the percentage of delta ferrite has an effect on ferrite number and thereby increases the hardness value in weldments. The increase in hardness value is correlated to the dispersion of high content of delta ferrite in the WM [13]. The delta ferrite (BCC structure) is not consistent with the austenite matrix (FCC structure) and can have a noticeable increase of hardness value in the FZ.

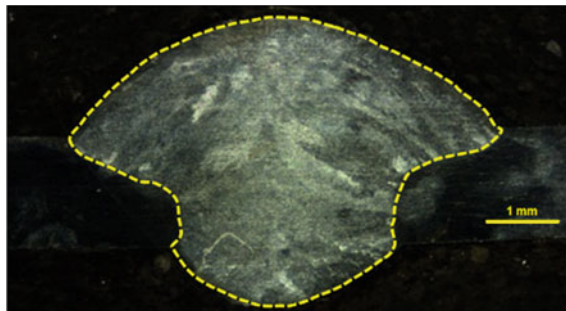
32.3.3 Microstructural Characterization

The optical macro-cross sections of CMT weldments in the various heat input conditions are described in Table 32.3. The input parameters are 95 A and 350 mm/min for a full depth of penetration in the joints. Macrograph of the CMT-welded sample reveals that there were no defects in the joint (Fig. 32.5). Three joints were prepared to examine the integrity of the joints using CMT process and metallurgical morphologies were evaluated.

Figure 32.6a shows the base metal microstructure at annealed condition before welding. The microstructure of the joint with full depth of penetration is examined at $200\times$ magnification which is displayed in Fig. 32.6b, c. The joint made by ER308L contains solidified austenitic structure and ferrite with delta ferrite in the WM after non-equilibrium cooling. Therefore, CMT welds have greater strength matched to the BM due to the incomplete delta ferrite to austenite transformation. Relating the micrographs in Fig. 32.6, the equiaxed fine grains are seen in the melting zone of the fusion zone as compared to the candidate metal.

The rapid cooling generally leads to the partial transformation of the ferrite during non-equilibrium solidification to austenite. This can happen because of the transformation process controlled by diffusion; the rapid cooling in the joining process does not provide adequate time to completely solidify after the phase transformation and bringing down to room temperature. The weld metal showed a combined morphology consisting of dark dendrites (delta ferrite) and equiaxed austenitic grains. Also, the morphology of the WM was completely different from the unaffected base material.

Fig. 32.5 Macrostructure of CMT weldment with full depth of penetration at $20\times$ magnification



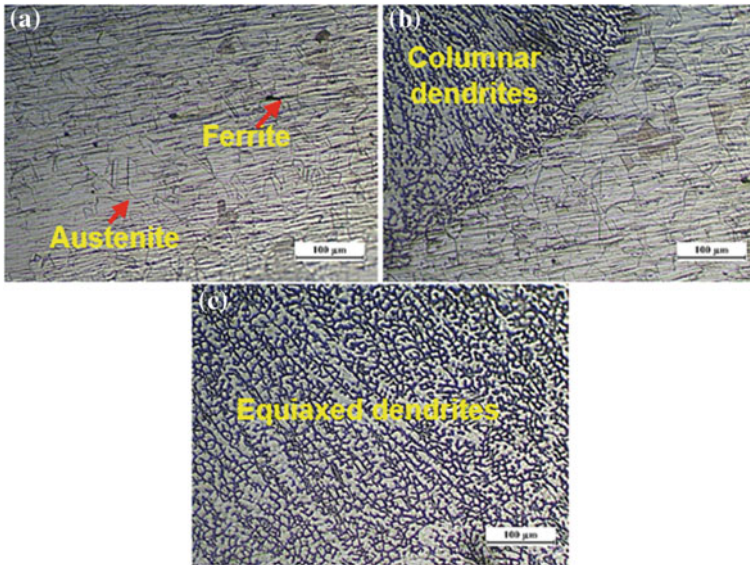


Fig. 32.6 Optical micrographs, **a** base metal, **b** and **c** CMT weldments of AISI 316L

32.3.4 XRD Results

X-ray diffraction (XRD) peaks were analyzed to recognize the phases present in the WM zone using Rigaku Ultima III XRD diffractometer with $\text{CuK}\alpha$ radiation of 40 kV. Two samples were examined, and the results were identical. The XRD pattern obtained from the analysis of BM and CMT joint is presented in Figs. 32.7 and 32.8. XRD plots for BM show peaks of austenite phase (FCC) at 43.48° , 50.66° , 47.48° , and 44.36° for the ferrite (BCC) and for CMT weld metal shows peaks at 43.62° , 50.74° , and 74.60° for the austenite phase and 44.64° to the ferrite phase. It reveals the existence of austenite (JCPDS No. 31-0619) and ferrite (JCPDS No. 06-0696) phases in both BM and WM from the XRD analysis [14, 15].

In addition, the ferrite-phase peak noticeably increased in the XRD plot as a result of increased delta ferrite (6.29 FN) in the weld metal. This result exactly correlates the effect of heat input used to produce weldments with an increase in FN.

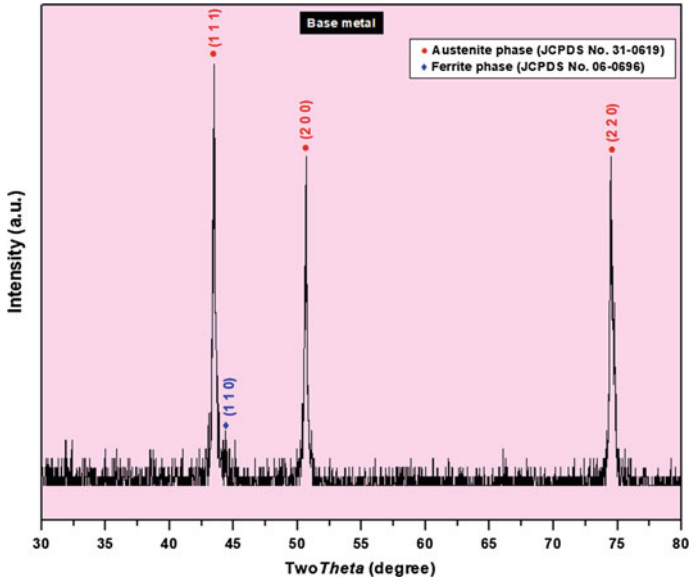


Fig. 32.7 XRD peaks for AISI 316L base metal

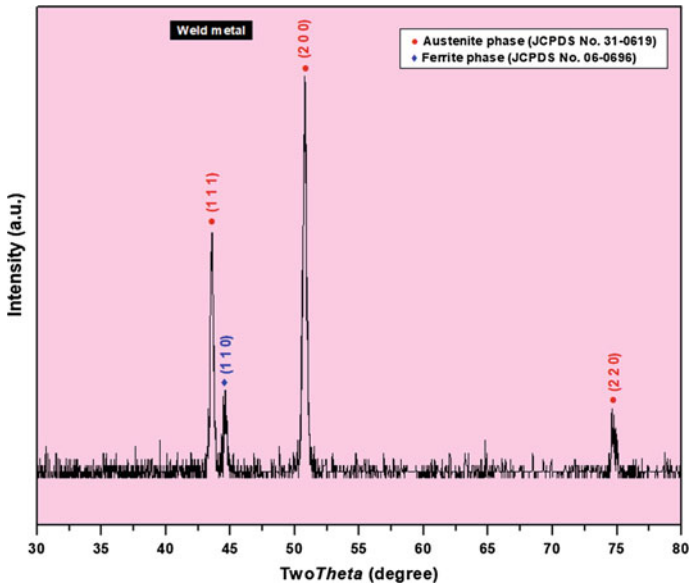


Fig. 32.8 XRD peaks for AISI 316L weld metal sample

32.3.5 Fractography Examination

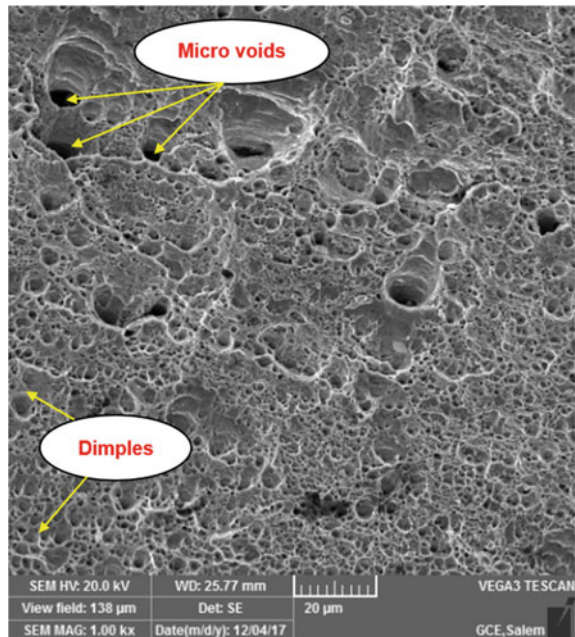
Therefore, in the viewpoint of metallurgy, the fine structure of the grain shows greater strength matched to the coarse structure of the grains. Figure 32.9 shows the failed specimen during a tensile test conducted at room conditions. The surface morphology of the fractured samples reveals a ductile mode of failure due to microstructural features of FZ with microvoids and dimples.

From the surface of the fractured weld sample, microvoids and fine dimples were observed compared to the BM and increase in the load-carrying capacity of the weld metal sample was attribute the presence of fine dimples. Therefore, the tensile strength of the CMT weldments is higher compared to BM. Also, the existence of microvoids observed at the fractured sample surface of the WM is higher than the BM.

32.4 Conclusions

Based on this research study, it is concluded that the microstructural and mechanical properties are not much affected by thermal cycles during welding. The following inferences are drawn from the experimental investigations:

Fig. 32.9 Fractograph of AISI 316L weld metal tensile fracture surface at 1000×



- Reasonably CMT joint (571 MPa) undergoes about 6.5% increase in tensile strength compared to the base metal (536 MPa).
- The maximum hardness of 189 HV in the fusion zone is due to the high amount of delta ferrite in the WM.
- The tensile samples failed at the ductile mode of fracture due to the existence of microvoids and fine dimples.
- The weldment microstructure consists of equiaxed grains in the FZ and was observed similar to base metal.
- The increase of delta ferrite in the FZ reduced the ductility of the WM and fracturing at HAZ during tensile tests
- The ferrite peak considerably increased in the XRD plot as a result of a higher amount of delta ferrite (6.29 FN) in the WM.
- The NSR ratio is higher than 1 for BM and WM, which makes to fall under the category of notch ductile materials.

References

1. Mishra, A., Chellapandi, P., Suresh Kumar, R., Sasikala, G.: Comparative study of cyclic hardening behavior of SS 316 L using time independent and dependent constitutive modeling: a simplified semi-implicit integration approach. *Trans. Indian Inst. Metals* **68**, 623–631 (2015)
2. Lu, B.T., Chen, Z.K., Luo, J.L., Patchett, B.M., Xu, Z.H.: Pitting and stress corrosion cracking behavior in welded austenitic stainless steel. *Electrochim. Acta* **50**, 3904–3911 (2005)
3. Liao, M.T., Chen, P.Y.: The effect of shielding—gas compositions on the microstructure and mechanical properties of stainless steel weldments. *Mater. Chem. Phys.* **55**, 145–151 (1997)
4. Amudarasan, N.V., Palanikumar, K., Shanmugam, K.: Mechanical properties of AISI 316L austenitic stainless steels welded by GTAW. *Adv. Mater. Res.* **849**, 50–57 (2014)
5. Zumelzu, E., Sepulveda, J., Ibarra, M.: Influence of microstructure on the mechanical behaviour of welded 316L SS joints. *J. Mater. Process. Technol.* **94**, 36–40 (1999)
6. El-Batahy, A.M.: Effect of laser welding parameters on fusion zone shape and solidification structure of austenitic stainless steels. *Mater. Lett.* **32**, 155–163 (1997)
7. Tsuchiya, K., Kawamura, H., Kalini, G.: Re-weldability tests of irradiated austenitic stainless steel by a TIG welding method. *J. Nucl. Mater.* **283**, 1210–1214 (2000)
8. Sireesha, M., Albert, S.K., Shankar, V., Sundaresan: A comparative evaluation of welding consumables for dissimilar welds between 316LN austenitic stainless steel and alloy 800. *J. Nucl. Mater.* **279**, 65–76 (2000)
9. Pickin, C.G., Williams, S.W., Lunt, M.: Characterisation of the cold metal transfer (CMT) process and its application for low dilution cladding. *J. Mater. Process. Technol.* **211**, 496–502 (2011)
10. Schierl, A.: The CMT-process a revolution in welding technology. *Weld World* **49**, 38 (2005)
11. Kumar, S., Shahi, A.S.: Effect of heat input on the microstructure and mechanical properties of gas tungsten arc welded AISI 304 stainless steel joints. *Mater Des* **32**, 3617–3623 (2011)
12. Lakshminarayanan, A.K., Shanmugam, K., Balasubramanian, V.: Effect of welding processes on tensile and impact properties, hardness and microstructure of AISI 409 M ferritic stainless joints fabricated by duplex stainless steel filler metal. *J. Iron. Steel Res. Int.* **16**, 66–72 (2009)
13. Yang, H., Yang, K., Zhang, B.: Pitting corrosion resistance of ‘La’ added 316L stainless steel in simulated body fluids. *Mater. Lett.* **31**, 1154–1157 (2007)

14. Mohan Kumar, S., Siva Shanmugam, N.: *Mater. Res. Express* **5**(10), 106524 (2018)
15. Tseng, K.H., Chen, K.L.: Comparisons between TiO₂- and SiO₂-flux assisted TIG welding processes. *J. Nanosci. Nanotechnol.* **12**, 6359–6367 (2012)

Chapter 33

Effect of Pre-weld Solution Treatment on Mechanical Properties and Microstructure of Micro-Plasma Arc Welded Inconel 718



Ajit Kumar Sahu  and Swarup Bag 

Abstract Welding of Inconel 718 is always a challenging task due to the presence of complex alloying elements, which segregates in the interdendritic region and form various brittle intermetallic secondary phases. Hence, in the current investigation, an attempt has been made to study the effect of pre-weld solution treatment on micro-plasma arc welded Inconel 718 microstructure and corresponding mechanical properties. Two different quenching medium, i.e., water and air cooling, were considered during the solution treatment at 980 °C to control the initial grain size and mechanical properties of the base material. The results of this study showed that change in quenching medium affected the grain size, tensile strength, yield strength, ductility, and heat input during the micro-plasma welding to achieve full penetration. The full weld penetrations of solution-treated sheets were achieved with lower heat input as compared to the as-received rolled sheets. Lower heat input during welding resulted in refined solidified microstructure and lower segregation in the interdendritic region, hence improving the joint efficiency of the micro-plasma arc welded Inconel 718.

Keywords Inconel 718 · Micro-plasma welding · Laves phase · Solution treatment · Cooling rate

33.1 Introduction

Inconel 718 is a nickel–iron-based precipitation-hardenable super alloy with a unique ability to retain its mechanical properties and oxidation resistance up to a high temperature of 650 °C [1]. It is one of the most preferred materials in the aerospace, aviation, and nuclear industries for making various critical components [2]. The use of Inconel 718 as turbine blades and disk material in gas turbine engines has increased significantly for its outstanding strength and microstructural stability at elevated tem-

A. K. Sahu (✉) · S. Bag
Department of Mechanical Engineering, Indian Institute of Technology Guwahati, Guwahati,
Assam 781039, India
e-mail: ajit.sahu@iitg.ac.in

© Springer Nature Singapore Pte Ltd. 2020
M. S. Shunmugam and M. Kanthababu (eds.), *Advances in Additive Manufacturing and Joining*, Lecture Notes on Multidisciplinary Industrial Engineering,
https://doi.org/10.1007/978-981-32-9433-2_33

373

perature [3]. Thin sheets are used for fan-containment applications around parts of the compressor and the turbine region in the commercial turbine jet engines because of its high ballistic impact strength [4].

Strengthening of Inconel 718 is based on solid solution and precipitation strengthening mechanism [5]. Hence, the heat treatment for Inconel 718 is divided into solution treatment and aging treatment [6]. Body-centered cubic (BCC) γ'' [Ni_3Nb] is the primary strengthening phase in Inconel 718 along with face-centered cubic (FCC) γ' [$\text{Ni}_3(\text{Al}, \text{Ti})$] and orthorhombic δ (NbC) phase [7]. Selection of standard solution treatment temperature is an important aspect for Inconel 718 as it is responsible for dissolution of Nb-rich Laves phases [$(\text{Ni}, \text{Fe}, \text{Cr})_2(\text{Nb}, \text{Ti}, \text{Mo})$] and carbides back into the metal matrix. Laves is a brittle intermetallic phase form in the interdendritic region during the cast solidification of Inconel 718. Dissolution of Laves and carbide phases will make ample amount of principal alloying elements available for the precipitation of principal strengthening phases. Hence, the selection of proper solid solution temperature is important for dissolution of various deleterious secondary phases and grain refinement before the fabrication of Inconel 718.

Inconel 718 possesses excellent weldability among the nickel-based super alloys. However several studies reported various defects like solidification cracking and micro fissuring in the weld zone and heat-affected zone (HAZ) which has detrimental effect on the mechanical strength [8, 9]. The main reason behind these defects is the segregation of Nb in the interdendritic regions and formation of intermetallic brittle Laves phase during weld metal solidification [10]. Formation of Laves phase and other carbides not only affects the weld quality but it also consumes a higher amount of favorable alloying elements from the metal matrix. Hence, various studies were focused on gas tungsten arc (GTA) welding, laser beam welding (LBW), and electron beam welding (EBM) techniques to minimize these defects [2, 11, 12]. When a heat source of higher power density is used for welding, the average welding heat input required for the joining reduces. Low heat input assures a steep temperature gradient during solidification as a result higher cooling rate is possible to achieve. It was reported that with an increase in weld cooling rate, the amount of segregation and formation of these deleterious phases reduces significantly. Higher cooling rate of the weld has reported in the microstructure refinement and improvement in the mechanical properties [12]. Techniques like beam oscillation and current pulsing were also reported to control the Nb segregation and laves phase formation [12, 13]. Very limited work has been reported on arc welding of Inconel 718 as compared to advanced LBW and EBW techniques. These advanced welding techniques have various limitations due to complex setup which cause a high inaccessible area while joining complicated shapes. Among all conventional arc welding techniques, plasma arc welding produces a constricted arc of higher energy density [14]. Hence in the present study, cost-effective micro-plasma arc welding (μ -PAW) in constant current mode is used to weld, as-received and solution-treated Inconel 718 sheets. The main focus of the present study is to analyze the effect of solution treatment on mechanical properties and welding parameter during the μ -PAW of Inconel 718.

33.2 Experimental Details

As rolled Inconel 718 sheets of thickness 0.7 mm were used for the current study in as-received and solution-treated conditions. Sheets were subjected to solution treatment at a temperature of 980 °C for 1 h followed by water quenching to room temperature named as ST1 and sheets subjected to air cooling was named as ST2. Solution treatments were done at different cooling medium to study the variation in grain refinement and corresponding effect on mechanical properties. Thus, three different specimens (as-received, ST1, and ST2) were prepared for the welding and the corresponding microstructures are shown in Fig. 33.1. The microstructure of as-received base materials consists of twinned grain, whereas homogeneous equiaxed grains were observed in ST1 and ST2 base material. The average grain diameter of the base materials was calculated by mean linear intercept method and found to be 61 μm (ASTM 5–6), 72 μm (ASTM 4–5), and 77 μm (ASTM 4–5) for as-received, ST1, and ST2 condition base materials, respectively. The chemical composition analysis of Inconel 718 is done by Energy-Dispersive X-ray (EDX) technique and the elemental distribution is shown in Fig. 33.2. Based on the EDX analysis, the resulted composition is given in Table 33.1.

The base materials were dimensioned into 90 mm (length) \times 60 mm (width) coupons with welding direction normal to the rolling direction. Autogenous butt

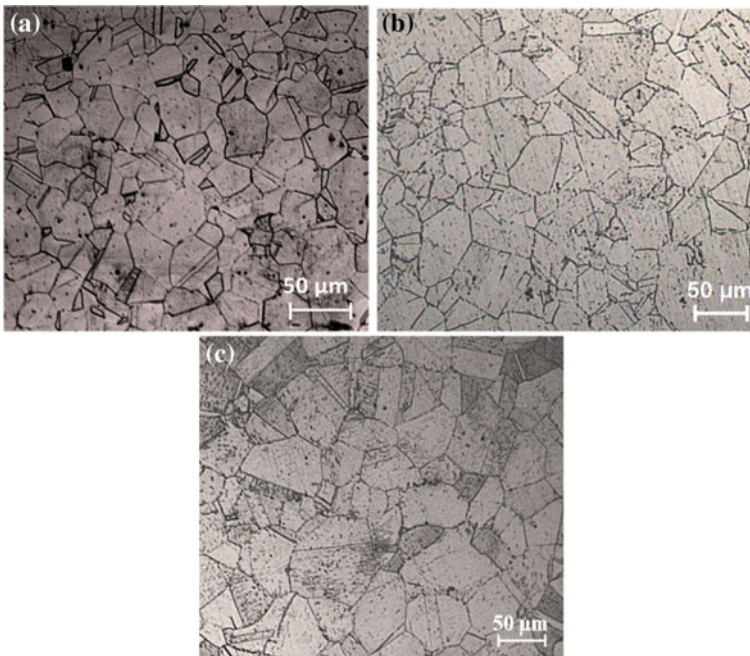


Fig. 33.1 Microstructure of base material in **a** as-received, **b** ST1, and **c** ST2 condition

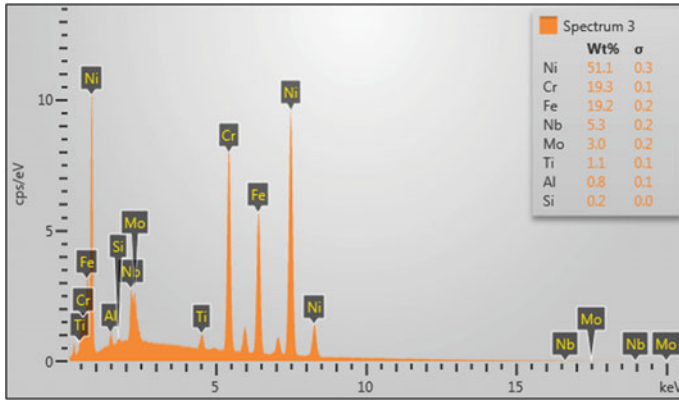


Fig. 33.2 EDX elemental analysis of the base material

Table 33.1 Chemical composition of Inconel 718

Elements	Ni	Cr	Nb	Mo
Composition (wt%)	51.1	19.3	5.3	3.0
Elements	Ti	Al	Si	Fe
Composition (wt%)	1.1	0.8	0.2	Bal.

configuration welds were prepared by micro-plasma arc welding machine with a 0.5–50 A DC power supply in constant current mode. The welding torch of micro-plasma setup is kept fixed, while the work piece is allowed to move at a constant velocity. Commercial pure argon (99%) is used as plasma gas to produce the plasma arc and as shielding gas for protection of weld pool. The shielding gas and plasma gas flow rate are maintained at 5 and 0.4 L min⁻¹. Respectively, with a nozzle standoff distance of 2 mm. Tungsten electrode of 1 mm diameter is used for generating the plasma arc during welding. The other welding parameters are listed in Table 33.2 which were obtained by a wide range of welding trials to achieve full penetration.

The heat input per unit length (J mm⁻¹) is calculated using the equation given below

$$H = \frac{V \times I}{S} \tag{1}$$

Table 33.2 Welding parameters employed in MPAW

Base plate	Current (A)	Welding speed (mm s ⁻¹)	Heat input (J mm ⁻¹)
As-received	14	4.3	78
ST1	13	4.2	74
ST2	13	4.4	71

where V , I , and S represent welding voltage, current, and speed, respectively. For microstructural study, the welded samples were sectioned normal to the welding direction and polished with various grades of emery paper followed by diamond polishing to obtain scratch-free surfaces. The polished specimens were etched in a solution of HCl, HF, and HNO₃ in the ratio of 2:1:1, respectively, for few seconds to reveal the microstructure. The microstructural analysis of the fusion zone and heat-affected zone (HAZ) was done with the help of optical microscope and field emission scanning electron microscope. EDX analysis was done for quantitative elemental analysis of the dendritic core and interdendritic regions. Vickers micro-hardness tests were implemented across the weld profile (covering the entire base metal, heat-affected zone, and fusion zone) with a spacing of 0.1 mm for each indentation. The hardness was measured at the middle section of the welded joint by using a load of 500 g for 15 s dwell time. The room temperature tensile tests of base materials and welded samples were conducted to analyze the effect of solution treatment and welding condition on yield strength, tensile strength, and percentage elongation of the gauge length. For each condition, three sub-size transverse specimens were prepared according to ASTM E8 M subsize-standard with a gauge length of 25 mm. The tests were carried out by a computer-controlled servo-hydraulic universal tensile testing machine with a strain rate of 0.5 mm min⁻¹.

33.3 Results and Discussion

33.3.1 Microstructural Analysis

Figure 33.3 shows the cross-sectional view of Inconel 718 welds for the different base material conditions. Full weld penetration achieved for all welding cases with a heat input of 78 J mm⁻¹, 74 J mm⁻¹, and 71 J mm⁻¹ for as-received, ST1, and ST2

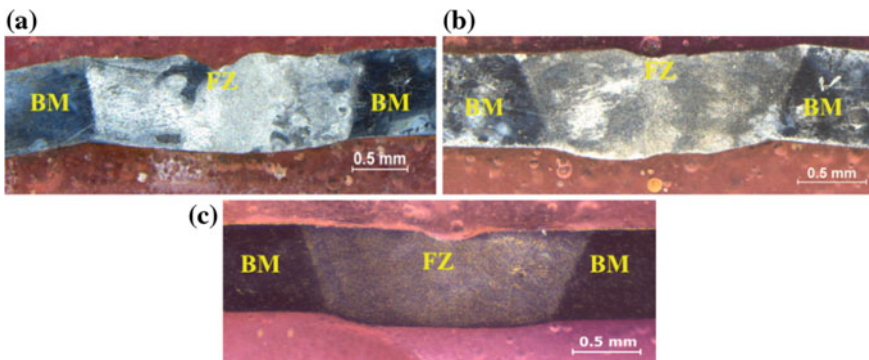


Fig. 33.3 Obtained weld bead from **a** as-received, **b** ST1 and **c** ST2 condition base material

condition base materials, respectively. The obtained weld beads are of trapezoidal shape with a small variation in weld width which is mainly due to variation in the heat input during welding. For as-received condition, the width of weld bead cap was found to be 2.5 mm, and for ST1 and ST2 conditions it was 2.08 and 1.6 mm, respectively. From optical microscopic analysis, it was found that the obtained weld beads were free from any type of surface defects.

Figure 33.4 shows the optical micrograph of weld fusion zone along with fusion boundary (FB) and heat-affected zone (HAZ) for all welded samples. Dendritic structures were seen in the weldment with the interdendritic regions etching dark as compared to the dendritic core. Coarse columnar dendrites grown from solid–liquid interface were seen in all welding conditions, which is mainly due to the higher temperature gradient in the fusion boundary [15], whereas fine and equiaxed dendrites were observed in the ST1 and ST2 weld interior. Figure 33.5 shows higher magnification FESEM micrographs of the as-received, ST1, and ST2 weld interior. Brighter Laves phase was seen in the interdendritic regions. The Laves particles in as-received weld were found to be coarser in the form of interconnecting long chains. The coarser columnar dendritic structure is attributed to the slow cooling rate of as-received weld [13]. When the heat input during welding is more, the weld pool

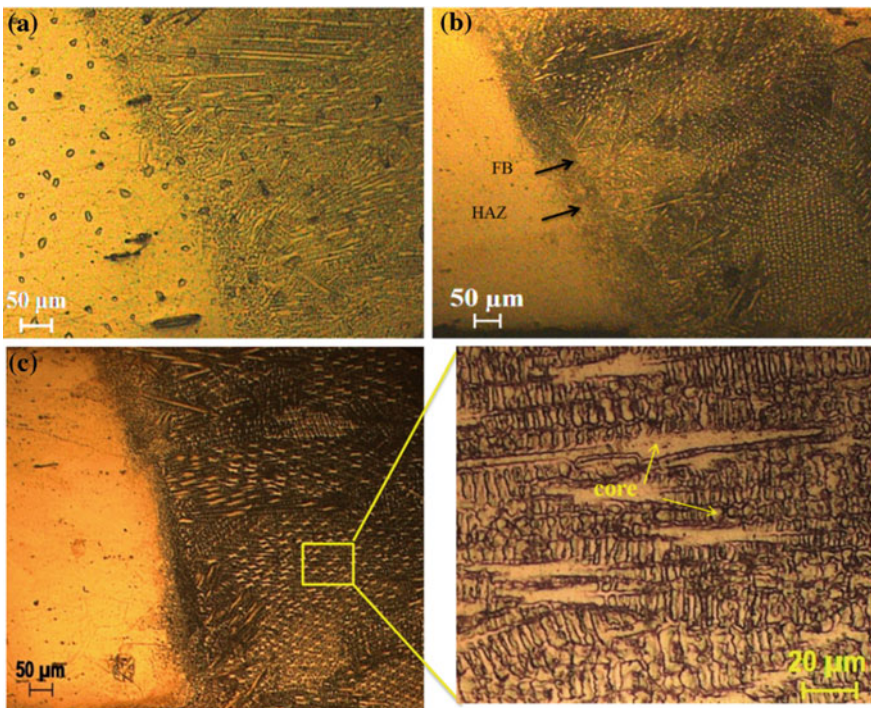


Fig. 33.4 Fusion zone microstructure near to fusion boundary for **a** as-received **b** ST1, and **c** ST2 condition weld bead

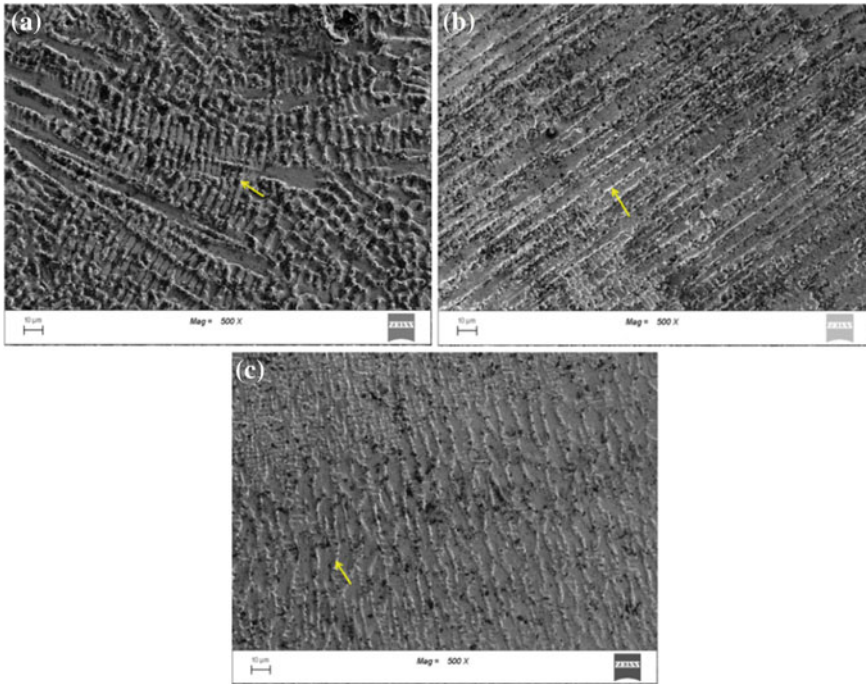


Fig. 33.5 SEM microstructure of **a** as-received, **b** ST1, and **c** ST2 weld interior

last for longer time period—as a result the cooling rate decreases [14], whereas the solidified microstructure of ST1 and ST2 weld were found to be finer as compared to as-received weld. ST2 weld found to have a mixed structure of fine columnar and equiaxed dendritic regions due to the higher cooling rate. Slow solidification rate provides sufficient time for solute redistribution as a result, segregation of Nb and other favorable alloying element takes place in the interdendritic region [16].

Figure 33.6 shows the elemental distribution of interdendritic and core region for the as-received weld through EDX analysis. It can be seen from the spectrum 1 (Fig. 33.6b) interdendritic regions are rich in Nb and Al as compared to the dendritic core (Fig. 33.6c). Hence higher segregation is consuming a significant amount of favorable alloying elements and promotes formation of brittle intermetallics Laves phase. The Laves formation can be controlled by refining the solidified structure which can be archived by controlling the welding heat input or weld solidification rate. The ST1 and ST2 weld bead were obtained at a lower heat input compared to as-received weld. As a result, the cooling rate is high and the obtained microstructures become finer and fragmented. Hence, the segregational effect is less and Nb-rich Laves phase formation also reduces.

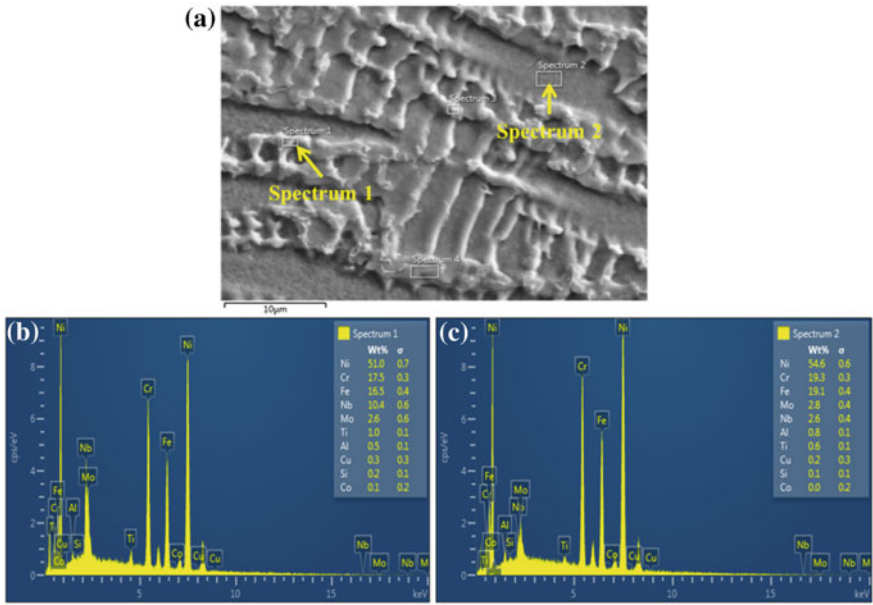


Fig. 33.6 EDAX analysis of the as-received the weld

33.3.2 Mechanical Properties

The base materials and weld metal tensile properties for all three conditions are given in Table 33.3. All the welded samples were failed in the weld zone. Tensile strength of the solution-treated sheets was found to be inferior to that of the as-received sheets, which is mainly due to the grain coarsening during solution treatment [4]. The ST2 base material shows excellent tensile ductility as compared to

Table 33.3 Tensile test results

Condition	0.2% PS (MPa)	UTS (MPa)	Elongation (%)
Base material, (as-received)	640	945	20
Base material (ST1)	561	938	23
Base material (ST2)	463	836	33.9
Weld, as-received	498	761	9.7
Weld, ST1	453	827	19.8
Weld, ST2	421	769	31.2

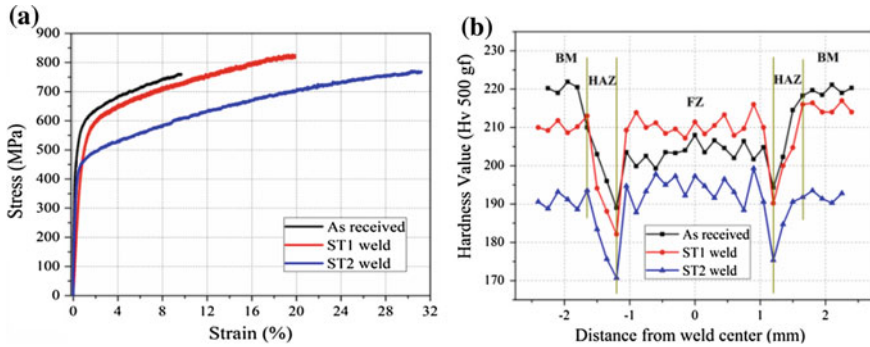


Fig. 33.7 Mechanical properties of the welded joints, **a** tensile strength and **b** micro-hardness distribution

other conditions because of slow air cooling during solution treatment. The ST1 base material shows moderate strength and ductility as compared to as-received and ST2 base material. The tensile properties of the base materials were found to be superior to the corresponding weld metals for all conditions due to the formation of brittle intermetallic phases in the interdendritic regions during weld solidification (Fig. 33.7).

The joint efficiency (with reference to UTS) of the as-received weld with respect to base material is found to be 80.5% with a 51% reduction in ductility, whereas the joint efficiency for ST1 and ST2 weld is found to be 88.2 and 92%, respectively with a reduction of 14 and 8% in the tensile ductility. UTS of the as-received weld was found to be marginally lesser than ST2 weld, but with a sharp fall in the ductility, whereas ST1 weld reported highest tensile strength with a moderate elongation of 20%. Pereira et al. [4] reported the same trend of results and concluded sheets with higher ductility has high impact strength which is a necessary parameter of the base material in fan containment application. The fine microstructure of ST1 and ST2 condition weld has shown significant improvement in tensile strength and ductility. The difference in the tensile properties is mainly due to the formation of intermetallic Laves phase. In as-welded condition, the fusion zone showed an ample amount of interdendritic Nb segregation and intermetallic Laves phase due to the microstructural coarsening. The laves phase not only consumes necessary alloying element from the metal matrix but also provides suitable site for crack initiation in the fusion and HAZ and cause early failure as shown in Fig. 33.8a [17], whereas the fracture surface of ST2 weld exhibits a very fine dimple structure with very less microvoids and cracks, resulting in a ductile mode of failure as compared to the as-received welded sample as shown in Fig. 33.8.

The hardness value of the as-received weld drops in the weld zone as compared to the base material which is due to the difference in precipitation of principal strengthening phase γ'' (Ni_3Nb). The coarse Laves of as-received fusion zone consumes ample amount of Nb that were originally present in the base material, makes less Nb available for the γ'' precipitation which is the main cause of hardness reduction.

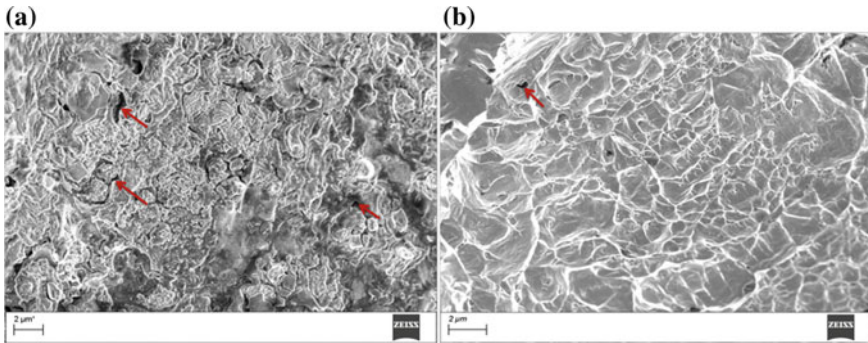


Fig. 33.8 Tensile fracture surfaces of **a** as-received and **b** ST2 weld

For ST1 and ST2 weld, the fusion zone hardness value is found to be almost equal to the base material due to the refined microstructure that hinders Nb segregation and Laves formation in the interdendritic region. The micro-hardness of the HAZ decreased in all the cases is mainly due to the grain coarsening in the region.

33.4 Conclusions

An experimental investigation based on micro-plasma arc welding of Inconel 718 thin sheets with different pre-weld solution-treated conditions was carried out, and following conclusions have been drawn.

- Significant grain coarsening was observed in the air-cooled solution-treated base material as compared to water-cooled base material.
- The solution treatment followed by air cooling of the base material reduces tensile strength by 11%, whereas ductility increased by 41%. For water-quenched base material, it was 12.5 and 13%, respectively.
- For as-received base material, full penetration was achieved at a higher heat input (78 J mm^{-1}) as compared to ST1 solution-treated condition (71 J mm^{-1}).
- The joint efficiency of ST2 welding condition is found to be 92%, whereas for ST1 and as-received welding condition it is 88 and 80%, respectively.
- The hardness variation in BM and FZ is found to be minimal in ST1 and ST2 welding condition as compared to as-received welding condition.
- The application of lower heat input for ST1 and ST2 weld resulted in remarkable refinement of the weld-solidified microstructure and reduces Nb segregation and formation of Laves phase in the fusion zone, resulting in improvement of the weld mechanical properties.

Acknowledgements The authors gratefully acknowledge the Central Instruments Facility (CIF), Central Workshop, Mechanical Engineering Department, Advanced Welding Laboratory, IIT Guwahati, India, for providing the experimental and analysis facility to carry out this research work.

References

1. Brooks, J.W., Bridges, P.J.: Metallurgical stability of Inconel alloy 718. *Superalloys* **88**, 33–42 (1988)
2. Radhakrishna, C., Rao, K.P.: Studies on creep/stress rupture behaviour of superalloy 718 weldments used in gas turbine applications. *Mater. High Temp.* **12**, 323–327 (1994)
3. Cao, X., Rivaux, B., Jahazi, M., Cuddy, J., Birur, A.: Effect of pre- and post-weld heat treatment on metallurgical and tensile properties of Inconel 718 alloy butt joints welded using 4 kW Nd:YAG laser. *J. Mater. Sci.* **44**, 4557–4571 (2009)
4. Pereira, J.M., Lerch, B.A.: Effects of heat treatment on the ballistic impact properties of Inconel 718 for jet engine fan containment applications. *Int. J. Impact Eng.* **25**, 715–733 (2001)
5. Sims, C.T., Hagel, W.C.: *The superalloys-vital high temperature gas turbine materials for aerospace and industrial power*. Wiley, Hoboken (1972)
6. Kuo, C.M., Yang, Y.T., Bor, H.Y., Wei, C.N., Tai, C.C.: Aging effects on the microstructure and creep behavior of Inconel 718 superalloy. *Mater. Sci. Eng. A* **510**, 289–294 (2009)
7. You, X., Tan, Y., Shi, S., Yang, J.-M., Wang, Y., Li, J., You, Q.: Effect of solution heat treatment on the precipitation behavior and strengthening mechanisms of electron beam smelted Inconel 718 superalloy. *Mater. Sci. Eng. A* **689**, 257–268 (2017)
8. Ram, G.J., Reddy, A.V., Rao, K.P., Reddy, G.M.: Microstructure and mechanical properties of Inconel 718 electron beam welds. *Mater. Sci. Technol.* **21**, 1132–1138 (2005)
9. Radhakrishnan, B., Thompson, R.G.: A model for the formation and solidification of grain boundary liquid in the heat-affected zone (HAZ) of welds. *Metall Mat. Trans. A.* **23**, 1783–1799 (1992)
10. Huang, C.A., Wang, T.H., Lee, C.H., Han, W.C.: A study of the heat-affected zone (HAZ) of an Inconel 718 sheet welded with electron-beam welding (EBW). *Mater. Sci. Eng. A* **398**, 275–281 (2005)
11. Gobbi, S., Zhang, L., Norris, J., Richter, K.H., Loreau, J.H.: High powder CO₂ and Nd-YAG laser welding of wrought Inconel 718. *J. Mater. Process. Technol.* **56**, 333–345 (1996)
12. Radhakrishna, C.H., Rao, K.P.: The formation and control of Laves phase in superalloy 718 welds. *J. Mater. Sci.* **32**, 1977–1984 (1997)
13. Janaki Ram, G.D., Venugopal Reddy, A., Prasad Rao, K., Madhusudhan Reddy, G.: Control of Laves phase in Inconel 718 GTA welds with current pulsing. *Sci. Technol. Weld. Joining* **9**, 390–398 (2004)
14. Kou, S.: *Welding metallurgy*. Wiley, New Jersey, USA (2003)
15. Janaki Ram, G.D., Venugopal Reddy, A., Prasad Rao, K., Reddy, G.M., Sarin Sundar, J.K.: Microstructure and tensile properties of Inconel 718 pulsed Nd-YAG laser welds. *J. Mater. Process. Technol.* **167**, 73–82 (2005)
16. Mei, Y., Liu, Y., Liu, C., Li, C., Yu, L., Guo, Q., Li, H.: Effect of base metal and welding speed on fusion zone microstructure and HAZ hot-cracking of electron-beam welded Inconel 718. *Mater. Des.* **89**, 964–977 (2016)
17. Vernot-Loier, C., Cortial, F., Loria, E.A.: *Superalloys 718, 625 and various derivatives*, pp. 409–422. Miner. Metals Mater. Soc., Warrendale, PA (1991)

Chapter 34

Refilling of Pinhole in Friction Stir Spot Welding Using Waste Chips



N. Bhardwaj , R. Ganesh Narayanan  and U. S. Dixit 

Abstract Friction stir welding (FSW) is considered as a sustainable and green alternative to conventional welding techniques. However, the pinhole left after welding is one of the major defects. This study discusses a novel technique of refilling the pinhole, left after conventional friction stir spot welding (FSSW) of aluminium alloy AA6082 overlapping sheets, using waste aluminium chips. The maximum load-bearing capacity of the refilled joint was found using T-peel test. The results were compared with that of conventional FSSW using a tool with pin and FSSW using pin-less tool. Further, the process parameters used for welding, viz. rotational speed, plunge depth during welding and plunge depth during refilling, have been optimized using evolutionary optimization technique to arrive at the optimum maximum load-bearing capacity of the joint for the mentioned process.

Keywords Sustainability · Refill-FSSW · Pinhole · Chips · Optimization

34.1 Introduction

Recent advances in automotive and aerospace applications have seen the rise in the use of lightweight materials like aluminium and magnesium alloys. These materials are difficult to weld using conventional welding techniques, which include problems of high heat conductivity, thermal distortion, oxide layer formation, etc. Resistance spot welding (RSW) has the demerits of very high operating and investment costs along with high distortion from heat. An alternative to conventional fusion welding is the friction stir welding (FSW) technique, which shows better mechanical properties, lesser heat distortion, lower power consumption, and lesser pollution. Along with high-energy efficiency, the process does not require any filler material during welding and helps saving weight and cost. The absence of arc flash, spatter, and pollution contributes to providing a safer working environment for the workers. As such, it is regarded as a sustainable and green welding technique. However, one of the major

N. Bhardwaj · R. Ganesh Narayanan (✉) · U. S. Dixit
Department of Mechanical Engineering, Indian Institute of Technology, Guwahati 781039, India
e-mail: ganu@iitg.ac.in

© Springer Nature Singapore Pte Ltd. 2020
M. S. Shunmugam and M. Kanthababu (eds.), *Advances in Additive Manufacturing and Joining*, Lecture Notes on Multidisciplinary Industrial Engineering,
https://doi.org/10.1007/978-981-32-9433-2_34

defects of FSW is the pinhole or exit hole that remains in the weld nugget after FSW process. The pinhole results in reduced bonding width in that region and lower strength of the welded joint. It also leads to stress concentration as well as increase in susceptibility to corrosion.

In order to solve the pinhole problem in FSW, runoff plates could be used, but it becomes particularly challenging in the case of circumferential welds or friction stir spot welding (FSSW) due to geometrical and metallurgical limitations. In order to eliminate the pinhole, FSW has been performed with pin-less tool by a few researchers. However, sufficient penetration of the stirred zone was not achieved which resulted in lower weld strength. Tozaki et al. [1] developed a new tool without pin with a scroll groove on its shoulder for effective friction stir welding. The spiral-shaped groove in the tool shoulder helped in more effective stirring of the metal and aided in increasing penetration depth to a certain extent. Aota et al. [2] had also attempted to use a tool without pin but sufficient depth of stir zone was not achieved. Allen et al. [3] and Uematsu et al. [4] had used double-acting tools for FSSW process consisting of outer shoulder and inner retractable pin. The tool refilled the pinhole successfully, but the system was complicated. A self-refilling friction stir welding (SRFSW) process to repair pinhole was introduced by Zhou et al. [5]. The pinhole was filled by combined effect of plastic deformation and flow of material around the pinhole. A series of tools were designed with changed pin diameter and lengths and used step by step. A spiral groove was also employed in the shoulder for better stirring. Huang et al. [6, 7] came up with a new technique of filling friction stir welding (FFSW) where a semi-consumable tool was used. A non-consumable shoulder with a consumable joining bit was used in this process in a two-stage process to fill the pinhole left after FSW. Zhang et al. [8] tried improving the consumable pin by using a T-shaped filler bit to fill the pinhole. Behmand et al. [9] discussed filling pinholes of FSW lap joints using consumable pin tools and investigated the effect of different geometries of the consumable pin. Reimann et al. [10] studied the microstructure and mechanical properties of pinhole repair welds in AA7075-T651 using refill friction stir welding where a retractable pin was employed to achieve a pinhole-free spot weld. However, the tool design used was complex.

In this study, a novel technique of refilling pinhole with waste chips has been introduced that does not require a complex mechanism to operate. The use of waste chips to fill the pinhole also adds to the sustainable nature of the FSW process. Further, the process parameters used in this method were optimized using evolutionary optimization.

34.2 Experimental Details

In this study on refilling pinhole in FSSW using waste aluminium chips, spot welding and T-peel tests were performed as part of experiments. The joint quality was evaluated by the results of the T-peel test. The following subsections describe the processes in details.

34.2.1 Welding

Two aluminium alloy AA6082 sheets of 1.5-mm thickness each were welded using friction stir spot welding (FSSW) and subsequently the pinhole was refilled by waste aluminium chips. The waste chips were derived from chips produced during turning of commercially available pure aluminium rod. The chips produced by turning have been termed “waste chips” since it does not find any usage and often discarded as scrap or recycled by re-melting which requires additional expenditure of energy. The chips belong to different grade as compared to base material. The base material properties found from tensile test are as given in Table 34.1. A vertical milling machine was used to perform FSSW. The welding operation involved two steps. In step 1, the two overlapping sheets were clamped and FSSW was performed using a tool with pin having shoulder diameter of 12 mm, pin diameter of 6.5 mm, and pin length of 1.2 mm. The rotational speed and the plunge depth were varied for the study. However, after this step, a pinhole of about 6.5 mm diameter remained in the weld spot. Step 2 involved refilling of the pinhole with waste aluminium chips. The amount of chip was derived from calculation of volume of pinhole and density of aluminium. A 20% more than calculated mass of chip was taken as a safety measure in order to compensate for waste in the form of flash and other losses. An amount of 0.12 g of chips was compacted into ball-shaped structures as shown in Fig. 34.1. The chips were then inserted into the pinhole. Subsequently a flat tool of diameter 14.4 mm was taken and stirred over the chip-filled pinhole with the same rotational speed and axis of rotation as that in Step 1. Different plunge depths during refilling were also used for the study. In all cases, a dwell time of 15 s was used. Thus, three variable process

Table 34.1 Tensile properties of AA6082

Property	Value
Ultimate tensile stress	350 MPa
Breaking stress	294 MPa
0.2% offset yield stress	314 MPa
Uniform elongation	10%
Total elongation	15%
Strain hardening exponent	0.1
Strength coefficient	485 MPa
Plastic strain ratio	0.7

Fig. 34.1 Chips compacted into ball-shaped structure



parameters, viz. rotational speed, plunge depth during welding (Step 1), plunge depth during refilling (Step 2), were considered for the study. During welding, the plunge depth is considered as the sum of plunge depth of the pin and the shoulder of the tool for convenience of calculation during optimization.

34.2.2 T-Peel Test

In order to compare the quality of the welded joints, T-peel test was conducted to find out the maximum load-carrying capacity of each joint. Samples were prepared according to AWS B4.0-2007 standards as shown in Fig. 34.2a. In order to keep the weld spot unaffected during sample preparation, the weld spot was fixed in a vice. The extended parts which were to be used for clamping were then bent to form the T-shaped sample for the test as shown in Fig. 34.2b. The samples were securely clamped, and test was performed as shown in Fig. 34.3 in a universal testing machine at room temperature. The test gave a plot of the load versus extension graph, where the extension is the opening of the root of the T as shown in Fig. 34.3. The extensions at maximum load and at failure were recorded during the test.

34.3 Evolutionary Optimization

To arrive at the best combination of process parameters for the welding process, evolutionary optimization technique, given by G.E.P. Box, was used. In this optimization technique [11], for an N -dimensional case, $2N + 1$ points are evaluated to find the best functional value or output. Starting from an initially assumed best point, \bar{x} , a hypercube is created around that point with $2N$ corner points where functional

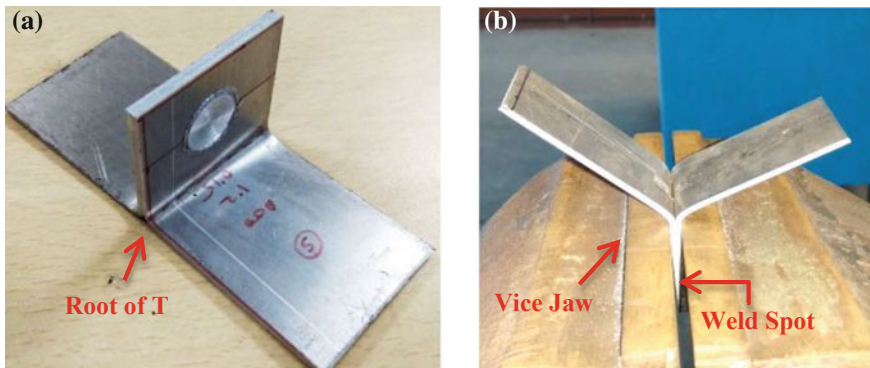
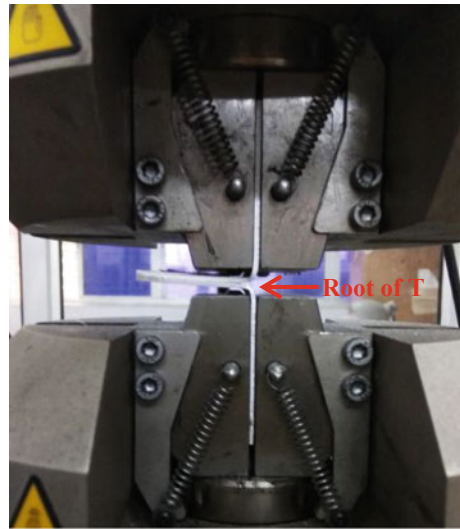


Fig. 34.2 a T-shaped sample prepared for T-peel test, b sample preparation for T-peel test

Fig. 34.3 T-peel test performed in a universal testing machine



value is evaluated. The size of the hypercube is given by Δ , known as reduction parameter. It denotes the length of each dimension of the hypercube, fixed according to precision required. A variation of $\pm\Delta/2$ is given to the best point, \bar{x} , to form the hypercube around it. The best functional value or output is found from the $2N + 1$ points, and the point which gives the best output value is chosen as the next \bar{x} . The process is repeated by choosing that point as the next best point. However, if no improvement is found, the size of the hypercube is reduced by reducing Δ only and repeating the process.

34.4 Results and Discussion

The results of refilling the pinhole are discussed in the following subsections. The T-peel tests results were used to employ evolutionary optimization. The detailed optimization process by using the T-peel test results in successive iterations is described.

34.4.1 Refilled Pinhole

The pinhole left after Step 1 was successfully refilled in Step 2 for all the cases. The stirring operation on filled waste chips was able to effectively refill the pinhole to give a surface with no depression mark as shown in Fig. 34.4a, b. Apart from aesthetic appearance of the weld spot, the refilled joint also showed better load-bearing capacity. A comparison of maximum load-bearing capacity in T-peel test

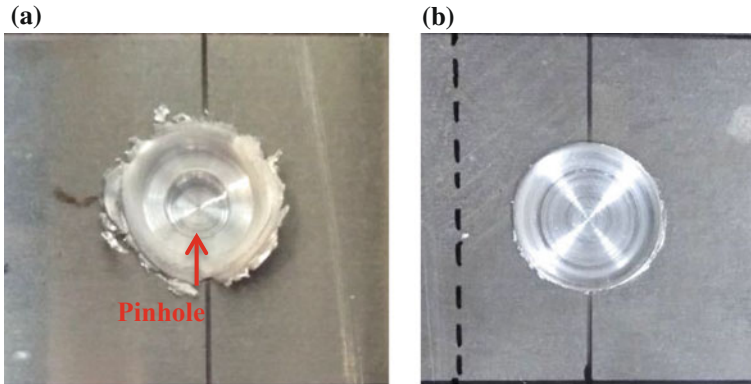


Fig. 34.4 Top view of **a** FSSW joint after Step 1 with pinhole, **b** refilled FSSW joint after Step 2

of (a) conventional FSSW joint made using a tool having pin, (b) FSSW joint with refilled pinhole using waste chips, and (c) FSSW using pin-less flat shoulder tool is given in Table 34.2. For conventional FSSW, rotational speed of 440 revolutions per minute (rpm) and plunge depth of 1.32 mm was used as in Step 1. For refilled FSSW, rotational speed of 440 rpm, plunge depth of 1.32 mm during welding and 0.18 mm plunge depth during refilling process was used. For FSSW with pin-less tool, 440 rpm was used as the rotational speed and 0.18 mm was used as the plunge depth during welding.

It can be seen from the results that refilling the pinhole with waste chips delivered 16% higher load-bearing capacity as compared to conventional FSSW with a tool having pin. The reason can be attributed to increase in bonded area from that of the joint with pinhole as well as reduction in stress concentration. The absence of pinhole would also result in lesser susceptibility to corrosion since there is no depression on the surface for accumulation of corrosive substances. The pinhole acts as a cavity for corrosive substances to get accumulated. The accumulation of chlorides on the surface may result in breaking of the protective passive oxide layer and lead to pitting corrosion. Corrosive liquid (e.g., saltwater) may fill the pinhole and with passage of time become more acidic in nature, as seen in crevice corrosion in aluminium and aluminium alloys, leading to corrosion [12]. The refilling of the pinhole eliminates the possibility of accumulation of corrosive substances on the surface of the product. On the other hand, an increase of 84% load-bearing capacity was observed as compared to joint made by a pin-less flat shoulder tool. The lack of sufficient penetration depth

Table 34.2 Maximum load-bearing capacity of different welded joints

Samples	Maximum load (N)
(a) FSSW joint with a tool having pin	838
(b) Refilled FSSW joint	972
(c) FSSW using pin-less tool	528

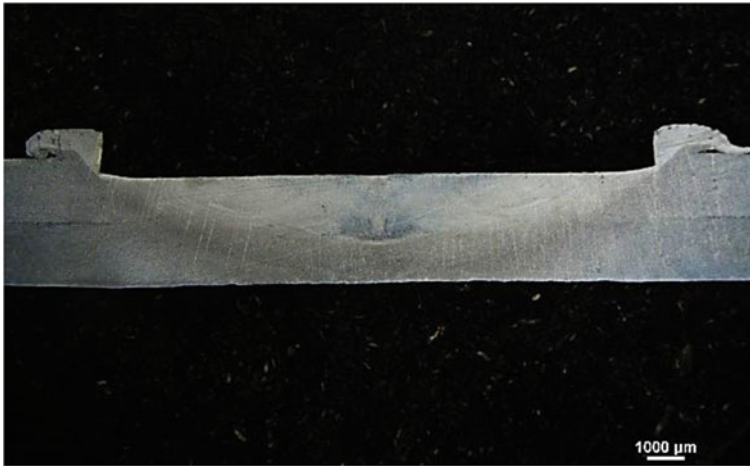


Fig. 34.5 Cross-section of refilled FSSW joint using waste aluminium chips

of stirring zone in case of pin-less flat shoulder tool resulted in a significantly lower maximum load-bearing capacity for the joint. Thus, it can be inferred that the tool pin plays an important role in stirring of the material and in order to refill the pinhole left after welding, use of waste aluminium chips is an effective solution. The cross section of the filled FSSW joint using waste aluminium chips is shown in Fig. 34.5 that shows an effective refilling of the pinhole and a seamless joint between the two plates. Here the stirred zone as well as refilled pinhole area can be visualized along with effective joining between the two plates.

34.4.2 Optimization of Process Parameters

For this study, as starting point, initial best point, \bar{x} , was assumed to have process parameters of 600 rpm as rotational speed, plunge depth during welding of 1.2 mm, and plunge depth during refilling of 0.15 mm (Sample S_0) which is tabulated in Table 34.3. The hypercube of 8 corner points was created around \bar{x} by giving $\pm 10\%$ variation to each of the three process parameters at \bar{x} . However, due to machine

Table 34.3 Initially assumed best point and load-carrying capacity in T-peel test

Sample	Rotational speed (rpm)	Plunge during welding (mm) Step 1	Plunge during refilling (mm) Step 2	T-peel test results		
				Maximum load (N)	Extension at maximum load (mm)	Extension at failure (mm)
S_0	600	1.20	0.15	883	4.21	10.56

constraints, rotational speed of 440 rpm was used for 10% lower value of 600 and 815 rpm was used for 10% higher value of 600 rpm. Also the plunge depth was constrained by the least count of 0.03 mm. The new set of 8 combinations is listed as shown in Table 34.4. The corresponding T-peel test results are also mentioned. The mathematically obtained combination of process parameters for $S_{1.3}$, $S_{1.4}$, $S_{1.7}$, and $S_{1.8}$ gave combinations where the shoulder of the tool did not come in contact with the base material. For conventional FSSW process to fabricate a successful spot joint, the shoulder of the tool must be in contact with the base material. Thus, the four points were discarded from actual experimentation and no tests were performed. For nomenclature of the samples, in the subscript of S , the digit on the left-hand side of the decimal denotes the iteration number, while the digit on the right-hand side of the decimal denotes the sample number in that iteration.

From the results of T-peel test and taking maximum load-bearing capacity as the deciding criteria, sample $S_{1.1}$ showed the highest load-bearing capacity among all the points. Hence, the next best point, \bar{x} , is chosen as the parameters corresponding to $S_{1.1}$ and the process was repeated. To form the hypercube, the next set of combination was obtained by giving $\pm 10\%$ variations to the process parameters of sample $S_{1.1}$. The combinations and the T-peel test results are tabulated in Table 34.5.

It can be observed from Table 34.5 that there was no improvement in the maximum load-bearing capacity for any of the new combinations with $\pm 10\%$ variation from sample $S_{1.1}$. For the next iteration, the point \bar{x} remained the same; however, the variation given to form the new hypercube was reduced to $\pm 5\%$ in order to refine the results. Since the rotational speed variation was limited by machine constraints and the plunge depth during refilling was constrained by the least count of 0.03 mm of the machine; only the plunge depth during welding was given a $\pm 5\%$ variation. Table 34.6 shows the combination as well as the T-peel test results. It can be observed that there was no improvement in maximum load-bearing capacity with $\pm 5\%$ variation given

Table 34.4 Load-carrying capacity for combination of parameters with $\pm 10\%$ variations from parameters of sample S_0

Sample	Rotational speed (rpm)	Plunge during welding (mm) Step 1	Plunge during refilling (mm) Step 2	T-peel test results		
				Maximum load (N)	Extension at maximum load (mm)	Extension at failure (mm)
$S_{1.1}$	440	1.32	0.18	972	4.99	13.80
$S_{1.2}$		1.32	0.12	678	3.51	8.55
$S_{1.3}$		1.08	0.18	–	–	–
$S_{1.4}$		1.08	0.12	–	–	–
$S_{1.5}$	815	1.32	0.18	684	3.40	7.82
$S_{1.6}$		1.32	0.12	782	7.74	13.84
$S_{1.7}$		1.08	0.18	–	–	–
$S_{1.8}$		1.08	0.12	–	–	–

Table 34.5 Load-carrying capacity for combination of parameters with $\pm 10\%$ variations from parameters of sample $S_{1,1}$

Sample	Rotational speed (rpm)	Plunge during welding (mm) Step 1	Plunge during refilling (mm) Step 2	T-peel test results		
				Maximum load (N)	Extension at maximum load (mm)	Extension at failure (mm)
$S_{2,1}$	325	1.44	0.21	834	5.93	13.93
$S_{2,2}$		1.44	0.15	512	3.22	10.11
$S_{2,3}$		1.20	0.21	794	6.64	12.35
$S_{2,4}$		1.20	0.15	549	5.54	5.62
$S_{2,5}$	600	1.44	0.21	664	7.13	13.96
$S_{2,6}$		1.44	0.15	789	8.49	15.64
$S_{2,7}$		1.20	0.21	972	9.02	18.17
$S_{2,8}$		1.20	0.15	964	8.23	15.07

Table 34.6 Load-carrying capacity for combination of parameters with $\pm 5\%$ variations from parameters of sample $S_{1,1}$

Sample	Rotational Speed (rpm)	Plunge during welding (mm) Step-1	Plunge during refilling (mm) Step-2	T-peel Test Results		
				Maximum Load (N)	Extension at maximum load (mm)	Extension at failure (mm)
$S_{3,1}$	440	1.26	0.18	937	8.49	11.66
$S_{3,2}$		1.38	0.18	862	4.96	10.28

to \bar{x} . Therefore, \bar{x} remained the same and to further refine the results, variation of $\pm 2.5\%$ was given as tabulated in Table 34.7. No improvement in result was observed even with $\pm 2.5\%$ variation and the least count constraint for variation of plunge depth during welding was also reached. Hence the point $S_{1,1}$, with parameters of 440 rpm, 1.32 mm plunge depth during welding, 0.18 mm plunge depth during refilling, was

Table 34.7 Load-carrying capacity for combination of parameters with $\pm 2.5\%$ variations from parameters of sample $S_{1,1}$

Sample	Rotational speed (rpm)	Plunge during welding (mm) Step-1	Plunge during refilling (mm) Step-2	T-peel test results		
				Maximum load (N)	Extension at maximum load (mm)	Extension at failure (mm)
$S_{4,1}$	440	1.29	0.18	956	8.94	25.43
$S_{4,2}$		1.35	0.18	824	5.64	12.87

regarded as the optimized combination of the process parameters with the maximum load-bearing capacity of 972 N and failure occurring at an extension of 13.80 mm. However, if the deciding criterion for optimization was chosen as extension at the maximum load or extension at failure, the resultant combination of parameters with optimized output would be different from this analysis. Depending on the required property, the deciding criteria for optimization can be chosen.

34.5 Conclusions

In this study, a novel method introduced to refill the pinhole in FSSW using waste aluminium chips showed higher load-bearing capacity as compared to both conventional FSSW using a tool having pin as well as FSSW using pin-less tool. The method of refilling imparts both aesthetic value as well as lesser susceptibility to corrosion in the weld spot formed. A seamless bonding of the two plates was also observed in the cross section of the weld spot with no trace of the pinhole. Thus, refilling pinhole with aluminium chips can be regarded as an effective method of elimination of the pinhole in FSSW.

The evolutionary optimization method revealed that rotational speed of 440 rpm, plunge depth during welding of 1.32 mm and plunge depth during refilling of 0.18 mm delivered the best results with 972 N maximum load-bearing capacity. A higher plunge depth resulted in thinning of the bonded region, while a lower plunge depth results in insufficient penetration of stirred zone. Thus, optimization of the process parameters delivered the best combination for this process to obtain the most favourable output. There is also a scope to study the refilling of pinhole with waste chips for materials other than aluminium. Further studies could be performed on the microstructural properties of the various regions in the weld spot.

References

1. Tozaki, Y., Uematsu, Y., Tokaji, K.: A newly developed tool without probe for friction stir spot welding and its performance. *J. Mater. Process. Technol.* **210**, 844–851 (2010)
2. Aota, K., Ikeuchi, K.: Development of friction stir spot welding using rotating tool without probe and its application to low carbon steel plates. *Q. J. Japan Weld. Soc.* **26**, 54–60 (2008)
3. Allen, C.D., Arbegast, W.J.: Evaluation of friction spot welds in aluminum alloys. *SAE Int.* 2005-01-1252 **1**, 107–113 (2005)
4. Uematsu, Y., Tokaji, K., Tozaki, Y., Kurita, T., Murata, S.: Effect of re-filling probe hole on tensile failure and fatigue behaviour of friction stir spot welded joints in Al–Mg–Si alloy. *Int. J. Fatigue* **30**, 1956–1966 (2008)
5. Zhou, L., Liu, D., Nakata, K., Tsumura, T., Fujii, H., Ikeuchi, K., Michishita, Y., Fujiya, Y., Morimoto, M.: New technique of self-refilling friction stir welding to repair keyhole. *Sci. Technol. Weld. Joining* **17**(8), 649–655 (2013)
6. Huang, Y.X., Han, B., Tian, Y., Liu, H.J., Lv, S.X., Feng, J.C., Leng, J.S., Li, Y.: New technique of filling friction stir welding. *Sci. Technol. Weld. Joining* **16**, 497–501 (2011)

7. Huang, Y.X., Han, B., Lv, S.X., Feng, J.C., Liu, H.J., Leng, J.S., Li, Y.: Interface behaviours and mechanical properties of filling friction stir weld joining AA2219. *Sci. Technol. Weld. Joining* **17**, 225–230 (2012)
8. Zhang, G.F., Jiao, W.M., Zhang, J.X.: Filling friction stir weld keyhole using pin free tool and T shaped filler bit. *Sci. Technol. Weld. Joining* **19**(2), 98–104 (2014)
9. Behmand, S.A., Mirsalehi, S.E., Omidvar, H., Safarkhanian, M.A.: Filling exit holes of friction stir welding lap joints using consumable pin tools. *Sci. Technol. Weld. Joining* **20**(4), 330–336 (2015)
10. Reimann, M., Goebel, J., dos Santos, J.F.: Microstructure and mechanical properties of keyhole repair welds in AA7075-T651 using refill friction stir spot welding. *Mater. Des.* **132**, 283–294 (2017)
11. Rao, S.S.: *Engineering optimization: theory and practice*, 3rd edn. New Age International (P) Ltd., Delhi (2010)
12. Oguzie, E.E.: Corrosion inhibition of aluminium in acidic and alkaline media by *Sansevieria trifasciata* extract. *Corros. Sci.* **49**(3), 1527–1539 (2007)

Chapter 35

Dissimilar Friction Stir Welding of DH36 Shipbuilding Steel and Mild Steel



Pardeep Pankaj , Avinish Tiwari , Saurav Suman , Abhishek Kumar , Rituraj Bhattacharjee , Subhashis Majumder and Pankaj Biswas

Abstract Tailor welded blanks are of increasing interest for various industrial applications. Many of the industries which are involved in welding of steel are now looking forward to the development of friction stir welding for joining of dissimilar grades of steel. In the present work, DH36 steel to mild steel sheets 4 mm in thickness were successfully joined by friction stir welding using non-consumable tungsten carbide tool at traverse speed of 132 mm/min and tool rotational speed of 600 rpm. Optical microscopy, SEM, EDX analysis, micro hardness testing, and tensile test were performed. Weld nugget exhibited the hardness higher than the mild steel base metal but lower than DH36 shipbuilding steel base metal. Maximum hardness was obtained in TMAZ at advancing side of dissimilar welded specimen. Tensile strength approximately 91.5% of the mild steel base metal strength was obtained.

Keywords Dissimilar friction stir welding · DH36 steel · Mild steel · Microstructure · Hardness · Tensile test

35.1 Introduction

Friction stir welding is a solid state welding process in which base materials are joined without melting and evaporation. This welding technique exhibits the advantages, i.e., less residual distortion, high integrity, and less residual stress in comparison with other to conventional welding process. FSW is highly used to join the aluminum alloys; however, recently higher temperature metals, i.e., structural steels, are also joined using FSW process. Over a past few years, joining of dissimilar metals became a fast developing area as it brings together materials having altered thermal and mechanical properties. The main advantage of joining dissimilar metals is to develop the intricate assemblies to construct the hybrid structures. The incompatibility in physical, chemical, thermal, and mechanical properties in dissimilar steels

P. Pankaj (✉) · A. Tiwari · S. Suman · A. Kumar · R. Bhattacharjee · S. Majumder · P. Biswas
Department of Mechanical Engineering, Indian Institute of Technology Guwahati, Guwahati
781039, Assam, India
e-mail: pankajpardeep22@gmail.com

© Springer Nature Singapore Pte Ltd. 2020
M. S. Shunmugam and M. Kanthababu (eds.), *Advances in Additive Manufacturing and Joining*, Lecture Notes on Multidisciplinary Industrial Engineering,
https://doi.org/10.1007/978-981-32-9433-2_35

makes the difficulty to produce the sound quality joint in terms of joint strength and welding efficiency. It makes dissimilar metal welding more challenging than similar metal welding process. DH36 shipbuilding steel is the high strength structural steel, and it is having the better corrosion resistance, good toughness properties, and excellent processing and welding properties. Mild steel is a low-carbon content structural steel with other alloying elements resulting in lower tensile strength in comparison with the DH36 shipbuilding steel. Nowadays, it is the most common type of the structural steel with lowest price and acceptable material properties for various industrial applications, i.e., metals chains, engine parts, wire ropes, auto body panels, nut, bolts, nails, and screws and bicycle rims.

The magnesium and aluminum alloy plates having thickness of 2 mm, were joined using friction stir process. The formation of mixed microstructural behavior of magnesium and aluminum alloys was observed adjacent to the weld interface. Tensile test showed no significant variation in the tensile strength which was the function of tool rotational speed. It was also reported that increasing tool rotational speed leads to smoother surface morphology of the stir zone [1]. The joining of Mg–Zn–Zr alloy (ZK60) and titanium plate's thickness of 2 mm was performed using FSW process with pin offset toward the ZK60 plate. Maximum tensile strength was achieved about 69% of the ZK60 parent metal strength and tensile specimens were ruptured at the stir zone in ZK6 due to the generation of Zn and Zr rich thin layer in the weld joint interface [2]. The aluminum plates and mild steel plates are joined using FSW technique to observe the effect of tool rotational speed, and tool offset on the microstructural behavior, and tensile properties of the weld joints. The tensile strength was reached maximum value which was about 86% of the aluminum alloy. The formation of lower extent of intermetallic compounds was observed in the top side of the steel and aluminum interface [3]. The friction stir lap welding was conducted for joining the Al–Si alloy and titanium sheets to study the microstructure and tensile behavior of welded specimens. The tensile strength of the weld specimen was reached about 62% of Al–Si alloy and fracture occurred at the joint interface [4]. The mild steel and aluminum alloy A7075-T6 sheets were welded using FSW process to observe the post weld properties. It was found that the joint strength of the aluminum alloy was greater than the steel/aluminum interface strength [5]. The FSW process was performed for 6061-T6 aluminum alloy and high strength steel thin sheets. The thickness of IMC layer was observed lesser than the value of 1 μm , and the composition of FeAl or Fe₃Al had a strong influence on the weld joint strength [6]. The friction stir welding was performed between aluminum and AISI 304 stainless steel plates having a thickness of 3 mm with a range of tool rotational speed (i.e., 200–1000 rpm) with an interval of 200 rpm with traverse speed of 60 mm/min. The formation of that intermetallic compounds like FeAl₂, Fe₄Al₃, and Fe₂Al₅ were observed in the interface during FSW of aluminum (CP Al) alloy and 304 stainless steel sheets [7]. The influence of tool rotational speed, traverse speed, and tool pin offset on mechanical properties and microstructure of FS welded joint between TRIP 780/800 steel and Al6061-T6511 sheets of 1.5 mm thickness was studied. The maximum tensile strength ~249 MPa which was approximately 85% of the aluminum base metal under 1800 rpm, 1.65 mm offset, and 60 mm/min was obtained [8]. So, from the above

literature review, it is observed that there are very few published literatures are available for dissimilar friction stir welded structural steel sheets. But there is no literature found on friction stir welding of DH36 shipbuilding steel and mild steel sheets. In the present work, DH36 steel to mild steel sheet of 4 mm in thickness was successfully joined by friction stir welding process under the tool rotational speed of 600 rpm and traverse speed of 132 mm/min. Single-pass butt weld free from any volumetric defect was produced using tapered non-consumable tungsten carbide FSW tool.

35.2 Experimental Details

In this experimental study, friction stir welding was performed to join the DH36 steel and mild steel sheet thickness of 4 mm under the rotational speed of 600 rpm and traverse speed of 132 mm/min using FSW machine and non-consumable tungsten carbide tool as shown in Fig. 35.1. The schematic illustration of friction stir welding technique for joining the dissimilar steels used in this study is represented in Fig. 35.2a. The FSW tool geometry and dimensions are shown in Fig. 35.2b. Welding was carried out with tool pin offset of 2 mm toward mild steel side of worksheet as shown in Fig. 35.2c. FSW tool used in the present experiment was made up of tungsten carbide (WC-10 wt% Co) [9]. The chemical composition of DH36 steel and mild steel is presented in Tables 35.1 and 35.2, respectively. The sheets were machined with dimension of 100 mm × 75 mm × 4 mm in square butt joint configuration before the welding process. Experiment was carried out under the ambient temperature condition. To avoid the generation of voids or groove-type defect, DH36

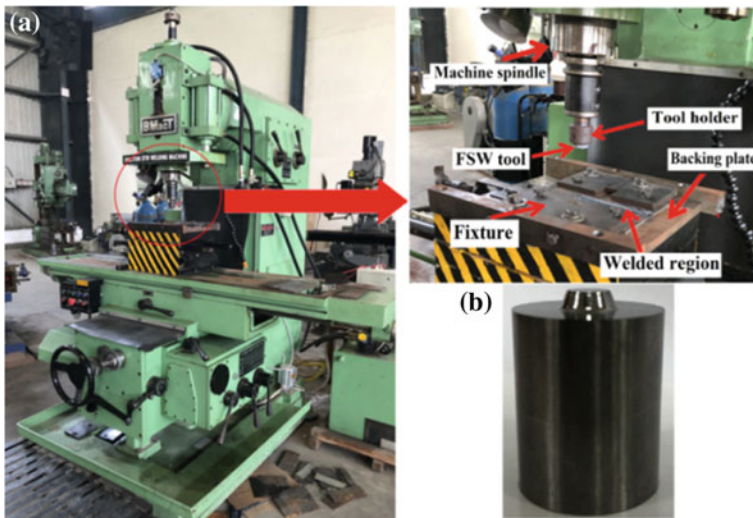


Fig. 35.1 a Friction stir welding experimental setup, b FSW tool

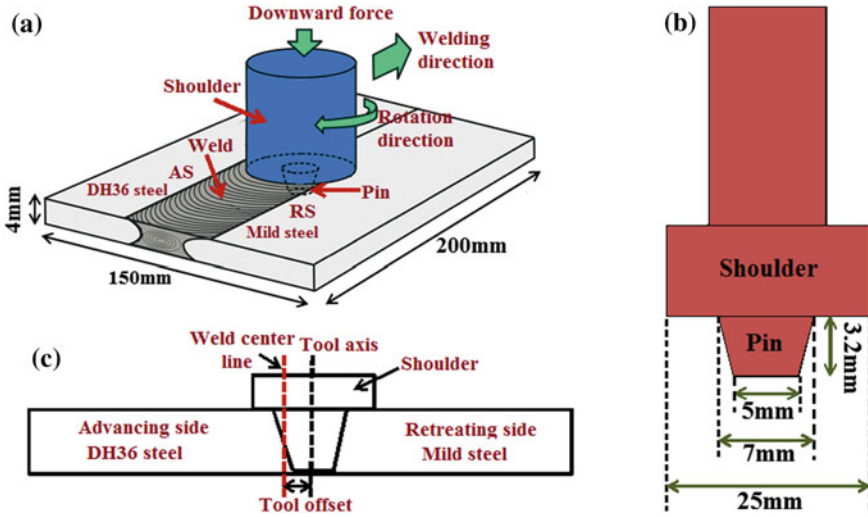


Fig. 35.2 a Schematic representations of FSW to join the DH36 steel to mild steel, b schematic illustration of FSW tool dimension, c position of the tool pin in worksheet

Table 35.1 Chemical composition and mechanical properties of DH36 steel

Chemical compounds		Mechanical properties	
Element	wt (%)	Yield strength (MPa)	385
C	0.16–0.18 max	UTS (MPa)	514
Mn	1.7	% Elongation	16
S	0.25–0.35	Hardness (HV _{0.5})	145
Si	0.45–6		
Cu	0.55–0.66		
Ti	0.05–0.06		
V	0.13–0.15		
Nb	0.05–0.06		
Fe	Rest		

Table 35.2 Chemical composition and mechanical properties of mild steel

Chemical compounds		Mechanical properties	
Element	wt%	Yield strength (MPa)	198
C	0.06–0.08	UTS (MPa)	304
Mn	0.25–0.4	% elongation	17.5
P	≤0.004	Hardness (HV _{0.5})	85
S	≤0.05		
Fe	Rest		

steel sheet was clamped on the advancing side (AS) and the mild steel sheet was fixed on the retreating side (RS). In reverse clamping condition, advancing side material starts to deform, however, retreating side material resists the deformation resulting from less heat generation. This leads to the inadequate metal flow and imperfect weld joint. As the FSW tool rotates and plunged inside the workpiece, the frictional heat between tool shoulder and worksheet responsible for excessive plastic deformation of the material under tool shoulder. The softened plasticized material transfers from the front to the back of the welding line due to the rotation of tool pin which leads to join the worksheets.

To perform the tensile test, the welded sheet was cut normal to the welding path and then machined into the tensile test sample as shown in Fig. 35.6a. The tensile test was performed in room temperature condition at constant 0.5 mm/min crosshead speed. The weld zone was positioned in the middle of the test samples. Metallographic behavior was studied using optical microscope and electron scanning microscopy which was equipped with an EDX system. The welded specimen was sectioned in the normal direction of weld to conduct the metallographic study. The standard metallographic procedure was used to polish the samples followed by the etching process. The welded specimen was etched by 2% nital. The Vickers microhardness test was performed to determine the hardness distribution on the cross section normal to the traverse direction as shown in Fig. 35.11a using 4.9 N load and dwell time of 15 s. The measurements were taken on three lines to determine the through thickness variation of hardness values in the cross section of welded specimen. The hardness values were taken from the mild steel side through to the DH36 steel side.

35.3 Results and Discussion

During the studies, many experiments were performed to find the sound quality of weld joint between DH36 steel and mild steel. Figure 35.3a represents the appearance

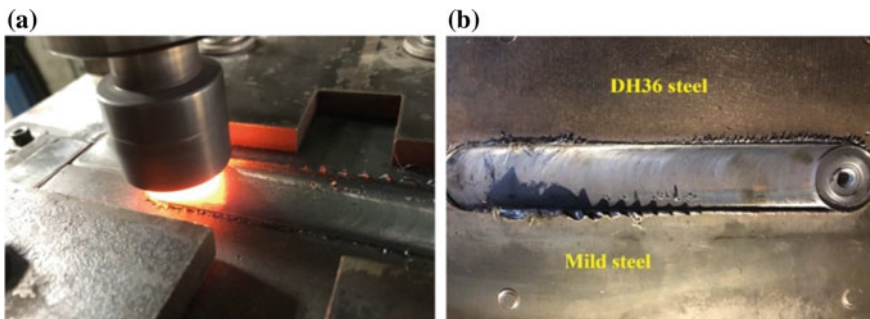


Fig. 35.3 a Appearance during friction stir welding of DH36 steel and mild steel, b surface appearance of friction stir welded joint

of friction stir welding of DH36 steel and mild steel butt joint. Figure 35.3b represents the surface appearance of weld joint produced by FSW process.

35.3.1 Microstructure

The microstructure of mild steel and DH36 steel under high magnification is shown in Fig. 35.4. The mild steel microstructure contained the equiaxed ferrite grains with fine pearlite grains as shown in Fig. 35.4a. The microstructure of DH36 steel exhibited the bands of equiaxed ferrite and pearlite as shown in Fig. 35.4b. Figure 35.5 represents the microstructure of various regions in friction stir welded DH36 steel to mild steel joint cross section. The dissimilar friction stir welded joints exhibits the distinct regions in microstructure in comparison with the similar aluminum alloys weld joints, i.e., base mild steel, heat-affected zone (HAZ) in mild steel side, thermo-mechanically affected zone (TMAZ) in mild steel side, TMAZ in DH36 steel side, HAZ in DH36 steel side, base DH36 steel, and weld nugget. The microstructure of these regions is shown in Fig. 35.5. Friction stir zone exhibited the equiaxed and fine grains with dislocation density which was slightly higher than that the DH36 steel and mild steel base metal. Grain refinement was observed in the TMAZ at the advancing side. The heat-affected zone (HAZ) was located between the parent metal and TMAZ at the advancing side contained equiaxed grain structure with a grain size substantively higher than that of the TMAZ and slightly higher than that of the DH36 base metal. There was also a heat-affected zone (HAZ) between TMAZ and parent mild steel zone at the retreating side. The microstructure of parent mild steel contained the characteristically coarse austenitic grains. The HAZ at the retreating side exhibited the similar microstructure to the parent mild steel.

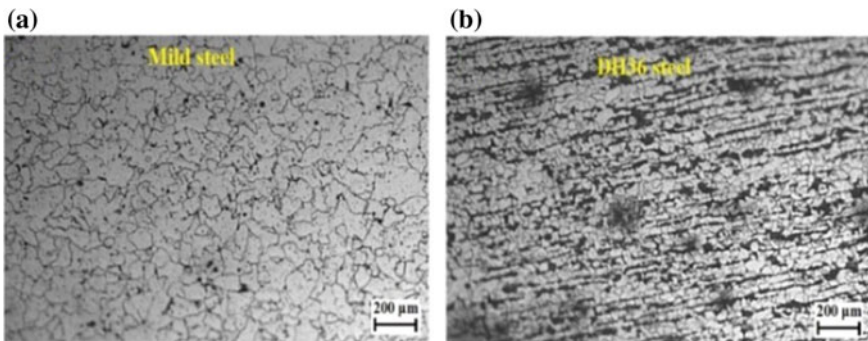


Fig. 35.4 Microstructure of **a** mild steel, **b** DH36 steel

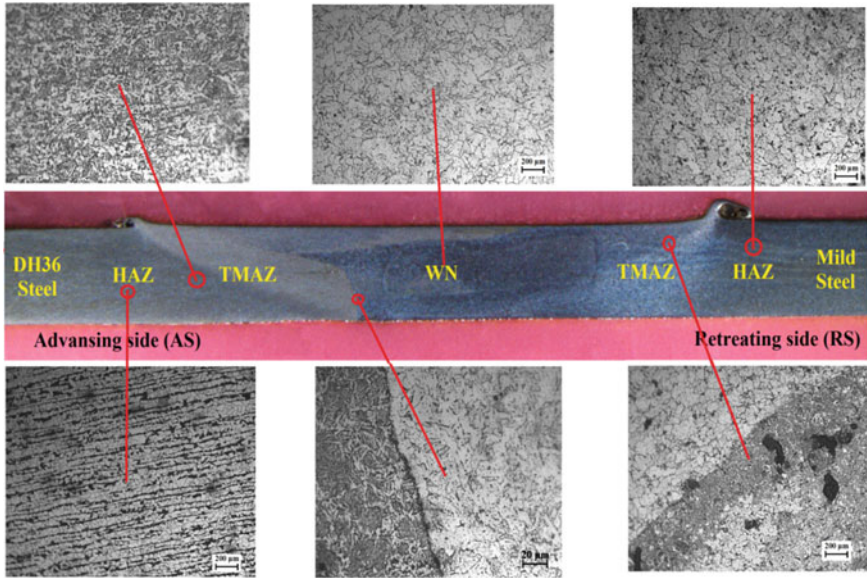
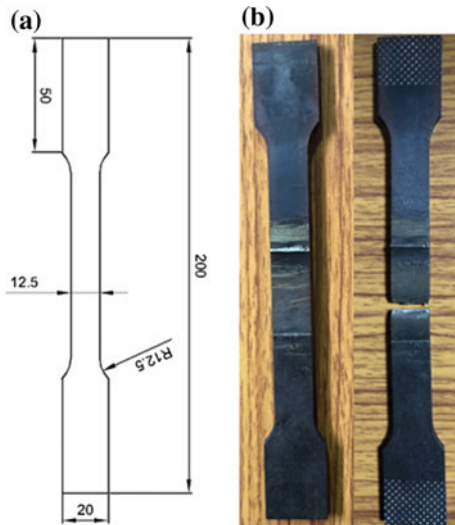


Fig. 35.5 Microstructures of FSW joint between DH36 steel and mild steel in various zones

35.3.2 Tensile Properties

Figure 35.6a represents the dimensions of tensile test specimen of dissimilar welded joint. Figure 35.6b represents the tensile fracture location of the dissimilar weld joint of DH36 steel and mild steel after the tensile test. The tensile specimen was

Fig. 35.6 a Dimensions of tensile specimen, b specimen before and after tensile test



ruptured at the weld joint center in the advancing side (DH36 steel) as shown in as shown in Fig. 35.6b. The sharpest hardness gradient was observed in this region as shown in Fig. 35.12. Figure 35.7 represents the comparison of tensile properties of base metals and friction stir welded specimen. It is observed that tensile strength of welded specimen was approximately 91.5% of the mild steel base metal strength, and yield strength was slightly higher than mild base metal.

Figure 35.8 represents the SEM appearance and energy-dispersive X-ray (EDX) area analysis of the tensile fractured surface. Concentration profiles of the major

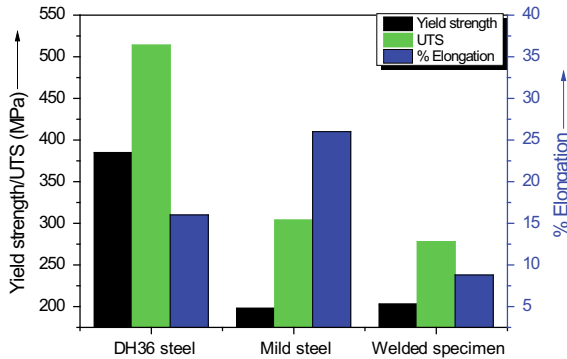


Fig. 35.7 Comparison of tensile properties of base metals and friction stir welded specimen

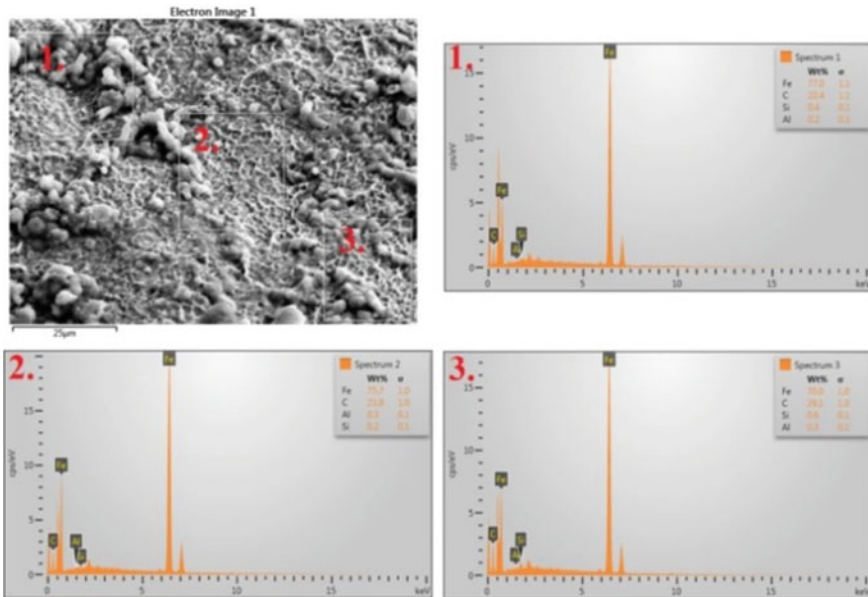


Fig. 35.8 SEM micrograph and EDX area analysis of fractured surface

elements (i.e., Fe, C, and Si) in dissimilar friction stir welded joint through the fractured surface are shown in Fig. 35.8. Figure 35.9 represents the EDX elemental mapping of these major elements (i.e., Fe, C, and Si) and other elements (i.e., O and Al) having very less concentration in the fractured surface.

Figure 35.10 represents the SEM examination of the fractured surfaces of tensile test specimen to observe the mode of rupture. The fractured surface of tensile specimen exhibited the very fine shallow dimples. The distribution of dimples in the fracture surface was also inhomogeneous as shown in Fig. 35.10. These dimples are corresponding to microvoids that initiate crack formation. These microcracks grow

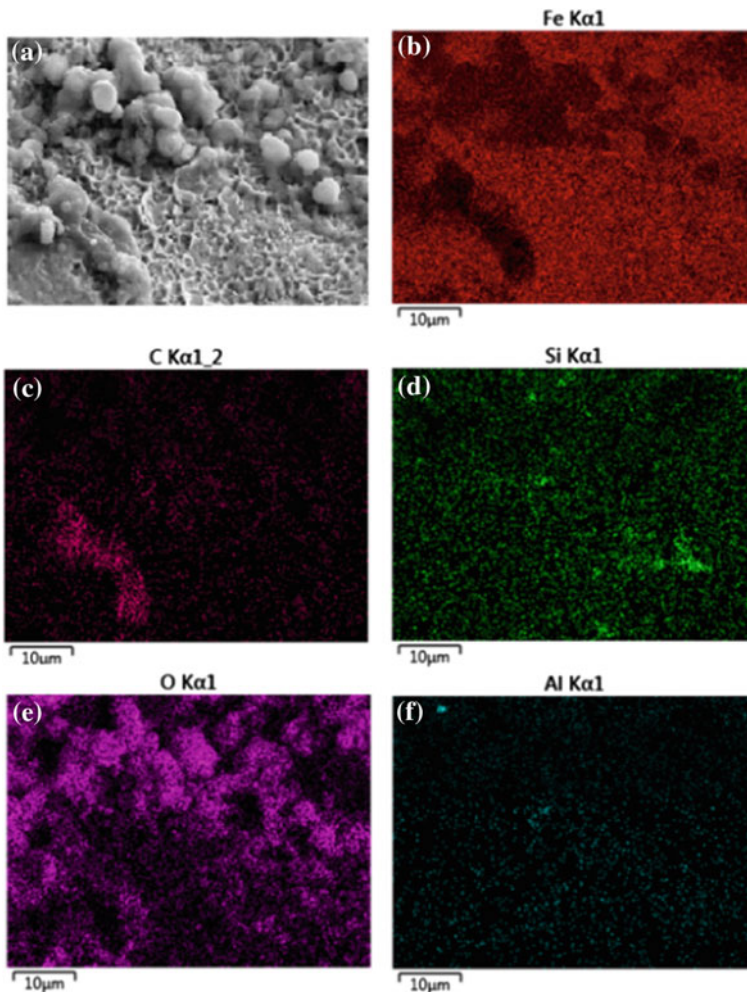


Fig. 35.9 a EDX analysis position, and corresponding EDX elemental maps for b Fe, c C, d Si, e O, f Al

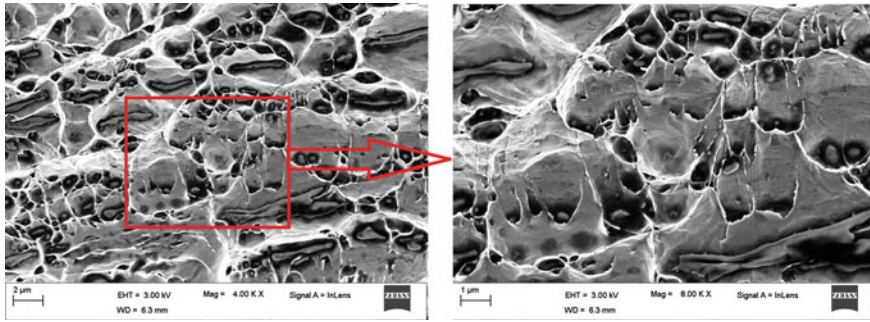


Fig. 35.10 SEM image of the fractured surface in tensile test specimen

and coalesce into the main crack which grows further under the straining conditions results in creation of fracture surface. Hence, the failure was the ductile mode of fracture in welded specimen.

35.3.3 Microhardness

Figure 35.11a represents the schematic diagram of welded specimen showing the location of sample extraction for hardness measurement. Figure 35.11b represents the hardness indentations on the top line, middle line, and bottom line in cross section of welded specimen. Figure 35.12 represents the microhardness distribution at the top line, middle line, and bottom line which were at 0.8, 1.6, and 2.4 mm, respectively, away from the top surface in welded specimen cross section, respectively.

The dissimilarity in the hardness magnitudes of the friction stir zone and TMAZ may be due to difference in microstructural evolution resulting from variance in peak temperature, strain rate, cooling rates, and material flow. DH36 steel side exhibited the hardness values greater than that of mild steel side. The bottom line the weld cross section contained the hardness value relatively lower than that the top line and middle line. The inhomogeneous hardness distribution was observed at the friction

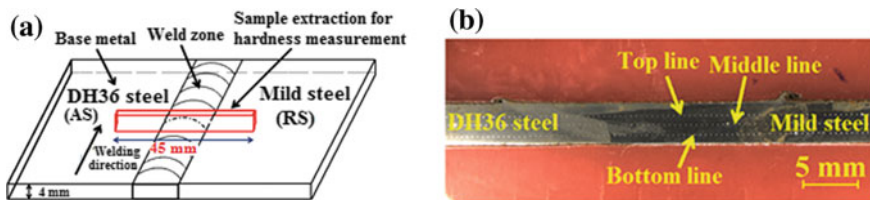
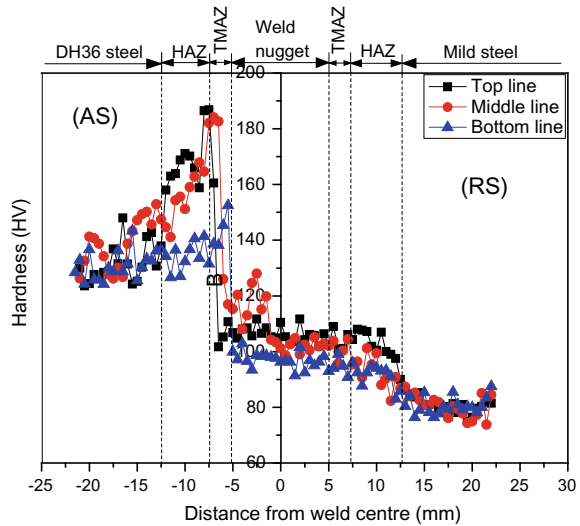


Fig. 35.11 a Schematic diagram of welded specimen showing the location of sample extraction for hardness measurement, b hardness indents at the upper line, middle line, and bottom line of the transverse cross section

Fig. 35.12 Microhardness profiles and hardness indents at the upper line, middle line, and bottom line of the transverse cross section



stir zone with average hardness value about 114 HV, which was lower than DH36 steel base metal (145 HV) and greater than the mild base metal (85 HV). This may be due to the fine recrystallized grains resulting from cruelly thermal cycle and plastic deformation. The TMAZ at the advancing side exhibited the grain refined ferrite structure with small amounts of pearlite resulted in maximum average hardness value (i.e., 184 HV) as compared other zones.

35.4 Conclusions

- In this experimental study, the DH36 steel and mild steel sheet thickness of 4 mm were successfully joined using FSW process at tool rotational speed of 600 rpm and traverse speed of 132 mm/min. The microstructural behavior and mechanical properties of friction stir welded DH36 steel and mild steel joint were studied.
- Optical investigation showed different microstructure zones which are base mild steel, heat-affected zone (HAZ) in mild steel side, thermo-mechanically affected zone (TMAZ) in mild steel side, TMAZ in DH36 steel side, HAZ in DH36 steel side, base DH36 steel, and weld nugget.
- The tensile strength of the welded specimen was achieved about 91.5% of the mild steel base metal strength. The fracture position was located at the weld joint center toward the advancing side, where the sharpest hardness gradient was observed. The failure was the ductile mode of fracture due to presence of the dimples in the fractured surface.

- Microhardness profiles showed the irregular distribution and the maximum average hardness value was observed in TMAZ at advancing side (DH36 steel). The stir zone of the welded joint exhibited the hardness higher than the mild steel and lower than DH36 base metal.






References

1. Kwon, Y.J., Shigematsu, I., Saito, N.: Dissimilar frictions stir welding between magnesium and aluminium alloys. *Mater. Lett.* **62**, 3827–3829 (2008)
2. Aonumaa, Masayuki, Nakatab, Kazuhiro: Dissimilar metal joining of ZK60 magnesium alloy and titanium by friction stir welding. *Mater. Sci. Eng., B* **527**, 5723–5727 (2010)
3. Watanabe, Takehiko, Takayama, Hirofumi, Yanagisawa, Atsushi: Joining of aluminum alloy to steel by friction stir welding. *J. Mater. Process. Technol.* **178**, 342–349 (2006)
4. Chen, Y.C., Nakata, K.: Microstructural characterization and mechanical properties in friction stir welding of aluminum and titanium dissimilar alloys. *Mater. Des.* **30**, 469–474 (2009)
5. Tanaka, Tsutomu, Morishige, Taiki, Hirata, Tomotake: Comprehensive analysis of joint strength for dissimilar friction stir welds of mild steel to aluminum alloys. *Scripta Mater.* **61**, 756–759 (2009)
6. Liu, X., Lan, S., Ni, J.: Analysis of process parameters effects on friction stir welding of dissimilar aluminium alloy to advanced high strength. *Mater. Des.* **59**, 50–62 (2014)
7. Murugan, Balamagendrarvarman, Thirunavukarasu, Gopinath, Kundu, Sukumar, Kailas, Satish V., Chatterjee, Subrata: Interfacial microstructure and mechanical properties of friction stir welded joints of commercially pure aluminum and 304 stainless steel. *J. Mater. Eng. Perform.* **27**(6), 2921 (2018)
8. Zhaoa, Sheng, Nib, Jun, Wangc, Guoqing, Wanga, Yuhana, Bia, Qingzhen, Zhaod, Yanhua, Liue, Xun: Effects of tool geometry on friction stir welding of AA6061 to TRIP steel. *J. Mater. Process. Tech.* **261**, 39–49 (2018)
9. Tiwari, A., Singh, P., Biswas, P., Kore, S.D.: Friction stir welding of low-carbon steel. *Adv. Mater. Mech. Ind. Eng.* (2019). https://doi.org/10.1007/978-3-319-96968-8_10

Chapter 36

Multi-step Radiographic Segmentation of Weld Defect Images



R. Sowmyalakshmi , M. R. Anantha Padmanaban ,
S. M. Girirajkumar , S. Benazir  and A. Farzana 

Abstract Non-destructive testing plays an important role in the evaluation of material properties as well as in the testing of a manufacturing system. The main objective of the proposed methodology is to improve the visual appearance of low contrast radiographic weld defect images without much loss of useful information by deploying multi-step radiographic enhancement (MSRE) and a subsequent region growing segmentation. The MSRE algorithm constitutes three major steps, namely linear weighting (LW), anisotropic diffusion filtering (ADF), and fuzzy image enhancement (FIE). This MSRE-based region growing segmentation methodology has addressed serious issues like amplification of noise, under and over enhancement, loss of edges, and image blurring. Further, the drawbacks of using single-step enhancement algorithms are overcome while preserving more useful image edges and details. This accounts for improving the segmentation accuracy of defective weld regions in non-destructive testing and evaluation (NDT&E). Following the three-step enhancement process, a region growing segmentation is performed on enhanced weld defect images to segment out the region-of-interest (ROI) defective regions. This multi-step segmentation methodology is tested on sample images from GDX-ray weld images database and the results are encouraging.

Keywords Radiographic weld images · Weld defects · Digital image processing · Multi-step radiographic enhancement · Region growing segmentation · Mean square error · Peak signal-to-noise ratio

R. Sowmyalakshmi (✉) · S. Benazir · A. Farzana
Department of Electronics and Communication Engineering, University College of Engineering,
BIT Campus, Trichy, India
e-mail: sowmya.anand2007@gmail.com

M. R. Anantha Padmanaban
Department of Mechanical Engineering, Saranathan College of Engineering, Trichy, India

S. M. Girirajkumar
Department of Instrumentation & Control Engineering, Saranathan College of Engineering,
Trichy, India

36.1 Introduction

Weld radiography comes under the umbrella of industrial radiography and is a non-destructive technique making use of ionizing radiation which penetrates into the inspected surface so as to detect internal discontinuities and weld deformities. Weld radiography finds a lot of applications, ranging from manufacturing, petrochemical, and petroleum industries and up to nuclear and power generation industries. Reliable inspection of welds contributes to quality assurance of the weld piece conforming to industry standards. As the human inspection and detection of weld defects is a subjective evaluation prone to fatigue, a good weld piece may be incorrectly identified as a faulty one, leading to false rejection or a weld piece with discontinuities may be identified as a good one resulting in false acceptance.

Advancements in computer vision and digital image processing techniques [3] have enabled the weld quality inspection as an automated and a more reliable task where the workload of radiographic inspector is reduced to the maximum extent. Digital image processing techniques coupled with machine learning algorithms are effective for weld quality inspection with respect to improvement of appearance of low contrast weld pieces, segmentation of region-of-interest, and extraction of discriminative features from weld pieces, thereby making the weld defects inspection process to be robust and systematic. Thus, the present work is focused toward the enhancement of weld defect images which otherwise could be a bad contrast image of low dimension with certain defects acquired on a radiographic film of noisy nature. Perfect knowledge of the geometry of these weld defects can be acquired by extracting discriminative features from the enhanced and segmented region-of-interest (ROI) weld region and these features are applied to a machine learning (ML) module for weld quality inspection and defects classification.

36.2 Conventional Methods of Weld Quality Inspection

The conventional weld quality inspection is done exclusively by a trained radiograph inspector, and such an inspection is prone to errors due to fatigue of the inspector in long run. In the past decades, the radiographic testing (RT) technology in industrial non-destructive testing and evaluation (NDT&E) has been evolved rapidly in field of weld inspection. RT is widely used as an inspection tool for detecting flaws inside welded structures, such as pressure vessels, structural members, and power plants. Extensive research has been carried out in this arena deploying digital image processing techniques in order to carry out successful automated weld quality inspection.

Weld defect classification can be automated by incorporating image processing techniques and pattern recognition tools. The process will no longer be a subjective one and will be more reliable than conventional weld quality inspection [1]. A comprehensive review of weld segmentation techniques, namely region growing, watershed, thresholding, split and merge, k -means clustering methods, were presented by

Karthikeyan et al. [4]. Nacereddine et al. [7] elaborated the concept of preprocessing to be performed initially on the selected image for weld defect detection in industrial radiography. There are many problems during all welding processes and most of them relate to non-integrity. The main weld quality criteria are integrity, shape, and required chemical and physical features [5]. Mu [6] proposed a segmentation method based on flooding to improve the speed and accuracy of defect segmentation for automated radiographic NDT. The first-level detection is done by analyzing the gray-level intensities profiles of a radiographic image and labels the defect found with a seed point. Then, the flooding is carried out using the line-flooding algorithm, in which water starts from a seed point and flows to the neighbor region in column-by-column order. The threshold value is determined by detecting an abnormal growth of flooded area. The concept of fuzzy-based multi-step radiographic enhancement of low-quality weld images was proposed by Dang et al. [2]. This particular work has motivated us to apply Multi-Step Radiographic Enhancement (MSRE) followed by region growing segmentation on weld images of GDX-Ray weld database.

36.3 Types of Weld Defects

The various possible weld defects are depicted in Fig. 36.1a–h, and the causes of these weld defects are described as follows.

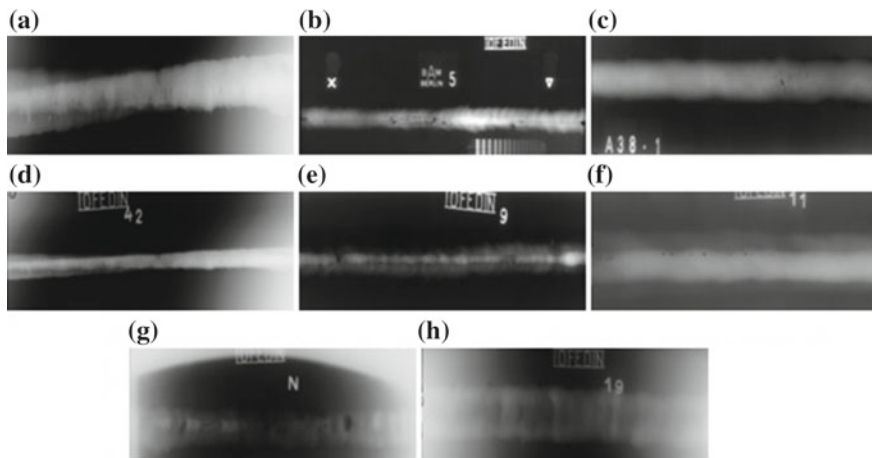


Fig. 36.1 a–h Various possible weld defects; **a** undercut, slag inclusion **b** centerline crack, cluster porosity **c** cluster porosity **d** root undercut **e** lack of root penetration **f** slag inclusion **g** transverse and longitudinal crack, undercut, porosity **h** transverse crack

Inclusion

Inclusions are developed whenever foreign matter or sand of low density captured in the molten metal do not dissolve in it. They have lower density when compared to gas voids and are characterized by irregular shapes in the weld piece.

Cracks

Cracks are developed whenever metal gets fractured either during or after its solidification. They are characterized by feathery or jagged, dark-colored linear indications.

Cluster Porosity

Cluster porosity is characterized by clusters of rounded or slightly elongated dark spots, developed due to the phenomenon of clusters of trapped gas.

Internal (Root) Undercut

Internal undercut is characterized by an irregular dark density in the weld image at its center. It is also called root undercut as it occurs along the edge of the root pass image. The existence of groove in the main object accounts for this particular weld defect.

Lack of Penetration

The weld defect called “Lack of penetration” is characterized by either continuous or intermittent dark-colored lines in the center of the weld. These defects occur due to a lack of fusion in the root of the weld or a gap left by the weld metal while filling the root.

Slag Lines

The weld defect called “Slag lines” is characterized by darker density lines of irregular width running parallel to the weld edges. Slag lines are produced due to the presence of elongated cavities containing slag or other low-density foreign matter.

Elongated Slag Inclusions

Elongated slag inclusions or “wagon tracks” appear as either single or parallel darker density line(s) of irregular width. The reason for these defects is that elongated cavities containing slag or foreign matter to be developed on both sides of the root.

Longitudinal Cracks

Longitudinal cracks are characterized by continuous or intermittent dark lines running along the entire weld length caused due to fractures throughout.

Transverse Cracks

Transverse cracks appear either as straight or wandering, fine dark lines running across a weld image caused due to fractures in the weld metal.

36.4 Radiographic Weld Images Database

Several organized collections of various types of digital images have been prepared by researchers working in varying areas of computer vision including biometrics, medical diagnostics, manufacturing industries, etc., and have been made mostly as either public or limited access to other researchers working in the same domain throughout the world. One such database is GDX-ray database. This database consists of around 19,400 X-ray images belonging to five groups of X-ray images, namely castings, welds, baggage, natural objects, and settings. Out of these groups, the present work is focused toward the weld images group of the GDX-ray database. GDX-ray is available for public access to researchers working in automated weld images processing and weld defects identification.

Input radiographic images for the present work are taken from the Welds group of GDX-ray database. In these, each class are identified and classified according to the ISO code.

36.5 Multi-step Radiographic Weld Image Segmentation System

Radiographic testing (RT) is one of the most important non-destructive testing techniques in industrial non-destructive testing and evaluation (NDT & E), and this is found to have a variety of applications in state-of-art manufacturing industries. But these RT images suffer from two serious drawbacks, namely low contrast and high noise etc., which will surely affect the subsequent image processing and automatic inspection system. Also, the automated weld defects identification is limited by serious problems. One is an improper segmentation algorithm and the other is the low visual quality of RT images. The main advantage of using the multi-step radiographic image enhancement (MSRE) algorithm is to overcome the above two problems. The proposed multi-step radiographic enhancement (MSRE)-based segmentation system is depicted in Fig. 36.2.

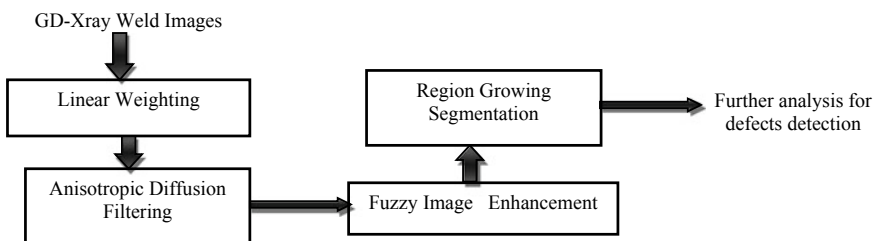


Fig. 36.2 Block diagram of proposed multi-step radiographic enhancement (MSRE)-based segmentation system

36.5.1 Multi-step Image Radiographic Enhancement (MSRE) Algorithm

It is difficult to segment defects accurately from low-quality RT images and improper segmentation may affect the accuracy of automated weld defects identification. So, it is essential to enhance the contrast of low-quality RT weld images before being segmenting the region-of-interest (ROI) weld region from them. Nowadays, many image pre-processing methods have been developed to improve the quality of RT images. The ROI weld defect region is segmented out from contrast-enhanced RT images, and discriminative features are extracted from ROI weld defect regions before performing defects identification. For RT images, the main focus on enhancement is contrast enhancement because low contrast is one of the inherent drawbacks of RT images. To improve the contrast of RT images, some conventional contrast enhancement techniques such as histogram equalization (HE), adaptive histogram equalization (AHE) may be carried out. In the present work, contrast-limited adaptive histogram equalization (CLAHE) is being done to enhance the contrast.

36.5.2 Various Steps Involved in Proposed System

Three major steps, namely linear weighting (LW), anisotropic diffusion filtering (ADF), and fuzzy image enhancement (FIE) are involved in the discussed system to overcome the drawbacks of the conventional enhancement methods by fully considering the proper segmentation requirement of weld defects as improper segmentation may affect the accuracy of weld defects identification. The very first step, i.e., linear weighting (LW) is used to improve contrast enhancement. This step is also advantageous in reducing the effects of amplified noise and background noise, thereby reducing the blurring of useful image details. The second step, i.e., anisotropic diffusion filtering (ADF) is used to smoothen the noise in the enhanced image while still preserving the useful defect edges. The third step is fuzzy image enhancement (FIE) which is implemented to further enhance the previously filtered image and obtain a relatively high quality enhanced RT image for subsequent segmentation and analysis.

By the use of linear weighting, we can enhance the contrast of the weld defect image. Filtering by ADF process can remove some noise and useless details efficiently while preserving the edges very well. Fuzzy image enhancement (FIE) technique improves the image visual quality. Final segmentation by the region growing method is performed to segment the defective regions from weld images.

Contrast Enhancement

It is difficult to segment defects accurately from low-quality RT images and is also difficult to detect the presence of small sized weld defects containing useful information. Contrast is defined as the difference between the maximum pixel value and

minimum pixel value of that image. Contrast enhancement is an essential preprocessing task in image processing, used to improve the overall appearance of an image which may be further processed by subsequent modules. There are various contrast enhancement methods which have been used in conventional techniques. Histogram equalization (HE) is the most frequently used technique in the contrast enhancement in which the visual appearance of the image is improved by assigning approximately equal numbers of pixels to all available intensity values. Ideal equalization is not possible for our problem, since digital RT images have only a finite number of gray-level values. Adaptive histogram equalization (AHE) can adaptively enhance the contrast of each pixel relative to its local neighborhood. As a result, over enhancement may occur and the enhanced RT images may look unnatural.

Adaptive histogram equalization is the extended version of the traditional histogram equalization technique. Contrast-limited adaptive histogram equalization (CLAHE) is a variant of adaptive histogram equalization which was originally developed for contrast enhancement of medical images. The image whose contrast is to be enhanced is divided into non-overlapping regions called “Image tiles.” Histogram equalization is applied to each image tile, thereby improving the contrast of each tile. The neighboring contrast improved image tiles are then combined using bilinear interpolation. The CLAHE technique accentuates the improvement of local contrast than of overall contrast unlike conventional histogram equalization.

Linear weighting (LW) is performed as the first-step enhancement by using an original RT image and its CLAHE image. CLAHE operation can thus increase the dynamic range of the subimage blocks (tiles) and enhance the local contrast. CLAHE is used along with LW to overcome the drawbacks due to noise if used separately. If $I_O(x, y)$ and $I_E(x, y)$ represent an original RT image and its CLAHE image, respectively, the resultant image $I_W(x, y)$ is given by the linear combination of $I_O(x, y)$ and $I_E(x, y)$ as in Eq. 36.1.

$$I_W(x, y) = w_1 I_O(x, y) + w_2 I_E(x, y) \quad (36.1)$$

where w_1 and w_2 denote the unique weighting coefficients, which are related to the contrast of the original RT image.

The coefficients “ w_1 ” and “ w_2 ” are chosen such that $w_1 + w_2 = 1$. By changing the weights w_1 and w_2 , the contrast of the linear weighted image can be adaptively adjusted.

Anisotropic Diffusion Filtering

Anisotropic diffusion filtering based on partial differential equations is carried out as the final step in this multi-step radiographic enhancement to remove the effects of noise and useless details. But, useful edge information is preserved very well. There have been several diffusion models for different applications of image processing. Therefore, only some equations optimized in MSRE are introduced as follows: The main iterative equation in the ADF is described by

$$I_{t+1} = I_t + \lambda(cN_{x,y} \cdot \nabla_N(I_t) + cS_{x,y} \cdot \nabla_S(I_t) + cE_{x,y} \cdot \nabla_E(I_t) + cW_{x,y} \cdot \nabla_W(I_t)) \tag{36.2}$$

where I_t and I_{t+1} represent the images of the previous and current iterations, respectively; t denotes the number of iterations; λ indicates a smoothing coefficient; $\nabla_N(x, y)$, $\nabla_S(x, y)$, $\nabla_E(x, y)$, $\nabla_W(x, y)$ represent the divergence equations in the four directions, respectively.

The number of iterations t is set according to the problem image, and k is related to the coefficient of thermal conductivity. Both k and λ have smoothening effect on the filtered image.

Fuzzy Image Enhancement

An adaptive algorithm of FIE is used in the proposed MSRE consisting of improved membership function, nonlinear transformation function and inverse transformation function. The following steps are involved in the adaptive algorithm of FIE.

Step 1: First, the filtered image obtained in the anisotropic diffusion filtering is normalized and the membership function transforming an image from the spatial domain to the fuzzy domain is defined as

$$P_{ij} = X_{ij} / (L - 1) \tag{36.3}$$

where X_{ij} denotes the gray level of the filtered image in pixel (i, j) , P_{ij} represents the membership degree in pixel (i, j) and L indicates the dynamic range of pixel values and is the constant for a given image.

Step 2: Otsu global thresholding algorithm is applied in order to compute the binarized image. Otsu sets the threshold so as to try to minimize the overlapping of the class distributions. Otsu’s method segments the image into two light and dark regions C_1 and C_2 , where C_1 and C_2 are the set of intensity levels. We can compute cross over point denoted as T for the normalized image. T is equal to the optimal threshold t , which maximizes the value of the improved Otsu.

Step 3: The membership degree $P_c(t)$ in the crossover point is calculated by the following formula,

$$P_c(t) = w_1(t) w_2(t) |U_1(t) - U_2(t)| \tag{36.4}$$

where $w_1(t)$ and $w_2(t)$ denote the number of pixels in $C1$ and $C2$ regions, respectively, and $U_1(t)$ and $U_2(t)$ represent the average gray level of all pixels in $C1$ and $C2$ regions, respectively.

Step 4: The normalized image I is fuzzily enhanced by a repeated non-linear transformation, and this process is described by

$$I_r(\mu_{ij}) = I_1(I_{r-1}(\mu_{ij})), r = 1, 2, 3, \dots \tag{36.5}$$

where $I_1(\mu_{ij})$ corresponding to the first (initial) iteration of this iterative FIE algorithm is determined according to Dang Changying et al.

Step 5: The last step in enhancement procedure is the inverse transformation (Defuzzification) in which the gray-level value of the enhanced image can be obtained by the following equation

$$X'_{ij} = P'_{ij}(L - 1) = I_{r-1}(\mu'_{ij})(L - 1) \tag{36.6}$$

where X'_{ij} and P'_{ij} represent the gray-level value and the membership degree of the enhanced image in pixel located at (i, j) , respectively.

Step 6: Repeat steps 1 through 5 till an enhanced version of the weld RT image from the GDX-Ray database is obtained.

Step 7: Region-based segmentation of the enhanced weld defect image is performed for subsequent analysis. Region growing segmentation was performed by proper selection of the growing seed and the region growing criteria. The enhanced image was normalized before the region growing segmentation, and the end threshold was 0.059. The segmentation integrity and accuracy of the weld defects are significantly improved by the proposed MSRE based segmentation technique.

36.6 Results and Discussion

The performance of the MSRE-based region-based segmentation of weld defect images in the GDX-Ray database can be evaluated by calculating the peak signal-to-noise ratio (PSNR) and the mean square error (MSE) by the following formulae.

$$MSE = \frac{1}{M \times N} \left(\sum_0^{N-1} \sum_0^{N-1} [I(x, y) - I'(x, y)]^2 \right)$$

$$PSNR = 20 \times \log_{10}(255/(MSE))$$

where $I(x, y)$ refers to the original radiographic weld defect image, $I'(x, y)$ is the enhanced version of the low contrast image $I(x, y)$, and $M \times N$ is the size of original image as well as that of enhanced image.

The screenshots of different stages of the above-described segmentation process for certain weld defects are shown in Figs. 36.3, 36.4 and 36.5.

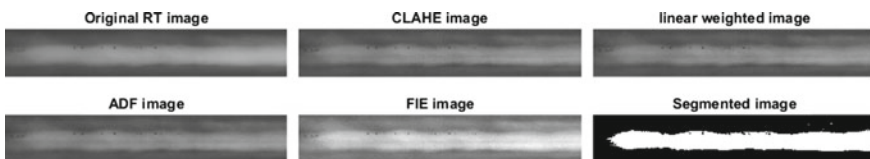


Fig. 36.3 Screenshot for MSRE-based segmentation for weld defect of slag inclusion

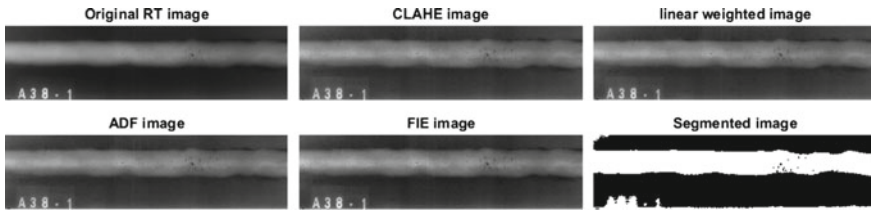


Fig. 36.4 Screenshot for MSRE-based segmentation for weld defect of cluster porosity

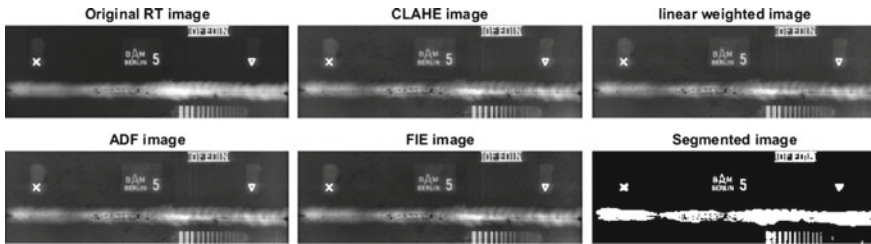


Fig. 36.5 Screenshot for MSRE-based segmentation for weld defect of centerline crack

The performance metrics for various types of weld defects are also compared in Table 36.1.

From Figs. 36.3, 36.4 and 36.5, it is obvious that the proposed MSRE-based segmentation technique has effectively segmented the weld defect region of interest from weld images in the GDX-Ray database and the segmented weld defect regions can be analyzed further. It is also evident from Table 36.1 that the multi-step radiographic enhancement (MSRE) has successfully improved the visual quality of the weld defect images with a relatively fair peak signal-to-noise ratio (PSNR) and a high degree of mean square error (MSE).

Table 36.1 Performance metrics for various types of weld defects

Sl. No.	Weld defects	PSNR (dB)	MSE
1	Slag inclusion	15.4105	1870.8
2	Cluster porosity	23.7270	275.67
3	Centerline crack	22.7955	341.61
4	Lack of root penetration	20.3918	594.15
5	Root undercut	21.3632	475.07
6	Transverse and longitudinal crack, undercut	21.2162	491.43
7	Transverse crack	22.4112	373.22

36.7 Conclusion

The present work has mainly focused on the enhancement of low-quality RT images using multi-step radiographic enhancement (MSRE) technique. The resulting enhanced images are then segmented for further analysis by suitable feature extraction techniques and machine learning module. Various issues in conventional segmentation techniques such as amplification of noise and image blurring have been addressed. The MSRE-based segmentation has effectively segmented the region of interest weld defect regions in the images of GDX-Ray weld images database.

References

1. Carvalho, A.A.D., Suita, R.C.D.S.B., Silva, R.R.D., & Rebello, J.M.A.: Evaluation of the relevant features of welding defects in radiographic inspection. *Mater. Res.* **6**(3), 427–432.
2. Dang, C., Gao, J., Wang, Z., Chen, F., Xiao, Y.: Multi-step radiographic image enhancement conforming to weld defect segmentation. *IET Image Proc.* **9**(11), 943–950 (2015)
3. Gonzalez, R.C., Woods, R.E.: *Digital Image Processing*. Pearson Education India (2002)
4. Karthikeyan, B., Vaithyanathan, V., Venkatraman, B., Menaka, M.: Analysis of image segmentation for radiographic images. *Indian J. Sci. Technol.* **5**(11), 3660–3664 (2012)
5. Marônek, M., Bárta, J.: *Multimedial Universal Guide of Welding Technology* (electr. monograph), pp. s. 340. AlumniPress, Trnava (2008)
6. Mu, W.L., Gao, J.M., Chen, F.M.: Weld radiographic image enhancement conforming to human visual system. *J. Xi'an Jiaotong Univ.* **46**(3), 90–93 (2012)
7. Nacereddine, N., Zemat, M., Belaifa, S.S.: Weld defect detection in industrial radiography based digital image processing. In: *Proceedings of International conference on World Academy of Science Engineering Technology*, Berlin, Germany, January 2005, pp. 112–115

Chapter 37

Thickness Evolution During End Forming Operations of Friction Stir Processed AA 6063-T6 Tubes at Different Tool Geometries



Arvind K. Agrawal , R. Ganesh Narayanan  and Satish V. Kailas 

Abstract The paper is concerned with thickness evolution in the end formed region of friction stir processed and unprocessed tubes at different pin profiles. Three end forming operations, namely end expansion, end reduction, and end beading, are conducted on AA 6063-T6 tubes for the purpose. Thinning and thickening are significant in the processed zone as compared to unprocessed zone in the cases of expansion and reduction for different pin profiles. During beading, the processed zone thickening is larger for tapered cylindrical pin as compared to unprocessed zone thickening, while in straight pin and stepped cylindrical pin, it is smaller. Lesser hardness/strength of the FSP zone leads to development of instability during end forming. In the case of expansion, failure is seen at the FSP zone. Wrinkling and overlapping are observed in the FSP zone during reduction. Fine cracks are observed in the base metal region of processed tubes in beading operation. Ductility of the FSP zone is responsible for relative thinning of processed tubes, while the strength of the zone is responsible for thickening for processed tubes in the case of end expansion and end reduction.

Keywords Thickness · End forming · Friction stir processing · Instability

37.1 Introduction

Tube end forming involves making of simple or complex shapes such as expansion, reduction, tapers, and flanges made at the end of the tube by simple or multiple metal forming operations. End formed tubes have a variety of applications in construction, agriculture, and automobile sectors. They are mainly used as a carrier of fluids such as oil, refrigerant, and water for agriculture sector. A few researches in the field of end forming of tubes are presented here. Gupta and Sahu discussed contraction of

A. K. Agrawal · R. Ganesh Narayanan (✉)
Department of Mechanical Engineering, Indian Institute of Technology Guwahati, Guwahati
781039, India
e-mail: ganu@iitg.ac.in

S. V. Kailas
Department of Mechanical Engineering, Indian Institute of Science, Bengaluru 560012, India

© Springer Nature Singapore Pte Ltd. 2020
M. S. Shunmugam and M. Kanthababu (eds.), *Advances in Additive Manufacturing and Joining*, Lecture Notes on Multidisciplinary Industrial Engineering,
https://doi.org/10.1007/978-981-32-9433-2_37

aluminum tubes under conical entry dies. The dies were made with semi-angles of 5° , 10° , 15° , and 20° [1]. The initial effort is larger for larger semi-angle. Yang et al. studied the plastic energy absorption behavior of expansion of tubes under axial compression by a conical-cylindrical die. Modeling for the process has been done in nonlinear finite element analysis code MSC.Marc [2]. Choi et al. studied the effect of impact velocity on the energy absorption characteristic during tube expansion. The whole length of the expanding tube has been divided into two different thicknesses, t_1 and t_2 ($t_1 < t_2$). The region with t_2 thickness requires larger load as compared to region having t_1 thickness. In addition, it has been observed that impact force increases with increase of impact velocities [3]. Tan et al. successfully developed axially displaced box-shaped ends having small corner radii from the experiments and FE simulation. The higher value of strain was observed around the corners, which is due to the compression of the circular ends into square corner radii [4]. Agrawal and Narayanan concluded that incorporation of failure criterion may improve the accuracy of predicted results during joining of a tube to a sheet [5].

Tubes are manufactured either by welding or by extrusion. Both the processes have their own merits and demerits. In welding processes, friction stir welding (FSW) has recently become popular for welding of aluminum and magnesium alloys due to its inherent merits such as low distortion of workpiece, absence of cracking, and other environmental benefits. Within aluminum alloys of different grades, 6000 series alloys exhibit acceptable ductility, corrosion resistance, and joinability [6]. A rolled plate or sheet of aluminum is first bent in the form of a pipe and then welded to convert sheet into pipe form. Instead of forming and then welding a sheet in the form of a pipe, a tube can be processed for certain property enhancement. For this purpose, fundamentals of friction stir processing (FSP) are utilized. FSP helps in modifying the microstructural and mechanical properties in the processed zone. Important process parameters such as tool rotational speed, tool traverse speed, tool geometry, tool plunge depth, tool axial force, and tool tilt angle control the quality of weld formed during FSW and FSP. Some of the contributions are presented here. Imam et al. [7] showed that square pin is better than tapered cylindrical and tapered square pins for FSW of 6063T4 plates. Hajideh et al. investigated the effects of tool geometry (threaded cylindrical, squared, triangular, and straight cylindrical) on dissimilar friction stir welding of polyethylene-polypropylene. The joint strength of the fabricated specimens with the threaded cylindrical tool is higher than other tool shapes [8]. Ramulu et al. studied the influence of shoulder diameter and plunge depth on formability of FSWed sheets AA 6061-T6. It has been observed that with an increase in shoulder diameter and plunge depth, the forming limit is found to improve considerably [9]. Khodabakhshi et al. studied the unique microstructural features of Al-matrix nanocomposites reinforced by grapheme nano-platelets (GNPs), fabricated by multi-pass friction stir processing (FSP). Yield strength of Al-Mg alloy improved from 68 to 148.7 MPa after nanocomposite fabrication [10]. Maamoun et al. studied the FSP effect on the microstructure evolution, microhardness, and the residual stresses of as-built and hot isostatic pressed AlSi10Mg parts. The optical microscope observation indicated a considerable reduction in void zone inside the friction stirred area as compared to HIP zone [11]. Though plenty of literature is

available on FSW/FSP of aluminum alloys sheets, scarce literature is available on FSW/FSP of tubes or pipes. FSW/FSP of tubes or pipes have their own challenges in terms of circularity of tubes, which prevents the full contact of shoulder with the workpiece. Internal mandrel requirement and clamping of tubes are other difficulties during FSP of tubes. FSW of AA 6061-T6 tubes [12] and steel tubes [13] are some contributions in the context.

The main aim of the present work is to conduct FSP of AA 6063-T6 tubes with three different tool pin profiles in defect-free conditions and study the thickness evolution at the end of the tube (in processed and unprocessed zones) during end forming operations. End forming operations also provide an idea of deformation behavior of different zones (processed or unprocessed) within the same tube. Such an attempt has not been made until now on tubes.

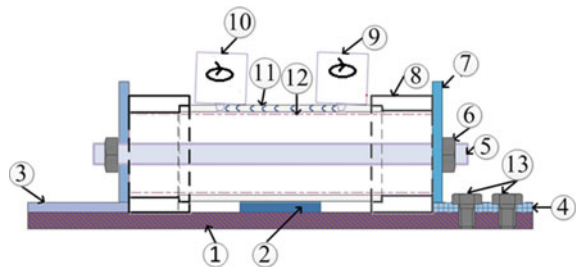
37.2 Methodology

37.2.1 Experimental Details

The material used for FSP of tubes is AA 6063-T6 with an outer diameter of 50.8 ± 0.2 mm and thickness of 3.17 ± 0.03 mm in as-received condition from supplier. For smooth conduction of FSP of tubes, a specially designed welding setup has been fabricated. Here the tube has been supported internally using a mandrel, which is longer than the tube. The extra length of the mandrel is threaded. This threaded portion is engaged with a capsule at both the ends. The tube is tightly clamped by this method. A circular rod passes through the center of the mandrel and it is tightened with two angle plates which are kept at two ends of the mandrel. The schematic along with nomenclature of parts for joining of tubes has been shown in Fig. 37.1.

Tools having same shoulder dimensions and different pin profiles have been fabricated to study the effect of different pin profiles during FSP of tubes. Tools are made of H13 steel in as-received condition. Here three different pin profiles, namely tapered cylindrical pin, straight cylindrical pin, and stepped cylindrical pin, have

Fig. 37.1 Experimental arrangement for FSP of tubes (Parts: 1: Bottom plate, 2: Support plate, 3: Fixed angle plate, 4: Slot, 5: Inside rod, 6 and 13: Nuts and bolts, 7: Movable angle plate, 8: Capsule, 9: FSP starts, 10: FSP ends, 11: Tube, 12: Mandrel)



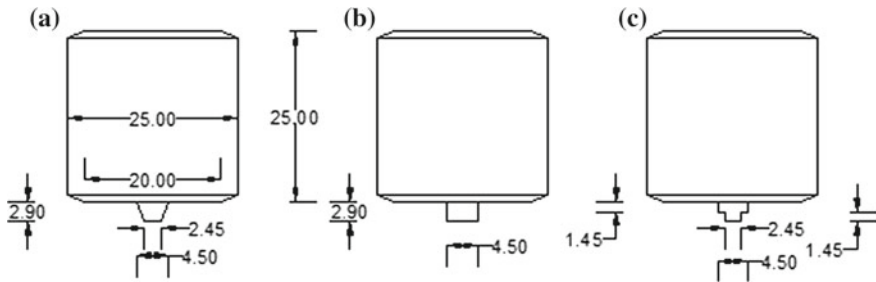


Fig. 37.2 Dimensions of different pin profiles, **a** tapered cylindrical pin, **b** straight cylindrical pin, and **c** stepped cylindrical pin (all dimensions in mm and not to scale)

been fabricated to study the effect of pin profiles during end forming operations. The schematic and dimensions of different pin profiles have been shown in Fig. 37.2.

FSP has been done at a tool rotational speed of 1350 rpm, tool traverse speed of 90 mm/min, tool tilt angle of 2° , and a tool plunge depth of 3 mm. At these set of process parameters, a defect-free zone has been obtained [14]. Later through macrostructural analysis, it has been confirmed that straight cylindrical pin as well as stepped cylindrical pin also have defect-free weld at these conditions. A backward tool tilt angle of 2° is generally used during FSW/FSP. A tool plunge depth of 3 mm means the insertion of tool inside the workpiece is sufficient to prevent the defects like kissing bonds and worm holes which occur due to lack of tool penetration.

37.2.2 Tensile Properties Evaluation and Thickness Evolution

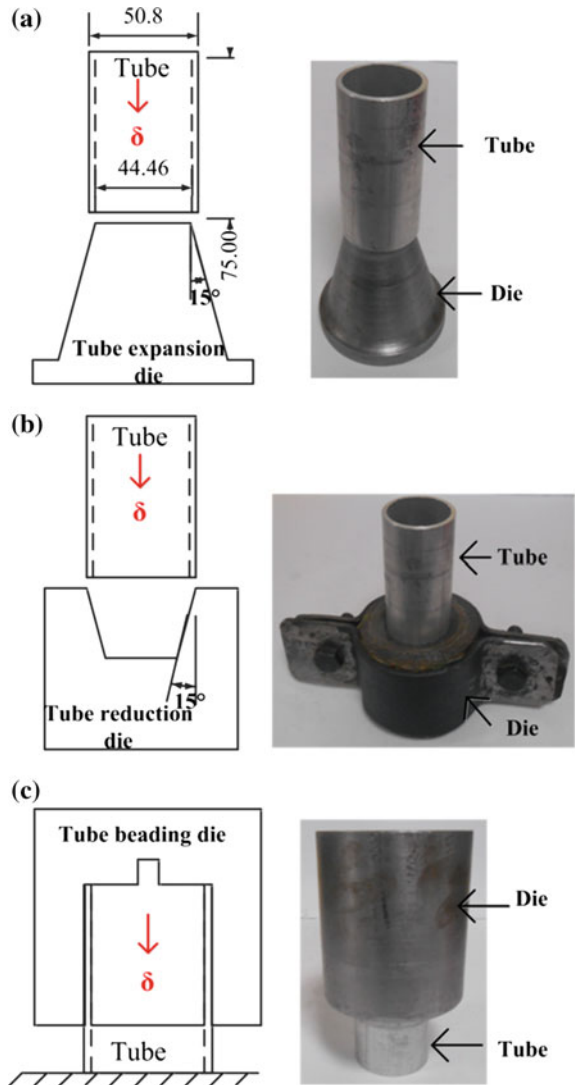
Tensile testing of processed and unprocessed zones has been conducted in UTM of load capacity 100 kN at a cross-head speed of 1 mm/min. The dimensions of processed zone have been determined based on availability of the weld zone. Here the gauge width has been taken as 16 mm, gauge length as 12.5 mm, shoulder length as 35 mm, shoulder width as 24 mm, and total length as 90.5 mm. To eliminate any discrepancy in the results due to difference in geometrical dimensions of the tensile specimen, tensile coupons for unprocessed zones (base metal) have been prepared with the same dimensions as that of processed zones. Load-displacement data have been captured during tensile testing. The engineering stress-strain behavior and true stress-strain behavior are calculated after that.

End forming operations conducted are tube end expansion, tube end reduction, and tube end beading. Dies have been fabricated from mild steel. The surface roughness was measured with the help of profilometer and is found to be 5.30 ± 0.81 , 4.10 ± 0.42 , and $2.89 \pm 0.65 \mu\text{m}$ for tube expansion, reduction, and beading dies, respectively. Taper angle of 15° has been provided for end expansion and reduction dies. A pair of split die is used for end reduction for easy removal of tube after

reduction process. For tube end beading, a certain length of tube is inserted inside a slot made in the die such that during compression, the unsupported length of the tube forms bead at its end.

During end forming operations, thickness is measured both in the processed zone and in the unprocessed zone at every 2 mm displacement. In the case of end expansion and end reduction, thickness is measured at the end of the tube. However, in beading, thickness is measured at the bulged region of the processed zone and in base metal region. The schematic of end forming tools and actual fabricated tools have been shown in Fig. 37.3. Thickness evolution helps in predicting the forming behav-

Fig. 37.3 Schematic and actual setup for end forming operations, **a** end expansion, **b** end reduction, and **c** end beading (all dimensions in mm and not to scale)



ior during end forming operations in different zones (processed and unprocessed). Important changes in the weld zone can be observed at subsequent steps during end forming operations. Thickness is quantified in the FSP zone or in unprocessed zone according to the equations,

$$t = \frac{t_i - t_f}{t_i} \text{ (for tube thinning),}$$

$$t = \frac{t_f - t_i}{t_i} \text{ (for tube thickening)} \tag{37.1}$$

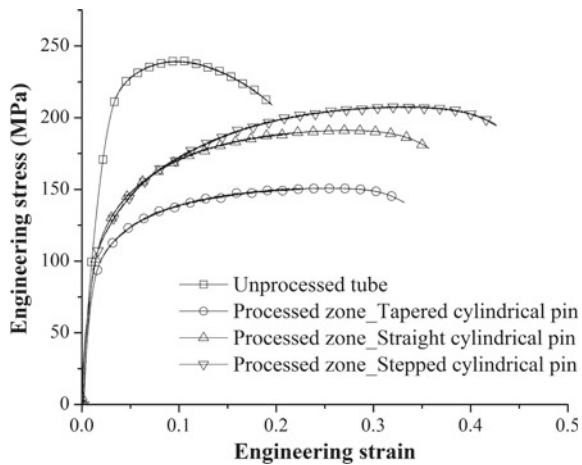
Here, t_i and t_f are the initial and final thicknesses of the processed or unprocessed zones. Tube thinning is shown as negative, while thickening as positive.

37.3 Results and Discussion

37.3.1 Tensile Properties

Base metal has larger tensile and yield strength as compared to processed zones (Fig. 37.4). However, ductility is less for base metal as compared to processed zones at different pin profiles. Within processed zones for different pin profiles, stepped cylindrical pin shows largest tensile strength as compared to other pin profiles. Hence, it is expected that hardness of the processed zone is less than as compared to unprocessed zone. Moreira et al. have shown similar results in their work. AA 6063-T6 has been FSPed and a hardness decrease of 25–35% has been observed [15].

Fig. 37.4 Engineering stress–strain curve for unprocessed tube and processed zones for different pin profiles



37.3.2 Thickness Evolution

Thinning is observed in processed zone as well as in unprocessed zone during end expansion of tube (Fig. 37.5a). Thinning is larger in the processed zone as compared to unprocessed zone for different tool pin profiles. Because of a softer weld zone, thinning is prominent in weld zone part as compared to unprocessed zone part.

During end reduction of tubes (Fig. 37.5b), thickening is observed for both processed and unprocessed zones (different pin profiles). Thickening is prominent in the case of processed zones as compared to unprocessed zones. Maximum thickening is observed for tapered cylindrical pin, and minimum thickening is observed for stepped cylindrical pin. Since the FSP zone is softer than the unprocessed zone, it is pushed inside and material accumulation occurs inside the FSP region from sideways. Because of this thickening observed in weld zone is more as compared to unprocessed zone. Since the processed zone for tapered cylindrical pin has lowest strength in comparison to processed zones for other pin profiles, maximum thickening is observed in this case.

In the case of end beading (Fig. 37.5c), thickening is observed for both processed zones and unprocessed zones as well as for unprocessed tubes. For stepped cylindrical pin and straight cylindrical pin, thickening observed is not so significant as compared to tapered cylindrical pin. Thickening (processed or unprocessed zone) depends on relative strength of unprocessed and processed zones. Actually, beading starts here initially in the form of bending and later on tube gets bulged due to compression of tube against the die and base plate. Because of this, stretching as well as compression occurs simultaneously in the end forming region. Thickening observed in the processed as well as in unprocessed regions shows the prominence of compression during end beading.

Maximum thinning in the processed zone is observed for stepped cylindrical pin during tube expansion (Fig. 37.6a). Because of larger ductility of weld zone for stepped cylindrical pin, thinning is severe in this case. Thinning observed in base metal zone is not so significant as compared to thinning observed in processed zones; however, a maximum thinning of 7.3% is observed for tapered cylindrical pin in base metal zone as compared to other pin profiles (Fig. 37.6b).

In the case of end reduction as the strength of weld zone increases for different pin profiles, thickening (%) decreases (Fig. 37.6a). A softer weld zone has thickened more. Thickening (%) in base metal zone for different pin profiles is almost same for different pin profiles (Fig. 37.6b). It means weld zone thickening has been largely affected by the use of different pin profiles and base metal zone thickening remains unaffected throughout the deformation for different pin profiles.

For beading, thickening (%) observed in FSPed zone is larger for tapered cylindrical pin as compared to thickening (%) observed in base metal zone (Fig. 37.6a). In other cases, like straight and stepped cylindrical pin, thickening (%) observed in base metal zone is larger as compared to corresponding weld zones. Since weld zone corresponding to tapered cylindrical pin is softer than other weld zones, thickening due to compression is prominent in this case as compared to other pin profiles. Here

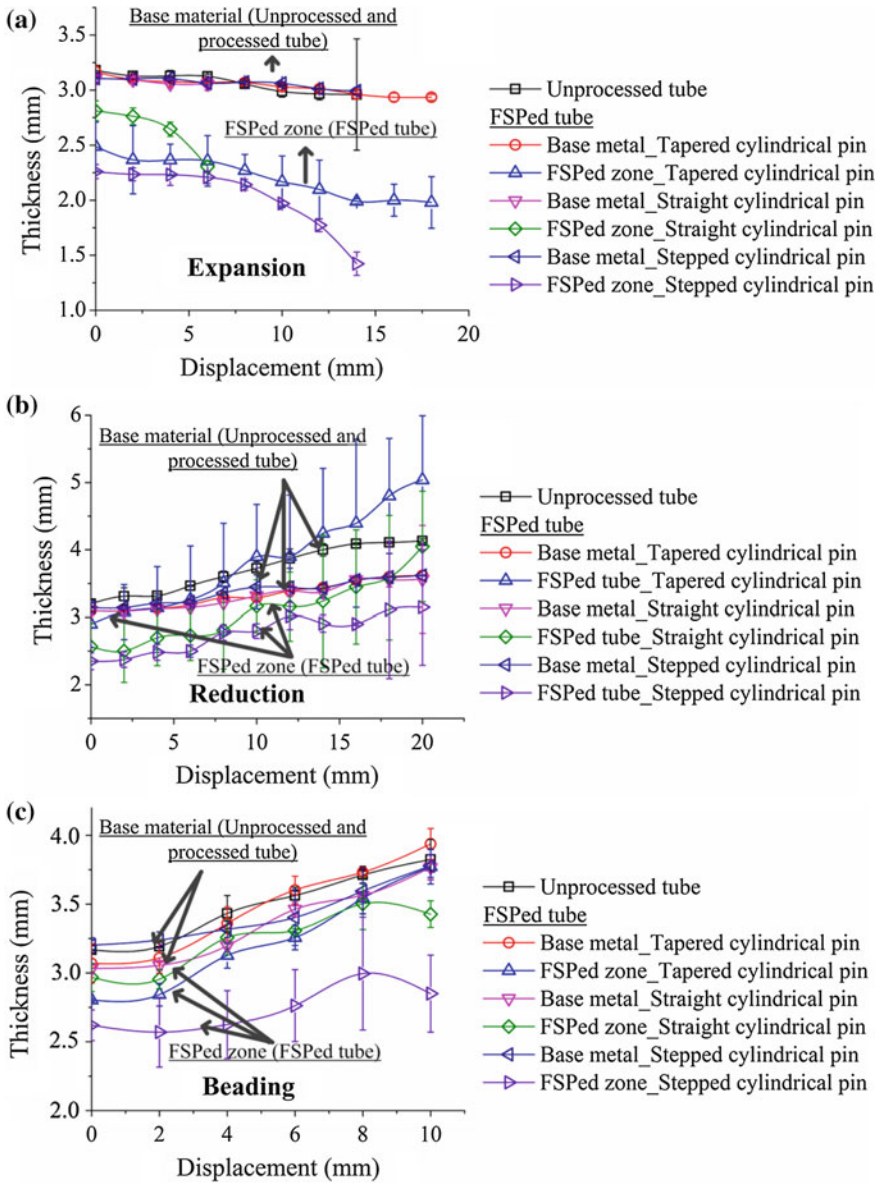
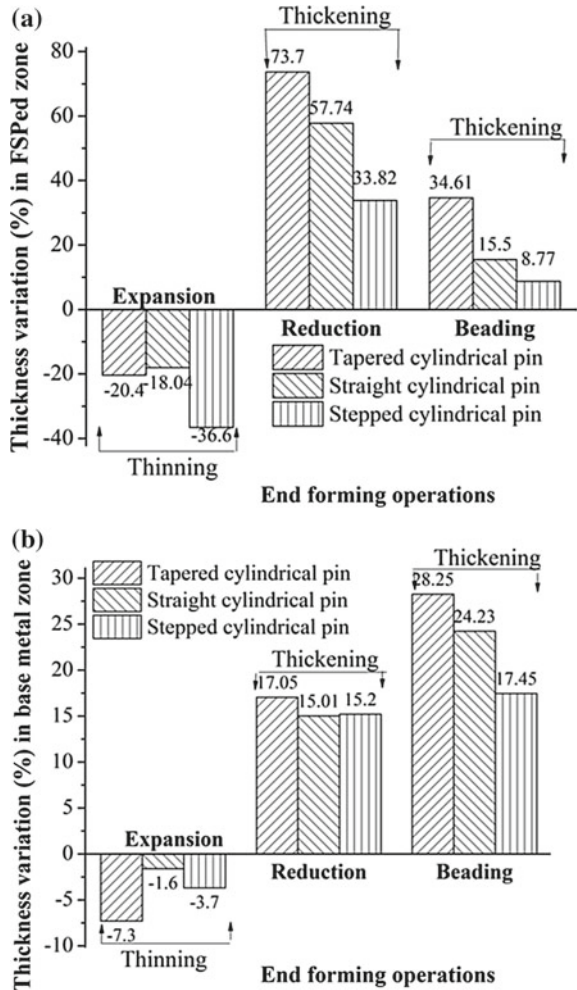


Fig. 37.5 Thickness evolution for unprocessed tube and processed tubes (base metal zone and processed zones) for different end forming operations, **a** end expansion, **b** end reduction, and **c** end beading

Fig. 37.6 Thickness variation for different tool pin profiles, **a** in FSPed zone and **b** in base metal zone



it is also observed that as the strength of pin profile increases, thickening (%) in the weld zone decreases. Similar trend is observed in base metal zones also (Fig. 37.6b).

37.3.3 Instability Development During End Forming

Instability in the form of crack is observed during end expansion of tube in the FSP zone. Due to stretching of the FSP zone (softer region), failure takes place at its middle (Fig. 37.7a).

In the case of end reduction of tubes, wrinkling and overlapping are observed in the FSP region. Because of softer FSP region, it is pushed in the inner direction as

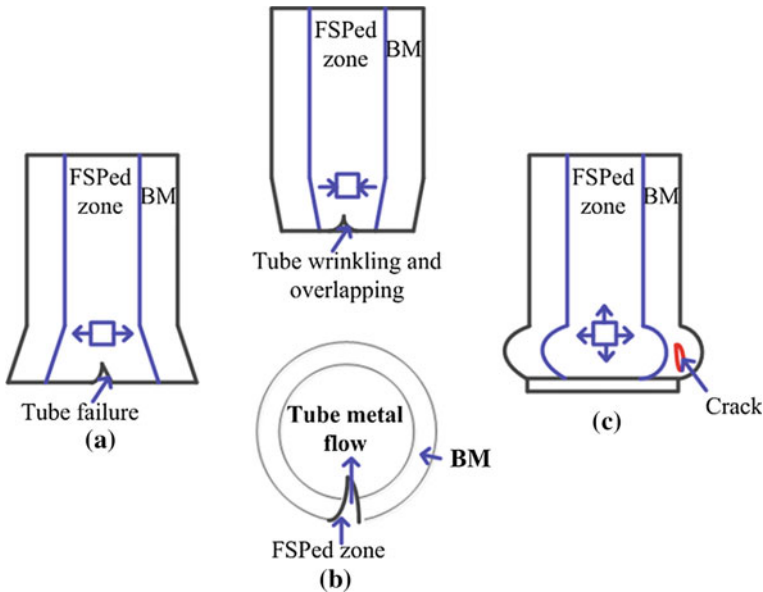


Fig. 37.7 Instability developed during, **a** end expansion, **b** end reduction, and **c** end beading

compared to base metal region, which is seen in the form of wrinkling and overlapping (Fig. 37.7b). In the case of end beading of tubes, fine cracks are observed in the base metal region. The difference in strength and strain hardening exponent in the FSP zone and the base metal region is responsible for this. This is predominantly because of reduced ductility of the base metal as compared to FSPed zone (Fig. 37.7c). Larger thickening in the base metal region leads to development of crack initiation.

Figure 37.8 shows the deformation behavior at the end of the tube for parent tubes and processed tubes for different end forming operations. Failure in the middle of the processed zone is observed in the case of end expansion (Fig. 37.8a). For tube reduction, wrinkling with overlapping can be observed in the processed zone, while such situation does not exist in case of unprocessed tube (Fig. 37.8b). For beading of tubes, parent tube actually fails at its peak bulged height, while very fine cracks are developed in base metal region for processed tubes (Fig. 37.8c).

In summary, it can be said that the relative difference in thickness evolution in the processed and unprocessed region during different end forming operations and for different pin profiles are governed by difference in hardness/strength between the processed and unprocessed regions. Within the processed tubes, ductility of FSP zone is responsible for thinning, while its strength is responsible for thickening in reduction and beading. The difference in strength between processed and unprocessed regions is also responsible for the development of instability in weld zone in the case of end expansion and end reduction. In the case of end beading, apart from difference in hardness, difference in strain hardening exponent is also responsible for instability development in unprocessed region.

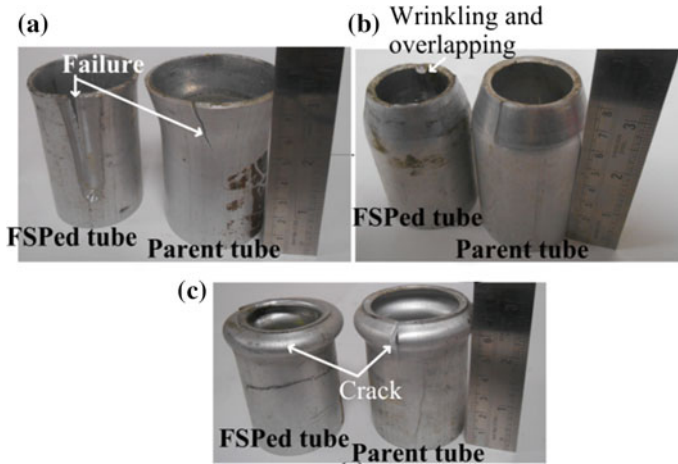


Fig. 37.8 Comparison in deformation behavior of FSPed tube and parent tube during, **a** end expansion, **b** end reduction, and **c** end beading

37.4 Conclusions

The following conclusions are drawn from the present work.

1. The strength of the processed zones is less than that of unprocessed zones for different pin profiles. It means that strength has decreased after FSP for different pin profiles. Larger strength is observed for stepped cylindrical pin, whereas it is lower in the case of tapered cylindrical pin.
2. Tube thinning is severe in the case of stepped cylindrical pin in processed zone in the case of expansion, while thickening is severe in the case of tapered cylindrical pin in the same zone in case of reduction and beading.
3. Thickening in weld zone for reduction and beading depends on strength of processed zone. Lower is the strength of the FSP zone, higher is the thickening in the zone. For reduction, base metal zone thickening is independent of tool pin profiles, while for beading, thickening in base metal zone decreases with an increase in strength of the processed zone.
4. Instability in the form of crack is observed in the FSP zone during end expansion. In tube reduction, it is in the form of wrinkling and overlapping in the FSP zone, while in the case of beading, it is in the form of fine cracks in the base metal of the processed tubes.

References

1. Gupta, P.K., Sahu, R.R.: Experimental and numerical studies on the tube contraction using a conical-cylindrical die. *J. Strain Anal. Eng. Des.* **48**(8), 482–493 (2013). <https://doi.org/10.1177/0309324713502200>
2. Yang, J., Luo, M., Hua, Y., Lu, G.: Energy absorption of expansion tubes using a conical-cylindrical die: experiments and numerical simulation. *Int. J. Mech. Sci.* **52**, 716–725 (2010). <https://doi.org/10.1016/j.ijmecsci.2009.11.015>
3. Choi, W.M., Kwon, T.S., Jung, H.S., Kim, J.S.: Influence of impact velocity on energy absorption characteristics and friction co-efficients of expansion tube. *Int. J. Crashworthiness* **17**(6), 621–629 (2012). <https://doi.org/10.1080/13588265.2012.704188>
4. Tan, C.J., Purbolaksono, J., Chong, W.T.: Forming box-shaped ends in circular tubes. *Int. J. Precis. Eng. Manuf.* **16**(9), 1975–1981 (2015). <https://doi.org/10.1007/s12541-015-0257-0>
5. Agrawal, A.K., Narayanan, R.G.: Joining of a tube to a sheet through end curling. *J. Mater. Process. Technol.* **246**, 291–304 (2017). <https://doi.org/10.1016/j.jmatprotec.2017.03.035>
6. Al-Fadhlah, K.J., Almazrouee, A.I., Aloraier, A.S.: Microstructure and mechanical properties of multi-pass friction stir processed aluminum alloy 6063. *Mater. Des.* **53**, 550–560 (2014). <https://doi.org/10.1016/j.matdes.2013.07.062>
7. Imam, M., Biswas, K., Racherla, V.: Effect of weld morphology on mechanical response and failure of friction stir welds in a naturally aged aluminium alloy. *Mater. Des.* **44**, 23–34 (2013). <https://doi.org/10.1016/j.matdes.2012.07.046>
8. Hajideh, M.R., Farahani, M., Alavi, S.A.D., Ramezani, N.M.: Investigations on the effects of tool geometry on the microstructure and the mechanical properties of dissimilar friction stir welded polyethylene and polypropylene sheet. *J. Manuf. Processes* **26**, 269–279 (2017). <https://doi.org/10.1016/j.jmapro.2017.02.018>
9. Ramulu, P.J., Narayanan, R.G., Kailas, S.V.: Forming limit investigation of friction stir welded sheets: influence of shoulder diameter and plunge depth. *Int. J. Adv. Manuf. Technol.* **69**, 2757–2772 (2013). <https://doi.org/10.1007/s00170-013-5245-x>
10. Khodabakhshi, F., Nosko, M., Gerlich, A.P.: Effects of graphene nano-platelets (GNPs) on the microstructural characteristics and textural development of an Al-Mg alloy during friction stir processing. *Surf. Coat. Technol.* **335**, 288–305 (2018). <https://doi.org/10.1016/j.surfcoat.2017.12.045>
11. Maamoun, A.H., Veldhuis, S.C., Elbestawi, M.: Friction stir processing of AlSi10Mg parts produced by selective laser melting. *J. Mater. Process. Technol.* **263**, 308–320 (2019). <https://doi.org/10.1016/j.jmatprotec.2018.08.030>
12. Lammlein, D.H., Gibson, B.T., Delapp, D.R., Cox, C., Strauss, A.M., Cook, G.E.: The friction stir welding of small-diameter pipe: an experimental and numerical proof of concept for automation and manufacturing. *Proc. Inst. Mech. Eng. B: J. Eng. Manuf.* **226**, 383–398 (2011). <https://doi.org/10.1177/0954405411402767>
13. Kang, S.H., Vadudevan, M., Noh, S., Jin, H.J., Jang, J., Kim, T.K.: Friction stir welding of F/M ODS steel plug and F/M steel tube. *Fusion Eng. Des.* **109–111**, 182–185 (2016). <https://doi.org/10.1016/j.fusengdes.2016.03.033>
14. Agrawal, A.K., Narayanan, R.G., Kailas, S.V.: End forming behaviour of friction stir processed AA 6063-T6 tubes at different tool rotational speeds. *J. Strain Anal. Eng. Des.* **52**(7), 434–449 (2017). <https://doi.org/10.1177/0309324717724662>
15. Moreira, P.M.G.P., Di Oliveira, F.M.F., De Castro, P.M.S.T.: Fatigue behaviour of notched specimens of friction stir welded aluminium alloy 6063-T6. *J. Mater. Process. Technol.* **207**, 283–292 (2008). <https://doi.org/10.1016/j.jmatprotec.2007.12.113>

Chapter 38

Geometric Model of the Weld Bead in DC and Square AC Submerged Arc Welding of 2.25 Cr-1 Mo Heat Resistant Steel



Uttam Kumar Mohanty, Abhay Sharma, Yohei Abe, Takahiro Fujimoto, Mitsuyoshi Nakatani, Akikazu Kitagawa, Manabu Tanaka and Tetsuo Suga

Abstract Weld bead shape is an important feature in arc welding that governs the mechanical behavior of the joint. The weld bead is significantly influenced by the type of power source used like alternating current (AC) or direct current (DC) as they affect the extent of heat generated at the electrode and workpiece. The present study identifies a way to represent the weld bead shape through composite geometrical functions. A case of bead geometry produced using DC and AC power source in submerged arc welding of 2.25 Cr-1 Mo is presented. The direct current electrode negative (DCEN) and direct current electrode positive (DCEP) polarities in DC power source and square waveform in the AC power source are used to deposit beads using constant welding conditions (like current and speed). The macrographs of the welded sample show different geometrical approximations for weld shape in DCEP, DCEN, and AC square waveform welds. Among the different polarity, the bead shape of an AC square waveform is distinct as compared to DC polarities and shows the ability to customize deposition and penetration by changing the frequency and the electrode negative ratio.

Keywords Power source · Bead geometry · Bead shape

38.1 Introduction

Heavy fabrication industries need semiautomatic submerged arc welding (SAW) with higher productivity in terms of strength, deposition rate, and quality of the weld. The SAW is known for efficient use of welding heat because the arc remains buried beneath the layer of flux, as shown in Fig. 38.1. The acceptable outcomes of SAW

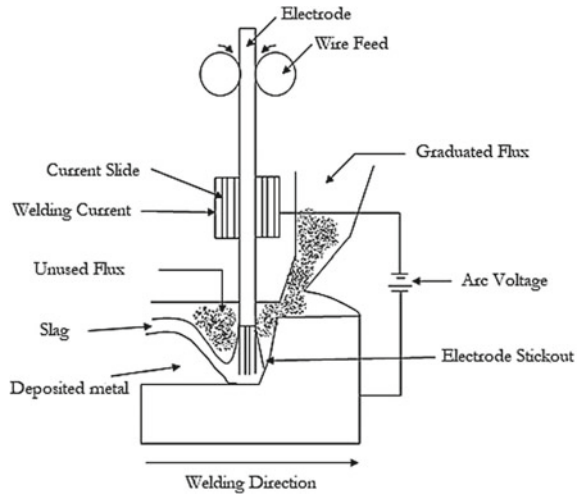
U. K. Mohanty (✉) · A. Sharma
Department of Mechanical and Aerospace Engineering, IIT Hyderabad, Sangareddy 502285, India
e-mail: me15resch11004@iith.ac.in

Y. Abe · T. Fujimoto · M. Nakatani · A. Kitagawa
Technical Research Institute, Hitachi Zosen Corporation, Osaka, Japan

M. Tanaka · T. Suga
JWRI, Osaka University, 5650871 Suita, Japan

© Springer Nature Singapore Pte Ltd. 2020
M. S. Shunmugam and M. Kanthababu (eds.), *Advances in Additive Manufacturing and Joining*, Lecture Notes on Multidisciplinary Industrial Engineering,
https://doi.org/10.1007/978-981-32-9433-2_38

Fig. 38.1 Schematic diagram of SAW



depend on the power source, i.e., either alternating or direct current power source. Depending on the requirement, DC power source uses either direct current electrode positive (DCEP) or direct current electrode negative (DCEN) polarity, whereas AC power source uses either triangular or square or sinusoidal waveform. The advantage of DCEP is the self-cleaning phenomenon which also improves the arc stability and reduces spatter. On the other hand, the merit of DCEN is that proper fusion of base plate takes place that leads to eliminate penetration defects due to excessive heat generation. The submerged arc welding process which is operating higher voltage (i.e. 24–38 V) creates the problem in the crossover when different waveforms like sine or triangular waveform of AC. The reason is that in case of sine or triangular waveform undergoes slow polarity reversal. However, square wave has a very fast crossover and tries to ignite the remaining arc. These power sources showing different weld bead geometry or bead shape which may be due to the different process parameters, polarity, materials, and welding technique.

Investigations have been conducted to understand the effect of power sources for different welding process and materials. Long et al. [1] compared the size of weld bead using DCEP and DCEN polarity in gas metal arc welding (GMAW) of Q235 steel in hyperbaric condition and observed that reinforcement and penetration remain larger, whereas bead width remains narrower at high pressures. Dutra et al. [2] observed that penetration and fusion area are large at larger electrode positive duration in aluminum using AC gas tungsten arc welding (GTAW) process. Singh et al. [3] studied the effect of DCEP and DCEN polarities on bead geometry (width, depth of penetration, penetration size factor, reinforcement, reinforcement form factor, and % dilution) in the SAW process for joining of mild steel and found that DCEP polarity yields a larger value of geometrical attributes except reinforcement. The comparative study of shielded metal arc welding process using different power sources like DCEP, DCEN, and AC to weld AISI 1020 steel [4] revealed that DCEN results in wider bead

and heat-affected zone than other polarities. It has been also reported that not only the polarity but also other process variables affect bead geometry. Vidyarthi et al. [5] obtained the direct relation between geometry of weld and process variables such as current and welding speed of for depositing ferritic stainless steel with DCEN polarity. Similarly, the effects of process variables such as wire feed speed, voltage, and contact tip to workpiece distance on the geometry of weld were analyzed in the bead-on-plate welding using DCEP GMAW process of mild steel [6]. The effect of electrode negative ratio on bead geometry was studied by Tong et al. [7] by using AC and DC pulse GMAW process to join AL6082 alloy and observed that AC pulse is more effective than DC pulse and results in shallow penetration due to high melting coefficient and low heat input. Some of the researchers have applied advanced mathematical tools like genetic algorithm, artificial neural network, and particle swarm optimization to obtain optimum process parameters to satisfy the requirement of the bead signature.

A mathematical model is an essential tool to determine the shape of penetration profile and reinforcement profile. Sharma et al. [8] suggested a composite trigonometric function such as cosine and parabolic and an elliptical segment for the prediction of penetration and reinforcement profile of twin-wire weld using both DCEP and DCEN polarity. Choudhury et al. [9] proposed bi-elliptic weld penetration profile for carbon steel welds produced using AC square waveform SAW. Kim et al. [10] observed finger-like penetration in mild steel in GMAW process. Circular and triangular sectors to represent the weld reinforcement and penetration profile, respectively, in SAW process of mild steel were suggested by Datta et al. [11]. Cao et al. [12] used logistic, parabolic, Gaussian, and sine function to fit the reinforcement profile of the GMAW welds in mild steel. Ridging et al. [13] divided the outer shape of the bead to predict the shape of weld using the artificial neural network technique. The literature review suggests a significant difference in bead geometry and bead shape of welds produced by different power sources and welding techniques. However, the effect of power source on bead geometry of heat-resistant steel is not revealed. The objective of this work is to explore the effect of power source on bead geometry (i.e., both penetration and reinforcement profile) and bead shape of heat-resistant steel using DCEP, DCEN, and AC square waveform power source of submerged arc welding. The outcomes of this research are expected to be useful for the end-user dealing with fabrication of thick plate welds that are required for pressure vessels.

38.2 Materials and Experiments

The SAW is widely used in the fabrication of pressure vessel used in the power sector, oil refineries, and petrochemical industries. These pressure vessels are fabricated with materials like 2.25 Cr-1 Mo heat-resistant steel because of high operating temperatures and pressures. The bead-on-plate welding experiments were conducted at Hitachi Zosen Corporation, Japan, using an AC square, DCEP, and DCEN polarity power sources. The workpiece, electrode, and flux material were 2.25 Cr-1 Mo steel

plate of 600 mm × 80 mm × 20 mm dimension, US-521S wire of 4 mm diameter, and PF-200, respectively. The chemical compositions of electrode and workpiece materials are given in Table 38.1.

A total of three experiments were conducted by taking constant input process parameters for both AC and DC SAW processes as shown in Table 38.2. The samples were obtained cutting the specimen normal to the direction of welding using wire cut EDM. The samples were polished by standard metallographic procedure and etched by using 5% nital solution to obtain weld macrograph which is shown in Fig. 38.2b–d. The parameters defining the signature of bead geometry are represented in Fig. 38.2a. The measured value of bead geometry is shown in Table 38.2.

P —depth of penetration (mm); W —bead width (mm); R —reinforcement height (mm); A_p —penetration area (mm²), and A_r —reinforcement area (mm²).

The weld bead shape model is developed for the AC and DC welding, as presented in the next section. The weld shape is closely related to the hardness, particularly in penetration zone. Therefore, hardness mapping of the penetration is an effective measure for validation of the predicted weld shape. The hardness of the weld is mapped over an array of points oriented in weld width and depth direction at a spacing of 0.2 mm. The parameters like indentation force, speed, and the holding time are 100 g, 35 μm/s, and 15 μs, respectively, used for Vicker microhardness test.

38.3 Geometric Model

The earlier literature suggests different geometric shapes for representation of a weld bead—e.g., circular, triangular, elliptic, parabolic, logistic, Gaussian, sine function, a composite function. These shapes do not fit well with the bead geometry obtained with the DC and AC power source in submerged arc welding of 2.25 Cr-1 Mo steel as presented in Fig. 38.2. A critical observation of the weld shape suggests that in order to fit the shape of the fusion zone, a combination of parabola and ellipse can be used. The penetration profile in an AC square waveform weld can be composed using parabolic (AB) and elliptical (BC) segments, as shown in Fig. 38.3a. For welds produced with DCEP and DCEN power source, a parabolic segment (AB) can be used to represent the profile of penetration which is shown in Fig. 38.3b. The geometrical representation of the parabola is represented by a focal length (a) and penetration (P) whereas ellipse is shifted by an offset ϕ_{h1} (the major axis of the ellipse is situated ϕ_{h1} distance from the surface of the weld which passes through origin “O”). The reinforcement profile can be represented by a parabolic segment (CD in Fig. 38.3a for AC square) with a focal length (a_1) and reinforcement (R), whereas an elliptical segment (BC in Fig. 38.3b for DC power source) having an offset ϕ_{h2} from origin “O.” The semi-major axis and semi-minor axis of the penetration and reinforcement of the ellipse are denoted by (a_{h1} , b_{h1}) and (a_{h2} , b_{h2}). The dotted curve represents the outer boundary of the bead.

The generic equation of an ellipse with an offset ϕ_{h1} and ϕ_{h2} to represent the outer boundary of bead can be expressed as

Table 38.1 Chemical composition (mass%) of workpiece and electrode material

Alloy	C	Si	Mn	P	S	Ni	Cr	Mo	Cu	Fe
2.25Cr-1 Mo steel	0.13	0.14	0.5	0.007	0.002	-	2.36	0.97	-	Balanced
US-521S wire	0.16	0.13	0.93	0.003	0.002	0.14	2.45	1	0.12	Balanced

Table 38.2 Experimental results

Power sources		DCEP	DCEN	AC square
Input process parameters	Frequency (Hz)	–	–	60
	EN ratio	0	1	0.5
	Current (Amp)	500	500	500
	Welding speed (cm/min)	30	30	30
Bead geometry	Depth of penetration (mm)	16.28	14.14	4.19
	Bead Width (mm)	19.6	16.8	24.15
	Reinforcement height (mm)	8.2	9.3	3.45
	Penetration area (mm ²)	189.94	158.61	50.29
	Reinforcement area (mm ²)	108.0708	117.705	44.32

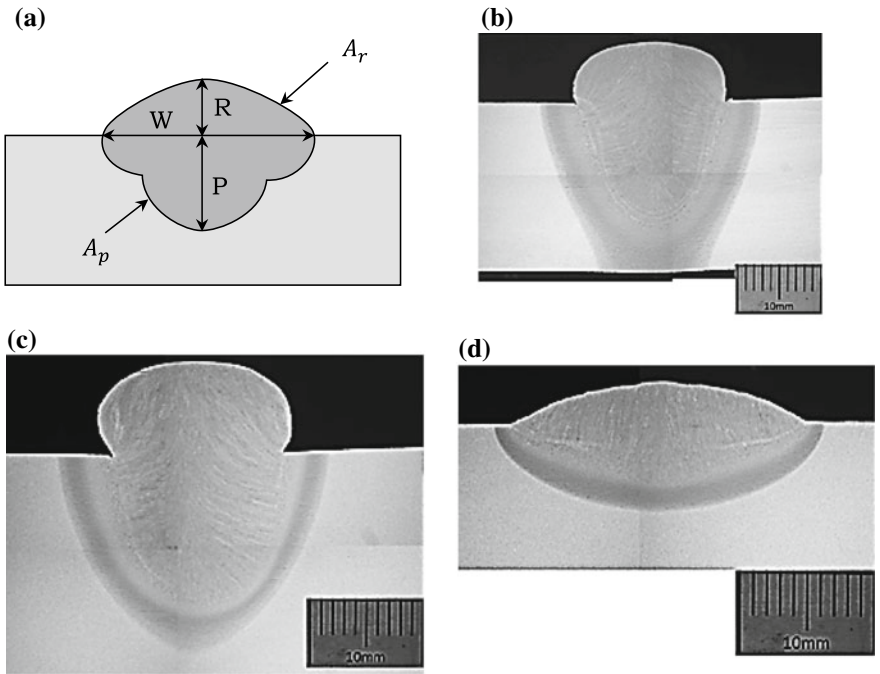


Fig. 38.2 Representation of a weld bead geometry; macrograph of b DCEP c DCEN, and d AC square weld bead

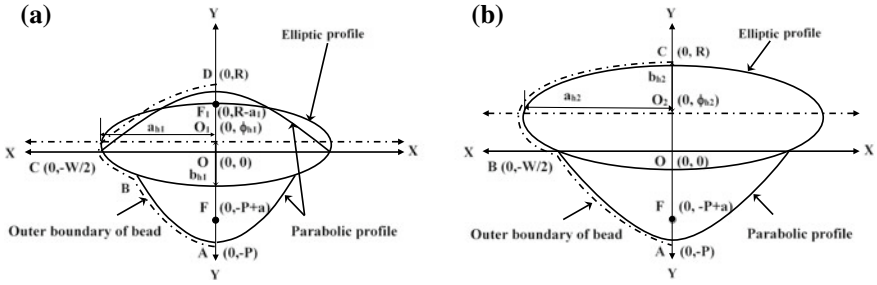


Fig. 38.3 Segment-wise representation of weld bead of **a** AC Square and **b** DC power source

For penetration profile [14]:

$$(x^2/a_{h1}^2) + (y - \phi_{h1})^2/b_{h1}^2 = 1 \tag{38.1}$$

For reinforcement profile [8]:

$$(x^2/a_{h2}^2) + ((y - \phi_{h2})^2/b_{h2}^2) = 1 \tag{38.2}$$

Similarly, the expression of parabola symmetric [14] with Y-axis to represent the penetration and reinforcement profile is given by

$$x^2 = 4a(y + P) \tag{38.3}$$

$$x^2 = 4a_1(y - R) \tag{38.4}$$

where P , R , and a_1 are the depth of penetration, reinforcement height, and focal length of reinforcement profile, respectively. The parameters of Eqs. 38.1–38.4 are calibrated with the experimental results as presented in the next section.

38.4 Results and Discussion

38.4.1 Model Calibration and Validation

The details of shape-defining parameters for AC and DC welds are given in Table 38.3. The weld produced by DCEP and DCEN fit a parabolic (AB) approximation for penetration profile, whereas the reinforcement profile fits well with an elliptic approximation (BC). Kim et al. [15] observed the similar result for the prediction of penetration profile. However, the profiles of reinforcement and penetration of an AC square waveform are found to be parabolic and a composite of elliptic and parabolic, respectively.

Table 38.3 Shape-defining parameters of the weld bead

Power sources	Profile details	Weld bead segment		
		AB	BC	CD
DCEP	Type of curve	Parabolic		Elliptic with offset
	Dimensions	$a = 1.85$ $P = 16.28$		$a_{h2} = 10.5$ $b_{h2} = 6.2$ $\phi_{h2} = 2$
DCEN	Type of curve	Parabolic		Elliptic with offset
	Dimensions	$a = 1.25$ $P = 13.91$		$a_{h2} = 10$ $b_{h2} = 6$ $\phi_{h2} = 3.5$
AC Square	Profile details	Weld bead segment		
		AB	BC	CD
	Type of curve	Parabolic	Elliptic with offset	Parabolic
	Dimensions	$a = 2.4$ $P = 4.24$	$a_{h1} = 12.3$ $b_{h1} = 2.23$ $\phi_{h1} = 0.2$	$a_1 = 10.65$ $R = 3.45$

The hardness mapping (left side), as shown in Fig. 38.4, fits very well with the penetration profile (right side). The hardness result validates the proposed penetration profile (i.e., parabolic in DC in Fig. 38.4a–b and composite parabolic and elliptic in AC square power source (Fig. 38.4c). The variation in power source leads to the formation of a different combination of parabolic and elliptic approximations, which are discussed in the next section.

38.4.2 Effect of Power Source on Bead Shape

Welding polarity produces a complex and sometimes conflicting bead shape due to the different behavior of deposition and penetration. The shape of weld bead can be quantitatively characterized by mapping the fusion zone as shown in Fig. 38.5. The most important features are the penetration and reinforcement profile, which are highlighted through A–B, B–C, and C–D segments for AC power source weld, and A–B and B–C segments for the DC power source weld. The sample macrograph shown in Fig. 38.2 shows that there is a significant change noticed in the bead shape with the variation of electrode polarity (e.g., difference in the shape of weld made with DC and AC polarity as seen in Fig. 38.5a–c).

With an increase in EN ratio, melting rate increases, which causes non-uniform reinforcement and penetration of the weld metal. In addition to this, the bead shape variation may occur because of polarity as discussed in the next section or may be

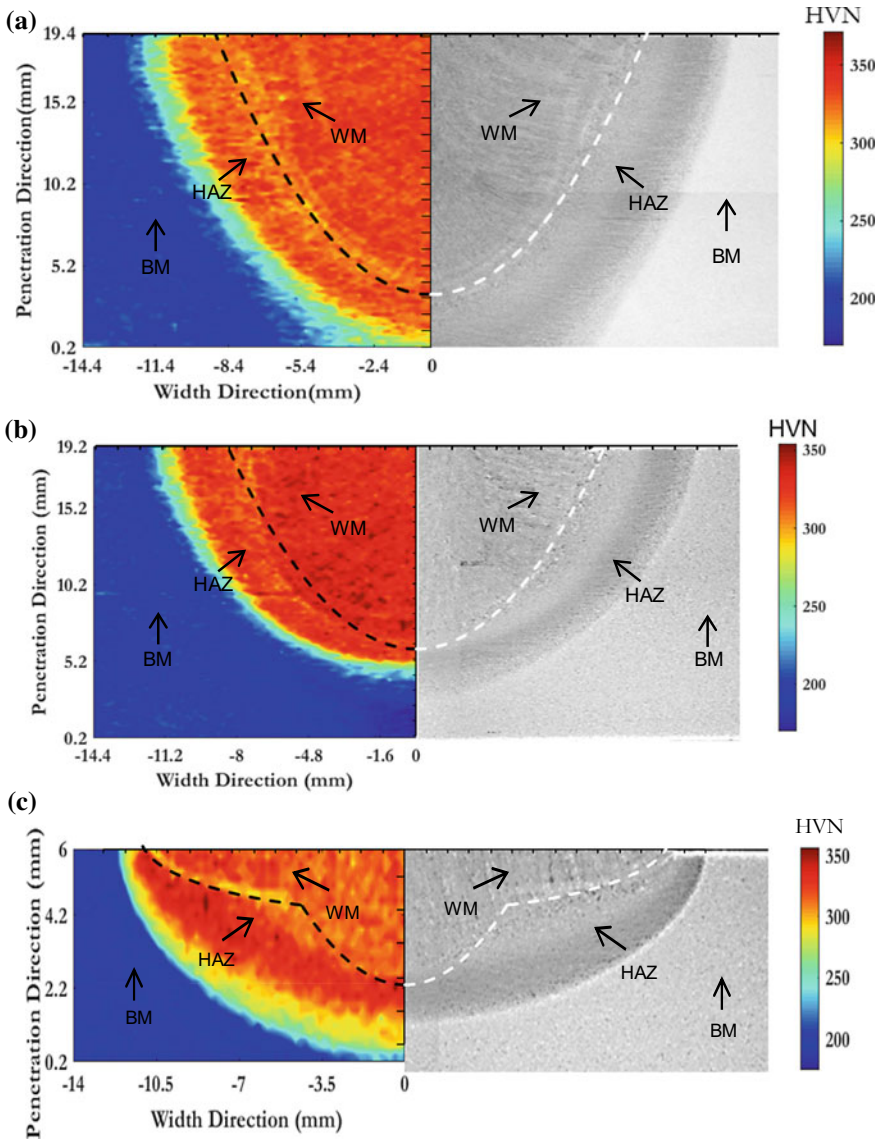


Fig. 38.4 Validation through hardness mapping of **a** DCEP **b** DCEN, and **c** AC square on weld bead shape (WM—weld metal; BM—base metal; HAZ—heat-affected zone; and HVN—vickers hardness number)

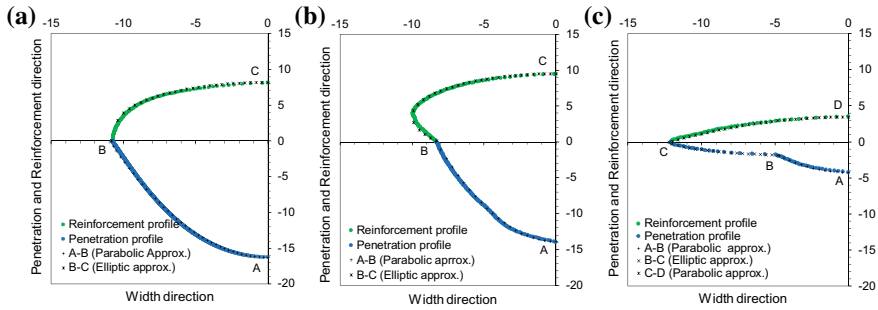


Fig. 38.5 Effect of **a** DCEP **b** DCEN, and **c** AC square on weld bead shape

due to the property of heat-resistant steel. The weld produced by AC square wave shows a composite parabolic (AB) and elliptic (BC) approximation for penetration profile, whereas the reinforcement profile is predicted by a parabolic approximation (CD), as shown in Fig. 38.5c.

38.4.3 Effect of Power Source on Bead Geometry

The effects of power sources on bead geometry for both DC and AC welding are shown in Fig. 38.6. The results show that the trend of variation in reinforcement height and reinforcement area is similar in Fig. 38.6a, b, respectively. The order of reinforcement height and reinforcement area in both AC and DC welding is DCEN > DCEP > AC square. The main reason is in DCEN power source, more heat is generated at the electrode than the workpiece [16]. In addition to this, the droplet size with DCEN polarity is larger than DCEP, which increases the overall melting rate. Therefore, the volume of material deposition is more in DCEN polarity than the DCEP polarity. Thus, the reinforcement profile deciding parameters such as reinforcement height and reinforcement area shows an increasing trend as compared to DCEP and AC square waveform power source. On the contrary, reverse phenomenon occurs in DCEP polarity. The parameters affecting penetration profile, i.e., depth of penetration and area of penetration increases in DCEP polarity (Fig. 38.6c, d) than DCEN which agrees with the work of Chandel et al. [17].

The increase in penetration and penetration area is because, in the case of DCEP polarity, the droplet flight time across the arc is reduced than the DCEN polarity, which indicates more force is acting on the weldment. A considerable increase in the width of an AC square weld is observed (Fig. 38.6e). The frequent polarity reversal promotes turbulence in arc plasma that allows the center core of the arc spread that leads to wider bead and lower penetration. The present work mainly emphasizes on SAW process to develop an analytical model to represent the actual shape of penetration and reinforcement profile of heat-resistant steel. This work can be extended to different arc welding process using DC and AC power source by

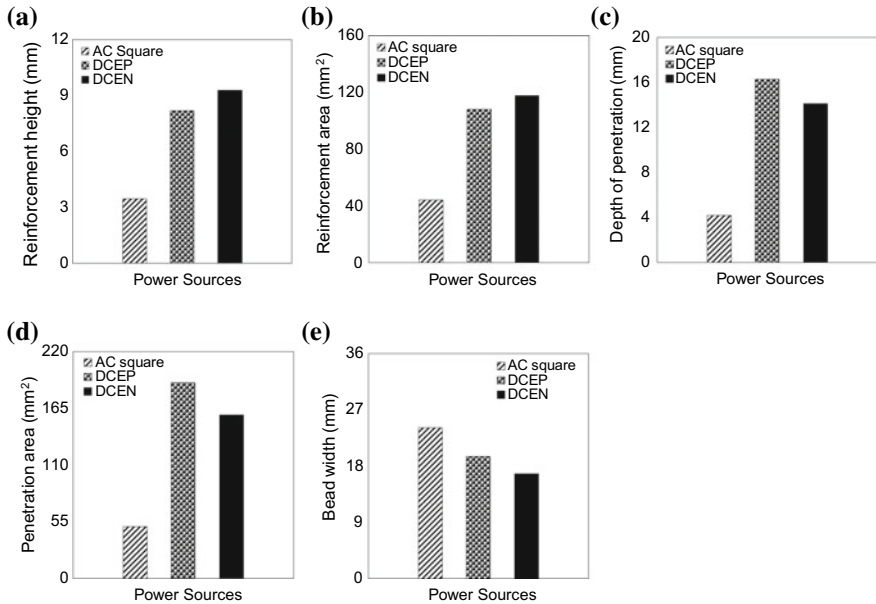


Fig. 38.6 Effect of power sources on **a** reinforcement height, **b** reinforcement area, **c** depth of penetration, **d** penetration area, and **e** bead width

varying different process variables like current, welding speed, and contact tip to work distance to compare the weld shape and bead geometry.

38.5 Conclusions

The major conclusions of this investigation are summarized as follows:

1. The developed geometrical approximation is reasonably accurate to predict the shape of penetration and reinforcement profiles of different weld produced by DCEP, DCEN, and AC square power source in heat-resistant steel.
2. The DCEP and DCEN weld shape can be approximated with elliptical reinforcement and parabolic penetration profile, respectively. The AC square welds are better represented by a combination of parabolic and elliptical segments for penetration profile and parabolic segment for reinforcement profile.
3. Among the different polarities, the bead shape of an AC square waveform is distinct as compared to DC polarities due to the ability to customize deposition and penetration by the change in frequency and EN ratio.
4. Bead width is the most affected by polarity, i.e., bead width of an AC square waveform is almost two times more than DCEP and DCEN welds which deviates the trend in other geometrical features (DCEN > DCEP > AC square).

5. The method of approximation is a generic approach which can be applied to other arc welding processes for determining the shape of penetration and reinforcement profile of a weld bead.

Acknowledgements The authors would like to acknowledge the support of Hitachi Zosen Corporation, Japan, JWRI, Osaka University, Japan, and IIT Hyderabad, India, for providing support for this research.

References





1. Xue, L., Wu, J., Huang, J., Huang, J., Zou, Y., Liu, J.: Welding polarity effects on weld spatters and bead geometry of hyperbaric dry GMAW. *Chin. J. Mech. Eng.* **29**(2), 351–356 (2016). <https://doi.org/10.3901/CJME.2015.1104.131>
2. Dutra, J.C., Cirino, L.M., Gonçalves e Silva, R.H.: AC–GTAW of aluminium—new perspective for evaluation of role of positive polarity time. *Sci. Technol. Weld. Joining* **15**(7), 632–637 (2010). <https://doi.org/10.1179/136217110X12813393169570>
3. Singh, R.P., Garg, R.K., Shukla, D.K.: Optimization of response parameters for polarity in submerged arc welding. *Multidiscipline Model. Mater. Struct.* **11**(4), 494–506 (2015). <https://doi.org/10.1108/MMMS-04-2015-0024>
4. Aloraier, A.S., Al-Fadhalah, K., Paradowska, A., Alfaraj, E.: Effect of welding polarity on bead geometry, microstructure, microhardness, and residual stresses of 1020 steel. *J. Eng. Res.* **24**, 2014. <https://doi.org/10.7603/s40632-014-0029-5>
5. Vidyarthi, R.S., Dwivedi, D.K., Muthukumar, V.: Optimization of A-TIG process parameters using response surface methodology. *Mater. Manuf. Processes* **33**(7), 709–717 (2018). <https://doi.org/10.1080/10426914.2017.1303154>
6. Adak, D.K., Mukherjee, M., Pal, T.K.: Development of a direct correlation of bead geometry, grain size and HAZ width with the GMAW process parameters on bead-on-plate welds of mild steel. *Trans. Indian Inst. Met.* **68**(5), 839–849 (2015). <https://doi.org/10.1007/s12666-015-0518-8>
7. Tong, H., Ueyama, T., Harada, S., Ushio, M.: Quality and productivity improvement in aluminium alloy thin sheet welding using alternating current pulsed metal inert gas welding system. *Sci. Technol. Weld. Joining* **6**(4), 203–208 (2001). <https://doi.org/10.1179/136217101101538776>
8. Sharma, A., Arora, N., Mishra, B.K.: Mathematical model of bead profile in high deposition welds. *J. Mater. Process. Technol.* **220**, 65–75 (2015). <https://doi.org/10.1016/j.jmatprotec.2015.01.009>
9. Choudhury, S., Sharma, A., Mohanty, U.K., Kasai, R., Komura, M., Tanaka, M., Suga, T.: Mathematical model of complex weld penetration profile: a case of square AC waveform arc welding. *J. Manuf. Proc.* **30**, 483–491 (2017). <https://doi.org/10.1016/j.jmapro.2017.10.015>
10. Kim, B.J.W., Na, S.J.: A study on the effect of contact tube-to-workpiece distance on weld shape in gas metal arc welding. *Weld. Res. Suppl.* 141–152 (1995). http://files.aws.org/wj/supplement/WJ_1995_05_s141.pdf
11. Datta, S., Bandyopadhyay, A., Pal, P.K.: Modeling and optimization of features of bead geometry including percentage dilution in submerged arc welding using mixture of fresh flux and fused slag. *Int. J. Adv. Manuf. Technol.* **36**(11–12), 1080–1090 (2008). <https://doi.org/10.1007/s00170-006-0917-4>
12. Cao, Y., Zhu, S., Liang, X., Wang, W.: Overlapping model of beads and curve fitting of bead section for rapid manufacturing by robotic MAG welding process. *Robot. Comput. Integr. Manuf.* **27**(3), 641–645 (2011). <https://doi.org/10.1016/j.rcim.2010.11.002>

13. Ridings, G.E., Thomson, R.C., Thewlis, G.: Prediction of multiwire submerged arc weld bead shape using neural network modelling. *Sci. Technol. Weld. Joining* **7**(5), 265–279 (2002). <https://doi.org/10.1179/136217102225006822>
14. Mohanty, U.K., Sharma, A., Nakatani, M., Kitagawa, A., Tanaka, M., Tetsuo, S.U.: A semi-analytical nonlinear model for weld profile prediction: a case of AC square waveform welded heat resistant steel. *J. Manuf. Sci. Eng.* **140**(11), 111013 (2018). <https://doi.org/10.1115/1.4040983>
15. Kim, G.H., Kang, S.I., Lee, S.B.: A study on the estimate of weld bead shape and the compensation of welding parameters by considering weld defects in horizontal fillet welding. In: *Third International Conference on Knowledge-Based Intelligent Information Engineering Systems*, Adelaide, Australia, pp. 212–216. IEEE (1999)
16. Sharma, A., Arora, N., Mishra, B.K.: A practical approach towards mathematical modeling of deposition rate during twin-wire submerged arc welding. *Int. J. Adv. Manuf. Technol.* **36**(5–6), 463–474 (2008). <https://doi.org/10.1007/s00170-006-0847-1>
17. Chandel, R.S., Bala, S.R.: Relationship between submerged-arc welding parameters and weld bead size. *Schweissen Schneiden.* **40**(2), 88–92 (1988). <https://scholar.google.com/scholar?q=Chandel,%20R.S.,%20Bala,%20S.,%201998.%20Relationship%20between%20submerged%20arc%20welding%20parameters%20and%20weld%20bead%20size.%20Schweissen%20Schneiden%2040,%20202831%20>

Chapter 39

Mechanical Characterization and Microstructural Investigation of MicroPlasma Arc Welded AISI 316L Thin Stainless Steel Sheets



Srikant Prasad , K. Vigneshwaran , Dibakor Boruah 
and Pintu Thakur 

Abstract The microplasma welding (MPAW) is the process of joining thin plate usually in the range 0.3–0.5 mm. The present work includes optimization of ultimate tensile strength (UTS), the effect of process parameters, the effect of hardness on mechanical properties, and metallographic investigation. The MPAW has been performed using 0.5-mm-thin stainless steel 316L sheets. Experiments were carried out based on Taguchi fraction factorial design approach using L27 orthogonal matrix. The tensile, hardness, and scanning electron microscope (SEM) sample were prepared to study the post-weld characterization. As a result of the optimization, UTS for the corresponding optimal setting was found to be 803.46 MPa, whereas predicted experimental result has incremented to 816 MPa. The overall mechanical properties analysis and optimization helps in the enhancement of strength, weld bead uniformity, defect-free weld. The output response of UTS, hardness, microstructure, and SEM, has been correlated with the weld. The optimal welding conditions help to maximize the productivity and minimize the total operating cost of the weld joint.

Keywords MPAW · Optimization · UTS · Hardness · SEM

S. Prasad (✉)

Indian Institute of Technology Guwahati, Mechanical Engineering, Guwahati 781039, Assam, India

e-mail: shrikant@iitg.ac.in

K. Vigneshwaran

JBM Auto System Pvt. Ltd., Maraimalai Nagar, Chennai 603209, Tamilnadu, India

D. Boruah

Faculty of Engineering, Environment and Computing, Coventry University, Coventry CV1 5FB, UK

P. Thakur

Girijananda Chowdhury Institute of Management and Technology, Tezpur 784501, Assam, India

© Springer Nature Singapore Pte Ltd. 2020

M. S. Shunmugam and M. Kanthababu (eds.), *Advances in Additive Manufacturing and Joining*, Lecture Notes on Multidisciplinary Industrial Engineering,

https://doi.org/10.1007/978-981-32-9433-2_39

39.1 Introduction

Microplasma arc welding is an economical and robust welding process for joining of metal sheets below 1 mm thickness. The pulse mode of MPAW produces deep penetration in the weld pool, resulting in welds with high tensile strength, high hardness, less distortion, less stress, good surface finish, fine grain in the weld zone. In the recent competitive manufacturing trend, quality, reliability, and productivity have importance, since it provides consumer satisfaction with the quality of weld joints that depends on the functional requirement which suits for various applications. PAW process does not require costly joint planning and diminishes the utilization of filler metal. The MPAW procedure has advanced electric control and along these lines better control of the procedure, however costly when contrasted with TIG welding hardware. In addition, parameter modification and control are likewise simple in MPAW process [1]. The Taguchi strategy is additionally one of the intense enhancement procedures which portray with enhancing the product quality and reliability at low cost. The working calculations for streamlining are computing signal-to-noise ratio (SN) proportions for every mix and after that the blend having a higher SN proportion is characterized as the ideal setting [2]. The weld quality is a mirror of mechanical properties, the bead geometry of the FZ (Fusion zone) and HAZ (Heat-affected zone), which in turn influences with metallurgical properties. The weld bead hardness influences the features of mechanical–metallurgical characteristics, which is directly related to the process parameters [3]. The process parameters affecting the weld quality of MPAW are mainly peak current, pulse time, pulse frequency, plasma and shielding gas flow rate, welding speed, nozzle diameter, weld materials, and thickness of base materials. The Taguchi method is a useful tool and technique to solve the optimization problem in various areas of manufacturing [4]. The statistical significance of the responses can be determined through analysis of variance (ANOVA). The Austenitic stainless steels 316L are characterized by good physical properties even at high temperatures. Higher chromium content in the material contributes to corrosion resistance behavior [5]. Control of weld bead shape is fundamental as the mechanical properties of welds are influenced by its shape [6]. Around the fusion zone, where the cooling rate is highest, a large increase in the hardness has been recorded [7, 8]. The extremely high rate of cooling of the weld causes hardening of the material in the HAZ. The principle parameters influencing the cooling cycle are welding velocity and heat input per unit length [9]. High cooling rates are accomplished in this cooling procedure, causing significant changes in the material properties of the weld and in heat-affected zone (HAZ) [10]. In the present work, the investigation was done to find the optimal parameter setting to get desirable responses such as mechanical properties of MPAW weld, and to get the effect of dominant parameters among welding speed, pulse time, stand-off distance, peak current, pulse frequency, and plasma gas flow rate. The welding was carried out in a direction perpendicular to the rolling direction. Taguchi fractional factorial design matrix approach with six parameters and three levels was adopted for the experiment. The reduced experimental run is a well-balanced set which gives output

as a signal-to-noise ratio (S/N). This ratio is the logarithmic function of output which consider mean and variance both as an account. The S/N ratio is the fingerprint of the process is to be optimized [11]. The rolling directions were identified with light scattering method and were chosen based on the fact that light on a rolled sheet will always scatter perpendicular to the rolling direction [12]. The additional experiment has been conducted for the validation of the predicted optimal setting of MPAW.

39.2 Experimental Methodology

The experiment was conducted using (Make-Arcraft plasma, model MP-50). The fixture has been modified to get proper alignment during welding to get proper weld on the joint interface. A pointer was fabricated and fixed in front of the nozzle to check the alignment by trail run of pug machine on which work table has been fixed. The torch holding device also modified in such a way that very precise stand-off distance in mm can be maintained. The modified fabricated fixture has been shown in Fig. 39.1. Various parameters which affect the quality of weld have been considered such as peak current (I_p) and base current (I_b), gas pre-flow, secondary upslope, secondary downslope pulse time (PT), pulse frequency (PF), plasma gas post-flow (PG), and stand of distance (SOD). In the experiment, the peak current and base current stability have been measured using a digital oscilloscope (Keysight infinition DSO-X-3024A).

The welding current is an important parameter and should be properly maintained to achieve a good-quality welded joint. It should be stable throughout the welding. In the present study, the base current was kept constant. The base current was set at a minimum level which can produce bead on the plate. The base current is responsible for the generation of a continuous arc and to maintain the arc flame at the tip of the nozzle. The effect of various parameters in three labels has been studied which has been shown in Table 39.1.

The independent machine and process parameters which were maintained constant during the experiments are given in Table 39.2.



Fig. 39.1 Modified and fabricated fixture

Table 39.1 Details regarding the welding parameters and the three levels

Sl. No.	Parameters	Level 1	Level 2	Level 3
1	Ip (A)	11.9	13.8	15.3
2	WS (regulator)	0.5 (2.5 mm/s)	1 (3.75 mm/s)	1.5 (4.75 mm/s)
3	PG (L/s)	0.6	0.7	0.8
4	PT (ms)	30	40	45
5	PF (Hz)	35	45	50
6	SOD (mm)	1	1.5	2

Table 39.2 Fixed machine and process parameters during the MPAW

Sl. No.	Fixed parameters	Quantity
1	Base current (Ib)	6.5 A
2	Shielding gas (argon)	2 LPM
3	Nozzle diameter	1.2 mm
4	Workpiece material	Stainless steel 316L
5	Material thickness	0.5 mm
6	Setback distance of the electrode	1 mm
7	Electrode tip angle	20°
8	Water temperature of the cooling tank	25 °C
9	Gas pre-flow	2.5 LPM
10	Secondary up slope current	2 A
11	Secondary downslope current	2 A
12	Secondary post-flow	2.5 LPM

The design matrix Taguchi L27 fractional factorial approach used for the present study has been shown as coded value in Table 39.3. The material used for the experiment was 0.5 mm-thin stainless steel sheet of grade SS 316L.

The fixture base plate for holding the sheet was made of copper and fixture clamp of mild steel which helps in heat removal from the weld plate and prevents the plasma arc deflection, respectively. Weld speed was precisely controlled using a pug machine moving along a rail track. The regulator unit for the weld speed of 0.50, 1.00, and 1.50 represents 2.50, 3.75, and 4.75 mm/s. Argon gas was used as the plasma and shielding gas for conducting the experiment. The factor-level range for the successful welding had been decided after a number of trial methods.

The metallographic investigation had been performed at the material science laboratory. The microstructure and SEM have been studied and correlated with weld quality. The well-polished weld samples were etched with Glyceregia. It is the fresh mixture of HCL, glycerol, and HNO₃ in a ratio of 3:2:1. The etchant was applied by swabbing technique [13]. The microstructural investigation had been performed

Table 39.3 Coded fractional factorial design for experiments

Exp. No.	Ip	WS	PG	PT	PF	SOD	UTS (MPa)
1	1	1	1	1	1	1	794.72
2	1	1	1	1	2	2	768.46
3	1	1	1	1	3	3	769.07
4	1	2	2	2	1	1	743.43
5	1	2	2	2	2	2	792.52
6	1	2	2	2	3	3	803.36
7	1	3	3	3	1	1	577.31
8	1	3	3	3	2	2	592.03
9	1	3	3	3	3	3	668.22
10	2	1	2	3	1	2	722.15
11	2	1	2	3	2	3	710.71
12	2	1	2	3	3	1	791.57
13	2	2	3	1	1	2	756.22
14	2	2	3	1	2	3	752.82
15	2	2	3	1	3	1	758.56
16	2	3	1	2	1	2	714.19
17	2	3	1	2	2	3	745.25
18	2	3	1	2	3	1	775.23
19	3	1	3	2	1	3	677.32
20	3	1	3	2	2	1	681.98
21	3	1	3	2	3	2	773.71
22	3	2	1	3	1	3	751.79
23	3	2	1	3	2	1	776.9
24	3	2	1	3	3	2	764.09
25	3	3	2	1	1	3	485.53
26	3	3	2	1	2	1	501.92
27	3	3	2	1	3	2	505.21

using an upright optical microscope (ZEISS AXIOCAM MRC) was used to see the microstructure and the weld bead zone.

Hardness was measured using Buehler, Lake bluff, Illinois USA, MODEL NO-75-20032-220, MSL laboratory. This test is conducted to determine the strength and quality of the welded joint. In the experimental investigation of MPAAV micro-Vickers hardness test method loads 500 g, idle time for loading was kept 20 s. The fractography samples were prepared from the tensile-tested sample. The test was carried out in a scanning electron microscope (make: Make: LEO, Model: 1430vp) at CIF laboratory. The fracture surface tip has been examined. The type of fracture reveals the brittle or ductile behavior of the weld.

39.3 Results and Discussions

39.3.1 Effect of Process Parameters

In the present investigation, the effect of process parameters on tensile strength has been studied using Taguchi's method. The welding sample of dimension (100 × 150) mm has been welded and tensile test was conducted as per ASTM-B557M-10 standard dimension of the tensile specimen which has been cut from the welded plate by CO₂ laser cutting machine. The standard dimension has been shown in Fig. 39.2. The edges were ground properly to remove heat-affected region from the edge of the tensile sample. The tensile sample has been shown in Fig. 39.3. The tensile test had been conducted using Instron digitally control closed loop servo-hydraulic 100 KN dynamic testing machine.

The stress–strain curve reveals the UTS up to 816 MPa was obtained for the welded joint. The good strength shows the quality welding defect-free weld (Fig. 39.4).

The response analyses are presented in Table 39.4; it shows the percentage contribution and ranking of significant parameters. The welding speed has very high influence 49% on the UTS property of the tensile sample which is followed by average pulse current contribution by 17% and plasma gas flow rate. Though the other parameters affect the welding process, their contribution is less compared to the above parameters. It is found that the stand-off distance has very less contribution to welding response (UTS). Since MPAW arc is columnar and concentric, no flaring is observed and hence the stand-off distance has the least effect on the response. The percentage contribution effect chart has been shown in Fig. 39.5.

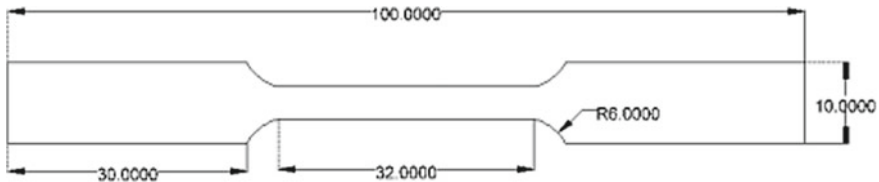


Fig. 39.2 Tensile sample dimension as per ASTM-B557M-10



Fig. 39.3 MPAW tensile sample

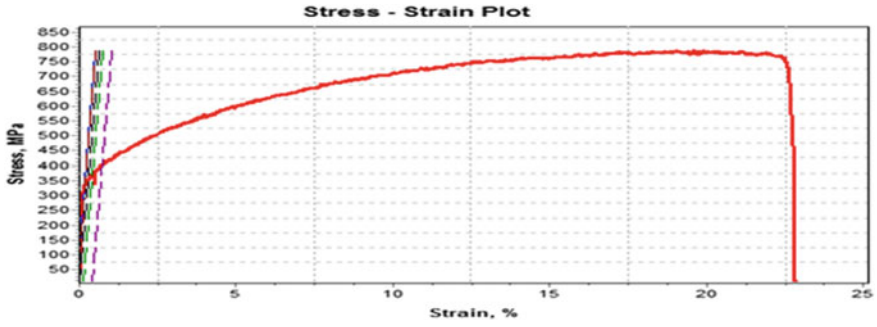


Fig. 39.4 Stress–strain curve for high UTS weld sample

Table 39.4 ANOVA response table for significant parameters

Source	DF	Seq SS	F	P	%C (%)
Ip	2	38,871	26.19	0	17
WS	2	114,479	77.13	0	49
Pg	2	39,431	26.57	0	17
PT	2	21,127	14.23	0	9
PF	2	8937	6.02	0.013	4
SOD	2	81	0.05	0.947	0
Residual Error	14	10,389			4
Total	26	233,315			100

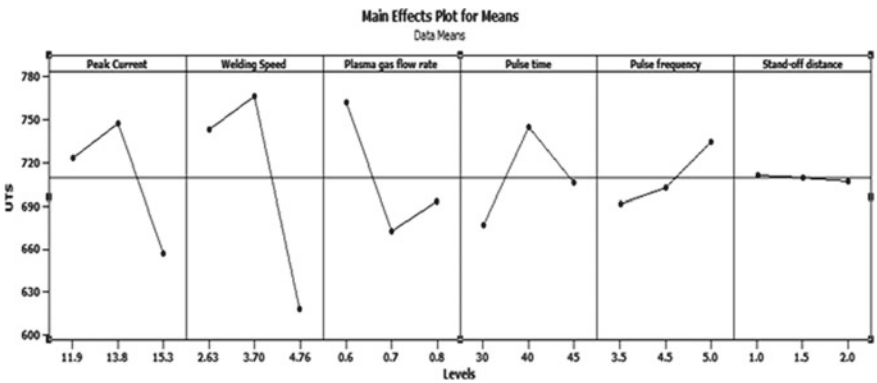


Fig. 39.5 Responses of main effects plot for mean of UTS

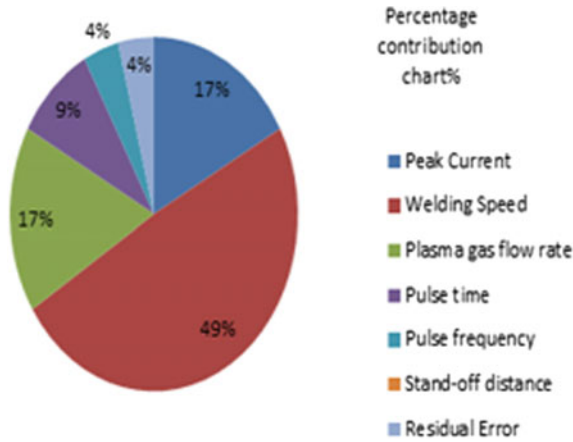


Fig. 39.6 The pie percentage contribution chart

The effect of process parameters on the UTS of the welded joints was investigated by carrying out with design of experiments (DOE) following the ANOVA response analysis. The main effect plot for means of UTS has been shown in Fig. 39.6. The maximum UTS was observed when plates were welded at peak current 13.8 A, welding speed 2.50 mm/sec, plasma gas flow rate 0.7 LPM, pulse time 40, pulse frequency 4.5, and stand-off distance 1 mm. The most influencing parameter was found as welding speed followed by pulse current and the plasma gas flow rate. The P value less than 0.5 show the significant parameters.

The optimized result found using MINITAB 16 was 919.99 MPa. The confirmation test had been conducted using the predicted setting, and it was found to be 816.00 MPa. The significant increment of 12.64 MPa in UTS has been achieved as a result of the optimization of the process. The best setting result and the predicted result are shown in Table 39.5.

Table 39.5 Evaluation of optimal and predicted experiments

Response characteristics	For best optimal factor setting	Optimal process condition	
	I_{p1} , WS_2 , $PG_{f/r2}$, PT_2 , PF_3 , SOD_3	Prediction with optimum setting I_{p3} , WS_1 , $PG_{f/r1}$, PT_2 , P_{f3} , SOD_2	Confirmation Experiment with the predicted condition
UTS (MPa)	803.36	919.99	816.00
Initial S/N ratio	58.10	59.75	58.91
Enhancement in UTS = (816.00-803.36) = 12.64 MPa			

39.3.2 Effect of Various Parameters on Welding Quality and Weld Geometry

The welding process parameters must be maintained carefully to achieve good stability of weld. Instability of welding can result in weld discontinuity such as excess penetration or incomplete penetration. High welding speed and low welding current will result in undercutting, which is shown in Fig. 39.7c, and incomplete penetration and no bead are formed [10]. Increasing the welding current within some ranges gives stronger heat and good welding joint as shown in Fig. 39.7d.

The welding speed is often determined by other welding parameters and factors such as welding current, type of plasma gas, and its flow rate and torch type. The melting efficiency characterizes as the heat energy required to initiate melting in the fusion zone divided by the net heat input. The melting efficiency increases or decreases rapidly with decrease and increase in welding speed, respectively. It is desirable to put low plasma gas flow rate nearly 0.2–0.4 LPM and shielding gas flow rate between 4 and 5 LPM to get a stable arc and shiny and strong weld. The formation of undercut determines the maximum welding speed allowed. The responsible entities for the weld bead properties and geometry. The geometry and quality are related to each parameters setting. So it needs to optimize the parameters so that we can get a quality weld to withstand the need and requirements. The welding current, welding speed, plasma gas flow rate, pulse time, pulse frequency, and stand-off distance all influence the heat-input per unit length, which have own contribution varied as per ranking shown in the result above.

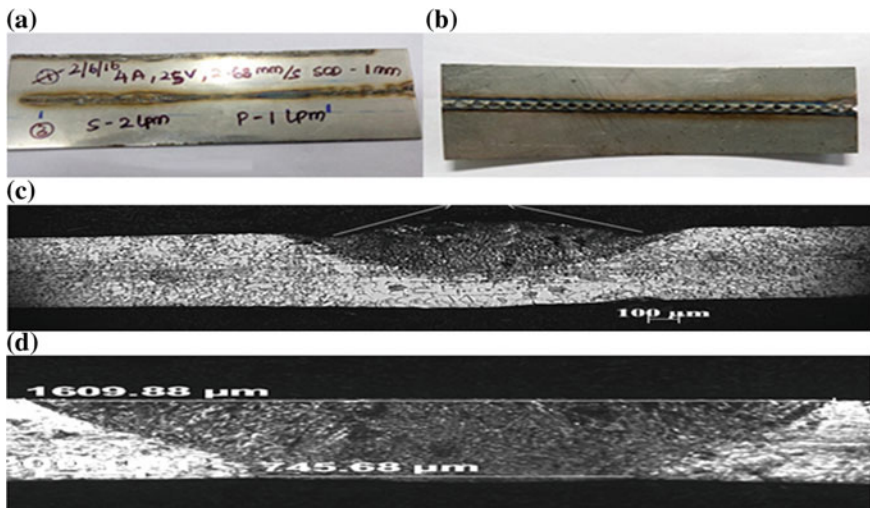


Fig. 39.7 Effect of welding current: **a** low and unstable welding current, **b** effect of high current and low welding speed, **c** undercut effect due to low current high voltage, **d** good and stable welding with optimized parameters

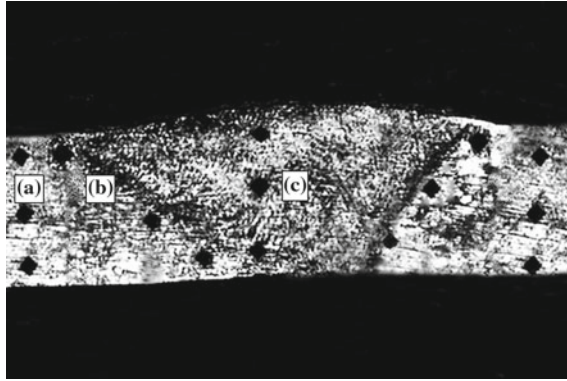


Fig. 39.8 Hardness indentation mark: **a** Fusion weld **b** HAZ zone 316L **c** base zone

39.3.3 *Effect of Hardness*

Hardness is the basic mechanical property of the material. The hardness values were measured at different zones: BZ (left), HAZ (left), FZ HAZ (right), and BZ (right) in accordance of top, center, and bottom of the weld joint. The indentation mark has been shown on the weld bead in Fig. 39.8. Hardness indentation is shown in (a) FZ, (b) HAZ, and (c) BZ. It was observed that the hardness at fusion zone is maximum at the top followed by HAZ and BZ hardness. Through the contour plot of hardness, we can measure hardness at any point within the weld zone.

The base material hardness for the rolled sheet plate has been found uniform compared to MPAW weld joint. From the plot, it is clearly revealing that at the top of the fusion zone hardness is highest due to recrystallization of fine grains, and the maximum hardness was observed at FZ top area followed by HAZ and BZ on both sides similarly. Hardness plot at the different zones of the weld joint is shown in Fig. 39.9.

39.3.4 *Metallographic Investigation*

The highest, lowest, and base metal UTS strength weld joint sample has been taken for metallographic study. From the microstructure, it is confirmed that in the melted zone, the grains are refined and dendrites were formed. At the interface of FZ and HAZ, the grain is columnar, which average size is nearly 50 μm . The length size of HAZ was found 300 to 400 μm . The grain size in HAZ varies from (30 to 70) μm . The microstructure reveals the grain in HAZ is coarse on both sides. In the base material, the grain size is almost uniform and evenly distribution of grains was observed. Twin deformation was observed in the base zone. In FZ, the grain recrystallization occurs

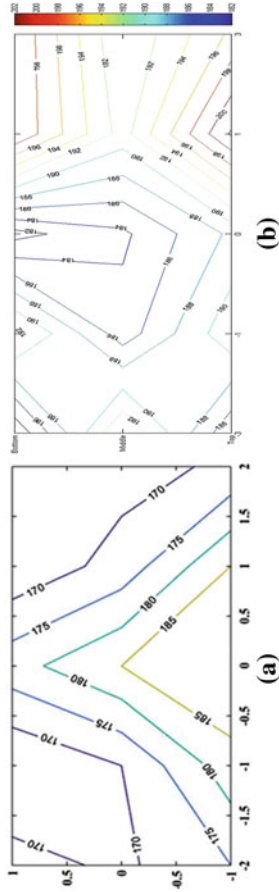


Fig. 39.9 Hardness contour plot for a MPAW weld and b base material 316L

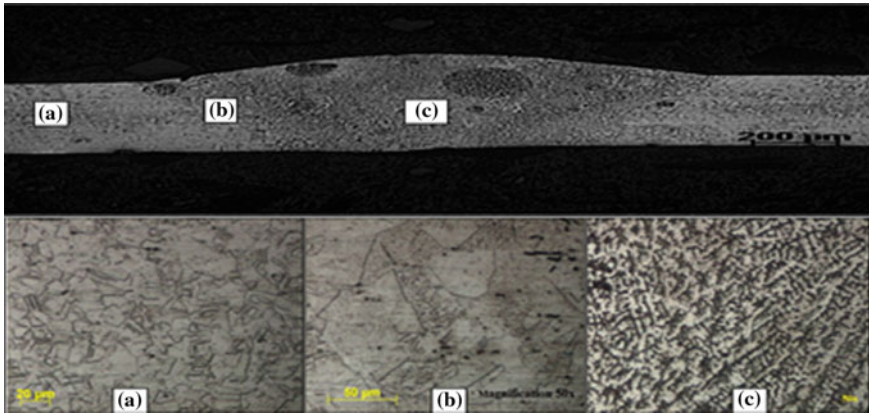


Fig. 39.10 Microstructures of the different zones: **a** base zone, **b** heat-affected zone, **c** fusion zone

so the grains are dendritic and very fine. It is very difficult to measure the grain size in FZ. Figure 39.10 shows the different zones of microstructure at 50x.

39.3.5 SEM Analysis for Tensile Fracture Sample

The fracture tensile samples were prepared from the tensile-tested sample. The test was carried out in a scanning electron microscope (make: Make: LEO, Model: 1430vp) at IIT Guwahati CIF laboratory. The fracture surface tip has been examined. The type of fracture reveals the ductile behavior of the weld. In the present investigation, two samples each, very high UTS strength fracture, very low UTS strength fracture, and base metal fracture, and average UTS strength fracture has been studied to find out the behavior of the fracture surface.

In the SEM fracture sample, dimples and black dark cavities were observed at the center of fracture specimen. It may be due to dimples grains in another part of the fracture. The deep cavity and diameters of the dimple are related to its tensile strength. High UTS sample shows higher deep cavity and diameters compared to the low UTS value sample. The size of dimples and cavity were found nearly of same size, which shows cavity is extracted dimples from the particular cavity. Figure 39.11 shows the fracture surface sample picture taken with a digital microscope to study in SEM.

In the fractured sample, typical size of the upper portion of cup diameter and cone diameter as measured with FESEM were in the range of 1.127–1.454 μm at 30KX and inside cone diameter was measured between average ranges of 220–260.1 nm.

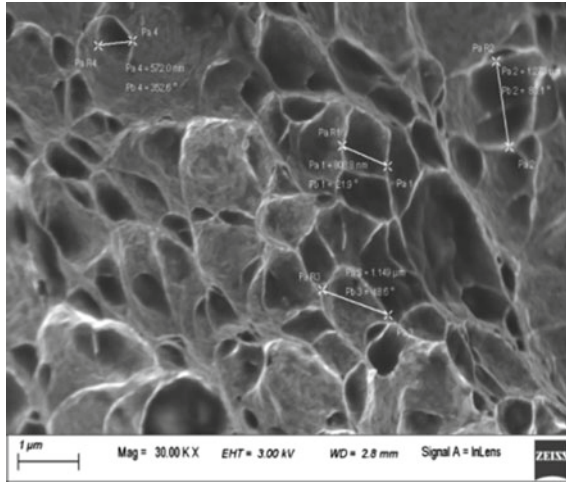


Fig. 39.11 Tensile fracture surface SEM images

39.4 Conclusions

- The optimum parameter setting for 316L austenitic stainless steel of 0.5 mm thickness for achieving maximum UTS were found to be peak current 13.8 A, welding speed 2.50 mm/s, plasma gas flow rate 0.7 LPM, pulse time 40, pulse frequency 4.5, and stand-off distance 1 mm. The experimental value of UTS for corresponding optimal setting was found to be 803.46 MPa, whereas predicted experimental result has an increment of 12.64 MPa.
- The most influencing parameter from ANOVA analysis was found to be welding speed, followed by peak current, plasma gas flow rate, and pulse frequency. The effect of stand-off distance on weld quality was observed to be negligible.
- It was observed that with the increase in welding current, penetration increases, whereas increased voltage results in increased bead width. The combination of low current and high voltage resulted in the undercut, which was clearly observed from experimental results.
- The trend in hardness pattern showing high hardness in Top FZ, followed by HAZ and base zone.
- At the interface of FZ and HAZ, the grain structure is columnar; the average size obtained was nearly 50 μm . The width of HAZ varies from 300 to 400 μm . The grain size in HAZ varies from (30 to 70) μm . The microstructure reveals the grain size in HAZ was coarse on both sides. In the base material, the grain size is almost uniform and even distribution of grains was observed. Twin deformation was observed in the base zone.
- It was observed from the broken tip of the tensile sample that the mode of fracture is ductile in nature.

References

1. Wu, C.S., Wang, L., Ren, W.J.: Plasma arc welding process, sensing, control and modeling. *J. Manuf. Pro.* **16**(1), 74–85 (2014)
2. Benyounis, K.Y., Olabi, A.G.: Optimization of different welding processes using statistical and numerical approaches. *Adv. Eng. Softw.* **39**, 483–496 (2008)
3. Datta, S., Bandyopadhyay, A., Pal, P.K.: Grey-based Taguchi method for optimization of bead geometry in submerged arc bead-on-plate welding. *Int. J. Adv. Manuf. Technol.* **39**, 1136–1143 (2008)
4. Rowlands, H., Antony, J., Knowles, G.: An application of experimental design for process optimization. *TQM Magazine* **12**(2), 78–83 (2000)
5. Ganesh, K.C., Balasubramanian, K.R., Vasudevan, M., Vasantharaja, P., Chandrasekhar, N.: *The Minerals, Metals & Materials Society and ASM International* (2016)
6. Connor, L.P.: *Welding handbook-welding processes*, 8th edn., vol. 2. American Welding Society (1991)
7. Bayraktar, E., Moiron, J., Kaplan, D.: Effect of welding conditions on the formability characteristics of thin sheet steels: mechanical and metallurgical effects. *J. Mater. Process. Technol.* **286**(1–3), 20–26 (2006)
8. Kaplan, A., Wiklund, G.: Advanced welding analysis methods applied to heavy section welding with a 15 kW fiber laser. In: *Proceedings of the International Conference on Welding of the IIW*, vol. 62, pp. 295–300 (2009)
9. Grigoryants, A.G., Shiganov, I.N., Misyurov, A.I.: *Grigoryants Technological Processes of Laser Treatment*. Bauman Moscow State Technical University, Moscow (2006)
10. Ion, J., Salminen, A., Sun, Z.: Process diagrams for laser beam welding of carbon manganese steels. *Weld. J.* **75**(7), 225 (1996)
11. Maghsoodloo, S., Ozdemir, G., Jordan, V., Huang, C.H.: Strengths and limitations of Taguchi's contributions to quality, manufacturing, and process engineering. *J. Manuf. Syst.* **23**(2), 73–126 (2004)
12. Yang, W.H., Tarn, Y.S.: Design optimization of cutting parameters for turning operations based on the Taguchi method. *J. Mater. Process. Technol.* **84**, 122–129 (1998)
13. Lamet Hubert, I.A.: *Metallography and Microstructures ASM Handbook*, vol. 9. UFRGS, Carnegie-Mellon University (1985)

Chapter 40

Comparison of Single- and Multiple-Spot Resistance Welding of Sub-millimeter Thick SS304 and SS316 Sheets



Dhanraj B. Waghmare and Partha Saha

Abstract Resistance spot welding is widely used for various industrial applications like in tailored blank welding. An attempt was made to study resistance welding process with multiple overlapped spots. Resistance spot welding machine was used to weld stainless steel sheets of sub-millimeter thickness. For this purpose, SS304 and SS316 sheets of 0.8 mm thickness were selected and welded. The welded joints were tested to check their tensile shear strength. It was observed that for both the stainless steel sheets, the shear strength of welded joint of multiple-spot welded joints was higher than single-spot welded joints. For both, single and multiple welded joints, the shear strength increased up to 20–25 welding cycles and thereafter got reduced, because of more HAZ. The coarsening of the grain structure which resulted in reduced strength was also verified by the microstructure analysis.

Keywords Resistance welding · Shear strength · Microstructure

40.1 Introduction

Resistance spot welding is one of the important welding processes used for sheet metal welding and it is used in automobile industry when permanent joining is required instead of joining by rivets or screws. This technique is being widely used by auto industry. It is well known that 4000–6000 resistance spot welds are required to assemble a car body. The importance of resistance welding is rightly mentioned by Tom Snow, who is chairman of Resistance Welding Manufacturing Alliance (RWMA), a Standing Committee of the American Welding Society (AWS), in the editorial of *Welding Journal* issue of May 2016. He says, “Today is an exciting time to be involved with resistance welding because the auto industry’s weight reduction efforts have increased the use of high-strength steels and aluminum, all of

D. B. Waghmare (✉)

Dr. Babasaheb Ambedkar Technological University, Lonere, Raigad 402103, India
e-mail: dbwaghmare@dbatu.ac.in

P. Saha

Indian Institute of Technology Kharagpur, Kharagpur 721302, India

© Springer Nature Singapore Pte Ltd. 2020

M. S. Shunmugam and M. Kanthababu (eds.), *Advances in Additive Manufacturing and Joining*, Lecture Notes on Multidisciplinary Industrial Engineering,
https://doi.org/10.1007/978-981-32-9433-2_40

which are more challenging to resistance weld than mild steel. These new materials have inspired more research into the process and many technological improvements.” Again resistance welding processing time is very short, it does not require any consumables such as welding rod, or solder or brazing material, etc. Thus it is not only advantageous in producing reliable thermo-mechanical joint, but also it is safe for operator and environment friendly.

As compared to another advanced welding processes such as laser beam welding (LBW), the joining efficiency ($\text{mm}^2 \text{kJ}^{-1}$) of resistance welding is 65–100, which is higher than LBW having joining efficiency of 15–25 [1]. The joining efficiency tells about the energy spent in unnecessary heating like HAZ or distortion of the components. It can also be used for joining reflective materials which are quite difficult for laser welding applications. Thus, the quality parameters like rate of weld production, low heat input, reliability of the equipment, deep penetration, no requirement of vacuum, welding magnetic materials are making it advantageous in joining process.

40.2 Process Mechanism

One of the important industrial joining processes is resistance welding process. The energy produced from a thermo-electric process is used to generate heat to form the coalescence at the interface of the mating parts. To achieve perfect joint, an electrical current is passed through the parts for certain time and under a controlled pressure. The heat is generated because of the resistance of the workpieces and electrodes. Figure 40.1 shows the resistance welding set up used for the experimentation. The electrode material used was copper–chromium–zirconium alloy. The amount of heat generated (Q) during welding depends upon three factors: (1) I = current (ampere); (2) R = resistance (ohms); and (3) t = duration of current (seconds). These three factors all together affect the heat generated as expressed in the following formula

$$Q = I^2 R t \quad (40.1)$$

The resistance R in the above expression is the total resistance of different resistances as shown in Fig. 40.2. This total resistance in the current flow path affects the magnitude of current. Thus, R can be expressed in the following expression,

$$R = R_{e1w1} + R_{w1} + R_{w1w2} + R_{w2} + R_{w2e2} \quad (40.2)$$

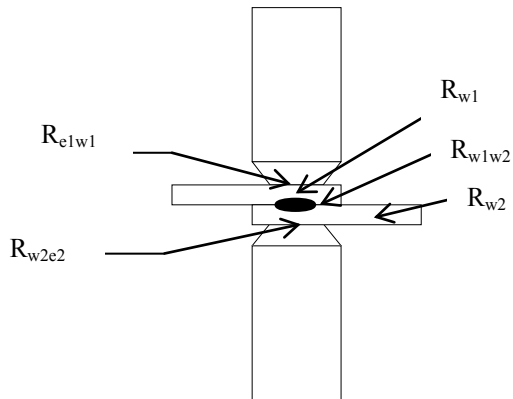
where

- R_{e1w1} the resistance between top electrode and work piece at top;
- R_{w1} the resistance of the work piece at top;
- R_{w1w2} the resistance between two workpieces at the interface;
- R_{w2} the resistance of the work piece at bottom;

Fig. 40.1 Resistance welding setup



Fig. 40.2 Resistances present in between the electrodes in RSW



R_{w2e2} the resistance between bottom electrode and work piece at bottom

Researchers had observed that the required resistance for resistance spot welding is offered by the resistance between the two workpieces R_{w1w2} as shown in Fig. 40.2. Higher weld ability can be achieved if R_{w1w2} is high. The magnitude of R_{w1w2} depends upon many factors such as dust-free, grease-free surfaces of the base metal, blackening of electrode surface, the size, and shape of the electrode face and electrode force.

Though the electrode surfaces are subjected to high temperature, the base metal does not melt during welding as electrodes are kept cool by passage of water [2].

The objective of studying resistance welding was to get some insight into this process and compare single-spot welding with multiple-spot welding. Hence, initially single-spot welding was carried out on SS304 and SS316 sheets of 0.8 mm thickness. Based upon the tensile shear strength obtained for single-spot welded joints, the performance parameters were finalized for conducting multiple-spot resistance welding.

40.3 Single-Spot Welding of SS304 and SS316

40.3.1 Material Selection and Process Parameters

Initially, the SS304 and SS316 sheets were cut into small coupons of 30 mm × 70 mm to be used for resistance welding. Based upon the literature survey [3, 4] and changing the values according to the available resistance welding set up, the values of the basic important process parameters—welding time, welding current, and electrode pressure—were selected after trial experiments as shown in Table 40.1. The welded samples were numbered based on the serial number of the actual experiment conducted. For example, RSW-B-1 means resistance spot welded SS316 sample of 0.8 mm thickness when experiment number 5 was done. The other samples have been designated in the same fashion. As mentioned previously, A stands for SS304 stainless steel sheet of 0.8 mm thickness and B stands for SS316 stainless steel sheet of 0.8 mm thickness. Though more number of experiments have been conducted, only the details of the relevant experiments have been shown here. All the experiments have been conducted in open atmosphere, without any filler material and without any shielding gas.

Table 40.1 List of the process parameters selected for resistance single-spot welding

Type of SS grade	Sample name	Welding time (cycles) (1cycle = 0.02 s)	Welding current (kA)	Pressure (bar)
SS316 (B)	RSW-B-1	15	7.6	1.5
	RSW-B-2	20	7.6	1.5
	RSW-B-3	25	7.6	1.5
	RSW-B-4	30	7.6	1.5
SS 304 (A)	RSW-A-1	15	7.9	3
	RSW-A-2	20	7.9	3
	RSW-A-3	25	7.9	3
	RSW-A-4	30	7.9	3

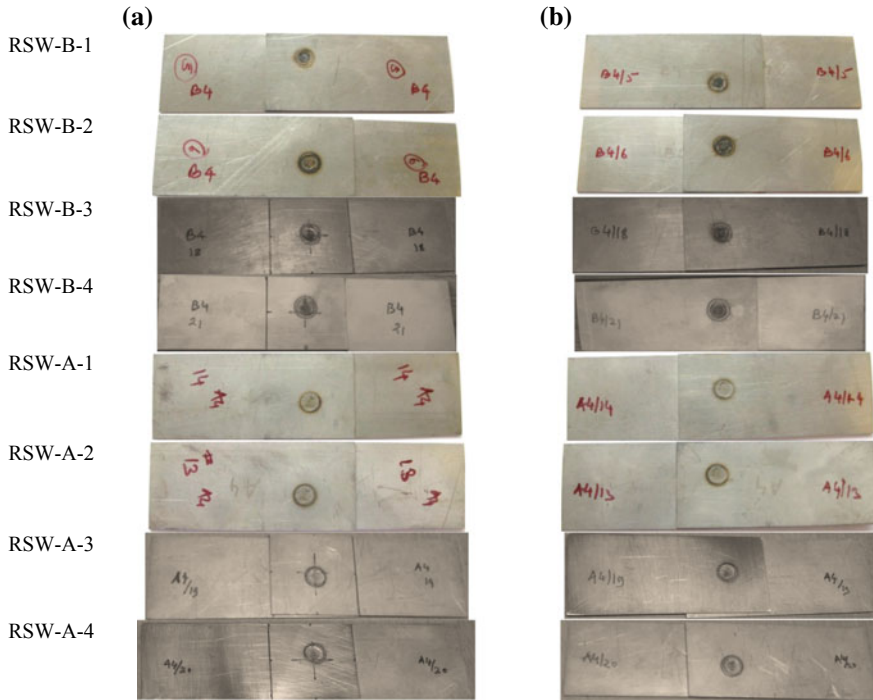


Fig. 40.3 Appearance of the resistance single-spot welded samples showing weld nugget from **a** top and **b** bottom

Here, the welding current and pressure or the electrode force are kept constant and the welding time varied from 15 cycles to 30 cycles with an increment of 5 cycles. The work holding time is kept as 30 cycles. Thus, the spot-welded samples show good surface appearance, which is one of the important quality parameters for resistance weld [5]. Figure 40.3 shows the appearance of the welded samples.

40.4 Results and Discussion

40.4.1 Tensile Shear Testing of Resistance Single-Spot Welded Samples

The mechanical strength of the welded joint is a very important parameter affecting the quality of welded joints. Hence, the procedure specified by ISO 14273:2000(E) was followed to measure tensile shear strength of the welded joints [6–9]. The Tinius Olsen H50KS universal testing machine was used, which satisfies the requirements laid down by ISO 7500-1. All the welded samples were tested with position rate of

1 mm/min. Figure 40.4 shows the photographs of tested samples after tensile shear testing.

It is clear from Fig. 40.4 that the failure occurred in the heat-affected zone (HAZ) of the welded samples. The failure is the tearing type of failure on the base material side. The values of tensile shear strength obtained are as shown in Table 40.2. It was observed that as the welding time was increased from 15 cycles up to 25 cycles, there was an increase in tensile strength of both the grades of stainless steel and reduces afterward. It was also seen that the tensile shear strength of all welded samples was higher than its base material which fractured at ultimate load of 2372 N (SS304) and 2310 N (SS316).

The highest value of tensile shear force obtained for SS316 is 6700 N, when welding time of 0.5 s (25 cycles) was used at constant current of 7.6 kA and constant electrode pressure of 1.5 Bar. Similarly, the highest value of tensile shear force obtained for SS304 is 7250 N, when welding time of 0.5 s (25 cycles) was used at constant current of 7.9 kA and constant electrode pressure of 3 Bar. Thus from Tables 40.1 and 40.2, it can be concluded that as the welding time increases from 15 cycles to 25 cycles amount of heat produced to form weld nugget increases [4, 10] and thus the amount of fused metal to form nucleus increases [1]. This leads to an increase

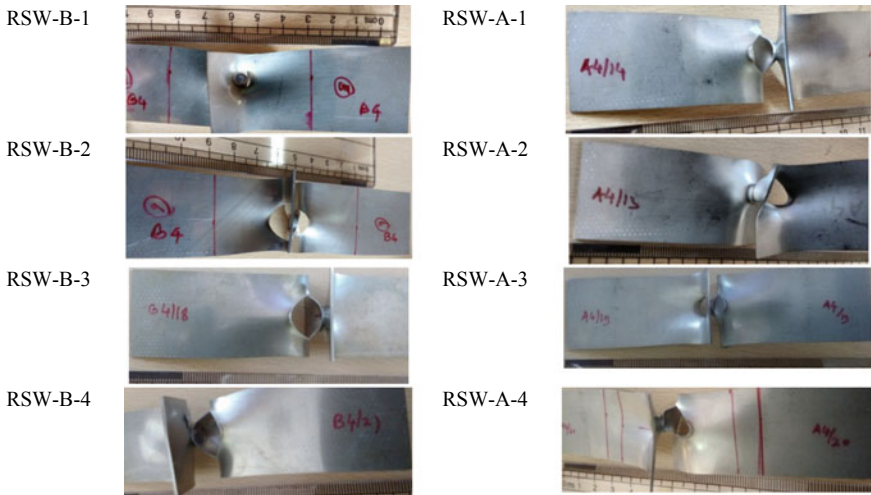


Fig. 40.4 Photographs of resistance single-spot welded samples after tensile shear testing

Table 40.2 Values of tensile shear strength of resistance single-spot welded samples

Sample name	Force (N)	Sample name	Force (N)
RSW-B-1	5880	RSW-A-1	6920
RSW-B-2	6600	RSW-A-2	6970
RSW-B-3	6700	RSW-A-3	7250
RSW-B-4	6630	RSW-A-4	6970

in tensile shear strength of welded joints. This is because the load-carrying cross section widens as weld nugget diameter increases [5] as shown in Table 40.2. But after welding time of 0.6 s, though weld nugget diameter increases, amount of further heat added reduces weld strength because of coarsening of microstructure of the weld nugget [11]. The effect of nucleus size on tensile shear strength in electrical resistance spot welding of chromided micro-alloyed steel sheets having 0.8 mm thickness and galvanized chromided micro-alloyed steel sheets having 1.0 mm thickness were investigated by Aslander [1] and found that the tensile shear strength increases up to 8 mm and reduces after 10 mm. The similar trend was followed for SS316, the tensile strength increases up to nugget diameter of 7.5 mm (RSM-B-3) and then reduces after 8 mm (RSM-B-4) diameter. The same trend was seen for SS304.

40.4.2 Multiple-Spot Welding of SS304 and SS316

Based on the data analysis of resistance single-spot welding of SS304 and 316 stainless steels, the experiments for multiple-spot welding were designed. It was decided to check the weld quality when overlapping of single spot over other spots was done. Same process parameters of single-spot welding as shown in Table 40.1 were used for multiple-spot overlap welding. There was small variation of welding current for different spots on the same sample; hence average of these values was used as shown in Table 40.3. Figures 40.5 and 40.6 shows the resistance of multi-spot welded samples of SS316 and SS304, respectively. Here, as the weld time increased, the size of the weld nugget also increased. Approximately 50% overlap was maintained between two spots. The more blackening of the welds was because of more heating due to overlapping of the spots.

These welds were then tested to check their tensile shear strength and microstructure. The sample nomenclature follows the name of the process, RMSW—Resistance

Table 40.3 List of the process parameters selected for resistance multi-spot welding

Type of SS grade	Sample name	Welding time (cycles) (1cycle = 0.02 s)	Welding current (kA)	Pressure (bar)
SS316 (B)	RMSW-B-1	15	6.94	1.5
	RMSW-B-2	20	7.3	1.5
	RMSW-B-3	25	7.66	1.5
	RMSW-B-4	30	7.46	1.5
SS304 (A)	RMSW-A-1	15	7.7	3
	RMSW-A-2	20	7.9	3
	RMSW-A-3	25	7.9	3
	RMSW-A-4	30	7.9	3

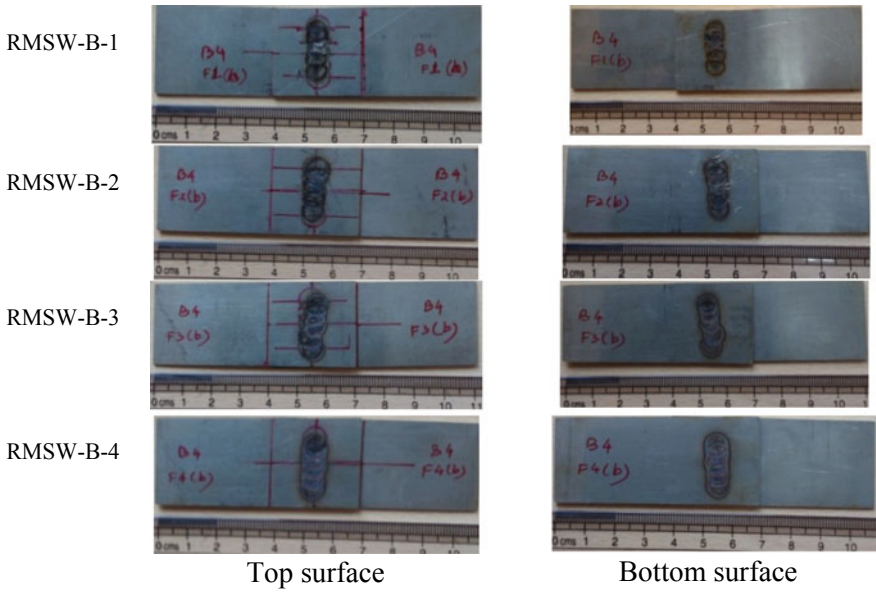


Fig. 40.5 Photographs of resistance multi-spot welded samples of SS316 of 0.8 mm thickness

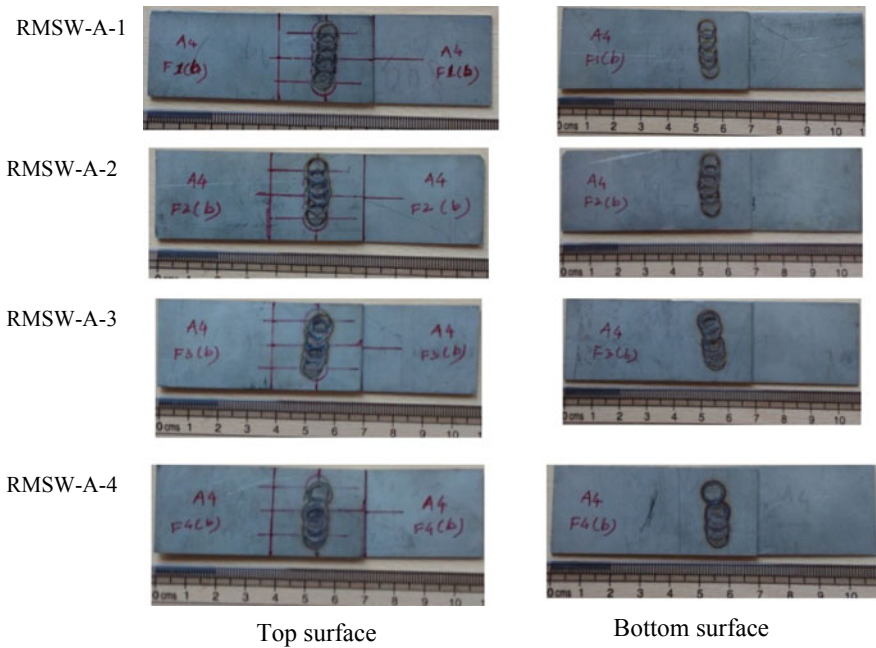


Fig. 40.6 Photographs of resistance multi-spot welded samples of SS304 of 0.8 mm thickness

Multiple-Spot Welding, specimen name—A(SS304)/B(SS316) and experiment number—1, 2, 3, 4.

40.4.3 Tensile Shear Strength Testing of Resistance Multi-spot Welded Samples

The tensile shear strength of these resistance multi-spot welded joints was checked by the procedure specified by ISO 14273:2000(E) by using the Tinius Olsen H50KS universal testing machine. All the welded samples were tested with position rate of 1 mm/min. Figure 40.7 shows the photographs of tested samples after tensile shear testing. From the photographs shown in Fig. 40.7 of resistance multi-spot welded samples, it can be seen that the welded samples failure started at the HAZ, not inside the weld interface [3] and further it progressed on the base material side. The same trend of increase in tensile shear strength was observed as compared to single-spot welding as shown in Table 40.4.

It is observed from Table 40.4 that, as the welding time increases from 15 cycles up to 25 cycles, there is an increase in tensile shear strength of both the grades of stainless steel. It is also seen that the tensile shear strength of all SS316 and SS304

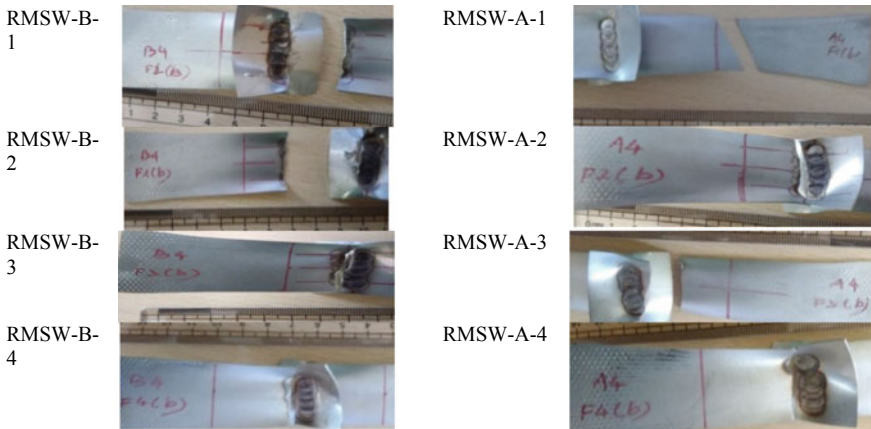


Fig. 40.7 Photographs of resistance multi-spot welded samples after tensile shear testing

Table 40.4 Values of tensile shear force of multi-spot resistance welded samples

Sample name	Force (N)	Sample name	Force (N)
RMSW-B-1	14,210	RMSW-A-1	14,240
RMSW-B-2	14,370	RMSW-A-2	15,070
RMSW-B-3	13,930	RMSW-A-3	15,440
RMSW-B-4	13,620	RMSW-A-4	14,850

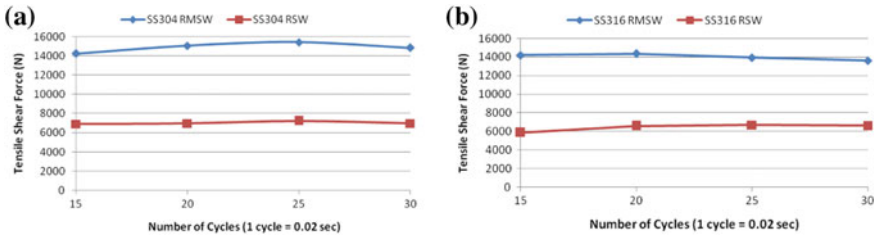


Fig. 40.8 Relationship between shear strength and welding cycle time **a** SS304 **b** SS316

welded samples is higher than its base material ultimate tensile strength of 2310 N and 2372 N, respectively. The highest value of tensile shear strength obtained for SS316 is 14370 N, when welding time of 0.4 s (20 cycles) is used at average current of 7.3 kA and constant electrode pressure of 1.5 Bar. Similarly, the highest value of tensile shear strength obtained for SS304 is 15440 N, when welding time of 0.5 s (25 cycles) is used at average current of 7.9 kA and constant electrode pressure of 3 Bar. Figure 40.8 shows the plot between tensile shear strength of SS304 and SS316 with an increase in weld cycle time.

Thus, it can be concluded from Fig. 40.8 that as the welding time increased at almost constant welding current and constant electrode pressure, amount of heat produced to form weld nugget increased resulting in an increase of weld nugget diameter, thus increasing the tensile shear strength [4]. This happened because the load-carrying cross section widens when weld zone area increases [5]. As the welding was done manually, it was difficult to maintain exact 50% overlap of weld spots. Because of this, the weld zone cross section length showed a slight decrease for welded samples RMSW-B-3 and RMSW-A-3 of both the grades. But after welding time of 0.6 s, though weld nugget diameter and weld zone length increased, the further heat addition resulted in reduction of weld strength because of more coarsening of microstructure of the weld nugget [11]. While discussing the effect of nugget diameter on tensile shear strength, Aslander [1] had explained the limitation of only using weld nugget diameter as a parameter to check weld quality and introduced the ratio of weld nugget diameter and nugget height as the most relevant parameter to check weld quality. After considering this ratio, it was observed that for SS316, maximum tensile shear strength was obtained for ratio of 0.12 and for SS304 it was 0.16, which is quite similar to the ratio obtained by Aslander [1].

40.4.4 Microstructure of Resistance Multi-spot Welded Samples

To study the effect of change in welding time on the microstructure of the weld zone, the samples were cut in the longitudinal and transverse directions of the weld zone (WZ). Thus, two samples from each welded samples were produced to study under

SEM (scanning electron microscope) as shown in Fig. 40.9. The longitudinal and transverse cross sections of all the welded samples were cut by using wire EDM (electric discharge machine). Then the metallographic sample preparation was done as per the ASTM (American Society of the International Association for Testing and Materials) standard E3.5569. After thoroughly cleaning and polishing the samples, etching of the samples was done by mixed acid solution containing equal amount of HCL, HNO₃, and acetic acid at room temperature. The etched samples reveal the microstructure as shown in Figs. 40.10 and 40.11. Figure 40.10 shows the microstructure of welded samples in the increasing order of welding time. Figure 40.10a shows the microstructure of the weld zone (WZ), heat-affected zone (HAZ), and the nearby

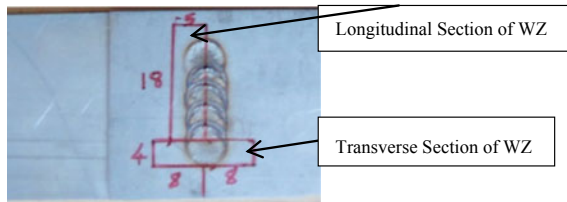


Fig. 40.9 Longitudinal and transverse cross sections marking on WZ

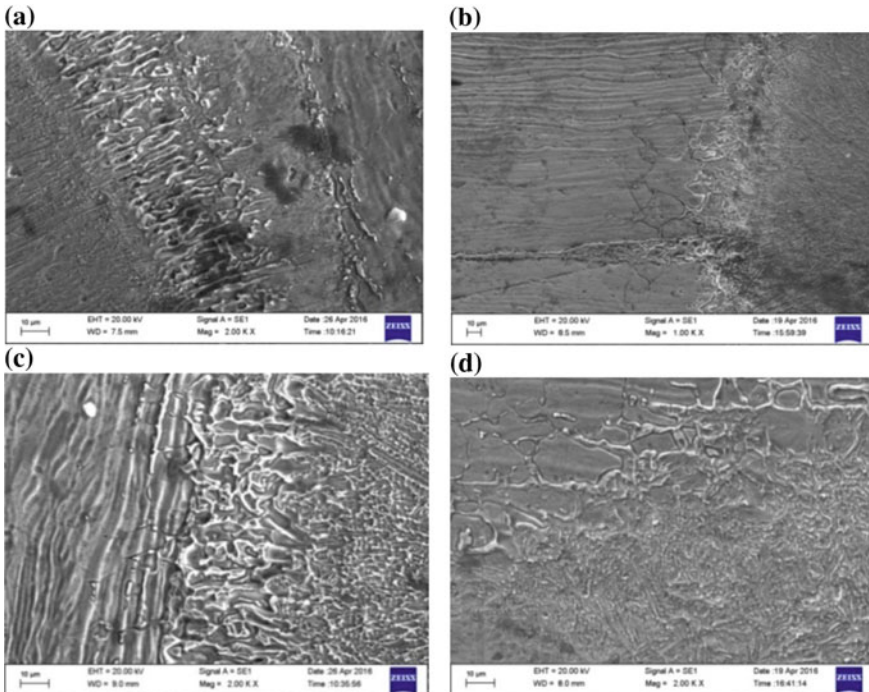


Fig. 40.10 Weld zone of SS316 multiple-spot welded samples of experiment a 1, b 2, c 3 and d 4

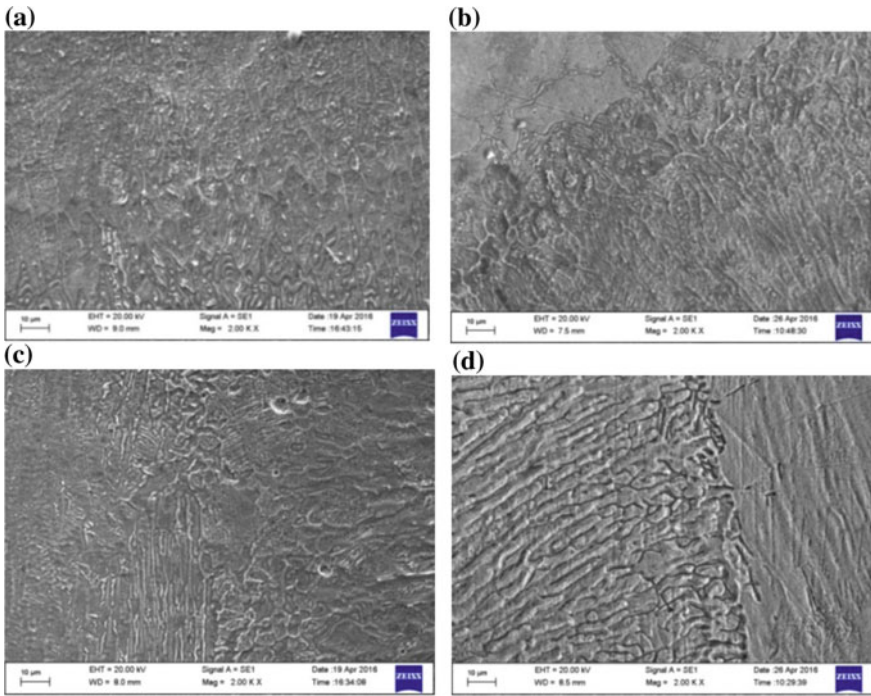


Fig. 40.11 Weld zone of A welded samples **a** F1, **b** F2, **c** F3 and **d** F4

base material of the SS316 welded sample when welding cycle of 15 cycles was used.

In the same way, remaining Fig. 40.10b–d show the microstructure when 20, 25, and 30 cycles were used, respectively, for welding. Figure 40.11a–d represent the microstructure of welded samples of SS304 when 15, 20, 25, and 30 cycles were used, respectively. It was observed that, for both the materials, the weld zone is having columnar structure. The grains in the weld zone and heat-affected zone are growing, because austenitic stainless steel does not show allotropic transformation during thermal cycles. As the welding cycle time goes on increasing, as shown in Figs. 40.10a–d and 40.11a–d in both the cases, there is a slight coarsening of the microstructure in WZ and HAZ.

In the weld nugget, the grains are elongated parallel to the electrode compression direction. Thus the increase in weld time resulted in increasing the heat input and leading to increase in weld nugget size and penetration. This finally resulted in an increase in tensile shear strength. This happened because rate of heat dissipation in the surrounding base metal decreased with an increase in weld time as large volume of base metal was heated [4]. This reduced temperature gradient between the base metal and weld nugget resulting in acceptable penetration. Thus weld having highest tensile shear strength was obtained when welding cycle time of 20–25 cycles was used.

40.5 Conclusions

The objective of the study was to study the effect of multiple overlapped spot welding on the strength of resistance spot-welded joints. An innovative approach of multiple-spot welding having overlapped spots was used. Thus, it can be concluded that the shear strength of resistance welded joints with only one spot can be increased by using overlapped spots instead of single spot. The cycle time of 20–25 cycles showed highest shear strength for the welded joints of SS304 and SS316 sheets of sub-millimeter thickness.

References

1. Aslanlar, S., et al.: The effect of nucleus size on mechanical properties in electrical resistance spot welding of sheets used in automotive industry. *Mater. Des.* **27**, 125–131 (2006)
2. Aslanlar, S., et al.: Welding time effect on mechanical properties of automotive sheets in electrical resistance spot welding. *Mater. Des.* **29**, 1427–1431 (2008)
3. Ozyurek, D.: An effect of weld current and weld atmosphere on the resistance spot weldability of 304L austenitic stainless steel. *Mater. Des.* **29**, 597–603 (2008)
4. Kacar, R., et al.: An effect of heat input, weld atmosphere and weld cooling conditions on the resistance spot weldability of 316L austenitic stainless steel. *J. Mater. Process. Technol.* **195**, 327–335 (2008)
5. Vural, M., et al.: On the resistance spot weldability of galvanized interstitial free steel sheets with austenitic stainless steel sheets. *J. Mater. Process. Technol.* **153–154**, 1–6 (2004)
6. Jou, M.: Real time monitoring weld quality of resistance spot welding for the fabrication of sheet metal assemblies. *J. Mater. Process. Technol.* **132**, 102–113 (2003)
7. Zhou, M., et al.: Relationships between quality and attributes of spot welds. *Suppl. Weld. J.* **72–77** (2003)
8. Harlin, N., et al.: Weld growth mechanism of resistance spot welds in zinc coated steel. *J. Mater. Process. Technol.* **143–144**, 448–453 (2003)
9. Cho, Y., et al.: New technology for measuring dynamic resistance and estimating strength in resistance spot welding. *Measur. Sci. Technol.* **1173–1178** (2000)
10. Moshayedi, H., Sattari-Far, I.: Resistance spot welding and the effects of welding time and current on residual stresses. *J. Mater. Processing Technol.* **214**(11), 2545–2552 (2014)
11. Martin, O., et al.: Quality prediction of resistance spot welding joints of 304 austenitic stainless steel. *Mater. Des.* **30**, 68–77 (2009)

Chapter 41

Effect of Tool Pin Profiles Using Tungsten Carbide Tool on Microstructure and Tensile Properties of Friction Stir Welded AA 6082-T6 Thin Aluminium Alloy Joints



M. D. Sameer  and Anil Kumar Birru 

Abstract In the current research, an effort was made to study the effect of tool pin profiles using tungsten carbide as the material to decide the weld quality of the friction stir welded AA 6082-T6 thin aluminium alloy. The employed profiles, straight cylindrical, tapered cylindrical, hexagonal, triangular and square, were compared with the joint fabricated with H13 tool steel with the straight cylindrical profile. Tool rotational speed and tool traverse speed were kept constant at 710 rpm and 40 mm/min, respectively. The highest tensile strength of 260.86 MPa was observed for the joint prepared with the hexagonal pin profile due to pulsating action. The highest impact strength of 7 J was observed for the hexagonal tool pin profile. The joint efficiency of the hexagonal pin profile was 83.1% when compared with other pin profiles. The examined outcomes were correlated with the microstructural and fractographic studies.

Keywords Friction stir welding · Aluminium alloy · Mechanical properties · Microstructure · Tungsten carbide

41.1 Introduction

AA 6082-T6 aluminium alloy has reasonable strength and consists of outstanding welding properties to that of high-strength aluminium alloys. Therefore, these series of alloy material are comprehensively used in aerospace, naval and other structural applications [1]. These Al–Mg–Si alloys suffer rigorous softening in heat-affected zone (HAZ) during conventional fusion welding process due to the dissolution of Mg₂Si precipitates caused by high heat supply. Therefore, these alloys' mechanical properties have to be enhanced by avoiding the softening of the HAZ. Friction stir

M. D. Sameer (✉) · A. K. Birru
Department of Mechanical Engineering, National Institute of Technology, Manipur 795004,
Imphal, India
e-mail: Sameer.mtech2010@gmail.com

© Springer Nature Singapore Pte Ltd. 2020
M. S. Shunmugam and M. Kanthababu (eds.), *Advances in Additive Manufacturing and Joining*, Lecture Notes on Multidisciplinary Industrial Engineering,
https://doi.org/10.1007/978-981-32-9433-2_41

welding is a solid-state welding process in which the material being weld does not melt or recast due to which it offers several advantages over the conventional welding processes. The fusion weld zone consists of coarser columnar grain structure due to high temperatures involved in fusion welding process leading to low mechanical properties. The design of the pin influences the flow of the material and affects the mechanical properties [2, 3]. Several studies have been conducted on the effect of pin profiles on the joining of various materials via friction stir welding (FSW). Elongovan et al. [4] considered the effect of tool pin profiles and tool rotational speed on 6-mm-thick rolled plate of AA 6061. They established that the weld produced with square pin profile and tool rotational speed of 1200 rpm showed excellent mechanical properties. Kumar and Survanaraju [5] conducted friction stir welding on copper sheets of 3 mm thickness with different tool pin profiles. They studied that square pin profile tool exhibited better mechanical properties due to pulsating action and dynamic volume to static volume ratio of 1.56. They further observed that microstructure of the stir zone (SZ) of the joint employing square pin profile has finer and more equiaxed grain structure than base metal. Ilongovan et al. [6] found the effect of tool pin profile on microstructure and tensile properties on dissimilar friction stir welding of AA 6061-AA 5086 aluminium alloy joints. They concluded that threaded and tapered cylindrical pin profile produced the sound defect-free weld. They observed that threaded pin profile pins showed superior performance than the tapered cylindrical tool. Mehta and Badheka [7] studied the influence of tool design and process parameters on copper and AA 6061 dissimilar joints via friction stir welding. They concluded that uniform mixing of the material was not achieved with the taper tool pin profile, whereas the cylindrical tool pin was suitable to achieve defect-free joint. Padmanabhan and Balasubramaniam [8] did FSW experimental investigation on AZ 31B magnesium alloy thickness of 6 mm by varying tool pin profile, shoulder diameter and tool material. They observed that joints produced by high carbon steel tool with threaded pin profile and shoulder diameter 18 mm showed excellent tensile properties. They also concluded that fine equiaxed grains in the nugget zone are the main cause for the higher hardness.

Sameer et al. [13, 14] did friction stir welding of DP 600 steel and AA6082-T6 aluminium alloy using tungsten carbide tool with tapered pin profile, and they reported that the successful joint can be achieved at process parameters conditions 700 rpm tool rotational speed, 40 mm/min traverse speed and tilt angle 0.5° . From the literature, it is evident that the very less amount of work has been done using different pin profiles and materials for joining. The FSW of thin aluminium alloy sheets of AA 6082-T6 of thickness 2 mm was not studied using tungsten carbide material and different pin profiles to the author's knowledge. Therefore, the present study is aimed to investigate the effect of straight cylindrical, tapered cylindrical, hexagonal, triangular and square pin profile on mechanical and microstructural properties and compared with the conventional tool material H13 fabricated joint.

41.2 Experimental Procedure

The base metal (BM) sheets of 2-mm-thick AA 6082-T6 aluminium alloy were friction stir welded (FSW) in butt joint configuration by using a modified vertical milling machine of HMT make with capacity of 1 HP spindle motor and 3000 rpm spindle speed. The mechanical properties and chemical composition of the base material are given in Tables 41.1 and 41.2, respectively. The tungsten carbide tool is used as the tool material due to its high-strength and wear resistance properties. For the comparison purpose, the H13 tool material joint is also fabricated. The initial experiments were conducted using straight cylindrical pin profile on AA 6082-T6 aluminium alloy by varying tool rotational speed and tool traverse speed. The condition for the defect-free joint parameters was obtained at 710 rpm and 40 mm/min rotational speed and traverse speed, respectively.

The optimum parameters were employed to achieve the better mechanical properties. Hence, the tool rotational speed 710 rpm and tool traverse speed 40 mm/min were kept constant, and different pin profiles were used such as straight cylindrical (SC), tapered cylindrical (TC), hexagonal (HX), triangular (TR) and square (SQ) for fabrication of joints. The tools used are shown in Fig. 41.1.

The process parameters and dimensions of the tools employed to obtain FSW joints are given in Tables 41.3 and 41.4, respectively.

The welds produced by employing the different pin profiles were defect free, and all the surface morphologies are presented in Fig. 41.2. From the surface appearances, the quantity of the flash was less for the joint produced with the hexagonal tool.

Samples were cut using electric discharge machine as shown in Fig. 41.3 perpendicular to the directions of the weld for the metallographic studies. They are mounted, polished and etched with Keller reagent. The etched samples are then examined by employing an optical microscope (Olympus make). The microhardness profiles were observed using micro-Vickers hardness testing machine at 100 Kgf load and applied dwell time for 10 s. Tensile test samples are prepared as per ASTM E8 standard guidelines as sub-size test specimen, and the average of three tensile specimens was recorded using the computerised universal testing machine. The V-notch Charpy

Table 41.1 Mechanical properties of AA 6082-T6

Alloy	Yield strength (MPa)	Ultimate tensile strength (MPa)	% Elongation	Hardness
AA6082	220	313	24	110 Hv

Table 41.2 Chemical composition of AA 6082-T6

Proportion of the constituting elements (wt%)								
Alloy	Mg	Zn	Cr	Si	Mn	Fe	Cu + Ag	Al
wt%	1.1	0.20	0.25	0.90	0.70	0.50	0.10	Bal

Fig. 41.1 Different tools used for the present investigation: **a** straight cylindrical, **b** tapered cylindrical, **c** triangular, **d** square, **e** hexagonal and **f** H13 tool steel straight cylindrical

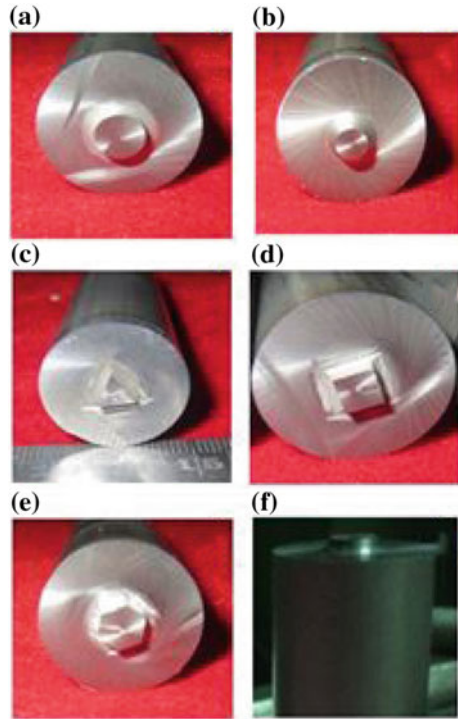


Table 41.3 Process parameters

S. No.	Tool rotational speed (rpm)	Tool travel speed (mm/min)	Pin profile
1	710	40	Straight cylindrical (SC)
2	710	40	Taper cylindrical (TC)
3	710	40	Hexagonal (HX)
4	710	40	Triangular (TR)
5	710	40	Square (SQ)
6	710	40	H13 straight cylindrical

Table 41.4 FSW tool dimensions used in experiments

Tool design	Pin profile	Edge size (mm)
Tool 1	Cylindrical	8 (dia)
Tool 2	Triangular	10
Tool 3	Square	7
Tool 4	Hexagonal	4
Tool 5	Taper straight cylindrical	4–6
Tool 6	H13 straight cylindrical	6

Fig. 41.2 Surface appearances of the fabricated joints: **a** SC, **b** TC, **c** HX, **d** TR, **e** SQ and **f** H13 SC

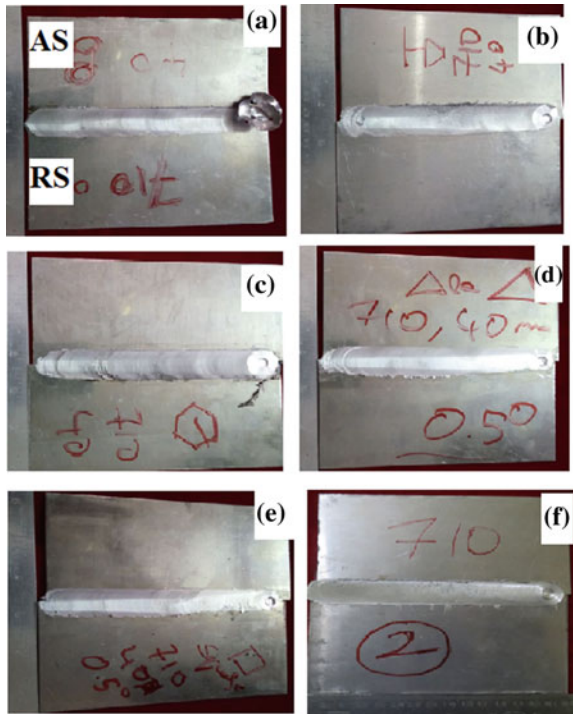
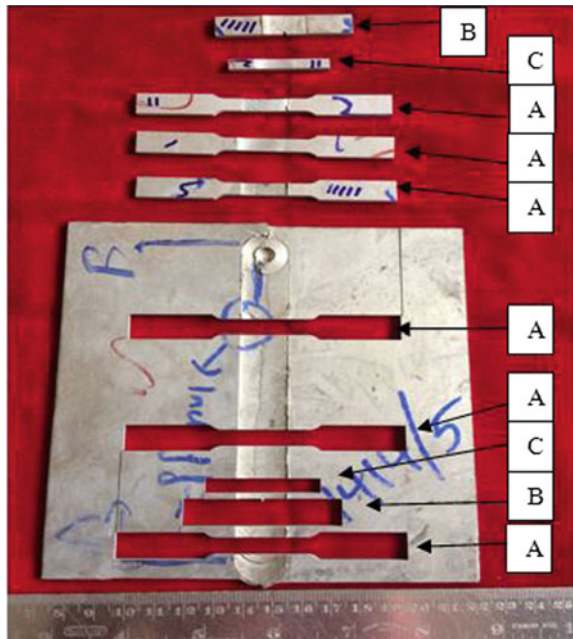


Fig. 41.3 Extraction of various samples for tests from the fabricated joint: **a** tensile test, **b** impact test and **c** microstructural sample and hardness test



impact tests were also conducted at the room temperature. The fractured surfaces were observed using scanning electron microscopy (SEM).

41.3 Results and Discussion

41.3.1 Macrostructure

The Macrostructure of the sample joint prepared with the triangular pin and hexagonal tool pin is shown in Fig. 41.4. These macrostructures are defect free, and distinct zones are clearly visible. These two structures have been studied because they have produced highest tensile strength from tensile test and compared with H13 tool steel weld specimen.

41.3.2 Microstructural Observations

FSW is a process which involves severe plastic deformation due to stirring action of the tool. As a result, the stir zone of the weld yields finer grains. The difference in the stir zone grain structure is studied by comparing the highest tensile strength joints produced by WC tool and compared with H13 tool steel produced joint. The microstructures of the considered joints are shown in Fig. 41.5. It is noticed that hexagonal tool pin profile, Fig. 41.5a, has finer grain structure compared to H13 tool steel produced joint. The high amount of frictional heat is generated due to the stirring of the tool which causes severe plastic deformation in the stir zone resulting in the formation of dynamic recrystallisation (DRX). The DRX usually gets refined, and

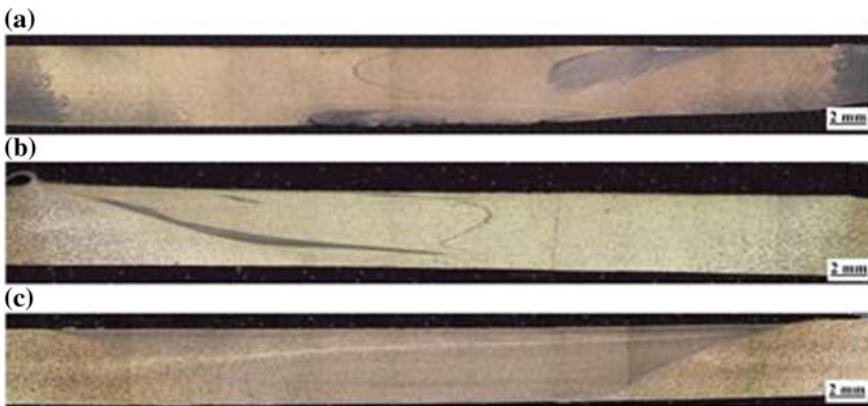


Fig. 41.4 Macrostructures of a triangular tool pin, b hexagonal tool pin and c H13 SC tool

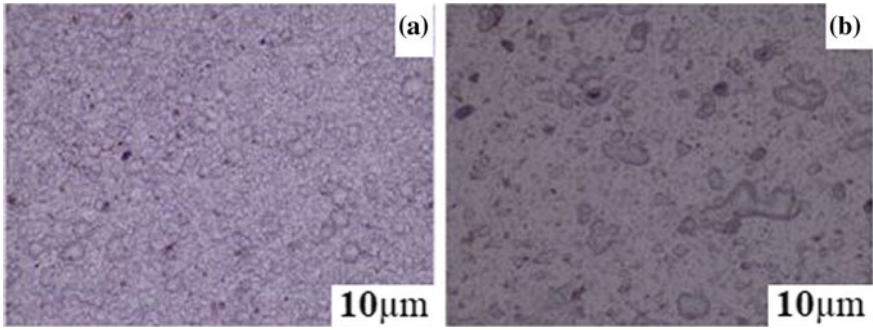
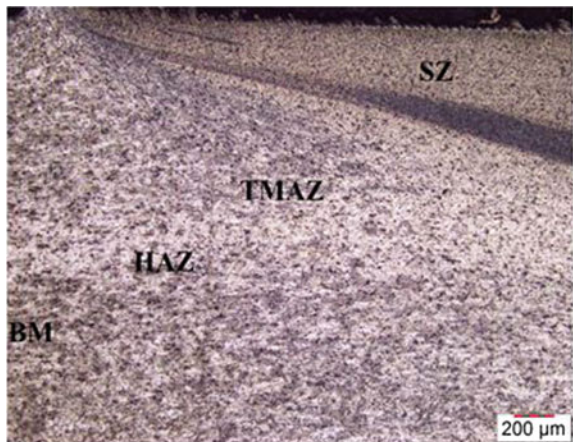


Fig. 41.5 Microstructures of the stir zone produced by **a** HX tool and **b** H13 SC tool

grain structure is modified [9]. The entire microstructure is shown in the Fig. 41.6. The thermomechanically affected zone (TMAZ) and heat-affected zone (HAZ) can be seen between the base metal (BM) and stir zone (SZ). The TMAZ consists of grain structure in form of slightly elongated structure. This elongated structure is the effect of annealing and severe plastic deformation. Between TMAZ and BM, there is a HAZ which has coarser grain structure to that of the base metal, due to heat affected during welding process [10]. DRX is the most significant zone for the formation of the finer grain structure. From the above results, it is clear that joint produced by hexagonal pin has superior grain structure than H13 tool steel produced joint. The variation in the grain size and homogeneous distribution of the strengthening precipitates are clearly visible in the microstructural images. The finer distribution of the precipitates and grain structure is attributed to the pulsating action of the hexagonal tool compared to the straight cylindrical tool. The tool material employed for aluminium alloys are generally tool steels due to its soft nature. However, to understand the effects of hard tool materials on the joint properties, the different tool pins are used and

Fig. 41.6 Microstructure of the entire weld shows WN, TMAZ and HAZ of HX tool



compared with the H13 tool steel material produced joint. The FSW tool plays a vital role in determining the quality of the joints. The coefficient of friction greater the heat generated will be greater which is very much needed for the formation of a defect-free weld. The friction is observed between the tool and the base material. The coefficient of friction is affected by the hardness of the tool. The joint exhibits a coarser and elongated structure if the frictional coefficient between the tool and base metal is less. On the other hand, if the friction between the tool and base metal is high, the material flow is not smooth, and as a result causes severe plastic deformation modifying the older grains and implements DRX.

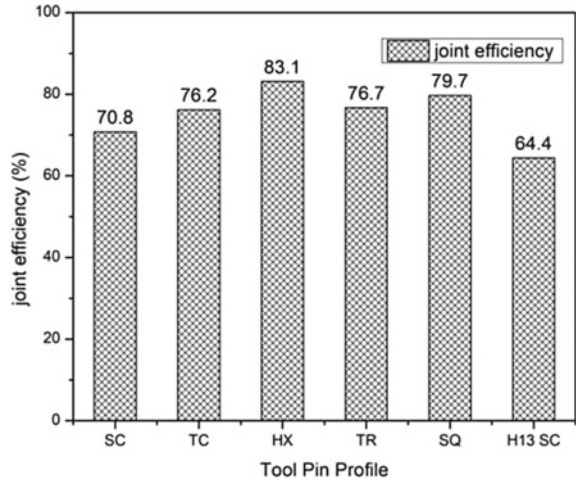
41.3.3 Mechanical Properties

Table 41.5 presents the mechanical properties of the FSWed joints with different tool pin profiles. It is shown that the hexagonal (HX) tool shows excellent tensile properties than to other pin profiles. The highest tensile strength of 260.86 MPa was reported for the hexagonal tool pin profile with the joint efficiency of 83.1%. The calculated efficiency values are illustrated in Fig. 41.7. The highest value of the tensile value of HX tool pin is due to the pulsating action of the tool. The number of pulsating action for the hexagonal tool is calculated according to the formula Pulses/second = Rotational speed (rps) \times no. of faces [4]. The polygonal edges of tool pin profiles have high tensile strength than cylindrical tool pin profile due to pulsating action. The straight cylindrical tool pins exhibited lower mechanical properties due to the absence of pulsating action resulting in less friction heat generation. The impact test results are also shown in Table 41.5 for different tool pin profiles. The HX tool pin profile has highest impact strength compared to its counterparts and strength almost near to base metal.

Table 41.5 Mechanical properties for different tool pin profiles

Pin profile	Tensile strength (MPa)	Yield stress (MPa)	% Elongation	Impact strength (J)
Straight cylindrical	222.33	194.5	7.6	6
Taper cylindrical	239.16	207.57	9.8	6
Hexagonal	260.86	216.4	15.9	7
Triangular	240.77	201.86	9.8	4.5
Square	250.34	200.89	14.8	6
H13 Straight cylindrical	202.19	185.58	8.8	6
Base material (unwelded)	313.82	230.32	24	8

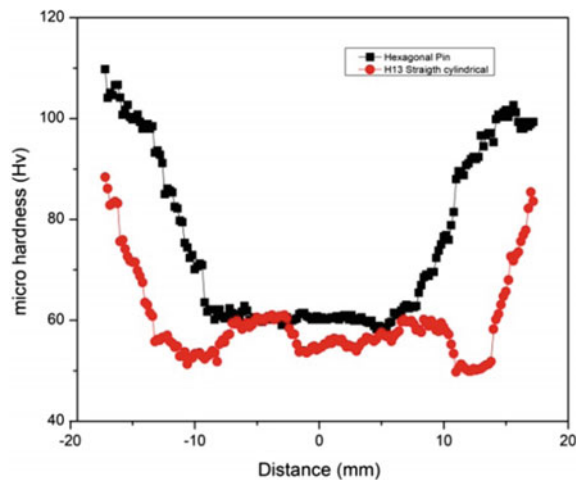
Fig. 41.7 Joint efficiency of different tool pin profiles



41.3.4 Microhardness

The hardness profiles of the hexagonal tool and H13 tool are shown in Fig. 41.8. The highest value of the hardness is found for the hexagonal tool with 60.13 Hv, and the lowest values are seen in H13 tool steel. The hardness of the base material is 110 Hv. The transition zone between the HAZ and TMAZ has the lowest hardness values. The highest value of the HX tool is attributed to finer grain structure in the stir zone. The hardness profiles of the joints are influenced by grain refinement and softening

Fig. 41.8 Hardness profile of HX tool pin joint and H13 SC tool pin joint



caused due to annealing [11]. The hardness of the stir zone is less compared to base metals in the joints fabricated due to the softening of the material and dynamic recrystallisation [12].

41.3.5 Fractography

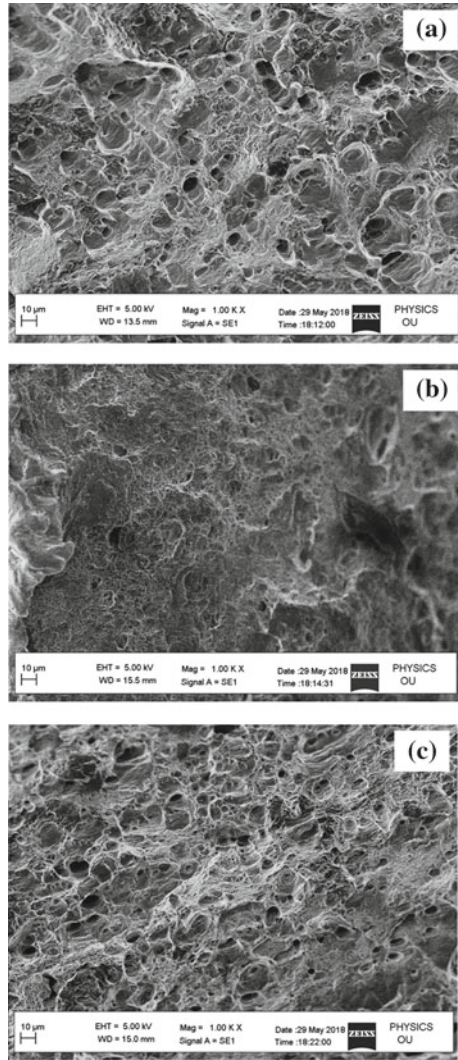
The fractured tensile specimens are observed under the scanning electron microscopy (SEM) for the examination of the mode of failure. The fractured surfaces of the tensile specimen of HX tool joint, H13SC tool joint and base metal are shown in Fig. 41.9. The joint produced by HX tool has fine dimple structure which indicates the ductile mode of failure; the dimple features are similar to the base metal dimples. The fracture surface of H13 tool produced joint when compared to fracture surface HX tool produced joint has fewer dimples. All the tensile specimens fractured at the lowest hardness zone are correlated with the fractographic results. Figure 41.9c shows smooth fractured appearance indicating low ductility of the joint fabricated by H13 tool steel SC tool.

41.4 Conclusions

The friction stir welding of AA 6082-T6 thin aluminium alloy sheets of 2 mm thickness was successfully joined using tungsten carbide tool; the results are compared with the traditionally used H13 tool steel produced joints and following conclusions are made

1. Joints fabricated with hexagonal tool pin profile have finer grain structure in the stir zone with a uniform distribution of strengthening precipitates.
2. The highest tensile strength and impact strength of 260.86 MPa and 7 J, respectively, were achieved for the hexagonal tool pin profile produced joint.
3. The highest joint of 83.1% was also achieved for the hexagonal pin profile.
4. The highest hardness of 60.1 Hv was exhibited for a hexagonal pin profile in the stir zone.
5. The fractured tensile specimen surface showed the fine deep dimples similar to the base metal as the ductile mode of failure.

Fig. 41.9 Fractured surfaces of the **a** HX tool pin profile joint, **b** H13 tool pin profile joint and **c** base metal



References

1. Hwan, T.K.; Soo, W.N.; Solidification cracking susceptibility of high strength aluminium alloy weldments. *Scr. Mater.* **34**(7), 1139–1145 (1996)
2. Yadava, M.K., Mishra, R.S., Chen, Y.L., Carlson, B., Grant, G.J.: Study of friction stir welding of thin aluminium sheets in lap joint configuration. *Sci. Technol. Weld Join* **15**(1), 70–75 (2010)
3. Choi, D.H., Ahn, B.W., Lee, C.Y., Yeon, Y.M., Song, K., Jung, S.B.: Effect of pin shapes on joint characteristics of friction stir spot welded AA5J32 sheet. *Mater. Trans.* **51**(5), 1028–1032 (2010)

4. Elangovan, K., Balasubramaniam, V., Valliappan, M.: Effect of tool pin profile and tool rotational speed on mechanical properties of friction stir welded AA6061 aluminium alloy. *Mater. Manuf. Processes* **23**(3), 251–260 (2008). <https://doi.org/10.1080/10426910701860723>
5. Kumar, A., Suvarna Raju, L.: Influence of tool pin profiles on friction stir welding of copper. *Mater. Manuf. Processes* **27**(12), 1414–1418 (2012)
6. Ilangovans, M., Rajendraboopathy, S., Balasubramaniam, V.: Effect of tool pin profile on microstructure and tensile properties of friction stir welded dissimilar AA 6061 and AA 5086 aluminium alloy joints. *Defence Technol.* **11**(2), 174–184 (2015)
7. Mehta, K.P., Badheka, V.J.: Influence of tool design and process parameters on dissimilar friction stir welding of copper to AA6061-T651 joints. *Int. J. Adv. Manuf. Technol.* **80**(9–12), 2073–2082 (2015)
8. Padmanaban, G., Balasubramaniam, V.: Selection of FSW tool pin profile, shoulder diameter and material for joining AZ31B magnesium alloy—an experimental approach. *Mater. Des.* **30**(7), 2647–2656 (2009)
9. Sun, Y.F., Fujii, H.: The effect of SiC particles on the microstructure and mechanical properties of friction stir welded pure copper joints. *Mater. Sci. Eng., A* **528**(16–17), 5470–5475 (2011)
10. Scialpi, A., Filippis, L.A.C.D., Cavaliere, P.: Influence of shoulder geometry on microstructure and mechanical properties of friction stir welded 6082 aluminium alloy. *Mater. Des.* **28**(4), 1124–1129 (2007)
11. Surekha, K., Botes, A.E.: Development of high strength, high conductivity copper by friction stir processing. *Mater. Des.* **32**(2), 911–916 (2011)
12. Hwang, Y.M., Fan, P.L., Lin, C.H.: Experimental study on frictions stir welding of copper metals. *J. Mater. Process. Technol.* **210**(12), 1667–1672 (2010)
13. Sameer, M.D., Birru, A.K.: Investigations on microstructural evolutions and mechanical properties of dual-phase 600 steel and AA6082-T6 aluminum alloy dissimilar joints fabricated by friction stir welding. *Trans. Indian Inst. Metals* (2018). <https://doi.org/10.1007/s12666-018-1487-5>
14. Sameer, M.D., Birru, A.K.: Optimization and characterization of dissimilar friction stir welded DP600 dual phase steel and AA6082-T6 aluminium alloy sheets using TOPSIS and Grey relational analysis. *Mater. Res. Express* (2019). <https://doi.org/10.1088/2053-1591/aafba4>

Chapter 42

Effect of Pin Diameter in Underwater Friction Stir Lap Welding of Dissimilar Materials: AA6061-T6 and AISI304



Raju Prasad Mahto, Manan Kinjawadekar, Chaman Gupta
and Surjya Kanta Pal

Abstract Friction stir welding has been used to produce lap welding between thin sheets of Al–Mg–Si alloy (AA6061-T6) and AISI304 austenitic stainless steel at different values of pin diameter in water medium. Three values of pin diameter have been used, 4, 5, and 6 mm, by maintaining constant values of other process variables. Results, such as axial component of weld force, weld strength, and weld interface characterizations, have been studied. Penetration of tool into steel substrate led to the formation of steel flash which got accumulated at the stir zone in aluminum substrate. Steel flash has led to the formation of hooking defects and weld cavities which were found to be dependent on the diameter of the pin. The distribution of steel flash has been analyzed by using X-ray micro-computed tomography that revealed a consequential hooking defect in retreating side at a pin diameter of 6 mm.

Keywords Dissimilar material welding · Intermetallic compound · Weld strength · Microstructure

42.1 Introduction

Welding of dissimilar materials such as aluminum and steel produces lightweight structures by maintaining good durability [1]. AA6061-T6 material is precipitate-hardened aluminum alloys where Mg and Si are major alloying elements. Addition of Mg and Si alloying elements in the aluminum matrix form strengthening precipitates such as Mg_2Si after heat treatment. Precipitate anchors the movement of dislocations leading to an improvement in the weld strength [2]. Similarly, AISI 304 is austenitic stainless steel which has good strength, high corrosion resistance, and low cost. The

R. P. Mahto (✉) · S. K. Pal
Friction Stir Welding Laboratory, Department of Mechanical Engineering, Indian Institute of Technology Kharagpur, Kharagpur 72302, West Bengal, India
e-mail: rajukec1@gmail.com

M. Kinjawadekar · C. Gupta
Department of Metallurgical and Materials Engineering, Indian Institute of Technology Kharagpur, Kharagpur 721302, West Bengal, India

© Springer Nature Singapore Pte Ltd. 2020
M. S. Shunmugam and M. Kanthababu (eds.), *Advances in Additive Manufacturing and Joining*, Lecture Notes on Multidisciplinary Industrial Engineering,
https://doi.org/10.1007/978-981-32-9433-2_42

welding of AA6061-T6 and AISI304 materials can meet better structural design for the automotive components at the minimum cost. However, welding of AA6061-T6 and AISI304 dissimilar materials is affected from heat and weld defects which are likely to form due to the difference in the melting points, coefficient of thermal expansions, and poor solid solubility. Particularly, fusion welding techniques such as laser beam welding, electron beam welding, and gas metal arc welding apply a greater amount of heat on the weld regions [3]. High heat input and wide thermal gradient cause residual stresses, solidification cracking, and dimensional instability (thermal distortion) [4]. In addition to that, low solid solubility between Al and Fe causes the formation of intermetallic compounds (IMCs) at the weld interface of aluminum and steel substrate which produces detrimental effects to the weld [5].

Many authors have used solid-state welding techniques such as friction stir welding (FSW) to produce weld between different grades of aluminum alloys and steel-based dissimilar materials [6, 7]. Solid-state nature of FSW reduces the weld defects related to the solidification in the welding of similar and dissimilar materials.

The process parameters of FSW are the tool rotational speed, welding speed, plunge depth, and tool tilt angle which affect the weld qualities. Increase in the rotational speed and plunge depth increases the heat input to the weld regions which resulting in the dissolution or coarsening of precipitate [2]. Also, the large amount of heat input increases the grain size and thickness of IMC layer [8–11] which produces an adverse to the weld strength. The effects of process parameters in the weld strength of Al-steel dissimilar materials have been well studied in [12, 13]. Other than the process parameters, weld strength is also affected from the welding defects which are produced due to the improper values of process parameters and faulty tool design [14–17]. In addition to the effect of dimensions and geometry of shoulder and pin, lap-welded structure is also affected from the pin size which has not been studied in the friction stir lap welding (FSLW) of AA6061-T6 and AISI304 steel.

Above problems related to high input and weld defects in FSW of Al-steel dissimilar materials in air can be tackled by using underwater FSW. In the present study, authors have studied the effect of the pin diameter in the underwater FSLW (UwFSLW) on AA6061-T6 and AISI304 by keeping a constant value to the process parameters. The influence of pin has been investigated on the axial weld force and weld strength. Later, the variation in the weld strength has been studied by the interface microstructural characterization. Scanning electron and optical microscopy have been used for weld interface characterizations.

42.2 Experimental Set-up

FSW has been carried out to produce lap welding on thin sheets of AA6061-T6 aluminum alloy and AISI304 stainless steel, each having thickness of 1 mm. Length and width of the each samples were 100 mm and 80 mm, respectively. For the present study, aluminum sheet was placed on the top of the steel sheet, as shown in Fig. 42.1a. The rigidly tightened samples were placed in water medium by using a water tank

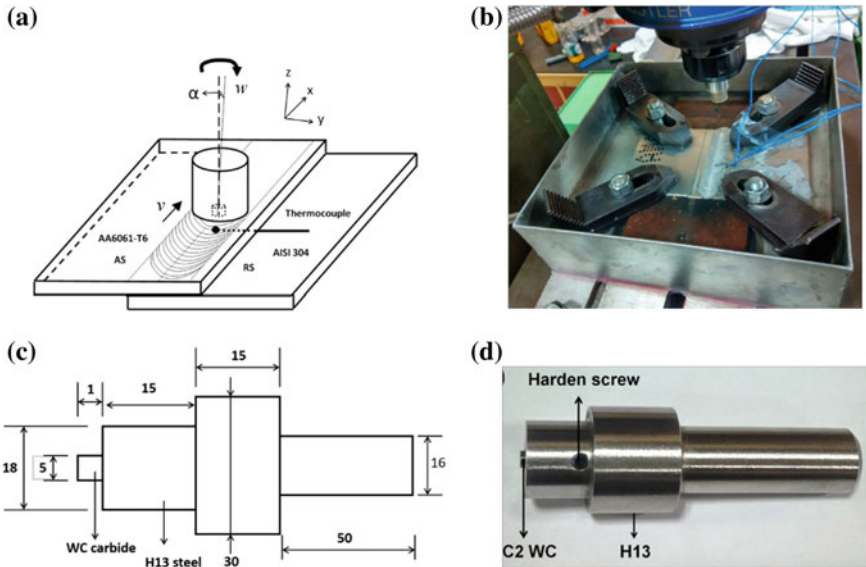


Fig. 42.1 a Schematic of FSLW, b actual experimental set-up of UwFSW, c schematic of FSW tool, and d actual FSW tool

having size of 300 mm × 280 mm × 250 mm, as shown in Fig. 42.1b. The chemical composition of AA6061-T6 base material in weight % is Si 0.57, Mg 1.17, Fe 0.45, Cu 0.265, and remaining Al. Similarly, chemical composition of AISI 304 in weight % is Cr 17.97, Ni 8.3, Mn 1.54, and remaining Fe. The FSW tool was made of two materials: H13 tool steel and C2 tungsten carbide. Pin of the tool was made up of tungsten carbide, whereas other parts such as shoulder and rest of the body of the tool were made up of H13 tool steel, as shown in Fig. 42.1c, d. The tool has flat shoulder having 18 mm diameter. The pin has cylindrical shape having diameter and height of 5 mm and 1 mm, respectively.

For the present study, tool rotational speed was kept at 900 rpm, welding speed was 125 mm/min, plunge depth was 0.2 mm and tool tilt angle was 1°. The diameter of pin has been varied: 4, 5, and 6 mm. All the experiments have been carried out in displacement controlled mode by using a manual FSW machine (BFW, VF 3.5) having wide range of spindle rotational speed from 35.5 rpm to 1800 rpm, and traverse speed of bed from 16 mm/min to 1600 mm/min.

A piezoelectric dynamometer (Kistler 9124B1111) was used to measure the vertical weld force and spindle torque. Lap shear tensile test specimens were cut along the traverse to welded samples by using a wire-cut electric discharge machining (Elektra, Maxicut 5231). Tensile testing was carried out at a cross-head speed of 0.5 mm/min by using a universal testing machine (Instron, 8825). Further, for weld interface characterizations, weld cross sections were cut transverse to the weld and hot mounted by using epoxy resin. The samples were polished by using silicon carbide emery papers having grit size of 200–2000 in an automatic polishing machine

(Bueler, 265). Later, for mirror polishing, samples were polished in automatic grinder and polisher machine by using diamond paste of grit size of 2 μm with the addition of hyphen fluid as lubricant. Scanning electron microscopy (Zeiss, EVO50) with an integrated energy dispersive spectroscopy (Oxford, INCA PentaFET $\times 3$) which has been used for the weld interface characterizations.

42.3 Results and Discussion

42.3.1 Axial Component of Welding Force and Torque

The magnitude of axial component of weld force is dependent on the weld materials, process parameters, and environments. Figure 42.2a shows the variation of axial weld force during the welding process at different diameters of the pin. It can be seen that, as the welding started by plunging of a rotating FSW tool into the base material, the tool has experienced a force. The magnitude of the force increased with the penetration of the tool into the sample and reached the maximum value when the shoulder penetrated. Later, in dwelling stage, the force reduced as a result of larger amount of heat and mechanical deformation. As the traverse of the weld started, the force was found to be almost consistent with slight fluctuations. Fluctuation in the force was due to the shearing of the steel substrate during welding. Similarly, the variation of spindle torque with time has shown in Fig. 42.2b, where it can be seen that, due to the static moment of inertia, the magnitude of spindle torque was higher at the beginning. Later, like axial component of the weld force, the value of spindle torque has varied depending on the welding stages.

The average value of the axial component of weld force has been calculated in the traverse stage and shown in Fig. 42.3, which has indicated that the weld force was found to be dependent on diameter of the pin. The average values of axial weld force

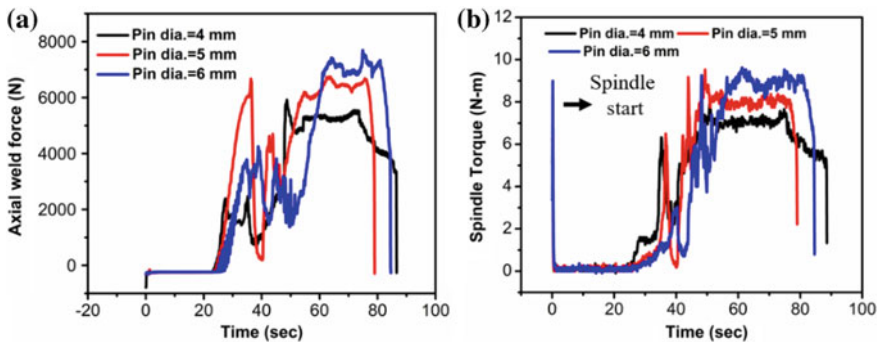
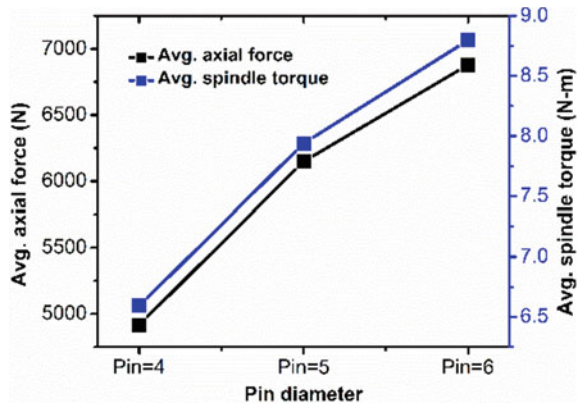


Fig. 42.2 Variation of the **a** axial weld force with **b** spindle torque with pin diameters during welding process

Fig. 42.3 Effect of pin diameters on the average (Avg.) value of axial weld force and torque



were 4917.32, 6149.39, and 6849 N for the diameter of the pin of 4 mm, 5 mm, and 6 mm, respectively. Similarly, the average value of spindle torque at different values of pin diameter in the welding stage has been shown in Fig. 42.2b. The average value of spindle torque was 6.6, 7.94, and 8.8 N-m at the diameter of the pin of 4, 5, and 6 mm, respectively. Hence, magnitude of the axial component of weld force and the spindle torques were increased with increase in the diameter of the pin.

42.3.2 Weld Strength

The variation of lap tensile load versus extension at different values of the pin diameter has been shown in Fig. 42.4a. Further, the maximum values of lap tensile load and extension at the different values of pin diameter have been shown in Fig. 42.4b. The maximum values of tensile load were 1814, 1939.25, and 1538 N at a pin diameter

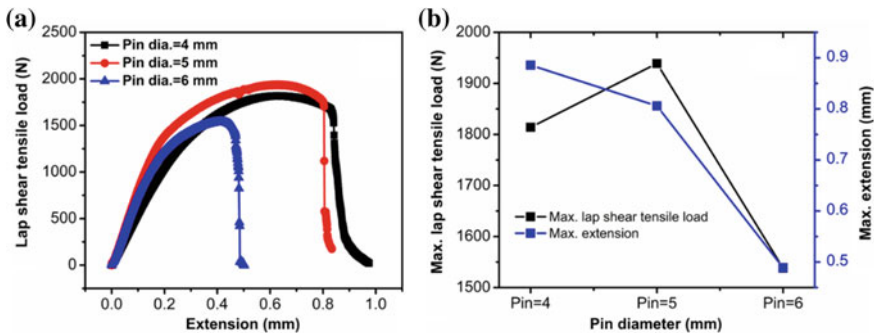


Fig. 42.4 Variation of **a** lap shear tensile load and extension, and **b** maximum value of lap shear tensile load and extension at different value of pin diameters

of 4, 5, and 6 mm, respectively. But, the maximum values of elongation were 0.8856, 0.8059, and 0.49 mm for the respective diameters of the pin. Thus, lap tensile load and extension were found to be reduced with an increase in the value of pin diameter. The variation in the weld strength can be understood by the weld interface characterization which was primarily dependent on the welding defects, microstructures, and IMCs.

42.3.3 Hooking Defects

Hooking defects have been found at the weld interface of aluminum and steel substrates. This defect was formed due to the presence of the steel flash in the aluminum substrate.

Steel flashes were produced due to the penetration of the FSW tool into the steel substrate. Penetration of the tool and its rotary action shear off the steel flashes into fragmented steel particles. These steel particles were found to be accumulated at the periphery of the pin (i.e., at SZ) in the aluminum substrate which led to the formation of the hooking defects. The distribution of steel flash was not uniformly distributed in the weld zone which has been verified after X-ray micro-computed tomography (X-ray micro-CT) on the samples. Results of micro-CT have been shown in Fig. 42.5, which revealed that the large amount of steel flash was found at RS which was found to be dependent on the value of pin diameter. As the pin diameter increased from 4 to 6 mm, a large amount of steel flash was formed which produced a consequential hooking defect.

Hooking defects reduced the thickness of aluminum sheet. Minimum sheet thickness of aluminium substrate above the steel hook has been defined as effective sheet thickness (EST). Consequently, the load bearing capacity of the samples against the transverse loading was reduced. The load bearing area is the $EST \times \text{width of the}$

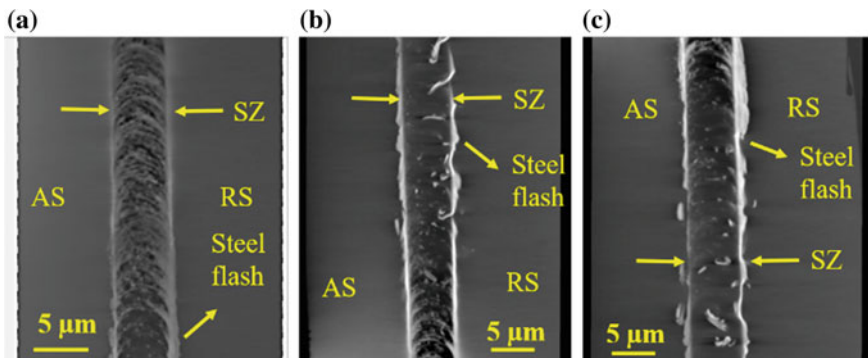


Fig. 42.5 X-ray micro-CT scans of welded samples at a pin diameter of **a** 4 mm, **b** 5 mm, and **c** 6 mm

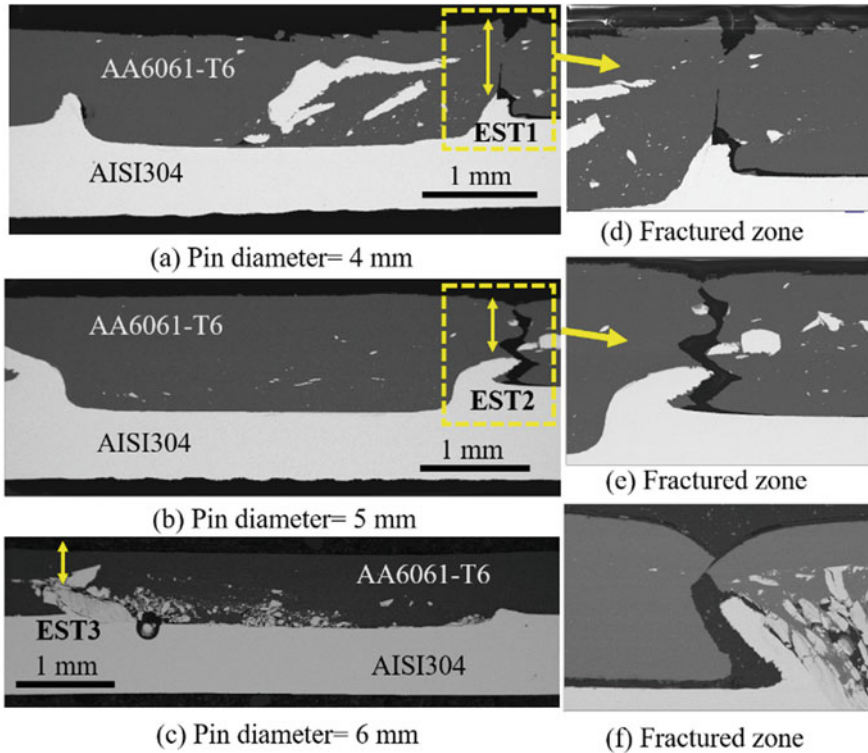


Fig. 42.6 SEM images of weld cross sections obtained at different values of pin diameter

sample. Figures 42.5 and 42.6 show that as the pin diameter increased, a large amount of steel flash has produced in the stir zone that led to the reduction in the EST of aluminum substrate, and consequently, load bearing area was reduced. Reduction in the load bearing area and the presence of hooking defects have led to the initiation of cracks just above the hook which can be verified from Fig. 42.6, where failure locations can be seen just above the hook regions. SEM images of the fractured surface have been shown in Fig. 42.7, which revealed cleavage-type of fracture in the weld obtained at the pin diameters of 5 and 6 mm, whereas quasi-cleavage fracture at pin diameter of 4 mm. In addition to that EDS result at a point shown in Fig. 42.7a indicated the presence of IMC. Results of point EDS can be seen in Fig. 42.7(S1).

42.3.4 Microstructure

Microstructure of different regions of aluminum and steel substrate for the weld cross section shown in Fig. 42.8 has been depicted in Fig. 42.9. Stir zone has fine and equiaxed grains in aluminum substrate which has average grain size of 5 μm .

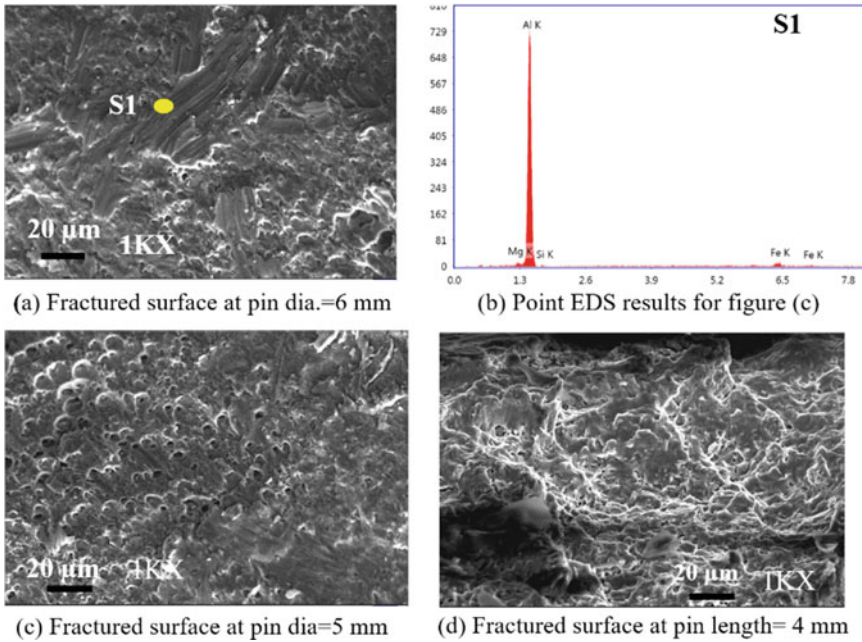


Fig. 42.7 Fractured surface of lap shear tensile samples

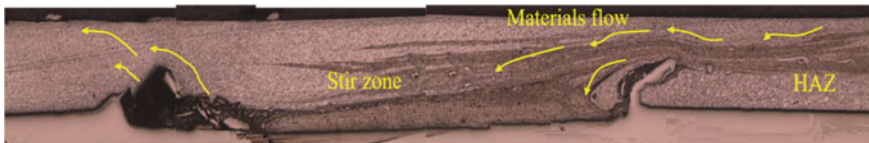


Fig. 42.8 Optical image of weld cross section at pin diameter of 4 mm

Beside stir zone, materials were affected from the heat and swirling action. The flow of materials surrounding the pin occurs due to the sticking and sliding actions. During FSW under the influence of relative rotary and transverse motions between the FSW tool and weld plates, materials tried to flow upward away from the stir zone along the advancing side (AS). But, along the retreating side (RS), materials moved toward the stir zone. The flow of materials was deflected from the hooking defects in both AS and RS. Flow patterns of materials have been shown by arrows in Fig. 42.8. Thus, the materials near hook region have been defined as hook-affected zone where elongated microstructures were observed. The average grain size at hook-affected zone of aluminum substrate was 4.5 μm. Heat-affected zone (HAZ) in aluminum substrate has coarse microstructure which has an average grain size of 15 μm.

FSW tool has penetrated the steel substrate by approximately 0.2 mm in the stir zone. Also, FSW tool has major contact with the aluminum substrate. Thus, the

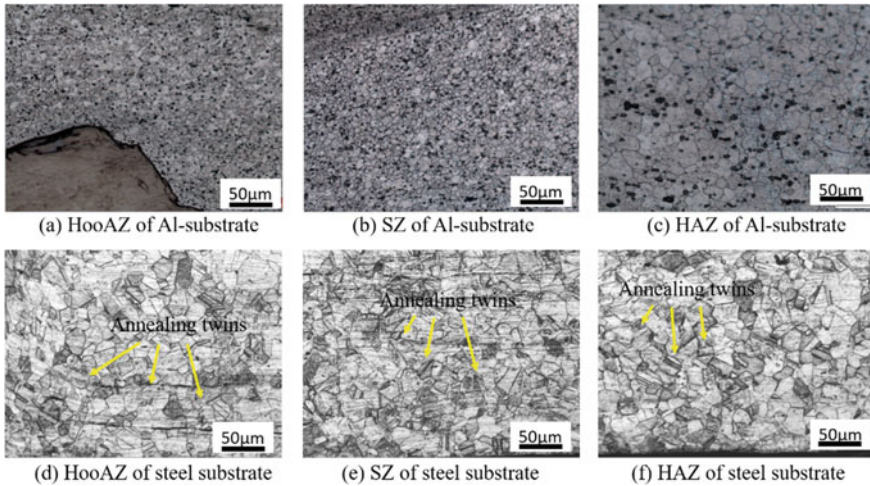


Fig. 42.9 Microstructure of aluminum and steel substrate in the weld cross section

majority of heat and mechanical deformation have been produced in the aluminum substrate. Also, heat generation in FSW is much lower than the melting point of base materials. Thus, at low heat input, there was a very minor change in the microstructure of steel substrate found. An average grain size of HAZ was $14.6 \mu\text{m}$ where grains were surrounded with annealing twins. The stir zone has average grain size of $12.3 \mu\text{m}$, but it has relatively higher numbers of twins. Hook-affected zone has average grains size of $10.3 \mu\text{m}$, and twins were found.

42.4 Conclusions

Underwater friction stir lap has been carried out on AA6061-T6 Al alloy and AISI304 steel at different values of pin diameter of FSW tool. The study has drawn following important conclusions.

1. The axial component of weld force increases with the increase in the pin diameter.
2. Asymmetric hooking defects occur between AS and RS in the lap welding which is dependent on the pin diameter. RS has larger hooking defect which recommends to place top sheet along AS for better weld strength.
3. Weld cavity, voids, etc., have been found near the steel flash.
4. Microstructure of weld zone was recrystallized. The stir zone has fine and equiaxed microstructure, whereas elongated and coarse grain microstructures have been found at the hook-affected zone and HAZ, respectively.

References

1. Kusuda, Y.: Honda develops robotized FSW technology to weld steel and aluminum and applied it to a mass-production vehicle. *Ind. Robot Int. J.* **40**, 208–212 (2013). <https://doi.org/10.1108/01439911311309889>
2. Tao, W., Yong, Z., Matsuda, K.: Precipitation in the nugget zone of AA6061-T6 by friction stir welding. *Chiang Mai J. Sci.* **43**, 409–419 (2016)
3. Ma, Z.Y., Feng, A.H., Chen, D.L., Shen, J.: Recent advances in friction stir welding/processing of aluminum alloys: microstructural evolution and mechanical properties. *Crit. Rev. Solid State Mater. Sci.* **8436**, 1–65 (2017). <https://doi.org/10.1080/10408436.2017.1358145>
4. Sree Sabari, S., Malarvizhi, S., Balasubramanian, V.: Characteristics of FSW and UWFSW joints of AA2519-T87 aluminium alloy: effect of tool rotation speed. *J. Manuf. Process.* **22**, 278–289 (2016). <https://doi.org/10.1016/j.jmapro.2016.03.014>
5. Mahto, R.P., Kumar, R., Pal, S.K., Panda, S.K.: A comprehensive study on force, temperature, mechanical properties and micro-structural characterizations in friction stir lap welding of dissimilar materials (AA6061-T6 & AISI304). *J. Manuf. Process.* **31**, 624–639 (2018). <https://doi.org/10.1016/j.jmapro.2017.12.017>
6. Mahto, R.P., Gupta, C., Kinjawadekar, M., Meena, A., Pal, S.: Weldability of AA6061-T6 and AISI 304 by underwater friction stir welding. *J. Manuf. Process.* (2019). <https://doi.org/10.1016/j.jmapro.2019.01.028>
7. Lee, W.B., Schmuecker, M., Mercardo, U.A., Biallas, G., Jung, S.B.: Interfacial reaction in steel-aluminum joints made by friction stir welding. *Scr. Mater.* **55**, 355–358 (2006). <https://doi.org/10.1016/j.scriptamat.2006.04.028>
8. Kimapong, K., Watanabe, T.: Lap joint of A5083 aluminum alloy and SS400 steel by friction stir welding. *Mater. Trans.* **46**, 835–841 (2005). <https://doi.org/10.2320/matertrans.46.835>
9. Bouché, K., Barbier, F., Coulet, A.: Intermetallic compound layer growth between solid iron and molten aluminium. *Mater. Sci. Eng. A.* **249**, 167–175 (1998). [https://doi.org/10.1016/s0921-5093\(98\)00573-5](https://doi.org/10.1016/s0921-5093(98)00573-5)
10. Mahto, R.P., Bhoje, R., Pal, S.K., Joshi, H.S., Das, S.: A study on mechanical properties in friction stir lap welding of AA 6061-T6 and AISI 304. *Mater. Sci. Eng., A* **652**, 136–144 (2016). <https://doi.org/10.1016/j.msea.2015.11.064>
11. Mahto, R.P., Anishetty, S., Sarkar, A., Mypati, O., Pal, S.K., Majumdar, J.D.: Interfacial microstructural and corrosion characterizations of friction stir welded AA6061-T6 and AISI304 materials. *Met. Mater. Int.* (2018). <https://doi.org/10.1007/s12540-018-00222-x>
12. Lan, S., Liu, X., Ni, J.: Microstructural evolution during friction stir welding of dissimilar aluminum alloy to advanced high-strength steel. *Int. J. Adv. Manuf. Technol.* **82**, 2183–2193 (2016). <https://doi.org/10.1007/s00170-015-7531-2>
13. Movahedi, M., Kokabi, A.H., Reihani, S.M.S., Cheng, W.J., Wang, C.J.: Effect of annealing treatment on joint strength of aluminum/steel friction stir lap weld. *Mater. Des.* **44**, 487–492 (2013). <https://doi.org/10.1016/j.matdes.2012.08.028>
14. Ramachandran, K.K., Murugan, N., Shashi Kumar, S.: Influence of tool traverse speed on the characteristics of dissimilar friction stir welded aluminium alloy, AA5052 and HSLA steel joints. *Arch. Civ. Mech. Eng.* **15**, 822–830 (2015). <https://doi.org/10.1016/j.acme.2015.06.002>
15. Dehghani, M., Amadeh, A., Akbari Mousavi, S.A.A.: Investigations on the effects of friction stir welding parameters on intermetallic and defect formation in joining aluminum alloy to mild steel. *Mater. Des.* **49**, 433–441 (2013). <https://doi.org/10.1016/j.matdes.2013.01.013>
16. Elangovan, K., Balasubramanian, V., Valliappan, M.: Influences of tool pin profile and axial force on the formation of friction stir processing zone in AA6061 aluminium alloy. *Int. J. Adv. Manuf. Technol.*, 285–295 (2008). <https://doi.org/10.1007/s00170-007-1100-2>
17. Mahto, R.P., Pal, S.K.: Friction stir lap welding of thin AA6061-T6 and AISI304 sheets at different values of pin penetrations. In: Vol. 2: Materials; Joint MSEC-NAMRC-Manufacturing USA, ASME, 2018, p. V002T04A041. <https://doi.org/10.1115/msec2018-6590>

Chapter 43

Brazeability of Synthetic Diamond with Steel Substrate Using Two Different Active Filler Alloys



Prithviraj Mukhopadhyay and Amitava Ghosh

Abstract Brazing of diamond to steel substrate using Ni-based filler alloy encounter several challenges like inferior joint strength and conversion of diamond to graphite. To overcome the problem, the present study tries to braze diamond to steel substrate using an Ag-based filler alloy. Two different weight percentages of an active element, titanium, were added to the Ag-based filler alloy to improve its wetting ability, i.e. 2 and 10 wt%, on the surface of the synthetic diamond grit. The characteristic quality of the brazed joint was subsequently inspected using a high-resolution electron microscope. Filler alloy containing 2 wt% of Ti as an active element showed better results in terms of grit retention ability compared to other combination of Ag-based and Ni-based alloy.

Keywords Diamond brazing · Micro-cracks · Reaction compounds

43.1 Introduction

Brazed super-abrasive diamond tools have gained a widespread recognition in modern manufacturing industries for machining of exotic non-ferrous and super hard materials. Improved joint strength and higher protrusion of the grits from the bond level make these tools to be used effectively under aggressive machining conditions. Additionally, the superior properties of synthetic diamond grits have also made an escalation in the demand for these tools in construction industries.

Synthetic diamond grits have always been difficult to join to a metal substrate because of its inherent inert characteristics [1]. The strong sp^3 bond existing between carbon-carbon atoms makes it difficult for the diamond grits to chemically adhere to the metal substrate easily. Filler alloys like Ni-Cr are known to be commonly used for brazing these diamond grits [2, 3]. These alloys are also recognized as hard-facing alloys as they possess an excellent abrasion resistance property. A good

P. Mukhopadhyay · A. Ghosh (✉)

Manufacturing Engineering Section, Department of Mechanical Engineering, Indian Institute of Technology Madras, Chennai 600036, India
e-mail: amitava_g@iitm.ac.in

© Springer Nature Singapore Pte Ltd. 2020
M. S. Shunmugam and M. Kanthababu (eds.), *Advances in Additive Manufacturing and Joining*, Lecture Notes on Multidisciplinary Industrial Engineering,
https://doi.org/10.1007/978-981-32-9433-2_43

abrasion resistance property of the filler alloy is necessary as it prevents the pull out of the grits due to the abrasive action of grinding swarfs. Chromium present within the filler alloy reacts with carbon atoms of the diamond grit to form metal carbide reaction compounds [4] at the interface by breaking the carbon–carbon bond. The metal carbides present near the interface play a vital role to improve the wetting ability of the filler alloy over diamond grit surface. However, these intermetallic compounds are highly brittle in nature and are prone to formation of micro-flaws during cooling of the brazed joint.

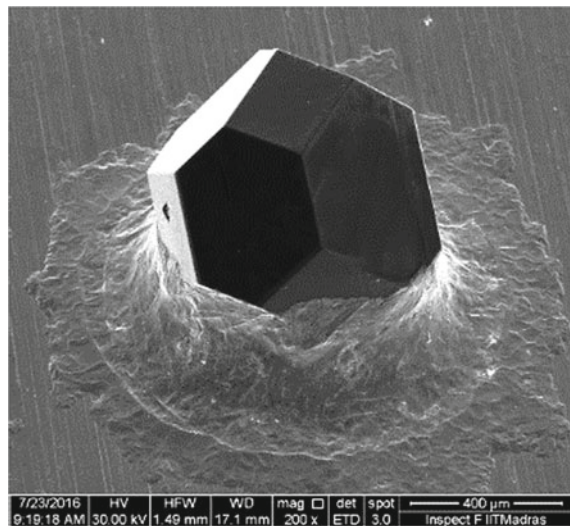
43.2 Experimental Methods

Brazing of synthetic diamond grits of SDB 1125 grade was done to a medium carbon steel substrate. Superior quality single-crystal synthetic diamond grits of 25/30 mesh size were chosen for this study. Two different filler alloys were chosen for brazing the diamond grits to the medium carbon steel substrate. One of them was a Ni-based filler alloy containing 7 wt% of chromium as the active element. Apart from chromium, the filler alloy also consisted of iron, boron and phosphorous. The presence of these elements aid in reducing the melting temperature of Ni–Cr filler alloy. In the second case, a eutectic silver–copper alloy was procured. Two different weight percentages of titanium were added to the filler alloy, i.e. 2 and 10 wt%. Titanium added to the filler alloy was in its hydride form. At higher brazing temperatures, hydrogen dissociates leaving behind titanium to react with diamond to form intermediate reaction compounds. The entire brazing experiment was conducted in a controlled vacuum environment. The vacuum level was maintained in the range of 10^{-6} – 10^{-7} mbar with the help of a turbo-molecular pump, backed up by a rotary pump. The temperature of the samples was measured using several flexible “N-type” thermocouples. To ensure a uniform heating, the samples to be brazed were made to rotate inside the heating chamber at 8–10 rpm. Both the filler alloys were heated above their corresponding liquidus temperature(s) based upon the available literature data. Ni–Cr alloy was heated to a temperature of 1050 °C. Ag-based passive filler alloy containing 10 wt% of Ti was heated to 920 °C, whereas the alloy containing 2 wt% of Ti was heated to 820 °C. High-resolution electron microscope operating at an accelerating voltage of 30 kV was used to observe the morphology of the brazed joint. EDS analyses were carried out to observe the composition of the reaction compounds developed at the interface. The strength of the brazed joint was evaluated with the help of an indigenously developed single-grit test rig. A horizontal load was applied on the grits at a particular height with the help of a carbide tool. This was done to mimic the line of action of the tangential force acting on diamond-abrasive grits in a grinding tool. The mode of failure of the grits was noted and has been discussed in detail in the subsequent section.

43.3 Results and Discussion

Nickel chromium alloys are known to exhibit an excellent wear resistance property. The high wear resistance property of the Ni–Cr alloy is attributed to the presence of hard reaction compounds within the filler alloy matrix after melting. A prior study revealed that the formation of compounds like Ni₃Si, chromium carbides and Fe₂B aids in improving the abrasion resistance property of the filler alloy [5, 6]. Because of its high hardness value, these alloys are widely accepted for brazing diamond grits to a metal substrate for developing single-layer super-abrasive tools. Filler alloys possessing poor abrasion resistance property are prone to abrasive wear. This will cause the filler alloy near the grit–alloy interface to rapidly wear out due to the abrasive action of the hard grinding swarfs. Therefore, the use of Ni–Cr has been widely considered to be the best possible composition for brazing diamond to steel substrate. Figure 43.1 shows the morphology of a synthetic diamond grit brazed with Ni–Cr filler alloy. From the figure, it can be noted that the filler alloy showcases an excellent wetting over the diamond grit surface. This is attributed to the formation of metal carbide compounds at the brazed interface, which fosters the filler alloy to nicely wet the surface of the diamond grit. Good wetting characteristics indicate a higher work of adhesion value [7]. Despite good wetting property of Ni–Cr alloy, it was observed that microscopic cracks were present at the interface of the as brazed joint. EDS analysis of the region possessing cracks revealed that the area was rich in chromium and carbon. The high weight percentage of chromium and carbon near the interface indicated that the compound was chromium carbide. These compounds have a high hardness value and are, therefore, brittle in nature. During brazing, local residual stress tends to develop near the interface of the brazed diamond joint. The existence of this stress near the interface can be attributed to two reasons. First, the

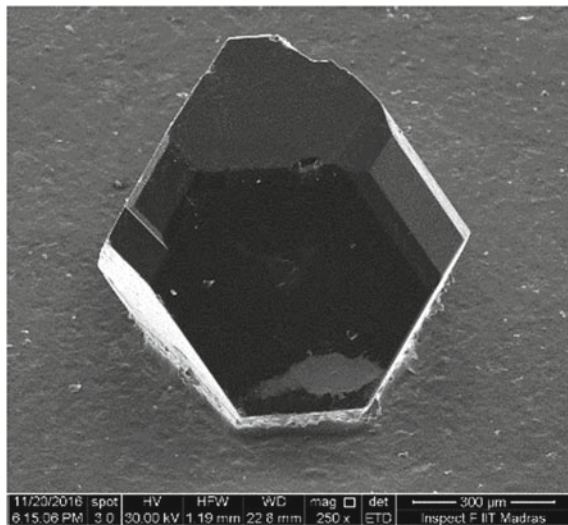
Fig. 43.1 Morphology of synthetic diamond grit brazed with Ni–Cr alloy



large difference in coefficient of thermal expansion value of the grit and the alloy. This can be mitigated by controlling the cooling rate of the brazed diamond joint. In the second case, the source of residual stress can be attributed to the presence of a partially coherent phase $[(Cr, Fe)_{23}C_6]$ in nickel-based alloy that causes local grain boundary stresses to develop [8]. In one of our prior study, it was demonstrated that cooling of the brazed joint alone in a programmed manner was not able to inhibit the formation of cracks [9]. Thus, it can be said that the combined effect of both thermal strain and the presence of partially coherent phase in Ni-based filler alloy is responsible for the development of residual stress. Additionally, the high brazing temperature associated with the use of Ni-Cr alloy has a detrimental impact on the surface of synthetic diamond grits. At higher brazing temperature, synthetic diamond tends to get converted to its more stable form, graphite. Formation of graphite on the surface of diamond grit will make the sharp edges of diamond grit to become blunt, making it ineffective to be used in an abrasive cutting tool.

From the above discussion, it can be imparted that the use of low temperature and the ductile Ag-based alloy is a suitable alternative to brazed synthetic diamond grits to steel substrate. Passive silver-based alloys show a poor wettability index on diamond grit surface. In order to ameliorate this phenomenon, the addition of an active element, titanium, is usually done. It is also necessary that an appropriate amount of the active element is added to the filler alloy. An excess addition of titanium has a detrimental effect on the joint strength. Increase in weight percentage of the active element also leads to the increase in the melting temperature of the resultant filler alloy. At the outset, 10 wt% of the active element, titanium, was added to the eutectic 72Ag–28Cu alloy. Figure 43.2 shows the morphology of the synthetic diamond grit brazed with active Ag–Cu alloy containing 10 wt% Ti. Since the alloy contains a higher weight percentage of the active element, the brazing temperature was set at

Fig. 43.2 Synthetic diamond grit brazed with (72Ag–28Cu)-10 wt% Ti filler alloy



920 °C. The alloy successfully wets the surface of the diamond grit by forming TiC compound near the brazed interface. It was noted that diamond grits brazed to the metal substrate using this alloy had an inferior joint strength. It could be attributed to the fact that at higher melting temperatures, the TiC intermediate compounds grow in size reasonably. Increase in the size of TiC reaction compound will cause a decrease in its fracture toughness values, as these compounds are brittle in nature. In a separate attempt, the weight percentage of the active element to be added to the filler alloy was reduced to 2 wt%. Figure 43.3 shows the SEM image of synthetic diamond grit brazed to a metal substrate using active Ag–Cu alloy containing two weight percentage of titanium. The wetting was observed to be superior to the filler alloy containing 10 wt% of titanium. The brazing of the grit was done at a temperature of 820 °C. The strength of the brazed joint was observed to be superior to the former case, wherein 10 wt% of the active element was added to the filler alloy.

The study of a brazed diamond joint quality remains incomplete without characterizing the failure of the brazed joint under the action of a horizontal load. To start with, a lateral load was applied to the diamond grit brazed with all three alloys. It was observed that in the case of Ni–Cr alloy, the failure took place at the bond level. Such a phenomenon was relatable to one of the prior studies where a similar trend was observed when Ni–Cr alloy was used for brazing synthetic diamond grit [10]. Figure 43.4 shows the characteristic bond level failure when Ni–Cr alloy is used for brazing synthetic diamond grit. In the case of an alloy containing 10 wt% of titanium, the failure took place due to grit pull out. It can be seen in Fig. 43.5 that at the brazed interface, no evidence of the ductile failure of the alloy was noticed. This clearly indicates that at higher brazing temperature the intermediate reaction compound grows in size and predominantly fails in a brittle manner, thereby reducing the brazed joint strength. For active Ag–Cu alloy containing 2 wt% of titanium,

Fig. 43.3 Synthetic diamond grit brazed with (72Ag–28Cu)-2 wt% Ti filler alloy

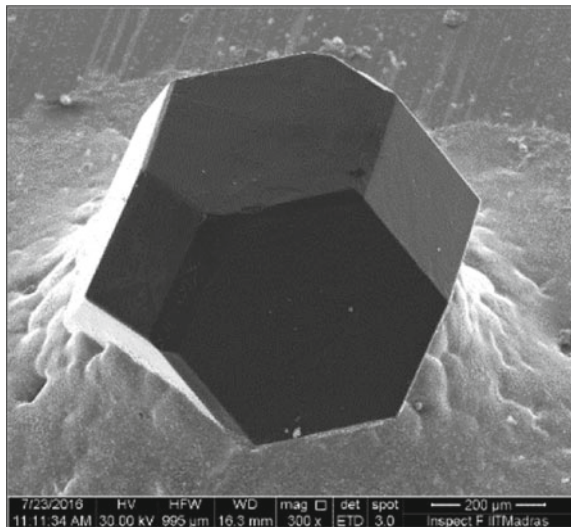


Fig. 43.4 Bond level failure of diamond grit brazed with Ni–Cr alloy

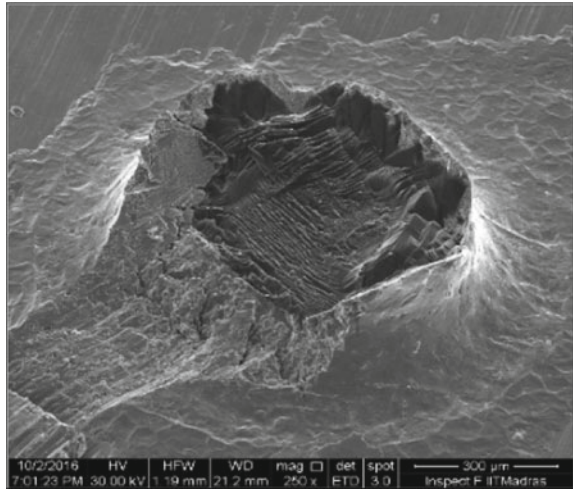
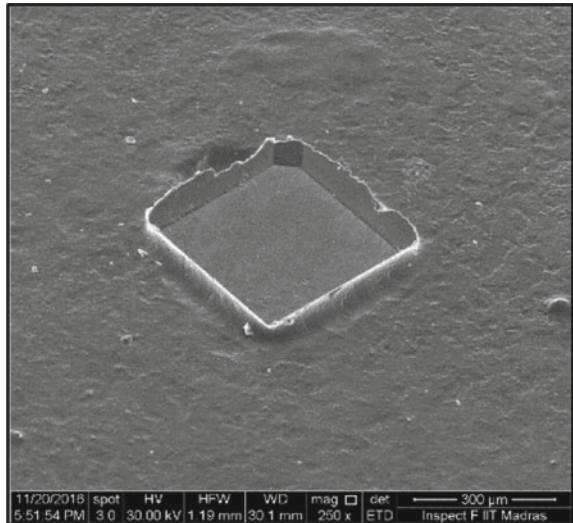


Fig. 43.5 Pull out of the grit brazed with (72Ag–28Cu)-10 wt% Ti



the interface failed majorly in a ductile manner resulting from pull out of the grit (Fig. 43.6). This was characterized by observing the failed morphology of the brazed joint at higher magnification. The failed region comprised multitudes of local cup (Fig. 43.7) and cone shapes, indicative of the ductile mode of failure of the joint.

The study points out that Ag–Cu alloy containing 2 wt% of titanium showcases a better resistance towards grit pull out, compared to Ag–Cu alloy containing 10 wt% of Ti. A lower percentage of Ti in the alloy restricts the growth of TiC within the filler alloy, and hence, improves the brazed joint strength. Ni–Cr alloys, although

Fig. 43.6 Failure of the brazed joint developed using (72Ag–28Cu)-2 wt% Ti

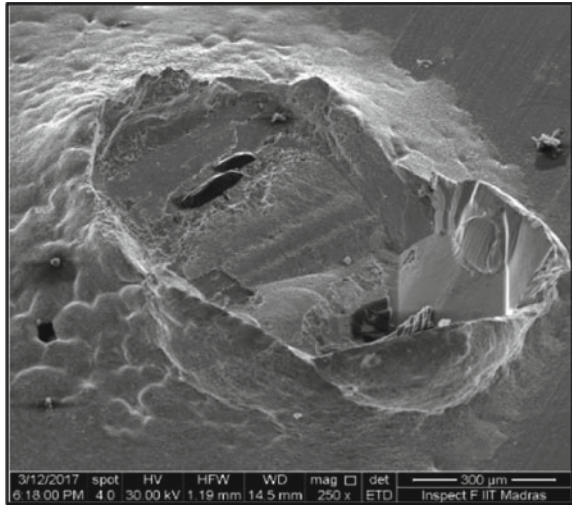
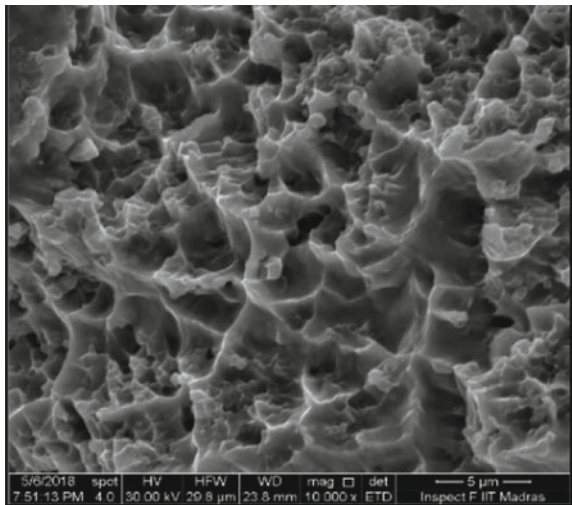


Fig. 43.7 Magnified image of (72Ag–28Cu)-2 wt% Ti filler alloy failed in ductile manner



possessing a superior abrasion resistance property, succumbed to bond level failure due to the presence of highly hard and brittle chromium carbide compounds at the interface of the brazed joint.

43.4 Conclusions

The study compares the effectiveness of brazing of synthetic diamond with Ni-based filler alloy and active Ag-based filler alloy containing two different weight percentages of titanium as the active element. Following inferences have been drawn out from this particular investigation:

- The brazed joint interface developed using Ni–Cr alloy is prone to formation of micro-cracks. Formation of the crack at the interface might be attributed to the presence of residual stress at the brazed joint.
- The combined effect of differential coefficient of thermal expansion of the grit, alloy, substrate and the presence of partially coherent phase in Ni-based alloy is responsible for the stress to develop at the brazed joint interface.
- Addition of 10 wt% of the active element, titanium, causes the silver-based alloy to flow more towards the base substrate. This results to improper wetting by the filler on diamond surface, resulting to reduction in brazed joint strength value.
- Increase in the weight percentage of Ti in silver–copper filler alloy increases the brazing temperature. In this study, the Ag–Cu alloy containing 10 wt% of Ti was used to braze diamond at 920 °C. The resultant filler alloy containing higher weight percentage of Ti had a poor grit retention ability, as the grits were pulled out relatively at a lower force applied in the lateral direction.
- Ag-based filler alloy containing 2 wt% of Ti as an active element was found to be a more promising composition. At a brazing temperature of as low as 820 °C, the filler alloy nicely wetted the surface of the grit and showed a superior resistance against grit pull out.

References

1. Sung, J.C., Sung, M.: The brazing of diamond. *Int. J. Refract. Met. Hard Mater.* **27**, 382–393 (2009). <https://doi.org/10.1016/j.ijrmhm.2008.11.011>
2. Chattopadhyay, A.K., Chollet, L., Hintermann, H.E.: Induction brazing of diamond with Ni–Cr hardfacing alloy under argon atmosphere. *Surf Coatings Technol* **45**, 293–298 (1991). [https://doi.org/10.1016/0257-8972\(91\)90235-O](https://doi.org/10.1016/0257-8972(91)90235-O)
3. Chattopadhyay, A.K., Chollet, L., Hintermann, H.E.: Experimental investigation on induction brazing of diamond with Ni–Cr hardfacing alloy under argon atmosphere. *J. Mater. Sci.* **26**, 5093–5100 (1991). <https://doi.org/10.1007/BF00549897>
4. Lee, C., Ham, J., Song, M., Lee, C.: The interfacial reaction between diamond grit and Ni-based brazing filler metal. *Mater. Trans.* **48**, 889–891 (2007). <https://doi.org/10.2320/matertrans.48.889>
5. Tanaka, K., Hidaka, K.: *Hard Facing Nickel Base Alloy* (1983)
6. Schwartz, C.: (Received February 7, 1986). **30**, 157–170 (1987)
7. Schwartz, M.M.: *Brazing*, second (2003). <https://doi.org/10.1361/brse2003p015>
8. Young, G., Capobianco, T.E., Penik, M., et al.: The mechanism of ductility dip cracking in nickel-chromium alloys. *Weld. J.* **87**:31S–43S (2008)

9. Mukhopadhyay, P., Raghava Simhan, D., Ghosh, A.: Challenges in brazing large synthetic diamond grit by Ni-based filler alloy. *J. Mater. Process. Technol.* **250**, 390–400 (2017). <https://doi.org/10.1016/j.jmatprotec.2017.08.004>
10. Mukhopadhyay, P., Ghosh, A.: On bond wear, grit-alloy interfacial chemistry and joint strength of synthetic diamond brazed with Ni–Cr–B–Si–Fe and Ti activated Ag–Cu filler alloys. *Int. J. Refract. Met. Hard. Mater.* **72**, 236–243 (2018). <https://doi.org/10.1016/j.ijrmhm.2017.12.033>

Chapter 44

Friction Stir Welding of Al–Cu Alloy Metal Matrix Composites Reinforced with B₄C and Graphite Particle Fabricated by Stir Casting and Thixoforming Method



K. Sekar  and P. Vasanthakumar 

Abstract Aluminum with high strength, improved corrosion resistance, lightweight-to-strength ratio, and toughness provides a technical challenge in the joining process. An attempt to weld Al–Cu alloy metal matrix composite reinforced with B₄C and graphite particle by friction stir welding (FSW). In this paper, stir casting and thixoforming method are used for fabricating AA2017 and its composite, which was reinforced with varying B₄C (0.5, 1 and 1.5 wt%) and constant graphite (1 wt%). The addition of B₄C improves the wear resistance, and graphite acts as solid lubricant for aluminum matrix. The microstructures of metal matrix composites studied by optical microscopy with the absence of defects and porosity and X-ray diffraction (XRD) patterns revealed the presence of reinforcement particles. SEM image confirms the reinforcement particles are well distributed and act as a bonding agent with the metal matrix. The hardness of composites AA2017+1.5% B₄C+1% graphite increased up to 19% compared to base alloy. The maximum increase in tensile strength from 224 to 251 MPa with strength increased up to 15.64%, in addition to 1 wt% boron carbide and 1 wt% graphite, was observed. The increase in B₄C particle generally increases the hardness and decreases the tensile strength and vice versa, due clustering of particles and segregation.

Keywords Friction stir welding · Aluminum alloy · B₄C+ graphite reinforcements · Stir casting · Thixoforming method

K. Sekar (✉) · P. Vasanthakumar

Department of Mechanical Engineering, National Institute of Technology Calicut, Kerala 673601, India

e-mail: sekar@nitc.ac.in

© Springer Nature Singapore Pte Ltd. 2020

M. S. Shunmugam and M. Kanthababu (eds.), *Advances in Additive Manufacturing and Joining*, Lecture Notes on Multidisciplinary Industrial Engineering,

https://doi.org/10.1007/978-981-32-9433-2_44

44.1 Introduction

Aluminum materials have the wide range of applications in everyday life from small wires to large automobiles and heavy machinery. Aluminum has the higher strength-to-weight ratio and second to steels in structural applications. In heat-treatable Al–Cu alloy, the principal alloying element copper of 1–6% and the small percentage of magnesium [1]. Aluminum metal matrix composite (AMMC) has attracted the attention due to their low weight, high stiffness, strength, low cost, and ease of fabrication. AMMC is desirable material for structural applications in aircraft, defense, and automotive industries. The particulate reinforcement B_4C , when added with aluminum alloy, provides high strength, high hardness, low density, and better chemical stability. The boron carbide is harder material next to diamond and boron nitride; expensive ceramic when compared with silicon carbide and Al_2O_3 . The mechanical properties like hardness and tensile strength improve with the addition of B_4C reinforcement particle [2]. The addition of B_4C particulates to the Al matrix leads to an increase in yield stress and ultimate tensile strength compared to the base metal but decreases in ductileness [3]. The aluminum composites having the different weight percentage of graphite particles fabricated, in that hardness of composites decreased with increase in weight percentage of graphite with some distributions and also the cluster of particles at the lower percentage of graphite up to certain amount [4].

Aluminum matrix composites (AMC) are fabricated by different methods such as spray atomization, stir casting, squeeze casting, plasma spraying, liquid infiltration, co-deposition, and powder metallurgy. Stir casting and thixoforming process enhance bonding between metal matrix and particulate reinforcement because of the stir action and high-pressure application. To improve the wettability between reinforcement and metal, added a small amount of magnesium with a stirring speed of 900 rpm and stirring time of 3–5 min [5]. The stirring speed and time provide the uniform dispersion of reinforcement particles in cast metal matrix composite. The clustering obtained at lower stir speed and time from the microstructural study [6].

The process parameters such as stir time, speed, casting temperature, and blade profile influence the tensile strength of aluminum matrix composites produced using stir casting method [7]. Thixoformed samples of Al2017 were prepared at an optimum temperature of 635–645 °C and a pressure of 100 MPa. Further, the squeezing operation reduces the porosity of the cast metal matrix composite and increases its strength [8]. The mechanical properties and microstructure of aluminum alloy formed by thixoforming have high strength at an isothermal temperature of 605 °C. The slight decrease in mechanical properties was due to microstructural change in coarsening the grains [9]. The microstructure and mechanical properties of aluminum alloy through thixoforming process show a significant change in ultimate tensile strength and yield stress [10].

Friction stir welding (FSW), a solid-state welding process, has great potential in joining aluminum materials, which could not be possible to join by conventional fusion welding technique. FSW of Al alloys has already implemented for the mass production of automotive structural components [11, 12]. The various process param-

Table 44.1 Composition of AA2017

Al	Cu	Mg	Mn	Si	Ti	Cr	Fe	Zn
91.55–94.15	3.5–4.5	0.4–0.8	0.4–1	0.2–0.8	0.15	0.1	0.7	0.25

eters like tool geometries, tool rotational speed, pin profiles, welding speed, and tool tilt angle affect the severe plastic deformation and dynamic recrystallization of the welded specimen. The fine equiaxed grains affect the microstructural characteristics and mechanical properties of aluminum alloy [13, 14]. It is very difficult to join the Al–Cu MMC by conventional fusion welding method. To overcome this difficulty, the research objective framed to address the solid state (FSW) joining of Al–Cu MMC fabricated by stir casting and thixoforming method.

44.2 Experimental Details

44.2.1 Materials

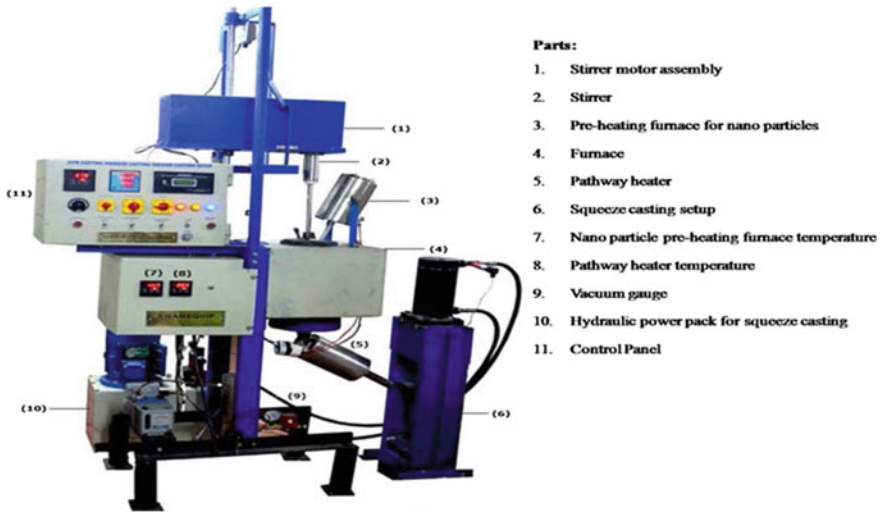
AA 2017 which has predominantly copper as an alloy shown in Table 44.1 was chosen owing to its high strength and superior heat treatability. The material specimen size: $45 \times 125 \times 650$ mm.

44.2.2 Stir Casting

Stir casting method is one of casting techniques for low melting point materials. The wt% of graphite held with constant while varying B_4C percentage with 0.5% increment in each cast as shown in Table 44.2. Total weight was decided based on the die used for casting which is 1160 g. 1 wt% of Zn and Mg each was added to increase wettability. The casting was done in an inert argon atmosphere to avoid oxidation. Refractory material (zirconium paste) was pasted inside die, crucible and on the stirrer to protect from high temperature. If the melting of the materials reached, then it is added with slag-removing agent bipotassium hexafluorotitanate (K_2TiF_6) in

Table 44.2 Castings

Cast No.	Castings
1	AA2017
2	AA2017+0.5% B_4C +1% graphite
3	AA2017+1% B_4C +1% graphite
4	AA2017+1.5% B_4C +1% graphite



- Parts:**
1. Stirrer motor assembly
 2. Stirrer
 3. Pre-heating furnace for nano particles
 4. Furnace
 5. Pathway heater
 6. Squeeze casting setup
 7. Nano particle pre-heating furnace temperature
 8. Pathway heater temperature
 9. Vacuum gauge
 10. Hydraulic power pack for squeeze casting
 11. Control Panel

Fig. 44.1 Multiple casting machine [15]

Table 44.3 Stir casting parameters

Parameters	Operating condition
Preheating temperature of reinforcements	750 °C
Preheating time	30 min
Stirrer speed	450 rpm
Stirring time	15 min
Weight of magnesium	11.6 g
Weight of zinc	11.6 g
Pressure of argon gas	1 MPa
Casting temperature	850 °C

powder form, and flux is used to remove impurities as slag. The photograph of the stir casting machine is shown in Fig. 44.1 and stir casting parameters in Table 44.3.

44.2.3 Thixoforming

After composite preparation, through stir casting, the thixoforming process was carried out to reduce porosity and defects in the cast as shown in Fig. 44.2. In thixoforming, the cast metal is reheated to an elevated temperature in solid state and then compressed by applying high squeeze pressure to decrease porosity, defects, and improved mechanical properties in the cast.

Fig. 44.2 Thixoforming setup [15]



44.2.4 Friction Stir Welding

The process of friction stir welding: The extruded plates of AA2017 and its composites of 4 mm thickness are welded by friction stir welding butt joint configuration. The size of the work specimens was 50 mm × 40 mm × 4 mm, and chemical composition of the AA2017 is shown in Table 44.1. The experiments were conducted in retrofitted vertical end milling machine as shown in Fig. 44.3a–d. The friction stir

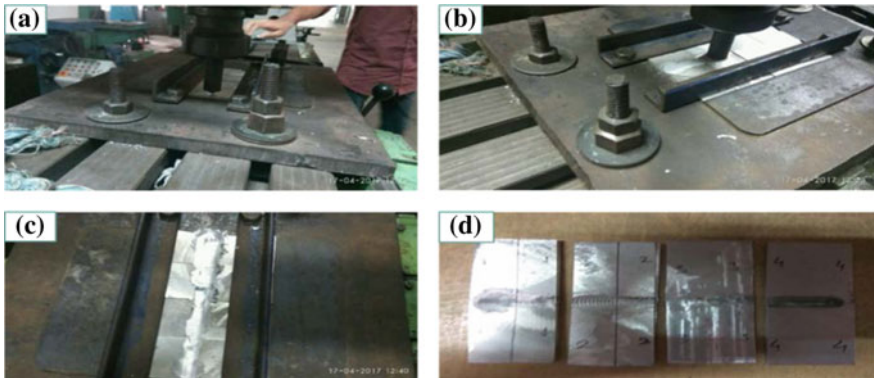


Fig. 44.3 Procedure of FSW in retrofitted vertical end milling machine

tools were made in OHNS die steel of pin diameter 6 mm, pin length 4 mm and tool shoulder diameter of 18 mm. With constant tool rotational speed 1000 rpm and the welding speed of 20 mm/min, FSW tool was rotated in the counterclockwise direction from advancing side to retreating side. The unthreaded tool was plunged at the center line of the specimen until the tool shoulder touches the surface of the plate, and the tool dwell time kept constant for 30 s. And then the tool was moving along the advancing side to obtain proper weld at faying surfaces.

44.3 Result and Discussion

44.3.1 Microstructural Studies

The microstructures of AA2017/B₄C/graphite hybrid composites are shown in Fig. 44.4a–d. The reinforced particles B₄C (0.5, 1, 1.5 wt%) and graphite (constant 1 wt%) added with AA2017. In AMMC, uniform dispersal of the reinforcements B₄C and graphite particles are observed clearly [3, 4]. Finely grained microstructures obtained in the addition of reinforcement 1.5 wt% B₄C and 1% graphite. Due to

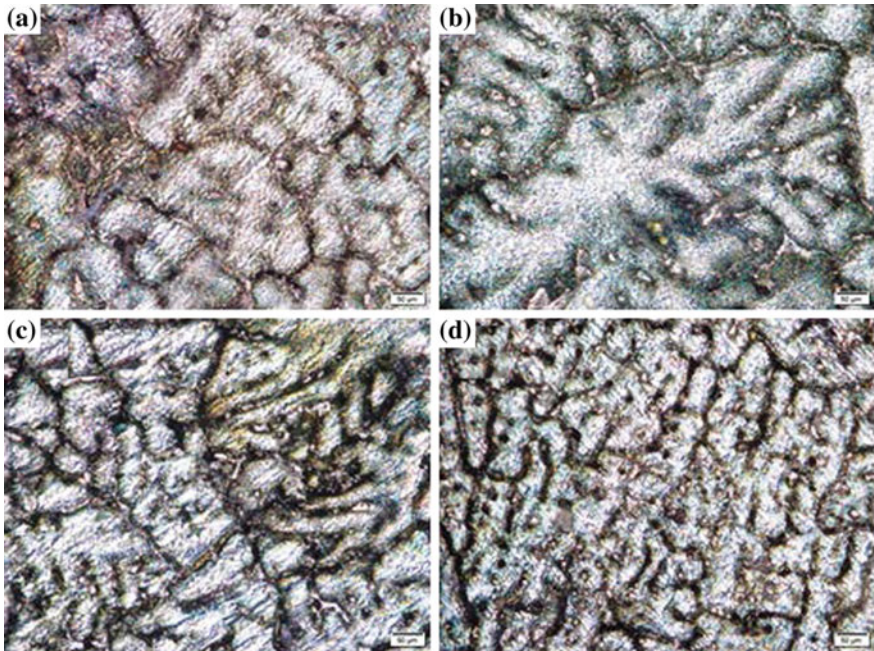


Fig. 44.4 Optical microstructure at 100X **a** AA2017, **b** AA2017+0.5% B₄C+1% graphite, **c** AA2017+1% B₄C+1% graphite, and **d** AA2017+1.5% B₄C+1% graphite

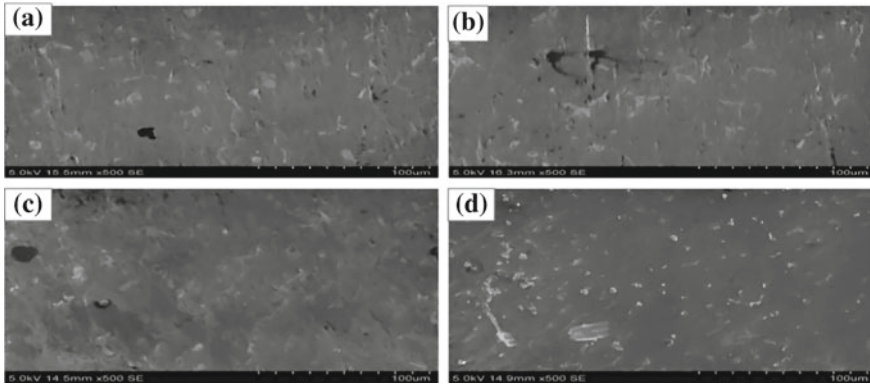


Fig. 44.5 SEM image **a** AA2017, **b** AA2017+0.5% B₄C+1% graphite **c** AA2017+1.5% B₄C+1% graphite, and **d** AA2017+1% B₄C+1% graphite

preheating, the reinforcement particle B₄C and graphite provide better bonding with the AA2017 metal matrix [15]. At higher magnification, microstructural images of the AA2017 composite provide the better interfacial bond between the B₄C particle and the metal matrix.

44.3.2 SEM Analysis

A complete microstructural study was carried out through scanning electron microscopy (SEM). The SEM microstructures were shown in Fig. 44.5a–d. In SEM image, there was the uniform distribution of reinforcement particle B₄C and graphite in the AA2017 metal matrix. The reinforcement particles are well distributed and act as a bonding agent with the metal matrix which leads to better mechanical properties. The preheating of the reinforcement particle provides proper bonding in the AA2017 metal matrix with enhanced microstructures and mechanical properties [15]. Most of B₄C and graphite reinforcement particles form a layer at the grain boundary and disperse gradually to inner grain [3, 4]. Because of stir casting followed by the thixo-forming process, B₄C particles have slightly settled in the grain boundary of the composite. No defects observed in the SEM image.

44.3.3 XRD Analysis

XRD analysis presented in Fig. 44.6a–c confirmed the presence of B₄C and graphite reinforcement within the matrix. Peaks of graphite obtained at $2\theta = 26^\circ$ and B₄C at $2\theta = 20^\circ, 36^\circ$. The only slight variation in peak intensity with the change in B₄C

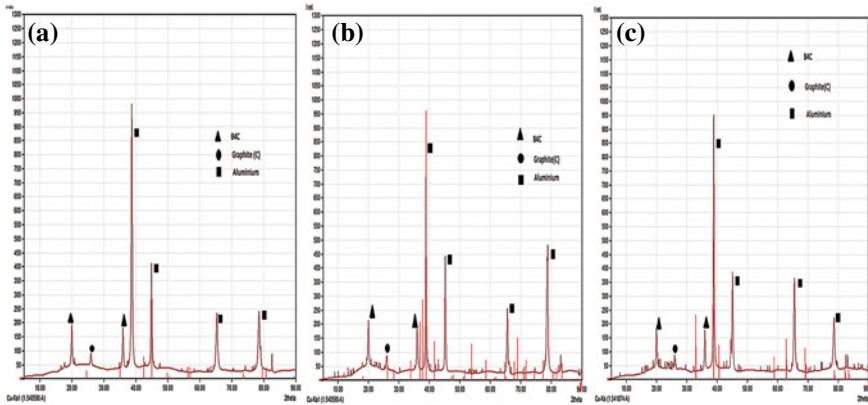


Fig. 44.6 a AA2017+0.5% B₄C+1% graphite, b AA2017+1% B₄C+1% graphite, and c AA2017+1.5% B₄C+1% graphite

weight percentage of reinforcements as the weight percentage of graphite remains constant.

44.3.4 Hardness Test

Hardness values measured across the weld are given in Fig. 44.7a–d. The hardness of the composite has increased with B₄C addition. Maximum hardness of 112 HV obtained by 1.5 wt% B₄C addition. The microstructure of different weld zone for the 1 wt% of B₄C and 1 wt% graphite welded specimen is as shown in Fig. 44.8a–d. There are four different zones in a welded region, weld or nugget zone (WZ), thermomechanically affected zone (TMAZ), heat-affected zone (HAZ), and unaffected zone.

It was clear from the images that the grain size was decreasing gradually from unaffected zone to TMAZ and then increases in weld or nugget zone. Grain size reaches the least value in TMAZ. This grain size distribution was due to dynamic recrystallization during friction stir welding [14]. The hardness trend obtained was in good agreement with grain size distribution. From the Hall–Petch equation, as grain size decreases, hardness increases. TMAZ has the highest hardness value and gradually decreases to unaffected zone. The small reduction in hardness in the weld region or nugget zone was due to an increase in grain size compared to TMAZ.

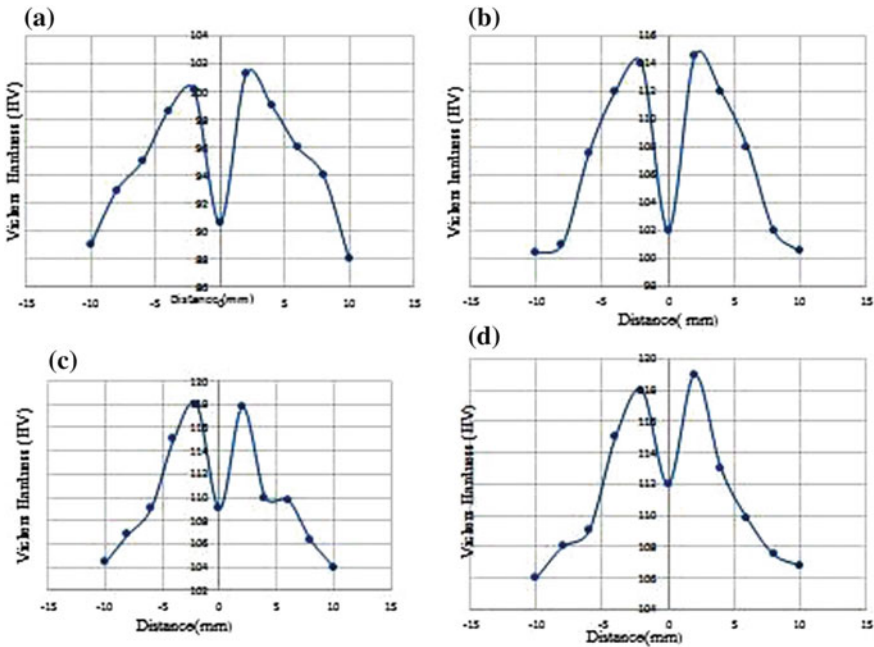


Fig. 44.7 Hardness distribution across the weld **a** AA2017, **b** AA2017 + 0.5% B₄C+1% graphite, **c** AA2017+1% B₄C+1% graphite, and **d** AA2017+1.5% B₄C+1% graphite

44.3.5 Tensile Test

The tensile test was performed to determine properties such as strength and ductility of a material. Test specimens are prepared as per ASTM E8M standard as shown in Fig. 44.9. In FSW, the tensile strength of joint measured and compared with that of base metal to determine the efficiency of the joint [11, 12]. For specimen reinforced with 0, 0.5, and 1% B₄C, the fracture obtained in the base metal rather than in the weld zone indicating a higher strength for particulate reinforced welds than base metal. For specimen reinforced with 1.5% fracture obtained in the near weld region due to the presence of the crack.

The ultimate tensile strength of the alloy and hybrid composites with constant 1 wt% of graphite and 0, 0.5, 1, 1.5 wt% of B₄C reinforcements as shown in Table 44.2. The true stress or ultimate strength as shown in Table 44.4 and Fig. 44.10 with varying composition of boron carbide and graphite particles. Due to the addition of boron carbide from 0 to 1 wt%, there was the increase in ultimate tensile strength. The increase of more than 1 wt% of the B₄C particles leads to the formation of agglomeration and clustering of particles which further decreases the tensile strength in the fourth cast. In addition to B₄C particulates of 0.5, 1, 1.5, and 1 wt% constant graphite-tested specimens the tensile strength increased when compared to the base alloy. The maximum increase in tensile strength from 224 to 251 MPa with strength

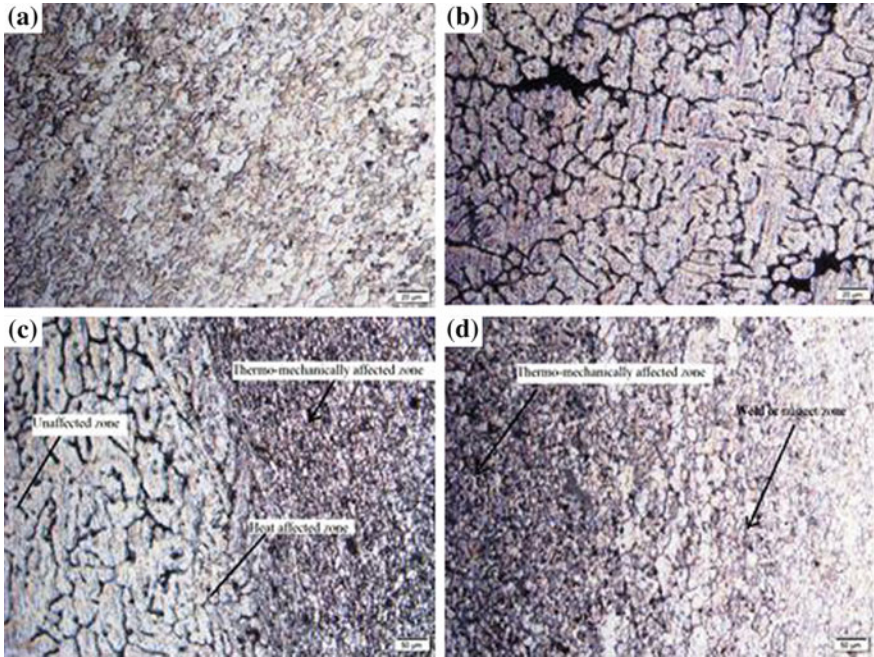


Fig. 44.8 **a** Microstructure of weld nugget zone, **b** microstructure of unaffected zone, **c** grain size variation in TMAZ, HAZ, and unaffected zone, and **d** grain size variation in TMAZ and weld nugget zone



Fig. 44.9 Tensile test specimens before and after fracture

increased up to 15.64%, on the addition of 1 wt% of boron carbide and 1 wt% of graphite as shown in Fig. 44.11. Due to severe plastic deformation in the weld nugget or stir zone during FSW provides excellent bonding of AA2017 metal matrix and B₄C and graphite reinforcements.

Fractographic study of the tensile test: Tensile fractured specimens of AA2017 and the composites with varying B₄C% are taken for study. The SEM images with the fractured surfaces are shown in Fig. 44.12a–d. SEM examines the fracture surfaces of 2017 aluminum alloy and composites; the fractured regions revealed fewer dimples for the unreinforced material. The fractured surface of the unreinforced metal contained a non-uniform distribution of small dimples like structure connected by

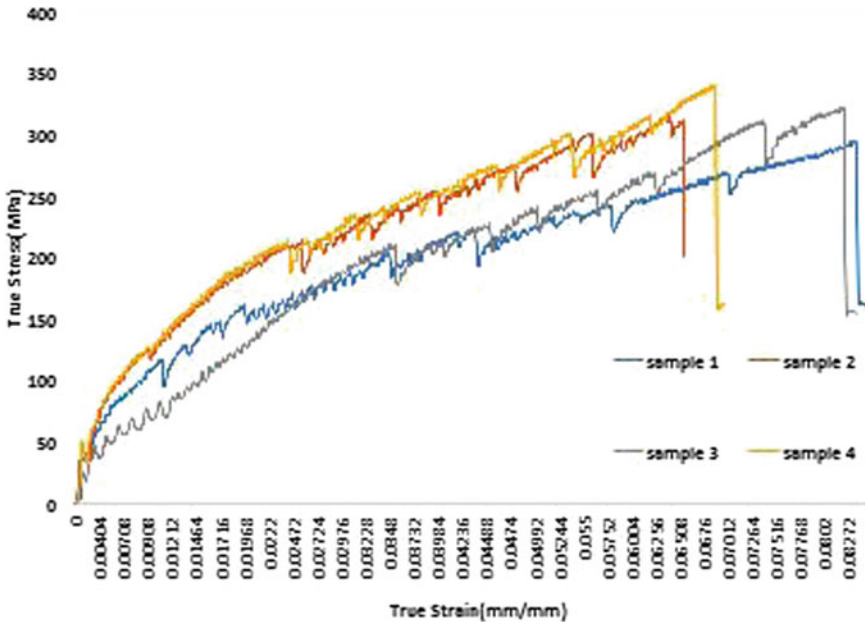
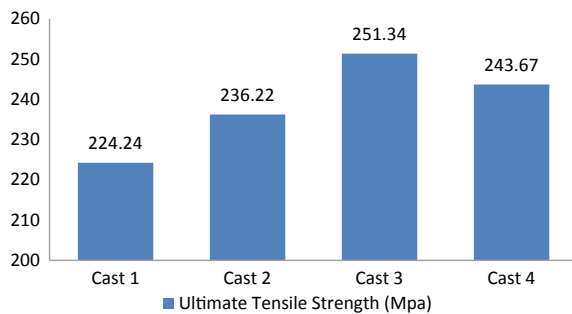


Fig. 44.10 True stress versus true strain graph for tensile test

Fig. 44.11 Ultimate tensile strength variation



sheets of the pattern resulting from ductile void growth coalescence and failure. The fractured surface of the reinforced aluminum composite contained more dimples than the fractured surface of the unreinforced material. But high weight percentage of B_4C and graphite leads to agglomeration in the fourth cast composites with brittle fracture failure. Only very few crack propagation noted as the fracture in SEM image, and there was an indication of ductile failure in the matrix [3, 4]. The fracture failure showed few longitudinally split and transverse as shown in Fig. 44.12.

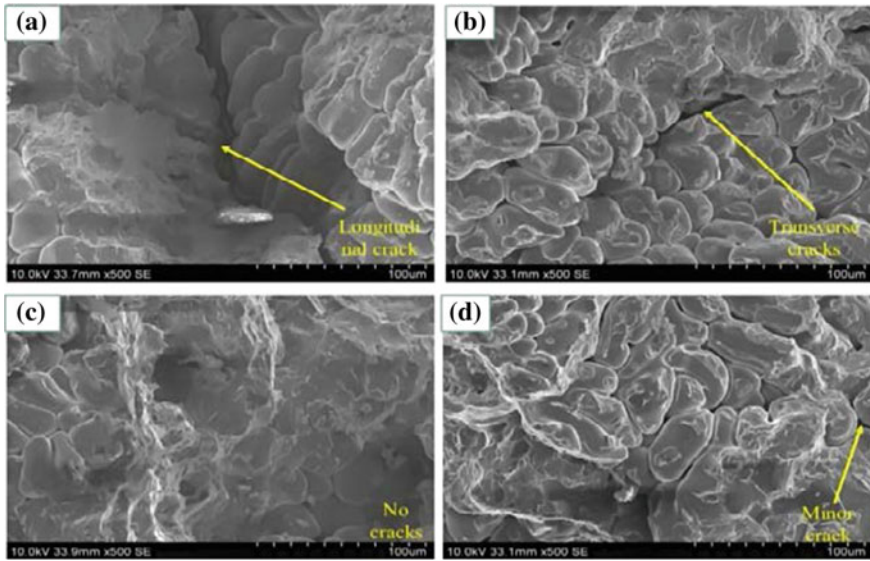


Fig. 44.12 Fractographic SEM image for tensile test at 100 μm **a** AA2017, **b** AA2017+0.5% B_4C +1% graphite, **c** AA2017+1% B_4C +1% graphite, and **d** AA2017+1.5% B_4C +1% graphite

Table 44.4 Stress–strain variation in tensile test

Sample No.	True stress (MPa)	Change in true stress (%)	Strain (mm/mm)
1	224.24	0	0.0822
2	236.22	5.44	0.0660
3	251.34	15.64	0.0721
4	243.67	9.86	0.0666

44.4 Conclusions

Friction stir welding of Al–Cu alloy metal matrix composites reinforced with B_4C and graphite particle fabricated by stir casting and thixoforming method concluded as follows:

- The optical microstructure study revealed the uniform dispersion of the reinforcement particles in the 2017 aluminum alloy matrix with the addition of reinforced B_4C and graphite particles. The absence of defects and porosity.
- SEM image shows reinforcement particles well distributed and acts as a bonding agent with the metal matrix.
- XRD analysis confirmed the presence of B_4C and graphite reinforcement particle within the AA2017 metal matrix composite.

- The hardness of hybrid composites was increased from 91 to 112 HV by addition of 1.5 wt% of B₄C, and 1 wt% of graphite and the hardness increases up to 19% compared to base alloy.
- The tensile strength increased from 224 to 251 MPa with strength increased up to 15.64%, on the addition of 1 wt% boron carbide and 1 wt% graphite compared to base alloy.
- The increase in B₄C particle generally increases the hardness and decreases the tensile strength and vice versa, due clustering of particles and segregation.

References

1. Davis, J.R.: Aluminum and Aluminum Alloys 351–416 (2001)
2. Kalaiselvan, K., Murugan, N., Parameswaran, S.: Production and characterization of AA6061–B₄C stir cast composite. *Mater. Des.* **32**(7), 4004–4009 (2011)
3. Auradi, V., Rajesh, G.L., Kori, S.A.: Processing of B₄C particulate reinforced 6061 aluminum matrix composites by melt stirring involving two-step addition. *Procedia Mater. Sci.* **6**, 1068–1076 (2014)
4. Sharma, P., Sharma, S., Khanduja, D.: Effect of graphite reinforcement on physical and mechanical properties of aluminum metal matrix composites. *Part. Sci. Technol.* **34**(1), 1722–1734 (2015)
5. Ghazi, J.H.: Production and properties of silicon carbide particles reinforced aluminum alloy composites. *Int. J. Min. Metall. Mech. Eng.* **1**, 2320–4052 (2013)
6. Balasivanandha Prabu, S., Karunamoorthy, L., Kathiresan, S., Mohan, B.: Influence of stirring speed and stirring time on distribution of particles in cast metal matrix composite. *J. Mater. Process. Technol.* **171**, 268–273 (2006)
7. Jebeen Moses, J., Dinaharan, I., Joseph Sekhar, S.: Prediction of influence of process parameters on tensile strength of AA6061/TiC aluminum matrix composites produced using stir casting. *Trans. Nonferrous Met. Soc. China* **26**(6), 1498–1511 (2016)
8. Ozdemir, I., Muecklich, S., Podlesak, H., Wielage, B.: Thixoforming of AA 2017 aluminum alloy composite. *J. Mater. Process. Technol.* **211**(7), 1260–1267 (2011)
9. Jufu Jiang., H.V. Atkinson., Ying Wang: Microstructure and mechanical properties of 7005 aluminum alloy components formed by thixoforming. *J. Mater. Sci. Technol.* **33** (4), 379–388 (2017)
10. Salleh, M.S., Omar, M.Z., Syarif, J., Alhawari, K.S., Mohammed, M.N.: Microstructure and mechanical properties of thixoformed A319 aluminum alloy. *Mater. Des.* **64**, 142–152 (2014)
11. Kumar, N., Yuan, W., Mishra, R.S.: Friction Stir Welding of Dissimilar Alloys and Materials (2015)
12. Khan, N.Z., Siddiquee, A.N., Khan, Z.A.: Friction Stir Welding: Dissimilar Aluminium Alloys (2017)
13. Meshram, S.D., Paradkar, A.G., Reddy, G.M., Pandey, S.: Friction stir welding: an alternative to fusion welding for better stress corrosion cracking resistance of maraging steel. *J. Manuf. Process* **25**, 94–103 (2017)
14. Rajakumar, S., Muralidharan, C., Balasubramanian, V.: Optimization of the friction-stir-welding process and tool parameters to attain a maximum tensile strength of AA7075-T6 aluminium alloy. *Proc. Inst. Mech. Eng. Part B J. Eng. Manuf.* **224** (8), 1175–1191 (2010)
15. Sekar, K., Allesu, K., Joseph, M.A.: Mechanical and wear properties of Al–Al₂O₃ metal matrix composites fabricated by the combined effect of stir and squeeze casting method. *Trans. Indian Inst. Metals* **68** (2), 115–121 (2015)

Chapter 45

Comparative Study of Feed-Forward and Recurrent Neural Networks in Modeling of Electron Beam Welding



Sanjib Jaypuria , Santosh Kumar Gupta  and Dilip Kumar Pratihar 

Abstract In this study, back-propagation neural network (BPNN) and recurrent neural network (RNN) were utilized for the modeling of electron beam welding of AISI 304 stainless steel. The input parameters considered in this study were accelerating voltage, beam current, and scanning speed. These primary parameters were modeled along with the responses like bead geometric parameters. The developed approaches of the modeling had been evaluated in terms of computational time and accuracy in prediction for the test data. The modeling capability of both BPNN and RNN was found to be significantly good, when it was compared with the experimental data. However, Elman recurrent neural network had shown the better accuracy in prediction compared to BPNN, due to the presence of feedback connection in RNN, which leads to capture the dynamics of the nonlinear system efficiently. In addition to this, BPNN was found to be computationally faster than RNN, as expected.

Keywords Electron beam welding · Modeling · Back-propagation neural network · Recurrent Elman neural network

45.1 Introduction

The recent era of industrialization demands automation and optimal use of resources in any kind of manufacturing process. However, it is not always possible to use the previous database in manufacturing industries because of machine, material, and man constraints. In addition to this, it is also not advisable to go with trial-and-error method, whenever there is an involvement of a significant chunk of capital investment. Welding is one of this kind of primary manufacturing process, where trial and error is

S. Jaypuria · D. K. Pratihar (✉)
Soft Computing Lab, Department of Mechanical Engineering, Indian Institute of Technology
Kharagpur, Kharagpur 721302, India
e-mail: dkpra@mech.iitkgp.ac.in

S. K. Gupta
Advanced Technology Development Centre, Indian Institute of Technology Kharagpur,
Kharagpur 721302, India

© Springer Nature Singapore Pte Ltd. 2020
M. S. Shunmugam and M. Kanthababu (eds.), *Advances in Additive Manufacturing and Joining*, Lecture Notes on Multidisciplinary Industrial Engineering,
https://doi.org/10.1007/978-981-32-9433-2_45

used most often before proceeding for the actual joint. This trial and error makes an inconvenience to automate the industry related to welding [1]. Electron beam welding (EBW) is the advanced fusion fabrication process, where an accelerated and focused electron beam acts as a heat source, and this high-velocity beam is converted into heat energy during the striking of the beam to plates to be joined. Electron beam involves multiple variables as primary (voltage, current, and scanning speed) and secondary (beam oscillation and focus coil current) input parameters [2, 3]. The primary responses of this welding are weld-bead geometry, which ensures a full-penetration and high strength of the weld joint. As a sophisticated and expensive process, there is a need for automation and control of this process.

Artificial neural network (ANN) is a popular machine learning tool, which can capture the implicit relationship between the input and output of any kind of nonlinear process and retrieve a generalized system. Here, a trained network is expected to capture the system characteristics and dynamics in their weights and bias [4]. There are two popular ANN architectures, namely multi-layer feed-forward network (MLFNN) and feedback-associated network (RNN). Back-propagation algorithm-tuned feed-forward neural network (BPNN) is one kind of multi-layer feed-forward neural network, which have three layers, namely input, hidden, and output layers. It is a multi-feed-forward network associated with gradient descent optimization method to minimize the difference between the model predicted and experimental value by adjusting the weights and biases [5, 6]. Recurrent neural network (RNN) is a system with a feedback connection. The feedback in the RNN network helps the activation function flow around the loop (from hidden layer to context layer), and it leads to capture the dynamics of a nonlinear system with a data-driven model [7, 8].

There were few reported studies on soft computing-based input–output modeling of welding. Some of those studies are discussed here. Dutta and Pratihari [9] modeled the input–output dependence of gas tungsten inert gas (TIG) welding with three approaches, namely the conventional regression, BPNN, and genetic algorithm-tuned neural network (GANN). From the results, it was concluded that the neural network has a more adaptive nature than conventional regression. Balasubramanian et al. [10] had done butt laser welding of stainless steel, using power, speed, and incidence angle as inputs and bead geometric parameters as the responses. They used the three-level Box–Behnken model to design the experiments. The prediction or modeling of the same was also done using BPNN and concluded that a comprehensive and usable prediction can be possible using a neural network. Jha et al. [11] attempted to model the relationship between input and output of the electron beam welding of SS 304 as a welding material. During the experimentation, three input parameters were considered, namely voltage, beam current, and scanning speed used the design matrix of central composite design (CCD). The parameters of the welding beads, i.e., bead width and penetration, and strength of the weld in terms of tensile strength were taken as the response variables. They carried out bidirectional (forward and reverse) predictions with both GANN and BPNN. It was found that GANN overcame the other two approaches in both direct and reverse mapping due to the full search capability of the genetic algorithm. Bagchi et al. [12] conducted Nd:YAG laser welding to predict the aspect ratio and peak temperature of Hastelloy. Taguchi L9 orthogonal array was

considered for designing the laser welding, where scanning speed, pulse frequency, and energy were taken as input parameters. It was also reported that the deviation of prediction was less than 10%, which showed the effectiveness of BPNN system.

Pradhan and Das [13] predicted the material removal rate of electro-discharge machining by implementing Elman recurrent neural network. The developed model was validated with test cases and had less than 6% mean percentage error in prediction of MRR. Manjunath Patel et al. [14] modeled the input–output of the squeeze casting process in bidirections using three approaches, namely BPNN, GANN, and Elman neural network. The result indicated a superior result for BPNN in forward modeling as compared to GANN and RNN. Bennett et al. [15] proposed recurrent nonlinear autoregressive with exogenous input (NARX) neural network to predict cylinder pressure using crank kinematics as input. This network helped them to calculate acceptably accurate cylinder pressure and accurate location of peak pressure without using a costly pressure sensor in closed-loop combustion control.

Although for modeling of welding, both conventional and various soft computing tools had been used as mentioned in the literatures, not much work has been reported on the recurrent neural network. Thus, in this study, an attempt was made to model the electron beam welding process through the recurrent neural network. Here, both back-propagation feed-forward neural network and recurrent neural network were used to map the input–output dependency (regression) of the electron beam welding process and to predict the weld response. Further, prediction accuracy and computational complexity were evaluated for each approach. RNN results were compared with that of BPNN and conventional regression analysis.

45.2 Experimentation and Data Generation

Bead-on-plate welding was performed on 150 mm × 100 mm × 5 mm plates of SS 304 [6]. Pre-welding preparation, i.e., cleaning and grinding, was carried out before testing. Accelerating voltage (V), beam current (I), and scanning velocity (S) were taken as input variables, whereas weld penetration, width, and height were regarded as responses, in this work. Each input variable was provided with three levels, which is, low, medium, and high values of the variables. In this study, data were collected based on design matrix of the central composite design (CCD) and a nonlinear regression analysis was performed to build the input–output relationships. Here, the experimental 51 compiled data points were used to train the neural network in batch mode. The test dataset for the verification of the developed model was also taken from Dey et al. [6]. Mathematical regression model equations for weld-bead height (BH), bead width (BW), and bead penetration (BP) obtained from Dey et al. [6] are shown below in equations from (45.1) to (45.3). Table 45.1 presents the combinations of the process parameters used as test cases.

Table 45.1 Test dataset

S. No.	V (kV)	I (mA)	S (cm/min)	BH (mm)	BW (mm)	BP (mm)
1	90	7	100	0.3392	1.6222	3.2846
2	75	8	80	0.3355	1.5709	3.1480
3	60	9	60	0.3976	2.0696	3.8733
4	90	7	100	0.3347	1.6568	3.5127
5	75	8	80	0.2956	1.6466	3.5377
6	90	7	60	0.4733	1.8236	4.1204
7	90	9	100	0.3840	1.8999	4.6063
8	60	8	80	0.3339	1.9531	3.4636

$$\begin{aligned} \text{BH} = & 0.2691 - 0.0162V + 0.1033I + 0.0008S + 0.0002V^2 + 0.0012I^2 \\ & + 0.00002S^2 - 0.0006VI - 0.00006VS - 0.0004IS, \end{aligned} \quad (45.1)$$

$$\begin{aligned} \text{BW} = & 6.6778 + 0.0103V - 0.8200I - 0.0437S - 0.00019V^2 \\ & + 0.0539I^2 + 0.0004S^2 + 0.0027VI - 0.00007VS - 0.0023IS, \end{aligned} \quad (45.2)$$

$$\begin{aligned} \text{BP} = & -11.2643 - 0.3047V + 4.9734I + 0.0697S + 0.0028V^2 \\ & - 0.2201I^2 - 0.0004S^2 - 0.0089VI - 0.00006VS + 0.0021IS, \end{aligned} \quad (45.3)$$

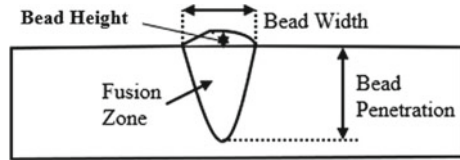
45.3 Proposed Algorithm

45.3.1 Neural Network

Artificial neural networks mimic a structure to simulate the processing capability of the complex human nervous system. ANN simulates the ability of human central nervous system to learn from available data and predict with experience. So, mostly these ANNs are used in practical applications for prediction and classification. ANN comprises processing members called neurons that operate in a complementary way between multiple layers [5]. The interconnection between different layers is conducted with the help of weight and bias parameters. These two parameters are optimized by any kind of traditional and evolutionary optimization algorithm during the processing to get the better prediction ability of the network.

The current study concerns with input–output modeling of EBW process. Figure 45.1 describes the weld-bead geometric parameters. It is difficult to model

Fig. 45.1 Schematic view of bead geometric parameters



input–output relationships of a highly nonlinear and complex process, such as welding by capturing its physics. For this purpose, two neural networks, namely BPNN and RNN, had been used in this study, which is described below.

45.3.2 Back-Propagation Neural Network

As shown in Fig. 45.2, BPNN is made of three interconnected layers, namely input, hidden, and output layers. During the training of this network, calculations were done in forward direction, and error values were then propagated back to the subsequent layer. Three inputs ($i = 3$), namely voltage, beam current, and scanning speed along with three outputs ($j = 3$), namely bead penetration, bead width, and bead height, were given as input to the network for its training. The hidden layer comprises K neurons; a suitable value of K was chosen through a detailed parametric study. The Levenberg–Marquardt algorithm was used for the training of the network. As there is no generalized method or formula to calculate the number of neurons in

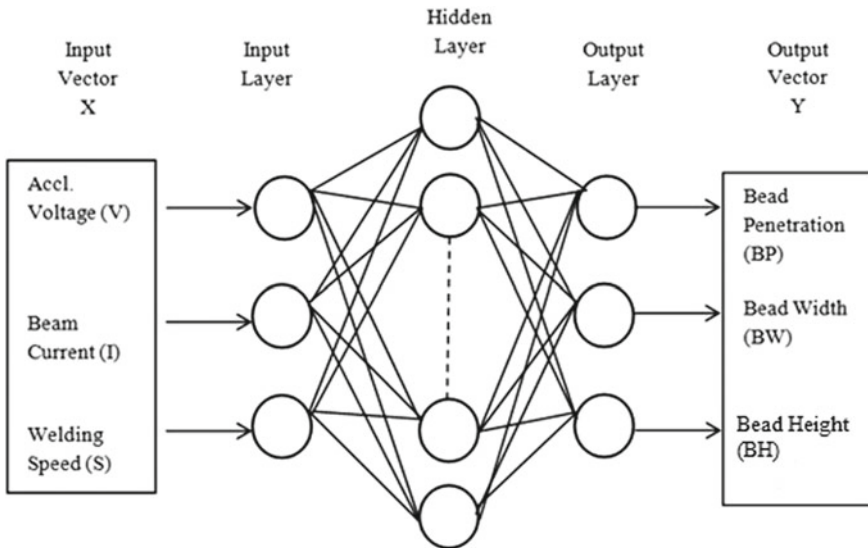


Fig. 45.2 Configuration of back-propagation feed-forward neural network (BPNN)

hidden layer and transfer function, parametric studies were conducted to get the optimized result. $[V]$ and $[W]$ are the connecting weights between input and hidden layers and hidden and output layers, respectively. In addition to this, here, these internal parameters were adjusted by the back-propagation algorithm and updated in subsequent iterations. Neural network toolbox under MATLAB R2015a software was used for developing the BPNN.

45.3.3 Recurrent Neural Network

Recurrent neural network (RNN) is a multi-layer neural network with a feedback connection, which forms a closed loop for the network. There are two primary ways, where feedback can be added to the multi-layer neural network. Practically, there are two popular forms of RNN, e.g., Elman network and Jordan network. Learning procedure of these networks also follows the gradient descent method.

Elman Network. Elman network is a multi-layer neural network with an extra context layer (input layer of Elman consists of both internal and external neurons). It has three layers, such as input, hidden, and output layers. The external inputs are fed into the network, and feedbacks are taken from the hidden neurons. The outputs of the hidden neurons are fed back as internal inputs to the network. Generally, the connecting weights between hidden and context neurons are kept fixed. These weights are updated during the training, and feedback connection weights are generally kept constant. The simplified view of this network is presented in Fig. 45.3. Here, W_1 , W_2 , and W_3 are weights between hidden and context layers, input and hidden layers, and hidden and output layers, respectively. The activation function of hidden layer in this RNN is a sigmoid function, and for the output layer, the used function is linear. If Y is output vector for k th neuron and $g(\cdot)$ represents the transfer function of output neuron, then it can be presented as Eqs. (45.4) and (45.5), respectively [7, 8].

$$Y(k) = g[W_3X(k)], \quad (45.4)$$

$$X(k) = f[W_1X_c(k) + W_2U(k - 1)], \quad (45.5)$$

where $X_c(k) = X(k - 1)$ and $f(\cdot)$ signifies the transfer function of the hidden layer, X_c denotes feedback or context layer vector, and U is the input vector of the considered system. The presence of context layer increases the probability of keeping track of previous dataset and refines it accordingly and able to capture the dynamic nature of the given network. Different combinations of several internal parameters and topology, i.e., hidden layer neurons, transfer function were tried. Levenberg—Marquardt algorithm was used for training of the network. Neural network toolbox under MATLAB R2015a software was used for developing the RNN. Here, Elman network parameters were also optimized through back-propagation algorithm to get a better comparison between multi-layer feed-forward and recurrent neural network.

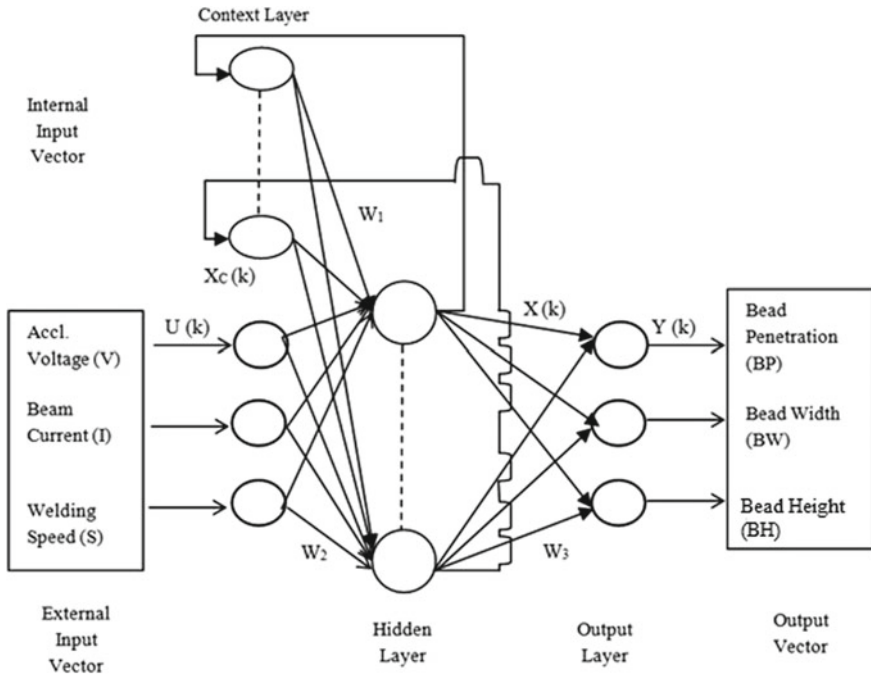


Fig. 45.3 Configuration of recurrent neural network (RNN)

45.4 Results and Discussion

Modeling of the EB welding with neural network consists of two phases, namely training and testing of the network with experimental welding results. For the training and testing, all experimental data were normalized in the range of 0–1. The performance criteria for the developed network were characterized by root mean square error (RMSE) and mean absolute percentage error (MAPE). The expressions used for evaluation of MAPE and RMSE are given in Eqs. (45.6) and (45.7), respectively.

$$MAPE = \frac{1}{n} \sum_1^n \left| \frac{y_{exp} - y_{cal}}{y_{exp}} \times 100 \right| \tag{45.6}$$

$$RMSE = \sqrt{\frac{1}{n} \left[\sum_1^n (y_{exp} - y_{cal})^2 \right]} \tag{45.7}$$

where y_{exp} is the target data found through experiment, y_{cal} is the predicted data by the network, and n is the number of training dataset.

The hidden layer neurons were varied from 2 to 10. The weights and biases were randomly initialized between -1 and 1 . Both the networks were trained with up to

1000 epochs. The modeling of the EBW process with the back-propagation network will be explained first. As shown in Fig. 45.2, three input parameters of the system were fed through three neurons in the input layer and passed through the hidden layer. At last, the output layer consists of three neurons, which would be nothing other than the outputs of the system. To fix up the hidden layer neurons and transfer functions of the different layers, a trial-and-error parametric study was performed. MAPE and RMSE values were used to converge during the training. From the parametric study, it was found that the minimum MAPE could be achieved as 4.740. This minimum MAPE was achieved using six neurons and tan-sigmoid transfer function at intermediate layer and linear transfer function at last layer. But, at the same time, if the convergence criteria were RMSE, then the network configuration changed to seven neurons and log-sigmoid transfer function at hidden layer. The minimum RMSE value was obtained as 0.117. From the above discussion, it could be concluded that there is no specific relationship among the number of neurons/topology with convergence criteria. No further reduction in RMSE and MAPE value was observed during the parametric study, even though the iteration number was increased. Figure 45.4a shows the variations of RMSE and MAPE with the number of neurons for BPNN. The network configuration of 3-7-3 with log-sigmoid function at intermediate layer and linear transfer function at final layer performed well as compared to other configurations tried during the parametric study. The average CPU time was 16–18 s in case of BPNN.

Next, the use of Elman network (RNN) to model electron beam welding process will be discussed. Here, the neurons at input layer were fed to hidden layer, and a feedback connection was established to get a context layer, which is having both external and internal input neurons. This cycle helped the network to compare and correct the deviation from the target. Here, the minimum MAPE and RMSE values were found as 4.645 and 0.116, respectively. These values pointed out the need of feedback in a dynamic system like welding. Although a similar trend was seen in case of MAPE for both the networks, a significant variation was visible in case of RMSE values for them. The network configuration corresponding to minimum MAPE observed was 3-9-3 with log-sigmoid transfer function at hidden layer. At the

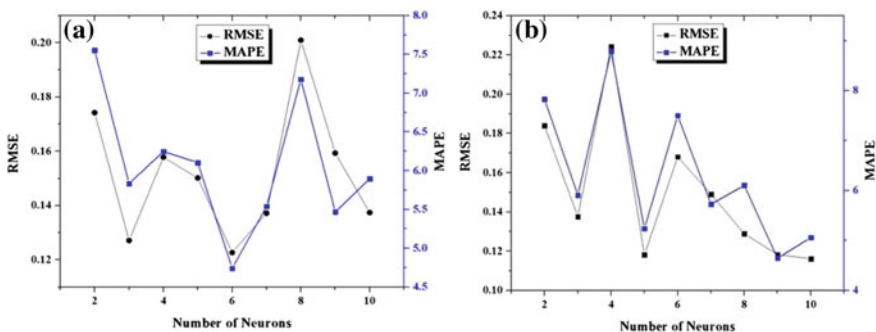


Fig. 45.4 Performance characteristics versus number of neurons a BPNN and b RNN

same time, the minimum of RMSE was achieved with the configuration of 3-10-3 with log-sigmoid transfer function. So, it was very hard to predict the optimized network for a given problem with multiple convergence criteria. But, this issue could be solved with one convergence criterion. The performance observed here led to a conclusion that recurrent network could be more precise with a proper parametric study and could outperform back-propagation feed-forward neural network. In other words, the recurrent neural network has better learning ability than the feed-forward neural. Figure 45.4b shows the variations of RMSE and MAPE with the number of neurons for RNN. For Elman algorithm, the optimized network configuration was obtained as 3-9-3 topology with log-sigmoid transfer function. The average CPU time was observed as 19–20 s for RNN.

Actual versus predicted values with different approaches are shown in Fig. 45.5 for bead penetration. From the figure, it could be seen that RNN had better predictability than feed-forward (BPNN) and regression, which was indicated by the higher R^2 value of RNN. It was also seen from the figure that the regression approach was not much precise in prediction of nonlinear process. Similar trend was also observed for BW and BH, so only for BP, the graph was shown.

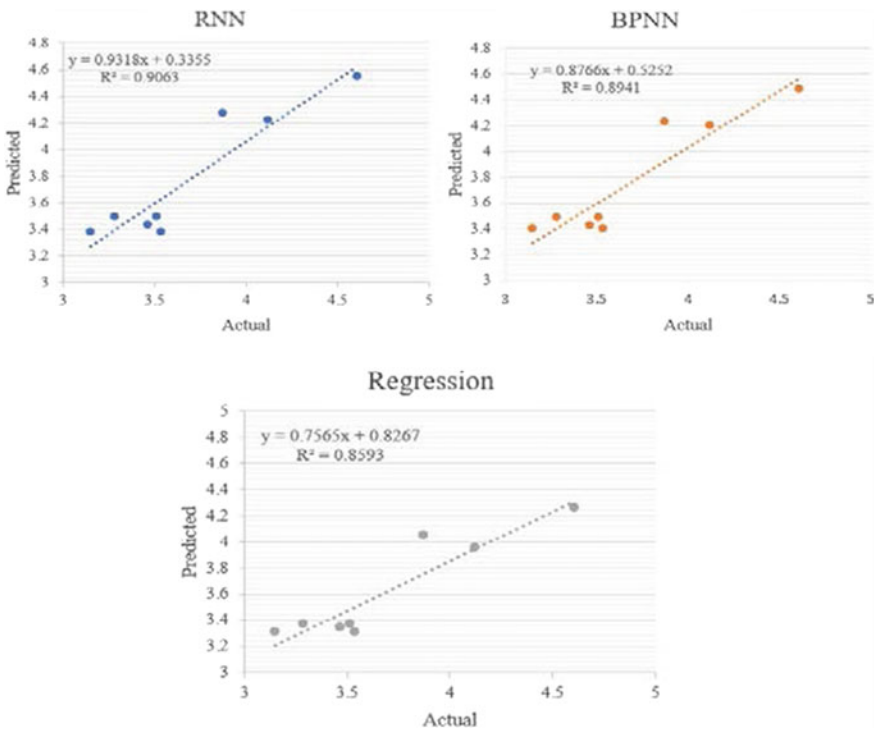


Fig. 45.5 Actual versus predicted values for test cases

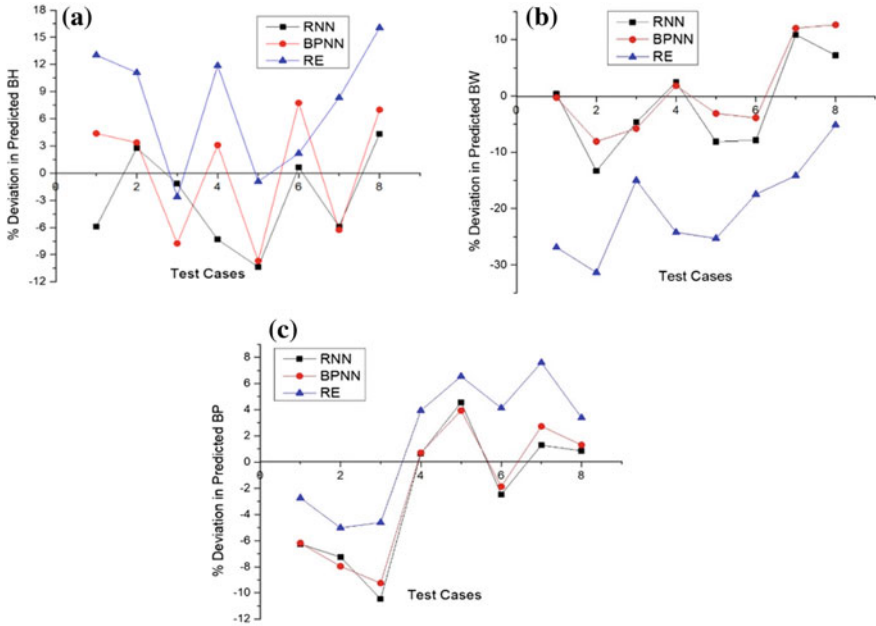


Fig. 45.6 Comparison of proposed approaches in terms of % deviation in predicted **a** BH, **b** BW and **c** BP on the test data

Comparisons were done on the basis of percent deviation in the prediction of bead width (BW), bead penetration (BP) and bead height (BH) on the test data with three approaches, namely BPNN, RNN, and regression analysis (RE). These results were shown in Fig. 45.6a–c. It was found that RNN and BPNN maintained similar trend for most of the configurations, but if the accuracies in predictions are considered, then RNN came out as clear winner over BPNN and conventional regression.

45.5 Conclusions

This study has described the applicability of both BPNN and RNN in modeling of input–output dependency of the electron beam welding process. The performances of these two approaches were also compared with the conventional regression analysis. The performance criteria (RMSE, MAPE) pointed out that RNN has better learning capability and adaptability for the dynamic system than BPNN and regression analysis. Although RNN has followed the same gradient descent method for learning, the presence of feedback makes the network more dynamic. The computation time of RNN is found to be 11% (around 2 s) higher than that of BPNN.

In future, a proper comparison among the various neural networks and neuro-fuzzy approaches for prediction capability will be considered for the study. In addition to

this, a suitable optimizer, namely, GA or PSO, will be associated with Elman network for tuning the internal parameters, so that a significant accuracy in prediction can be achieved.

Acknowledgements The authors thank the support received from Board of Research in Nuclear Science (BRNS), India, and from the Indian Institute of Technology (IIT) Kharagpur, for carrying out this study. The authors thank Dr. M. N. Jha for his valuable comment and suggestion.

References

1. Islam, M., Buijk, A., Rais-Rohani, M., Motoyama, K.: Process parameter optimization of lap joint fillet weld based on FEM-RSM-GA integration technique. *Adv. Eng. Softw.* **79**, 127–136 (2015)
2. Jaypuria, S., Doshi, N., Pratihari, D.K.: Effects of welding parameters on mechanical properties in electron beam welded CuCrZr alloy plates. *IOP Conf. Series Mater. Sci. Eng.* **338**(1), 012013 (2018)
3. Schultz, H.: *Electron Beam Welding*. Abington Publishing, England (2004)
4. Zhao, D., Ren, D., Zhao, K., Pan, S., Guo, X.: Effect of welding parameters on tensile strength of ultrasonic spot-welded joints of aluminum to steel—by experimentation and artificial neural network. *J. Manuf. Process.* **30**, 63–74 (2017)
5. Pratihari, D.K.: *Soft Computing: Fundamentals and Applications*. Narosa Publishing, New Delhi (2014)
6. Dey, V., Pratihari, D.K., Datta, G.L., Jha, M.N., Saha, T.K., Bapat, A.V.: Optimization of bead geometry in electron beam welding using a genetic algorithm. *J. Mater. Process. Technol.* **209**(3), 1151–1157 (2009)
7. Medsker, L.R.: *Recurrent Neural Networks: Design and Applications*. CRC Press LLC, Boca Raton (2001)
8. Lin, T., Horne, B.G., Tino, P., Giles, C.L.: Learning long-term dependencies in NARX recurrent neural networks. *IEEE Trans. Neural Netw.* **7**(6), 1329–1338 (1996)
9. Dutta, P., Pratihari, D.K.: Modeling of TIG welding process using conventional regression analysis and neural network-based approaches. *J. Mater. Process. Technol.* **184**(1–3), 56–68 (2007)
10. Balasubramanian, K.R., Buvanashakaran, G., Sankaranarayanan, K.: Modeling of laser beam welding of stainless steel sheet butt joint using neural networks. *CIRP J. Manuf. Sci. Technol.* **3**(1), 80–84 (2010)
11. Jha, M.N., Pratihari, D.K., Dey, V., Saha, T.K., Bapat, A.V.: Study on electron beam butt welding of austenitic stainless steel 304 plates and its input–output modelling using neural networks. *Proc. Inst. Mech. Eng. Part B J. Eng. Manuf.* **225**(11), 2051–2070 (2011)
12. Bagchi, A., Saravanan, S., Kumar, G.S., Murugan, G., Raghukandan, K.: Numerical simulation and optimization in pulsed Nd: YAG laser welding of Hastelloy C-276 through Taguchi method and artificial neural network. *Optik-Int. J. Light Electron Opt.* **146**, 80–89 (2017)
13. Pradhan, M.K., Das, R.: Recurrent neural network estimation of material removal rate in electrical discharge machining of AISI D2 tool steel. *Proc. Inst. Mech. Eng. Part B J. Eng. Manuf.* **225**(3), 414–421 (2011)
14. Manjunath Patel, G.C., Shettigar, A.K., Krishna, P., Parappagoudar, M.B.: Back propagation genetic and recurrent neural network applications in modelling and analysis of squeeze casting process. *Appl. Soft Comput.* **59**, 418–437 (2017)
15. Bennett, C., Dunne, J.F., Trimby, S., Richardson, D.: Engine cylinder pressure reconstruction using crank kinematics and recurrently trained neural networks. *Mech. Syst. Signal Process.* **85**, 126–145 (2017)

Chapter 46

Effect of Beam Offset on Dissimilar Laser Beam Welding of Ti6Al4V and Inconel 718 Superalloy



Anitesh Kumar Singh , Kalinga Simant Bal , Suman Sharma ,
Aditya Harbajanka , Mukesh Prasad , Dipanjan Dey 
and Asimava Roy Choudhury 

Abstract In the present investigation, an attempt has been made to identify the probable cause of welding defects, e.g. weld separation and crack, in the dissimilar welding of Ti6Al4V superalloy and Inconel 718 superalloy. Ti6Al4V and Inconel 718 sheets have been welded through offsetting the laser beam by 0.5 mm on either side of the weld centreline line. It was observed that weld separation occurred in the welded sample when the laser was offset towards Inconel 718; while the crack was observed in the welding area when the laser was offset towards Ti6Al4V. It might be possible that crack occurred as a result of chromium segregation due to supersaturation of solid solubility limit of chromium in both the alloys. Weld separation might have occurred due to the difference in coefficient of thermal expansion between Ti6Al4V and Inconel 718. Relatively higher cooling rate along with higher shrinkage tensile stress of Inconel 718 offset dissimilar weld caused weld separation.

Keywords Ti6Al4V · Inconel 718 · Dissimilar welding · Beam offset · Crack

46.1 Introduction

Titanium-based alloys and nickel-based alloys are two of the most extensively used super alloys in a variety of fields. Titanium alloys, specifically Ti6Al4V, are widely applicable in aerospace, biomechanical and automotive industries due to characteristics properties like (a) excellent corrosion resistance, (b) higher strength to weight ratio, (c) creep resistance, (d) toughness, (e) high yield stress and (f) biocompatibility. One of the major applications in the aerospace industry is to make components of the turbine engines [1]. Nickel-based Inconel 718 is also broadly used in aerospace industries due to its excellent mechanical properties and high resistance to oxidation at higher temperatures. These alloys are used to manufacture parts for elevated-temperature regions of gas turbines and aerospace engines [2]. During last

A. K. Singh · K. S. Bal · S. Sharma · A. Harbajanka · M. Prasad · D. Dey · A. Roy Choudhury (✉)
Laser Material Processing Laboratory, Mechanical Engineering Department, Indian Institute of
Technology Kharagpur, Kharagpur 721302, West Bengal, India
e-mail: archie@mech.iitkgp.ac.in

© Springer Nature Singapore Pte Ltd. 2020

533

M. S. Shunmugam and M. Kanthababu (eds.), *Advances in Additive Manufacturing and Joining*, Lecture Notes on Multidisciplinary Industrial Engineering,
https://doi.org/10.1007/978-981-32-9433-2_46

few decades, welding of dissimilar metals is attracting wide attention as it exploits the benefit of characteristics properties of both the joining materials, and also it can save material cost, improve design complexity and flexibility, as well as enhance the functionality of the product [3]. But the problem arises because of difference in the chemical and physical properties of dissimilar welding materials and brittle intermetallic phases formation, which degrade the mechanical properties of weld zone [4–6]. Titanium-based superalloy and nickel-based superalloy are used together specifically in the compressor section of gas turbine industries. Chen et al. [2] carried out a continuous-wave fibre laser welding of Ti6Al4V and Inconel 718. Presence of (a) welding defects such as cracks and pores and (b) brittle intermetallic phases were observed in the weld zone [2]. Gao et al. [7] have studied the pulsed laser beam welding of Ti6Al4V superalloy and Inconel 718 superalloy using niobium as an interlayer to prevent the precipitation of intermetallic brittle phases such as Ti–Cr, Ti–Ni and Ti–Fe. Krishnamoorthi [8] studied the microstructural characteristics of dissimilar laser joining of Inconel 718 and Ti6Al4V with and without interlayer addition in the weld zone. Chen et al. [9] have studied the mechanical properties and carried out microstructures analysis of dissimilar arc-welded Ti3Al and Inconel 718 with Ti–Ni–Nb filler alloy and Ti–Nb filler alloy. They observed that welding with Ti–Nb-type filler (a) produces less amount brittle interfacial phases and (b) improve tensile strength as compared to the addition of Ti–Ni–Nb-type filler alloys. Masayuki et al. [10] studied friction stir welding of pure titanium and Inconel 625, and observed the formation of two types of interface reaction layer on each side (i.e. titanium side and Inconel side). The reaction layers were found to contain titanium and nickel. Janasekaran et al. [11] studied the laser beam welding of Ti6Al4V and Inconel 718, and observed the intermetallic layers as NiTi and NiTi₂. It was reported that NiTi phase was produced due to primary recrystallization, while NiTi₂ phase was precipitated by reaction between NiTi phase and the cooling after NiTi columnar dendrite melting [11]. It has been reported [12] that when a bulk of the weld zone is solidifying, there is a narrow band of unmixed zone at the weld interface which solidified before mixing with the weld metal. This causes the brittle intermetallic phases formation. Zoeram et al. [13] observed that the brittle intermetallic phase (Ti₂Ni) reduces due to copper interlayer insertion, also it reduced the transverse cracks through the fusion zone and improves the mechanical properties of the laser-welded Ti6Al4V and Nitinol joint. Previous literatures show that welding of Ti6Al4V superalloy and Inconel 718 superalloy has weld defects such as cracks and pores, and the same has been reduced using selection of proper process parameters and selection of suitable interlayer at the joint interface. However, the cause–effect of laser beam offset on weld defects has not been studied. In the present investigation, an approach has been made to study the cause of welding defects in laser beam welding of Ti6Al4V superalloy and Inconel 718 superalloy sheets with the help of laser beam offset.

46.2 Experimental Detail

Ti6Al4V and Inconel 718 material sheets of 2.5 mm thick and dimension of 20 mm × 15 mm were sectioned in wire-EDM. Edge preparation was carried out by polishing the butt interface with SiC paper and cleaned with acetone before welding. These dissimilar alloys were then butt joined together by fibre laser operated in continuous-wave mode. The elemental composition is given in Table 46.1.

A 2 kW, 5-axis ytterbium fibre laser with the Gaussian intensity of 1070 nm wavelength and a spot diameter of laser beam 0.3 mm was used in this study. Argon shielding inert gas was supplied at the flow rate of 10 l/min to cover the fusion zone from contamination during welding. Dissimilar sheets were butt welded by keeping laser spot focused on the top surface with 1200 W laser power and 1200 mm/min welding speed. To study the effect of offset on the laser welding performance characteristics, at first, the laser beam was moved 0.5 mm (offset) from the joining line towards Ti6Al4V sheet and in the second case, towards Inconel 718. Microstructural analysis has been carried out on the samples. X-ray diffraction (XRD) of the weld zone was carried out with a scan angle (2θ) varying from 20° to 160°. The welded sample was sectioned perpendicular to the weld direction. Polishing has been done on MetaServ® 250 Grinder-Polisher with series of SiC paper of grade 400, 600, 800, 1200, 1500, 2500 and finally finished using 1 µm diamond abrasive. Keller's reagent (190 mL distilled water, 5 ml HNO₃, 3 ml HCl and 2 ml HF) was used to etch the sample for further analysis. Scanning electron microscope (SEM) and energy-dispersive X-ray spectroscopy (EDS) of the weld zone were performed to study the microstructure and weld bead profile to check the presence of any weld defects. Vickers microhardness test of the welded sample was carried out in tester at an indentation load of 50 g for a dwell time of 10 s.

Table 46.1 Elemental composition (wt%) of Ti6Al4V and Inconel 718

Elements	Ti6Al4V	Inconel 718
Al	6.49	0.49
Nb	–	3.85
Mo	–	2.16
Ti	86.64	0.99
V	5.43	0.59
Cr	–	17.88
Mn	–	0.88
Fe	1.44	18.60
Ni	–	54.55

46.3 Result and Discussion

46.3.1 Microscopic Analysis of the Laser Beam Welded Sample

Figure 46.1a, b shows the image of the laser-welded sample when the beam is offset on the Ti6Al4V side and Inconel 718 side, respectively. It could be observed from Fig. 46.1a that, when the beam of laser was offset to Ti6Al4V side, only crack was formed. On the other hand, when the beam of laser was offset to Inconel 718 side, weld separation occurred. Both the crack and resulting weld separation were longitudinal. Figure 46.2a shows the SEM image of weld profile for Ti6Al4V side offset-welded sample. A neck-tie-shaped weld zone was formed. Figure 46.2b shows the formation of a crack on welded zone near Inconel 718 side when offset was towards Ti6Al4V. This crack was observed to pass through the fusion boundary of the weld zone at the Inconel 718 interface of the weld. However, no weld separation was observed.

On the other hand, weld separation occurred in the Ti6Al4V interface when the laser was offset on the Inconel 718 side as could be seen from Fig. 46.2c, d. However, a difference in the weld crack propagation was observed in both cases. For sample welded with beam offset on the Ti6Al4V side, crack was found to follow the fusion boundary; while for sample welded with beam offset on Inconel 718 side, the crack (or weld separation) was found to travel straight along the weld interface between Inconel 718 and Ti6Al4V side instead of fusion boundary.

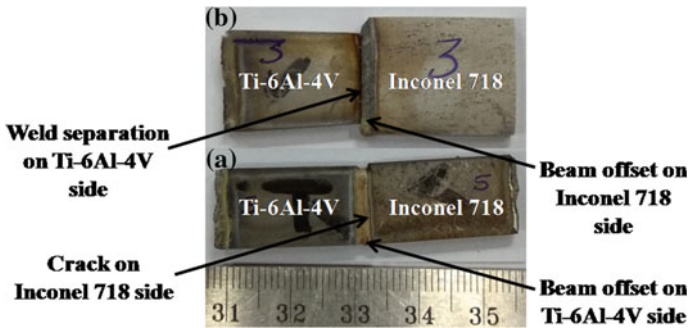


Fig. 46.1 Image of laser beam welded sample when beam is offset on **a** Ti6Al4V side and **b** Inconel 718 side

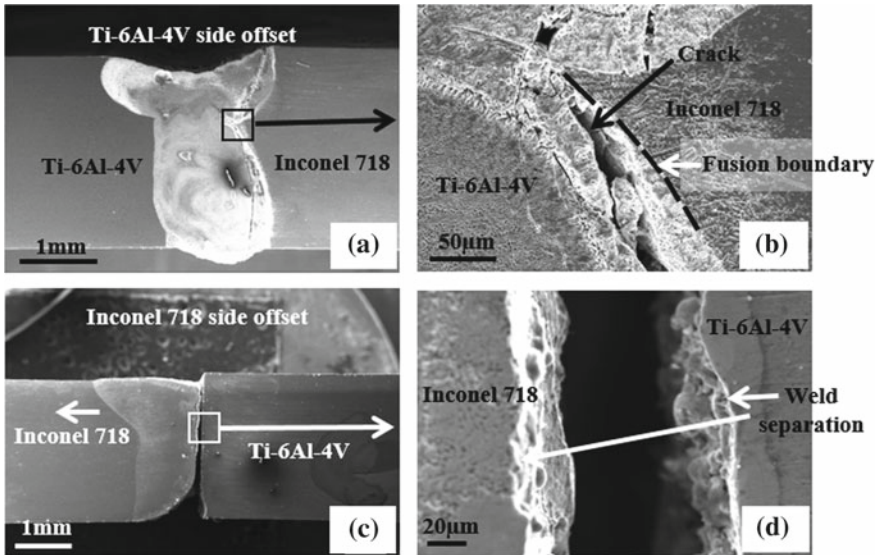


Fig. 46.2 SEM image of **a** weld profile, **b** crack near Inconel base, for Ti6Al4V side offset-welded sample. SEM image of **c** Inconel 718 side weld profile, **d** Ti6Al4V side weld profile, for Inconel 718 side offset-welded sample

46.3.2 Analysis of Crack Formation and Weld Separation

Crack and weld separation in the dissimilar joining of Ti6Al4V and Inconel 718 might have occurred due to following reasons:

- (a) Segregation of elements in the weld zone
- (b) Formation of intermetallic brittle phases in the welded zone
- (c) Difference in coefficient of thermal expansion of Ti6Al4V and Inconel 718

The points as mentioned earlier have been discussed below in detail.

Segregation of elements in the weld zone

When offset of the laser beam is on Ti6Al4V side

It has been reported [2] that Ti6Al4V has almost half of the thermal conductivity as compared to Inconel 718. The low thermal conductivity of Ti6Al4V would cause (a) excessive melting of the Ti6Al4V side of the dissimilar weld, and (b) concentration of heat at the interface between Ti6Al4V and Inconel 718. Also, simultaneous melting of Inconel 718 occurs due to its lower melting point. Melting of both the alloys leads to diffusion of elements. Elements from either side of the alloys would start to mix with each other in the bulk molten pool. Table 46.2 shows the result of EDS analysis carried out at various locations in the weld zone when the laser is offset on the Ti6Al4V side of the dissimilar joint. It was observed that Cr, Fe and Nb were

Table 46.2 EDS result for Ti6Al4V side offset

Element	Composition of Ti6Al4V base metal	Inconel 718 side of the weld zone	Crack in the weld zone	Ti6Al4V side of the weld zone	Composition of Inconel 718 base metal
Al	6.49	3.42	0.44	0.73	0.49
Nb	–	1.48	5.30	4.09	3.85
Mo	–	1.26	2.93	2.06	2.16
Ti	86.64	49.28	17.10	1.16	0.99
V	5.43	2.32	1.30	–	0.59
Cr	–	8.01	20.26	18.85	17.88
Mn	–	1.07	1.96	1.22	0.88
Fe	1.44	8.86	19.73	19.17	18.60
Ni	–	24.30	30.98	52.72	54.55

found to have a large difference in elemental composition in different regions of the welded sample. Melting causes diffusion of these elements from Inconel 718 towards the weld zone to mix with Ti6Al4V. Since Ti-matrix has definite solubility limit for Cr, Fe and Nb, the excessive concentration of these elements would cause saturation or supersaturation of the Ti6Al4V matrix. This causes segregation of elements and might lead to the formation of Cr–Fe–Nb-rich phase after weld zone solidification. Since Inconel 718 has a lower melting point, continued movement of Cr, Fe and Nb would cause saturation or supersaturation of Ti–Ni matrix at the fusion boundary. While Ti6Al4V weld side would have solidified earlier and could not dissolve any further elements segregated from the Inconel 718 side, the segregated elements or phase would solidify at last. The segregating elements are concentrated at the fusion boundary due to non-diffusion (caused due to saturation or supersaturation of Ti–Ni matrix) on either side. Hence, the crack would follow the path of the fusion boundary as shown in Fig. 46.2b.

Figure 46.3 shows the X-ray map image of the crack surrounded region at the interface of Ti6Al4V and Inconel 718 weld zone when the beam offset was towards Ti6Al4V sheet. The figure shows the presence of a higher concentration of Cr, Nb

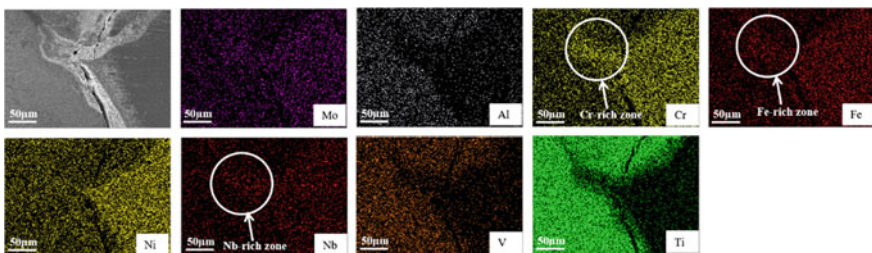


Fig. 46.3 X-ray map image of the crack surrounded region in the weld zone

and Fe. Hence, the supersaturation of these elements in the weld zone might be one of the reasons for crack formation.

When offset of the laser beam is on Inconel 718 side

When the laser is offset on Inconel 718 side, due to higher conductivity of Inconel 718, heat is conducted faster and simultaneously higher melt pool volume is formed due to the lower melting point of Inconel 718. Higher melting means more diffusion of elements in the molten pool of the weld zone. Table 46.3 shows the result of EDS analysis carried out at various locations in the weld zone when the laser is offset on the Inconel 718 side of the dissimilar joint. When Cr and Fe dissolution exceeds the Ti6Al4V limit, then these elements would get saturated or supersaturated at the interface of Ti–Ni weld matrix. This might lead to the formation of the highly segregated zone and would solidify at last. This unmixed zone of weld metal could have resulted in crack initiation followed by weld separation.

Figure 46.4 shows the X-ray map image of the weld separation region present at the interface of Ti6Al4V and Inconel 718 weld zone, when the beam offset was towards Inconel 718 sheet. It shows the presence of a higher concentration of Cr and Fe. Hence, the supersaturation of these elements in the weld zone might be one of the reasons for weld separation.

Table 46.3 EDS result for Inconel side offset

Element	Ti6Al4V side of the weld zone	Weld separation zone	Inconel 718 side of the weld zone
Al	4.36	2.67	1.30
Nb	0.83	1.04	6.83
Mo	0.33	0.40	2.98
Ti	52.61	12.09	2.84
V	3.59	1.81	0.78
Cr	6.23	21.82	17.11
Mn	1.02	2.72	1.14
Fe	6.26	15.08	15.71
Ni	24.27	42.37	51.32

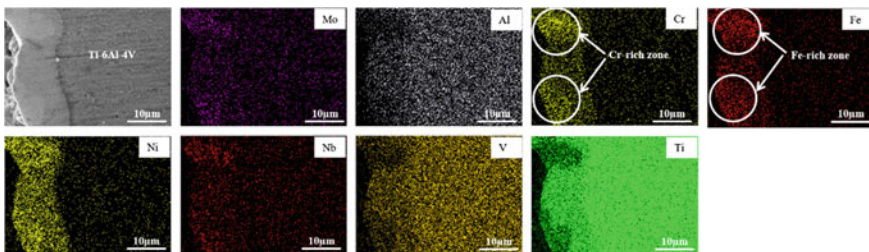


Fig. 46.4 X-ray map image of the weld separation region

Formation of intermetallic phases

It could be observed that segregation of elements had occurred in the weld joint of dissimilar laser-welded Ti6Al4V and Inconel 718 when the laser was offset on either side of the weld centreline. This would have resulted in the formation of intermetallic in the welded zone. XRD analysis was carried out to identify the various phases of formation in the weld zone. Figure 46.5a, b show the X-ray diffraction analysis of weld zone for dissimilar laser-welded Ti6Al4V and Inconel 718 when the laser is offset on Ti6Al4V side and Inconel 718 side, respectively.

It was observed that irrespective of the position of beam offset, γ' phase that mainly consisting of all the major elements such as Ni, Fe, Cr, Nb, Mo, Ti and Al were found in the welded zone. In addition, the formation of (a) Ni₂Ti phase consisting of Al, (b) Al-rich phase (i.e. Al-Fe and Al-Ni) and (c) Cr-Ti was also

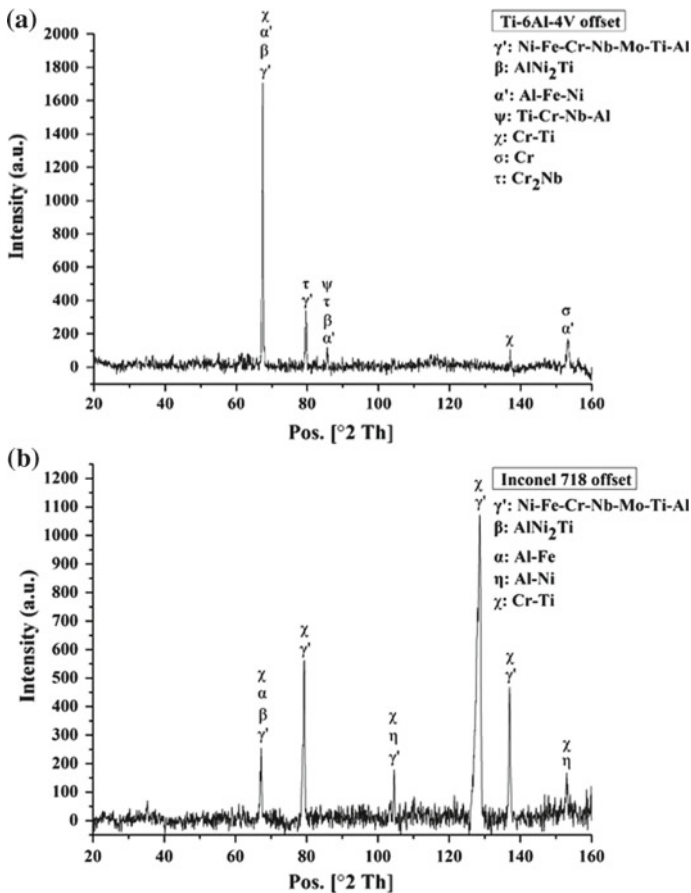


Fig. 46.5 X-ray diffraction analysis of weld zone for dissimilar laser-welded Ti6Al4V and Inconel 718 when beam is offset on **a** Ti6Al4V side and **b** Inconel 718 side

formed in the weld zone for both the cases. When the laser was offset on the Ti6Al4V side, intermetallic phases such as Ti–Cr–Nb–Al, Cr–Ti, Cr and Cr–Nb were formed. Similar intermetallics phases were found in the weld zone when the laser was offset on Inconel 718 side, except for the intermetallic phases were consisted mainly of Al and Cr. However, the major difference between the two cases for beam offset was found in the presence and absence of peaks such as 85°, 104° and 128°. The result of microhardness test of the weld zone is shown in Fig. 46.6a, b for both the cases of beam offset.

It was observed that, when the laser was offset on the Ti6Al4V side (Fig. 46.6a), the hardness of the weld zone was found to increase while moving from Ti6Al4V superalloy side to Inconel 718 superalloy side. When the laser was offset on the Inconel 718 side (Fig. 46.6b), the hardness of the weld zone was found to increase while moving from Inconel 718 side to Ti6Al4V side. However, hardness of the weld zone or intermetallic phases (when beam was offset on Ti6Al4V side as shown in Fig. 46.6a) were found to be more as compared to the hardness of the weld zone or intermetallic phases formed when laser was offset on Inconel 718 side (Fig. 46.6b). This could have been possible due to the formation of Al- and Cr-rich intermetallic phases inside the weld zone when the laser was offset on the Ti6Al4V side. It was interesting to note that the crack region (Fig. 46.6a) and weld separation region (Fig. 46.6b)

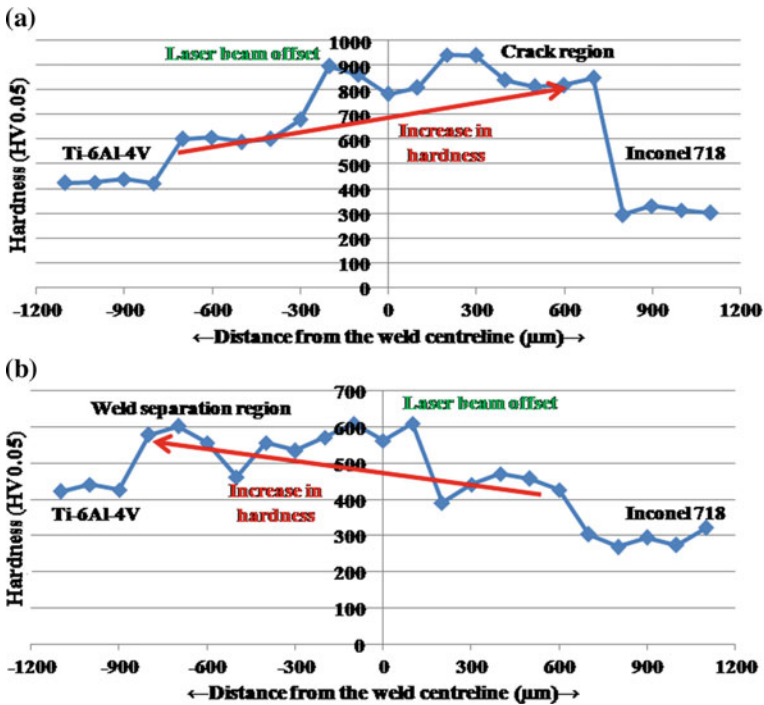


Fig. 46.6 X-ray diffraction analysis of weld zone for dissimilar laser-welded Ti6Al4V and Inconel 718 when beam is offset on a Ti6Al4V side and b Inconel 718 side

(Fig. 46.6b) found to higher hardness as compared to the other regions in the weld zone for dissimilar laser-welded Ti6Al4V and Inconel 718.

Difference in coefficient of thermal expansion of Ti6Al4V and Inconel 718

During welding, cracks or weld separation could form due to the difference in coefficient of thermal expansion and contraction of the Ti6Al4V and Inconel 718. It has been reported [2] that the coefficient of thermal expansion of Ti6Al4V is two-thirds of the coefficient of thermal expansion of Inconel 718. Since Inconel 718 expands and contracts more as compared to Ti6Al4V, this difference in expansion and contraction would result in differential shrinkage during the cooling cycle of the welding. Inconel 718 with a higher coefficient of thermal expansion would shrink more, and this differential shrinkage induces tensile stress in the Inconel 718 side of the weld, while comparatively less tensile stresses would develop on the Ti6Al4V side of the weld.

Figure 46.7 shows the value of residual stress about the weld separation when the laser was offset on Inconel 718 side. Development of tensile stresses during cooling might has resulted in the formation of cracks. Weld separation might be possible if the tensile stress exceeds the ultimate tensile stresses of one of the joining metal. In the present study, higher tensile stress, i.e. 303.80 MPa in Inconel 718 interface as compared to 194.32 MPa in Ti6Al4V interface was developed after weld solidification that led to the formation of cracks at the fusion boundary. Also, a difference in thermal conductivity produces differential rates of heating and cooling

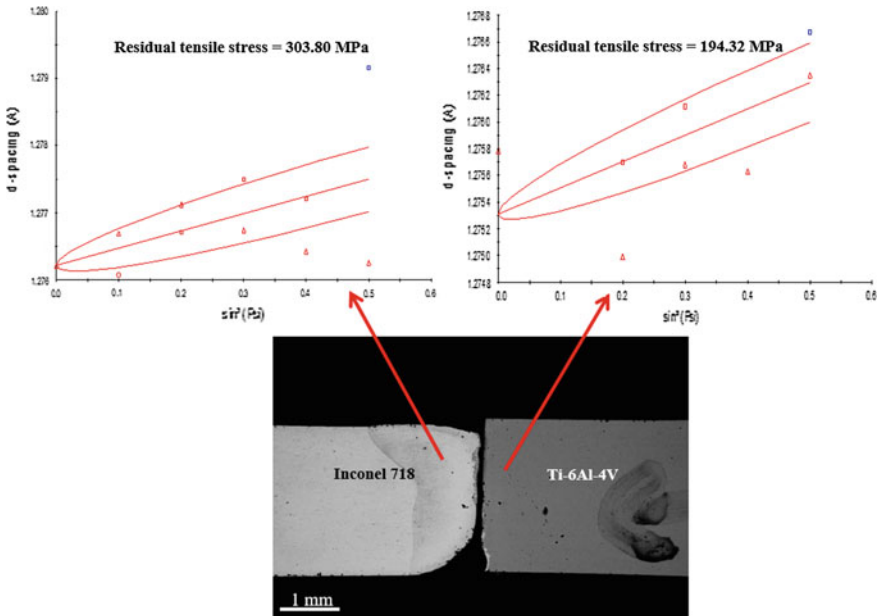
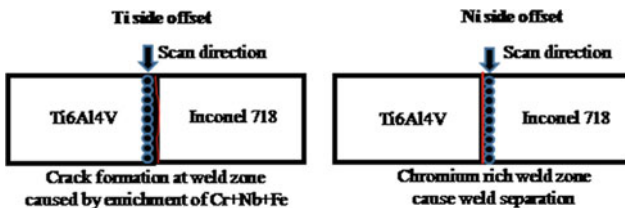


Fig. 46.7 Residual stress measurement about the weld separation

on the two sides of the weld joint during and after the welding cycle. Inconel 718 would draw heat away and would melt fast as compared to Ti6Al4V, and the uneven heat flow would lead to incomplete dilution or fusion of Inconel 718 elements. Uneven heat flow leads to thermal gradient and results in the development of thermal stresses.

46.4 Conclusion

1. In the present investigation, a study on the cause of cracks in the welded zone of dissimilar laser-welded Ti6Al4V and Inconel 718 has been carried out with the help of beam offset about the centreline. It was observed that weld separation occurred in the sample, when offset of the laser beam was on Inconel 718 side; while a crack was observed in the welded sample, when the laser was offset towards Ti6Al4V.
2. While Ti6Al4V solidifies first, Inconel 718 is still to get solidified, and hence the formation of intermetallic phase rich in Cr, Nb and Fe at the end of the solidification might have led to crack formation when offset of the beam was on the Ti6Al4V side.
3. When the laser was offset on Inconel 718 side, weld separation might have occurred due to the formation of the intermetallic phase rich in Cr, Al and Fe. Also, higher shrinkage tensile stresses developed in the Inconel 718 side of the weld zone might be one of the factors that could result in weld separation.
4. It was observed that the region near the crack and weld separation was found to higher hardness as compared to the other regions in the weld zone. Hence, the formation of hard and brittle intermetallic secondary phases could have formed in the dissimilar weld zone.
5. It might be possible that crack and weld separation occurred as a result of chromium segregation due to supersaturation of solid solubility limit of chromium in both the alloys.



References

1. Shen, Y., Liu, Y., Sun, W., Dong, H., Zhang, Y., Wang, X., Zheng, C., Ji, R.: High-speed dry compound machining of Ti6Al4V. *J. Mater. Process. Technol.* **224**, 200–207 (2015). <https://doi.org/10.1016/j.jmatprotec.2015.05.012>
2. Chen, H.C., Pinkerton, A.J., Li, L.: Fibre laser welding of dissimilar alloys of Ti6Al4V and Inconel 718 for aerospace applications. *Inter. J. Adv. Manuf. Technol.* **59**, 977–987 (2011). <https://doi.org/10.1007/s00170-010-2791-3>
3. Olabi, A.G., Alsinani, F.O., Alabdulkarim, A.A., Ruggiero, A., Tricarico, L., Benyounis, K.Y.: Optimizing the CO₂ laser welding process for dissimilar materials. *Opt. Laser. Eng.* **51**, 832–839 (2013). <https://doi.org/10.1016/j.optlaseng.2013.01.024>
4. Anawa, E.M., Olabi, Abdul-Ghani: Control of welding residual stress for dissimilar laser welded materials. *J. Mater. Process. Technol.* **204**, 22–33 (2008). <https://doi.org/10.1016/j.jmatprotec.2008.03.047>
5. Lee, W.B., Schmuecker, M., Mercado, U.A., Biallas, G., Jung, S.B.: Interfacial reaction in steel–aluminum joints made by friction stir welding. *Scripta Mater.* **55**, 355–358 (2006). <https://doi.org/10.1016/j.scriptamat.2006.04.028>
6. Torkamany, M.J., Tahamtan, S., Sabbaghzadeh, J.: Dissimilar welding of carbon steel to 5754 aluminium alloy by Nd:YAG pulsed laser. *Mater. Des.* **31**, 458–465 (2010). <https://doi.org/10.1016/j.matdes.2009.05.046>
7. Gao, X.L., Liu, J., Zhang, L.J.: Dissimilar metal welding of Ti6Al4V and Inconel 718 through pulsed laser welding-induced eutectic reaction technology. *Int. J. Adv. Manuf. Technol.* **96**, 1061–1071 (2018). <https://doi.org/10.1007/s00170-018-1633-6>
8. Krishnamoorthi, J.: Studies on joining of Ti 6Al 4V with inconel 718 and stainless steel 304l by diffusion bonding and friction welding. *Shodhganga* (2012). <http://r.inflibnet.ac.in:8080/jspui/handle/10603/17485>
9. Chen, B., Xiong, H., Sun, B., Tang, S., Du, B., Li, N.: Microstructures and mechanical properties of Ti3Al/Ni-based joints arc welded with Ti–Nb and Ti–Ni–Nb filler alloys. *Prog. Nat. Sci. Mater. Int.* **24**, 313–320 (2014). <https://doi.org/10.1016/j.pnsc.2014.06.003>
10. Masayuki, A., Taku, I., Isao, N., Yoshikazu, T., Kazuo, M.: Dissimilar lap joining of commercial pure titanium to nickel-based alloy by friction stir welding. *Weld. Soc. Pap.* **35**, 85–88. <https://doi.org/10.2207/qjwvs.35.85s>
11. Janasekaran, S., Tan, A., Yusof, F., Abdul Shukor, M.: Influence of the overlapping factor and welding speed on T-joint welding of Ti6Al4V and Inconel 600 using low-power fiber laser. *Metals* **6**, 134 (2016). <https://doi.org/10.3390/met6060134>
12. Anthony, R. (Ed.): *Encyclopedia of Chemical Processing and Design*, Vol. 69 (Supplement 1). CRC Press, New York (2001)
13. Zoeram, A.S., Akbari Mousavi, S.A.A.: Laser welding of Ti–6Al–4V to nitinol. *Mater. Des.* **61**, 185–190 (2014) <https://doi.org/10.1016/j.matdes.2014.04.078>

Chapter 47

Study on the Dissimilar Joining of Martensitic Stainless Steel and Carbon Steel Using TIG Welding



S. Karthi , S. P. Kumaresh Babu , S. Shanmugham  and V. P. Balaji 

Abstract Dissimilar metal joints are of great interest in many industries. This paper deals with the study on dissimilar fillet joints made by tungsten inert gas welding (TIG) with various shielding gas and filler combinations. Design of experiments performed to optimize the right combination of the process. Metallurgical and mechanical characterization on the dissimilar joints made by TIG welding process was carried out and compared with dissimilar joints made by friction welding. Weldment corrosion behavior was studied by using the potentiodynamic instrument. Dissimilar welding is done by TIG welding process using duplex stainless filler wire with argon shielding gas shown an appreciable increase in pull out strength while compared with other combinations. The dissimilar joint made by duplex stainless steel filler (ER2209) exhibits better pitting corrosion resistance than austenitic stainless steel filler (ER309L).

Keywords Dissimilar welding · Low-carbon steel · Martensitic stainless steel · Microstructure · Duplex filler wire · Potentiodynamic polarization

47.1 Introduction

Dissimilar joining is of great importance in automotive industries to improve fuel economy with maintaining or improving safety and performance by the best combination of different strength materials in the structure. Multi-material perception including a hybrid of light metals is now a trend for the automotive industry. Examples of dissimilar welding in the automotive industry such as body structure, power train parts like turbocharger impeller, etc., steels, owing to their interesting properties such as reusability, matured state of the art, and relatively low cost, have historically

S. Karthi (✉) · S. P. Kumaresh Babu · S. Shanmugham
Department of Metallurgy and Materials Engineering, National Institute of Technology,
Tiruchirappalli, India
e-mail: vinoth.karthi@gmail.com

V. P. Balaji
Research and Development, WABCO India Limited, Chennai, India

© Springer Nature Singapore Pte Ltd. 2020
M. S. Shunmugam and M. Kanthababu (eds.), *Advances in Additive Manufacturing and Joining*, Lecture Notes on Multidisciplinary Industrial Engineering,
https://doi.org/10.1007/978-981-32-9433-2_47

been the favored choice for structural application in automotive industry. However, it is appropriate that not a single material can fit all applications. These situations give rise to dissimilar metal welds. Dissimilar metal welding refers to the joining of two different alloy systems. In fact, all fusion welds are dissimilar metal welds. Since the metals are being joined have a wrought structure and the welds have cast structure. Frequently, the corresponding composition filler metal deliberately alters the weldment from the base alloy [1]. The importance of joining dissimilar materials often arises in industrial materials to impart complex shape, different loading or performance conditions needed in different parts of the wide variety of assembly such as high strength and corrosion resistance [2, 3]. Friction/friction stir welding is the most widely used process for joining of different materials, and enough researches are carried out [4]. Very limited work is carried on fillet joint dissimilar welding by an arc welding process, especially for industrial application. This research work aims to study the effect of various filler and shielding gas combination on dissimilar joints by TIG welding process and compare with the dissimilar joints made by the friction welding process.

47.2 Experimental Work

The push rod assembly is the combination of rod and plate. Plate material is made of FE 410 low-carbon steel sheet of 8 mm thickness, and rod material made of AISI 420 martensitic stainless steel rod with 16 mm diameter was used in these experiments. The chemical composition and mechanical properties of base materials and filler wires are listed in Tables 47.1 and 47.2. Microstructures of the base materials are

Table 47.1 Chemical composition of the base materials and filler wires

Composition wt%								
Specimen materials	C	Mn	Si	P	S	Cr	Ni	Mo
Stainless steel	0.187	0.71	0.55	0.03	0.017	12.79	0.06	0.023
Steel	0.072	0.296	0.022	0.0063	0.007	0.009	0.008	0.005
ER309L	<0.03	1–2.5	0.3–0.65	<0.03	<0.03	23–25	12–14	<0.75
ER2209	<0.03	0.5–2	<0.9	<0.03	<0.03	21.5–23.5	7.5–9.5	2.5–3.5

Table 47.2 Mechanical properties

Mechanical properties	Stainless steel	Low-carbon steel	ER2209	ER309L
Tensile strength (N/mm ²)	777	449	723	600
Yield strength (N/mm ²)	598	370	555	400
Elongation (%)	16	36	26	40

shown in Fig. 47.1. 3% nital is used to etch the steel part, and kalling's reagent is used to etch the stainless steel [5]. Push plate microstructure consists of a mixture of ferrite and pearlite, and rod microstructure consists of fully martensite structure. Duplex stainless steel (ER2209) and austenitic stainless steel (ER309L) filler wires of 2 mm diameter have chosen for this research work to join the push plate and push rod [6]. Duplex stainless filler wire offers excellent pitting resistance and twice as strong as austenitic filler grades. Argon (Ar) and oxygen (O_2) gases were used as shielding gases with a flow rate of 8 LPM for all the trials. The applied voltage is 18 V, and maintained current is 140 A. Calculated heat input value for all the trial is 2.1 kJ/mm. Figure 47.2 shows the push rod assembly part after welding.

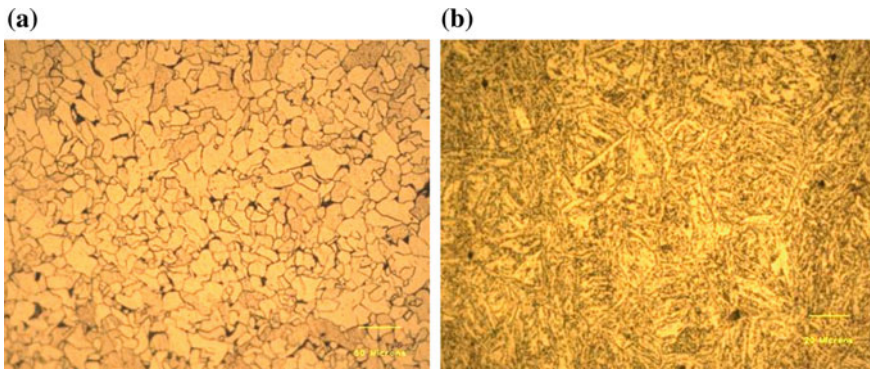


Fig. 47.1 Base material microstructures. **a** Push plate material etched with 3% nital @ 200 \times magnification. **b** Rod material etched with kalling's reagent @ 500 \times



Fig. 47.2 Push rod assembly welded with different filler wires and gas mixtures

47.3 Results and Discussions

Design of experiment (DOE) study conducted to choose the minimum sample size for the pull out testing, and results are analyzed with the help of Minitab tools. DOE is planned with two factors such as filler metal and shielding gas. Table 47.3 indicates the variable factor and the design of experiment plan. The full factorial design is used for DOE considering two factors with two levels and two replicates. Based on design of experiment, eight runs of experiments were done.

47.3.1 Pull Out Test

Pull out test is performed to find out the weld separation load, and the results were compared with friction-welded sample. Pull out test results are presented in Tables 47.4 and 47.5, respectively. Samples were welded with duplex stainless steel filler wire (ER2209) with 100% Ar shielding gas combination resulted in higher pull-

Table 47.3 Variable factor

Factors	Parameter	1	2
A	Filler	ER2209	ER309L
B	Shielding gas	100% Ar	98% Ar + 2% O ₂

Table 47.4 Pull out load

DOE trial	Filler metal	Shielding gas	Pullout load (KN)
1	ER2209	100% Ar	126.7
2	ER2209	98% Ar + 2% O ₂	118.75
3	ER309L	98% Ar + 2% O ₂	101.4
4	ER2209	98% Ar + 2% O ₂	102.85
5	ER309L	100% Ar	100.2
6	ER2209	100% Ar	115.9
7	ER309L	98% Ar + 2% O ₂	95
8	ER309L	100% Ar	96.8

Table 47.5 Friction-welded sample pull out load

Sample ID	Pull out load (KN)
Sample 1	105
Sample 2	93

out load than other combinations. Approximately 15% increase in pullout strength is observed when compared with friction-welded sample. Effect of varying filler wire is analyzed by using the main effect plot as shown in Fig. 47.3.

The analysis shows that ER2209 filler wire is having higher pullout load than other combinations. Pareto chart worked out to know the influence of different factors as shown in Fig. 47.4 which clearly indicated that filler wire influenced the weld strength than shielding gas.

Fig. 47.3 Main effect plot

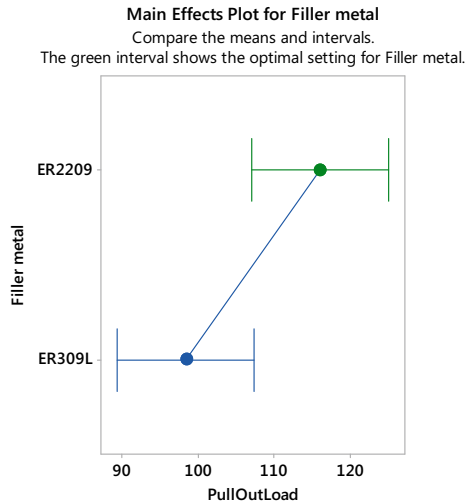
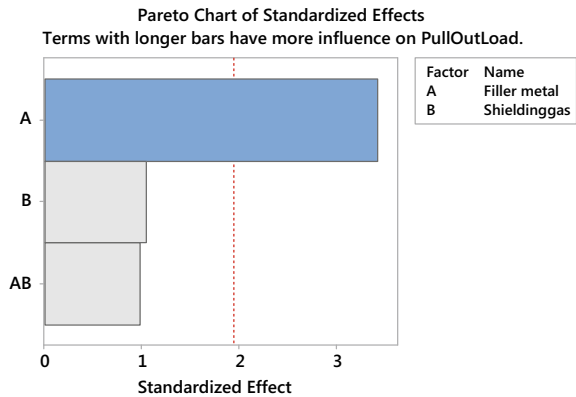


Fig. 47.4 Pareto chart



47.3.2 Hardness Survey

In order to understand the higher pullout load in duplex stainless steel (ER2209) filler wire, hardness survey was carried out using Shimadzu micro-Vickers hardness tester (model number HMV-2TE) on ER2209 + 100% Ar weldment sample, and results are compared with a friction-welded part. While hardness testing, 300 g test force applied. Traverse hardness survey was taken from the center of weld face to the base metal (low-carbon steel side), i.e., from weldment to plate side as shown in Fig. 47.5. Observed hardness in sample welded with ER2209 + 100% Ar is quite higher than friction-welded sample which is in linear relation with pull out load as shown in Fig. 47.6. This hardness increased mainly due to the presence of hard-phase microstructure constituents of acicular martensite structure.

47.3.3 Microstructure Analysis

To study the microstructural features of the welded part, the cut section is made from the selective portion of the push rod sample. Cut portion is properly grounded and molded with plastic material. The molded portion is polished with silicone carbide

Fig. 47.5 Refer the actual molded sample

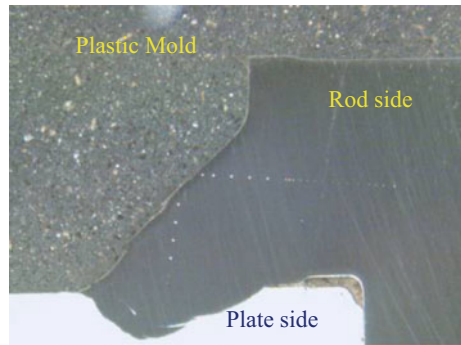
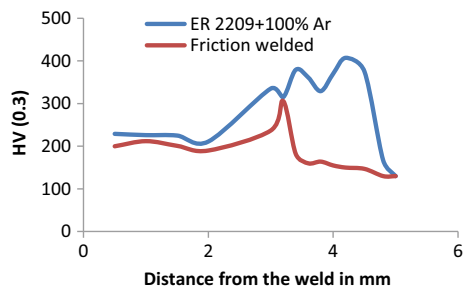


Fig. 47.6 Hardness survey from weldment to carbon steel



abrasive sheets. Final polishing was done using 0.5 μm diamond suspension fluid and etched with 3% nital solution and then examined the surface with help of optical microscope. Filler metal composition, cooling rate, and dilution were the important elements to decide the weldment microstructure [7]. Figure 47.7 represents the microstructure of various zones. Figure 47.7a represents heat-affected zone of the push plate welded by the friction welding process. Ferrite and pearlite structures were observed. Remaining microstructure denotes the weldment structure joined by TIG welding process by using different filler wires and shielding gas combinations.

Figure 47.7b denotes the microstructure of acicular ferrite (α -ferrite-darker area), austenite (Lighter area) along with upper bainite and which is responsible for ER2209 weldment higher pull out strength. These weldment microstructural features are not seen in ER309L and friction-welded samples. ER2209 weldment had an equal proportion of both α -ferrite and austenite phase with the matrix comprising ferrite and which is an advantage in terms of mechanical and corrosion behavior. In ER309L weldment, between base metal and weld, the formation of equiaxed austenite grains noticed as shown in Fig. 47.8c, d [8]. Dendritic coring is characteristic of rapidly

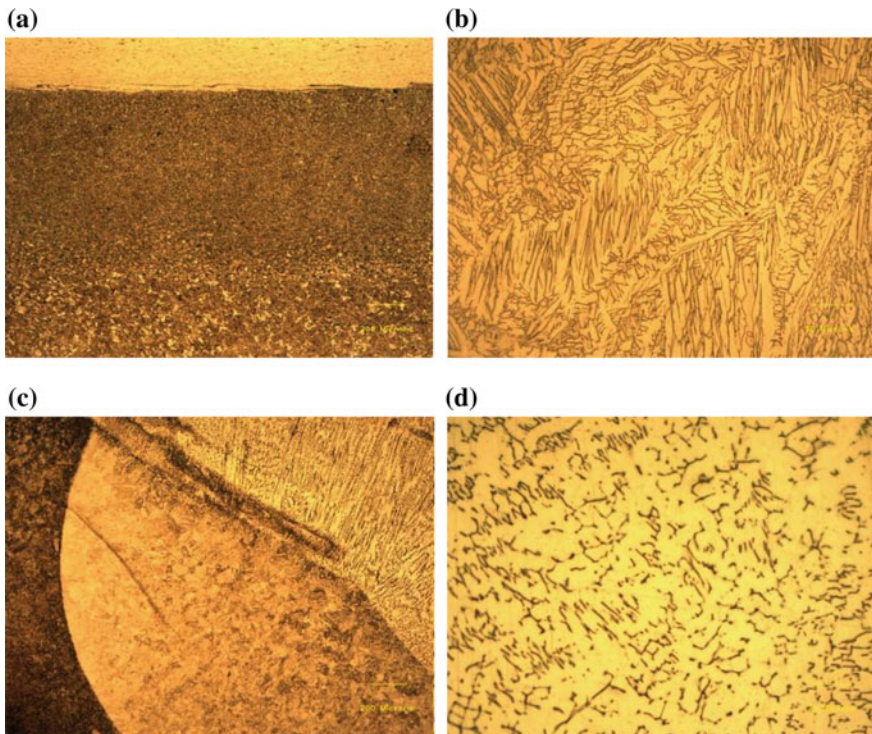


Fig. 47.7 a Friction-welded HAZ zone @ 50 \times . b Weldment of ER2209 filler @200 \times . c, d Show the HAZ and weldment structures of ER309L magnified with 50 \times and 200 \times , respectively

frozen austenitic weld metal. The composition of the bead depends not only on the compositions of the base and filler metals but also on the extent of dilution.

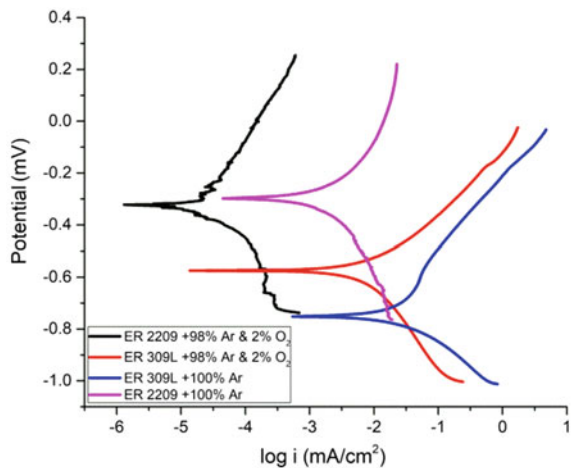
47.3.4 Corrosion Study

In order to study the effect of dissimilar material in the joints on corrosion, the potentiodynamic study was conducted. Weldment samples were cut from the actual pushrod sample for standard potentiodynamic polarization tests. Electric wires were attached on top of the weldment samples, and samples were covered by polypropylene based material in order to expose weldment alone.

Polished weldment is exposed to the testing and remaining surfaces covered with plastic film. Exposed surface was thoroughly cleaned by acetone solvent and dried in air. 1 cm × 1 cm area of the sample was exposed to 5% sodium chloride electrolyte. Saturated potassium chloride is taken as the reference electrode and platinum wire as the counter electrode. Potentiodynamic experiments were carried out according to ASTM G-61 [9]. pH of the electrolyte solution is 7.2, and the conductivity of the solution is 39 $\mu\text{S}/\text{cm}$.

Figure 47.8 represents the potentiodynamic polarization test results. The corrosion behavior of weldment using ER2209 filler exhibits superior resistance for corrosion pit initiation than weldment of ER309L filler wire [10]. Duplex phases are grades which are highly resistant to chloride stress-corrosion cracking and have excellent resistance to pitting and crevice corrosion [11]. It is about twice as strong as the standard austenitic stainless steel. Combination of alloying elements such as molybdenum and chromium is beneficial for the pitting corrosion of the weldment in ER2209 while compared with ER309L.

Fig. 47.8 Potentiodynamic polarization test results for various dissimilar weldments



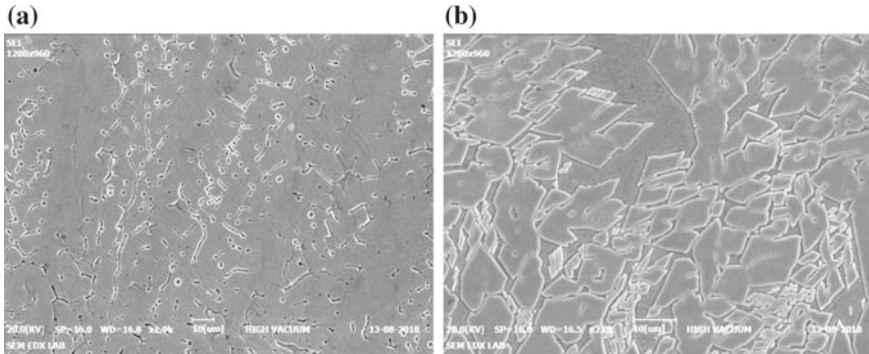


Fig. 47.9 **a** ER309L weldment SEM-EDAX analysis results and **b** represents the ER2209 weldment SEM-EDAX analysis

Table 47.6 EDAX compositions of the weldment

Composition wt%					
Specimen	Si	Mn	Cr	Ni	Mo
ER2209 weldment	0.4	1.16	17.72	5.57	1.87
ER309L weldment	0.23	1.02	15.24	6.29	0.08

47.3.5 SEM-EDAX Analysis

In order to understand the micro structural and chemical features of the dissimilar weldments, cut portion of the weldment is exposed to scanning electron microscope. Figure 47.9a, b represent the SEM analysis of duplex filler (ER2209) weldment and austenitic filler (ER309L) weldment, respectively. SEM structure also confirms the austenite coring structure in ER309L weldment and duplex microstructure in ER2209 weldment.

Table 47.6 shows EDAX values of both ER309L and ER2209 weldment, respectively. ER2209 EDAX pattern shows higher molybdenum in the weldment while compared with ER309L weldment. Pitting Resistance Equivalent Number (PREN) for ER2209 and ER309L weldments is 23.9 and 15.4, respectively, which is the clear evidence of higher corrosion resistance of ER2209 weldment

47.4 Conclusions

AISI 420 Martensitic stainless steel and Fe 410 low-carbon steel can be welded together with TIG welding process by using ER2209 or ER309L with proper argon and oxygen gas mixture. ER2209 with 100% Ar combination resulted in 15% higher pullout strength than friction-welded sample and other combinations. Presence of

hard-phase microstructure constituents in ER2209 weldment resulted in higher hardness and higher strength than friction-welded sample. Austenitic steel (ER309L) weldment shows lesser corrosion resistance for pitting corrosion than duplex stainless (ER2209) weldment due to lower PREN value. Dilution effect and higher alloying elements along with dual-phase microstructure resulted the better corrosion and mechanical properties in ER2209 while compared with ER309L and friction-welded parts.

Acknowledgements The authors would like to acknowledge the WABCO India Limited, to support this research work.

References

1. Bailey, N.: *Welding Dissimilar Metals*. The Welding Institute, Cambridge, UK (1986)
2. Shahid, F.: *Mechanical and Microstructural Analysis of Dissimilar Metal Welds*. Department of Aeronautics and Astronautics, Institute of Space Technology, Islamabad
3. Kumar, N., Yuan, W., Mishra, S.R.: *Friction Stir Welding of "Dissimilar Alloys and Materials"*. Butterworth-Heinemann, Oxford (2015)
4. Ma, H., Qin, G., Geng, P., Li, F., Fu, B., Meng, X.: Microstructure characterization and properties of carbon steel to stainless steel dissimilar metal joint made by friction welding. *Mater. Des.* **86**, 587–597 (2015)
5. *Metals Handbook: Atlas of Microstructures of Industrial Alloys*, Vol. 7. American Society for Metals, USA (1973)
6. AWS A5.9/A5.9M:2012: *Specification for Bare Stainless Steel Welding Electrodes and Rods*. American Welding Society, USA (2012)
7. Barnhouse, E.J., Lippold, J.C.: Microstructure/property relationships in dissimilar welds between duplex stainless steel and carbon steels. *Weld. Res. J.* **77** (1998)
8. Ku, S.: *Welding Metallurgy*, 2nd edn. (2002)
9. ASTM G-61:1986: *Standard Test Method for Conducting Cyclic Polarization Measurements for Localized Corrosion Susceptibility of Iron, Nickel or Cobalt-Based Alloys*
10. Xiong, J., Tan, M.Y., Forsyth, M.: The corrosion behaviors of stainless steel weldments in sodium chloride solution observed using a novel electrochemical measurement approach. *Desalination* **327**, 39–45
11. Davis, J.R.: *Corrosion of Weldments*. ASM International, Materials Park, USA (2006)

Chapter 48

Influence of Tool Probe Offset and Traverse Speed on Microstructure and Mechanical Properties of Friction Stir Weld Dissimilar Joints of AA2024-T351 and AA7075-T651



K. S. Anil Kumar , S. M. Murigendrappa  and Hemantha Kumar 

Abstract The effect of tool probe offset and varying traverse speed on the mechanical and metallographic characteristics of friction stir weld dissimilar joints of AA2024-T351 to AA7075-T651 in butt joint configuration produced using taper-threaded tool with constant tool rotation speed, 650 rpm and plunge depth, 6.2 mm are investigated. The tool traverse speed was varied from 20 to 120 mm/min along the weld length with the different tool probe offset condition. Optical microscopy and scanning electron microscopy are used to characterize the grain size and microstructural modification at the weld nugget zone (WNZ). The effect of different tool offset conditions in conjunction with varying traverse speed results in banded structure of alloys, partial material mixing and unmixed region at the WNZ. The combination of tool offset distance of 1 mm towards AA7075-T651 with traverse speed, 110 mm/min yields maximum ultimate tensile strength, 436 MPa, yield strength, 375 MPa, elongation, 14% and weld joint efficiency, 92%.

Keywords Dissimilar alloys · Friction stir welding · Aluminium alloy · Tool offset · Tool traverse speed · Microstructure

48.1 Introduction

Friction stir welding (FSW) technique invented and patented by the welding institute (TWI) shown its capability as a most promising method of solid-state metal joining technique in joining similar or dissimilar metals and presents several advantages of over the occurrence of the types of defects (e.g. porosity, slag inclusion, cracks) in the joints fabricated by conventional fusion welding method like TIG, laser technique [1, 2]. The joining process in FSW involves the action of a rotating tool plunged

K. S. Anil Kumar (✉) · S. M. Murigendrappa · H. Kumar
Department of Mechanical Engineering, National Institute of Technology Karnataka, Surathkal
575025, India
e-mail: anilkumar_aks@rediffmail.com

© Springer Nature Singapore Pte Ltd. 2020
M. S. Shunmugam and M. Kanthababu (eds.), *Advances in Additive Manufacturing and Joining*, Lecture Notes on Multidisciplinary Industrial Engineering,
https://doi.org/10.1007/978-981-32-9433-2_48

into butting material to be joined and traversed along the weld path. As a result, the material from the leading edge of the tool transfers towards the trailing edge causing simultaneously the plastic flow and mixing of the materials. The successful joining of dissimilar material aluminium alloys is of great interest as these alloys have been extensively used to produce aircraft components such as fuselage, upper wing, lower wing and skeleton parts. Selection of a FSW parameters and joining process for dissimilar materials, aluminium alloys like AA2024-T3 to AA7075-T6 [3–7], AA6061 to AA7075 [8, 9], AA5052-H32 to AA6061-T6 [10], AA6061-T6 to AA7050 [11] and aluminium to copper [12] was found more complicated FSW process compared to joining process of similar materials. This is because the two materials which were need to be joined consist of different chemical composition and physical characteristics. Also, lack of equality in temperature exposure was found during joining dissimilar alloys by FSW technique. In addition, the location of the materials in FSW of dissimilar alloys also plays a significant role in the metallurgical and mechanical properties of the weld joints. Thus, the selection of FSW parameters in order to produce dissimilar joints of different materials is a challenging task for many researchers. The effect of positioning of the plates to obtain high weld joint strength of FSW dissimilar material joints between Al alloys has been focused by many investigators [7, 8, 10, 13] and suggested that high-strength material should be placed in the retreating side (RS) in order to obtain the higher weld joint strength. The weld properties are more dependent on the alloy on the RS because the stir zone (SZ) or weld nugget zone (WNZ) mainly consists of material from RS. The analysis of these studies led to the conclusion that by placing the higher-strength material in the advancing side (AS) results in the development of high flow stress which prevents the flow of low-strength material towards SZ from the RS. Khodir and Shibayanagi [7] in their investigation in joining AA2024-T3 to AA7075-T6 reports that by locating lower hardness AA2024-T3 in the AS and the weld joint yields higher tensile strength and better metallurgical properties. Similarly, investigation of FSW joints of AA6061 to AA7075 placing the AA6061 in the AS [8], AA5052-H32 to AA6061-T6 by placing AA5052-H32 in the AS [10], and AA6061 to A356 [13] with A356 Al fixed at the AS reports an effective material mixing at the SZ and higher tensile properties of the weld joint when low-strength and relatively soft material kept in the AS. On the contrary to the studies [7, 8, 10, 13], several investigations [3, 11, 14] documented that the dissimilar weld joint strength and material flow depend on selected FSW parameters (tool rotation speed, welding speed, etc.) and processing conditions rather than the position of the plate. Several literatures [5, 9, 12, 15] report the implementation of tool offset as a method to diminish the effect of strength reduction in the production of joints with dissimilar materials. Tool offsets found to be beneficial in enhancing the flow of the material and exhibit higher properties of the dissimilar weld joints.

Despite the investigation of in joining dissimilar material of AA2024-T351 and AA7075-T651 by FSW technique using FSW major parameters [3, 4], effect of location of material and welding speed [7], to the author's knowledge there are few studies [e.g. 5] focusing on the effect of tool offset distance from the joint interface of AA2024-T351 and AA7075-T651 FSW dissimilar joints. Also, the studies on the

effect of combining the different tool offset distance and varying tool traverse speed (VTS) on microstructure, grain size and intermixing of the two dissimilar materials along the weld length of dissimilar joints of 2024-T351 and 7075-T651 are found to be scant. Therefore, in this present study, the FSW technique for joining AA2024-T351 and AA7075-T651 in butt joint configuration with different tool offset condition and VTS range 20–120 mm/min were investigated to find its effect on mechanical, microstructure and fracture analysis of the weld.

48.2 Experimental Procedure

48.2.1 Materials and Methods

In the present study, plates of AA2024-T351 and AA7075-T651 in the as-rolled condition having a thickness of 6.35 mm and cut into dimensions of 200 mm × 100 mm. The chemical composition, average tensile and hardness properties of both the plates are presented in Table 48.1. Both the plates are properly fixed and rigidly clamped on the working table in butt joint configuration such that the position of AA 2024-T351 plate is always on the AS, while the higher-strength AA7075-T651 is on the RS. The FSW process performed using a taper-threaded tool made from hot die steel (HDS) material having the geometry of taper-threaded pin with top diameter, 7.5 mm and bottom diameter, 6 mm and pin probe length, 5.8 mm. A 5-axis FSW machine (Make BISS technology Pvt. Ltd.) is used to carry out the experiments. Figure 48.1 illustrates the schematic of the experimental trials carried out with two different tool axis offset (1 mm towards 2024-T351 and 7075-T651) condition by VTS from the range 20–120 mm/min. The other two parameters optimized FSW parameters tool rotation speed, 650 rpm, and plunge depth, 6.2 mm, selected from the early investigation [8] are kept as constant. The combined experiment of tool axis offset and VTS is carried out in two sets of experiment trials by plunging the tool to a depth, 6.20 mm. In the first set of experiment trial, the experiment is conducted by considering the tool offset distance of 1 mm (indicated as –1) towards AA2024-T351 from the joint interface as shown in the Fig. 48.1a, and the traverse speed is varied from 20 to 120 mm/min for weld length, 150 mm. This experimental procedure is schematically shown in Fig. 48.1c. Also, the second experiment is done with tool offset 1 mm towards AA7075-T651 (indicated as +1) from the joint interface as shown in Fig. 48.1b.

Figure 48.2 depicts the schematic of the tensile test specimen and macro/microstructure specimen removal layout from the dissimilar welded joints for different tool offset FSW experimental conditions. The tensile specimens were denoted as ‘T’, and macro/microstructure specimens are denoted as ‘M’. Tensile specimens are prepared according to ASTM code of E8M-04. The strength of the FSW dissimilar weld joint specimens are evaluated for tensile properties such as ultimate tensile strength (UTS), yield strength (YS) and % elongation using SHI-

Table 48.1 Chemical composition, tensile properties and hardness value

Material type	Cu	Mg	Cr	Zn	Mn	Si	Fe	Ti	Al
AA2024-T351	4.37	1.5	0.01	0.02	0.49	0.05	0.12	0.05	Balance
AA7075-T651	1.4	2.3	0.19	5.6	0.03	0.03	0.14	0.05	Balance
Tensile properties and hardness value									
Material type	YS (MPa)	UTS (MPa)	Elongation (%)	Vickers microhardness at 1 kg of load at 15 s (Hv)					
AA2024-T351	410	476	15	139					
AA7075-T651	528	568	12	175					

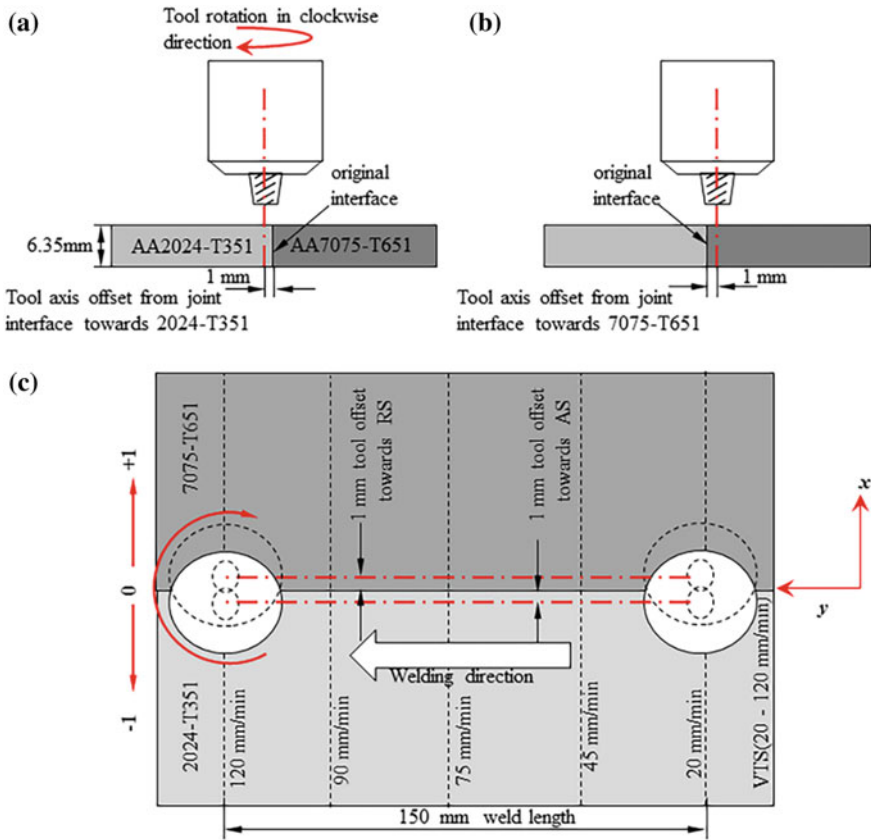


Fig. 48.1 Schematic illustration of tool offset and varying traverse speed (VTS) experiment carried out with tool offset distance of **a** 1 mm towards AA2024-T351 and **b** 1 mm towards AA7075-T651, **c** tool traverse direction with VTS along the weld length of 150 mm

MADZU hydraulic tensile testing machine (100 kN capacity). The tensile properties of the tested specimens were recorded and transformed to plot the graph. The specimens for metallographic examination were prepared to study the microstructure at the WNZ. The microstructure specimens are prepared by following standard metallographic procedures and etched with Keller’s reagent (1 ml of HF, 2.5 ml of HNO₃, 1.5 ml of HCL and 95 ml of distilled water). The detailed investigation of microstructure analysis of the specimens was carried out using JEOL (type JSM-6380 LA) scanning electron microscopy (SEM).

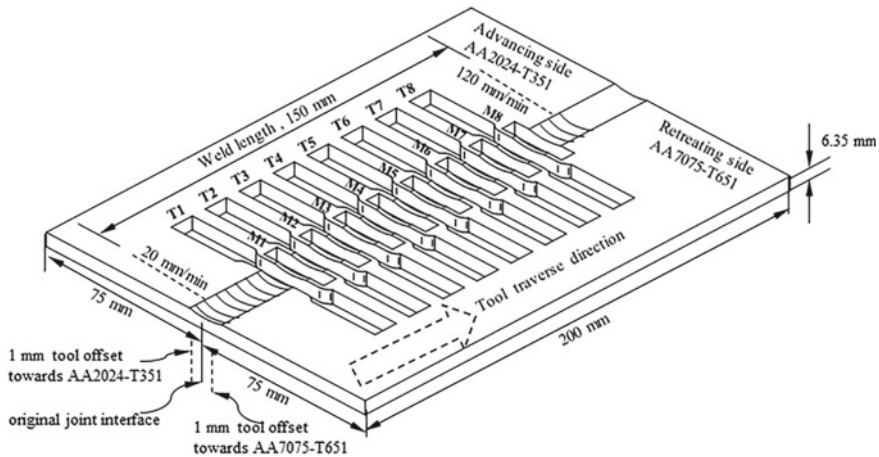


Fig. 48.2 Schematic showing the locations for removing the tensile and microstructure specimens from dissimilar weld joints

48.3 Results and Discussions

48.3.1 Macro and Microstructure of the Joints

The microstructure analysis is carried out for exploring the effect of tool axis offset position, i.e. 1 mm towards 2024-T351 (−1), 1 mm towards AA7075-T651 (+1) from the joint interface in conjunction with VTS range 20–120 mm/min.

Effect of tool offset towards AA2024-T351 and traverse speed. Influence of 1 mm tool offset condition (−1) towards AA2024-T351 in conjunction with VTS 20–120 mm/min on WNZ, thermomechanically affected zone (TMAZ) and heat-affected zone (HAZ) can be seen from Fig. 48.3a–j. The SEM images are shown in Fig. 48.3a–j which depict an evolution on the mixing state starting from mechanically mixed region (MMR) evidenced with intense mixing condition of 2024-T351 and 7075-T651 at lower VTS range 25–40 mm/min, partially mixing condition observed at AS and bottom of the WNZ for VTS range 45–55 mm/min followed by unmixed region (UMR) condition observed at the RS of the WNZ for the VTS range above 55 mm/min. The light-coloured etched bright layers are of 7075-T651, whereas the dark-coloured etched dull regions are of 2024-T351. In Fig. 48.3a, b, obtained traverse speed, 25 mm/min, results in intensive mixing of both the alloys at the WNZ. The increase in the tool residence time in the WNZ at lower traverse speed results in higher heat input and stronger stirring of both the alloy. The high-magnification back-scattered emission (BSE) image in Fig. 48.3b shows the WNZ is composed of alternate layer-by-layer banded structure (BS) consisting of both 2024-T351 and 7075-T651. The classical ‘onion ring’ structure formation that was observed for traverse speed 25 mm/min at the WNZ could not be seen at higher traverse speed

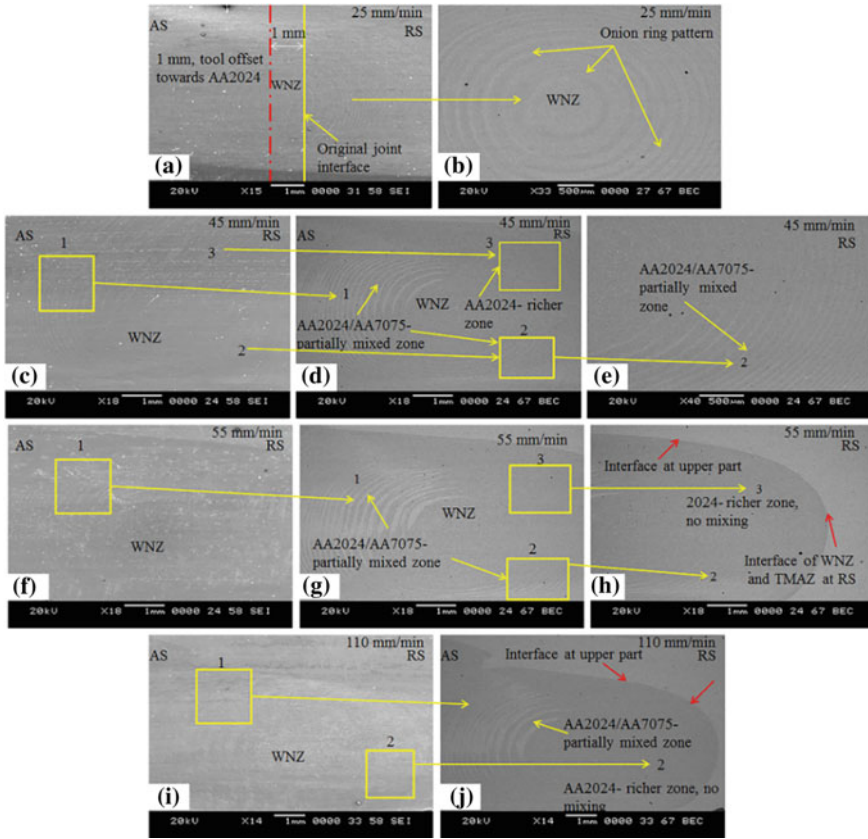


Fig. 48.3 SEM images for tool offset distance 1 mm towards AA2024-T351 and VTS range 20–120 mm/min

(>45 mm/min) at the WNZ. Figure 48.3c–e observes a three distinct region (marked as 1, 2 and 3) at the WNZ. The visible WNZ is mainly composed of material located in the AS (i.e. 2024-T351) and observes a lack of symmetry in material mixing. The BSE images of Fig. 48.3d, e show the AS region marked ‘1’ (Fig. 48.3d), and bottom region of WNZ region marked ‘2’ (Fig. 48.3e) observes a partial mixing of two alloys. The RS region marked ‘3’ (Fig. 48.3d) observes no material mixing condition or UMR in the WNZ consisting of only AA2024-T351. Also, three distinct regions (marked as 1, 2 and 3) can also be noticed in the BSE images of FSW dissimilar weld joint section in Fig. 48.3f–h for traverse speed, 55 mm/min. Thus, as described in most of the literature of FSW dissimilar joints [3, 6], increasing the traverse speed observes the WNZ without any alternate layers of 2024-T351/7075-T651. Further, for the tool traverse speed to 110 mm/min, Fig. 48.3i, j observes a UMR marked as ‘2’ in the RS of WNZ. During tool traversing, the material flow depends upon the amount of heat generated thereby the amount of softening of the material. Observing

these Fig. 48.3a–j, the three regions (marked as 1, 2 and 3) observed at the WNZ are attributed to the tool traverse speed and tool offset condition. As the tool distance is offset towards AA2024-T351, the amount of heat acting on the higher-strength alloy, i.e. 7075-T651 is less and the proportion of heat generated at the WNZ reduces with higher traverse speed. As a result, the flow stress on the high-strength material AA7075 increases causing a reduced amount of material flow from leading edge to the trailing edge. Thus, the WNZ observes a partial material mixing ratio with an increase in the traverse speed. In addition, with the increasing the traverse speed (>55 mm/min), the RS observes a sharp interface boundary between WNZ, TMAZ and upper part of the WNZ (see Fig. 48.3h, j). These sharp boundaries become the primary region of discontinuity and promote fracture at these points causing early failure of the weld joints.

Effect of tool offset towards AA7075-T651 and traverse speed. The microstructure of the WNZ of the joint specimen fabricated for tool offset of 1 mm (+1) towards AA7075-T651 for the VTS from 20 to 120 mm/min are shown in the SEM images of Fig. 48.4a–i. The lower traverse speed range 25–45 mm/min results in a well-developed WNZ composed of banded alternate lamellae pattern of both the aluminium alloys which resembles classical ‘onion ring’ structure that was observed (Fig. 48.4a–c). However, the material mixing and composition at the WNZ change with respect to the VTS range above 55 mm/min (Fig. 48.4d–i). It can be seen from Fig. 48.4d–i that increasing the tool traverse speed with tool offset condition (+1),

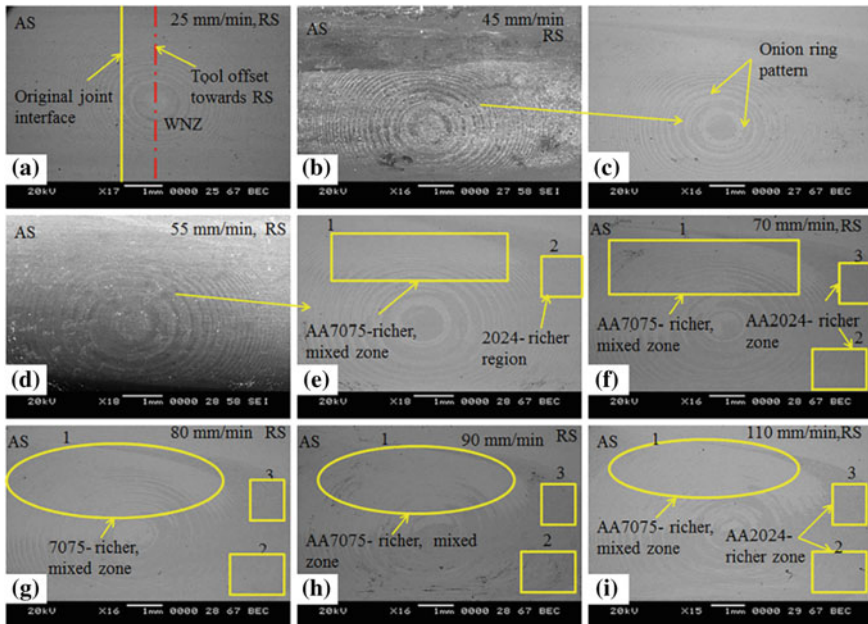


Fig. 48.4 SEM images for tool offset distance 1 mm towards AA2024-T351 and VTS range 20–120 mm/min

the amount of material drawn from the RS increases and WNZ loses its symmetry about the weld joint centreline. For the same traverse speed parameters unlike for the tool offset condition (−1), the mixing state of the two alloys at the WNZ for tool offset condition (+1) appears to be different and composed the material mainly located at the RS (i.e. 7075-T651). As shown in Fig. 48.4d–i, there has been a bulk transference of AA7075-T651 material from RS to the AS. Tool axis offset is considered one of the important parameters in controlling the mixing of two dissimilar materials ratio at the WNZ and weld quality of the joints [12]. The tool offset condition (+1) helps in the material AA7075-T651 placed in the RS being dragged to the AS by the shoulder at the trailing side of the tool. As presented in the SEM images, Fig. 48.4d–i, the material AA7075-T651 transports from the RS towards AS which occurs at the top region of the WNZ. Also, as clearly visible from the BSE images of Fig. 48.4, at lower traverse speed, the gap between the alternate lamellae pattern of the two alloys is clearly visible in the WNZ top portion. However, increasing the tool traverse speed (>55 mm/min), the lamellae pattern observed at the top region of WNZ becomes dense and separation between them diminishes with the increase in the speed. Since the two alloys, 2024-T351 and 7075-T651, having different etching responses, the material flow from both the AS and RS can be clearly visible in the WNZ. Judging from the etching response, it can be seen from BSE images in Fig. 48.4d–i the area marked as ‘1’ at the top side of the WNZ consists of mainly AA7075-T651. Similarly, in Fig. 48.4d–i, the area marked as ‘2’ at the bottom of WNZ and ‘3’ at the RS of the WNZ mainly consists of mainly 2024-T351.

Figure 48.5a–c shows the grain size measurement at the WNZ obtained from the microstructure sample specimen produced for traverse speed, 25, 55 and 110 mm/min, respectively, for tool offset condition of 1 mm towards AA2024-T351. Figure 48.5a shows a higher grain size range 5.5–7.5 μm in the WNZ. As expected this is due to the higher heat generation and severe plastic deformation of the material

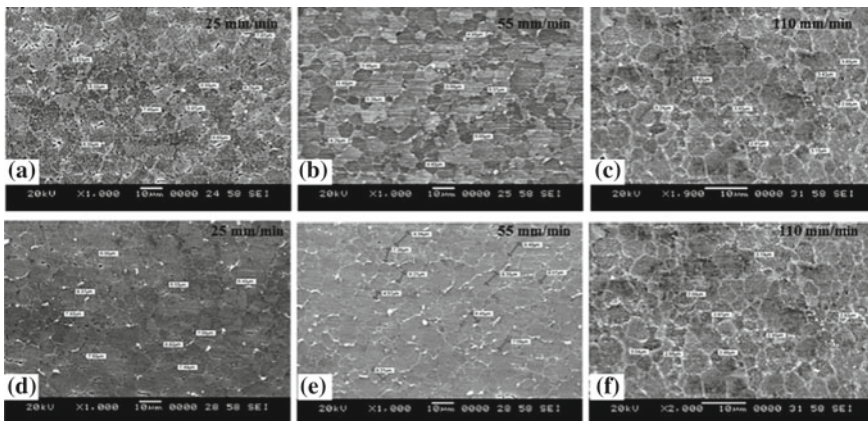


Fig. 48.5 Grain size at the WNZ for tool offset distance. **a–c** 1 mm towards 2024-T351, **d–f** 1 mm towards 7075-T651, obtained at various levels of tool traverse speed

during FSW of dissimilar joints. Increasing the traverse speed from 25 to 55 mm/min has shown decreased grain size range of 3.5–5.5 μm in the WNZ. Further increase in the traverse speed results in decreased grain size range 2.9–5 μm . This decrease in the grain size with an increase in the traverse speed is attributed to the lower heat input the WNZ. Figure 48.5d–f observes a similar variation in the grain size at the WNZ for the tool offset distance 1 mm towards 7075-T651. Irrespective of the tool offset conditions (-1 , $+1$), the microstructure at the WNZ of all the specimens consists of grains similar in size and varies according to the traverse speed condition and heat input.

48.3.2 Tensile Properties

The result of the tensile properties from the tested specimen for tool offset conditions of -1 , $+1$ with VTS range 20–120 mm/min is as shown in Fig. 48.6. It is interesting to note that the increase in VTS from the range 20–120 mm/min for tool offset condition -1 (Fig. 48.6a) results in decreasing trend in tensile properties of the weld joints, while for tensile properties for tool offset condition $+1$ (Fig. 48.6b) follows an increasing trend. Maximum tensile strength was obtained for the combination of tool offset condition of $+1$ (i.e. tool offset towards 7075-T651) and higher traverse speed above 100 mm/min compared to the tool offset condition of -1 . Dissimilar FSW joint specimen produced with tool offset condition of $+1$ and for traverse speed of 110 mm/min has shown maximum UTS of 436 MPa, YS of 375 MPa, % elongation of 14 and weld joint efficiency of 92%.

One can observe from Fig. 48.6a that, with the traverse speed of 25–40 mm/min, the tensile properties show a decreasing trend. Due to the increase in the tool residence time at lower traverse speed range 25–40 mm/min results in higher heat input and softened WNZ. As a result, UTS in the range of 347–356 MPa, YS of 210–264 MPa and % elongation of 8.6–11.6 was observed for the VTS 20–45 mm/min. A similar

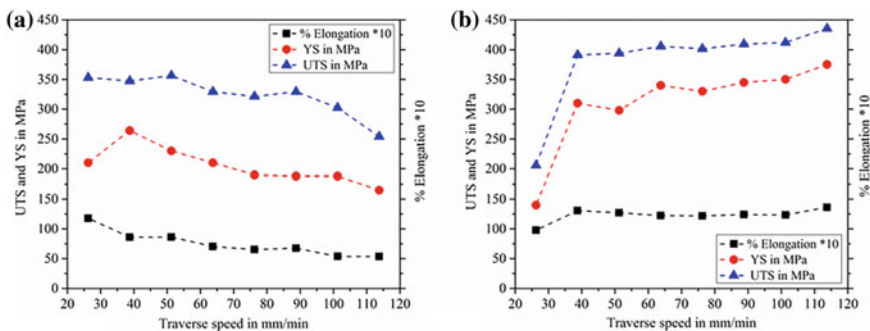


Fig. 48.6 Variation of tensile strength for tool offset distance of **a** 1 mm towards AA2024-T351, **b** 1 mm towards AA7075-T651 for varying the traverse speed range 20–120 mm/min

observation in regard to the lower tensile properties can also be observed for the tool offset condition of +1 for lower traverse range 20–30 mm/min. Further, the combination of tool offset condition of –1 and the traverse speed, 110 mm/min has shown lower tensile properties with UTS of 253 MPa. However, for tool offset condition +1 (towards AA7075-T651) for traverse speed of 110 mm/min, higher UTS of 435 MPa, YS of 375 MPa and elongation of 14% were observed for a tested tensile specimen of the dissimilar weld joint. The tool offset into the AS results in higher temperature than the RS, and local temperature determines the weld strength [9]. Thus, the tool offset condition –1 results higher local temperature and observes a reduction in the tensile properties. Thus, a lower tensile property was observed as a result of higher temperature on the AS and reduced MMR at the WNZ with the increase in the traverse speed. In the present study, the tool offset condition of +1 (i.e. towards AA7075-T651) results in increased amount of material flow of AA7075-T651 into the WNZ resulting in enhanced tensile properties of the weld joint. Cole et al. [9] also report the similar observation in the dissimilar joints of AA6061-T6 kept in the AS to the AA7075-T651 in the RS. Further, they report the colder welds and tool offset into the higher hot strength material helps in retaining the strength of the material in the dissimilar weld. From this experimental investigation, it can be concluded that the combined effect of moving the tool offset towards AA7075-T651 and higher traverse speed results in increased amount of flow of higher-strength material AA7075-T651 and decreased amount of heat input to the WNZ, respectively.

48.3.3 Fractography

Figure 48.7a–c, d–f shows SEM images of fracture specimen after the tensile test for the tool offset conditions 1 mm towards AA2024-T351 and 1 mm towards AA7075-T651, respectively. For the tool offset condition –1, invariably all the specimens except that the one dissimilar joint specimen produced for traverse speed 25 mm/min were fractured at the joint interface between WNZ and TMAZ. The sharp boundary and lack of metallurgical bonding between the joint interface of WNZ and TMAZ of the two materials exhibit fracture surface morphology as depicted in Fig. 48.7a–c evidenced with lack of metallurgical bonding and consisting of smoothly curved fracture surface features. The higher magnified SEM images (Fig. 48.7c) show the presence of a good number of dimples and confirm the failure characteristics which resemble that of a ductile fracture. Figure 48.7d–f shows SEM images of the specimen that produced the best joint strength for tool offset condition +1 for traverse speed of 110 mm/min, and failure was away from the WNZ and at the HAZ of AS. The analysis of the fracture surface in Fig. 48.7d, f observes the presence of microvoids and dimples.

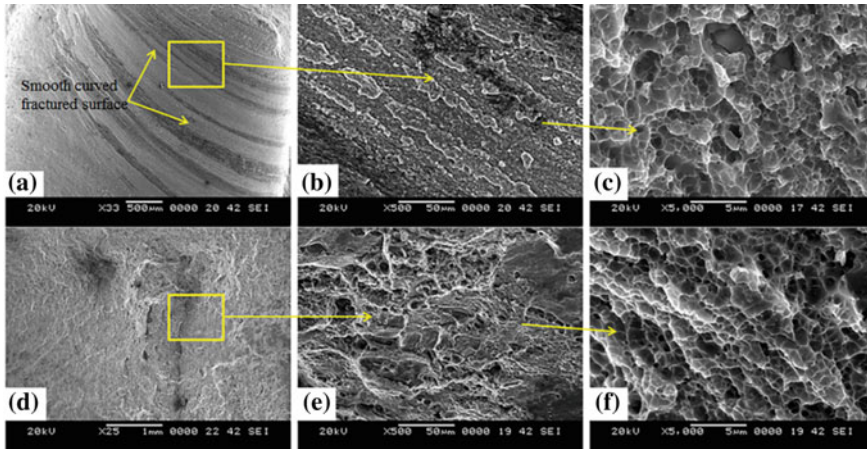


Fig. 48.7 Fracture surface appearance of FSW joint specimen for tool offset distance of **a–c** 1 mm towards AA2024-T351, **d–f** 1 mm towards AA7075-T651

48.4 Conclusions

In the present study, the combined effect of tool offset distance and VTS range from 20 to 120 mm/min on the microstructure and mechanical properties of FSW joints were investigated. The following conclusions can be drawn from the experiment.

1. Tool offset of 1 mm towards AA2024-T351 and higher traverse speed of 110 mm/min have shown the reduction in the tensile properties.
2. The tool offset of 1 mm towards AA7075-T651 results in increased amount of material flow of AA7075-T651 into the WNZ and with the traverse speed above 110 mm/min yields higher tensile properties for the specimen of FSW joint.
3. The grain size at the WNZ remains same in both tool offset condition (–1, +1) with respect to the varying traverse speed range 20–120 mm/min.
4. For the tool offset of 1 mm towards AA2024-T351, almost all the specimens of dissimilar weld joint were fractured at the joint interface of the WNZ and TMAZ. The specimen that produced the best joint strength for tool offset condition +1 for traverse speed of 110 mm/min, failure location, was found to be away from the WNZ and at the HAZ of AS.

References

1. Thomas, W.M., Nicholas, E.D., Needham, J.C., Murch, M.G., Templesmith, P., Dawes, C.J.: Friction stir welding. GB Patent Application No. 9125978.8 and US Patent No. 5460317, Oct 1995 (1991)
2. Mishra, R.S., Ma, Z.Y.: Friction stir welding and processing. *Mater. Sci. Eng. R Rep.* **50**(1–2), 1–78 (2005). <https://doi.org/10.1016/j.mser.2005.07.001>
3. Da Silva, A.A.M., Arruti, E., Janeiro, G., Aldanondo, E., Alvarez, P., Echeverria, A.: Material flow and mechanical behaviour of dissimilar AA2024-T3 and AA7075-T6 aluminium alloys friction stir welds. *Mater. Des.* **32**(4), 2021–2027 (2011). <https://doi.org/10.1016/j.matdes.2010.11.059>
4. Cavaliere, P., Nobile, R., Panella, F.W., Squillace, A.: Mechanical and microstructural behaviour of 2024–7075 aluminium alloy sheets joined by friction stir welding. *Int. J. Mach. Tools Manuf.* **46**(6), 588–594 (2006). <https://doi.org/10.1016/j.ijmachtools.2005.07.010>
5. Cavaliere, P., Panella, F.: Effect of tool position on the fatigue properties of dissimilar 2024–7075 sheets joined by friction stir welding. *J. Mater. Process. Technol.* **206**(1–3), 249–255 (2008). <https://doi.org/10.1016/j.jmatprotec.2007.12.036>
6. Kumar, K.A., Murigendrappa, S.M., Kumar, H.: A bottom-up optimization approach for friction stir welding parameters of dissimilar AA2024-T351 and AA7075-T651 alloys. *J. Mater. Eng. Perform.* **26**(7), 3347–3367 (2017). <https://doi.org/10.1007/s11665-017-2746-z>
7. Khodir, S.A., Shibayanagi, T.: Friction stir welding of dissimilar AA2024 and AA7075 aluminium alloys. *Mater. Sci. Eng. B* **148**(1–3), 82–87 (2008). <https://doi.org/10.1016/j.mseb.2007.09.024>
8. Guo, J.F., Chen, H.C., Sun, C.N., Bi, G., Sun, Z., Wei, J.: Friction stir welding of dissimilar materials between AA6061 and AA7075 Al alloys effects of process parameters. *Mater. Des.* (1980–2015) **56**, 185–192 (2014). <https://doi.org/10.1016/j.matdes.2013.10.082>
9. Cole, E.G., Fehrenbacher, A., Duffie, N.A., Zinn, M.R., Pfefferkorn, F.E., Ferrier, N.J.: Weld temperature effects during friction stir welding of dissimilar aluminum alloys 6061-t6 and 7075-t6. *Int. J. Adv. Manuf. Technol.* **71**(1–4), 643–652 (2014)
10. Park, S.K., Hong, S.T., Park, J.H., Park, K.Y., Kwon, Y.J., Son, H.J.: Effect of material locations on properties of friction stir welding joints of dissimilar aluminium alloys. *Sci. Technol. Weld. Joining* **15**(4), 331–336 (2010). <https://doi.org/10.1179/136217110X12714217309696>
11. Rodriguez, R.I., Jordon, J.B., Allison, P.G., Rushing, T., Garcia, L.: Microstructure and mechanical properties of dissimilar friction stir welding of 6061–7050 aluminum alloys. *Mater. Des.* **83**, 60–65 (2015). <https://doi.org/10.1016/j.matdes.2015.05.074>
12. Sahu, P.K., Pal, S., Pal, S.K., Jain, R.: Influence of plate position, tool offset and tool rotational speed on mechanical properties and microstructures of dissimilar Al/Cu friction stir welding joints. *J. Mater. Process. Technol.* **235**, 55–67 (2016). <https://doi.org/10.1016/j.jmatprotec.2016.04.014>
13. Lee, W.B., Yeon, Y.M., Jung, S.B.: The mechanical properties related to the dominant microstructure in the weld zone of dissimilar formed Al alloy joints by friction stir welding. *J. Mater. Sci.* **38**(20), 4183–4191 (2003). <https://doi.org/10.1023/a:1026337807920>
14. Dinaharan, I., Kalaiselvan, K., Vijay, S.J., Raja, P.: Effect of material location and tool rotational speed on microstructure and tensile strength of dissimilar friction stir welded aluminum alloys. *Arch. Civ. Mech. Eng.* **12**(4), 446–454 (2012). <https://doi.org/10.1016/j.acme.2012.08.002>
15. Liang, Z., Chen, K., Wang, X., Yao, J., Yang, Q., Zhang, L., Shan, A.: Effect of tool offset and tool rotational speed on enhancing mechanical property of Al/Mg dissimilar FSW joints. *Metall. Mater. Trans. A* **44**(8), 3721–3731 (2013). <https://doi.org/10.1007/s00170-013-5485-9>

Chapter 49

Joining of Different Thickness Dissimilar Materials SS 316L/SS 310 By μ -PAW Process



Swagat Dwibedi , Swarup Bag , Deepak Kumar Lodhi 
and Arindam Kalita 

Abstract The utility of recent manufacturing concepts and advanced materials is of greater interest to manufacturers of automobile and aerospace industries to reduce weight, cost and enhance part performance. In spite of various advantages associated with the use of tailor-welded blanks (TWBs), joining of TWBs is challenging due to the variation in their properties and thickness. The principal objective of this paper is to make a detailed study for microstructural (optical microscopy) and mechanical characterization (uniaxial tensile test, Vickers micro-hardness) of the steel assemblies formed by autogenous joining of SS 316L (0.8 mm) and SS 310 (0.6 mm) using micro-plasma arc welding process (μ -PAW). This study constructs the capability of μ -PAW process for joining dissimilar materials of different thickness autogenously and producing good quality joint using considerably reduced power as compared to laser and electron beam welding processes.

Keywords Micro-plasma arc welding (μ -PAW) · SS 316L-SS 310 · Autogenous joining

49.1 Introduction

The weight of automobiles has been continuously increasing over the years since the overall features have widened and a heavy number of electric and electronic parts have been included to fulfil expanding demands regarding safety and comfort. As higher weight directs increased fuel consumption, tailored blanks are used to reduce the weight, which results in increase in fuel efficiency and reduction in cost due to use of less material [1]. Tailor-welded blanks (TWBs) are manufactured by welding together sheets of different grades or thicknesses. Generally in steel TWBs, the weld is characterized with lower ductility and higher strength than base materials [2]. Steels of different class (Fe360, interstitial free steel—IFS and high resistance

S. Dwibedi (✉) · S. Bag · D. K. Lodhi · A. Kalita
Department of Mechanical Engineering, Indian Institute of Technology Guwahati, Guwahati
781039, Assam, India
e-mail: swagatsudhadwibedi@gmail.com

© Springer Nature Singapore Pte Ltd. 2020
M. S. Shunmugam and M. Kanthababu (eds.), *Advances in Additive Manufacturing and Joining*, Lecture Notes on Multidisciplinary Industrial Engineering,
https://doi.org/10.1007/978-981-32-9433-2_49

steel—HR) were used to the study TWBs (welded and then formed) [3]. Plasma arc welding was used to join two sheets of stainless steel having 0.1 and 0.3 mm thickness using high-power density. It was reported that the welding capability is not influenced by the stand-off distance (i.e. distance between the exit of nozzle and workpiece surface) [4]. Tensile strength of the weldment was prepared from AISI SS 304 TWBs with a thickness combination of 1 and 1.2 mm using electron beam welding to analyse characteristics of weldment of the heterogeneous tailor-welded blank (TWB) and its base metal [5]. Mild steel (MS) sheets having thickness of 0.6 and 1.2 mm, and a high-strength steel sheet was used as materials to prepare TWBs using Nd:YAG laser welding [6]. In the present investigation, different materials having different thickness (SS 316L—0.8 mm and SS 310—0.6 mm) were joined to form TWB butt joints using μ -PAW process. Various liquid-state welding processes, namely metal inert gas (MIG) welding, tungsten inert gas (TIG) welding, laser beam welding (LBW), electron beam welding (EBW) and plasma arc welding (PAW), have been used for joining of tailored blanks. Since austenitic stainless steel (SS) sheets may undergo certain changes during manufacturing, it is essential to employ an acceptable degree of control during joining of austenitic SS sheets to forbid any probable harmful effects and to maintain identical level of resistance to corrosion and strength in the weld zone as compared to that of the base metal. Choice of appropriate joining process, process parameters (optimized) and procedure can help to solve these problems to a considerable extent [7]. Micro-plasma is one of the relatively inexpensive techniques for metal joining used widely for micro-scale utilization due to its built-in characteristics of governing constricted arc with very low value of current. μ -PAW utilizes a variable and low-cost heat source and is a vital joining process due to its ability to create an intense, controlled and directed arc at a very low current in micro-scale. Low power combined with high flux density heat source is an essential experimental characteristic for welding of micro-scale components, since it is constricted to comparatively insignificant region. Therefore, plasma as a heat source (high energy density) is preferred for welding utilization at micro-scale as contrast to other arc welding processes [8].

49.2 Materials and Methods

Materials selected for the present research work are SS 316L (0.8 mm) and SS 310 (0.6 mm). SS 316L is a variant of SS 316 with an extra low carbon that restricts detrimental precipitation of carbides that occurs because of welding [7]. SS 310 is a grade (highly alloyed) of austenitic stainless steel developed for high-temperature services. Presence of high chromium and nickel composition allows this highly alloyed steel to withstand oxidation while in service at high temperatures (up to 1200 °C) in absence of reduced sulphur gases [9]. Table 49.1 shows the chemical composition of AISI SS 316L and AISI SS 310.

Table 49.1 Chemical composition of AISI SS 316L and SS 310 by wt% [7, 10]

Elements	C	Mn	Mo	Ni	Cr	Fe
SS 316L	0.021	1.51	2.16	10.21	17	Balance
SS 310	0.07	0.95	0.25	19	25	Balance

49.3 Experimentation

49.3.1 Experimental Procedure

A micro-plasma arc welding (MPAW) machine with a direct current (DC) power supply with current ranging from 0.05 to 50 A is used to perform the experiments. The plasma torch is stationary while the workpiece advances on a rail-guided PUG machine. Argon gas (industrially pure) is used both for shielding and generating plasma gas. The joining of TWB joint has been carried out with suitable parameters, because the range of parameters to form proper weld joint exists in narrow regions. For current in the ranges of 7–15 A for different speeds, bead on plate (BOP) welding is carried out at varying plasma (gas) flow rate to estimate the feasible domain of process parameters. BOP welding completely removes the effect of the joint gap on weld bead shape and size. Preliminary runs were accomplished by changing one process parameter while keeping others (parameters) constant. The weld quality depends on the integration of (i) welding current, (ii) welding speed and (iii) plasma (gas) flow rate. Plasma arc welding (PAW) remains less responsive to stand-off distance (SOD); therefore, value of SOD is varied at a narrow range [8]. Value of plasma gas and shielding gas flow rate is varied in the range used in past work [7]. Welding speed is bracketed by trial on minimum speed and then varied at orderly interval. The proper welding current for sound weld joint is bracketed after a lot of preliminary trials. It is noted that 2.25 mm/s as the minimum welding speed and 8 A as the minimum current required to produce proper weld joint. The current is then increased from 8 A until melt through of the material appears.

49.3.2 Experimental Setup

SS 316L (0.8 mm) and SS 310 (0.6 mm) sheets were prepared for welding by cutting large pieces into 100 × 50 mm sizes by using shearing machine. Edges were prepared properly to maintain the joint gap at a minimum level, and then the polished edges were cleaned with acetone for removal of all dirt particles. A suitable fixture with copper as backing plate assured small angular distortions of the weld joint due to enhanced rate of heat transfer. A packing sheet was used below the sheet having lower thickness (SS 310) so as to maintain the level of the sheets of different thickness. The sample pieces are arranged in square butt joint configuration in the fixture and are

Table 49.2 Ranges of parameters used for welding of SS 316L and SS 310

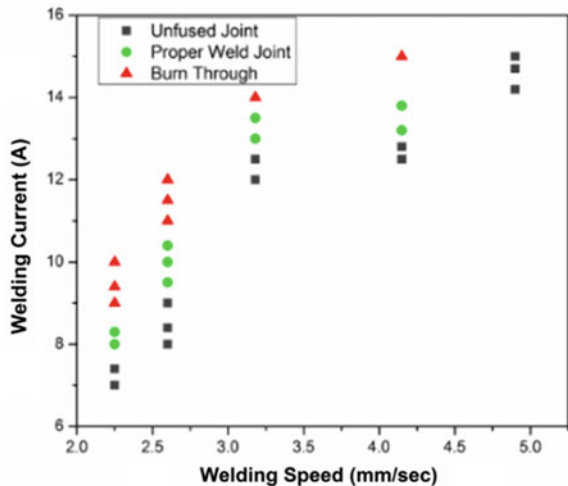
Welding parameters	Values
Welding current (A)	7–15
Welding speed (mm/s)	2.25, 2.60, 3.18, 4.15, 4.9, 6.15, 6.4, 6.98
Plasma gas flow rate (lpm)	0.7
Shielding gas flow rate (lpm)	6–8
Stand-off distance (mm)	1.7
Fixed parameters	Copper nozzle diameter 1.2 mm, electrode diameter 1.2 mm, torch position: vertical

mounted on a PUG machine while the torch is held stationary above it in a vertical manner. The various process parameters used for the present investigation are shown in Table 49.2.

49.3.3 Welding Parameters

Welding current and welding speed are the most prominent process parameters owing to the fact that both affect bead shape, heat-affected zone (HAZ), the depth of penetration (DOP) and the volume of base material melted. The total volume of weld pool is positively correlated to the welding current. Figure 49.1 depicts weld quality at various combination of welding current and welding speed for TWB butt joint. Identified optimum combination of welding current and welding speed at which proper weld joint was achieved are (8 A, 2.25 mm/s), (10 A, 2.60 mm/s) and (13.5 A, 2.60 mm/s).

Fig. 49.1 Weld quality at various combination of welding current and welding speed for TWB joint



3.18 mm/s). Theoretically, the weld width increases in size with increase in heat input (i.e. increase in current or decrease in welding speed; keeping other parameters constant). For the present work, calculated heat input required to form proper TWB butt joint is shown in Table 49.3.

Need for proper heat input for joint formation can be observed from Fig. 49.2. When the applied heat input is not sufficient to melt the base material, only heating takes place without joint formation. If the applied heat input is higher than the required value, excessive penetration occurs and may result in a burn through. Optimum heat input results in regular weld bead with no visual imperfection and high joint efficiency.

Table 49.3 Heat input required for proper weld joint

Case	Current (A)	Speed (mm/s)	Heat input (J/mm)
1	8	2.25	58.67
2	10	2.60	63.46
3	13.5	3.18	70.04

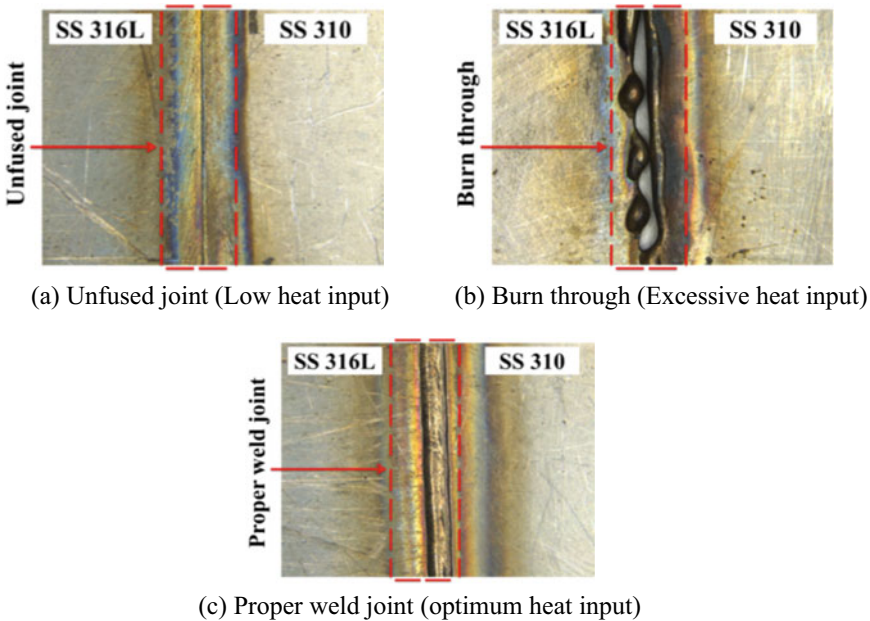


Fig. 49.2 Weld quality at different heat input

49.4 Results and Discussion

49.4.1 Influence of Heat Input on Weld Bead Size

As greater heat input results in a bigger and wider weld zone, increase in the value of heat input increases the width of the weld zone. A positive linear relation between heat input and weld width can be observed from Fig. 49.3, in which different TWBs butt joint are formed at different heat input value, increasing from Fig. 49.3a–c.

49.4.2 Characterization of the Weld Joints

Tensile Strength A total of nine TWB butt joint samples are tested on an UTM machine for three cases with three tensile specimens considered for every welding condition, and the mean value is considered for parameters yielding proper weld joint. The test is carried out at a constant rate of 0.5 mm/min. Among the nine samples, six samples failed at the weld region (average UTS of 552 MPa), while three samples failed at base material (average UTS of 604 MPa), towards SS 310 (0.6 mm) side, which is attributed to lower thickness of SS 310 (0.6 mm) as compared to SS 316L (0.8 mm) side. Highest tensile strength is observed for the samples that failed at the

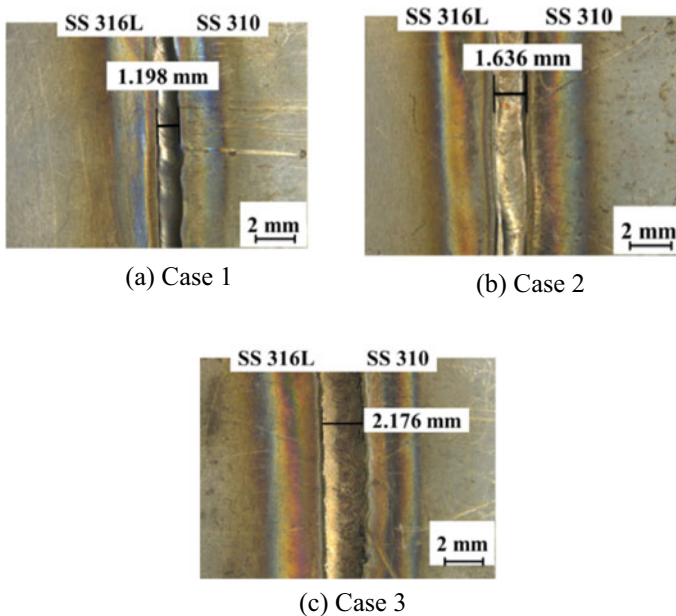
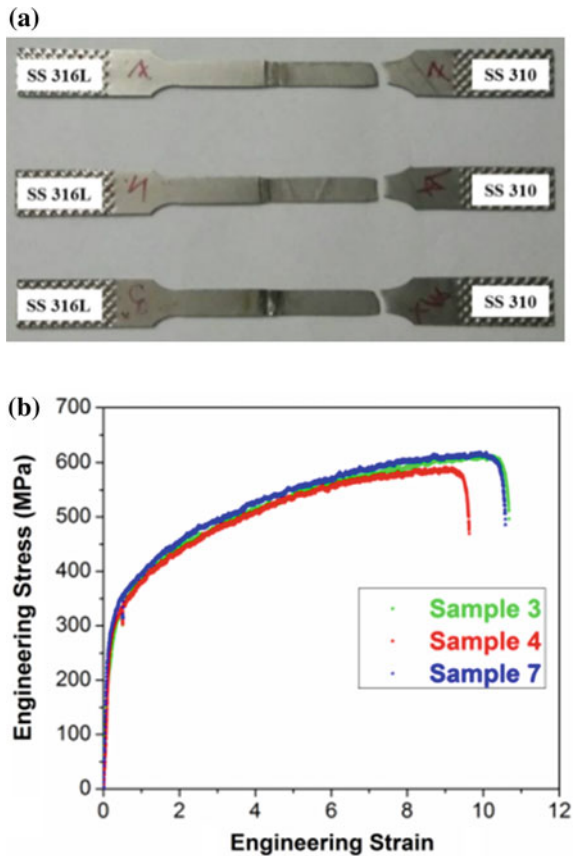


Fig. 49.3 Weld bead size with increasing heat input from **a** case 1, **b** case 2 and **c** case 3

gauge length of base material like in sample 3, 4 and 7. Among these three samples, 3 and 7 belong to case 1 while sample 4 belongs to case 2. Failed tested samples are shown in Fig. 49.4a, and engineering stress–strain curve for TWB joint obtained for samples 3, 4 and 7 is shown in Fig. 49.4b. TWB joints formed at a lower heat input had higher value of ultimate strength as compared to joints formed at a lower heat input value. This can be attributed to the high cooling rate achieved with lower heat input, resulting in fine grains, thus enhancing the joint strength.

Microstructure To reveal the microstructure of welded samples, Glyceregia (HCl-15 cc + Glycerol-10 cc + HNO₃-5 cc) is used as etchant onto the polished surface for duration of 25 s. Figure 49.5a–c shows weld zone and weld zone boundary with the base materials. Figure 49.5d, e shows grain size of weld zone and heat-affected zone (HAZ). In Fig. 49.5d, e, it can be observed that the grains’ size in the weld zone is significantly smaller than the heat-affected zone (HAZ). It is noticed that microstructure of base metal consists of major content as ferrite in the matrix. Amount of heat inputs dictates the microstructure of the weld zone, i.e. with low value

Fig. 49.4 a Failed tensile test specimens for case 1 and case 2 and b engineering stress–strain curve for TWB butt joints at optimum welding parameters



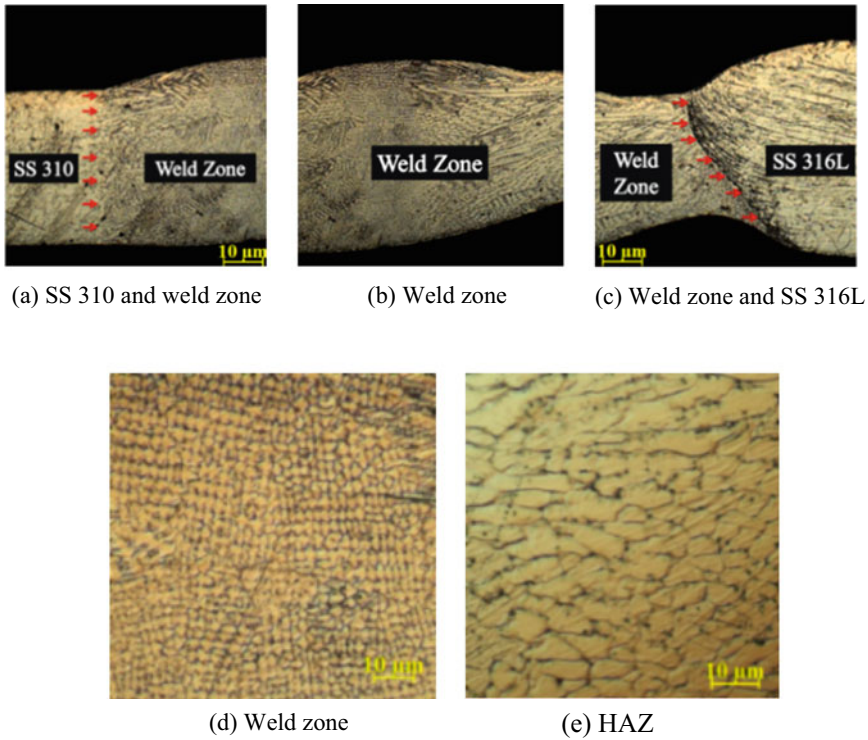
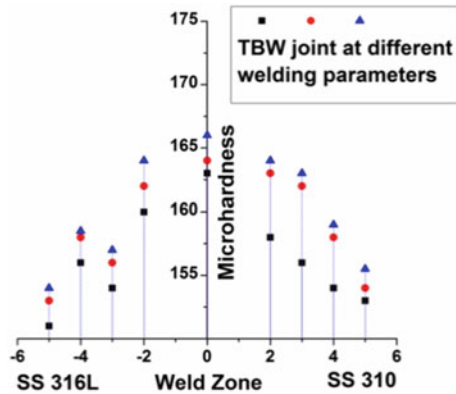


Fig. 49.5 Optical microstructures of different zones of TWB butt joint at heat input of 58.67 J/mm

of heat input resulting in smaller size dendrites, average heat input value results in δ ferrite and high heat input values results in coarse microstructure. Therefore, the value of Vickers micro-hardness of the weld zone is higher compared to that of base materials. The red arrows in the Fig. 49.5a, c show the boundary of the fusion zone with SS 310 and SS 316L.

Micro-hardness The Vickers micro-hardness test is performed in different zones, i.e. weld zone (WZ), heat-affected zone (HAZ) and base metal (BM). The measurements for Vickers (HV) micro-hardness are made using 500 g of indentation load with a dwell time of 10 s. The Vickers micro-hardness obtained for three different samples is shown in Fig. 49.6. It is observed that the weld zone has higher hardness than the HAZ on both sides; this is due to the presence of fine grains in the weld zone, as compared to coarse grains in HAZ. The presence of fine grains is confirmed with increase in hardness, strength and decrease in ductility (i.e. low value of percentage elongation obtained in tensile test results).

Fig. 49.6 Variation of Vickers micro-hardness along the weld zone and HAZ at identified optimum welding parameters



49.5 Conclusions

This paper contributes on experimental analysis of weld joint formed by dissimilar materials having different thickness using μ -PAW process. Effect of heat input on the tensile strength, microstructure and micro-hardness has been studied. It can be concluded that a weld joint with high quality, regular fusion zone and no visible flaw is obtained under controlled process parameters. The major conclusions drawn from the present investigation are as follows:

- The feasible process parameters to produce proper weld joint by micro-plasma arc welding of SS 316L (0.8 mm) and SS 310 (0.6 mm) are evaluated. Increase in amount of heat input results in increase in size of weld bead up to a certain limit and then melt through occurs. Selection of optimum amount of heat input results in a sound weld joint with uniform weld bead.
- Joint efficiency calculated for different combination welding parameters is found to be more than 100% with reference to ultimate tensile strength (UTS) with maximum UTS of 618 MPa and minimum of 542 MPa, which is higher than the UTS of the base materials.
- Microstructural analysis reveals that the grain size in the weld zone is significantly smaller than the base materials and HAZ. Microstructure and solidification of the weld pool is a direct function of amount of heat input, which in turn dictates mechanical property of the resulting weld joint. Thus, selection of heat input value plays an important role for achieving sound weld joint.
- Micro-hardness of the weld zone is found to be higher than that of the base material and HAZ. This is attributed to the presence of fine grains in the weld zone which results in high value of joint strength and hardness but low value of ductility.
- To accomplish uniform fusion, i.e. without melt through, it is necessary that the edges are machined to perfection, i.e. the two edges of sheets are perfectly aligned along the entire length of the joint. TWB butt joint formed at optimum welding parameters is considered to be defect free due to no surface defects (confirmed from macrographs) and no internal defects due to use of argon as shielding gas.

References

1. Merklein, M., Johannes, M., Lechner, M., Kuppert, A.: A review on tailored blanks—production, applications and evaluation. *J. Mater. Process. Technol.* **214**(2), 151–164 (2014). <https://doi.org/10.1016/j.jmatprotec.2013.08.015>
2. Rojek, J., Hyrcza-Michalska, M., Bokota, A., Piekarska, W.: Determination of mechanical properties of the weld zone in tailor-welded blanks. *Arch. Civ. Mech. Eng.* **12**(2), 156–162 (2012). <https://doi.org/10.1016/j.acme.2012.04.004>
3. Bayraktar, E., Kaplan, D., Yilbas, B.S.: Comparative study: mechanical and metallurgical aspects of tailored welded blanks (TWBs). *J. Mater. Process. Technol.* **204**(1–3), 440–450 (2008). <https://doi.org/10.1016/j.jmatprotec.2007.11.088>
4. Yoshioka, S., Miyazaki, T., Kimura, T., Komatsu, A., Kinoshita, N.: Thin-plate welding by a high-power density small diameter plasma arc. *CIRP Ann. Manuf. Technol.* **42**(1), 215–218 (1993). [https://doi.org/10.1016/s0007-8506\(07\)62428-7](https://doi.org/10.1016/s0007-8506(07)62428-7)
5. Cheng, C.H., Jie, M., Chan, L.C., Chow, C.L.: True stress–strain analysis on weldment of heterogeneous tailor-welded blanks—a novel approach for forming simulation. *Int. J. Mech. Sci.* **49**(2), 217–229 (2007). <https://doi.org/10.1016/j.ijmecsci.2006.08.012>
6. Morishita, Y., Kado, T., Abe, S., Sakamoto, Y., Yoshida, F.: Role of counterpunch for square-cup drawing of tailored blank composed of thick/thin sheets. *J. Mater. Process. Technol.* **212**(10), 2102–2108 (2012). <https://doi.org/10.1016/j.jmatprotec.2012.05.011>
7. Dwibedi, S., Jain, N.K., Pathak, S.: Investigations on joining of stainless steel tailored blanks by μ -PTA process. *Mater. Manuf. Process.* (2018). <https://doi.org/10.1080/10426914.2018.1476766>
8. Baruah, M., Bag, S.: Influence of heat input in microwelding of titanium alloy by micro plasma arc. *J. Mater. Process. Technol.* **231**, 100–112 (2016). <https://doi.org/10.1016/j.jmatprotec.2015.12.014>
9. Norton, J.F., Baxter, D.J., Santorelli, R., Bregani, F.: The corrosion of AISI 310 stainless steel exposed to sulphidizing/oxidizing/carburizing atmospheres at 600 °C. *Corros. Sci.* **35**(5–8), 1085–1090 (1993)
10. Hosseini, H.S., Shamanian, M., Kermandpur, A.: Characterization of microstructures and mechanical properties of Inconel 617/310 stainless steel dissimilar welds. *Mater. Charact.* **62**(4), 425–431 (2011). <https://doi.org/10.1016/j.matchar.2011.02.003>

Chapter 50

Modification of Aluminium Alloy Surface Composite Reinforced with ZrO₂ Particles Fabricated Through Friction Stir Processing



Surendra Kumar Patel , Virendra Pratap Singh  and Basil Kuriachen 

Abstract The improvement in mechanical behaviour of the modified surface composite was accredited to development of the microstructural structures. This was reached by fine spreading of zirconium dioxide (ZrO₂) particles into the A6063 alloy. The bulk amounts of stir zone (SZ) microhardness for fabricated composite were equated to the results calculation by a Hall–Petch-type equation between obtained hardness versus particle grain size. The effect of surface-particle distribution over the material flow around the pin was also examined using scanning electron microscope (SEM). Additionally, compared with the base metal, both the microhardness and tensile strengths of the friction stir processed (FSP) composites were progressively improved with gradually increases the number of FSP passes. Adding the ZrO₂ ceramic particles, the applied severe plastic deformation and elevated the strain rate of the materials during FSP. As possibly will be seen, adding the ZrO₂ particles resulted in an enhancement in the microstructural behaviour tensile strength and microhardness.

Keywords Friction stir processing · Al–ZrO₂ composite · Mechanical properties · Nanocomposites · Strain rate

50.1 Introduction

Friction stir processing (FSP) is a solid-state material processing method based on the concepts of friction stir welding (FSW) which was invented at The Welding Institute (TWI) in 1991, UK [1]. During this process, severe plastic deformation (SPD) occurs as the stirring action forced by the tool throughout FSP, and it is to be controlled to numerous interesting applications, as microstructural characteristic modification, homogenization of alloys and homogenization of metal matrix composites (MMCs). The extremely fine structural formation feature of Al-based alloys at standard tem-

S. K. Patel · V. P. Singh · B. Kuriachen (✉)
Department of Mechanical Engineering, National Institute of Technology Mizoram, Aizawl
796012, Mizoram, India
e-mail: Basilkuriachen@gmail.com

© Springer Nature Singapore Pte Ltd. 2020
M. S. Shunmugam and M. Kanthababu (eds.), *Advances in Additive Manufacturing and Joining*, Lecture Notes on Multidisciplinary Industrial Engineering,
https://doi.org/10.1007/978-981-32-9433-2_50

perature and pressure with the uniform crystal structure requires grain refinement. It has been exposed that the aluminium alloys with fine grain microstructures become much more feasible at slightly pre-eminent temperatures [2]. Such features are proposed to be applied in the supercomputer, automobile industry and communication, for developing complex components through press forming technique. The friction stir processing can be significant in refining the ultra-grain size and equal distribution the microstructure (uniform the local solute structures) in particular positions of needful consideration [3]. It has indicated that FSP is used as an experimental approach to fabricating the surface composites. For example, to fabricate aluminium surface composited via FSP, reinforcements such as SiC and Al₂O₃ powders are implanted into the Al-alloying matrix, and also Nickel and SiC powders which are much useful to modify the surface of a plate during the FSP. The SiC residues can be overflowing into a groove on a plate earlier the FSP. Addition of SiC particles to the surface of plate was accredited to improvement the influenced strain and the pinning effect. The momentous increase into the hardness of stir zone (SZ) was credited to the refinement of grains as well as the effect of SiC particles [4]. In addition to avoid the particles from being exiled out of the groove throughout the FSP, a surface was proficient with an improved FSP tool had a pinless shoulder during the FSP. To obtain the SiC grains to be homogeneously spread over the matrix, the dispensation process was repetitive under the same conditions associated with the stiffness of the SZ. Remarkably, hardness increased from 70 to 110 Hv owing to the occurrence of the SiC grains. It is seen that particle spreading was mainly pretentious through FSP parameters such as rotating speed, traverse speed and FSPed pass [5]. A good particle spreading was primarily accomplished at higher rotating speed than the traverse speed. FSP includes compound material line-up and plastic distortion. Movement conception and approximation of the strain rate at significant position mostly found in composite manufacture since it would help to recognize, how the subdivision atoms are dispersed and thus forecast the accepted properties [6]. In response to industrial requirements, several wear-resistant steels have been commercialized by the manufacturers. Generally, the commercial materials are identified by their hardness to show their wear resistance. Based on the practical experiences of the current authors, the hardness is not a reliable factor for judgment of the wear resistance such that Al-alloy with identical hardness may exhibit different life under different working conditions. For example, it is experienced that one might exhibit longer life when it is used as a boiler, whereas the other one might be more appropriate to be used in screw conveyors. It is worthwhile to mention that such an ambiguous relation between the hardness and wear resistance has been reported in the literature. For instance, it has been proved that hardness is a reliable wear index only when chemical compositions and microstructures of the samples are identical [7]. To clarify this matter and to reveal the relations between the wear resistance and hardness of the target materials, a part of the current research is focused on this issue. To provide a better sense about the deviations, standard deviation per cent is plotted versus the elevation. Here, STD per cent at each elevation is calculated via dividing of the STD by the average value at that elevation [8]. It is observed that, by going up along the pot height, the slurry concentration is decreased and the deviation per cent is increased. For the five

bottom elevations, STD per cent is less than 18%, whereas it is around 32% for the highest point [9]. In other words, at lower elevations, the concentrations are close at different sampling times, whereas more deviated amounts of concentration are obtained at the upper positions. As an identical sampling procedure was applied for all valves, such differences between the data of different valves should be related to the flow not to sampling error. As an explanation, this might be due to the fact that, at lower elevations, the slurry is denser and the particles have to move on smoother streamlines, which causes forming more uniform flow regime leading, in turn, to more stable sampling [10].

Thus, numerous studies have been designated the material flow about the pin and calculate the amount of the strain rate throughout this severe plastic distortion in order to accomplish a better empathetic of the process. Investigator pictured out the material flow through surrounded indication materials. In current work, micro-particles of ZrO_2 were further to the surface of A6063 alloy to develop a surface composite surface through FSP. The influences of ZrO_2 particles on the microstructural and mechanical properties were calculated.

50.2 Materials and Experimental Procedure

The specimens of 180 mm × 120 mm × 4 mm were cut from A6063 alloy. Nanoparticles of stabilized zirconium dioxide with the average particles size of 50 μm were used in volume percentage (15 vol%) to produce surface composites thickness on the surface of the A6036 alloy. The specifics of the A6063 alloy are specified in Table 50.1. The tool was made of WC. The shoulder diameter was 20 mm, while the height and diameter of the pin were, respectively, 4 mm and 6 mm. The applied rotating and traverse speeds were 1200 rpm and 20 mm/min, individually. The tool tilt was set to 3° and rotation direction in clockwise. In order to develop a surface composite, a groove with same depth and width of 2 mm was designed along the plate length, which was then covered with ZrO_2 reinforcement and was pad-locked

Table 50.1 Chemical compositions of Al-alloy (A6063)

Elements	wt%
Si	0.2–0.6
Fe	0.0–0.35
Cu	0.0–0.1
Mn	0.0–0.1
Mg	0.45–0.9
Zn	0.0–0.1
Ti	0.0–0.1
Cr	0.1 max
Al	Balance

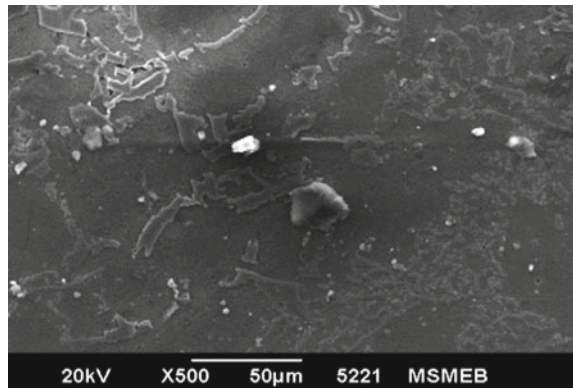
with a pinless tool. The microstructural growth examination during the FSP was characterized with a scanning electron microscope (SEM). To evaluate the mechanical properties of the fabricated surface composite, tensile and hardness tests were carried out. The hardness tests were observed under indentation/dent load of 100 g for time of 15 s. The dimensions of tensile samples which were prepared conferring to ASTM E8-04.

50.3 Results and Discussion

The SEM micro-image obtained from the composite surface is presented in Fig. 50.1. In the SEM results, the existence of ZrO_2 particles in the metal matrix shown by grains marked. The composition of the ceramic (ZrO_2) particles with base material, indicated in micrograph.

The microstructure of the processed composite obtained from base metal and two-pass of the FSP is shown in Fig. 50.2a, b. However, Fig. 50.2c shows the micrograph of fictional surface composite after four passes through FSP. The outcomes designate that the original microstructure of the base metal is made up of coarse and non-uniformity grains having average grain size of about 50 μm . It can be seen in Fig. 50.2a, after addition the reinforcement particles ZrO_2 , the particle grains became too much finer, considering an average grain size of around (6–10) μm . After four-pass of the FSP, the grains even refinement leading to become a grain size of around 4 μm as shown in (Fig. 50.2c). The ZrO_2 particles spread over the grain interface in stirred zone. The establishment of ultra-fine grains refinement can be credited to the Zener effect in pinning the grain interface. The developments of the dynamically recrystallized grains are pointedly withdrawn through Zener pinning effect. Actually, the grains to be disposed and produce for the effect of high temperatures; however, the reinforcement particles avoid its progress by pinning effect. The better dispersal

Fig. 50.1 SEM view of ZrO_2 dispersion in A6063 matrix



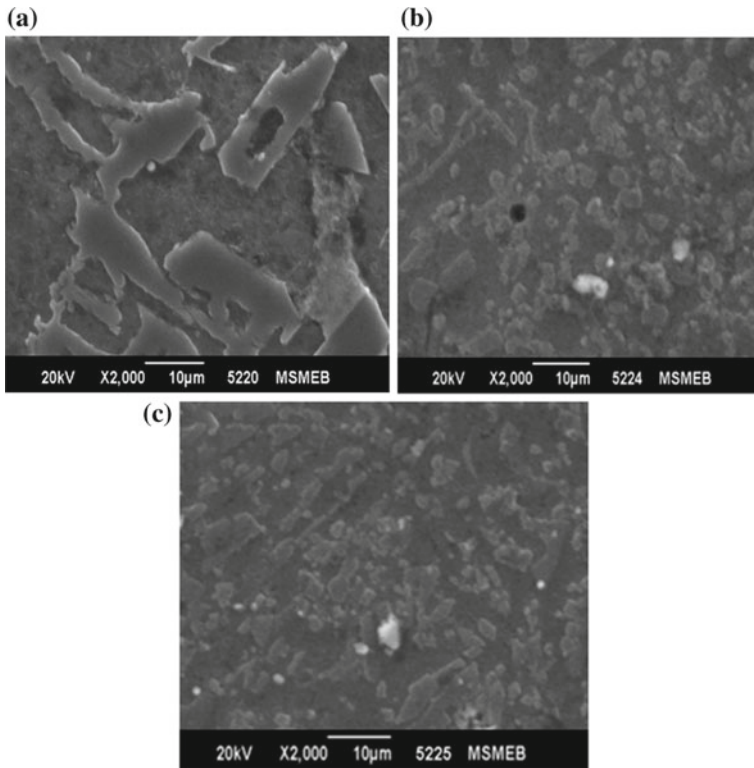


Fig. 50.2 Microstructure of the stir zone: **a** base metal, **b** after two-pass and **c** four-pass of FSP with ZrO_2

of the particles after four-pass of the FSP caused in the improved pinning result of zirconium dioxide (ZrO_2) particles.

The microhardness of numerous FSP passes are specified in Table 50.2 and Fig. 50.3. The observation of the data evidently validates that the hardness values are significantly affected through number of passes. It could be credited to ultra-fine grains microstructure with tool design due to the sufficient heat and materials flow obtained through processed surface made using conical-tool profile. This result is in

Table 50.2 Microhardness values of base metal and FSPed composites (two and four passes)

Samples	Microhardness (HV)						
	Distance from centre (mm) in stir zone						
	-3	-2	-1	0	1	2	3
Base metal	56.9	53.4	51.6	52.8	53.7	52.8	53.2
Two-pass	58.6	72.6	68.9	64.5	65.6	66.7	66.2
Four-pass	64.5	83.5	87.2	86.9	83.8	87.9	85.9

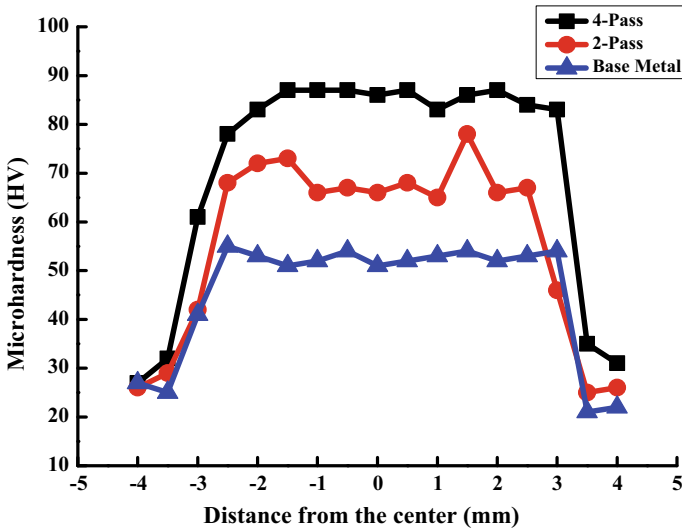


Fig. 50.3 Microhardness graph of base metal and FSPed composites (two and four passes)

promised with SEM images which shown in Fig. 50.2. In fact, ultra-fine grains consequence of a developed resistance and it is the sign of displacements and develop the hardness and strength of the fabricated surface composite. The considered microhardness of the (A6063 alloy) as-received aluminium plate, the two-pass FSPed surface composite and the four-pass FSPed surface composites were, respectively, around 54, 75 and 89 Hv. This shows a better agreement among the considered and measured values of microhardness.

In the current research, the wear behaviour of four commercial aluminium was studied. It was observed that the hardness reduces along the depth of the samples. Regarding the microstructural evolutions, in all sample martensite was the main phase, while small fractions of retained austenite and ferrite also existed. It was revealed that alloy has the finest and the most homogeneous martensitic phase, while coarse martensite was present aluminium alloy. Regarding the decrease in hardness along the depth, the samples ranked from the best to the worst. The lower quenching rate in the depth of the plates can be likely an important reason for the degradation of the hardness through the depth of the plates.

Appropriate examination of the effect of the zirconium dioxide particles on the mechanical characterization, such as tensile tests were found out, the outcomes of which are shown in Table 50.3 and Fig. 50.4. Possibly, it will be seen that adding the zirconium dioxide (ZrO_2) ceramic particles resulted into improved tensile strength from 47 to 120%, respectively, for two and four passes as compared to base metal.

Table 50.3 Tensile properties of the A6063 and friction stirred (two and four passes) specimens

Samples	Yield stress (MPa)	Ultimate stress (MPa)	% Elongation
Base metal	54.80	148.70	31.10
Two-pass	81.20	152.20	23.40
Four-pass	121.40	177.40	27.50

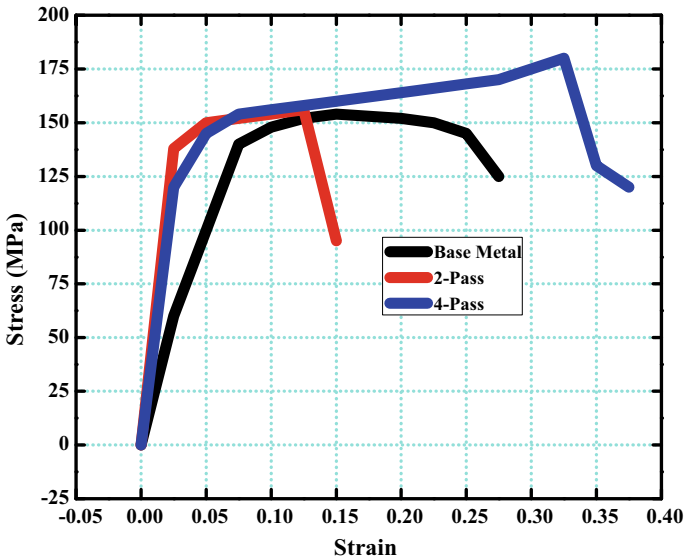


Fig. 50.4 Stress–strain (tensile) curves of A6063 and FSPed composites (two and four passes)

50.4 Conclusions

Zirconium dioxide reinforced into A6063 aluminium metal–matrix composites with substantial control over the microstructural behaviour and properties were fabricated through FSP technique. The number of FSP passes has been considered as an effective process parameter to optimize the performance of the final product. While the four-pass composites exhibited the homogeneity over the surface and the improvement in mechanical properties such as tensile strength and microhardness. The modified surface composite was credited to the finer grains concerning the pinning effect of the ZrO₂ nanoparticles. The increase in the FSP passes leads to finer grains as well as less accumulation refinement of the particles, consequently enhancing the pinning effect of particles.

References

1. Paik, JeomKee: Mechanical properties of friction stir welded aluminum alloys 5083 and 5383. *Int. J. Naval Architect. Ocean Eng.* **1**(1), 39–49 (2009)
2. Mishra, R.S., Ma, Z.Y.: Friction stir welding and processing. *Mater. Sci. Eng., R* **50**(1–2), 1–78 (2005)
3. Pozdniakov, A.V., Zolotorevskiy, V.S., Barkov, R.Y., Lotfy, A., Bazlov, A.I.: Microstructure and material characterization of 6063/B₄C and 1545 K/B₄C composites produced by two stir casting techniques for nuclear applications. *J. Alloy. Compd.* **664**, 317–320 (2016)
4. Xie, S., Li, R., Yuan, T., Chen, C., Zhou, K., Song, B., Shi, Y.: Laser cladding assisted by friction stir processing for preparation of deformed crack-free Ni–Cr–Fe coating with nanostructure. *Opt. Laser Technol.* **99**, 374–381 (2018)
5. Esmaily, Hossein, Habibolahzade, Ali, Tajally, Mohammad: Parametric investigation of Al5456/BNi-2 composite properties fabricated by friction stir processing. *J. Alloy. Compd.* **725**, 1044–1054 (2017)
6. Qian, J., Li, J., Xiong, J., Zhang, F., Lin, X.: In situ synthesizing Al₃Ni for fabrication of intermetallic-reinforced aluminum alloy composites by friction stir processing. *Mater. Sci. Eng.* **A550**, 279–285 (2012)
7. Navazani, M., Dehghani, K.: Fabrication of Mg–ZrO₂ surface layer composites by friction stir processing. *J Mater. Process. Technol.* **229**, 439–449 (2016)
8. Khodabakhshi, F., Simchi, A., Kokabi, A.H., Gerlich, A.P., Nosko, M.: Effects of post-annealing on the microstructure and mechanical properties of friction stir processed Al–Mg–TiO₂ nanocomposites. *Mater. Des.* **63**, 30–41 (2014)
9. Ke, L., Huang, C., Xing, L., Huang, K.: Al–Ni intermetallic composites produced in situ by friction stir processing. *J. Alloy. Compd.* **503**, 494–499 (2010)
10. Shojaefard, M.H., Akbari, M., Khalkhali, A., Asadi, P.: Effect of tool pin profile on distribution of reinforcement particles during friction stir processing of B₄C/aluminum composites. *Mater. Des. Appl.* <https://doi.org/10.1177/1464420716642471> (2016)

Chapter 51

Investigation of General Welding Defects Found During Friction-Stir Welding (FSW) of Aluminium and Its Alloys



Virendra Pratap Singh , Surendra Kumar Patel , Basil Kuriachen 
and Saurav Suman 

Abstract Friction-stir welding (FSW) of aluminium and its alloys are presently employed in numerous modern industries. The weld joint should have enough elastic–plastic behaviour and formability levels same as parent metal. Being a solid-state joining process, friction-stir welding method has been extensively used for soft material like aluminium, magnesium and its alloys. Aluminium and its alloys have magnificently remunerated to meet the escalating demand for lightweight (weight to density) products. Remarkable growths in aluminium alloys and welding procedures have resolute many welding concern complications, even though a few problems remain to be pointed out. The present investigation efforts to provide an outline for the various types of defects and its fundamental factors associated to the development of defects in friction-stir welding process usually used for aluminium and its alloys.

Keywords Friction-stir welding · Defects · Aluminium alloys · Process parameters

51.1 Introduction

The FSW process developed at The Welding Institute (TWI), UK, in 1991, is a solid-state welding technique which circumvents the development of solidification defects like cracking and voids accompanied by fusion welding. Additionally, it substantially enhances the weld properties and has been comprehensively realistic in welding soft metals, particularly for aluminium and its alloys [1].

Since several years, aluminium alloys have been one of the principal contestants stick with material choice in various industries, counting with the commercial, military aircraft and marine sectors, primarily because of its renowned mechanical behaviour (strength), ease with design and machinability [2]. The classical set for such multi-material structures are reflected as Advanced High-Strength Steel (AHSS)

V. P. Singh · S. K. Patel · B. Kuriachen (✉) · S. Suman
Department of Mechanical Engineering, National Institute of Technology Mizoram, Aizawl
796012, Mizoram, India
e-mail: Basilkuriachen@gmail.com

and aluminium alloys. But, such dissimilar metals are challenging to join through fusion welding because of dissimilarities in its physical and mechanical properties and tendency towards the development of huge quantities of brittle intermetallic compounds (IMCs). Aluminium is having unique properties concerning to weld metal as compared to ferrous alloys, because aluminium alloys shows absence of a solid-state microstructural transformation during cooling. Thus, its microstructural changes determine only by solidification [2, 3].

The factors promoting the FSW defects in aluminium alloys are complex, and as FSW is an intricate hot shear (high strain rate) and forging method, one cannot able to find out the source of defects straightforward. The residual stresses and defects formation into weld zone are significantly affected through the intricate plastic deformation (distortion) process. In this paper, the key parameters of FSW have been investigated in addition to the various collective joining defects which take place if an unsuitable set of parameters are used.

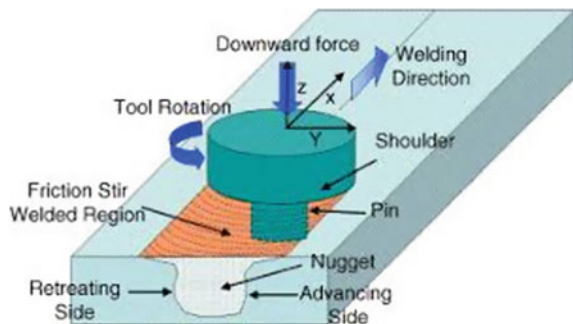
51.2 Friction-Stir Welding Features

Friction-stir welding technique has been deliberated among the most substantial progress of metal joining in the last few decades. It comes under green technology because of its energy saving proficiency, ecological friendly and its flexibility. The vast application of FSW has been expanded to noticeable contribution in the fabrication of highly incorporated welds in solid phase of 2000, 5000, 6000, 7000 and Al–Li series Al alloys and its metal matrix composites [2, 3].

51.2.1 Process Principles

In FSW process, the steps follow successive order; the frictional heat (pre-heat), early deformation, forging process and upon cooling metallurgical changes. Figure 51.1 represents the schematic diagram of FSW. The welding process starts as the heat

Fig. 51.1 Schematics of the friction-stir welding process [2]. ©Elsevier. Reproduced by permission of Elsevier. Permission to reuse must be obtained from the rights holder



generated (frictional heat) between the surface of the workpiece surface and the shoulder material, causing softening of material which tends to severe permanent deformation [2]. The soft material is stirred from the front to trailing edge of the tool, where forging action takes place into a proper joint. Thus, the FSW process is a thermal process and a mechanically deformation process, taking place in a solid phase; it employs deformational and frictional heat as the source to have a bond between metals under vertical axial force [4].

There are basically two positions known as advancing side (AS) and retreat side (RS) with respect to FSW tool rotation and welding speed. The FSW welds have some extent to dissimilar microstructure to welds obtained through fusion welding procedures, because of the maximum generated temperature (peak temperature) around heat-affected zone (HAZ) is considerably very less as solidus temperature [2]. Figure 51.2 shows thermo-mechanically affected zone (TMAZ), where grain deformation takes place by keeping the original microstructures as usual that lies between the heat-affected zone (HAZ) and stirred zone (SZ). The flowability of the plastically deformed material is highly dependent on process parameters [2].

So, it is necessary to pay attention while selecting process parameters to avoid possible defects at the TMAZ/WNZ interface [4]. Taking an example of ‘onion ring’ defects at SZ, which is known for most severe plastic deformation, is an effect of the material deposition, through front and the back action with different dimensions tool.

51.2.2 Issues in FSW of Aluminium and Its Alloys

In FSW, various thermo-mechanical practices occur at the same time, comprising variations in heating, cooling and softening of material during operation. During FSW

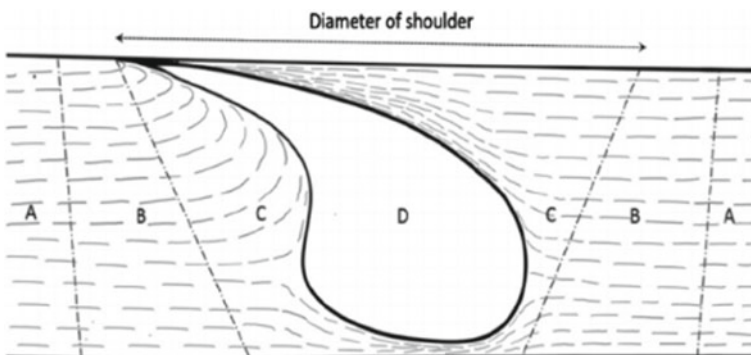


Fig. 51.2 Typical FSW weld region: **a** base metal, **b** heat-affected zone, **c** thermo-mechanically affected zone and **d** weld nugget zone/stirred zone [3]. ©Springer. Reproduced by permission of Springer. Permission to reuse must be obtained from the rights holder

operation, no liquid state occurs [2, 3]. Defects like hot cracking and porosity are generally not found in FSW welds being a solid-state joining technique, and welding takes place well under the melting point of base metal. FSW is also liable of forming flaw due to unevenness among the various welding zones. Defects such as void formation (non-bonding) may take place at very low welding temperature, because of inadequacy in material flow. Because of excess in material flow, decline in the joint interface tensile strength may ensure at hot circumstances [5]. Furthermore, defects can be predicted if the abutting plate's gap is not closely controlled. Substantial decrease in fatigue strength has been reported with the gap concerning the plates to be welded.

51.3 Commonly Found Friction-Stir Welding Defects in Aluminium and Its Alloys

51.3.1 Development of an Onion Ring Structure

Onion ring defects in FSW welds in aluminium alloys may perceive as a group around weld nugget zone (WNZ). The microstructures have distinguished by dark and bright alternative bands, the gap among the bands must be identical as tool onward motion in each revolution. Material conceded through weld of retreating side (RS) is collected to put into the cavity with the help of the pin [4]. Therefore, the weld nugget contains the blending of two flows of stream of material having different historical path and mechanical properties that probably enhance the onion skin structure. The onion skin defects can be seen in Fig. 51.3.

Increase in the welding temperature considerably affects the development of onion structure and that form a crack initiation around WNZ placed under fluctuating load. It is shown clearly that an onion skin structure is directly influence by changing the pitch of the tool throughout the weld joint interface. Subsequently, the chance of changing the process parameters optimization to alter the weld microstructure, strengthen the properties of material and mentioning the fracture toughness also [4].

Fig. 51.3 Onion ring defects [4]. ©Elsevier. Reproduced by permission of Elsevier. Permission to reuse must be obtained from the rights holder

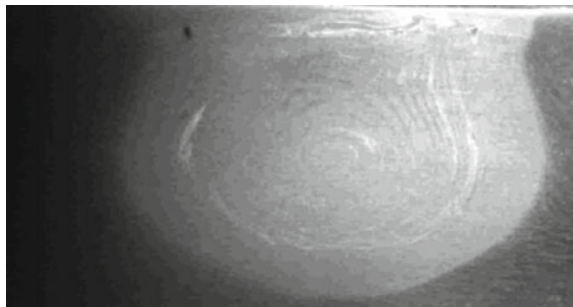
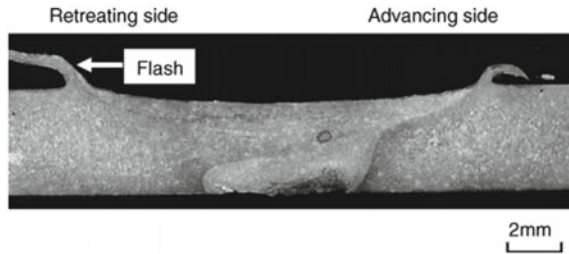


Fig. 51.4 Flash defects [6].

©Elsevier. Reproduced by permission of Elsevier. Permission to reuse must be obtained from the rights holder



51.3.2 Flash Defects Formation

The workpiece being welded practices very high temperature around the weld interface as tool pin rotational speed is very high. Thus, too much heat generates, resulting the material get soften around the tool pin and tool shoulder and ejects huge amount of material as surface flash [5]. The flash defects can be seen in Fig. 51.4.

As the tool pin plunge depth is more, the softened material around the tool probe is forced out, which effects into bond flash. So, the probe depth should be selected properly, in addition to this high tool tilt angle also leads to inadequate softening of material rests to seal the cavity over the WNZ and extra flash seems at retreating side (RS) [6].

51.3.3 Tunnel Defects Formation

As expressed already, as the welding parameters, i.e. welding speed (traverse speed), tool rotatory speed, tool tilt angle, etc., are unable to create the prerequisite heat for material bonding, insufficient mixing of material and forging action, causing into the appearance of tunnel defects [3]. Previous experimental results recommended that the tunnelling defects may occur in weld zone, as any increment in linear speed. As shoulder dimension increases, the heat generation also increases that openly advances the weld metal flow ability within the cavities. Hence, to reduce the tunnelling defects and to evade the cold processing situations, the heat input and flowability of weld material should be optimized. The incorporation of fragmented oxide layer by means of dark zigzags (wavy) line or we can have called it kissing-bond defects as shown in Fig. 51.5a, b. In Fig. 51.5b, weld defects highlighted by arrows. In Fig. 51.5c, d, defects are shown in enlarged outlook. Figure 51.5a, b may occur due to low heat generation in welds [2, 6]. Optimized process parameters of FSW abolish the development of zigzag weld lines, resulting in enhanced mechanical properties.

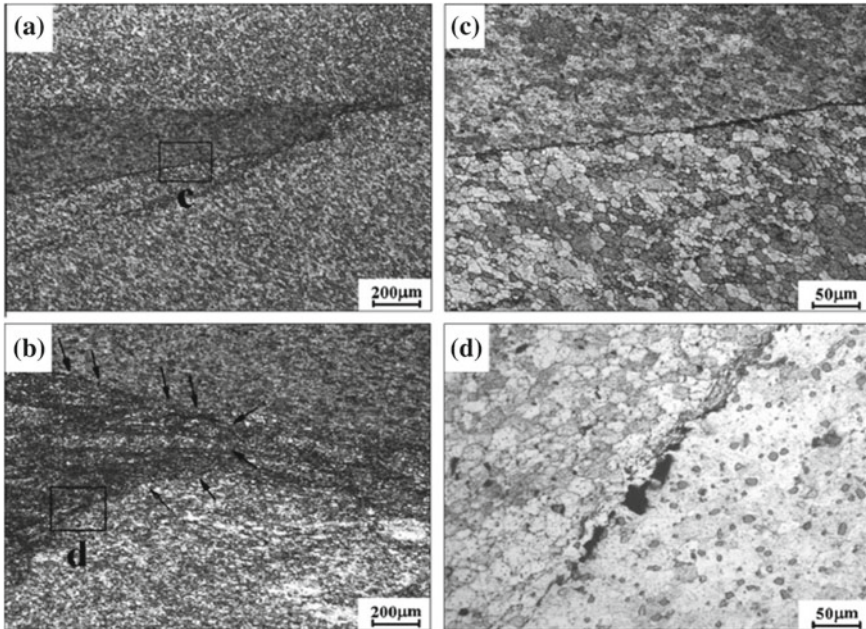


Fig. 51.5 Microstructure of kissing-bond or zigzag line defects [5]. ©Elsevier. Reproduced by permission of Elsevier. Permission to reuse must be obtained from the rights holder

51.3.4 Crack-Like Root Defects Formation

Welding parameters express a crucial part during the development of root defects or crack defects. These defects come up with inadequate heat generation or may be because of inadequate fragmentation of surface aluminium oxide films. When the tool probe plunging length is short, then grooving defect may take place over the advancing side (AS) [5]. Crack-like root imperfections as shown in Fig. 51.6a, b ensue because of the deficiency in probe depth as compared to workpiece depth.

At lesser tool tilt angle, lack of plunging force obtained leads to groove formation like defects [5].

51.3.5 Voids Formation Defects

Voids formation in the FSW weld is a very common defect. The dynamic forces related by means of deformed flow into weld nugget area show a crucial part in the development of these voids defects [7]. The voids defects can be seen in Fig. 51.7.

Even at higher linear speed the FSW joints shows reasonable strength and higher productivity, but beyond a certain limits it may promote the voids formation [7].

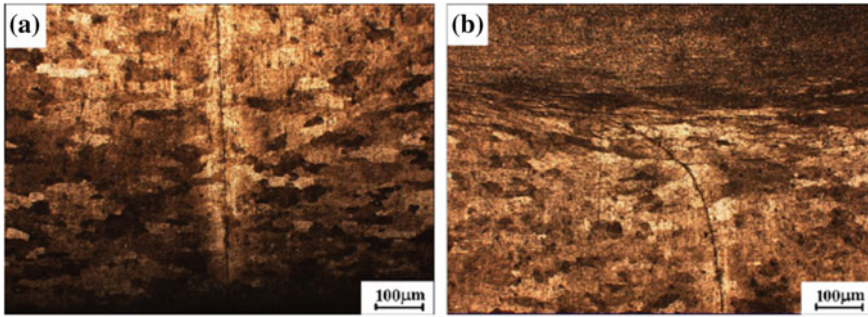
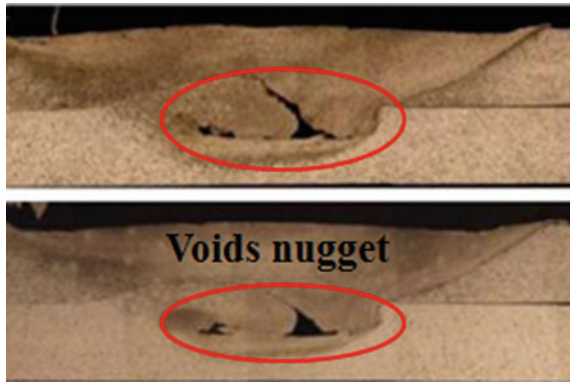


Fig. 51.6 Highlights the microstructure of the crack-like root defects [5]. ©Elsevier. Reproduced by permission of Elsevier. Permission to reuse must be obtained from the rights holder

Fig. 51.7 Voids defects [4]. ©Elsevier. Reproduced by permission of Elsevier. Permission to reuse must be obtained from the rights holder

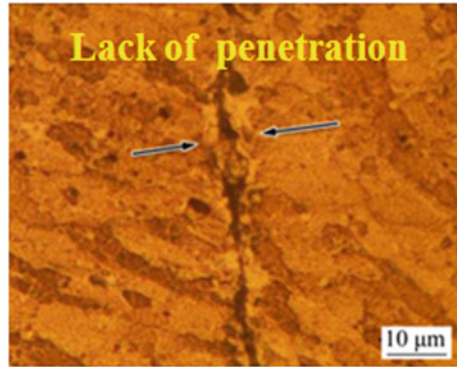


51.3.6 Lack of Penetration Defects

Lack of penetration is one of the usually found weld defects in dissimilar material FSW. This kind of defects generally found at the lowermost surface of the weld joint, and samples are isolated or not having proper joints consequently obtained weak bond between the welds [8].

It may be deliberated a crack initiation where stress corrosion aspect considers, deprived fatigue toughness and having less tensile strength, which leads to deformation. The lack of penetration defects can be seen in Fig. 51.8. This kind of defects may be identified by means of bend test which evaluate both the ductility and soundness of a material [8].

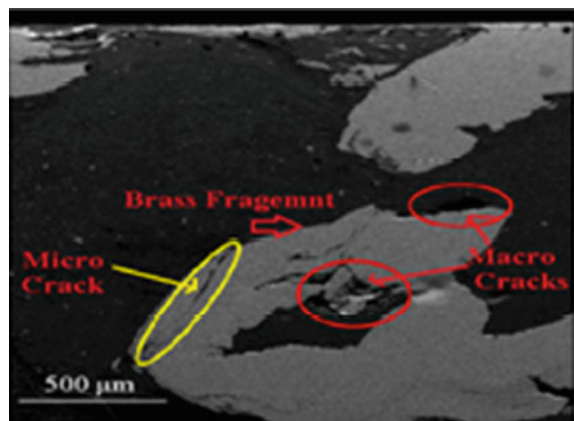
Fig. 51.8 Lack of penetration defects [5]. ©Elsevier. Reproduced by permission of Elsevier. Permission to reuse must be obtained from the rights holder



51.3.7 Fragmented Defects

These defects are exclusively set up in the course of dissimilar FSW of Al–Cu material and usually not shown for similar FSW material. The copper hard particles embedded into aluminium metal matrix which is deliberated as fragmented defect. The fragmented defects can be seen in Fig. 51.9. The incorrect metal flow cannot dispense the fragmented copper homogeneously; therefore, selection of optimized welding parameters particularly the low tool rotational speed and suitable offset of tool pin can decrease these kinds of defect [9, 10].

Fig. 51.9 Fragmented defects [6]. ©Elsevier. Reproduced by permission of Elsevier. Permission to reuse must be obtained from the rights holder



51.4 Conclusions

FSW evades difficulties associated with melting of materials, casting microstructure development and weld solidification shrinking zone which is usually found with fusion welding. FSW welding defects are somewhat different as compared to fusion welding defects. In this paper, the most common FSW defects that are associated because of setting wrong combination of process (welding) parameters (primarily traverse/welding speed and tool rotational speed). FSW defects comprises an onionskin structure, porosity, tunnel voids, defective tightness, kissing-bond defects, excessive flash and crack-like root flaws. To circumvent these defects, the thermo-mechanical properties of weld material must be recognized and the working temperature and its processing rate employed consequently. The fashion in which temperature hits metal properties differs considerably to various aluminium alloys. Though these welding parameters are designated suitably, the defects may take place because of incorrect tool tilt angle, wrong tool geometry (shoulder diameter and pin length) or improper control panel. Therefore, FSW welding parameters fit for dealing out one set of series of aluminium alloys, and it may vary significantly for that which is appropriate for other series of aluminium alloys.

References

1. Thomas, W.M, Nicholas, E.D., Needham, J.C., Church, M.G., Templesmith, P., Dawes, C.J.: Friction stir welding. International Patent Application no. PCT/GB92102203, (1991) Great Britain Patent Application No. 9125978.8
2. Mishra, R.S., Ma, Z.Y.: Friction stir welding and processing. *Mater. Sci. Eng., R* **50**, 1–78 (2005)
3. Paul, K., Richard, R., Jukka, M., Raimo, S.: Investigation of weld defects in friction-stir welding and fusion welding of aluminium alloys. *Int. J. Mech. Mater. Eng.* **10**(26), 1–10 (2015)
4. Krishnan, K.N.: On the formation of onion rings in friction stir welds. *Mater. Sci. Eng., A* **327**, 246–251 (2002)
5. Bo, L., Yifu, S., Weiye, H.: The study on defects in aluminium 2219-T6 thick butt friction stir welds with the application of multiple non-destructive testing methods. *Mater. Des.* **32**(4), 2073–2084 (2011)
6. Kim, Y.G., Fujii, H., Tsumura, T., Kumazemi, T., Nakata, K.: Three defect types in friction stir welding of aluminium die casting alloy. *Mater. Sci. Eng., A* **415**(1–2), 250–254 (2006)
7. Tae-Jin, Y., Jung-Gil, Y., Chung-Yun, K.: Formation mechanism of typical onion ring structures and void defects in friction stir lap welded dissimilar aluminium alloys. *Mater. Des.* **90**, 568–578 (2016)
8. Khan, N.Z, Khan, Z.A., Siddiquee, A.N., Al-Ahmari, A.M, Abidi, M.H.: Analysis of defects in clean fabrication process of friction stir welding. *Trans. Nonferrous Met. Soc. China* **27**, 1507–1516 (2017)
9. Esmaeili, A., Givi, M.B., Rajani, H.Z.: A metallurgical and mechanical study on dissimilar Friction Stir welding of aluminium 1050 to brass (CuZn30). *Mater. Sci. Eng., A* **528**(22), 7093–7102 (2011)
10. Singh, V.P., Patel, S.K., Kumar, N., Kuriachen, B.: Parametric effect on dissimilar friction stir welded steel-magnesium alloys joints: a review. *Sci. Technol. Weld. Joining.* <https://doi.org/10.1080/13621718.2019.1567031>

Chapter 52

Study of Heat Treatment Effect on Microstructure of PTA Weld Deposited Surface of SS 316L Steel



H. V. Naik , D. D. Deshmukh  and V. D. Kalyankar 

Abstract Plasma transferred arc (PTA) welding process is established method for surface modification by weld deposition of alloying elements. In this article, experimental investigation is performed with chosen parameters on ASTM 316 L steel as substrate with Stellite 6 as coating material by PTA process. Microstructural analysis was performed with scanning electron microscope (SEM). From the SEM micrographs, it is revealed that as-deposited coating region comprises uneven grain structures which are uniformly distributed in the eutectic matrix. Further, for studying the effect of heat treatment process on coating and substrate material, solution heat treatment followed by age hardening was adopted. After heat treatment, poor grouping amongst the Co-based solid solution and eutectic were observed for coarser arrangement which made ease for eutectic region to shed from the coatings. Microhardness of as-deposited surface was observed at 439 HV. After the two-stage heat treatment process, 7% upsurge in hardness was observed for the heat-treated coating for selected range of temperature and time. Similar kinds of results were observed in substrate regions, where 14% increase in hardness was recorded during testing of heat-treated sample. However, in interface regions, the hardness value decreased around 11%.

Keywords Plasma transferred arc (PTA) · Stellite 6 · Heat treatment · SEM · Microstructure

52.1 Introduction

The exploration for advanced grade engineering materials used in the fabrication of components which may operate under severe working environment is critical issue in manufacturing industries these days. The deposition of coatings by PTA to shield components made of high-strength engineering materials is a significant procedure

H. V. Naik (✉) · D. D. Deshmukh · V. D. Kalyankar
Department of Mechanical Engineering, S.V. National Institute of Technology, Surat 395 007,
Gujarat, India
e-mail: naik.hardik.v@gmail.com

© Springer Nature Singapore Pte Ltd. 2020
M. S. Shunmugam and M. Kanthababu (eds.), *Advances in Additive Manufacturing and Joining*, Lecture Notes on Multidisciplinary Industrial Engineering,
https://doi.org/10.1007/978-981-32-9433-2_52

for protecting such materials, according to the reports by Goncalves et al. [1] in their summarized work. From the literature study, hardness [2, 3], corrosion resistance [4, 5], wear resistance [6–8] and impact strength [9, 10] have been improvised by optimization of process parameters and selection of suitable alloying elements by various researchers. For engineering valve applications, components are exposed to very harsh working conditions such as wear, high contact stress, corrosion and erosion [11, 12]. Therefore, reduction in surface damage as well as improvement in hard facing layer becomes focused area of investigation for the benefits of valve industries [11, 13, 14]. Many research works have been reported in terms of weld deposition of Stellite 6 as coating material on engineering materials used such as AISI 316 stainless steel, AISI 309 stainless steel in valve industries [15, 16]. The given combination of AISI 316 Steels with Stellite 6 coating material is frequently used as optimum combination in supporting bearings [16], engineering valves [10] in turbine components, bush [6], sleeve in sink roll [15], etc., for many years. Therefore, many research works are reported in terms of investigations for betterment of the mechanical properties as an outcome [4, 9, 11, 17–19]. For example, size of dendrites in Stellite 6 on AISI 316 stainless steel was examined, and the effect of various process parameters such as arc current, oscillation width, preheat temperature and powder feed rates was considered [6, 15]. It is observed that high wear resistance is associated with high quantity of retained austenite and strain induced transformation [20, 21]. Another reason is the presence of fine carbide particles and eutectic carbide network for improvised hardness [22–24]. Although Stellite 6 was found to be more suitable for valve industries, there were some problems observed due to insufficient hardness [25]. Under such difficult working conditions, the hardness of the weld surfacing has to be at least 505 HV, though Stellite 6 is having hardness about 388 HV [25]. However, over the years, heat treatment process has been beneficial in terms of refinement of mechanical properties as it causes the microstructural changes in engineering materials. Further, various heat treatments such as annealing [26], tempering [27] and ageing [28] have been reported for the examination on microstructural changes which eventually affect microhardness and wear resistance of weld deposited surfaces and substrates. For example, Hou et al. [28] studied the effect of heat treatment by selecting 600 °C temperature and soaking time of 60 h on cobalt-based coating and 0.12 wt% carbon steel as base material. During this experimental work, poor wear resistance and negligible improvement in terms of microhardness were observed due to coarser microstructure. Few attempts have been reported related to the application of different heat treatment processes on various coating materials such as Co-based alloy [18, 20, 29], TiC–Cr powder [19, 30, 31], Fe-based alloy [21, 32] and Ni-based alloy [30, 33, 34].

Various experimental investigations have been directed towards the consequence of different heat treatment processes on coating materials. Gurumoorthy et al. [35] studied the effect of heat treatment by selecting 650 °C temperature and soaking time of 250 h on Ni-based coating and 316 L (N) stainless steel as base material. In this work, there was no effect over hardness observed after heat treatment process due to stability in microstructure. Shi et al. [27] studied the effect of various tempering temperature (200, 400, 600 °C) and constant soaking time of 2 h on TiC–Cr powdered

coating and low-alloyed grey cast iron as substrate material. In this work, microhardness was decreased with increase in heating temperature due to depletion of Cr and formation of α -Fe content. Huayi et al. [36] conducted the experimental investigations by considering 600 °C temperature and soaking time of 0.67 h on Fe-based coating and low-carbon steel as substrate material. With the help of SEM, resolving of eutectic structure at annealing temperature was observed which resulted in poor nanohardness compared to as-deposited samples. Considering improvement aspect on PTA coatings, there have been very undesirable results in terms of microhardness obtained after heat treatment process.

Few attempts in terms of experimental works have been applied for studying transformation of the microstructure by tempering treatment, and there were still many unexplored heat treatment processes such as solution heat treatment, case hardening techniques and age hardening which were seldom applied. Further, most of the research works were based on the subsequent heat treatment study of laser cladding, and very inadequate research work was existing on PTA even though its benefits are well recognized [37, 38]. Therefore, in this experimental work, a comprehensive study on the influence of solution heat treatment followed by age hardening process on microstructure and microhardness of Stellite 6 hardfacing deposited on stainless steel 316 L through PTA welding process was attempted.

52.2 Experimental Details

52.2.1 *Experimental Material*

In this work, a stainless steel 316 L code named ASTM 316 L steel was used. It was obtained from the casting process followed by cold working process with a chemical composition presented in Table 52.1. The Co–Cr powder was selected as coating materials in the ratio as per the Stellite 6 composition which is shown in Table 52.1. For this experimental work, size of Co–Cr powder was used of 45–125 μm .

52.2.2 *Experimental Methods and Process Parameters*

Necessary experiments were performed on the specimen of ASTM 316 L substrate material of size 120 × 150 mm cut from the 16-mm-thick plate. Preheating of 200 °C was provided to all samples applied before weld deposition for avoiding the crack formation. Multi-track deposition was prepared on the sample by maintaining nearly 50% overlapping, and 250 °C interpass temperature was maintained. For the deposition process, 4 mm diameter and 2% throated tungsten electrode with torch of 25 mm diameter was utilized. Pure argon (Composition: 99.99% Ar) was utilized at a constant flow rate as per different requirements, i.e. for shielding purpose 13–15 L/min,

Table 52.1 Chemical composition of substrate material and coating material (wt%)

Composition %	C	Si	Cr	Co	W				
Co- Cr alloy	1.08	1	28.75	Balance	4.37				
Composition %	C	Si	Cr	Ni	P	S	Mo	Mn	N
SS 316L	0.02	0.3	16.5	10	0.032	-	2.01	1.2	-

Table 52.2 Details of optimized parameters

Parameters for PTA process	
Transferred arc current	140 (A)
Travel speed	180 (mm/min)
Powder flow rate	14 (gms/min)
Oscillation speed	650 (mm/min)
Stand-off distance	10 (mm)

for plasma centre gas 3.5–4 L/min and for powder flow 2–3 L/min, and same was maintained during the experimentation and 1G groove welding position with DCEN polarity was used. Further, Table 52.2 gives the details of processing parameters used for the tracks deposition. After the deposition of Stellite 6 coating on ASTM 316 L material by PTA process, the samples were classified into two groups. Further, obtained coating thickness for both samples is identical of 3 mm after machining. The first group of samples was remained to be in original status of as-deposited condition, whereas the second group was classified as heat-treated sample.

Here, both samples were cut by abrasive cutting machine from the same plate which was constructed using optimized parameters mentioned in Table 52.1.

52.2.3 Heat Treatment Process Details

With the view of studying the effect of the heat treatment process on PTA coatings, solution heat treatment process followed by age hardening process was adopted for the second group of samples. During the first phase of heat treatment process, temperature was selected at 1050 °C at which point alloying constituents are taken into one solid solution (i.e. brought near their melting point), prior to a fast quenching (water as medium) and soaking time was 30 min based on Co–Cr phase diagram [39]. This process helps in retaining the grain structure but forces softness in the material. Hence, it necessitates a subsequent ageing operation to increase the hardness. Therefore, age hardening process was performed at 600 °C for 60 min soaking time followed by furnace cooling.

52.2.4 Detailed Description of Sample Preparation

Steps involved for the preparation of metallographic specimens are described here for microhardness and microstructural investigations. Sectioning, mounting, rough grinding, polishing and chemical etching are necessary steps which are followed in order to achieve less depth of microstructural damage on samples. Sectioning was done in perpendicular direction to welding track with the help of abrasive cutting machine in order to reduce chances of less heat generation. Mounting of specimen

is done with help of hot mounting process and Bakelite as a powder material. Afterwards, grinding and polishing are final steps conducted over prepared metallographic specimen. Grinding is followed by subsequent polishing paper so that mirror image can be acquired. After acquiring mirror image, the samples are then etched with etchants containing CuCl_2 and HNO_3 .

52.2.5 Characterization of Heat Treatment

The heat treatment effects on microstructure and microhardness were analysed underneath the subsequent procedures. Both groups were cut parallel to the length direction, and proven approaches of metallographic sample preparation were performed. Microstructural investigations were examined by Hitachi S3400N, SEM and ZEISS Axio Observer, optical microscope (OM). For the measurement of microhardness, Vickers microhardness testing machine (HM-211, manufactured by Mitutoyo Corporation, Japan) was used and for the current research purpose, and 1000 gf load was applied for 10 s for all indentations carried out on both samples.

52.3 Results and Discussions

52.3.1 Microstructural Analysis

SEM images as per the Fig. 52.1a, b show microstructural characteristics of the bonding zone between the substrate and coating materials. It can be observed that the ASTM 316 L steel substrate and the Stellite 6 coating are of high-quality and crack-free metallurgical bonding having noticeable gradient microstructure. From the SEM micrographs, it is revealed that the microstructure of the PTA weld surfacing coating region comprises uneven grain structures which are uniformly distributed in the eutectic matrix, as shown in Fig. 52.1a, b, whereas after solution heat treatment followed by ageing treatment, sample shows different microstructure with the exposure to 1050 and 600°C temperatures and varied cooling rates. As shown in Fig. 52.1c, after the heat treatment coating region contains uneven surface and some portion of unmelted elements which has resulted in marginal difference and change in microhardness. At the interface region, as-deposited samples are observed with uniform and finer defect-free bonding due to process capability of PTA weld surfacing, whereas after heat treatment process, it is observed with some minor deformation as well as non-uniform structure which are less fine than the previous one. Hence, observed mechanical properties in terms of hardness may be varied which further is validated by mechanical testing.

From Fig. 52.1d, furthermore, it can be seen that the eutectic assembles with large network with coarser structure than as the previous group of samples with deposited

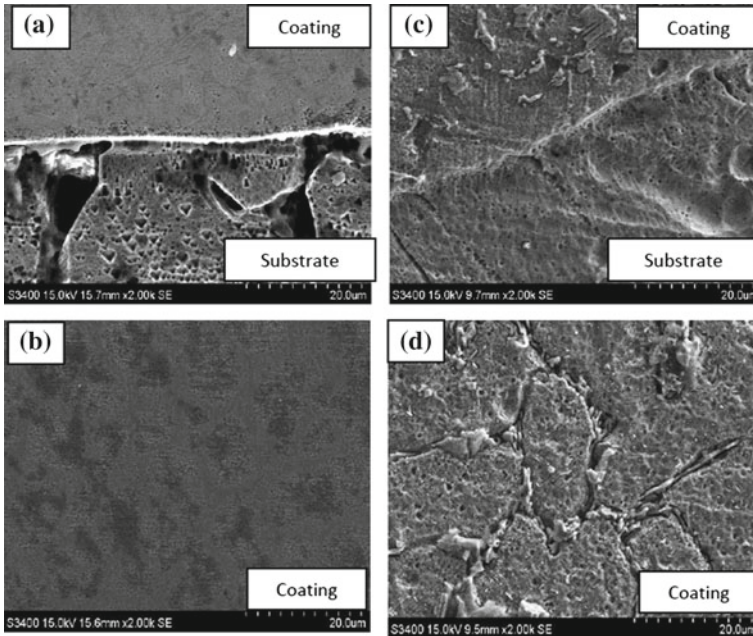


Fig. 52.1 SEM micrographs of **a** as-deposited sample—interface region, **b** as-deposited sample—coating region, **c** heat-treated sample—interface region, **d** heat-treated sample—coating region (Magnification: 2000X)

conditions. Poor combination amongst the Co-based solid solution and eutectic were responsible for this arrangement which resulted in ease for eutectic region to shed from the coatings. This can be resulted in cracks during service conditions as this line indicates the higher stress concentration in grain boundaries. The deformed grains are resulted by the uneven cooling rates during heat treatment; hence, possible stress relieving techniques shall be included in future.

As shown in Fig. 52.2a, b, substrate region was observed having very finer structure after heat treatment process as temperature of first phase was selected in accordance with making one solid solution. As shown in Fig. 52.2, main difference observed in microstructure was in terms of refinement of grains and grain boundaries after heat treatment. There are number of uneven grain orientation observed in as-deposited samples whereas, after heat treatment it has improved marginally by forming uniform grain orientation. Therefore, an increment in microhardness was observed in the coating region as well as substrate region than that of as-deposited specimens, whereas in interface, there was very marginal fall of microhardness and few cracks observed.

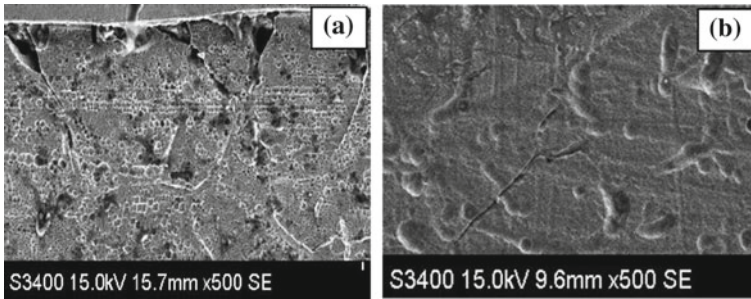
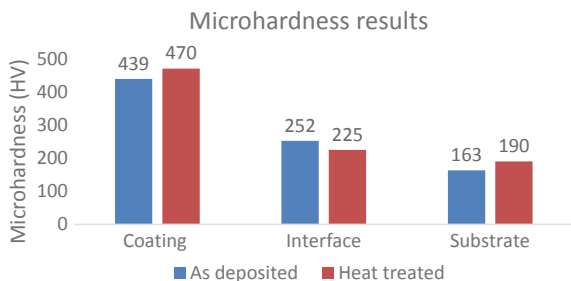


Fig. 52.2 SEM micrographs of substrate region **a** as-deposited sample and **b** heat-treated sample (Magnification: 500X)

52.3.2 Hardness Study

Further, for the measurement of microhardness, Vickers microhardness testing machine (HM-211, manufactured by Mitutoyo Corporation, Japan) was used and for the current research purpose, 1000 gf load was applied for 10 s for all indentations carried out on both samples. Figure 52.3 shows the comparison between as-deposited surface and heat-treated surface categorized in three regions, namely coating, interface and substrate. Microhardness of the as-deposited surface was observed at 439 HV. After the two-stage heat treatment process, 7% upsurge in hardness was detected for the heat-treated coating for selected range of temperature and time. Similar kinds of results were observed in substrate regions, where 14% increase in hardness was recorded during testing of heat-treated sample. However, in interface regions, the hardness value decreased around 11%. In coating and substrate region, uniform microstructure was observed and further, there were no involvement of metallurgical bonding. Due to the existence of variance in thermal expansion at the interface regions, there were non-uniform microstructure distribution observed which resulted in decrement in microhardness at particular region.

Fig. 52.3 Vickers microhardness taken on the surface of heat treated and the as-deposited coating



52.4 Conclusions

- Wear-resistant and hard Co–Cr powder (Stellite 6) coating was deposited on a substrate of ASTM 316 L steel by the technique of PTA weld surfacing using chosen parameter successfully.
- After heat treatment, it can be seen that the eutectic assembles with large network with coarse grain structure than as the previous group of samples with deposited conditions. Bad combination between the Co-based solid solution and eutectic were responsible for this arrangement which resulted in ease for eutectic region to shed from the coatings.
- Microhardness of as-deposited surface was observed at 439 HV. After the two-stage heat treatment process, 7% upsurge in hardness was observed for the heat-treated coating for selected range of temperature and time. Similar kinds of results were observed in substrate regions, where 14% increase in hardness was recorded during testing of heat-treated sample. However, in interface regions, the hardness value decreased around 11%.
- The overall influence of heat treatment on microhardness was very marginal due to formation of coarser and non-uniform microstructure. Further, improper cooling rate has led to generation of residual stress which may result in cracks.

In future, after the application of hardfacing by PTA process, stress relieving technique or samples can be exposed to aggressive service conditions for validation of its durability in high-temperature/pressure conditions. Since all tests are conducted at room temperature, it is evident to check the mechanical performance of coatings in service conditions.

References

1. Goncalves, R.H., Dutra, J.C.: PTA process—a literature review as basis for innovations. Part 1 of 2: constructive elements. *Soldagem & Inspecao* **17**(1), 76–85 (2013)
2. Dai, W., Miao, Y., Li, J., Zheng, Z., Zeng, D., Huang, Q.: Investigation on morphology and micro-hardness characteristic of composite coatings reinforced by PTA copper alloying on nodular cast iron. *J. Alloy. Compd.* **689**, 680–692 (2016). <https://doi.org/10.1016/j.jallcom.2016.08.007>
3. Da Silva, L.J., D'Oliveira, A.S.C.: NiCrSiBC alloy: microstructure and hardness of coatings processed by arc and laser. *Weld. Int.* **31**(1), 1–8 (2017). <https://doi.org/10.1080/09507116.2016.1218608>
4. Zhang, S., Wang, S., Wu, C.L., Zhang, C.H., Guan, M., Tan, J.Z.: Cavitation erosion and erosion-corrosion resistance of austenitic stainless steel by plasma transferred arc welding. *Eng. Fail. Anal.* **76**, 115–124 (2017). <https://doi.org/10.1016/j.engfailanal.2017.02.007>
5. Kesavan, D., Kamaraj, M.: Influence of aging treatment on microstructure, wear and corrosion behavior of a nickel base hardfaced coating. *Wear* **272**(1), 7–17 (2011). <https://doi.org/10.1016/j.wear.2011.05.041>
6. Wang, S., Li, H., Chen, X., Chi, J., Li, M., Chai, L., Xu, H.: Improving microstructure and wear resistance of plasma clad Fe-based alloy coating by a mechanical vibration technique during

- cladding. *Mater. Sci. Eng., A* **528**(1), 397–401 (2010). <https://doi.org/10.1016/j.msea.2010.09.021>
7. Hou, Q.Y., Huang, Z., Wang, J.T.: Influence of nano- Al_2O_3 particles on the microstructure and wear resistance of the nickel-based alloy coating deposited by plasma transferred arc overlay welding. *Surf. Coat. Technol.* **205**(8–9), 2806–2812 (2011). <https://doi.org/10.1016/j.surfcoat.2010.10.047>
 8. Gallo, S.C., Alam, N., O'Donnell, R.: In-situ precipitation of TiC upon PTA hardfacing with grey cast iron and titanium for enhanced wear resistance. *Surf. Coat. Technol.* **214**, 63–68 (2013). <https://doi.org/10.1016/j.surfcoat.2012.11.003>
 9. Sundaramoorthy, R., Tong, S.X., Parekh, D., Subramanian, C.: Effect of matrix chemistry and WC types on the performance of Ni–WC based MMC overlays deposited by plasma transferred arc (PTA) welding. *Wear* **376**, 1720–1727 (2017). <https://doi.org/10.1016/j.wear.2017.01.027>
 10. Deshmukh, D.D., Kalyankar, V.D.: Deposition characteristics of multitrack overlay by plasma transferred arc welding on SS316L with Co–Cr based alloy—influence of process parameters. *High Temp. Mater. Processes.* <https://doi.org/10.1515/htmp-2018-0046> (2018)
 11. DeshmukhDD, Kalyankar V.D.: Recent status of overlay by plasma transferred arc welding technique. *Int. J. Mater. Prod. Technol.* **56**(1–2), 23–83 (2018). <https://doi.org/10.1504/IJMPT.2018.089118>
 12. Deng, X., Zhang, G., Wang, T., Ren, S., Cao, Q., Bai, Z., Liu, Z.: Microstructure and wear resistance of Mo coating deposited by plasma transferred arc process. *Mater. Charact.* **131**, 517–525 (2017). <https://doi.org/10.1016/j.matchar.2017.07.044>
 13. Cao, H.T., Dong, X.P., Pan, Z., Wu, X.W., Huang, Q.W., Pei, Y.T.: Surface alloying of high-vanadium high-speed steel on ductile iron using plasma transferred arc technique: microstructure and wear properties. *Mater. Des.* **100**, 223–234 (2016). <https://doi.org/10.1016/j.matdes.2016.03.114>
 14. Cao, H.T., Dong, X.P., Huang, Q.W., Pan, Z., Li, J.J., Fan, Z.T.: Effect of scanning speed during PTA remelting treatment on the microstructure and wear resistance of nodular cast iron. *Int. J. Miner. Metall. Mater.* **21**(4), 363–370 (2014). <https://doi.org/10.1007/s12613-014-0917-6>
 15. Bohatch, R.G., Athayde, J.N., Siqueira, J.C.M., Scheid, A.: Influence of processing on the microstructure and properties of CoCrMoSi alloy PTA coatings. *Soldagem & Inspecao* **20**(2), 219–227. DOI: <https://doi.org/10.1590/0104-9224/si2002.09> (2015)
 16. Lu, F., Li, H., Ji, Q., Zeng, R., Wang, S., Chi, J., Li, M., Chai, L., Xu, H.: Characteristics of the functionally graded coating fabricated by plasma transferred arc centrifugal cladding. *Surf. Coat. Technol.* **205**(19), 4441–4446 (2011). <https://doi.org/10.1016/j.surfcoat.2011.03.071>
 17. Gnyusov, S.F., Degterev, A.S., Tarasov, S.Y.: The effect of plasma torch weaving on microstructural evolution in multiple-pass plasma-transferred arc Fe–Cr–V–Mo–C coating. *Surf. Coat. Technol.* **344**, 75–84 (2018). <https://doi.org/10.1016/j.surfcoat.2018.03.002>
 18. Kilicay, K., Ulutan, M.: Effect of cryogenic treatment on tribological behaviour of TiC composite coatings. *Surf. Eng.* **33**(12), 886–894 (2017). <https://doi.org/10.1080/02670844.2017.1317452>
 19. Sawant, M.S., Jain, N.K.: Investigations on wear characteristics of stellite coating by micro-plasma transferred arc powder deposition process. *Wear* **378**, 155–164 (2017). <https://doi.org/10.1016/j.wear.2017.02.041>
 20. Degterev, A.S., Gnyusov, S.F., Tarasov, S.Y.: Structural modification in a reheated bead-overlapping zone of the multiple-pass plasma-transferred arc Fe–Cr–V–Mo–C coating. *Surf. Coat. Technol.* **329**, 272–280 (2017). <https://doi.org/10.1016/j.surfcoat.2017.09.054>
 21. Hu, Y., Wan, J., Yuan, L., Zhang, T., Cao, J., Li, F., Cheng, X., Jie, X., Zhang, H.: Influence of the phase composition and microstructure of plasma cladding Fe–Cr–Ni–C alloy coating on residual stress and crack formation. *Int. J. Adv. Manuf. Technol.* **96**(5–8), 1607–1613 (2017). <https://doi.org/10.1007/s00170-017-0765-4>
 22. Ulutan, M., Kilicay, K., Celik, O.N., Er, U.: Microstructure and wear behaviour of plasma transferred arc (PTA)-deposited FeCrC composite coatings on AISI 5115 steel. *J. Mater. Process. Technol.* **236**, 26–34 (2016). <https://doi.org/10.1016/j.jmatprotec.2016.04.032>

23. Sigolo, E., Soyama, J., Zepon, G., Kiminami, C.S., Botta, W.J., Bolfarini, C.: Wear resistant coatings of boron-modified stainless steels deposited by plasma transferred arc. *Surf. Coat. Technol.* **302**, 255–264 (2016). <https://doi.org/10.1016/j.surfcoat.2016.06.023>
24. Motalebzadeh, A., Atar, E., Cimenoglu, H.: Sliding wear characteristics of molybdenum containing Stellite 12 coating at elevated temperatures. *Tribol. Int.* **91**, 40–47 (2015). <https://doi.org/10.1016/j.triboint.2015.06.006>
25. Ding, Y., Liu, R., Yao, J., Zhang, Q., Wang, L.: Stellite alloy mixture hardfacing via laser cladding for control valve seat sealing surfaces. *Surf. Coat. Technol.* **329**, 97–108 (2017). <https://doi.org/10.1016/j.surfcoat.2017.09.018>
26. Rajeev, G.P., Kamaraj, M., Bakshi, S.R.: Hardfacing of AISI H13 tool steel with Stellite 21 alloy using cold metal transfer welding process. *Surf. Coat. Technol.* **326**, 63–71 (2017). <https://doi.org/10.1016/j.surfcoat.2017.07.050>
27. Shi, K., Hu, S., Liang, L.: Effect of tempering treatment on microstructure and fatigue life of TiC–Cr overlay, produced by plasma transferred arc alloying. *J. Mater. Sci.* **47**(2), 720–729 (2012). <https://doi.org/10.1007/s10853-011-5845-5>
28. Hou, Q.Y., Gao, J.S., Zhou, F.: Microstructure and wear characteristics of cobalt-based alloy deposited by plasma transferred arc weld surfacing. *Surf. Coat. Technol.* **194**(2–3), 238–243 (2005). <https://doi.org/10.1016/j.surfcoat.2004.07.065>
29. Bond, D., D'Oliveira, A.S.C.M.: Effect of current and atomized grain size distribution on the solidification of plasma transferred arc coatings. *Mater. Res.* **15**(5), 770–774. DOI: <https://doi.org/10.1590/s1516-14392012005000101> (2012)
30. Zhao, H., Li, J.J., Zheng, Z.Z., Wang, A.H., Huang, Q.W., Zeng, D.W.: Microstructure and high-temperature wear properties of in situ TiC composite coatings by plasma transferred arc surface alloying on gray cast iron. *Int. J. Miner. Metall. Mater.* **22**(12), 1273–1282 (2015). <https://doi.org/10.1007/s12613-015-1195-7>
31. Gallo, S.C., Alam, N., O'Donnell, R.: In situ synthesis of TiC–Fe composite overlays from low cost TiO₂ precursors using plasma transferred arc deposition. *J. Therm. Spray Technol.* **23**(3), 551–556 (2014). <https://doi.org/10.1007/s11666-013-0052-3>
32. Veinthal, R., Sergejev, F., Zikin, A., Tarbe, R., Hornung, J.: Abrasive impact wear and surface fatigue wear behaviour of Fe–Cr–C PTA overlays. *Wear* **301**(1–2), 102–108 (2013). <https://doi.org/10.1016/j.wear.2013.01.077>
33. Dikici, B., Ozel, S., Gavgali, M., Somunkiran, I.: The effect of arc current on the corrosion behaviour of coated NiTi alloy on AISI304 by plasma transferred arc process. *Prot. Metals Phys. Chem. Surf.* **48**(5), 563–567 (2012). <https://doi.org/10.1134/S2070205112050024>
34. Demian, C., Denoirjean, A., Pawlowski, L., Denoirjean, P., El Ouardi, R.: Microstructural investigations of NiCrAlY + Y₂O₃ stabilized ZrO₂ cermet coatings deposited by plasma transferred arc (PTA). *Surf. Coat. Technol.* **300**, 104–109. DOI: <https://doi.org/10.1016/j.surfcoat.2016.05.046> (2016)
35. Gurumoorthy, K., Kamaraj, M., Rao, K.P., Rao, A.S., Venugopal, S.: Microstructural aspects of plasma transferred arc surfaced Ni-based hardfacing alloy. *Mater. Sci. Eng., A* **456**(1–2), 11–19 (2007). <https://doi.org/10.1016/j.msea.2006.12.121>
36. Huayi, L., Guolu, L., Haidou, W., Binshi, X.: Influence of heat treatment on microstructure and mechanical properties of iron-based coating. *Mater. Des.* **32**(5), 3004–3007 (2011). <https://doi.org/10.1016/j.matdes.2010.12.055>
37. Bourithis, L., Papaefthymiou, S., Papadimitriou, G.D.: Plasma transferred arc boriding of a low carbon steel: microstructure and wear properties. *Appl. Surf. Sci.* **200**(1–4), 203–218 (2002)
38. Ozel, S., Kurt, B., Somunkiran, I., Orhan, N.: Microstructural characteristic of NiTi coating on stainless steel by plasma transferred arc process. *Surf. Coat. Technol.* **202**(15), 3633–3637 (2008). <https://doi.org/10.1016/j.surfcoat.2008.01.006>
39. Li, Z., Mao, H., Korzhavyi, P.A., Selleby, M.: Thermodynamic re-assessment of the Co–Cr system supported by first-principles calculations. *Calphad* **52**, 1–7 (2016). <https://doi.org/10.1016/j.calphad.2015.10.013>

Chapter 53

Modelling of Welding Sequences for Minimization of Weld-Induced Distortions and Residual Stresses



Saurav Suman , Avinish Tiwari , Pradeep Pankaj , Pankaj Biswas , Basil Kuriachen  and Abhijit Sinha 

Abstract In this work, thermal elastic–plastic analysis (TEPA) has been performed to analyse the fillet welded joint to minimize the weld-induced residual stresses and distortions. Various possible welding sequences, considering the start and end positions of the heat source along with their directions of motion, were decided. Those sequences were simulated and analysed for prediction of the weld-induced residual stresses and distortions. The whole process involves a moving heat source, temperature-dependent thermal and mechanical properties of the weld plate, and different relevant boundary conditions. As a result, an overall optimum welding sequence was identified which turns out to produce minimum welding-induced distortions and residual stresses.

Keywords Welding sequence · Modelling · Fillet weld · Arc welding

53.1 Introduction

An arc welding is extensively used in various fabrication industries like automobiles, ship panels, pressure vessels, etc. The fillet (single-sided and double-sided) joints are an integral part in most of the stiffened plated onshore and offshore ship structures, automobile chassis structures, bridges and such others large weld structures. Many analytical models have been developed from last two to three decades to develop an appropriate heat source model to estimate the temperature fields. Rosenthal [1] developed a heat source as a point heat source which moves at the speed same as welding speed to obtain the temperature distribution over the weld joints. Tsai et al. [2] attempted to improve the Rosenthal's model and introduced a 2D heat source

S. Suman (✉) · B. Kuriachen · A. Sinha
Department of Mechanical Engineering, National Institute of Technology Mizoram, Aizawl
796012, Mizoram, India
e-mail: sauravnitmz@gmail.com

S. Suman · A. Tiwari · P. Pankaj · P. Biswas
Department of Mechanical Engineering, Indian Institute of Technology Guwahati, Guwahati
781039, Assam, India

© Springer Nature Singapore Pte Ltd. 2020
M. S. Shunmugam and M. Kanthababu (eds.), *Advances in Additive Manufacturing and Joining*, Lecture Notes on Multidisciplinary Industrial Engineering,
https://doi.org/10.1007/978-981-32-9433-2_53

model which has Gaussian distribution. In the process of such improvement, some 3D heat source models were developed of different shapes varying with different arc welding processes [3]. Deo et al. [4] firstly demonstrate the transient thermal tensioning technique to minimize the buckling distortion. Adak et al. [5], Yang et al. [6] investigated the various welding distortion control techniques like weld optimization, pre-straining, pre-cambering and optimum welding sequence, etc. Watanabe et al. [7] studied the effect of welding sequences on the residual stress build-up. Fu et al. [8] investigated the influence of welding sequences on the results of residual stresses and distortions of fillet weld structure. However, welding sequences mentioned by them were not the only possibilities in this regards.

The present work includes a numerical analysis to investigate the effect of welding sequences on the weld-induced distortions and residual stresses in a double-sided fillet welded joint. The joint has been modelled with a mild steel plate under the arc welding process. A Gaussian-distributed heat source model has been used as the moving heat flux in weld zone to simulate the actual welding process. A total of ten welding sequences are simulated based on the initial and final positions of the heat source as well as their direction of movement. The welding speed and other parameters remained constant. The analysis also involves the comparison of the distribution of residual stresses and distortion for regular weld bead joint. The most suitable weld bead geometry and dimensions are taken for the given thickness of the plate. Weld strength is calculated under the transverse and longitudinal loads acting on the welded plates. The results were compared for the residual stress distribution in transverse and longitudinal directions and also for the deformation along the edge as well as in the transverse direction.

53.2 Methodology

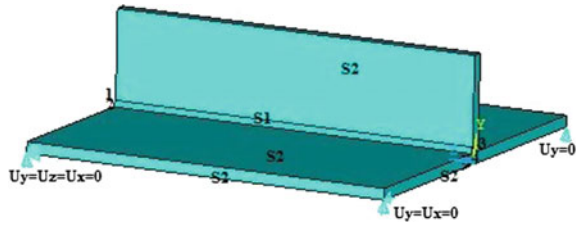
53.2.1 Thermal Model

The heat distribution pattern in the vicinity of the weld zone, fusion zone and heat-affected zone (HAZ) is greatly affected by the type of heat source model applied while modelling an arc welding process. The plate thickness number for submerged arc welding process is near about 0.88. Therefore, two-dimensional or surface heat flux load is sufficient to model the SAW process. Assuming that the heat from the welding arc is applied at any given instant of time as Gaussian-distributed heat flux, then the rate of heat generation can be given as in Eq. (53.1):

$$q_{\text{sup}}(r) = \frac{3Q}{\pi R^2} \exp\left[-3\left(\frac{r^2}{R^2}\right)\right] \quad (53.1)$$

where Q = heat input from arc given by the product of welding source voltage (V), current (I) and arc efficiency (η), r = distance of the heat source from the plate and

Fig. 53.1 Thermal and structural boundary conditions



R = effective arc radius to cover the region of 95% of deposited heat flux [3]. In submerged arc welding process, except the welding zone of the weld structure, rest of the weld joint part remains in the solid state, so a 3D conduction model can be considered to analyse the thermal distribution. Hence, in the schematic of the weld joint model as shown in Fig. 53.1, the throat or weldment top surface indicated as S_1 was subjected to a conduction heat flux load as a moving heat source model at the rate of welding speed. Convection load was applied on rest of the areas indicated as S_2 to incorporate the heat loss at the same time. Ambient temperature (T_∞) was taken as an initial condition or initial temperature, and the other two boundary conditions were taken as in Eqs. (53.2) and (53.3):

(a) Conduction over surface is S_1

$$Q_n = -Q_{sup.} \tag{53.2}$$

(b) Convection loss over surface area is S_2

$$Q_n = -Q_{convec.} \tag{53.3}$$

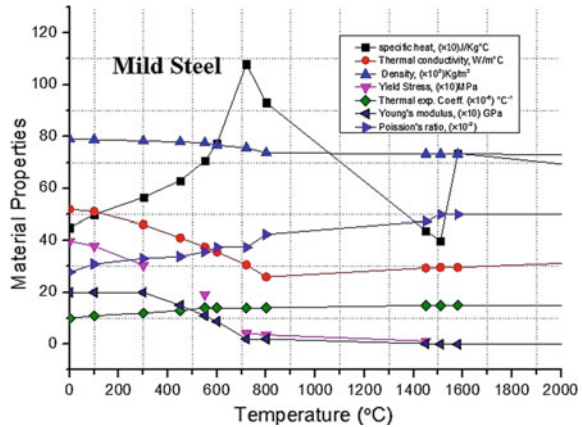
$$\Rightarrow Q_n = h_f(T - T_\infty) \tag{53.4}$$

where Q_n = Normal component of conduction heat flux, $Q_{sup.}$ = Heat flux applied on the work face, $Q_{convec.}$ = Convective heat loss and T = Welding plate surface temperature. Equation (53.2) explains the heat supply through conduction along the normal of the weldment top surface. Equation (53.3) describes the heat loss through convection from all the surface areas except weldment area, which is equal to the heat gain through the normal components of the heat flux applied.

53.2.2 Structural Model

For structural analysis, the boundary conditions were applied as constraints to prevent the rigid body motion of the weld plate as shown in the same schematic of the weld model in Fig. 53.1. The structural boundary conditions were applied as zero displacement load on all the bottom corner of the web plate as ($U_x = U_y = U_z = 0$),

Fig. 53.2 Mechanical and thermal properties [9]



($U_x = U_y = 0$), ($U_y = 0$), ($U_z = 0$), respectively, where U_x , U_y and U_z indicate the displacement load in x , y and z directions, respectively. The plastic deformation was assumed as rate dependent and modelled with von Mises yield criterion and bilinear kinematic hardening behaviour along with associated flow rule with temperature-dependent mechanical and physical properties of the weld and plate materials [9]. The density of the work was assumed to be constant throughout the welding process as it slightly varies with the temperature. The temperature-dependent material properties are shown in Fig. 53.2.

53.2.3 Welding Sequences

The sequences were marked by varying the direction of movement of the welding torch, initial and final positions of the welding torch and positions of the weldment welded. The positions of the weldments show the type of welding sequences and are shown in Fig. 53.3. For all those welding conditions, the welding parameters were kept constant. As it is already mentioned, the welding sequences are categorized on the ground of heat source position and the direction of the movement. Those welding sequences are enlisted in the Table 53.1. An uncoupled thermal–structural analysis was performed to model this welding sequence for fillet weld joints. Hence, welding and cooling process for all the tabulated welding sequences were performed in one of the finite element software package, i.e. ‘ANSYS APDL’. In thermal analysis, the best suitable element was chosen as ‘SOLID70’ which is a 3D element with single degree of freedom and allow the transient thermal analysis. The thermal analysis result is obtained in terms of nodal temperature values. And, ‘SOLID185’ a 3D element with three translational degrees of freedom was selected to apply the nodal temperature load to conduct the structural analysis. The heat flux was applied using load steps varying with corresponding time steps and substeps. Similarly, nodal

Fig. 53.3 Welding sequences

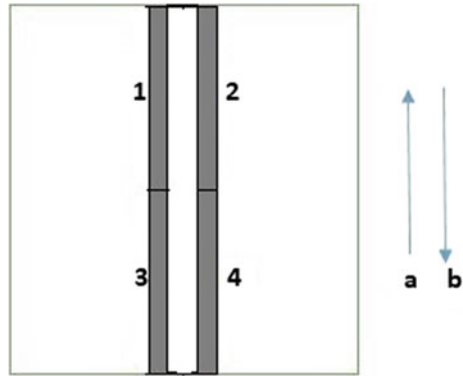


Table 53.1 Welding sequences for regular welding joint

S. No.	Welding sequences	Welding direction			
		1	2	3	4
1	1,3,4,2	b	a	b	a
2	1,3,2,4	b	b	b	b
3	1,2,4,3	b	b	a	a
4	1,3,2,4	b	b	a	a
5	1,4,2,3	b	b	a	a
6	1,2,4,3	b	b	b	b
7	1,4,3,2	b	b	a	a
8	1,4,2,3	b	b	b	b
9	1,3,2,4	a	a	b	b
10	1,3,4,2	a	a	b	b

temperature varying with time was also applied using load steps associated with the transient thermal analysis results.

The positions of welding torch for each sequence were modelled taking its initial positions as a reference. The corresponding weldment was applied with the moving surface heat flux. The structural analysis results in terms of welding-induced deformation (edge deflection and angular deformation) and residual stresses (longitudinal and transverse directions) were observed to verify the effect of welding sequences to recognize the best suitable welding sequences with minimum welding-induced deformation and residual stresses.

53.3 Result and Discussion

The double-sided fillet welded joint was successfully modelled and simulated for different ten welding sequences. The results were analysed for edge deflection of the web plate, angular deformation of the web plate and the distribution of residual stresses for the same web plate in transverse and longitudinal directions. The edge deflection in terms of the deformation for the top surface of the plate is plotted as shown in Fig. 53.4. From Fig. 53.4, it is observed that minimum distortion at the edge occurs in case of welding sequence '1' followed by sequence no. '4' and '10'. For rest of the welding sequences, deflection is not even near to the distortion values as obtained for sequences '1', '4' and '10'.

Similarly, from Fig. 53.4, it can also be observed that the minimum angular deformation is obtained for welding sequence '3' followed by sequences no. '4', '5' and '7'. It was observed that the conventional welding sequences '1' and '2' result higher angular deformation values than other welding sequences, whereas edge deflection was found to be minimum for the same conventional welding sequence '1'. Therefore, based on the observations done for edge deflection and angular deformation the best suitable welding sequence for minimum edge deflection is '1', and if angular deformation is the main objective for mitigation then sequence '3' will be the best possible welding sequence cases. For combined minimum value for both edge deflection and angular deformation, welding sequence '4' is the best apposite welding sequence. Taking residual stresses into the consideration, the distribution of transverse and longitudinal stresses can be observed from Fig. 53.5. On the observation of the comparative plots for residual stresses for both the directions, welding sequence '5' shows the minimum transverse residual stress. From Fig. 53.5, it can be observed that other sequences apart from welding sequence '5' has negative or say compressive residual stress values. Welding sequence '2' shows the minimum value of longitudinal stress with positive numerical value. For welding sequence '5', the value of longitudinal stress is comparatively lesser than the other welding sequence cases for positive numerical value. It was also observed that the conventional welding

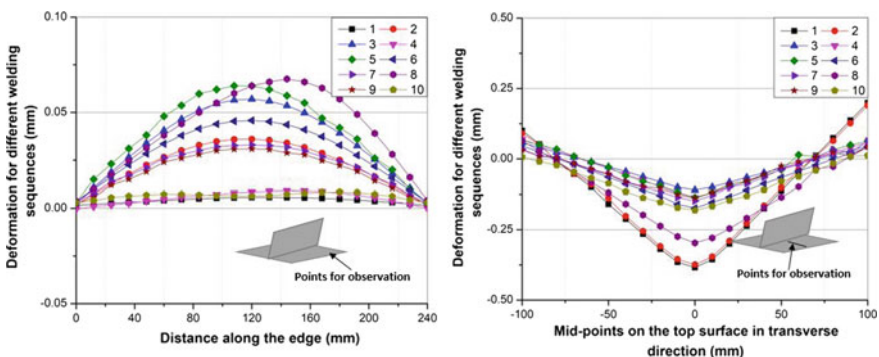


Fig. 53.4 Comparative edge deflection plots and angular deformation plots

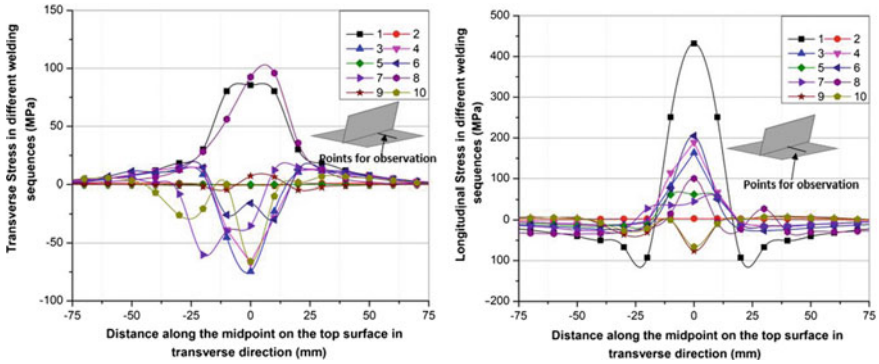


Fig. 53.5 Distribution of transverse residual stress for all the enlisted welding sequences

sequence ‘1’ showed the maximum residual stress distribution for both the directions, transverse and longitudinal. Therefore, collectively welding sequence ‘5’ should be the best suitable welding sequence for minimum possible residual stresses value. Figures 53.6 and 53.7 finally show the welding sequence ‘4’ and welding sequence ‘5’, respectively. Figures 53.6 and 53.7 present the four stages of welding process for welding of a double-sided fillet weld joint. Welding sequence ‘4’ starts with the

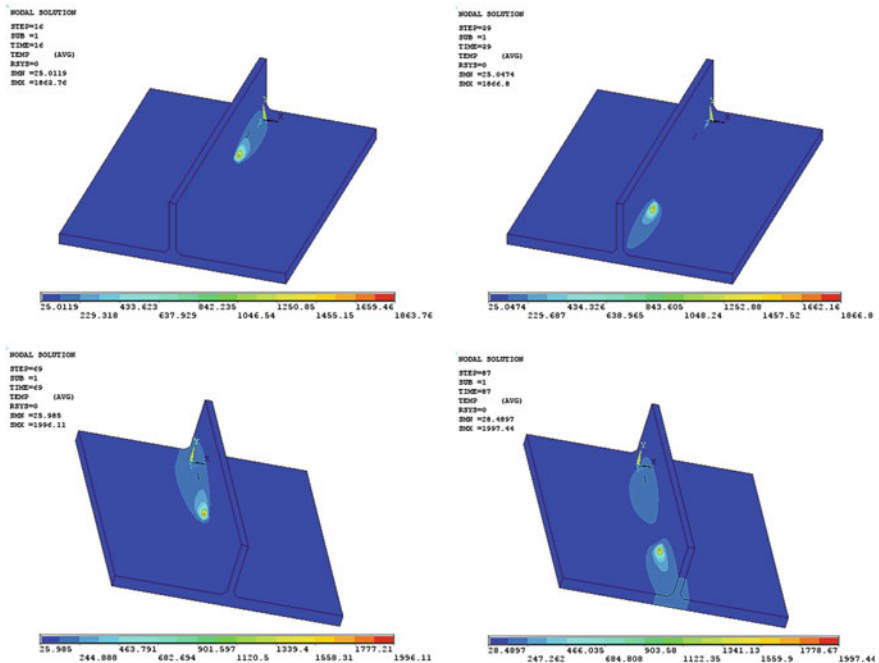


Fig. 53.6 Welding sequence ‘4’ (best suitable for minimum welding-induced distortions)

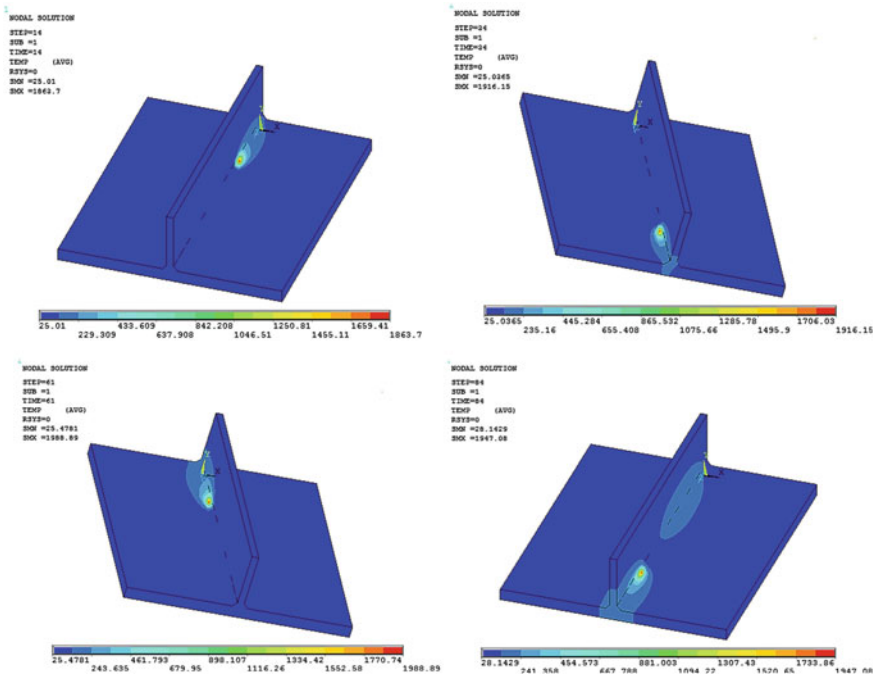


Fig. 53.7 Welding sequence ‘5’ (best suitable for minimum residual stresses value)

initial position of the welding torch at one of the end of the web plate as shown in Fig. 53.6. The first weldment was welded on the left-hand side of the flange till the mid-point of the web plate in the longitudinal direction. In the next sequence, the next half of the weldment was welded on the same side of the flange, starting from the other end of the web plate. Similarly, the other side of the flange was also welded as shown in Fig. 53.6. In welding sequence number ‘5’, welding started in the same manner as in the welding sequence ‘4’.

However, next sequence started for the right-hand side of the weldment starting from another end of the web plate. The next third sequence started from the end point of the web plate on the same right-hand side to weld rest of the half of the weldment. The last sequence welded the left side of the flange for rest of the weldment to complete the double-sided fillet weld as shown in Fig. 53.7.

53.4 Conclusion

The double-sided fillet welded joint was modelled and simulated for ten welding sequences with regular weldment. The comparative study finally provides an optimal welding sequence, which generates a fillet joint with least welding-induced distor-

tions and comparatively less residual stresses. The welding sequences which were identified for such minimum deformation and residual stress distribution are welding sequence '4' and '5'. Hence, this welding sequence may be a positive replacement for any type of arc welded double-sided fillet weld joint.

References

1. Rosenthal, Daniel: Mathematical theory of heat distribution during welding and cutting. *Weld. J.* **20**, 220s–234s (1941)
2. Eagar, T.W., Tsai, N.S.: Temperature fields produced by travelling distributed heat sources. *Weld. J.* **62**(12), 346–355 (1983)
3. Goldak, J., Malcolm, B., Aditya, C.: A Double Ellipsoid Finite Element Model for Welding Heat Sources. International Institute of Welding (1985)
4. Deo, M.V., Michaleris, P.: Mitigation of welding induced buckling distortion using transient thermal tensioning. *Sci. Technol. Weld. Joining* **8**(1), 49–54 (2003)
5. Adak, M., Mandal, N.R.: Numerical and experimental study of mitigation of welding distortion. *Appl. Math. Model.* **34**(1), 146–158 (2010)
6. Yang, Y.P., Dong, P.: Buckling distortions and mitigation techniques for thin-section structures. *J. Mater. Eng. Perform.* **21**(2), 153–160 (2012)
7. Watanabe, Masaki, Satoh, Kunihiko: Fundamental study on buckling of thin steel plate due to bead-welding. *J. Jpn. Weld. Soc.* **27**(6), 313–320 (1958)
8. Fu, G. et al.: Influence of the welding sequence on residual stress and distortion of fillet welded structures. *Mar. Struct.* **46**, 30–55 (2016)
9. Suman, S., Biswas, P., Sridhar, P.V.S.S.: Numerical prediction of welding distortion in submerged arc welded butt and fillet joints. In: *Proceeding of International Conference on Design and Manufacturing, IITDM, Chennai* (2016)

Chapter 54

Effect of Different Activated Fluxes on Mechanical Properties of DSS 2205 in Pulsed Tungsten Inert Gas Welding



Dhananjay S. Satelkar, Bhagwan F. Jogi and Shrikant B. Thorat

Abstract The present study relates investigating the effect of four kinds of fluxes: SiO_2 , MnO_2 , TiO_2 , and Al_2O_3 , and no flux was used in activated-pulsed tungsten inert gas (A-PTIG) welding process on ultimate tensile strength (UTS), yield strength (YS), elongation, and weld morphology of duplex stainless steel SS2205. This study involves a novel variant of the activated-pulsed TIG welding process and was applied to 6-mm-thick DSS 2205 plate through a thin layer of flux to join plate-to-plate using a butt joint. The oxide fluxes used were employed in powdered form. The experimental results indicate that using SiO_2 , MnO_2 , TiO_2 , and Al_2O_3 fluxes leads to a significant increase in the capacity of TIG welds. The employed activated-pulsed TIG welding showed increase in joint penetration and weld depth-to-width ratio, thereby reducing the angular distortion of the weldments. Weld morphology of all the weld was studied and correlated with the mechanical properties.

Keywords Oxide fluxes · Pulsed TIG · DSS 2205 · Mechanical properties

54.1 Introduction

The duplex stainless steels have a variety of industrial applications in the field of oil and gas, paper and pulp, petrochemical industries, and in power generation because of their superior corrosion resistance, strength, and a combination of both properties by virtue of their precise composition control and microstructural balance. Excellent mechanical properties (high strength combined with high toughness) are associated with the presence of duplex structures with a perfect balance in the proportion of austenite/ferrite, which is usually 50/50. The phase transformation plays a significant role in affecting the properties of the material. The phase balance in base metals is

D. S. Satelkar (✉) · B. F. Jogi · S. B. Thorat
Department of Mechanical Engineering, Dr. Babasaheb Ambedkar Technological University,
Lonere, Raigad 402103, Maharashtra, India
e-mail: dsatelkar1993@gmail.com

B. F. Jogi
e-mail: bfjogi@dbatu.ac.in

© Springer Nature Singapore Pte Ltd. 2020
M. S. Shunmugam and M. Kanthababu (eds.), *Advances in Additive Manufacturing and Joining*, Lecture Notes on Multidisciplinary Industrial Engineering,
https://doi.org/10.1007/978-981-32-9433-2_54

achieved by an appropriate combination of composition and solution heat treatment. Change in microstructural features affects the properties and corrosion resistance. In addition to this, the high chromium and molybdenum content exhibit excellent corrosion resistance, high pitting, crevice corrosion resistance, and good sulfide stress corrosion cracking resistance [1, 2].

Owing to its numerous applications, DSS emerged as an essential material, where it endures with the welding process, in which heat energy is used to join two parts. The mechanical and metallurgical properties of the DSS at weld zone and around (Heat Affected Zone) were significantly affected by the heating cycles of the welding. Subsequently, high thermal conductivity and lower thermal coefficient of expansion do not give highly intensified thermal stresses at welded joints due to the presence of austenite and ferrite phases. However, DSS consists of austenite and ferrite contents almost in the equal ratio [3]. In the welded zone, it exhibits excellent mechanical strength and superior corrosion resistance; it is in demand for welding applications. In welding, heating and cooling cycles impart the changes in the microstructure. However, in fusion welding, change in the microstructure are due to induced austenite grain size (at intergranular and intragranular) with coarse ferrite grains. Characteristically, the islands of the austenite were located partially as well as transverse direction concerning the rolling direction in the DSS. It is evident by the microstructure of the HAZ and weld zone affected by the peak temperature and cooling rate [4, 5]. The optimum welding process can be obtained through better quality of the welds to ferrous and non-ferrous alloys. It does not seem suitable for thick material. Therefore, active chemical elements such as sulfur and oxygen were used to enhance the depth of penetration. It provides the maximum depth of penetration at minimum heat input. The activated fluxes exhibit the behavior as per the Marangoni convection effect, where active elements of the molten pool change the surface tension to positive from negative; this changes the coefficient of the temperature of the material which can lead to the flow of convection from outward to inward. Hence, it increases the depth of penetration of the joint [6–8].

Further, in pulsed TIG welding deep penetration is obtained with less heat input to the joint. The pulsed arc agitates the molten weld metal. During the off-position, the electrode is kept sufficiently active by retaining the ionized column so that the arc is not extinguished. The minimum heat input advances the grain structure and the mechanical properties of the weld. The weaving is not required because the pulsed current is sufficient to melt the base metal area. Molten metal deposited in each pulse starts solidifying from the periphery toward the center; it may produce defect-free joints [9, 10].

The significant concern with duplex stainless steel is that TIG welding can degrade the strength and corrosion resistance, by imparting residual stresses, producing unbalanced ferrite–austenite content in the weld metal. And also TIG welding cannot weld thick weld; maintaining of phase balance in weld metal is a crucible for sustaining original chemical and physical properties. Therefore, the technique that may control the ferrite/austenite content of the weld is very important. Hence, this study uses five different kinds of a component of flux on the appearance, morphology, and distortion of DSS 2205 weld. This paper mainly studies the cumulative effect of both activated

oxide flux and pulsed current on mechanical properties, viz. UTS, YS, and elongation of the weld metal.

54.2 Materials and Method

The experimental setup of the activated-pulsed TIG (Maxstar DX 210 120–480 V of miller) is shown in Fig. 54.2. A DC power supply was used, the output current of which can be regulated from 50 to 1000 A. The workpieces used in this study were S2205 DSS having dimensions of 100 mm × 50 mm × 6 mm thick. The chemical composition of the base metals is reported in Table 54.1.

Before welding, two workpieces with a Y-groove were fixed, roughly polished with grit silicon carbide paper to remove surface contamination, and then cleaned with acetone. Figure 54.1 shows specimen with clamping flat welding position. Activating flux was prepared using four kinds of single component oxides (SiO_2 , MnO_2 , TiO_2 , and Al_2O_3) packed in powdered form with about 30–60 μm particle size. These powders were mixed with acetone to prepare a paint-like. Before welding, a thin layer of the flux was brushed onto the surface of the joint to be welded. The coating density of flux was about 5–6 mg/cm^2 , and then they were butt welded. Table 54.2 illustrates the constant parameters.

Considering the domain of activated-pulsed TIG welding, the welding current, frequency, and activating flux affect the formation of the weld. Also, this welding has effects on weld bead profile. Therefore, mainly the welding current, frequency, and activating flux are adjusted after the arc length and tungsten electrode diameter are appropriately fixed. The control variable method was applied in this study to test the effects of welding current, frequency, and activating flux on the weld geometry profile. The ranges of the welding parameters are mainly based on the reference data and the penetration of the workpiece. The experiment consists of Test Nos. 1–12, and the welding parameters are listed in Table 54.3. The universal testing machine was employed to observe the tensile strength. The samples were prepared as per ASTM e8 standards (Fig. 54.2).

54.3 Result and Analysis

Figures 54.4, 54.5 and 54.6 show the effect of peak current on ultimate tensile strength, yield strength, and elongation. These responses mainly depend on the central region of the weld, fusion boundaries, and heat-affected zone (HAZ) shown in Fig. 54.3, whereas HAZ can be divided into overheated and partially annealed zones concerning to heat input/induced in the material. A lower amount of austenite characterizes the overheated zone (Zone 4) compared to the melted and partially annealed zones. Subsequently, it imparts the high level of the ferrite content to this region. It is due to the induced peak temperature which was very high during the welding

Table 54.1 Chemical composition of SS2205 DSS

Element	C	Mn	P	S	Si	Cr	Ni	Mo	N	Cu
SS2205 (wt%)	0.03	0.82	0.02	0.01	0.93	25.7	6.3	3.4	0.23	0.61

Fig. 54.1 DSS 2205 specimen with clamping flat welding position



Table 54.2 Constant process parameters for welding of DSS 2205

Process parameters	Constant value
Electrode diameter (mm)	2.4
Tip angle of the electrode (°)	45
Electrode gap (mm)	1–2
Shielding gas	Ar
Gas flow rate (L/min)	14
Pulse ratio (%)	50

Table 54.3 Process parameters of activated-pulsed TIG welding of SS2205 DSS

Test no.	Welding current (A)	Frequency (Hz)	Fluxes
1	60	4	SiO ₂
2	80	4	SiO ₂
3	120	4	SiO ₂
4	160	4	SiO ₂
5	200	4	SiO ₂
6	80	2	SiO ₂
7	80	6	SiO ₂
8	80	8	SiO ₂
9	80	4	TiO ₂ ,
10	80	4	MnO ₂
11	80	4	Al ₂ O ₃
12	80	4	No flux

Fig. 54.2 Experimental setup of activated-pulsed TIG welding process



Fig. 54.3 Schematic representation of different regions subjected to ferrite measurement on the welded specimen

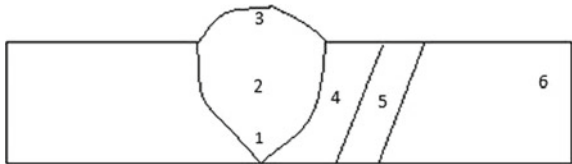


Fig. 54.4 Effect of peak current on ultimate tensile strength

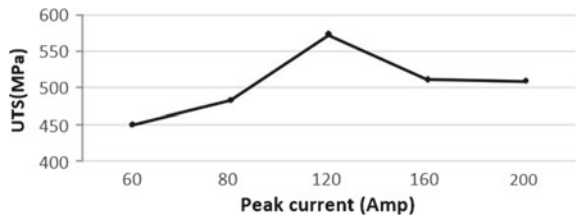


Fig. 54.5 Effect of peak current on yield strength

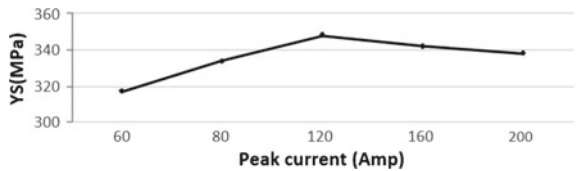
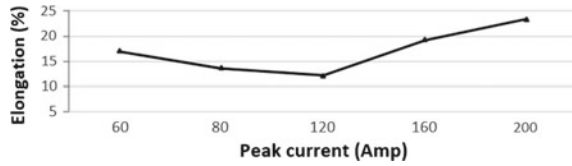


Fig. 54.6 Effect of peak current on elongation



operation. The high temperature was the result of the high peak current. The heat induced was directly proportional to the peak current and peak temperature. However, during heating, the ferrite region is transformed into the ferrite phase, albeit, on cooling the austenite grain were reforms. In the cooling cycle, the partial transformation of the ferrite to austenite occurs in this region due to insufficient diffused chromium content throughout phase in inadequate time. Substantially, the incomplete grain growth occurred at HAZ (Zone 5, in Fig. 54.3) in comparison with the base metal. In HAZ, the two-phase domain was heated up to recrystallization temperature. This imparts the transformation into ferrite content at maximum level. It increases the ratio of ferrite to austenite. The HAZ was enriched with ferrite content due to the accumulation of the delta ferrite. It enhances the ultimate tensile strength (UTS) and yield strength (YS) of the weld zone. It also increases the hardness of the weld joint. Simultaneously, this region lowers the percentage of the austenite content. Therefore, the cumulative effect of the undiffused austenite, high content delta ferrite, and lowered grain growth reduce the toughness of the weld zone, which relatively decreases the ductility and ultimately elongation. Figure 54.3 depicts the effect of the peak current on the elongation.

Concerning the peak current 160 and 200 A, the tensile strength is reduced. The behavior of the graph is bell-shaped. In high peak current, the elasticity of the weld remains maintains and showed the maximum elongation. This result is due to weld heat input. Heat input relatively measures of the heat energy transferred per unit length of the weld. Since calculated heat input is proportional to the measured arc voltage, the applied current increases the heat input. Therefore, there is an increase in the peak temperature of the weld metal and a reduction in the cooling rate. In this case, the transformation of delta ferrite to austenite is complete or ceases to attain the equilibrium phase, resulting in lower ferrite content in DSS 2205. As a result, the higher content of austenite improves ductility which consequences that the higher elongation at high peak current.

The DSS 2205 used as a base material has tensile strength and elongation 765 MPa and 35%, respectively. Figures 54.7, 54.8 and 54.9 depict the effect of activated fluxes on mechanical properties, viz. ultimate tensile strength, yield strength, and elongation, respectively. The used base material has better mechanical properties than as-welded alloy because of work hardening. From figure, it is clear that the joints obtained using A-PTIG process with fluxes presented equal or better ultimate tensile strength and yield strength than that of weldment made without flux; however, the use of SiO_2 , MnO_2 , TiO_2 , and Al_2O_3 fluxes produced relatively deep penetration in TIG process. This will increase in the weld depth-to-width ratio; therefore, it provides a better joint. In the condition of activated TIG welding, adding surface-

Fig. 54.7 Effect of activated fluxes on ultimate tensile strength

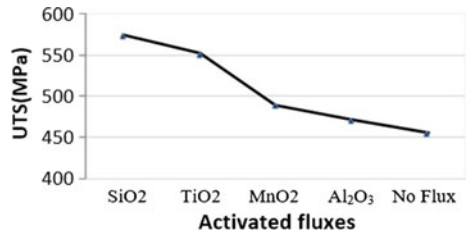


Fig. 54.8 Effect of activated fluxes on yield strength

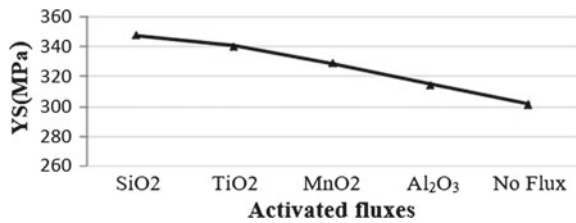
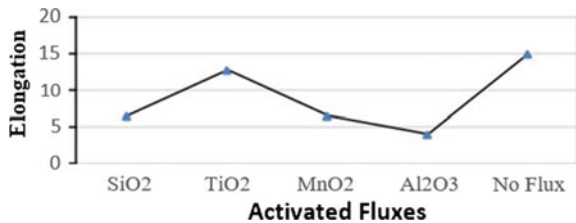


Fig. 54.9 Effect of activated fluxes on elongation



active element oxygen to the molten pool can drastically change the temperature dependence of surface tension. In this condition, the surface tension will highest at pool center, creating an inward surface fluid flow. It exhibited this fluid flow pattern that produces a narrow and deep weld. While SiO₂, MnO₂, and TiO₂ have the better ultimate tensile strength and yield strength, whereas Al₂O₃ has equal and over performance as compared to no flux. However, the dependence of elasticity, as a percentage of elongation, shows a reduction with the use of flux. Ordinarily, strengthening of an alloy decreases the ductility. In addition to this pulsed TIG, minimize the residual stresses and angular distortion of the weld sample.

Figure 54.10 depicts that the surface appearance of the weld metal is carried out using different oxide fluxes in standard welding conditions. Figure 54.10a shows the results of pulsed TIG with MnO₂ flux, which produced excessive residual slag and spatters. Figure 54.10b shows the use of TiO₂ flux produced residue and small spatters. Figure 54.10c shows a satisfactory surface appearance in pulsed TIG of DSS 2205 which is carried out using SiO₂ flux. Figure 54.10d shows that Al₂O₃ produced litter residual slag with smut formation and small spatters. Figure 54.10e shows that smooth and clean surface appearance is the result of pulsed TIG welding without flux. The experimental results indicate that the activated-pulsed TIG welding produced surface contributed to smut formation, residual slag, and spatters. Moreover, activated-pulsed TIG welding produces a small amount of fumes. Figures 54.11,

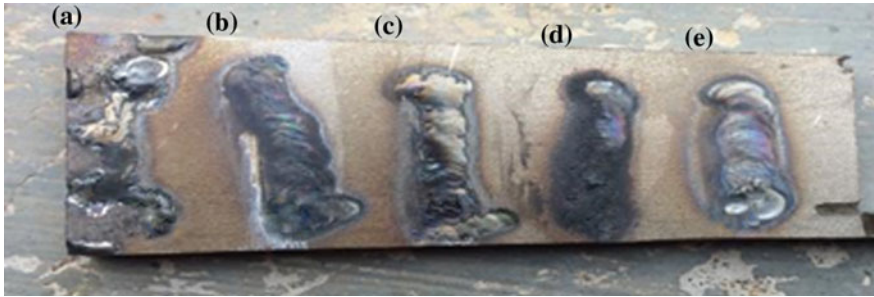


Fig. 54.10 Effect of oxide flux on surface appearance

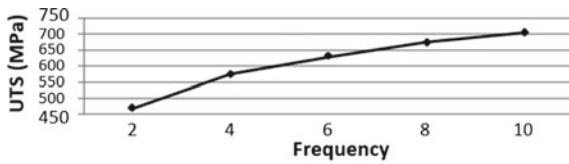


Fig. 54.11 Effect of frequency on ultimate tensile strength

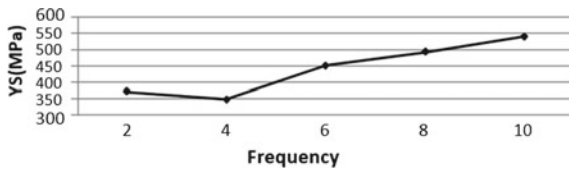


Fig. 54.12 Effect of frequency on yield strength

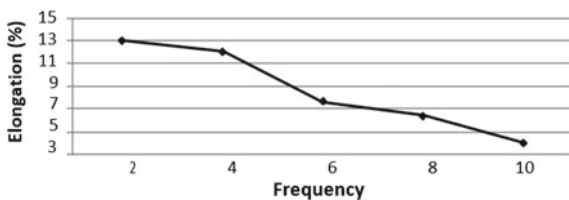


Fig. 54.13 Effect of frequency on elongation

54.12 and 54.13 show the effect of the frequency on the mechanical properties. Lower the frequency, higher is the duration for peak current, i.e., maximum heat input to the material, i.e., maximum temperature. There may be the possibility of transformation of delta ferrite to austenite. Frequency is the occurrence of a number of pulse cycles, whereas 1 pulse cycle consists of base time (duration of base current) and pulse time (period of peak current). As frequency increases, pulse with of peak

current is reduced. There is minimum pulse width, i.e., the minimum contact period of peak current. The generated heat is unable to transform delta ferrite to austenite. Therefore, the maximum amount of delta ferrite is present in the weld bead/matrix.

54.4 Conclusions

This study investigated the effect of SiO_2 , MnO_2 , TiO_2 , and Al_2O_3 , and no flux on ultimate tensile strength, yield strength, elongation, and weld morphology obtained with A-PTIG process employed to weld 6-mm-thick DSS 2205 plate. By primary results and analysis, the following conclusion is drawn:

- Activated-pulsed TIG welding can increase the joint penetration and weld depth-to-width ratio, and significantly reducing the angular distortion of the weldment.
- Pulsed TIG welding with SiO_2 , MnO_2 , and TiO_2 fluxes achieves an increase in weld depth and decrease in bead width, respectively, whereas Al_2O_3 flux led to a deterioration in the penetration compared to the conventional TIG process for DSS2205.
- Peak current, activated flux, and frequency were essential parameters; they substantially affect the UTS, YS, and elongation of weld metal of DSS 2205.
- Since the activated-pulsed TIG welding can increase the arc voltage, the amount of heat input per unit length in a weld is also high, and therefore, the delta ferrite content in weld metal will be increased. The applied pulsed current significantly reduces residual stresses and distortion. The generated heat input in pulsed-activated TIG welding was found to be decreased than activated TIG and TIG welding process.

References

1. Badji, R., Bouabdallah, M., Bacroix, B., Kahloun, C., Belkessa, B., Maza, H.: Phase transformation and mechanical behavior in annealed 2205 duplex stainless steel welds. *Mater. Charact.* **59**(4), 447–453 (2008)
2. Cui, S., Shi, Y., Sun, K., Gu, S.: Microstructure evolution and mechanical properties of keyhole deep penetration TIG welds of S32101 duplex stainless steel. *Mater. Sci. Eng. A* **709**, 214–222 (2018)
3. Verma, J., Taiwade, R.V.: Effect of welding processes and conditions on the microstructure, mechanical properties and corrosion resistance of duplex stainless steel weldments—a review. *J. Manuf. Process.* **25**, 134–152 (2017)
4. Pramanik, A., Littlefair, G., Basak, A.K.: Weldability of duplex stainless steel. *Mater. Manuf. Process.* **30**(9), 1053–1068 (2015)
5. Korra, N.N., Balasubramanian, K.R., Vasudevan, M.: Optimization of activated tungsten inert gas welding of super duplex alloy 2507 based on experimental results. *Proc. Inst. Mech. Eng. Part B: J. Eng. Manuf.* **229**(8), 1407–1417 (2015)
6. Sakthivel, T., Vasudevan, M., Laha, K., Parameswaran, P., Chandravathi, K.S., Mathew, M.D., Bhaduri, A.K.: Comparison of creep rupture behavior of type 316L (N) austenitic stainless steel

- joints welded by TIG and activated TIG welding processes. *Mater. Sci. Eng. A* **528**(22–23), 6971–6980 (2011)
7. Tathgir, S., Bhattacharya, A., Bera, T.K.: Influence of current and shielding gas in TiO₂ flux activated TIG welding on different graded steels. *Mater. Manuf. Process.* **30**(9), 1115–1123 (2015)
 8. Tseng, K.H., Hsu, C.Y.: Performance of activated TIG process in austenitic stainless steel welds. *J. Mater. Process. Technol.* **211**(3), 503–512 (2011)
 9. Chern, T.S., Tseng, K.H., Tsai, H.L.: Study of the characteristics of duplex stainless steel activated tungsten inert gas welds. *Mater. Des.* **32**(1), 255–263 (2011)
 10. Ahmad, A., Alam, S.: A review on pulsed TIG welding. *J. Recent Act. Prod.* **2**(1, 2) (2017)

Chapter 55

Effect of Pre- and Post-welding Processes on the Distortion Pattern in a SAW-Welded Butt Joint of P91 Steel Plate



Saurav Suman , Pradeep Pankaj , Avinish Tiwari , Pankaj Biswas , Basil Kuriachen  and Abhijit Sinha 

Abstract In this investigation, a comparative study has been done to show the effect of prewelding and post-welding processes on the weld-induced distortion in a submerged arc-welded butt joint of P91 steel plate. An optimal set of welding parameters are selected beforehand for conducting the experiment to prepare single-sided and double-sided weld joints. The experiment samples were prepared for four different welding cases as with and without preheating and with and without post-welding heat treatment (PWHT). The distortion was measured for the points on the top surface of the plate. Edge deflection or say buckling distortion on both the edges and angular deformation in transverse direction of the weld line direction was measured at the start, end, and middle portions of the welded joint. The comparison of the results concludes that both preheating and post-welding heat treatment collectively influence the overall distortion pattern in the welded plate in positive direction.

Keywords SAW · P91 steel · Distortion · Preheating · PWHT

55.1 Introduction

Cr–Mo steel is one of the best materials with high creep strength, which is widely used in fabrication of structural components related to pressure vessels, power systems, nuclear, chemical, food processing, and petroleum industries. In particular, P91 steel is extensively used in many advanced reactor systems like the very-high-temperature reactor and the sodium fast reactor owing to their excellent combination of elevated temperature strength, thermal fatigue resistance, and immunity from stress corro-

S. Suman (✉) · B. Kuriachen · A. Sinha
Department of Mechanical Engineering, National Institute of Technology Mizoram, Aizawl
796012, Mizoram, India
e-mail: sauravnitmz@gmail.com

S. Suman · P. Pankaj · A. Tiwari · P. Biswas
Department of Mechanical Engineering, Indian Institute of Technology Guwahati, Guwahati
781039, Assam, India

© Springer Nature Singapore Pte Ltd. 2020
M. S. Shunmugam and M. Kanthababu (eds.), *Advances in Additive Manufacturing and Joining*, Lecture Notes on Multidisciplinary Industrial Engineering,
https://doi.org/10.1007/978-981-32-9433-2_55

sion cracking in aqueous and chloride environments low susceptibility to irradiation embrittlement [1]. P91 steel has shown susceptibility to a number of phenomena, particularly in the case of welds, which invariably have the potential to reduce work efficiency and shorten service life [2]. The problems encountered in welding joints of these steels under creep conditions, both in base metal (BM) and weld metal (WM), are the result of type IV cracking, i.e., crack initiation in the region of the heat-affected zone (HAZ), immediately next to the BM [3]. Most of the literatures found in the field of P91 steel are related to the study of microstructure, characterizations, and creep and fatigue analysis with both experimental and numerical analysis. The effect of PWHT on microstructure and mechanical properties was also investigated for different fusion welding processes. Polcik et al. analysed microstructural data for creep of the tempered martensitic 9 wt.% CrMoV steel P91 at 873 K [4]. Zubairuddin et al. analyzed the effect of preheating process on the residual stresses and distortion in a GTAW-welded P91 steel butt joint [5]. Both preheating and PWHT processes are found to be the most pre- and post-welding processes to improve the overall weld quality of P91 steel joints. P91 steel is generally subjected to PWHT to reduce stress and improve ductility, toughness, and other mechanical properties [6]. It has been noticed that when PWHT is performed at relatively low temperature, the impact toughness is found to be poor, whereas if performed at very high temperature, then the excessive tempering of the martensite decreases the creep rupture and tensile strength [7, 8]. From the above literature, we found that most of the studies are confined to the study of microstructures, mechanical properties, and residual stresses. However, very few literatures have been found in the field, particularly no literature is there especially for submerged arc-welded P91 steel joints. Rao and Kalyankar conducted the SAW on P91 steel to obtain optimal set of welding parameters for different responses like weld bead width, weld reinforcement, weld penetration, weld tensile strength, and weld hardness [9]. Still, there is lack of literatures on the analysis of distortion and residual stresses of SAW-welded P91 steel plate.

The present work is all about measuring the weld-induced distortion pattern of the butt joint of P91 steel plate. The whole process involves preheating the tack-welded butt joint plate and welding the plate with square butt joint under the most suitable welding parameters, and finally post-welding heat treatment was done in a furnace with the proper temperature–time control. The square butt joints were prepared for both single-sided and double-sided welding. The distortions were measured in terms of Z or say vertical displacement of the measuring point on the top surface of the weld plate. And finally, those were compared on the graph of edge deflection of both the edge along the welding line direction and angular deformation along the transverse direction of the welding line at the start, middle, and end regions. It was found that the angular deformation value in both the single-sided and double-sided welded joints improved with the implementation of any one of both the processes and collectively gave the better result for the angular deformation value. While for edge deflection, it showed slightly negative effect on the overall edge deflection or say vertical displacement value on the edges. So, taking the improvement in mechanical properties and microstructure under consideration, preheating and post-welding heat treatment positively improve the weld quality in terms of weld-induced distortion.

55.2 Experiment Details and Methodology

55.2.1 Selection of Welding Materials

Hot rolled SA387 Grade 91 CL.2 steel plates of thickness 11 mm were procured in the normalized (30 min. at 1050 °C) and tempered (30 min at 770 °C) condition. Keeping the various problems involved with the submerged arc welding of modified Cr-Mo steel, a 3.1-mm low-alloyed, copper-coated ESAB make wire was selected. The manufacturer has coded the wire as OK AUTROD 13.20 (EB-3-21/4Cr1Mo) with the wire electrode classification as AWS A5.23: EB3R. The mechanical properties for the electrode wire were taken almost closer and better than the base metal.

The ESAB makes agglomerated fluoride basic flux suitable for submerged arc welding of Cr-Mo group of steels, and best suitable for OK AUTROD 13.20 wire was selected which was coded as OK FLUX 10.62. The grain size of the flux varies from 0.2 to 1.6 mm. The weld joint specimen was prepared as per the ASTM standard with the dimensions as 150 × 75 × 11 mm for each plate. The most suitable root gap for the given thickness was taken as 2.5 mm. The weld joint was prepared with no edge preparation, i.e., as a simple square butt joint. The schematic diagram of weld joint plate with full details about dimensions is shown in Fig. 55.1.

55.2.2 Submerged Arc Welding Set up

A 1250-A automatic submerged arc welding machine with IGBT inverter technology equipped with mounting tractor head was used to conduct all the welding experi-

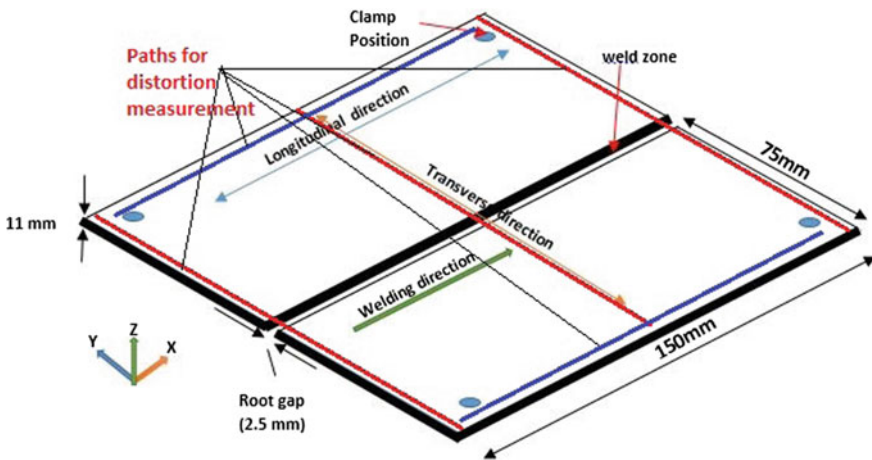


Fig. 55.1 Schematic diagram of butt weld sample

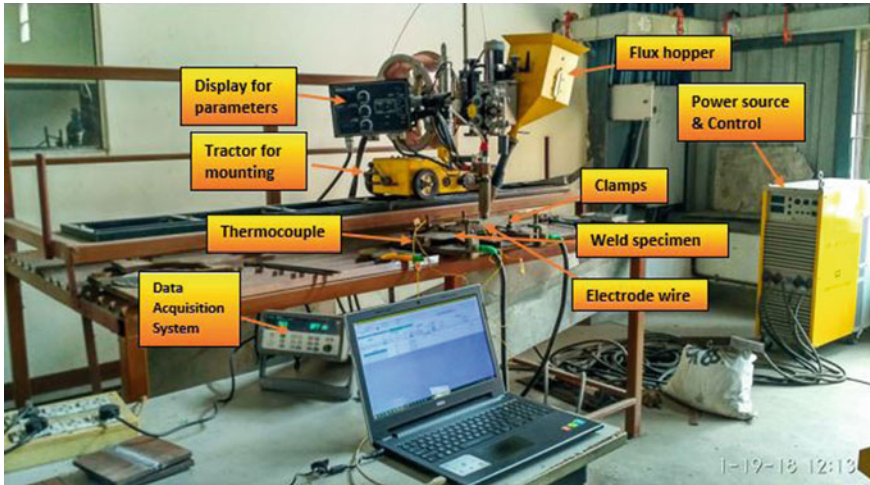


Fig. 55.2 Submerged arc welding setup with thermocouple attachments

ments. The K-type thermocouple was used to record the thermal history of the welding process on the top surface of the weld plate using a data acquisition system. At first, the point on the weld plate surface is prepared to attach the thermocouple wire by making a groove, after that the tip of the thermocouple wire is welded with the help of spot welding machine. The other end of the wire is attached with data acquisition system, which is connected to the computer, preloaded with the AGILENT software to read and store the data generated from the system. The whole setup is shown in Fig. 55.2.

55.2.3 Preheating and PWHT Set up

Preheating involves heating the base metal, either in its entirety or just the region surrounding the joint, to a specific desired temperature, called the preheat temperature, prior to welding. Heating may be continued during the welding process, but frequently the heat from welding is sufficient to maintain the desired temperature without a continuation of the external heat source.

It lowers the cooling rate in the weld metal and base metal, producing a more ductile metallurgical structure with greater resistant to cracking. It reduces the shrinkage stresses in the weld and adjacent base metal, which is especially important in highly restrained joints. Mostly, the preheating temperature range for P91 steel varies in between 200 and 300 °C [10]. PWHT is mandatory regardless of the component wall thickness in order to reduce the hardness and improve the ductility and toughness of the weld/HAZ. Lower PWHT temperature can result in larger differences in the hardness between the type IV position and the coarse grain HAZ and weld metal,

which adversely affects the strain accumulation in the soft type IV region, increasing its susceptibility to creep failure.

55.2.4 Distortion Measurement

The welding-induced deformation was measured directly with the help of Coordinate Measuring Machine (CMM). The welded plate or workpiece was placed on a V-block and is positioned on the horizontal bed of the machine. Probe was impinged on the marked points for measuring the separate coordinate of each point. The machine was interfaced with USoft software for collecting and analyzing data. For edge deflection, reference point was taken on both the end points along the welding direction. For angular deformation, the reference points were taken near the weld bead, i.e., values of vertical deformation were assumed to be zero near the weld bead. Therefore, the deformation values can be different on the same point for edge deflection plot and angular deformation plot.

55.3 Result and Discussion

The thermal history was recorded on a data acquisition system during the preheating and actual welding processes. Both the thermal profiles are shown in Fig. 55.3. It shows the thermal history in case of both single-sided and double-sided welding without preheating, whereas Fig. 55.4 shows both single-sided and double-sided weld joints for welding with preheating.

The single-sided and double-sided joints were prepared simultaneously. Those welded samples then heated up inside an automatically controlled electric furnace with proper time–temperature control to fulfill the requirement. The samples were first heated at the rate of 100–150 °C up to 760 °C. It was then kept at the same temperature, i.e., 750–760 °C and then cooled down inside the furnace again at the rate of 100–130 °C followed by air cooling after 4 h of furnace cooling. The welded

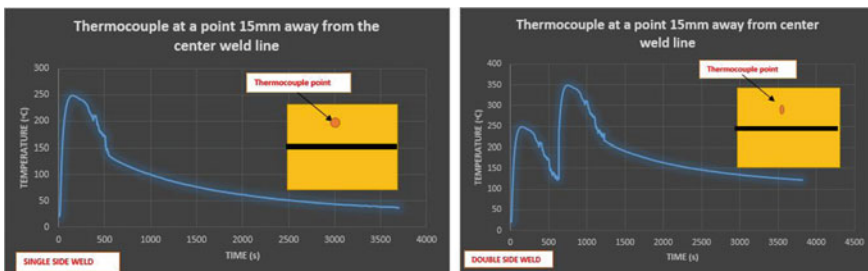


Fig. 55.3 Thermal history in case of both single-sided and double-sided welding without preheating

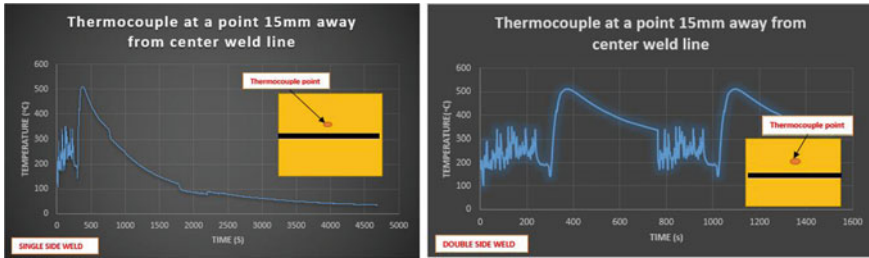


Fig. 55.4 Thermal history in case of both single-sided and double-sided welding with preheating

samples are collectively shown in Fig. 55.5 for single- and double-sided welded joints along with the cross-sectional view of the joints. After completing the welding experiment, the distortion was measured for all the eight welded butt joints separately. The distortion patterns were measured at five different regions of the plate, which are two sides of the edges along the welding line direction and three start, end, and mid-portions of the weld plate in the weld line direction along the transverse direction, which were shown in Fig. 55.1 in the earlier section. The distortion pattern at the edges as well as for the transverse directions is lesser for the Case I.

It shows that practicing of those pre- and post-welding processes effectively improves the weld quality also in terms of weld-induced distortion. The edge deflection values were plotted taking end points as reference points. Therefore, the maximum edge deflection in terms of bending deformation values was observed to be around 0.25 mm for both the single-sided and double-sided welds. In all the distor-

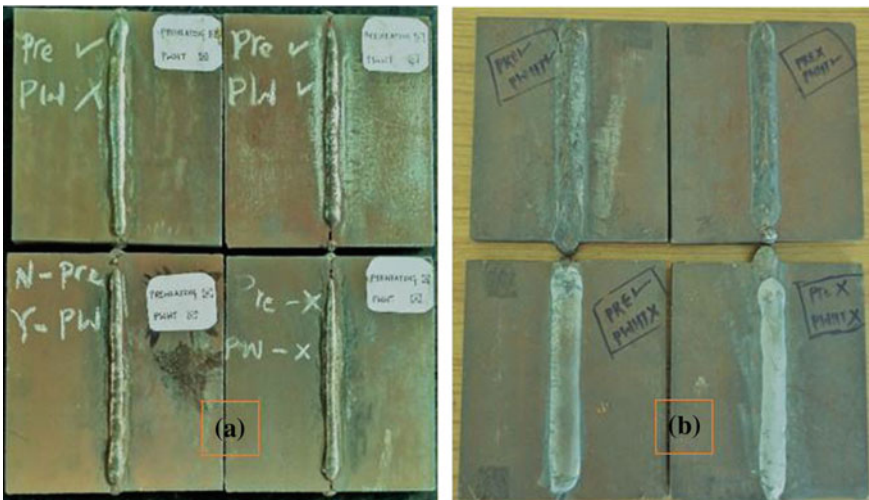


Fig. 55.5 a Single-sided weld joints (bottom surface) and b double-sided weld joints (bottom surface)

tion results, preheated and post-weld heat-treated weld sample shows the minimum distortion, though the difference is not as much effective in terms of edge deflection, which is clearly observable in Figs. 55.6 and 55.7. However, the angular deformation pattern shows a good improvement in the maximum value of z-displacement or vertical deformation results, which shows the improvement in between 30 and 40% of the maximum deformation value as observed in the case of no preheating and no post-weld heat treatment. It is easily visible in Figs. 55.8 and 55.9 representing the deformation patterns on the line at the end region and mid-region of the weld plate in the transverse direction, respectively. As per the expectations, the deformation values are found to be more in case of single-sided weld joint. It was also observed that only post-weld heat treatment only causes slight difference in the deformation values, whereas both processes improve it significantly to some extent.

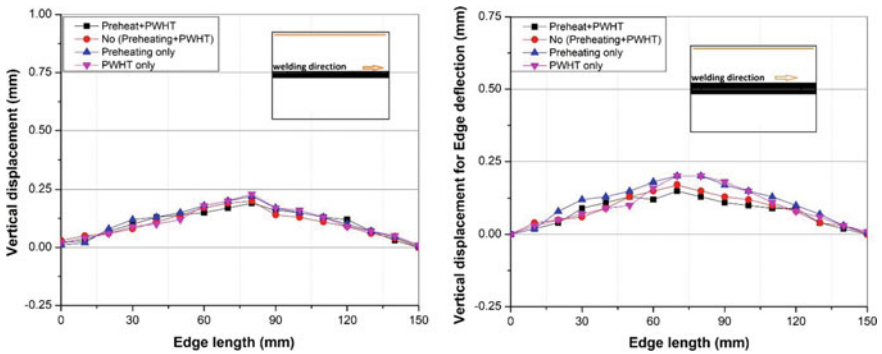


Fig. 55.6 Edge (left) deflection for single-sided and double-sided welds (left to right)

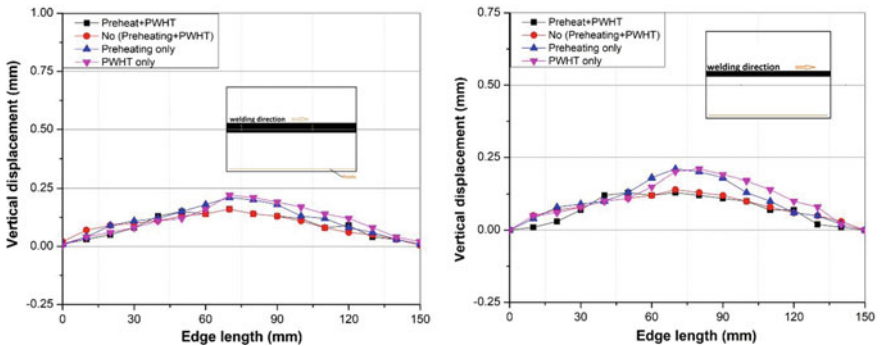


Fig. 55.7 Edge (right) deflection for single-sided and double-sided welds (left to right)

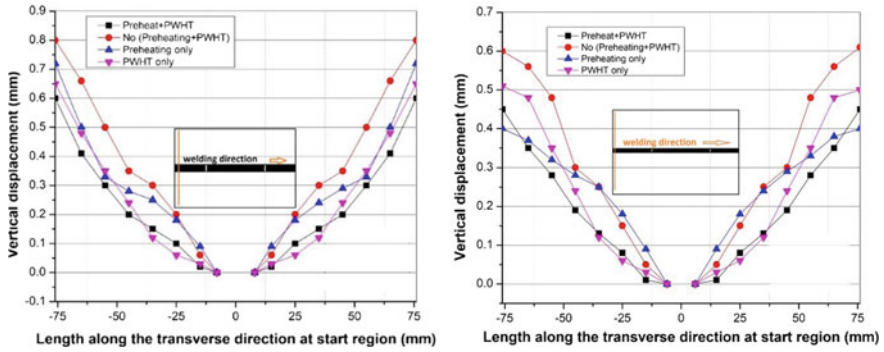


Fig. 55.8 Angular deformation at start or end region along the transverse direction for single-sided and double-sided welds (left to right)

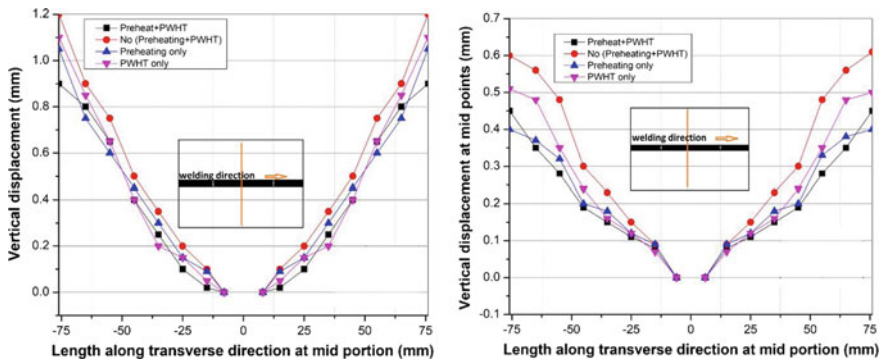


Fig. 55.9 Angular deformation at mid-region along the transverse direction for single-sided and double-sided welds (left to right)

55.4 Conclusion

The study was done to investigate the effect of those prewelding and post-welding processes on the overall weld-induced distortion. The main conclusion is as follows:

- Thermal history was tracked for both single-sided and double-sided welds.
- The distortion pattern in terms of edge deflection was not as much affected with preheating and post-welding heat treatment processes.
- The edge deflection values are more or less for both the single and double-sided weld joints.
- The angular deformation pattern was improved with 30–40% with the application of preheating and post-welding heat treatment processes.

References

1. Kumar, S., et al.: Residual stresses in laser welded ASTM A387 Grade 91 steel plates. *Mater. Sci. Eng. A* **575**, 160–168 (2013)
2. Kamal, H.D., Vishvesh, J.B.: Effect of activating fluxes on weld bead morphology of P91 steel bead-on-plate welds by flux assisted tungsten inert gas welding process. *J. Manuf. Process.* **17**, 48–57 (2015)
3. Das, C.R.: Influence of boron on microstructure and mechanical properties of modified 9cr-1mo steel weldments, Ph. D thesis. IIT, Madras (2011)
4. Polcik, P., Sailer, T., Blum, W., Straub, S., Bursk, J., Orlova, A.: On the microstructural development of the tempered martensitic cr-steel p 91 during long term creep a comparison of data. *Mater. Sci. Eng. A* **260**(1), 252–259 (1999)
5. Zubairuddin, M., Albert, S.K., Mahadevan, S., Vasudevan, M., Chaudhari, V., Suri, V.: Experimental and finite element analysis of residual stress and distortion in GTA welding of modified 9cr-1mo steel. *J. Mech. Sci. Technol.* **28**(12), 5095–5105 (2014)
6. Murugan, N., Parmar, R.S., Sud, S.K.: Effect of submerged arc welding process variables on dilution and bead geometry in single wire surfacing. *J. Mater. Process. Technol.* **37**, 767–780 (1993)
7. Chandel, R.S., Seowl, H.P., Cheong, F.L.: Effect of increasing deposition rate on the bead geometry of submerged arc welds. *J. Mater. Process. Technol.* **72**, 124–128 (1997)
8. Brito, V.L.O., Voorwald, H.J.C., Neves, N., Bott, I.S.: Effects of a postweld heat treatment on a submerged arc welded ASTM A537 pressure vessel steel. *J. Mater. Eng. Perform.* **10**, 249–257 (2001)
9. Rao, R.V., Kalyankar, V.D.: Experimental investigation on submerged arc welding of Cr–Mo–V steel. *Int. J. Adv. Manuf. Technol.* **69**(1–4), 93–106 (2013)
10. Pre-Heat Calculator.: Metallurgy of carbon steel. www.gowelding.com/weld/preheat/preheatcalc.html. 13 Apr 2002, 12:00

Chapter 56

Effect of Welding Parameters on Tensile Strength of AA7075-T₆ Friction Stir Welded Joints



Mallapuram Bala Chennaiah , Podaralla Nanda Kumar 
and Karanam Prahlada Rao 

Abstract In the present work, influential process parameters will yield enhanced tensile strength and joint efficiency of 6.35-mm-thick plate friction stir welded AA7075-T₆ aluminium alloy. Evaluate the effect of welding process parameters like rotational speed, welding speed and tool geometry on the tensile strength of butt joints of Al 7075-T₆ alloy fabricated using friction stir welding technique. Tensile strength and efficiency of the joint decreased with increasing rotational and welding speeds. It is found that similar aluminium (7075-T₆) joint fabricated at a tool rotational speed of 1340 rpm and welding speed of 11 mm/min, and geometry showed excellent tensile strength properties. The tool for this investigation is made up of stainless steel material. The tensile strength and efficiency of friction stir welded Al7075-T₆ aluminium alloy are 382 MPa and 79%, respectively. The results were confirmed by further experiments.

Keywords Tool rotational speed (rpm) · Welding speed (mm/min) · Tensile strength and efficiency

56.1 Introduction

Aluminium is one of the majorly flexible, inexpensive and attractive properties of material for a wide range of uses from soft, highly ductile wrapping foil to the most challenging engineering, industrial applications [1, 2]. These alloys are second only to steels in used in structural applications. One of the best known properties of aluminium is that it is light, with a density (2.7 g/cm³) one-third that of steel. Such a lightweight structures are particularly helpful for space vehicles, aircraft and all types

M. Bala Chennaiah (✉)
V.R. Siddhartha Engineering College, Vijayawada, India
e-mail: chennai303.mech@vrsiddhartha.ac.in

P. Nanda Kumar
N.B.K.R Institute of Science & Technology, Nellore, India

K. Prahlada Rao
J.N.T.U.A, Ananthapuramu, India

© Springer Nature Singapore Pte Ltd. 2020
M. S. Shunmugam and M. Kanthababu (eds.), *Advances in Additive Manufacturing and Joining*, Lecture Notes on Multidisciplinary Industrial Engineering,
https://doi.org/10.1007/978-981-32-9433-2_56

of land- and water-borne vehicles [3, 4]. Friction stir welding (FSW) was invented at The Welding Institute (TWI) of UK in 1991, as a solid-state joining technique, and it was originally applied to aluminium alloys. A rotating tool is non-consumable with a different tip-pin, and shoulder is inserted into the adjacent to edges of sheets or plates to be joined and traversed along the length of plate [5, 6]. Tool rotational and welding speeds are the important parameters of FSW. Before the welding, the non-consumable tool is inserted into the spindle of milling machine. The plates were rigidly clamped on the work table of machine. Then the required spindle speed and welding speed are given with the help of levers present on the machine. The spindle motor is switched on. The tool is allowed to reach the required speed. Then the tool is inserted slowly into the joint of two aluminium plates. The pin will be fully inserted in the plates. After that the shoulder will be slightly lowered into plates. This is done by lowering the spindle a little bit after the pin is fully inserted into the joint. Then the tool is allowed to rotate for some time to raise the temperature around the pin [7]. The tool rotating about an axis and travel along the edges of the plates, due to this heating of work-piece and movement of material to produce the joint. The heating is accomplished by friction between the tool and the base material and plastic deformation of base material plate. Once the material around pin softens, then the rotating tool is traversed along the length of joint [8]. When the tool reaches the other end, then the tool is lifted up. After this, the clamps are loosened and plates are taken out. The same process is repeated for other joints. Welding was performed using three rotational speeds 760, 1340 and 2000 rpm with advancing speed of 11, 18 and 25 mm/min. In order to control welding parameters in FSW, a 6.25-mm-thick aluminium plate was friction stir welded using three parameters and three levels for each parameter in the present study [9, 10]. The aim is to investigate the influence of non-consumable tool rotational speed and welding speed on the tensile strength, joint efficiency and grain size of 7075-T₆ joints.

56.2 Experimental Procedure

Rolled plates of 6.35 mm thick, AA7075-T₆ aluminium alloy base material, were cut to the required size of 150 mm × 50 mm by hacksaw cutting. The base material chemical composition properties and mechanical properties are presented in Tables 56.1 and 56.2.

Non-consumable stainless steel tool is used to fabricate the joints. Various tool materials can be used for friction stir welding. We have used a stainless steel rod for welding. The shoulder and pin were machined using a CNC machine. The shoulder

Table 56.1 Base material chemical properties (wt%)

Element	Mg	Mn	Zn	Fe	Cu	Si	Al
(7075-T ₆)	2.1	0.12	5.1	0.35	1.2	0.58	Remaining

Table 56.2 Base material mechanical properties

Material	Yield strength (MPa)	Tensile strength (MPa)	Elongation (%)
(7075-T ₆)	410	485	12

Fig. 56.1 Stainless steel tool used in this experiment**Table 56.3** Tool specifications

Parameter	Value
Pin taper angle	4.6 degrees
Pin length	6.35 mm
Shoulder diameter	15 mm

profile was flat. The pin profile is machined in the form of a tapered cylindrical pin shown in Fig. 56.1.

The tool shoulder and pin specifications were mentioned in Table 56.3. The joints were fabricated on a conventional vertical milling machine. The tool is made from stainless steel rod of diameter 20 mm. Single-pass tool travel procedure was followed to make the joints. The faces of the plates which are to be joined are made flat and parallel by milling for proper joining. To investigate the effect of tool rotational and welding speed, we have chosen three different rotational speeds and three welding speeds. The three different tool rotational speeds (760, 1340 and 2000 rpm) are selected from possible minimum, intermediate and maximum spindle speeds (11, 18 and 25 mm/min) of the machine. The three welding speeds are also selected in the similar manner. A total of 18 plates were joined to get 9 joints. The plates are held rigidly by clamps during welding. The FSW was carried out by using a conventional milling machine whose specifications are mentioned in Fig. 56.2 and Table 56.4.

56.3 Results and Discussion

56.3.1 Tensile Test

The ultimate strength of Al7075-T6 weld joints is investigated. The Al7075-T6 plates were welded by friction stir welding technique with each input condition means the three levels of heat inputs. The finished joints are shown in Figs. 56.3, 56.4 and 56.5.

Fig. 56.2 Conventional milling machine used in this experiment



Table 56.4 Machine specifications

Company	ALTO
Model	HV3CW
Serial No	201304017 N
Spindle speed	Min: 60 rpm
	Max: 2000 rpm
Voltage	415 V
Phase	3 PH
Total power	4.1 kW
Net weight	2200

Fig. 56.3 FWS produced at 760 rpm with 11, 18, 25 mm/min



The weldments before taking to destructive testing are subjected to dye penetrant test and X-ray test to find the surface and subsurface defects. Then they are subjected to tensile and hardness tests. The results are presented (Table 56.5).

Fig. 56.4 FWS produced at 1340 rpm with 11, 18, 25 mm/min



Fig. 56.5 FWS produced at 2000 rpm with 11, 18, 25 mm/min



Table 56.5 Ultimate tensile strength of various joints in MPa

Process parameters	11 mm/min	18 mm/min	25 mm/min
760 rpm	189	233	214
1340 rpm	382	310	275
2000 rpm	252	221	205

56.3.2 Effect of Tool Rotational Speed on UTS and Efficiency of Joints

The above two figures show the effect of increasing tool rotational speed on UTS and joint efficiency at a constant welding speeds of 11, 18 and 25 mm/min, respectively. We can observe that at a constant welding speed, the ultimate tensile strength and joint efficiency first increase with increasing rotational speed and then decrease with additional increase in tool rotational speed. Of all the joints, the joints fabricated at

a tool rotational speed of 1340 rpm and a welding speed of 11 mm/min showed the highest ultimate tensile strength and joint efficiency. In FSW, the rotational speed of the tool increases; consequently, the heat also increases. This experience can be explained by the following two reasons: first, the rubbing surfaces between tool and base material co-efficient of friction decreases when a local melt occurs, and subsequently decreases; on the other, the rotational speed of the tool increases, and the heat generated at the stirred zone also increases due to the higher friction heat which in turn result in more intense stirring and mixing of materials. As the tool rotational speed increased from 760 to 1340 rpm, the strength is improved, reaching maximum strength before falling again at high rotational speeds of the tool. Higher heat is generated due to the higher tool rotational speed, and this leads to the excessive release of stirred material to the upper surface, which resultantly produced microvoids in the stir zone (Figs. 56.6 and 56.7).

Fig. 56.6 Effect of rotational speed on UTS

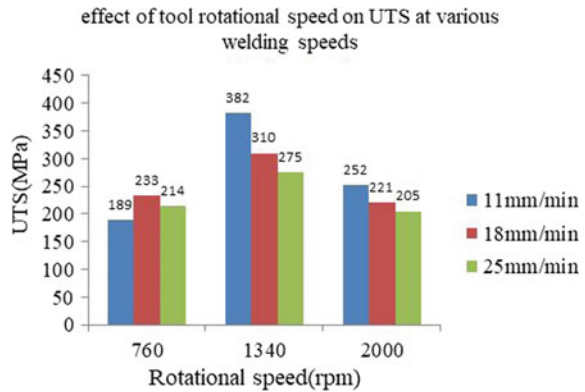
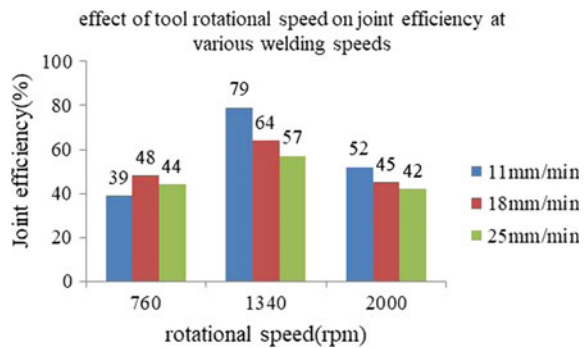


Fig. 56.7 Effect of rotational speed of tool on joint efficiency at various welding speeds



56.3.3 Effect of Welding Speed on UTS and Efficiency of Joints

The above two figures show effect of increasing welding speed on UTS and joint efficiency at a constant tool rotational speeds of 760, 1340 and 2000 rpm, respectively. We observe that as the speed increases from welding of 760 rpm, the tensile strength and joint efficiency first increase and then decrease. The ultimate tensile strength and joint efficiency are observed at 1340 rpm and 11 mm/min, respectively. At higher welding speed, the softened base plate area is narrower than the lower welding speed. Thus, the ultimate tensile strength of welded joint has a relative with lower welding speed. Higher speeds give faster cooling rates of friction stir welded joint and may cause lack of penetration and the formation of defects in stirred zone side poor strength properties. Finally, the width of the heat-affected zone and the value of the maximum strain decreased and the location of the maximum strain gradually moved to the diminishing side from the advancing side of the joint (Figs. 56.8 and 56.9).

56.4 Conclusions

In this experiment, the two process parameters of FSW, i.e. tool rotational speed and welding speed, are varied to find the effect of process parameters on microstructural and mechanical properties of Al 7075-T6 alloy friction welded plates of thickness 6.35 mm. In these experiments, three tool rotational speeds and three welding speeds were employed. As a result, nine joints were fabricated. Each joint is subjected to tensile test to know their mechanical properties. The conclusions are listed below from the experiments.

Fig. 56.8 Effect of welding speed on UTS at various tool rotational speeds

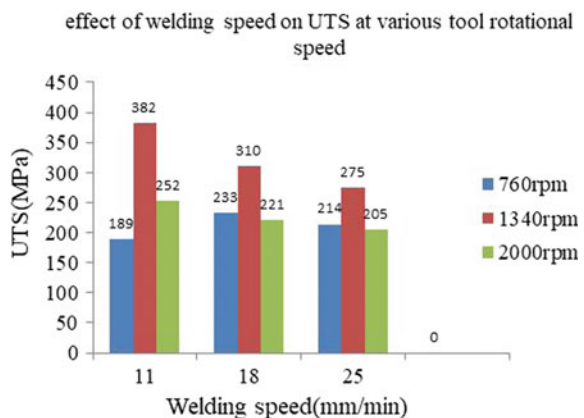
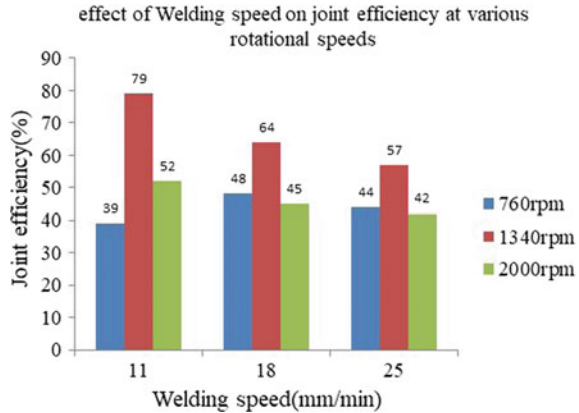


Fig. 56.9 Effect of welding speed on joint efficiency at various tool rotational speeds



- The experiment it is found that the aluminium 7075-T₆ alloy plates can be successfully welded by using a tool made of stainless steel rod having a flat shoulder and cylindrical tapered pin profile.
- From the non-destructive test, defect-free joints were obtained at tool rotational speeds of 760–2000 rpm, speeds of 11–25 mm/min.
- Tensile strength of the joints (Al7075-T₆) increases along with tool rotational speed maximum at 760–1340 rpm and again decreases with beyond the 1340 rpm of tool rotational speed.
- At tool rotational speed of 760 rpm and welding speed of 11 mm/min, the tensile test, was 189 MPa and increased to 382 MPa as the tool rotational speed was increased to 1340 rpm. Then decreased to 252 MPa at the rotational speed of tool 2000 rpm.
- The tensile strength obtained at tool rotational speed of 760 rpm, welding speed of 25 mm/min, was 214 MPa, increased to 275 MPa as the tool rotational speed was increased to 1340 rpm and then decreased to 205 MPa at the tool rotational speed of 2000 rpm. Mechanical properties of joints decreased with increase in welding speed.

Acknowledgements We sincerely thanks to VR Siddhartha Engineering College management providing necessary resources and Dr. N. Vijaya Sai, Head of the Department, Mechanical Engineering, VRSEC, for his continued encouragement to completion of this work.

References

1. Mendes, N., Neto, P., Loureiro, A., Moreira, A.P.: Machines and control systems for friction stir welding: a review (2015). <https://doi.org/10.1016/j.matdes.2015>. <https://doi.org/10.124>
2. Shah, P.H., Badheka, V.J.: Friction stir welding of aluminium alloys: an overview of experimental findings—Process, variables, development and applications. Proc. IMechE Part L: J. Mater. Des. Appl. **0**(0):1–36 (2017)

3. Rai, R., De, A., Bhadeshia, H.K.D.H., DebRoy, T.: Review: friction stir welding tools. *Sci. Technol. Weld. Joining* **16**(4), 325–342 (2011)
4. Zhang, Y.N., Cao, X., Larose, S., Wanjara, P.: Review of tools for friction stir welding and processing. *Can. Metall. Q.* **51**(3), 250–261 (2012)
5. Yuqing, M., Liming, K., Fencheng, L., Yuhua, C. and Li, X.: Effect of tool pin-tip profiles on material flow and mechanical properties of friction stir welding thick AA7075-T6 alloy joints. *Int. J. Adv. Manuf. Technol.* **88**, 949–960 (2017)
6. Shah, P.H., Badheka, V.J.: An experimental insight on the selection of the tool tilt angle for friction stir welding of 7075 T651 aluminum alloys. *Indian J. Sci. Technol.* **9**(S1)
7. Shah, P.H., Badheka, V.J.: An experimental investigation of temperature distribution and joint properties of Al 7075 T651 friction stir welded aluminium alloys. *Proced. Technol.* **23**:543 – 550
8. Bayazida, S.M., Farhangia, H., Ghahramania, A.: Effect of pin profile on defects of friction stir welded 7075 aluminum alloy. *Proced. Mater. Sci.* **11**, 12–16 (2015)
9. Srinivasa Rao, T., Madhusudhan Reddy, G., Koteswara Rao, S.R.: Microstructure and mechanical properties of friction stir welded AA7075 – T651 aluminum alloy thick plates. *Trans. Nonferr. Met. Soc. China* **25**, 1770–1778 (2015)
10. Gemme, F., Verreman, Y., Dubourg, L., Wanjara, P.: Effect of welding parameters on microstructure and mechanical properties of AA7075-T6 friction stir welded joints. *Fatigue Fract. Eng. Mater. Struct.* **34**, 877–886 (2011)

Chapter 57

Effect of Tool Plunge Depth on the Mechanical Performance of Joints Fabricated by Dieless Friction Stir Form Joining of Dissimilar Grade Aluminum Alloys



Tinu P. Saju  and R. Ganesh Narayanan 

Abstract Dieless friction stir form joining is a new eco-friendly solid-state spot joining technique for dissimilar sheet metals (Indian Patent Application No. 201741040528). The process has the advantage of enabling joint formation by simultaneous mechanical interlocking and metallurgical bonding. The hook defect and pin hole formation commonly found in friction stir spot welding have been successfully eliminated. The effect of tool plunge depth on the joint formation and joint strength is elaborately discussed in this paper. Lap shear strength of samples joined with the new process is compared with that of conventional processes. Maximum lap shear fracture load of 7.71 kN was recorded at 0.4 mm tool plunge depth. The detailed characterization of the joint macrostructure of a typical high-strength sample is also presented.

Keywords Dieless friction stir forming · Tool plunge depth · Lap shear test · Macrostructure

57.1 Introduction

Energy conservation has been achieved at most importance in all major engineering fields including automobile sector. Improving the fuel efficiency and attaining mass reduction are the major measures to realize energy conservation in automobiles. Joining of sheet metals like aluminum to steel and joints between dissimilar grades alloys of aluminum especially for tailor welded blanks are some of the major issues associated with the objective of weight reduction. Solid-state welding technologies can play a significant role in such applications.

T. P. Saju · R. Ganesh Narayanan (✉)
Department of Mechanical Engineering, Indian Institute of Technology Guwahati, Guwahati
781039, India
e-mail: ganu@iitg.ac.in

© Springer Nature Singapore Pte Ltd. 2020
M. S. Shunmugam and M. Kanthababu (eds.), *Advances in Additive Manufacturing and Joining*, Lecture Notes on Multidisciplinary Industrial Engineering,
https://doi.org/10.1007/978-981-32-9433-2_57

Dieless friction stir form (DFSF) joining is a new solid-state, spot joining process by which lap joints can be produced in similar and dissimilar sheet metal combinations by simultaneous mechanical interlocking and metallurgical bonding. The use of a friction stir tool to obtain mechanical interlocking and metallurgical bonding is a novel concept. This process is a modified form of friction stir forming (FSF). Both FSF and DFSF processes yield advantages like less added mass due to the absence of traditional rivets, no chips, no fume, and no by-product formation. A better understanding of FSF process is a prerequisite for introducing DFSF process.

Friction stir forming (FSF) is a spot joining process, which relies on the principle of stir heating of the upper sheet accompanied by forging and extruding the plasticized upper sheet metal into the anvil cavity through a pre-drilled hole in the lower sheet. A flat-faced rotating stir tool is plunged into the surface of the upper sheet metal, which generates frictional heat. The plasticized upper sheet metal is able to flow through the pre-drilled hole in the lower sheet. The flown metal finally forms a mechanical rivet like interlock by acquiring the shape of the cavity feature on the anvil surface.

FSF process was initially proposed by Nishihara [1]. FSF joints were made between dissimilar metals like galvanized steel sheet and aluminum alloy sheets such as AISI 5182 and AA6014 [2]. The lap shear test and microstructure analysis had been conducted. Experimental observations proved that FSF is an excellent alternative for other joining processes like self-pieced riveting (SPR) for which the lap shear strength nearly twice of that of SPR had been recorded. Traversing FSF was experimented for cladding of AA6061-T6 over S45C steel sheet [3]. FSF of dissimilar grade aluminum alloys such as AA 5052-H32 and AA 6061-T6, each of 2 mm thickness, was performed [4, 5]. The effect of tool rotational speed and tool plunge depth on the joint strength and joint formation was experimentally investigated. It was reported that the exact mechanical interlocking was absent in aluminum-to-aluminum sheet metal combination. The pre-drilled hole had undergone severe deformation at high tool rotational speeds like 3000 rpm. The chance of closure of the pre-drilled hole was more at high tool plunge depths. Although the two sheets were metallurgically bonded, the extruded upper sheet metal was isolated from the rest by the pre-drilled hole closure. Thus, FSF is not a suitable choice for lap joining dissimilar aluminum alloy sheets. Therefore, in the present work, we propose a modified spot joining technique, namely DFSF, in which the two aluminum sheets are joined by simultaneous mechanical interlocking and metallurgical bonding.

The complete process sequence is schematically illustrated in Fig. 57.1. The anvil cavity employed in FSF process is removed in DFSF process because the joint is not realized by the formation of an extruded rivet like pin. The stir tool is rotated and plunged into the upper sheet (Stage 1). The upper sheet metal is plasticized at elevated temperature and extruded into the pre-drilled hole in the lower sheet. The pre-drilled hole also undergoes plastic deformation by the conducted heat from the upper sheet. The mechanical interlocking is enabled by the controlled deformation of the pre-drilled hole in the lower sheet (Stage 2). The top of the pre-drilled hole forms an inward collar, which locks the extruded upper sheet metal. The extruded upper sheet metal is prevented from retraction by the neck formation produced by the inward collar. Meanwhile, the interface between the two sheets is metallurgically bonded.

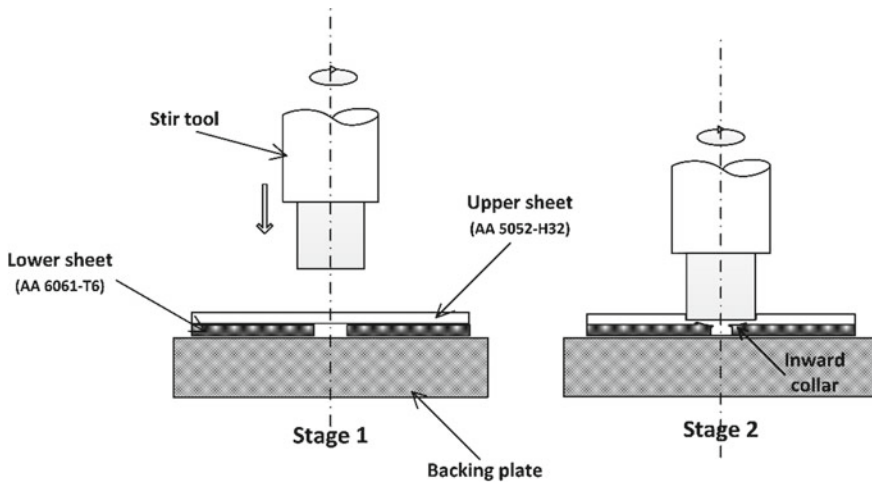


Fig. 57.1 DFSF process sequence

Thus, simultaneous mechanical interlocking and metallurgical bonding realize the joint formation. The process has the advantage of producing single-pin and multi-pin configurations. DFSF varies slightly from friction stir spot welding (FSSW), since the stirring in a DFSF process is intended to produce plasticized upper sheet metal, whereas in FSSW, the stirring results in mixing of the plasticized metal of the upper and lower sheets. The hook defect and pin hole defect commonly found in FSSW impair the joint strength. DFSF process has been successful in eliminating these defects. The flat-faced pinless stir tool prevents keyhole formation. Since low plunge depth is employed in the DFSF process, the chance of hook defect is very less.

The present work provides a critical understanding about the potential of the DFSF process in creating joints in dissimilar aluminum alloys, namely AA5052-H32 and AA6061-T6, each of 2 mm thickness. The effect of the tool plunge depth (TPD) on the joint formation and the joint macrostructure is elaborately discussed. But the exact process analysis and the effects of other critical process parameters on the quality of the DFSF joint are kept for future investigation.

57.2 Methodology

57.2.1 DFSF Joining Experiments

The effectiveness of the formation of a DFSF joint can be evaluated on the basis of the resulting joint strength and the produced geometrical interlocking features. The DFSF samples were prepared using a fixture setup mounted on a milling machine (Kirkoskar Viking KTM 40). The basic elements of the experimental setup are friction

Fig. 57.2 Experimental setup

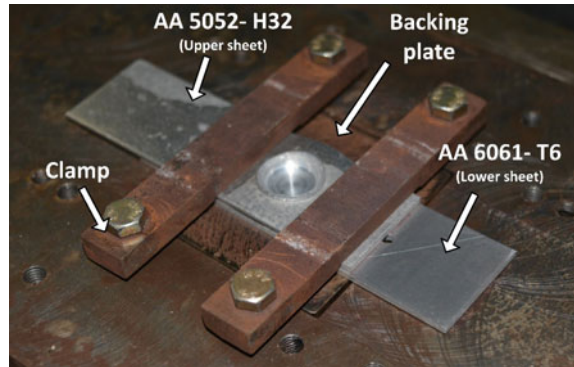


Table 57.1 Tool and backing plate details

Tool	Material	H13 tool steel
	Feature	Pinless flat face
	Diameter and length of the shoulder	14 and 25 mm
Backing plate	Material	Mild steel
	Feature	Flat surface without anvil cavity

stir tool, backing plate, and clamps, as shown in Fig. 57.2. Details about the backing plate and the stir tool are given in Table 57.1. AA 5052-H32 metal strips which form the upper coupon were stir heated and form joined into the lower strips of AA 6061-T6 alloy. The DFSF joints were fabricated at various TPD levels—lower levels at 0.25 and 0.3 mm, medium levels at 0.35 and 0.4 mm and higher levels at 0.45 and 0.5 mm. Throughout the experiments, the plunge rate, rotational speed, and direction of tool rotation were kept constant as 0.002 mm/second, 500 rpm, and clockwise direction, respectively. The parameters were decided based on previous experimental trials.

A hole of 3 mm diameter was pre-drilled into the lower AA 6061-T6 strip to enable the extrusion of the plasticized upper sheet metal during the process. The proper alignment of stir tool center, pre-drilled hole center on lower sheet, and anvil cavity center are important for the formation of a sound DFSF joint. Two samples were prepared for each TPD to obtain average data.

57.2.2 Lap Shear Test

Lap shear test was conducted in order to evaluate the sample joint strength under shear loading condition, in which tensile load was applied perpendicular to the axis of the joint. The axis of a DFSF joint can be considered to be perpendicular to the plane of the sheets and passing through the center of the stir spot. The metal strips

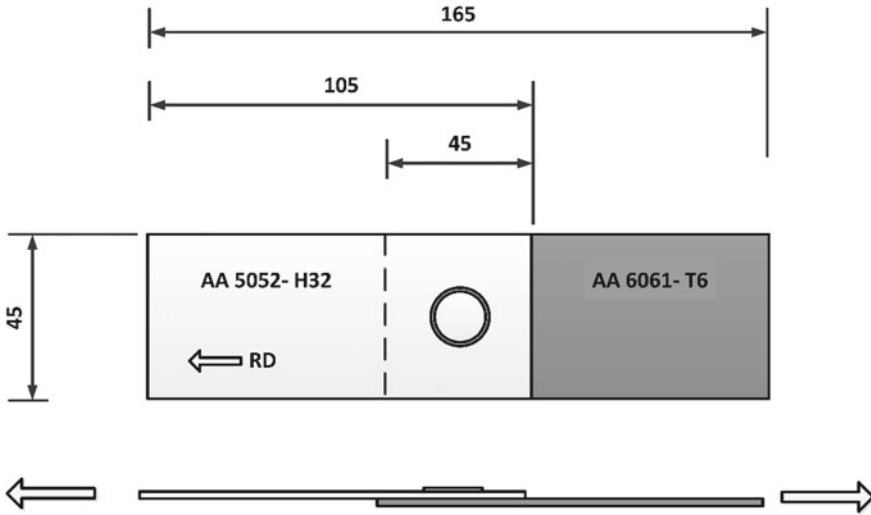


Fig. 57.3 Schematic diagram of a lap shear test sample with all dimensions in mm

for lap shear samples were shear cut from large sheets such that the sheet rolling direction (RD) is oriented along the length of the sample. The sample dimensions are shown in Fig. 57.3.

Lap shear tests were carried out on a 250 kN servo hydraulic UTM (BISS Median 250). The extension rate was kept at a standard value of 1 mm/min. The samples were subjected to tensile load until failure, and the maximum load at which failure occurred and load-progression behavior were recorded.

Lap shear test was also performed on samples joined with FSF and FSSW processes to compare their strengths with DFSF samples. A flat pinless stir tool having 14 mm shoulder diameter and anvil cavity diameter of 3.5 mm and cavity depth of 0.55 mm were employed for FSF process. A stir tool of 14 mm shoulder diameter with a pin of 4 mm diameter and 1 mm length was used for FSSW process. All other parameters were kept same as that in DFSF.

57.2.3 Macrostructure

The macrostructure analysis provides information about the effectiveness of the joint formation, material flow evolution, defect formation, and distinction of various zones in a DFSF joint. The DFSF sample fabricated at 0.5 mm TPD was cut along the center of the spot perpendicular to the length direction of the sample so that the joint cross section was obtained. The cross section was initially rough finished with emery paper with grit size ranging from 60 to 2000, and fine finish was obtained by polishing with a velvet cloth treated with polishing liquid. The polished sample was mildly etched

with Keller's reagent (190 mL distilled water, 5 mL HNO₃, 3 mL HCl, and 2 mL HF) for 20 s. The macrostructure image was taken using Zeiss Axiocam MR3 Microscope.

57.3 Results and Discussion

57.3.1 Lap Shear Test Results

The average fracture load (kN) for lap shear samples is plotted against corresponding TPDs in Fig. 57.4. The fracture load remains nearly same about 6–7 kN throughout the TPD range except at 0.25 mm. This indicates that at lower TPD of 0.25 mm, the chance of formation of a sound joint is less. Maximum lap shear fracture load of 7.71 kN was recorded at 0.4 mm TPD. The extension at fracture remains more or less same about 1 mm. Therefore, a consistent mechanical performance has been obtained for DFSF samples throughout the TPD range. Throughout the TPD range, the samples are equally strengthened by simultaneous mechanical interlocking and metallurgical bonding. From lap shear test results, it can be concluded that DFSF joints can be fabricated successfully at a minimum TPD of 0.3 mm.

DFSF samples show superior lap shear fracture load than FSSW and FSF samples. Lap shear tests were also performed in FSF and FSSW samples for the same material combination. The comparison of lap shear fracture load of samples fabricated at

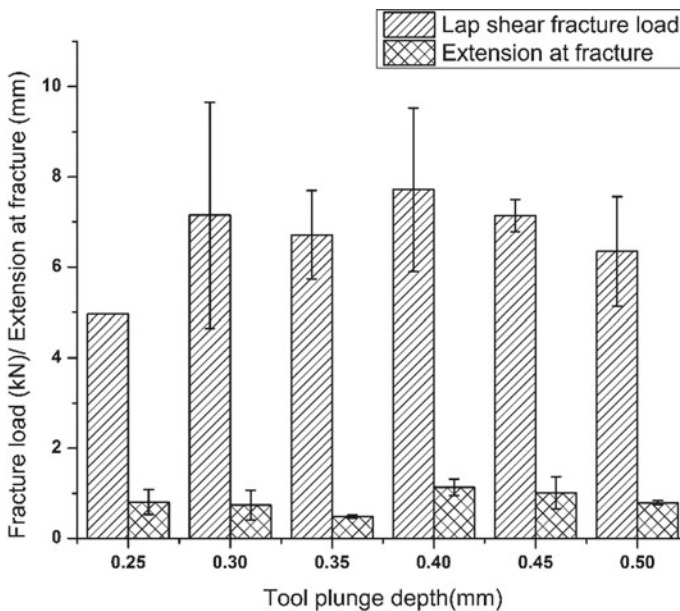


Fig. 57.4 Comparison of fracture loads and extension at fracture for various TPDs

Table 57.2 Comparison of the lap shear fracture load of DFSF samples with conventional FSF and FSSW samples

Joining technique	Fracture load (kN)
DFSF	7 ± 2.49
FSF	3.276 ± 0.46
FSSW	4.4 ± 0.35

0.3 mm TPD is shown in Table 57.2. It can be observed that the DFSF samples possess lap shear fracture load, which is 113% better than FSF and 60% better than FSSW samples at 0.3 mm TPD. In addition to the superiority in strength, the aesthetic appearance of DFSF samples is much better than its counterparts. The pin hole defect in FSSW samples and rivet head formation in FSF samples are eliminated in DFSF samples.

57.3.2 Macrostructure Analysis

The complete macrostructure of the joint cross section fabricated at 0.5 mm TPD with the schematic representation of various zones is shown in Fig. 57.5. The various zones that can be distinguished in the cross section of the DFSF samples are stir zone (SZ), thermo-mechanically affected zone (TMAZ), and plastically deformed metal flow zone (PDZ).

SZ is located symmetrically at the center of the stir spot, where the tool face touches the upper sheet. The SZ has maximum depth at the center of the spot. The direction of metal flow and the amount of plastic deformation under the tool varies from center to the periphery of the tool. Unique pattern is produced by the stirring of the material inside the SZ. This is due to the dynamic recrystallization of the stirred upper sheet material. The SZ also possesses another localized annular ring-shaped region, annular stir zone (ASZ), appearing outside the central region. This shows that a discontinuity is present in the SZ formation toward the periphery of the stir tool.

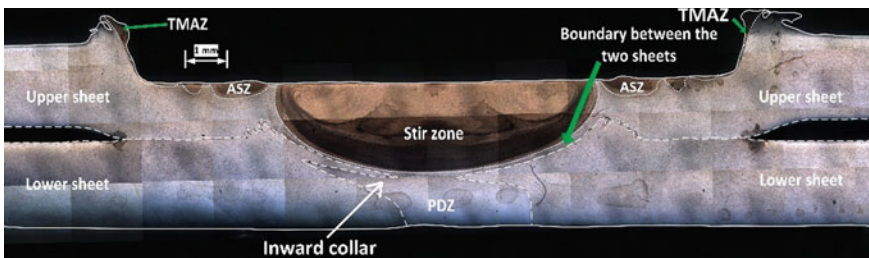


Fig. 57.5 Sample macrostructure with schematic representation of joint zones

The TMAZ is visible on the side walls of the stir spot. This region is generated due to the frictional contact of the lateral surface of the rotating stir tool on the top of the upper sheet. The TMAZ has also been dynamically recrystallized under the influence of the rotating stir tool and the frictional heat flux.

Plastically deformed metal flow zone (PDZ) is located below the SZ inside the pre-drilled hole, where the stirring of the plasticized upper sheet metal is absent. The PDZ metal is extruded, and metal flow occurs radially inward into the pre-drilled hole due to plunge force generated by the downward movement of the stir tool.

The interface between the two sheets is metallurgically bonded. In addition, the two sheets are mechanically interlocked by the controlled deformation of the pre-drilled hole. The mechanical interlocking is visible in the form of an inward collar, which grows from the top of the pre-drilled hole. This prevents the retraction of the extruded PDZ. The inward collar creates neck on the extruded metal. The collar edges are closer at 0.5 mm TPD. Therefore, employing TPD beyond 0.5 mm may result in closure of the pre-drilled hole for the selected material combination of 2 mm thickness.

57.4 Conclusions

The effect of TPD on the mechanical performance and joint formation of DFSF joints of dissimilar grade aluminum alloys has been conducted. The following are the conclusions from the results.

- Lap shear fracture load of 6–7 kN is obtained throughout the TPD range chosen for DFSF samples, which is better than that of FSSW and FSF samples. The hook defect and pin hole defect in FSSW have been successfully eliminated.
- The macrostructure analysis revealed the presence of three distinct zones, namely stir zone, annular stir zone, thermo-mechanically affected zone, and plastically deformed metal flow zone.
- The samples are strengthened by simultaneous mechanical interlocking and metallurgical bonding.

Past research is focused on applying already available technique such as FSF for spot joining lightweight sheet metals such as aluminum alloys. The present work describes a modified process, namely DFSF joining, which eliminates the defects and shortcomings encountered in the previous work. The significance of critical process parameter such as TPD is revealed through the present work.

Acknowledgements The authors thank the mechanical testing facility extended by the Department of Mechanical engineering, IIT Guwahati, for conducting the lap shear test.

References

1. Nishihara, T.: Development of friction stir forming. *Mater. Sci. Forum* **426–432**, 2971–2978 (2003)
2. Lazarevic, S., Miller, S.F., Li, J., Carlson, B.E.: Experimental analysis of friction stir forming for dissimilar material joining application. *J. Manuf. Process.* **15**, 616–624 (2013). <https://doi.org/10.1016/j.jmapro.2013.05.004>
3. Nishihara, T., Ito, A.: Measurement of die temperature during friction stir forming. *Weld. World* **49**(3–4), 22–26 (2005)
4. Saju, T.P., Narayanan, R.G.: Friction stir forming of dissimilar grade aluminum alloys: influence of tool rotational speed on the joint evolution, mechanical performance, and failure modes. *Int. J. Adv. Manuf. Tech.* **95**, 1377–1397 (2018). <https://doi.org/10.1007/s00170-017-1322-x>
5. Saju, T.P., Narayanan, R.G.: Effect of tool plunge depth on joint formation and mechanical performance of friction stir forming joints made between AA 5052-H32 and AA6061-T6 sheet metals. *Trans. Nonferrous Met. Soc. China* **28**, 613–628 (2018). [https://doi.org/10.1016/S1003-6326\(18\)64694-1](https://doi.org/10.1016/S1003-6326(18)64694-1)

Chapter 58

Influence of Perturbations on Actuation Characteristics of Friction Stir Welded Shape Memory Alloy



S. S. Mani Prabu , R. Mithun , Suhel Khan , S. Jayachandran , M. Manikandan , Yeshwanth Sai , M. Anbarasu and I. A. Palani

Abstract In this work, the actuation behavior of friction stir welded nitinol shape memory alloy (SMA) was studied. A welded rectangular strip was used for actuation studies. The electrical actuation of the welded sample was performed in cantilever configuration along with a bias load attached to the free end. A maximum displacement of 17.8 mm was attained at a current of 4A against the biased load at room temperature. Using finite element method (FEM), the influence of environmental perturbation on the actuation characteristics of welded nitinol has been simulated. The change in actuation characteristics with respect to ambient temperature and air flow velocity is described in detail.

Keywords Shape memory alloy · Nitinol · Friction stir welding · Actuation

58.1 Introduction

Shape memory alloys are one of the widely used smart materials for their unique shape memory and superelasticity. The diffusionless solid-state phase transformation is the phenomenon driving the distinctive behavior of this material. It has been used as actuator in the form of wires, springs, ribbon, and various geometric structures. Many interesting applications can be seen such as valves (safety valves, anti-clad valve, and transmission valve), morphing aircraft, robotics, and other mechanical systems [1–5]. Especially, the NiTi SMAs are very attractive due to good biocompatibility,

S. S. Mani Prabu (✉) · Y. Sai

Metallurgy Engineering and Materials Science, Indian Institute of Technology Indore, Indore, India

e-mail: maniprabu.sakthivel@gmail.com

R. Mithun

Mechanical Engineering, A.C. G. College of Engineering and Technology, Karaikudi, India

S. Khan · S. Jayachandran · M. Manikandan · I. A. Palani

Mechanical Engineering, Indian Institute of Technology Indore, Indore, India

M. Anbarasu

Electrical Engineering, Indian Institute of Technology Indore, Indore, India

© Springer Nature Singapore Pte Ltd. 2020

M. S. Shunmugam and M. Kanthababu (eds.), *Advances in Additive Manufacturing and Joining*, Lecture Notes on Multidisciplinary Industrial Engineering,

https://doi.org/10.1007/978-981-32-9433-2_58

high work density, and good thermomechanical stability. These alloys have been employed in many biomedical applications notably as cardiovascular stents, permanent bone implants, and biopsy forceps. The SMAs actuate or regain its original position through heating above the austenite temperature. There are many ways to heat or actuate the SMA such as hot water actuation, electrical actuation, laser actuation, and electromagnetic heating. Depending on the application requirements, the actuation method has to be selected wisely. In case of contactless and long-distant actuation, laser actuation is preferred over other methods. In case of safety valves, the hot fluidic actuation can be used where the working fluid will actuate the SMA element above the safety threshold temperature. However, the electrical actuation has been widely used for its efficient control and simple design. The speed of actuation can be easily controlled by simply varying the current. During actuation, the environmental disturbances such as ambient temperature and air flow velocity affect heating (rate the heat transfer) which eventually change the actuation behavior. The understanding of actuation behavior, i.e., the power requirement, frequency of actuation, etc., with respect to environmental perturbations is crucial for practical actuator applications. Because the ambient will influence the actuation behavior, and understanding of the behavior change is very important for successful implementation of SMA. Due to low formability of nitinol, welding has been used to fabricate complex geometrical structures of SMA components as demanded by the application. Differently shaped structures will be required for vibration damping of civil structures where the SMA will be used as braced frames. Fusion welding processes like gas tungsten arc welding, plasma arc welding, resistance welding, laser welding, electron beam welding, etc., have been widely used to weld nitinol [6–8]. During fusion welding, the high temperature has triggered the formation of undesirable brittle intermetallics which in turn affects the weld structural integrity and the shape memory effect. During welding of SMA, retaining the shape memory effect in the weld is crucial. In case of fusion welded nitinol, there exists either the reduction in the shape memory effect or a change in phase transformation temperatures in the weld. The weld having the different phase transformation temperatures will generate stresses when actuated together as a component. Recently, friction stir welding under the class of solid-state welding process has proved to be viable to weld nitinol without formation of brittle intermetallics and with retention of shape memory behavior [9]. The shape memory effect has been retained after friction stir welding with minimal change in phase transformation behavior. Friction stir welding (FSW) is a solid-state welding process which uses both heating and pressure to weld the joints together. Here, the high-strength materials having adequate hot hardness are used as a non-consumable welding tool. The tool will plunge into the abutting edges of the plates to be joined and traverse along the line of joint to accomplish the proper consolidation of the edges to form a joint. The welding temperature normally lies in the range from 60 to 85% of the melting point of the material being welded together. As the operating temperature is comparably lesser than the fusion welding techniques, the thermal distortion and residual stresses produced due to welding will be less. Most importantly, the autogenous weld capability of the FSW relieves the issue of compositional compatibility of the weld. The NiTi alloy is very sensitive to compositional

change as it will affect the phase transformational behavior of the weld. In this work, an attempt has been made to find the influence of ambient temperature and air flow velocity on the actuation characteristics of welded nitinol SMA. Initially, the electrical actuation characteristics at room temperature have been studied. Furthermore, finite element method was used to study the actuation behavior of welded nitinol against the environmental disturbances.

58.2 Experimental Work

The austenitic shape memory alloy sheet of thickness 1.5 mm was friction stir welded using the Densimet (Tungsten alloy) tool. Initially, the edges of the plates were grounded using abrasive papers and clamped in a special fixture made for holding thin sheets intact during welding. The tool had a pin length of 1.2 mm and diameter of 5 mm along with the shoulder diameter of 22 mm. The tool rotational speed of 1000 rpm and a traverse of 50 mm/min were used for welding at room temperature [9]. No special cooling medium was used during welding of the nitinol plates. After welding, the sample was annealed at 450 °C for 1 h and furnace cooled to convert the nitinol from superelastic to shape memory state, i.e., from austenite to martensite phase at room temperature [10]. A rectangular strip of dimension 70 mm × 2 mm was cut across the weld and used for actuation studies, i.e., the weld was in the center of the strip. The surface oxide layer of the sample was abraded using silicon carbide papers. The actuation setup consists of a programmable power supply, data acquisition system (DAQ), and a laser displacement sensor (LDS). The power supply will supply the required electrical input, while the LDS will measure the change in displacement upon actuation. The schematic of the actuation configuration and the setup is shown in Figs. 58.1 and 58.2. The actuation was carried out by fixing the sample in a cantilever configuration, and a bias load of 50 g was attached to free end of the sample. The bias load will serve as a counterforce to achieve the two-way shape memory effect. During the electrical actuation studies of the welded strip, the room temperature was maintained at 20 °C.

58.3 Results and Discussion

After attaching the bias load in the free end, the welded strip was electrically biased using the programmable power supply. A constant current of 4A was applied to the welded strip. The current was selected based on the trials conducted to actuate the sample against the bias load. Due to the flow of current across the sample, the temperature was increased due to Joule heating. On heating, the sample tried to lift up against the bias load due to the shape memory effect. The resulted displacement change was measured using LDS. After reaching the maximum displacement (satu-

Fig. 58.1 Schematic of configuration used for actuation analysis of the strip having the weld in the center

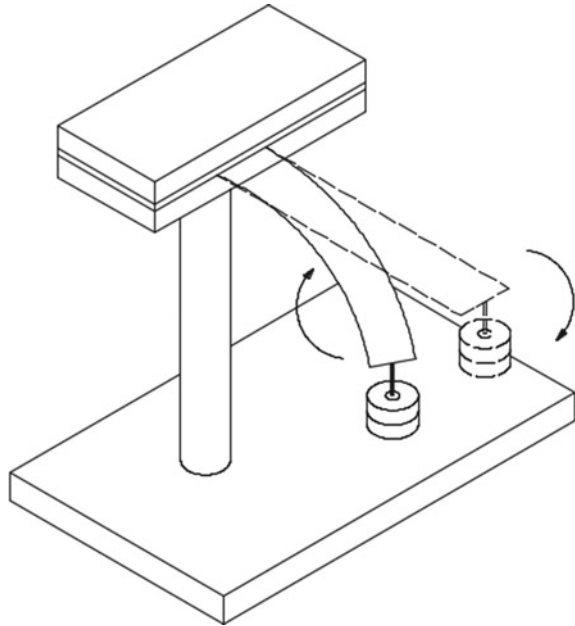
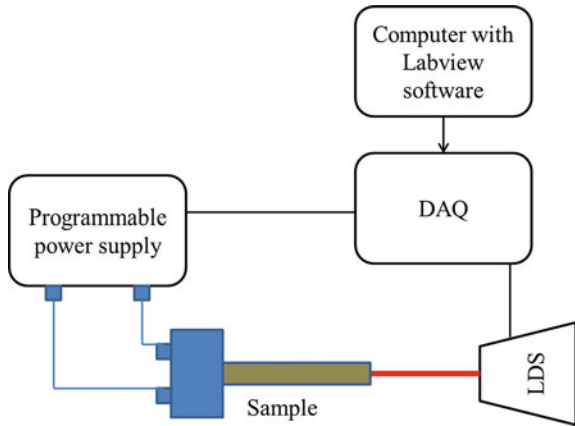


Fig. 58.2 Schematic of experimental setup used for actuation analysis of the welded strip



ration of the displacement), the electricity was cut off which enables cooling of the sample. During heating, the shape memory effect has acted upon the sample due to the solid-state transformation from martensite to austenite. On cooling, the transformation from austenite to martensite takes place, and the bias load has taken the welded strip to the initial position. The temperature during actuation was recorded using K-type thermocouple. A steady increase in temperature of the strip was noticed during heating cycle, and the maximum temperature of 40 °C was recorded at the end of heating cycle.

Figure 58.3 shows the displacement change of the SMA strip during heating and cooling cycles triggered by electrical actuation. A maximum displacement of 17.8 mm has been reached in 65 s. To study the effect of ambient temperature and flow velocity on the current required for actuation, the FEM was used. The simulation was done to get the maximum temperature of 40 °C with variation in current against the environmental perturbations. COMSOL Multiphysics 4.3a was used for simulating the mentioned conditions. The standard material properties of the nitinol SMA were used. The governing equations of the FEM used for the simulation are given in the following.

The heat generation in the welded SMA strip during electricity supply is given by,

$$J = \sigma E \tag{58.1}$$

$$E = -\nabla V \tag{58.2}$$

where J —current density, E —electric field, V —electric potential.

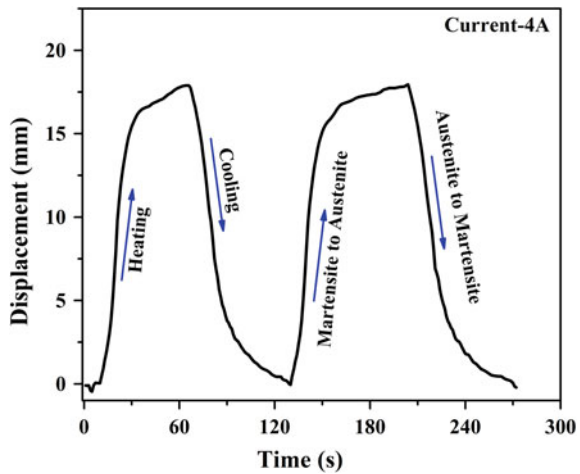
The heat transfer due to conduction and convection from the welded strip to the surrounding is given by

$$\rho C_p u \cdot \nabla T + \nabla \cdot q = Q \tag{58.3}$$

$$q = -k \nabla T \tag{58.4}$$

$$q = h_c A d T \tag{58.5}$$

Fig. 58.3 Heating and cooling cycles during electrical actuation of the welded NiTi strip against the bias load



where ρ —density of the sample, C_p —specific heat, u —velocity of flow, k —thermal conductivity, A —exposed surface area, and h_c —convective coefficient.

The Navier–Stokes and continuity equation governing the fluid motion are given by

$$\rho(u \cdot \nabla)u = \nabla \cdot [-pI + \mu(\nabla u + (\nabla u)^T)] + F \quad (58.6)$$

$$\rho \nabla \cdot (u) = 0 \quad (58.7)$$

where u —fluid velocity, p —pressure applied to the fluid, ρ —density of fluid, I —identity matrix, F —external force, and μ —dynamic viscosity of fluid.

The meshed model of the sample and the flow domain are shown in Fig. 58.4. The model was solved for the required actuation temperature against the variation in ambient temperature and airflow velocity. The ambient temperature was changed in the range from -5 to 25 °C, and the flow velocity was varied from 1 to 15 m/s. These values were selected based on the geographical variation of the temperature and air flow velocity across the countries. The temperature distribution of the sample is shown in Fig. 58.5. Figure 58.6 shows the current required for actuation of SMA strip at various ambient temperatures and air flow velocities. A linear relationship between the required current against ambient temperature and air flow velocity was observed. The decrease in temperature has linearly increased the required current for actuation. Highest current of 6.9 A was required to get the actuation temperature at -5 °C ambient temperature. In case of higher air flow of 15 m/s, the sample needs 6.8 A to actuate. The decrease in ambient temperature or increase in airflow velocity leads to increase in heat transfer from the sample. Due to the increased heat transfer from the sample, the sample drains more electrical energy for actuation.

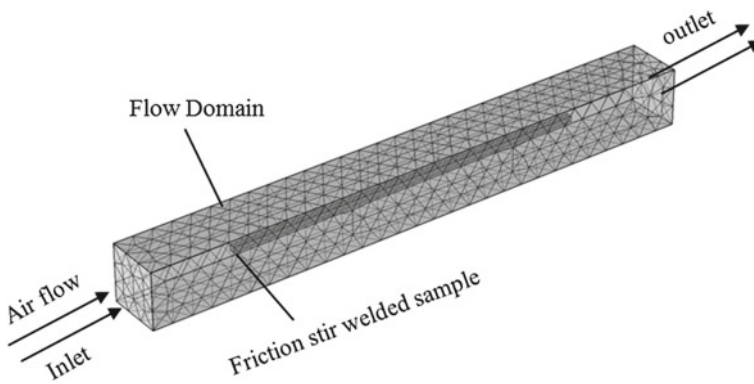


Fig. 58.4 Meshed model for FEM having the sample in the center of the flow domain

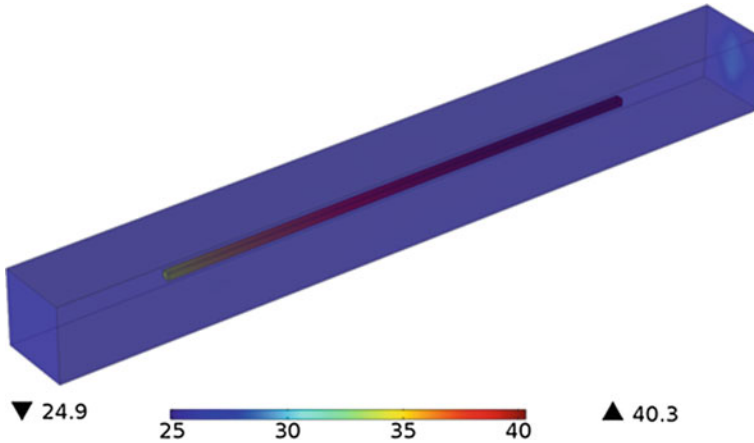
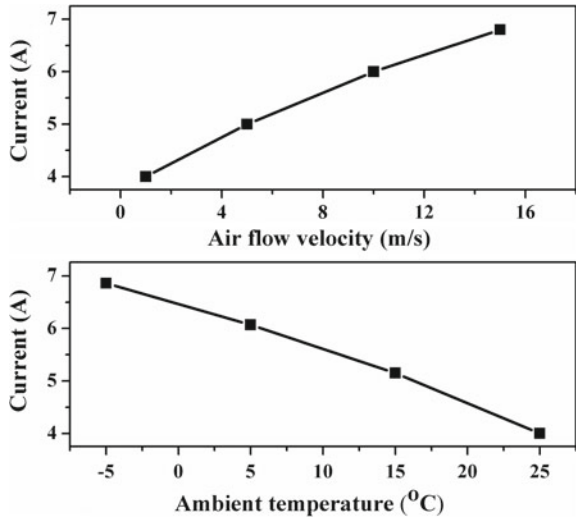


Fig. 58.5 Temperature distribution during heating cycle of the welded strip

Fig. 58.6 Effect of ambient temperature and flow velocity of actuation behavior of the welded strip



58.4 Conclusions

The electrical actuation characteristics of the friction stir welded nitinol have been studied against the environmental perturbations, and the following conclusions can be derived.

- The two-way shape memory effect was achieved during the electrical actuation of welded nitinol strip with the help of bias load attached to the free end in a cantilever configuration. A maximum displacement of 17.8 mm has been achieved at a time of 65 s during the application of 4 A current.

- The decrease in ambient temperature has significantly increased the current required for actuation. A maximum current of 6.9 A was required for actuation at an ambient temperature of -5°C .
- The increase in airflow velocity has increased the actuation current. A maximum current of 6.8 A was required at air flow velocity of 15 m/s.

Acknowledgements The authors are grateful to Prof. Satish V. Kailas of IISc Bangalore, for providing the welding facility. The authors are thankful to Madhu H. C and Chandra S. Perugu of IISc Bangalore, for their valuable assistance during welding. The author M P is thankful to Akash K for his valuable support.

References

1. Kim, H.-J., Song, S.-H., Ahn, S.-H.: A turtle-like swimming robot using a smart soft composite (SSC) structure. *Smart Mater. Struct.* **22**, 014007 (2013). <https://doi.org/10.1088/0964-1726/22/1/014007>
2. Mohd Jani, J., Leary, M., Subic, A., Gibson, M.A.: A review of shape memory alloy research, applications and opportunities. *Mater. Des.* **56**, 1078–1113 (2014)
3. Han, M.W., Rodrigue, H., Cho, S., Song, S.H., Wang, W., Chu, W.S., Ahn, S.H.: Woven type smart soft composite for soft morphing car spoiler. *Compos. Part B Eng.* **86**, 285–298 (2016). <https://doi.org/10.1016/j.compositesb.2015.10.009>
4. Murugan, S., Woods, B.K.S., Friswell, M.I.: Hierarchical modeling and optimization of camber morphing airfoil. *Aerosp. Sci. Technol.* **42**, 31–38 (2015). <https://doi.org/10.1016/j.matdes.2009.09.011>
5. Barbarino, S., Bilgen, O., Ajaj, R.M., Friswell, M.I., Inman, D.J.: A review of morphing aircraft. *J. Intell. Mater. Syst. Struct.* **22**, 823–877 (2011). <https://doi.org/10.1177/1045389X11414084>
6. Kannan, T.D.B., Ramesh, T., Sathiya, P.: A review of similar and dissimilar micro-joining of nitinol. *J. Miner. Met. Mater. Soc.* **68**, 1227–1245 (2016). <https://doi.org/10.1007/s11837-016-1836-y>
7. Van Der Eijk, C., Fostervoll, H., Sallom, Z.K., Akselsen, O.M.: Plasma Welding of NiTi to NiTi, Stainless Steel and Hastelloy C276, pp. 13–15 (2003)
8. Oliveira, J.P., Barbosa, D., Fernandes, F.M.B., Miranda, R.M.: Tungsten inert gas (TIG) welding of Ni-rich NiTi plates: functional behavior. *Smart Mater. Struct.* **25**, 1–7 (2016). <https://doi.org/10.1088/0964-1726/25/3/03LT01>
9. Prabu, S.S.M., Madhu, H.C., Perugu, C.S., Akash, K., Kumar, P.A., Satish, V.K., Manivannan, A., Palani, I.A.: Microstructure, mechanical properties and shape memory behaviour of friction stir welded nitinol. *Mater. Sci. Eng., A* **693**, 233–236 (2017)
10. Yoon, S.H., Yeo, D.J.: Phase transformations of nitinol shape memory alloy by varying with annealing heat treatment conditions. *Proc. SPIE.* **5648**, 208–215 (2005). <https://doi.org/10.1117/12.582381>

Chapter 59

Ultrasonic Welding of Molybdenum Using Aluminium Interlayer



Sanjay Kumar Patel, Harshit K. Dave  and Himanshu V. Patel 

Abstract The ultrasonic metal welding is an industrial technique whereby high-frequency ultrasonic acoustic vibrations are locally applied to the workpiece being held together under pressure to create a solid-state weld. In the present study, ultrasonic metal welding was successfully carried out on the material 0.3-mm molybdenum TZM alloy with pure aluminium interlayer. Al interlayer of 0.2, 0.25 and 0.3 mm thickness is inserted in between the faying surface. Experiments of ultrasonic metal welding were performed using Taguchi's L27 orthogonal array. The weld strength of the welded joints is measured using tensometer. Results show that weld strength is increasing with an increase in pressure and weld time. Further, ANOVA result indicates that pressure and weld time have a maximum contribution on weld strength.

Keywords USMW · Interlayer · Weld strength · Aluminium · Molybdenum

59.1 Introduction

Welding is a process of joining two similar or dissimilar metallic components with the application of heat and with or without the application of pressure and filler metal. In ultrasonic welding, high-frequency ultrasonic vibrations are produced to create relative motion between surfaces held under pressure. This motion produces shearing, deformation and flattening of surface asperities and disperses interface contaminants and oxides, and metal-to-metal bond is formed between surfaces. Temperature is raised due to combined effects of interfacial slip, elastic hysteresis and plastic deformation. Figure 59.1 shows a schematic representation of the weld interface in ultrasonic metal welding [1].

Matsuoka [2] has given a description of an experimental study on ultrasonic welding of ceramics and metals using inserts. Ultrasonic welding can weld various ceram-

S. K. Patel · H. K. Dave · H. V. Patel (✉)

Department of Mechanical Engineering, Sardar Vallabhbhai National Institute of Technology,
Surat 395007, Gujarat, India

e-mail: hpsvnit07@gmail.com

© Springer Nature Singapore Pte Ltd. 2020

M. S. Shunmugam and M. Kanthababu (eds.), *Advances in Additive Manufacturing and Joining*, Lecture Notes on Multidisciplinary Industrial Engineering,

https://doi.org/10.1007/978-981-32-9433-2_59

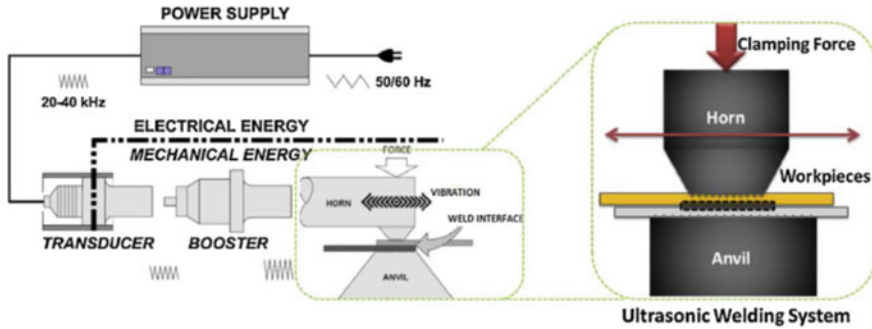


Fig. 59.1 Ultrasonic metal welding [1]

ics such as Al_2O_3 , SiC, Si_3N_4 and AlN to metals at room temperature more easily relatively to other welding methods. Elangovan et al. [3] have used response surface methodology (RSM) with a genetic algorithm (GA) to obtain the optimum process parameter for maximum weld strength. They observed that as pressure increases, weld strength decreases, because relative motion between weld surfaces reduces. They have observed that for any value of pressure weld strength increases up to weld time 3 s. After 3 s weld time increases, it disturbs the contact and changes the orientation of the bond region and they get stretched. On the other hand, increasing amplitude causes more area for rubbing leading to higher weld strength.

Patel and Dave [4] worked to understand the relation between weld strength and other welding parameters by Taguchi's L27 orthogonal array. They have identified the optimal combination of input parameters for ultrasonic welding of Al–Al for maximum weld strength. Optimal input parameters were amplitude $18\ \mu\text{m}$, pressure 3 bar, weld time 1 s and thickness ratio 0.7. Pradeepkumar and Prakasan [5] have discussed the weld strength of the welded joint between the copper wire and copper sheet using ultrasonic welding. The experiment was conducted using full factorial design according to varying weld pressure, amplitude and welding time. The standard tensile test was selected to extract quality response. Using ANOVA, the percentage contribution of each factor is determined. From the study, it can be seen that the experimental and predicted value of weld strength shows good agreement with 2.32 average percentage error. From analysis of variance (ANOVA), it can be found that weld pressure contributes 50% to the response characteristics, i.e. weld strength. Balasundaram et al. [6] studied welding of Al and Cu while using $50\ \mu\text{m}$ thick Zn interlayer and observed that micro hardness of Al to Cu joint reduces as weld energy increases. Al–Cu weld strength increases when zinc interlayer inserted in between Al–Cu due to Al–Zn eutectic film produced. Wang et al. [7] studied welding between Ti and Al alloys with or without pure aluminium intermediate layer and investigated microstructure, hardness and tensile strength. They concluded that At 1000 J energy and $75\ \mu\text{m}$ Al interlayer thickness gave 206 MPa weld strength. Further increases in Al interlayer thickness with constant weld energy have no significant change on strength.

Literature shows that ultrasonic welding operations have been employed on thin sheets of similar as well as dissimilar metal sheets. However, very less literature is observed to the best of authors' knowledge that reports the effect of varying inserts thickness during ultrasonic welding. In the present investigation, an attempt is made to the effect of interlayer thickness along with amplitude, pressure and weld time on weld strength. Experiments were performed using Taguchi method, and results were analysed using analysis of variance (ANOVA).

59.2 Experimental Study

59.2.1 Experimental Set-Up

The experiments were conducted on a 3 kW power rating ultrasonic welding machine manufactured by Roop Telsonic Ultrasonix Limited (RTUL) which is shown in Fig. 59.2. The sonotrode used along with machine is made of hardened steel. Anvil block has knurling impressions to provide grip to the specimen placed on it, and it is made up of steel. The parameters that can be varied on this machine tool set-up are amplitude, pressure and weld time. Additionally, to study the effect of the interlayer, one more factor is taken into account, i.e. interlayer thickness.

Experiments of ultrasonic welding were carried out with different interlayer thicknesses, i.e. 0.2, 0.25 and 0.3 mm of pure aluminium. The specimens are prepared as per ASTM D-1002 [8]. Weld strength is measured with a tensometer which is shown in Fig. 59.3.

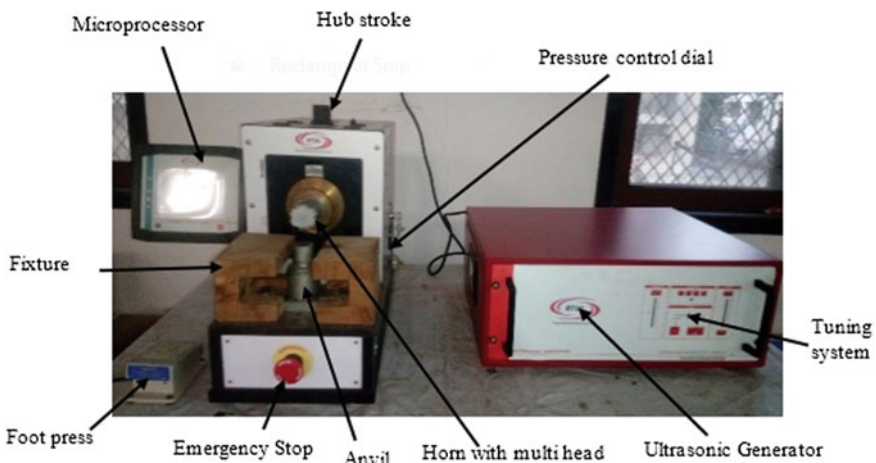


Fig. 59.2 Ultrasonic metal welding

Fig. 59.3 Tensometer set-up



59.2.2 Material Selection

In this study, Molybdenum TZM alloy of 0.3 mm thickness sheet selected for welding. Pure Aluminium sheet as an interlayer of 0.2, 0.25, 0.3 mm thickness inserted between the molybdenum alloy strips. Molybdenum strips of 100 × 20 mm size are cut from the metal sheets of thickness, viz. 0.3 mm for experimentation. The parts are prepared for experiments as per ASTM D1002-01 standard [8]. The overlap distance during the welding of parts is maintained at 6 mm. Tables 59.1 and 59.2 show the chemical composition of the molybdenum TZM alloy and aluminium.

59.3 Design of Experiments

Taguchi’s L27 orthogonal array method has been used for the experiment and subsequent analysis of the data collected. The L27 orthogonal array is meant to understand the effect of four independent variables factor with each having three-level values [9]. The focus of this study is to maximize the weld strength, and hence, weld strength is larger-the-better-type response characteristic as per Eq. 59.1. Higher signal-to-noise ratio corresponds to better performance with minimum variation.

Table 59.1 Chemical composition of the molybdenum TZM alloy (wt%)

Molybdenum, Mo	Titanium, Ti	Zirconium, Zr
99	0.50	0.10

Table 59.2 Chemical composition of the pure aluminium (wt%)

Aluminium, Al	100
---------------	-----

Table 59.3 Controlled factors with level

Factors	Units	Symbol	Level 1	Level 2	Level 3
Pressure	bar	p	1.5	2	2.5
Amplitude	μm	a	16	18	20
Weld time	s	t_w	1	1.5	2
Interlayer thickness	mm	t	0.2	0.25	0.3

$$\text{Signal-to-noise ratio } \eta_{LB} = -10 \log \frac{1}{n} \left(\sum_{i=1}^n \frac{1}{Y_i^2} \right) \quad (59.1)$$

In the present work, amplitude, pressure, weld time and interlayer thickness are considered as the controlled factors and varied at three levels as shown in Table 59.3. In present work, amplitude range is selected from 16 to 20 μm to utilize the maximum capacity of the machine tool. The parametric range of pressure and weld time are selected based on some preliminary trials during which it has been observed that welding of Mo strips occurs within the selected range of pressure and weld time. All experimental runs have been conducted three times. Table 59.4 shows the experimental plan containing factors with their real values.

59.4 Result and Discussion

The effect of controlled input parameters, namely amplitude, pressure, weld time and thickness ratio on weld strength, is plotted using the mean of SN ratios and shown in Fig. 59.4. Further, to identify the contribution of parameters, ANOVA is performed. ANOVA is a mathematical technique which breaks total variation down into accountable sources [10]. The results of the analysis of variance are shown in Table 59.5. It can be seen that the higher value of coefficient determination $R^2 = 85.49\%$, where DOF is a degree of freedom, SS is the sum of square and MS is mean square.

59.4.1 Effect of Pressure on Weld Strength

Pressure has an important role in ultrasonic welding. It holds the workpiece at anvil during the welding process. It provides proper contact between two specimens which result in energy transfer between interfaces. Due to pressure better intimate contact produces between the workpieces which lead to good weld strength. The effect of pressure on weld strength can be observed by plotting a graph between the SN ratio of weld strength and the various levels of pressure, as shown in Fig. 59.4. It can be observed that the weld strength of the specimen is increasing with the increase in

Table 59.4 Real values of parameters

Exp. no.	Pressure p (bar)	Amplitude a (μm)	Weld time t_w (s)	Insert thickness t (mm)
1	1.5	16	1	0.2
2	1.5	16	1.5	0.25
3	1.5	16	2	0.3
4	1.5	18	1	0.25
5	1.5	18	1.5	0.3
6	1.5	18	2	0.2
7	1.5	20	1	0.3
8	1.5	20	1.5	0.2
9	1.5	20	2	0.25
10	2	16	1	0.2
11	2	16	1.5	0.25
12	2	16	2	0.3
13	2	18	1	0.25
14	2	18	1.5	0.3
15	2	18	2	0.2
16	2	20	1	0.3
17	2	20	1.5	0.2
18	2	20	2	0.25
19	2.5	16	1	0.2
20	2.5	16	1.5	0.25
21	2.5	16	2	0.3
22	2.5	18	1	0.25
23	2.5	18	1.5	0.3
24	2.5	18	2	0.2
25	2.5	20	1	0.3
26	2.5	20	1.5	0.2
27	2.5	20	2	0.25

pressure. At 2.5 bar maximum, weld strength was achieved. From the ANOVA as in Table 59.5, the significant effect of the pressure can be seen on the weld strength, i.e. 71.30%.

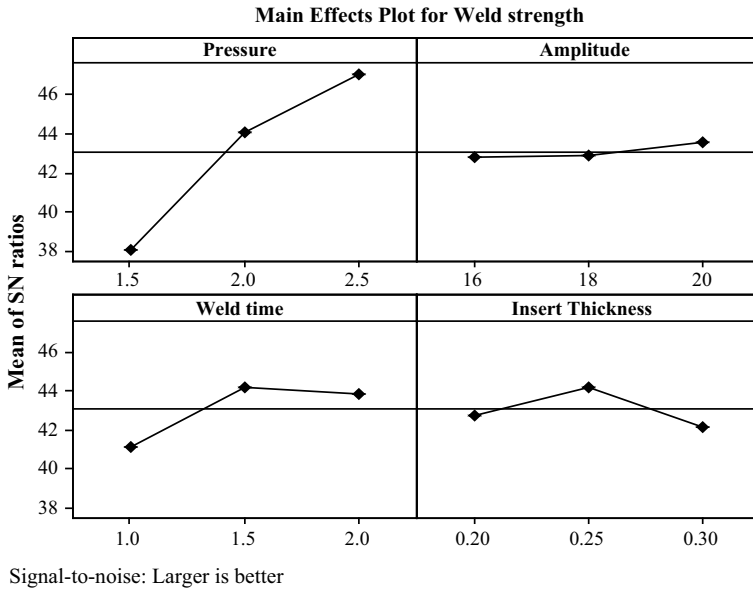


Fig. 59.4 Main effect plots for weld strength

Table 59.5 Analysis of variance for weld strength

Factor	DOF	SS	MS	F-value	P-value	Contribution (%)
Pressure	2	379.738	189.869	44.23	0.000	71.30
Amplitude	2	3.476	1.738	0.40	0.673	0.65
Weld time	2	51.278	25.639	5.97	0.010	9.63
Interlayer thickness	2	20.788	10.394	2.42	0.117	3.90
Error	18	77.278	4.293			14.51
Total	26	532.558				100.00

59.4.2 Effect of Amplitude on Weld Strength

Figure 59.4 shows the effect of a change in amplitude applied to the specimen on weld strength in ultrasonic welding. When amplitude increases, the movement of the tool is more with its mean position. High heat is generated by rubbing action. Due to this, plastic deformation of materials takes place. Fresh metal-to-metal contact with applying pressure causes better bonding. Therefore, it combines the action of pressure and amplitude to enhance the weld strength of joints.

59.4.3 Effect of Weld Time on Weld Strength

Weld time is an important parameter in the ultrasonic welding process. From Fig. 59.4, the effect of weld time on weld strength can be observed. Welded joint strength increases as weld time increases because vibrational amplitude and pressure remain for more time. Due to this, more heat generation and better bonding will occur, but a further increase of weld time will decrease weld strength because excess heat generation damages the microbonding between the atoms. The thermal energy stays on the welding spot for the longer time span. With the increase in weld time, the vibration energy transfer duration increases at the interface which results in the better weld joint. The ANOVA results show 9.63% contribution of weld time for weld strength.

59.4.4 Effect of Interlayer Thickness on Weld Strength

Effect of interlayer thickness on weld strength is plotted and shown in Fig. 59.4. Aluminium is soft and having low melting temperature metal compared to molybdenum. When Al insert kept in between the Mo Sheets insert melts at low temperature and produces a good bond with Mo. From Fig. 59.4, it can be observed that when insert thickness increases, initially weld strength increases and then decreases because at high thickness sufficient heat does not transfer for bond formation. The higher thickness of the material is one of the limitations of ultrasonic metal welding.

59.5 Conclusions

The following conclusions are made after the performance of experiments.

1. Weld strength increases as the pressure increases. Increased pressure provides better holding to the workpieces. It produces more frictional heat which leads to better weld strength.
2. It was found that the amplitude has very less impact on weld strength.
3. As the weld time increases, weld strength also increases because longer welding time provides more vibration amplitude and pressure which results in better weld strength.
4. It was found that as the interlayer thickness increases, sufficient heat does not transfer for bond formation due to that weld strength decreased.

References

1. Nong, L., Shao, C., Kim, T.H., Hu, S.J.: Improving process robustness in ultrasonic metal welding of lithium-ion batteries. *J Manuf. Syst.* (2018)
2. Matsuoka, S.I.: Ultrasonic welding of ceramics/metals using inserts. *J. Mater. Process. Technol.* **75**(1–3), 259–265 (1998)
3. Elangovan, S., Venkateshwaran, S., Prakasan, K.: Experimental investigations on optimization of ultrasonic welding parameters for copper to brass joints using response surface method and genetic algorithm. *Int. J. Adv. Eng. Res. Stud.* **1**, 55–64 (2012)
4. Patel, H.V., Dave, H.K.: Effect of parameters on weld strength during ultrasonic welding of Al–Al strip. *J. Manuf. Engineering* **11**(3), 121–125 (2016)
5. Pradeepkumar, J., Prakasan, K.: *Int. J. Mech. Prod. Eng. Res. Dev. (IJMPERD)* **2**, 21–29 (2012)
6. Balasundaram, R., Patel, V.K., Bhole, S.D., Chen, D.L.: Effect of zinc interlayer on ultrasonic spot welded Aluminium-to-copper joints. *Mater. Sci. Eng., A* **607**, 277–286 (2014)
7. Wang, S.Q., Patel, V.K., Bhole, S.D., Wen, G.D., Chen, D.L.: Microstructure and mechanical properties of ultrasonic spot welded Al/Ti alloy joints. *Mater. Des.* **78**, 33–41 (2015)
8. ASTM International: Standard Test Method For Apparent Shear Strength of Single-Lap-Joint Adhesively Bonded Metal Specimens by Tension Loading (Metal-to-Metal). ASTM international (2010)
9. Phadke, M.S.: *Quality Engineering Using Robust Design*. Prentice Hall PTR (1995)
10. Ross, P.J.: *Taguchi Techniques in Quality Engineering*. Tata McGraw-Hill, New Delhi (2005)

Chapter 60

Experimental Investigation and Mechanical Characterization of Double-Sided Submerged Arc Welding of AISI 304 Austenitic Stainless Steel



P. V. S. S. Sridhar , Shailesh Kumar , Kaushik Pal ,
Bhaskar Kumar Chakraborty , Rituraj Bhattacharjee ,
Subhashis Majumder , Pankaj Biswas and Pinakeswar Mahanta

Abstract The austenitic stainless steels are widely used in chemical, metallurgical, conventional, nuclear power plants and industrial applications due to their excellent corrosion resistance and formability. For welding plates of higher thickness, the submerged arc welding is a suitable technique, as it offers higher deposition rate, good bead shape and deeper penetration. To get a sound welded joint without defects, suitable welding parameters should be carefully chosen to weld austenitic stainless steel as they are sensitive to heat input. In this study, austenitic stainless steel plates were joined using double-sided submerged arc welding, and key welding parameters such as voltage, current and welding speed were established to get a defect-free joint. The effectiveness of double-sided welding is evaluated from microstructural and mechanical characterization. From the macroscopic examination, the two weld seams, i.e. initial run and second run intersect at the middle, which is an indication of the defect-free weld. The microstructure of the fusion zone consists of dendritic grains and coarse columnar grains. The microhardness tends to increase in the weld zone for initial weld run followed by second weld run and lowest in the middle of the weld seam. The result of the tensile test indicates that elongation of the welded joint surpasses that of parent metal elongation, and fracture occurs at base zone. The

P. V. S. S. Sridhar (✉) · S. Kumar · P. Biswas · P. Mahanta
Department of Mechanical Engineering, Indian Institute of Technology
Guwahati, Guwahati 781039, Assam, India
e-mail: p.sridhar@iitg.ac.in

K. Pal · B. K. Chakraborty
Department of Production Engineering, National Institute of Technology
Agartala, Agartala, India

R. Bhattacharjee
Department of Mechanical Engineering, National Institute of Technology
Agartala, Agartala, India

S. Majumder
Department of Mechanical Engineering,
Coochbehar Government Engineering College, Cooch Behar, West Bengal, India

© Springer Nature Singapore Pte Ltd. 2020
M. S. Shunmugam and M. Kanthababu (eds.), *Advances in Additive Manufacturing
and Joining*, Lecture Notes on Multidisciplinary Industrial Engineering,
https://doi.org/10.1007/978-981-32-9433-2_60

field emission scanning microscopy examination of the broken surfaces of the tensile sample reveals the nature of fracture mode is ductile. In this paper, heat input controlling method was successfully introduced for welding of austenitic stainless steels of higher thickness with a simple double-sided submerged arc welding (DSSAW).

Keywords Submerged arc welding · Microstructure · Microhardness

60.1 Introduction

In the early 1930s, submerged arc welding (SAW) was developed with an aim to produce high-quality weld deposits [1]. The key advantages of SAW are that it is easy to automate, minimum operator skill requirement, high deposition rate, excellent weld quality, surface finish and deeper penetration which means ability to join thick plates with single pass and clean operation without fumes [2]. In submerged arc welding (SAW), an arc is struck between bare electrode wire and the parent metal. The arc electrode end and molten pool are submerged in an agglomerated or fused flux, which turns into a slag in its lower layers under the heat of the arc and protects the weld from contamination [2]. The fluxes used in the SAW are granular fusible minerals containing oxides of manganese, silicon, titanium, aluminium, calcium, zirconium, magnesium and other compounds of calcium fluoride. The fluxes may be fused or agglomerated. Typically, the power unit used was DC generator or transformer–rectifier with output voltage in the range of 30–55 V, and currents can be as high as from 200 to 2000 A. Normally, electrode is connected to positive, and workpiece is connected to negative when the requirement is to join the materials [3]. The proper control variables in SAW are necessary to control for attaining good quality welds, namely welding current, voltage, welding speed and length of stick out. The welding current controls the electrode melting and metal deposition. The shape of fusion zone and external bead appearance is governed by welding voltage, whereas welding speed influences bead size and penetration. When welding current is kept constant, the electrode extension influences the deposition rate by 25–50% [4]. Due to application of heat, there is a possibility of deformations in the fabricated structure. For minimizing the angular distortions, adequate top and bottom reinforcements are required in a single-pass welding, which is not always possible if the plate thickness is more. In heavy engineering works, like ship building, welding of bridge large structures bead geometry is prescribed for attaining reliability of the structure in field. If first pass produces sufficient reinforcement, it will minimize the angular distortion as it acts like a hurdle when second pass is attempted. One way to minimize the angular distortions is to fabricate the plates using double-sided welding. The procedure to weld 12-mm-thick plates with minimum angular distortion by double-sided submerged arc welding with top and bottom reinforcements was developed, and numerical results are validated [5]. In their work, a distributed heat source, reinforcements, filler material deposition in each pass of welding and temperature-dependent material properties were considered. The experimental tem-

perature distribution results were co-related with numerical results which indicate the adequacy of the developed model [5]. The effect of heat input on bead geometry in single-wire and double-wire SAW for ASTM A709 Grade 50 steel for a 20-mm-thick plate was studied. With increase in heat input, there observed an increase in electrode melting efficiency in single-wire SAW, while plate melting efficiency does not change with single-wire and double-wire SAW [6]. Subsequently, the effect of welding process parameters on double-sided welding of SA516 grade 70 steel of 17 mm for various welding currents and traverse speeds was chosen for study. It was concluded that welding current directly affects the electrode melting rate, cooling rates and weld metal chemistry. Also, traverse speed has dominant effect on final fusion zone microstructure than welding current [7]. From [8] and [9], it is observed that DSSAW yields suitable quantities of microconstituents, namely ferrite and austenite in fusion zone and HAZ for duplex stainless steels. Their post-weld heat treatment studies revealed that σ phase was not present closer to the fusion-heat-affected zone vicinity, and σ phase increased in the weld zone with post-weld heat treatment [9]. Even though austenitic stainless steels were very often used material in process, manufacturing and metallurgical industries' technical literature on fabrication using submerged arc welding is rarely published. The austenitic stainless steels possess about 45% more coefficient of thermal expansion, higher electrical resistance and lower thermal conductivity than mild steels. In this regard, special precautions should be exercised for minimizing the warpage, distortion and importantly undesirable metallurgical changes in the resultant joint as they are sensitive to heat input. The studies on austenitic stainless steel SS304 with double-sided welding were not found in the published literature. In this paper, double-sided submerged arc welding of 10-mm-thick plates was successfully fabricated, and microstructural and mechanical studies were conducted to evaluate the performance of the welded joint.

60.2 Materials and Experimental Procedure

The AISI SS304 austenitic stainless steel of 10-mm-thickness plates (200 × 100 × 10 mm) were submerged arc welded using 3.2-mm-diameter ADOR welding electrode (ER SS 308L), and OK 10.92L (Make: ESAB), a chromium-compensating flux, was used in this study. The weld samples were sectioned using wire electric discharge machine (WEDM) after which they were cleaned and degreased with acetone. As there is negligible heat input during cutting with EDM, the formation of prior HAZ is eliminated leading to good post-weld mechanical properties.

Prior to welding, the samples were tack welded using manual metal arc welding by ER308L electrode with a uniform root gap of 2.5 mm between the weld plates. The double-sided SAW samples were joined in square butt configuration. The schematic representation of submerged arc welding is shown in Fig. 60.1.

In this experiment, the same heat inputs were applied to the both sides of the weld plates. The heat input was calculated using the following formula

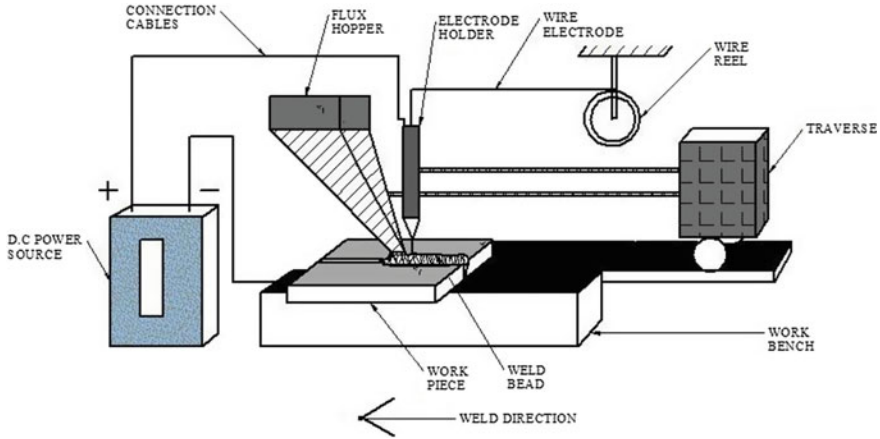


Fig. 60.1 Schematic representation of SAW welding machine

$$Q_w = \frac{\eta V I}{S}$$

where V is arc voltage, I is the welding current and S is welding speed, the arc efficiency (η) as 0.95 [6, 7] considered in this study.

The welds were made with constant current power source with positive terminal to the electrode and negative connected to workpiece. The welding current, voltage and speed used in the present study are 380A, 26 V and 6.66 mm/s, respectively. The heat input calculated using the above equation is found to be 1409.31 J/mm.

The samples for microstructural examination were ground using silicon carbide papers of grades 320, 600, 800, 1000, 1200, 1500 and 2000 grit size. These samples were then polished using 0.3 micron Al_2O_3 (Buehler, USA) on a velvet cloth. The mirror finish samples were then etched with Glyceregia (3 parts of glycerol, 2–5 parts of HCl and 1 part of HNO_3) to reveal the microstructure of the base metal, HAZ, fusion zone and interface zone. The etched samples are washed thoroughly and dried with a dryer. The microstructure at distinct locations in the sample of study was viewed and captured with an upright optical microscope (Make: Carl Zeiss) coupled with AxioVision image analysis software. The macrostructure is examined using Nikon SMZ25 Stereomicroscope. The Vickers microhardness of the welded sample is recorded with 0.5 kg load and a dwell time of 15 s. For measuring mechanical properties of the DSSAW sample, tensile test was conducted with INSTRON 8801. The cross-head speed of 1 mm/min is given, and an extensometer is fitted in the gage length to record the elongation. The scheme of sample extraction from the welded sample for microstructure, hardness and tensile test is shown in Fig. 60.2.

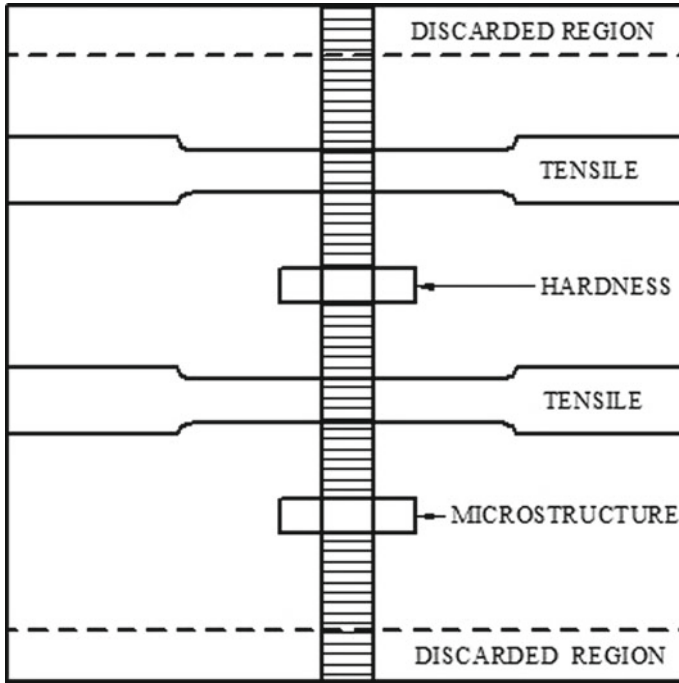


Fig. 60.2 Scheme of microstructure, hardness and tensile sample extraction from welded plate

60.3 Result and Discussions

60.3.1 Macrostructure and Microstructure

The square butt geometry without root gap and DSSAW joint configuration is shown in Fig. 60.3a, b. It is observed that both welds run, namely initial and second run,

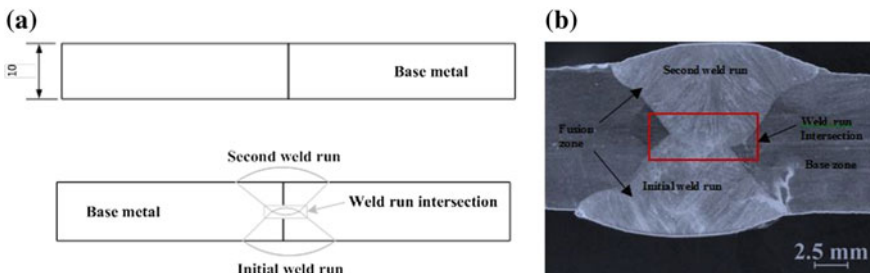


Fig. 60.3 a Square butt joint configuration without root gap. b Illustration of double-sided SAW method and c DSSAW macrostructure

intersect in the middle of the plate, hence creating a defect-free joint and is shown in Fig. 60.3c.

The microstructure of the parent metal and various regions of weld zone is shown in the below Fig. 60.4. The parent metal contains equiaxed grains with few twinings. The microstructure of the fusion zone comprises dendrites of delta ferrite in a matrix of austenite. The evolution of dendritic microstructure in the fusion zone is a result of directional solidification. The solidified portion of the weld consists of complex combination of austenitic–ferrite structure. This complex structure is a result of both material solidification behaviour and transformation which are directed by cooling rate of the material. The dark region corresponds to delta ferrite phase in the austenitic matrix. This delta ferrite transforms from vermicular to lath morphology as it approaches to the middle of the weld zone.

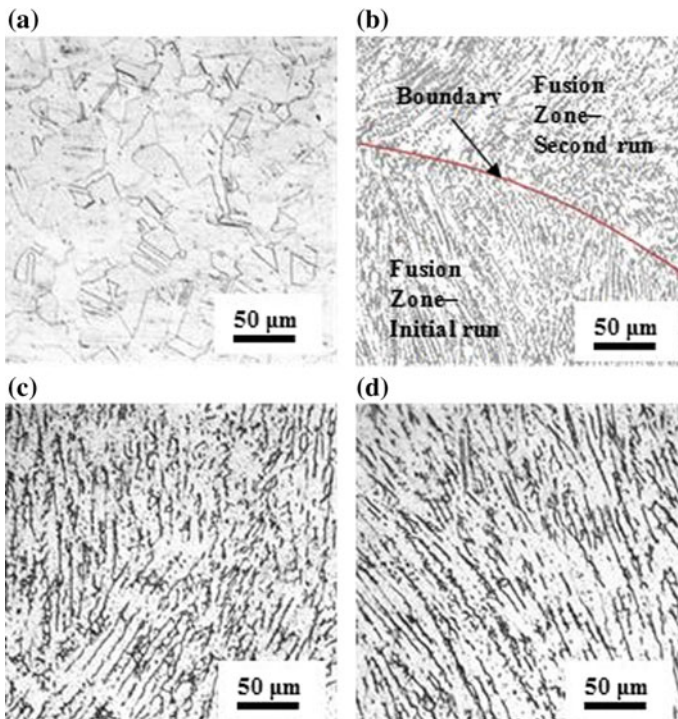


Fig. 60.4 Microstructure of **a** parent metal, **b** weld zone intersection initial run and second run, **c**, **d** dendritic structure of the weld zone

60.3.2 Microhardness

The microhardness is recorded 2 mm from the top and bottom weld bead and along the weld transverse centreline. The microhardness of the base material is the average of five measurements taken at an interval of 0.5 mm, and hardness was found to be ~214 HV. The Vickers hardness indentation in the weld zone is shown in Fig. 60.5.

The microhardness of the fusion zone was highest which ranges from 260 to 290 HV. The hardness of HAZ is higher than that of parent metal. The higher hardness was recorded in all zones on the second run compared to centre line and initial weld run. This could be due to the prior exposure of the metal to high temperature in the initial weld run.

The microhardness distribution in the (a) initial run, (b) weld intersection and (c) second run is shown in Fig. 60.6. The initial run recorded the more hardness ~272 HV, while the intersection region and second run are ~227 HV and ~252 HV, respectively. The transport of thermal energy in the welds depends on direction of application of heat. From Fig. 60.5, it observed that at the intersection region, grains appear to be skeletal dendritic and some segregation is noticed. Finally, the intersection portion of the weld gets remelted during second run leading to dissolution and reduction of other phases, thus less the hardness when compared to the second run weld.

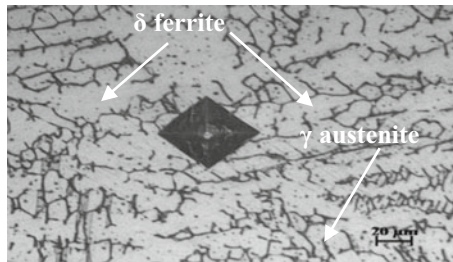


Fig. 60.5 Sample of hardness indentation in the weld zone

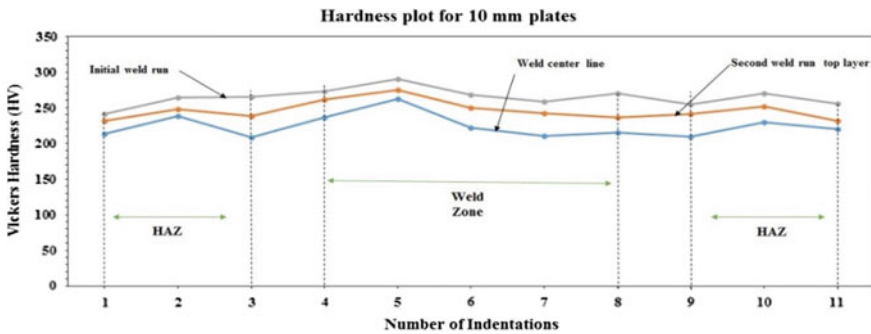


Fig. 60.6 Hardness plot representing three zones in DSSAW

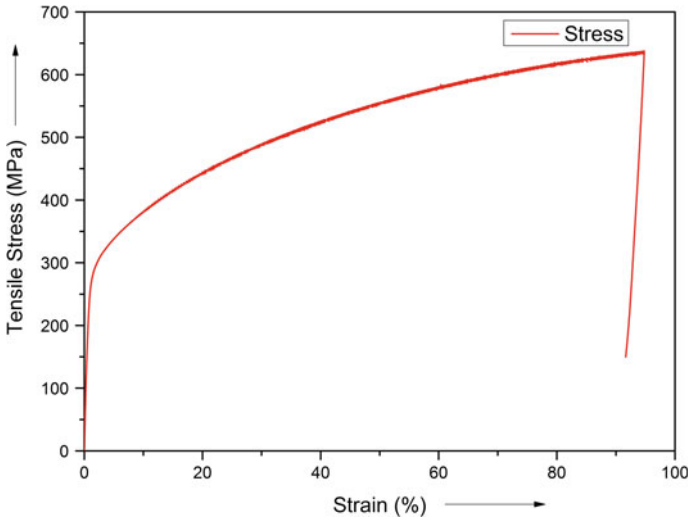


Fig. 60.7 Tensile curve for 304 austenitic steel joint welded by DSSAW

60.3.3 Tensile Test

The tensile test was conducted at ambient temperature, and the UTS of the tested samples was found to be 637.57 and 645.93 MPa, respectively. The average tensile strength of the welded sample was found to be 641.75 MPa. The tensile test curve for double-sided austenitic steel is shown in Fig. 60.7.

The fracture of the sample occurs much away from the weld zone and in the region of the base material. The failed region of the tensile sample is sectioned for study of mode of the fracture, and the sample is shown in Figs. 60.8 and 60.9. The examination of tensile sample reveals that it contains large cups, which was a result of plastic deformation that experienced by the material during testing. Also more is the depth of the dimples, more is the material has experienced plasticity.

It is also observed from fracture image Fig. 60.9 that large pull outs were experienced in some regions of the sample, which is a result of strong welding.

60.4 Conclusions

- The double-sided submerged arc welding was successfully conducted with both beads intersecting in the weld zone. No defects were observed in the macrostructure of the DSSAW.
- Apart from austenite and delta ferrite, there were no other phases found during metallurgical examination of welded samples.

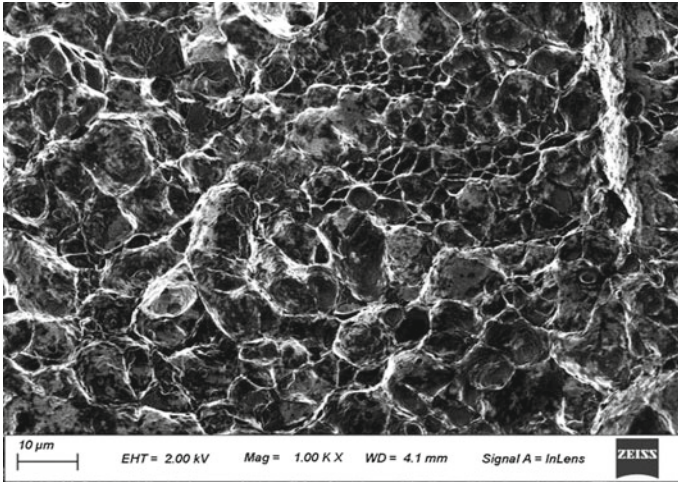


Fig. 60.8 Tensile fracture of 10-mm-thick DSSAW Sample

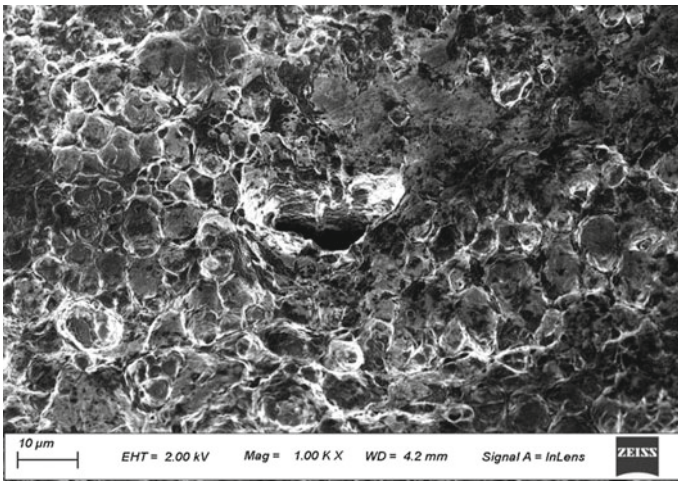


Fig. 60.9 Tensile fracture sample with large pull out

- The segregation of delta ferrite appears in the intersection zone and morphology of delta ferrite appears to shift from skeletal to lath morphology in some regions of weld zone microstructure. The orientation of the dendrites is also non-consistent in nature in the weld zone.
- It was observed that microhardness at the centre of intersection of weld zone is low when compared with other regions of weld zone.
- The average value of tensile strength is 641.75 MPa, and percentage of elongation was about 91%. The fracture occurred at the base zone of the tensile sample. The

fractured surfaces which exhibit cup appearance, which indicates the mode of fracture, is ductile in nature.

- The square butt geometry eliminates the cost of edge preparation and enhances the productivity of the process. This method can be successfully applied to join plates of thickness from 8 mm up to 20 mm.

References

1. Cary, H.B.: *Modern Welding Technology*. Prentice-Hall, Englewood Cliffs, NJ (1989)
2. ASM Handbook: *Welding Brazing and Soldering*, vol. 6, 9th edn. ASM International, Metals park, OH, USA (1983)
3. Davis, A.C.: *The Science and Practice of Welding*. vol. 1, 10th edn. Cambridge University Press (1992)
4. Mandal, N.R.: *Welding Techniques, Distortion Control and Line Heating*. Narosa Publishing House Pvt. Ltd. (2009)
5. Mahapatra, M.M., Datta, G.L., Pradhan, B, Mandal, N.R.: Modelling of angular distortion of double-pass butt-welded plate. *Proc. IMechE, Part B: J. Eng. Manuf.* **222**(3), pp 391–401 (2008). doi.org/<https://doi.org/10.1243/09544054jem995>
6. Shen, S., Oguocha, I.N.A., Yannacopoulos, S.: Effect of heat input on weld bead geometry of submerged arc welded ASTM A709 Grade 50 steel joints. *J. Mater. Process. Technol.* **212**(1), 286–294 (2012). <https://doi.org/10.1016/j.jmatprotec.2011.09.013>
7. Amanie, J., Oguocha, I.N.A., Yannacopoulos, S.: Effect of submerged arc welding parameters on microstructure of SA516 steel weld metal. *Can. Metall. Q.* **51**(1), 48–57 (2013). <https://doi.org/10.1179/000844311X13117643274794>
8. Luo, J., Yuan, Y., Wang, X., Yao, Z.: Double-sided single-pass submerged arc welding for 2205 duplex stainless steel. *J. Mater. Eng. Perform.* **22**(9), 2477–2486 (2013). <https://doi.org/10.1007/s11665-013-0529-8>
9. Luo, J., Dong, Y., Li, L., Wang, X.: Microstructure of 2205 duplex stainless steel joint in submerged arc welding by post weld heat treatment. *J. Manuf. Process.* **16**(1), 144–148 (2014). <https://doi.org/10.1016/j.jmapro.2013.06.013>

Chapter 61

A Study on Hardness of CRNO Electrical Sheets for Edge Joining Through TIG Welding



Bhushan Y. Dharmik and Nitin K. Lautre

Abstract Tungsten inert gas (TIG) welding is gaining popularity on welding of cold-rolled non-oriented (CRNO) electrical steel. The process deals with welding of stacks of thin sheets generally used as cores of electric vehicles and other electrical systems. Welding of thin sheets is affected by large amount of heat input. An investigation on the hardness of material post-welding is carried out. The hardness of the base metal, heat-affected zone, and fusion zone shows a different trend for an input current. The observed current setting at 60 A generated a minimum hardness on welded sheets from the selected range from 30 to 110 A. The output performance of the process is analyzed through various regression models with best-fit R^2 ranging from 0.9738 to 1. The hardness value can be used to estimate the variation in material property, mechanical plastic strain, and electrical losses post-welding.

Keywords Electrical steel · Hardness · CRNO · TIG · Thin sheets

61.1 Introduction

In the twenty-first century, the effective use of energy resources and environmental protection has been considered as one of the most important issues. The viewpoint of energy saving has led to the development of high-efficient electric motors. The other electrical equipments such as generators, transformers, ballasts, alternators, and refrigerators are also responsible for the major part of electric consumption. Accordingly, a lot of effort has been made toward increasing the efficiency of the electrical motors. The higher-efficient motors are expected to be developed for electric vehicles (EV) as the performance of electric storage cells and the efficiency of engine motors greatly influence energy efficiency and driving performance [1]. The efficiency of the motors can be largely improved by material properties (mechanical

B. Y. Dharmik · N. K. Lautre (✉)

Department of Mechanical Engineering, Visvesvaraya National Institute of Technology (VNIT), Nagpur 440010, India

e-mail: nfl_123@rediffmail.com

© Springer Nature Singapore Pte Ltd. 2020

M. S. Shunmugam and M. Kanthababu (eds.), *Advances in Additive Manufacturing and Joining*, Lecture Notes on Multidisciplinary Industrial Engineering,

https://doi.org/10.1007/978-981-32-9433-2_61

and electrical). One of such critical issues is the manufacturing of the core used in the motors.

A popular electrical steel material is used for manufacturing of cores used in electric motors and transformers. The electrical steel based on the orientation of the grains is either cold-rolled grain oriented (CRGO) or cold-rolled non-grain oriented (CRNGO, CRNO) [2]. The CRGO electrical steels are mainly used in cores of high-capacity transformers for power distribution and also in small transformers, whereas the CRNO electrical steels are used in making of cores of electric motors and also in small and medium current transformers, alternators, pump motors [2, 3].

The CRNO electrical steels are usually available in size of 0.5 mm thickness for cores of motors [4]. The thin steel sheets are stacked together and clamped in the hydraulic press at a pressure of approx. 50–60 kg/cm² and welded along the circumference by using TIG welding. One of the main reasons for the generation of the losses in the cores is the manufacturing process used in the joining of the core laminations [5]. A TIG welding process is commonly used for joining thin laminations of CRNO electrical steels [4].

TIG welding is an arc welding process carried out in argon environment using a tungsten electrode and is preferred for its easy operations and reduced cost [6]. However, it is also responsible for generation of large amount of thermal and residual stresses on the welded material [7, 8]. An interlocking factor is predicted to estimate the core losses due to interlink magnetic flux. The plastic strains are correlated to micro-Vickers hardness, which if increased increases the iron loss [7]. An investigation of variation in hardness distribution of electron beam welding (EBW) [8] and TIG was found influential in developing thermal and residual stresses. It leads in degradation of CRNO material properties in terms of grain orientation and grain degradation [9, 10].

The aim of present study is to obtain experimental data to understand the variation of micro-hardness in and around the weld. The work focuses on the effect of the TIG welding on the mechanical properties of CRNO through variation in the hardness post-TIG welding. The hardness of the electrical steels is one of the concerned issues as the drastic increase in the hardness level of CRNO can cause sudden failure of core of electric motors [7–10]. The reasons of the failure are buildup of plastic strain and development of cracks due to increase of hardness. The study also aims to develop relationship between micro-hardness and TIG input current for different regions and trends to hardness.

61.2 Experimentation

61.2.1 Material Selection

The mechanical properties such as hardness of the material, from an engineering and design point of view, is one of the important parameters in considering the nature of the material. The study involves the investigation on the influence of welding current

on the hardness levels of the material. The material used in the study is CRNO electrical steels 0.5 mm thick of M-45 grade. The cores of most of the electric motors are made of thin sheets of low-carbon steel. The material CRNO is easily available and manufactured than CRGO. The welding of thin CRNO is challenging due to striking of high thermal energy on thin sheets. The chemical composition of the material as per element (% mass fraction) for CRNO electrical steel (Grade-M45) is C(0.008), Si(2.54), Mn(0.22), P(0.0245), S(0.0075), Cr(0.0448), Ni(0.0205), Al(0.41), Fe(96.72). The compositions are estimated by using a SPECTROMAXx Metal Analyzer. It employs a tungsten filament as a heat source to heat the surface of the material for detecting the chemical composition. The argon gas (at a pressure 3 bar) is used as a primary gas during the chemical analysis.

The pilot runs on TIG welding are attempted on the coated CRNO samples without using filler material. However, this resulted in the generation of porosity and incomplete fusion on CRNO. To eliminate porosity on the material surface, filler SS308L was selected as it is commonly used for joining low-carbon plates. The composition of the material as per element (% mass fraction) for SS308L (Filler) is C(0.03), Si(0.45), Mn(1.5), P(0.02), S(0.03), Cr(20.5), Ni(10.5), Mo(0.45), Cu(0.70) as described by AWS 5.9 [10].

61.2.2 Parameter Selection

The TIG welding parameters are selected from the recommended specifications of the supplier EWAC alloys of Larsen & Toubro Limited. The model TIG Zuper 400i was used with available current range from 10 to 400 A, DC and 100% duty cycle. However, based on pilot experiments, it was observed that the welding of the CRNO electrical steel depends on variation of current ranging from 30 to 110 A. The current steps are fixed as 10 A for detail study of variation. The other constant parameters are shielding gas of argon as 10 L/min and weld speed as 2.5 mm/s. The TIG voltage variation was between 15 and 20 V, which was self-adjusting and fluctuating according to the current input.

61.2.3 Sample Preparation

The sample used in study consists of stacked CRNO sheets in a group of 15 per samples. The stack is further clamped by fixture and welded in the direction perpendicular to the edge of plate as shown in Fig. 61.1. The sheets are pressed by approx. 50–60 kg/cm² or at a pressure sufficient to eliminate any air gaps between the sheets. The CRNO plates of ± 7.5 mm (15 Nos. \times 0.5 mm thick) thickness after being welded are cut to obtain small samples mechanically for further study of hardness variation.

A total of 18 samples were prepared to analyze hardness in two replicates for accurateness of reading. The effect of different welding current ranging from 30 to

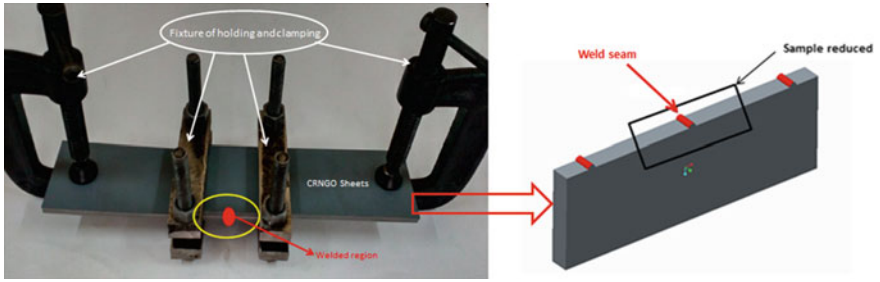


Fig. 61.1 Clamp and fixture for holding CRNO sheets

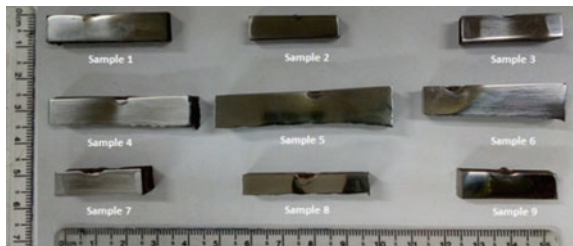
110 A, in step of 10 A, is implied in two different blocks. A sample set of one block of nine samples are shown in Fig. 61.2. The cut samples are polished by abrasive carbide papers of 80, 320, 600, 800, and 1000 grit size, for removing the material coating. The polished samples as shown in Fig. 61.3 are then observed under Mitutoyo, Japan make Vickers micro-hardness tester. The hardness measurement was performed at a load of 100 N for 10 s.

The samples are examined across the weld bead in two directions from the weld bead. The measurement was done at distance of ± 2.5 mm ($-1, +1$), ± 5 mm ($-2, +2$), and 7.5 mm ($-3, +3$) from the center of the weld bead as shown in Fig. 61.4. The measurement distances are selected to ensure that the Vickers hardness is measured in heat-affected zone (HAZ) as formed by the TIG current.

Fig. 61.2 Welded samples



Fig. 61.3 Polished welded samples



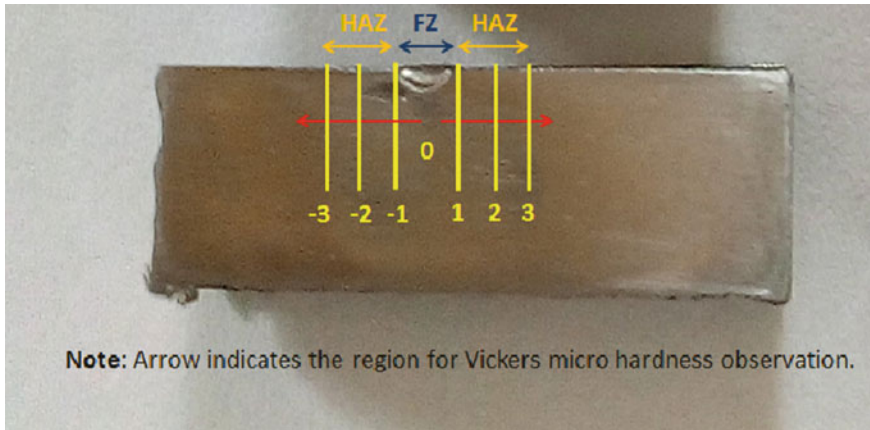


Fig. 61.4 Micro-hardness

61.3 Results and Discussion

The visual examination of samples as shown in Figs. 61.2, 61.3, and 61.4 reveals fusion zone (FZ) of about 4 mm and heat-affected zone (HAZ) around 16 mm. It is due to the fact that the input parameter selection is not significant in generating FZ and HAZ. In pilot experimentation, the HAZ on each side measures around 6 mm on which the Vickers micro-hardness is measured as shown in Table 61.1. The generalized specification of Vickers hardness at a current of 30 A is 251.75HV10.2/10, where 251.75 is average of hardness number of two blocks of reading, HV is hardness scale, 10.2 is constant applied load in Kgf, and 10 is loading time in seconds. The variation of hardness for all the variation of TIG current is shown in Fig. 61.5.

Table 61.1 Experimental observations of CRNO hardness in HAZ

(A)	At HAZ (2.5 mm)			At HAZ (5 mm)		
	H1	H2	(HV)	H1	H2	(HV)
30	251.2	252.3	251.75	243.5	245.8	244.65
40	253.5	252.5	253	245.6	243.6	244.6
50	255.6	253.4	254.5	247.8	245.6	246.7
60	254.3	251.3	252.8	239.2	240.2	239.7
70	257.3	255.2	256.25	246.3	244.9	245.6
80	253.2	260.3	256.75	242.3	245.2	243.75
90	253.2	255.5	254.35	245.3	245.1	245.2
100	253.6	255.3	254.45	241.3	242.9	242.1
110	260	257.3	258.65	242.9	243.9	243.4

(A) = Current, H1, H2 = Hardness, HV = Average hardness

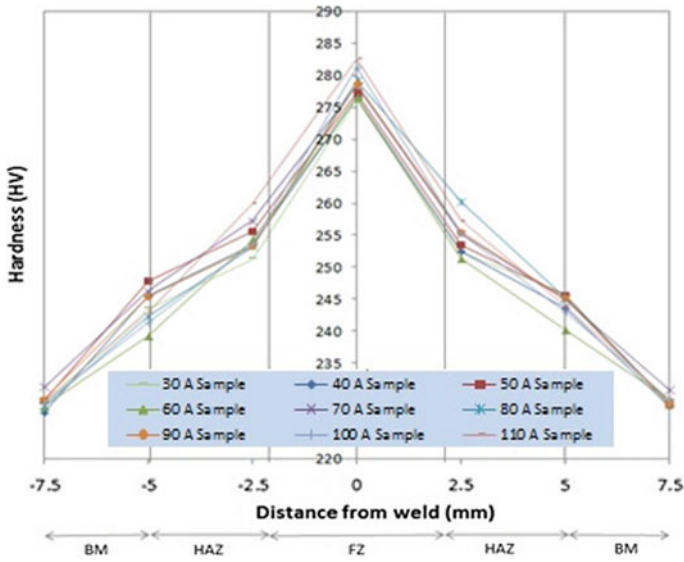


Fig. 61.5 Distribution of hardness over current variation

The maximum average hardness value of 282.5HV_{10.2/10} is recorded at the center of fusion zone at 110 A.

The base metal (BM) measured near to HAZ, 7.5 mm from center of FZ (-3, +3 as shown in Fig. 61.4), shows an average hardness value of 228.88 HV ± 0.914. The trend of hardness recorded near the HAZ, but favorably in BM is shown in Fig. 61.6. The average hardness value in the HAZ is 249.34 HV ± 5.90. The increase in hardness

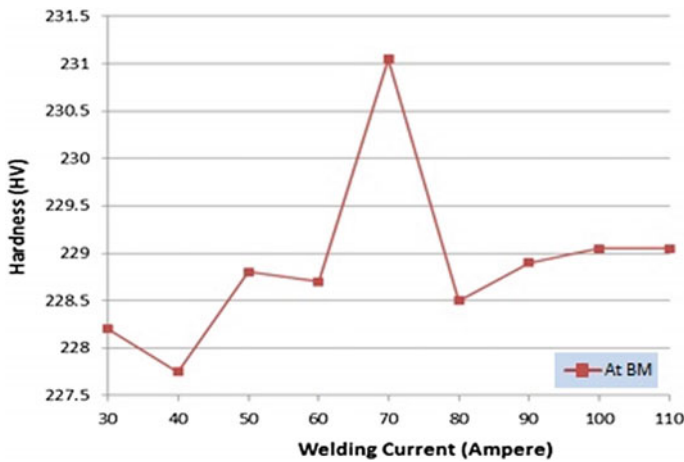


Fig. 61.6 Trend for hardness at base metal

of 20.46 HV over BM is observed for HAZ. The material at BM is the less affected from the heat input due to welding, and no such variation from the data at BM of the samples is observed. The variation in hardness value ranging from 227.75 to 231 HV is observed at BM zone. The maximum HV recorded as 231.05 HV at 70 A shows the influence of diffusion of heat outside the considered range of HAZ on the basis of pilot experiments. However, the maximum BM hardness (231.05 HV at 70 A) is found to be less than the minimum hardness 239.7 HV recorded at 60 A, 5 mm distance in HAZ. It may be due to the more conductive heat transfer in BM at input of 70 A.

The HAZ of the samples shows a continuous but less variation in the micro-hardness values starting from 252 HV (for 30 A) to 258 HV (for 110 A) as shown in Fig. 61.7. A drop in hardness value as observed close to FZ at 60 and 90 A. The hardness value away from FZ shows a cyclic trend in hardness value which is observed from 40 to 60 A, 60 to 80 A, and 80 to 100 A with peak at 50, 70, and 90 A, respectively. The lowest hardness as recorded at 60 A in HAZ is 239.7 HV, away from FZ and 252.8 HV, near to FZ. The regression model for HAZ region and near to FZ is $HV = 0.0013 A^2 + 0.0375 A + 249.5$, $HV = -0.0148 A^2 + 2.262 A + 170.15$, and $HV = 0.0205 A^2 - 3.885 A + 37.95$, for 30–50 A, 60–80 A, and 90–110 A, respectively. The model for HAZ region away from FZ is $HV = -0.0455 A^2 + 4.305 A + 145.2$, $HV = -0.0388 A^2 + 5.627 A + 41.55$, and $HV = -0.0227 A^2 + 4.0125 A + 68.35$, for 40–60 A to 80–100 A, respectively.

The trend of hardness in fusion zone is generally increasing from 276.1 to 282.5 HV, with the increase in current value from 30 to 110 A. This reveals that with the increase in heat input of the material the hardness also increases. However, after 50 and 80 A the hardness value drops. The best-fit regression model for 30–50 A was $HV = 0.02 A^2 - 0.1 A + 277.3$, which shows an increasing trend. The other trend shows a decreasing trend as $HV = -0.005 A^2 + 0.83 A + 244.8$ for 60–80 A and $HV = -0.006 A^2 + 1.39 A + 202.2$ for 90–110 A.

A hardness value in FZ is maximum for all the current values. The percentage variation in hardness is estimated from these maximum hardness values of FZ for

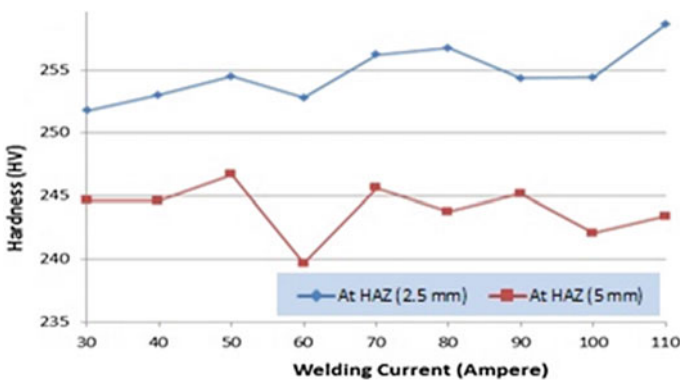


Fig. 61.7 Trend for hardness at HAZ

analyzing and comparing the relative hardness in different region of the specimen. The trend observed in fusion zone is increasing if analyzed in a set of three current values starting from 30–60–90 A, 40–70–100 A, and 50–80–110 A as shown in Figs. 61.8, 61.9, and 61.10, respectively.

The maximum hardness value of 278.7 HV is used to compare other HV in a set of 30–60–90 A as shown in Fig. 61.8. The percentage variation in the hardness shows a significant variation from the fusion zone (FZ) to the base metal (BM). The percentage degradation of 8% is observed in FZ with mostly linear trend for all values of current in HAZ from FZ. The degradation (10%) is nonlinear and different at different values of current. The model for one side of FZ for 30 A is $\%HV = 0.0009 \text{ mm}^2 - 0.02 \text{ mm} + 0.994$ ($R^2 = 97.47\%$). The model for 60 A is $\%HV = 0.0021 \text{ mm}^2 - 0.0377 \text{ mm} - 0.997$ ($R^2 = 99.2\%$) and for 90 A is $\%HV = 0.0009 \text{ mm}^2 - 0.03 \text{ mm} + 0.996$ ($R^2 = 98.64\%$).

The maximum hardness value is 281.2 HV at 100 A in a set of 40–70–100 A as shown in Fig. 61.9. The 100% (281.2 HV) is used as reference to compare the variation at other setting. Not much variation was observed in terms of degradation of hardness as noticed with 30–60–90 A combination. A significant variation of hardness is noticed when compared with 282.5 HV of 110 A in a set of 50–80–110 A as shown in Fig. 61.10. The degradation of hardness in FZ is similar for 50 and 110 A. The hardness variation at 80 A is not matching with other in any region of FZ, HAZ, and BM. The current parameters 50–80–110 A are influential parameters for the variation in hardness. The regression models for degradation of HV are different for the set of current value. The model at 50 A for one side is $\%HV = 0.001 \text{ mm}^2 - 0.029 \text{ mm} + 0.994$ ($R^2 = 97.38\%$). The model for 80 A is $\%HV = 0.0003 \text{ mm}^2 - 0.0264 \text{ mm} + 0.99$ ($R^2 = 100\%$) and for 110 A is $\%HV = 0.0015 \text{ mm}^2 - 0.035 \text{ mm} + 0.997$ ($R^2 = 99.44\%$).

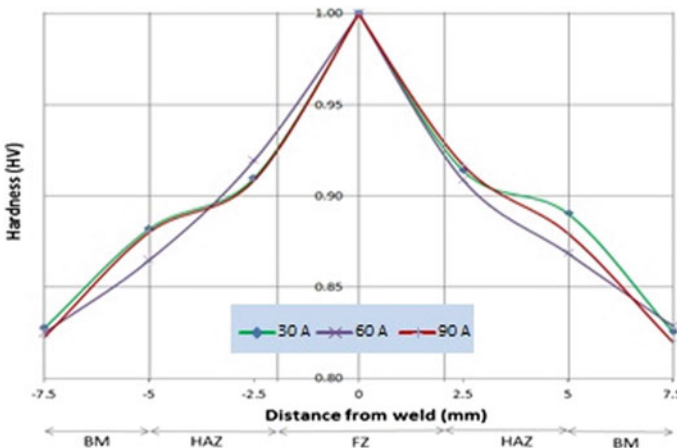


Fig. 61.8 Percentage variation in hardness weld zone for 30, 60, and 90 A

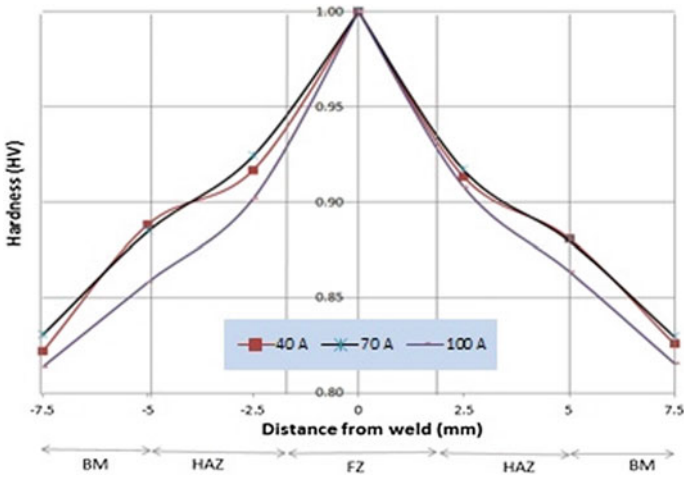


Fig. 61.9 Percentage variation in hardness with weld zone for 40, 70, and 100 A

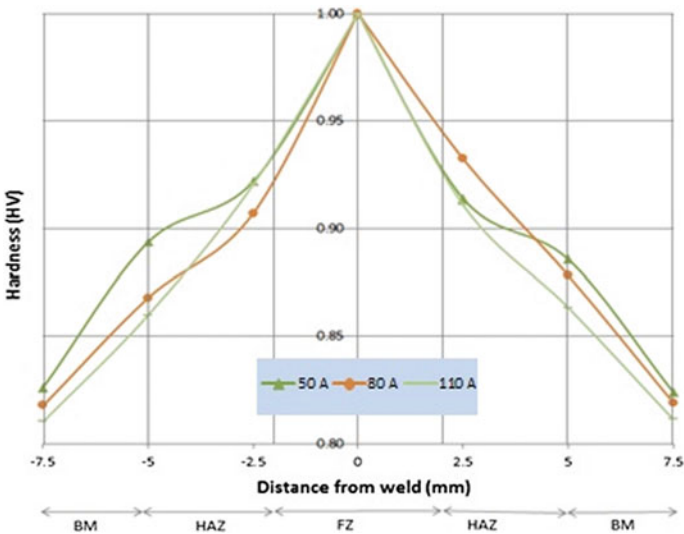


Fig. 61.10 Percentage variation in hardness with weld zone for 50, 80, and 110 A

61.4 Conclusions

The study involving TIG welding of CRNO electrical steel sample shows a significant increase in the micro-hardness values from the welded zone to the base material. The average hardness variation was from 228.88 ± 0.914 HV at BM, 249.34 ± 5.9 HV at HAZ to 278.5 ± 2.19 HV in FZ. However, the variation has shown different trends

in FZ, HAZ, and BM. The best regression models are developed for all possible variation of current and trends observed in FZ, HAZ, and BM. The model helps in predicting the hardness value at suitable current value ranging from 30 to 110 A. The issue of sudden cracks on the material surface and accumulation of plastic strain can be avoided by controlling the hardness. The regression model developed is helpful in predicting and adjusting the hardness value at different setting of current values. The hardness of the CRNO sheets has a significant role in the variation in mechanical behavior of the material.

References

1. Lei, G., Zhu, J., Guo, Y., Liu, C., Ma, B.: A review of design optimization methods for electrical machines. *Energies* **10**(12), 1962 (2017)
2. Mahajan, V.V., Gore, P.P.N.: Role of insulation coating in electrical steels and their final applications. *Int. Res. J. Eng. Technol.* **4**(4), 1248–1251 (2017)
3. Lindenmo, M., Coombs, A., Snell, D.: Advantages, properties and types of coatings on non-oriented electrical steels. *J. Magn. Magn. Mater.* **215**, 79–82 (2000)
4. Kurosaki, Y., Mogi, H., Fujii, H., Kubota, T., Shiozaki, M.: Importance of punching and workability in non-oriented electrical steel sheets. *J. Magn. Magn. Mater.* **320**(20), 2474–2480 (2008)
5. Kraemer, A., Veigel, M., Pontner, P., Doppelbauer, M., Lanza, G.: Influences of separation and joining processes on single tooth laminated stacks. In: *Proceedings of International Electrical Drives Production Conference, Germany*, pp. 178–185 (2016)
6. Senda, K., Toda, H., Masaki Kawano, M.: Influence of interlocking on core magnetic properties. *IEEE J. Ind. Appl.* **4**(4), 496–502 (2014). <https://doi.org/10.1541/ieejia.4.496>
7. Vourna, P.: Characterization of electron beam welded non-oriented electrical steel with magnetic Barkhausen noise. *Key Eng. Mater.* **605**, 39–42 (2014). <https://doi.org/10.4028/www.scientific.net/KEM.605.39>
8. Lamprecht, E., Homme, M., Albrecht, T.: Investigations of eddy current losses in laminated cores due to the impact of various stacking processes In: *Proceedings of International Electrical Drives Production Conference, Germany*, pp. 1–8 (2012)
9. Zhang, Y., Wang, H., Chen, K., Li, S.: Comparison of laser and TIG welding of laminated electrical steels. *J. Mater. Process. Technol.* **247**, 55–63 (2017). <https://doi.org/10.1016/j.jmatprotec.2017.04.010>
10. <https://www.aircraftmaterials.com/data/weld/er3081.html>

Chapter 62

Friction Stir Welding for Joining of Dissimilar Materials



Suryakanta Sahu, Omkar Mypati, Soumya Sangita Nayak, Pooja Sarkar, Surjya Kanta Pal and Shiv Brat Singh

Abstract In the present work, friction stir welding (FSW) of aluminum (AA 6061-T6) to austenitic stainless steel (AISI 304) has been performed. A tungsten carbide tool with a tapered cylindrical pin has been used. The tool rotational speed (ω) and welding speed (v) are found to be the most influential factors in the welding process. To understand the influence of ω and v , tensile strength, optical micrographs, SEM, and XRD analyses have been performed. A maximum joint strength of 7.6 kN in terms of tensile load of the base aluminum alloy has been found out at 1600 rpm and 100 mm/min.

Keywords Friction stir welding · Dissimilar joints · Joint strength · IMCs

62.1 Introduction

The global laws toward the control of environmental carbon content and saving of energy are effectively imposing the transport industries to use hybrid or multi-material structures in component manufacturing. To fulfill the demand, it is essential to choose a combination of materials that cannot only reduce the weight of the component but also provide adequate strength during crashing circumstances. From these considerations, aluminum (Al) alloys and steel proved themselves to be the best choices in the transport industries because of their combined specific light weightiness and cost-effectiveness. Al alloys provide low density, high strength, and good

S. Sahu (✉) · S. S. Nayak · P. Sarkar
Advanced Technology Development Centre, Indian Institute of Technology Kharagpur,
Kharagpur 721302, India
e-mail: suryakanta@iitkgp.ac.in

O. Mypati · S. K. Pal
Department of Mechanical Engineering, Indian Institute of Technology Kharagpur, Kharagpur
721302, India

S. B. Singh
Department of Metallurgical and Materials Engineering, Indian Institute of Technology
Kharagpur, Kharagpur 721302, India

© Springer Nature Singapore Pte Ltd. 2020
M. S. Shunmugam and M. Kanthababu (eds.), *Advances in Additive Manufacturing and Joining*, Lecture Notes on Multidisciplinary Industrial Engineering,
https://doi.org/10.1007/978-981-32-9433-2_62

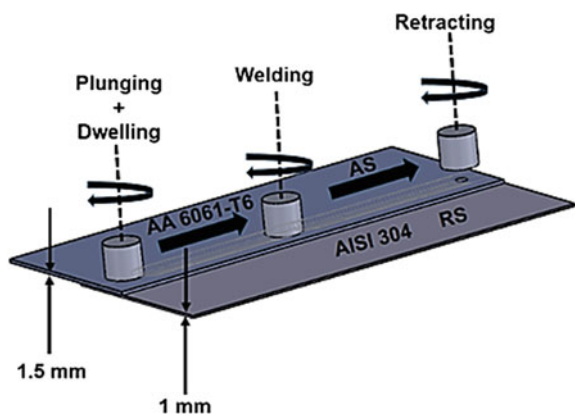
formability while steel contributes to strength and stiffness to the components. Hence, to acquire the advantages of both the materials, reliable and cost-effective dissimilar joining technique is necessary [1].

Joining of Al to steel is difficult due to the significant difference in their physical and mechanical properties. Different joining techniques like ultrasonic welding [2], friction welding [3], and laser welding [4, 5] have been employed to join them. While friction welding is limited to joint configuration, ultrasonic and laser welding are limited to joining of thin sheets. The problems associated with these techniques are formation of porosity, hot cracks, oxidation, hydrogen solubility, and distortion. Other complications such as formation of Al-rich intermetallic compounds (IMC) (FeAl_2 , FeAl_3 , and FeAl_5) exist which lowers the joint strength. Various hybrid welding methods have been developed in this regard [6–8]. These techniques produce sound joint yet are not cost-effective. Thus, achieving a weld with considerable strength at a low cost is a challenging task.

Friction stir welding (FSW), a solid-state joining process was patented by The Welding Institute (TWI), UK in 1991 [9]. It comprises of four stages namely plunging, dwelling, welding, and retracting as depicted in Fig. 62.1. FSW was developed to join low melting point materials like Al and magnesium (Mg). However, with time FSW is capable of joining high-temperature melting point materials like steel, titanium, copper, etc. [10]. The process variables responsible for controlling FSW are tool rotational speed (ω), tool traverse speed (v), tool tilt angle (α), plunge depth (pd), and tool profiles. Among them, ω and v are the most crucial parameters that significantly affect the joint quality. Usually, higher ω produces higher heat input, whereas higher v reduces heat input by shortening the contact time between tool and workpiece.

The studies illustrating the effect of process parameters on joint properties in FSW have been reported in [11–15]. Welds with good metallurgical bonding and mechanical mixing have been obtained with high ω and low v . It is seen that ω has a significant effect than v on the formation of IMCs. Though IMC formation is necessary for improving weld strength, presence of brittle and thick IMC layers formed by higher ω has a detrimental effect on joint strength. Further, the volume

Fig. 62.1 Different stages of FSW in lap configuration



of defects reduced and strength increased with decreasing v due to the formation of Fe-rich IMCs.

From the literature, it can be concluded that research on joining of thin sheets in lap configuration by using FSW is scarce, and the present work addresses the same.

62.2 Experimental and Characterization Details

The base materials used along with their chemical composition are mentioned in Tables 62.1 and 62.2, respectively. A tapered cylindrical (TC) pin made of tungsten carbide with a shoulder diameter of 16 mm was used for welding. The top and bottom diameters of the pin were 5 and 4 mm, respectively. Experiments were conducted in a three-axis NC FSW machine (ETA, WS004). The complete experimental setup along with data acquisition (DAQ) card and location of thermocouples during the welding process are shown schematically in Fig. 62.2. All the welds have been fabricated in lap configuration, placing Al sheets above the steel sheets. The optimum process parameters considered during the experiments are mentioned in Table 62.3.

For determining the tensile strength of the base materials and weld joints, tensile test specimens were prepared in rectangular shape [16]. All specimens were tested in a 50 kN SHIMADZU AG-5000G Universal Testing Machine. Tensile failure samples were investigated by SEM to perform the fracture surface analysis. The specimens for microstructural investigations were prepared as per ASTM E3-11 [17]. The microstructure of weld cross sections was captured with Leica optical microscope. The IMC thickness at the joint interface was observed with an analytical SEM (A-SEM, ZEISS). For identifying the phases of IMCs, X-ray diffraction (XRD) test (X-pert software) was performed employing a target of Cr K α at a voltage of 30 kV and a current of 55 mA in the scanning range of $20^\circ \leq 2\theta \leq 160^\circ$ with PANalytical X-ray diffractometer.

62.3 Result and Discussion

62.3.1 Temperature Variations

The temperature history was noted for dissimilar thickness welds. For lap welds, a significant portion of the shoulder remains in contact with material on top (Al here), thus the majority of frictional heat is generated in Al only. The consequence of ω on temperature distribution at a constant v of 100 mm/min has been shown in Fig. 62.3a. It can be seen that an increase in ω increases the temperature due to rising friction between the tool and the workpiece. The influence of v can also be realized in Fig. 62.3b. The decline in temperature occurs with increasing v due to

Table 62.1 Chemical composition of AA6061-T6 (wt%)

Elements	Mn	Fe	Mg	Si	Cu	Zn	Ti	Cr	Al
AA 6061-T6	0.042	0.428	1.125	1.172	0.326	0.084	0.015	0.294	90.545

Table 62.2 Chemical composition of AISI 304 (wt%)

Elements	Mn	Fe	P	Si	Cu	Zn	Ni	Cr	C
AISI 304	1.382	69.807	0.03	0.323	0.384	0.288	7.863	18.168	<0.08

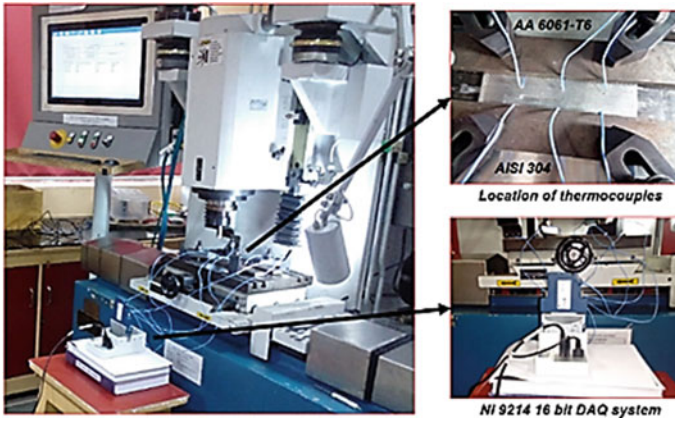


Fig. 62.2 Experimental details

Table 62.3 Optimum process parameters

ω (rpm)	v (mm/min)	α (°)	pd (mm)	Tool configuration
800	50	2	0.2	Tapered cylindrical (TC) pin
	100			
	200			
1600	50			
	100			
	200			
2400	50			
	100			
	200			

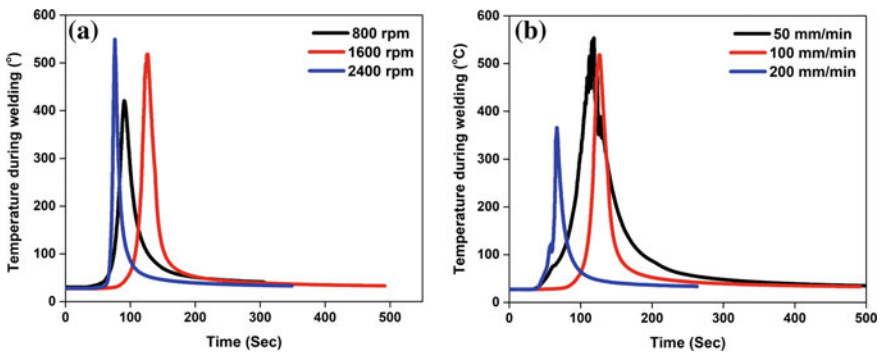


Fig. 62.3 Temperature profiles at a constant v of 100 mm/min and b constant ω of 1600 rpm

loss in contact time. Hence, the time for conduction of heat to the parent part of Al is higher resulting in lower temperature.

62.3.2 Force and Torque Variations

The variation of average axial Z-load during the welding with different parameters can be viewed in Fig. 62.4. From the figure, it can be understood that with increasing ω , the Z-load is decreasing, which is due to the increase in the generation of frictional heat. This consequently softens the materials and reduces the Z-load. However, with v , it can be observed that as it increases, there is increase in Z-load. This is due to decrease in time for stirring phenomenon and frictional heat availability. This results in the reduction of the viscoplastic state of the weld material promoting increase in Z-load.

Spindle torque exhibits an important characteristic of FSW machine by indicating the power consumption during the process. The change in torque with different parameters is represented in Fig. 62.5a–c. It can be observed that the spindle torque increases during plunging and then rises to a maximum value during impingement of

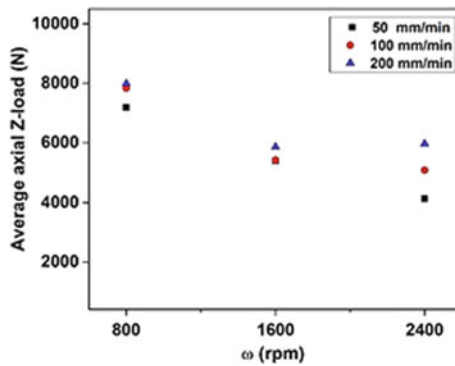


Fig. 62.4 Average axial Z-load variation with different ω and v

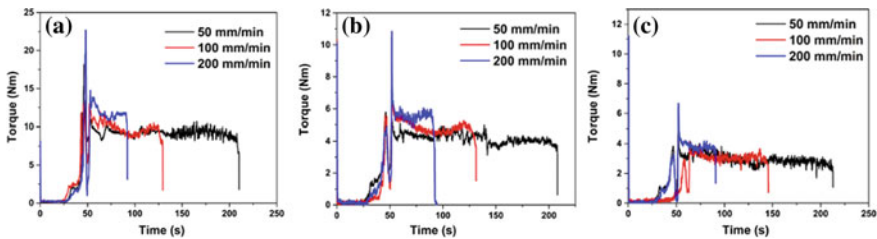


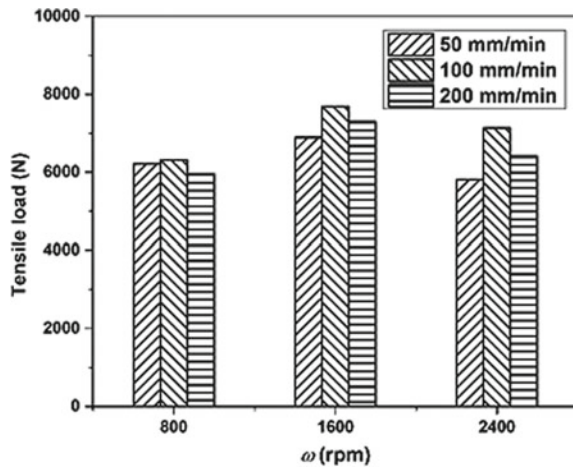
Fig. 62.5 Variation of torque for: **a** $\omega = 800$ rpm, **b** $\omega = 1600$ rpm, and **c** $\omega = 2400$ rpm

the shoulder, drops in dwelling phase, and reaches a constant value during welding. It can also be witnessed that the spindle torque reduces with increasing ω due to ease in the flow of material with high-temperature generation. In contrast to this, with an increase in v , the torque also increases because of the decrease in frictional heat thereby minimizing the rise in temperature. Due to this, workpiece resistance increases and hence torque increases.

62.3.3 Tensile Strength and Fractography

The tensile strength was studied in terms of tensile load. Figure 62.6 shows the variation of the tensile load for different parametric conditions. At 1600 rpm and 100 mm/min, a maximum tensile load of 7.6 kN has been achieved. Fracture of the tensile specimens occurred in between stir zone (SZ) and advancing side (AS) and only a few samples failed due to shear. Further, with an increase in ω and decrease in v , the joint strength was found to be decreasing. The possible reason for this is the softening of materials in the weld zone due to high heat input. The high heat input results in faster diffusion of atoms leading to the formation of coarser grains populating the dislocations to move faster. IMC sizes also altered the joint strength in FSW process. It has also been observed that at 1600 rpm and 100 mm/min, the IMC thickness is minimum. Figure 62.7 shows the SEM of the fracture surface. It can be reasoned that the fracture was of ductile nature that was caused due to the presence of voids.

Fig. 62.6 Tensile load for dissimilar thickness



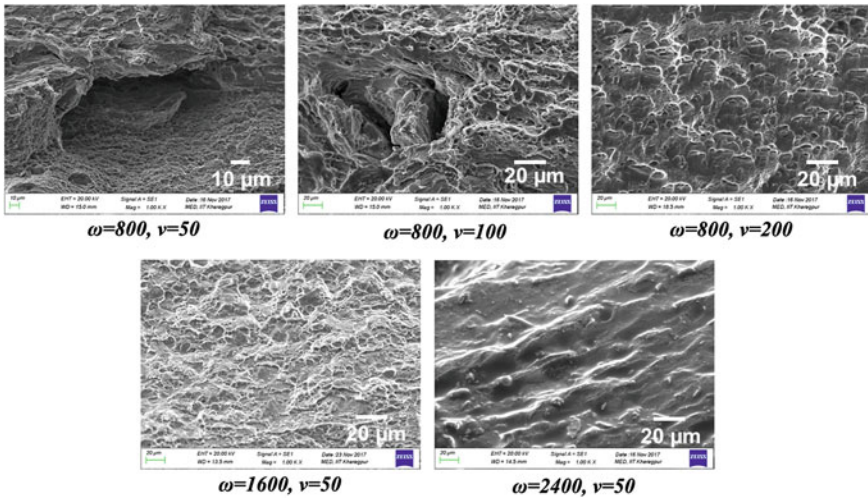
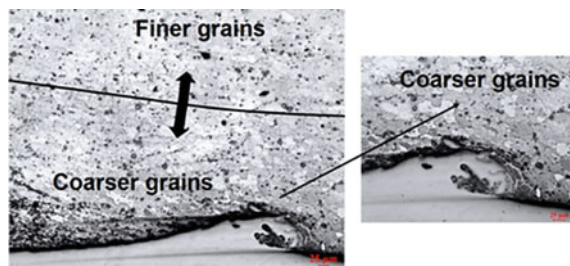


Fig. 62.7 Fractured surface morphology

62.3.4 Microstructure Analysis

The evolution of microstructure in the interface of SZ depends on the recrystallization temperature and the cooling rate of the welding region. The SZ of welded plates were cooled by surrounding air. The microstructures at the interface, for all the weld conditions, revealed that coarser grains were formed neighboring to the interface of the weld because of the slow rate of cooling. Unlike the interface region, the weld materials beneath the tool shoulder were subjected to higher heating and mechanical deformations which led to the formation of finer grains, as shown in Fig. 62.8. At low ν of 50 mm/min, the microstructure shows a deformed and coarser grain size. This is due to the additional heat input which leads to severe plastic deformation of the metals beneath the shoulder. At 100 mm/min also, the microstructure shows deformed, and coarse grains but the deformation and size are less than that observed with 50 mm/min. Thus, ν controls the frictional heat input per unit length during the welding, which further controls the grain size during the FSW process.

Fig. 62.8 Optical image of welded cross section for $\omega = 1600$ rpm and $\nu = 100$ mm/min



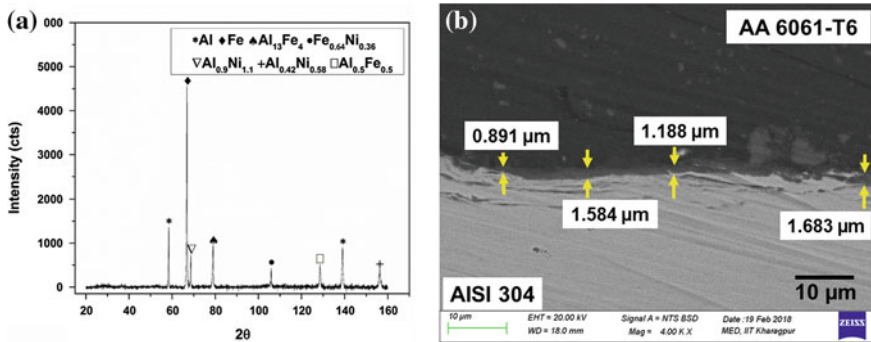


Fig. 62.9 a XRD plot and b measured IMC thickness for $\omega = 1600$ rpm and $v = 100$ mm/min

62.3.5 IMCs and Their Thickness

From XRD results, IMCs like $\text{Al}_{13}\text{Fe}_4$, AlFe , FeAl_3 , Al_5Fe_2 , Fe_2Si , $\text{Al}_{0.4}\text{Fe}_{0.6}$, $\text{Al}_{0.5}\text{Fe}_{0.5}$, $\text{Al}_{0.42}\text{Fe}_{0.58}$, FeNi , $\text{Fe}_{0.64}\text{Ni}_{0.36}$, FeSi , $\text{Al}_{0.42}\text{Ni}_{0.58}$, Mg_2Si , $\text{Al}_{1.1}\text{Ni}_{0.9}$, and $\text{Al}_{0.9}\text{Ni}_{1.1}$ were observed. While Al-rich IMCs like $\text{Al}_{13}\text{Fe}_4$, FeAl_3 , and Al_5Fe_2 decreased the joint strength, AlFe , AlFe_3 , $\text{Al}_{0.4}\text{Fe}_{0.6}$, $\text{Al}_{0.5}\text{Fe}_{0.5}$, $\text{Al}_{0.42}\text{Fe}_{0.58}$, and FeNi increased it due to high composition of Fe. The plot with respect to ω of 1600 rpm and v of 100 mm/min is shown in Fig. 62.9a, b shows the IMC thickness variations measured with Digimizer software for $\omega = 1600$ rpm and $v = 100$ mm/min, which is found to be within 1–2 μm . With the increase in ω from 800 to 1600 rpm and increase in v from 50 to 100 mm/min, the IMC thickness decreased, and it increased significantly with the increase in ω from 1600 to 2400 rpm. The least thickness was observed at $\omega = 1600$ rpm and $v = 100$ mm/min.

62.4 Conclusions

In this study, FSW has been used to join AA6061-T6 and AISI 304 in lap configuration. High frictional heat is generated at higher ω , which results in decreasing Z-load, due to the high plasticization of material. The optimum parametric combination obtained from the present study is $\omega = 1600$ rpm and $v = 100$ mm/min with a tensile load of 7.6 kN. Fe-rich IMCs like $\text{Al}_{0.5}\text{Fe}_{0.5}$ and $\text{Fe}_{0.64}\text{Ni}_{0.36}$ with average thickness of 1.33 μm were observed at this combination.

Acknowledgements This work has been supported by Department of Science and Technology (DST), Science and Engineering Research Board (SERB), New Delhi with sanction number: **EMR/2015/001588**. The authors would like to extend their gratefulness toward Dr. Debalay Chakrabarti, Associate Professor, Department of Metallurgical and Materials Engineering for extending tensile testing facility.

References

1. Liu, X., Lan, S., Ni, J.: Analysis of process parameters effects on friction stir welding of dissimilar aluminum alloy to advanced high strength steel. *Mater. Des.* **59**, 50–62 (2014)
2. Watanabe, T., Sakuyama, H., Yanagisawa, A.: Ultrasonic welding between mild steel sheet and Al–Mg alloy sheet. *J. Mater. Process. Technol.* **209**, 5475–5480 (2009)
3. Taban, E., Gould, J.E., Lippold, J.C.: Dissimilar friction welding of 6061-T6 aluminum and AISI 1018 steel: properties and microstructural characterization. *Mater. Des.* **31**(5), 2305–2311 (2010)
4. Torkamany, M.J., Tahamtan, S., Sabbaghzadeh, J.: Dissimilar welding of carbon steel to 5754 aluminum alloy by Nd:YAG pulsed laser. *Mater. Des.* **31**(1), 458–465 (2010)
5. Tricarico, L., Spina, R.: Experimental investigation of laser beam welding of explosion-welded steel/aluminum structural transition joints. *Mater. Des.* **31**(4), 1981–1992 (2010)
6. Qin, G., Su, Y., Wang, S.: Microstructures and properties of welded joint of aluminum alloy to galvanized steel by Nd:YAG laser + MIG arc hybrid brazing-fusion welding. *Trans. Nonferrous Met. Soc. China* **24**, 989–995 (2014)
7. Gao, M., Chen, C., Mei, S., Wang, L., Zeng, X.: Parameter optimization and mechanism of laser-arc hybrid welding of dissimilar Al alloy and stainless steel. *Int. J. Adv. Manuf. Technol.* **74**(1–4), 199–208 (2014)
8. Chang, W.S., Rajesh, S.R., Chun, C.K., Kim, H.J.: Microstructure and mechanical properties of hybrid laser-friction stir welding between AA6061-T6 Al alloy and AZ31Mg alloy. *J. Mater. Sci. Technol.* **27**(3), 199–204 (2011)
9. Thomas, W., Nicholas, E., Needham, M., Temple-Smith, P., Dawes, C.: Friction stir butt welding. GB Patent No. 9125978.8, International Patent Application No. PCT/GB92/02203 (1991)
10. Thomas, W., Nicholas, E., Needham, M., Temple-Smith, P., Dawes, C.: Friction stir welding for the transportation industries. *Mater. Des.* **18**, 269–273 (1997)
11. Pourali, M., Abdollah-zadeh, A., Saeid, T., Kargar, F.: Influence of welding parameters on intermetallic compounds formation in dissimilar steel/aluminum friction stir welds. *J. Alloys Compd.* **715**, 1–8 (2017)
12. Movahedi, M., Kokabi, A.H., Reihani, S.M.S., Najafi, H.: Effect of tool travel and rotation speeds on weld zone defects and joint strength of aluminium steel lap joints made by friction stir welding. *Sci. Technol. Weld. Join.* **17**(2), 162–167 (2012)
13. Mahto, R.P., Bhoje, R., Pal, S.K., Joshi, H.S., Das, S.: A study on mechanical properties in friction stir lap welding of AA 6061-T6 and AISI 304. *Mater. Sci. Eng., A* **652**, 136–144 (2016)
14. Mahto, R.P., Kumar, R., Pal, S.K., Panda, S.K.: A comprehensive study on force, temperature, mechanical properties and micro-structural characterizations in friction stir lap welding of dissimilar materials (AA6061-T6 & AISI304). *J. Manuf. Process.* **31**, 624–639 (2018)
15. Mahto, R.P., Pal, S.K.: Friction stir lap welding of thin AA6061-T6 and AISI304 sheets at different values of pin penetrations. In: Vol. 2: Materials. Joint MSEC-NAMRC-Manufacturing USA, p. V002T04A041 (2018)
16. Rao, H.M., Jordon, J.B., Yuan, W., Ghaffari, B., Su, X., Khosrovaneh, A.K., Lee, Y.L.: Fatigue behavior of friction stir linear welded dissimilar aluminum-to-magnesium alloys. *Frict. Stir Weld. Process.* VIII **82**, 145–152 (2016)
17. ASTM International: ASTM E3-11. Standard guide for preparation of metallographic specimens. *Am. Soc. Test. Mater.* **11**(Reapproved 2017), 1–17 (2001)

Chapter 63

Effect of Process Parameters on Quality Characteristics of Al/Cu Dissimilar Friction Stir Welding Joint



A. Mandal, J. D. Barma and A. Bandyopadhyay

Abstract Friction stir welding (FSW) is a useful technique to join dissimilar materials. The aim of present study is to find the effect of process parameters on the mechanical properties and metallurgical properties of joining of aluminium and copper dissimilar metals using FSW. The friction stir welding of aluminium and copper have been conducted by varying the tool traverse speed and the tool rotational speed. The result of tensile strength as an output parameter has been included in this study for the above input process parameters range.

Keywords FSW · IMCs · Aluminium alloy · Commercially pure copper · Microstructure · Tool traverse speed · Tool rotational speed

63.1 Introduction

Copper is the most suitable material for manufacturing electric switch, electrical equipment and cable, etc. as it has good electrical and thermal conductivity. But electric industries bear the huge cost for the shortage of copper and high price of copper. Aluminium and aluminium alloy have excellent electrical, mechanical, thermal properties like copper and also have properties of low density and high specific strength as well. In addition, the price of aluminium is lower than that of copper, so the aluminium replaces the copper partially or totally in some cases in order to save the production cost [1]. The joining of dissimilar metals is very much important due to their numerous advantages in industrial applications including the chemical, nuclear, aerospace, transportation, power generation and electronic industries. However joining of dissimilar materials by conventional fusion welding is very difficult due to their different chemical, mechanical and thermal properties and formation of

A. Mandal (✉) · A. Bandyopadhyay
Department of Mechanical Engineering, Jadavpur University, Kolkata 700032, India
e-mail: abhishekmandal72@gmail.com

J. D. Barma
Department of Mechanical Engineering, National Institute of Technology, Agartala 799046,
Tripura, India

© Springer Nature Singapore Pte Ltd. 2020
M. S. Shunmugam and M. Kanthababu (eds.), *Advances in Additive Manufacturing and Joining*, Lecture Notes on Multidisciplinary Industrial Engineering,
https://doi.org/10.1007/978-981-32-9433-2_63

711

hard and brittle intermetallic compounds (IMCs) in large scale at weld interface, thus solid-state joining process can solve this difficulty [2, 3].

Previous studies show sound dissimilar FSW joints obtained but it also shows that the dissimilar FSW joints usually failed at the nugget or along the interface between the two materials during mechanical tests [4–8]. For FSW joints of dissimilar Al/Cu, IMCs like CuAl_2 , CuAl and Cu_9Al_4 , etc. are easily formed in the nugget zone due to severe plastic deformation and thermal exposure. Thick intermetallic layer increases the brittleness of the joint as IMCs brittle in nature and [6–10]. Therefore, it is worthwhile to study mechanical properties and metallurgical properties on the size and distribution of the IMCs which is generally responsible for crack formation. In this paper, sound FSW Al–Cu joints were successfully achieved by offsetting the tool to the aluminium side and controlling the FSW parameters. The purpose of this study is to show the relation between FSW parameters and bonding strength in dissimilar welding joints and the metallurgical properties on the different process parameters.

63.2 Experimental Set-up and Procedure

Aluminium alloy (Table 63.1) and commercially pure copper (Table 63.2) have been cut into pieces of 300 mm × 65 mm × 3 mm for welding purpose. The copper sheets have been heat-treated at 650 °C, holding for 1 h and then cooled in the open air. The surfaces of sheets have been cleaned by emery paper to remove the oxide layers. The copper sheets positioned on the advancing side and aluminium sheets on the retreating side. The welding sheets have been supported by backing plate and clamp rigidly on the anvil along the welding direction to prevent the sliding movement of the sheets. FSW processes have been carried out on three-Ton FSW set-up, made by ETA technologies, India. The rotational speed varies from 800 to 1400 rpm keeping traverse speed constant at 1.5 mm/s and also the traverse speed varies from 0.9 to 2.1 mm/s when rotational speed keep constant at 1000 rpm which have been already furnished in Table 63.3. The tool, made of heat-treated H13 tool steel, has been used in these experiments with tapered hexagon pin having concave shoulder of 16 mm in diameter and the diameter of the circle inscribed hexagon at the bottom part is 5.2 mm, whereas that one is 3.6 mm at the top part (Fig. 63.1).

The tool tilt angle has been 2° from the normal surfaces to the plates. The tool pin offset has been 1.5 mm to the aluminium side for this study. The plunge depth of the tool shoulder was controlled manually for the quality of weld formation. The welded samples have been prepared for tensile samples according to ASTM E8 standard. Tensile test has been carried out on UTM-H50KS, made by Tinius Olsen, UK. Tensile

Table 63.1 Chemical composition of aluminium alloy

Elements	Si	Fe	Cu	Mn	Al
wt%	0.23	0.70	0.09	0.01	99.0

Fig. 63.1 Tool

test is carried out at an initial strain rate of $1 \times 10^{-3} \text{ s}^{-1}$. For microstructure, samples have been polished using rough emery, followed by water emery sheets of various grit sizes ranging from 1000 to 2000 grit. Then, weld area was polished with 3 and 1 μm diamond paste and then etched. Aluminium side have been etched using modified Keller's solution made of 190 ml of distilled water, 5 ml of HNO_3 , 3 ml of HCL and 3 ml of HF . Copper side has been etched using a solution of 5 g FeCl_3 , 50 ml HCL and 100 ml H_2O . Microstructures have been analysed using optical LEICA DM LM microscope, Germany.

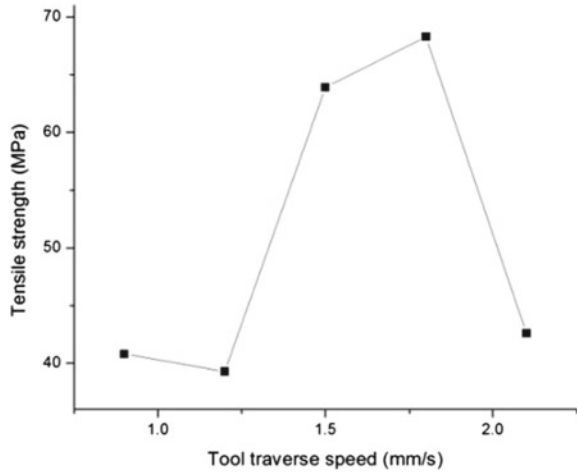
63.3 Results and Discussion

63.3.1 Tensile Properties

Figure 63.2 shows the tensile properties for different tool travel speeds ranging from 0.9 to 2.1 mm/s when tool rotational speed is constant at 1000 rpm. At the lower travel speed of 1.2 mm/s, tensile strength is lowest in this range of 39.3 MPa and then tensile strength increases with the increase of tool travel speed up to 1.8 mm/s is 68.3 MPa. Figure 63.2 also shows the tensile properties at different tool rotational speed ranging from 800 to 1400 rpm when traverse speed is constant at 1.5 mm/s. Results show higher tensile strength at 1000 rpm when tool traverse speed 1.8 mm/s (Tables 63.3 and 63.4).

Heat generation at stir zone is excess when tool traverse speed is low. So, different flow stresses of Al and Cu at weld nugget produce turbulent material and the weak consolidation of material and so defects are formed during low travel speed. Similarly, strength is lower at low traverse speed. High strengths of joint have been achieved at tool traverse speed of 1.2–1.8 mm/s. It depends on the distribution of fine particles and reduction of excessive intermetallic compounds formation and grain boundary strengthening zone. Stirring action of the tool extracted Cu particle from Cu side and distributed in the nugget zone and Cu particles mix with aluminum trans-

Fig. 63.2 Tensile strengths at various tool travel speeds



formed into hard intermetallic. This also improves the joint strength by the dispersion strengthening mechanism.

Figure 63.3 shows the tensile properties for different tool rotational speeds ranging from 800 to 1400. Low tool rotational speed 800 rpm causes low stirring action which causes improper mixing of Al and Cu particle and aluminium and copper cannot completely transfer into hard intermetallics which reduce the strength also. At 1000 rpm, mixing of fine Cu particle with aluminium properly takes place which simultaneously increases the joint efficiency. Again at higher rotational speed, heat generation is very high which causes generation of large amount of IMCs and also higher volume of flash which weakens the joints.

Fig. 63.3 Tensile strengths at various tool rotational speeds

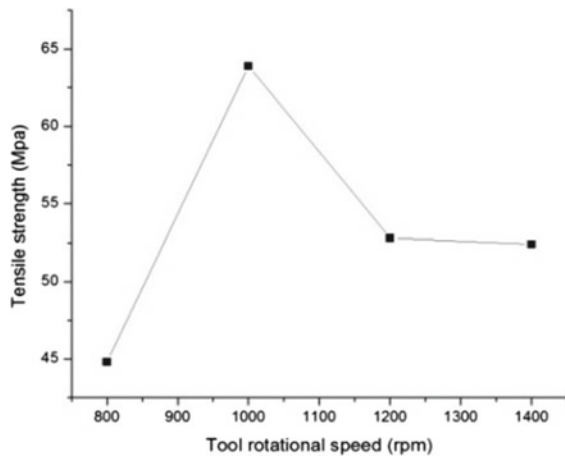


Table 63.2 Chemical composition of commercially pure copper

Elements	Cu	C	Ti	Zn	Cr	P
wt%	99.97	0.002	0.0003	0.01	0.0006	0.0009

Table 63.3 Tensile test results of FSW joints

S. No.	Tool rotational speed (rpm)	Tool traverse speed (mm/s)	Tensile strength (MPa)
1	1000	0.9	41.8
2	1000	1.2	39.3
3	1000	1.5	63.9
4	1000	1.8	68.3
5	1000	2.1	42.6
6	1200	1.5	52.8
7	1400	1.5	52.4
8	800	1.5	44.8

Table 63.4 Tensile test results of base metals

Base material	Tensile strength (MPa)
Aluminium alloy	124
Commercially pure copper	185

63.3.2 *Microstructure of Dissimilar Joints*

Since the melting point of copper is higher than aluminium, aluminium will have better flowability at the same temperature. By plunging tool pin into the aluminium side, Al/Cu joint can be formed. FSW tool pin has been set 1.5 mm to the aluminium side during welding. The welding zone is covered by the layer of aluminium. The nugget zone is made of aluminium and copper, and its structure depends on the material flow.

Low traverse speed causes high heat generation at nugget zone which forms more IMCs and along with defects. The laminated structures have been observed on the dissimilar materials and also the intercalated flow patterns due to the complex flow Al and Cu. When tool traverse speed increases from 1.2 to 1.8 mm/s, high generation decreases to the stir zone and simultaneously reduces the excessive plasticization which reduces the formation of turbulent flow. Low rotational speed reduces heat generation which lowers the plasticity of materials. This causes improper mixing of Al and Cu particles and when rotational speed increases from 800 to 1000 rpm, heat generation increases which increases plasticity and swirling of Al and Cu increase. When rotational speed increases from 1000 to 1400 rpm, high heat generation is produced which increases excessive plasticity and produces turbulent material (Figs. 63.4 and 63.5).

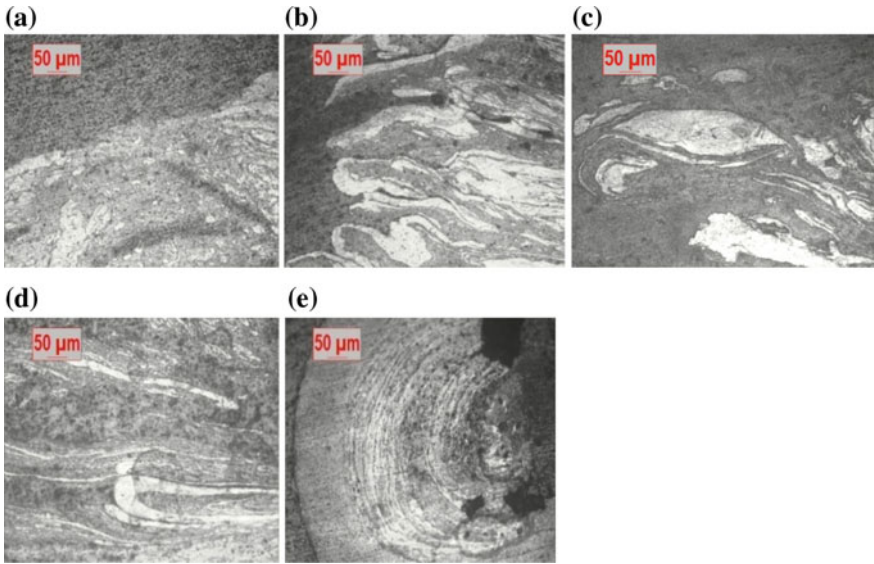


Fig. 63.4 Interfacial microstructure of Al/Cu joint produced at constant tool rotational speed 1000 rpm and various tool traverse speed at **a** 0.9 mm/s, **b** 1.2 mm/s, **c** 1.5 mm/s, **d** 1.8 mm/s and **e** 2.1 mm/s

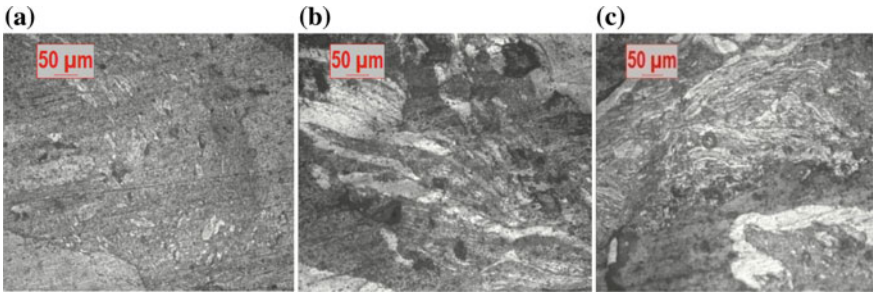


Fig. 63.5 Interfacial microstructure of Al/Cu joint produced at constant tool traverse speed 1.5 mm/s and various tool rotational speed at **a** 1200 rpm, **b** 1400 rpm and **c** 800 rpm

63.4 Conclusion

In summary, the effects of tool traverse speeds and tool rotational speeds on the tensile strength, microstructure of Al/Cu dissimilar friction stir welded joints extensively studied.

Al/Cu are joined successfully when tool traverse speed varies from 0.9 to 2.1 mm/s at constant tool rotational speed of 1000 rpm and also when tool rotational speed varies from 800 to 1400 rpm at constant traverse speed 1.5 mm/s.

Superior tensile properties are obtained on the distribution of fine particles and reduction of excessive intermetallic compounds formation and grain boundary strengthening zone. Stirring action of the tool extracted Cu particle from Cu side and distributed to the nugget zone and Cu particles mix with aluminum transformed into hard intermetallic. This also improves the joint strength by the dispersion strengthening mechanism.

Excess heat generation due to high tool rotational speed and low tool traverse speed causes excessive formation of intermetallic which reduces the joint strength due to brittle in nature tensile strength have been obtained.

Optimum heat input, at the tool traverse speed 1.8 mm/s when tool rotational speed 1000 rpm, reduces the diffusion of Al and Cu interfaces which results high tensile strength.

References

1. Man, Z.: *Hot Work. Technol.* **38**, 116–119 (2009). (In Chinese)
2. Li, Y.J., Wu, H.Q., Chen, M.A., Yang, M., Feng, T.: *Chin. J. Nonfer. Met.* **11**(3), 424–427 (2001)
3. Chen, X.D., Song, Q., Yu, W.Y., Song, C.Y.: *Trans. China. Weld Inst.* **24**(1), 40–43 (2003)
4. Uzun, H., Donne, C.D., Argagnotto, A., Ghidini, T., Gambaro, C.: *Mater. Des.* **26**, 41–46 (2005)
5. Liu, P., Shi, Q.Y., Wang, X.D., Wang, W.: *Mater. Lett.* **62**, 4106–4108 (2008)
6. Yan, J.C., Xu, Z.W., Li, Z.Y., Yang, S.Q.: *Scripta Mater.* **53**, 585–589 (2005)
7. Lee, W.B., Jung, S.B.: *Mater. Res. Innov.* **8**, 93–96 (2004)
8. Zettler, R.: *Adv. Eng. Mater.* **8**, 415–421 (2006)
9. Ouyang, J.H., Yarrapareddy, E., Kovacevic, R.: *J. Mater. Process. Technol.* **172**, 110–122 (2006)
10. Stao, Y.S., Park, S.H.C., Michiuchi, M., Kokawa, H.: *Scripta Mater.* **50**, 1233–1236 (2004)

Chapter 64

Numerical Simulation to Predict Temperature Distribution and Weld Profile in Laser Beam Welding of Carbon Steel St37 and Mechanical Properties



Pramod Kumar and Amar Nath Sinha

Abstract In the present research work, a numerical simulation of temperature distribution for laser beam welding of St37 carbon steel has been investigated. The geometry created for this model is similar to the butt joint of 1.4-mm-thick material, and cooling effect caused by the free convection and radiation in ambient air is taken into account. The effect of average beam power and laser spot diameter on the transient temperature distribution and peak temperature has been investigated. It has been found the peak temperature increases with increase in average beam power and decreases with increase in spot diameter at constant welding speed. The mechanical properties such as microhardness and ultimate tensile strength of the welded joint have also been studied.

Keywords Laser beam welding · Spot diameter · Temperature distribution · Butt joint · ANSYS

64.1 Introduction

Welding is one of the most widely used joining methods and is applicable in different fields of industry such as automotive, oil and gas industry. Advantages of welded joints are high ultimate tensile strength and reduced weight weldment. Laser beam welding (LBW) has many specific features like smooth weld surface and defect-free joint due to which it is gaining popularity for effective operation.

Numerical modeling has been widely used for describing the physical phenomenon used in complicated joining processes. LBW is a non-conventional welding process applicable for joining similar and dissimilar set of materials. Many researchers have been working in the area of numerical modeling of laser welding for determining the temperature distribution and weld bead geometry. Chukkan et al. [1] have studied the temperature profile using FEM and observed that it pro-

P. Kumar (✉) · A. N. Sinha

Department of Mechanical Engineering, National Institute of Technology Patna, Ashok Rajpath, Patna 800005, India

e-mail: pramod.me14@nitp.ac.in

© Springer Nature Singapore Pte Ltd. 2020

M. S. Shunmugam and M. Kanthababu (eds.), *Advances in Additive Manufacturing and Joining*, Lecture Notes on Multidisciplinary Industrial Engineering,

https://doi.org/10.1007/978-981-32-9433-2_64

vided accurate numerical results for simplified numerical model using different heat sources. Kumar et al. [2] studied numerical simulation of temperature distribution in dissimilar laser beam welding of St37 steel and 304L steel and validated the numerical results. Tsirkas et al. [3] studied the numerical simulation of laser welding process for determining the distortion in the welded joint using SYSWELD software package, and the results were experimentally validated with good agreement. Frewin and Scott [4] studied numerical model for heat flow of pulsed LBW using FEM. Carmignani et al. [5] have studied LBW of 304L stainless steel for measuring the residual stresses and strains produced in the weldments of 10-mm-thick sheet using beam power of 15 kW in Abaqus. Spina et al. [6] have predicted the induced distortions in thin plates and T-joints of aluminum alloys and observed that a correct thermal analysis is mandatory to predict welding-induced distortions and residual stresses in laser beam welding of AA5083 alloys. De et al. [7] have explored the temperature contour of the laser spot weldments for measuring the size of the weld bead. Kumar et al. [8] investigated the numerical simulation of temperature distribution in laser welding of 304L austenitic stainless steel using Gaussian 3D conical moving heat source. Kumar et al. [9] also studied the microstructure and mechanical properties of laser welding of carbon steel (St37) at different laser parameters.

The aim of the current study is to explore the effect of LBW parameters such as beam power (W), scanning speed (mm/s) and laser spot diameter (mm) on temperature profile and weld bead size of carbon steel (St37) of 1.4-mm-thick sheet. The mechanical properties of welded material have also been studied.

64.2 Material Properties

The carbon steel St37 is selected for the transient thermal analysis. St37 is widely used in structural components. The microstructure of carbon steel St37 consists of a fully medium-sized ferrite grain in a solution-quenched condition. The chemical composition (wt%) of St37 is shown in Table 64.1. The melting point of the St37 is 1500 °C. The temperature-dependent thermo-physical properties of St37 are shown in Table 64.2 [10].

Table 64.1 Chemical composition of St37 in weight %

C	Si	Mn	P	S	Cr	Mo	Ni	Fe
0.102	0.15	0.49	0.019	0.005	0.002	0.01	0.03	Bal.

Table 64.2 Thermo-physical properties of stainless steel St37 [10]

Temperature (°C)	Thermal conductivity (W/m °C)	Density (Kg/m ³)	Specific heat (J/kg K)
0	45.9	7900	444
100	44.8	7880	472
200	43.4	7830	503
300	41.4	7790	537
400	38.9	7750	579
600	33.6	7660	692
800	28.7	7560	837
1200	28.6	7370	860
1300	28.6	7320	860
1600	29.5	7320	863

64.3 Numerical Simulation

The physics incurred in describing the governing equation for heat conduction of transient temperature is described by Eq. 40.1 [3].

$$\rho c \frac{\partial T}{\partial t} + v \rho c \frac{\partial T}{\partial y} = \frac{\partial}{\partial x} \left(k \frac{\partial T}{\partial x} \right) + \frac{\partial}{\partial y} \left(k \frac{\partial T}{\partial y} \right) + \frac{\partial}{\partial z} \left(k \frac{\partial T}{\partial z} \right) + Q(x, y, z) \quad (40.1)$$

where T is the temperature (°C) which is a function of time and space, ρ is the density of the material (kg/mm³), c is the specific heat of the material (J/kg °C), v is the laser scanning speed or welding speeds (mm/s), k is the thermal conductivity of the material (W/mm °C) and Q is the heat source defining the heat generation per unit volume (J/mm³). The Gaussian distribution of heat flux is given by Eq. 40.2.

$$Q(z) = \frac{2Q_{\text{keyhole}}}{\pi r_o^2 H} e^{-\left(\frac{x^2 + (y-vx)^2}{r_o}\right)^2} (1 - z/H) \quad (40.2)$$

where Q_{keyhole} is the absorbed laser power (52%), H is the sheet thickness, r is the current radius, z is the current depth and r_o is given as in Eq. 40.3.

$$r_o = r_e - (r_e - r_i) \left(\frac{z_e - z}{z_e - z_i} \right) \quad (40.3)$$

where z_e and z_i are the z-coordinates at top and bottom surfaces, respectively. r_e and r_i are the radii at top and bottom surfaces, respectively.

In laser welding, quick heating and cooling of the weldment occur as it is a fast welding process. Overlapping spot welds formed on the weld bead surface are the

consequences of many spot welds which can be numerically modeled for better results. ANSYS APDL multipurpose physics has been used to numerically simulate the 3D transient analysis of temperature distribution. The sheet dimension of 50 mm × 25 mm × 1.4 mm is used in the current study. The numerical model explored has been used to analyze the peak temperature and temperature profile and their influence on laser parameters (beam power and scanning speed). The mesh size of the weld geometry should be fine, for analyzing heating and melting of narrow weld zone, but fine mesh of complete weld geometry raises the computational time for the whole analysis. Fine mesh near the weld line and coarser mesh away from the weld line with element size increasing are done to minimize the whole computational time. The complete mesh geometry is shown in Fig. 64.1. The size of the element adjacent to the weld line is 0.2 mm × 0.2 mm × 0.2 mm with total of 82,530 nodes and 78,750 elements in the entire body of the weld geometry. The initial temperature considered for the analysis was 35 °C as per the surrounding.

The LBW parameters incorporated in the current numerical study for measuring the temperature distribution are shown in Table 64.3.

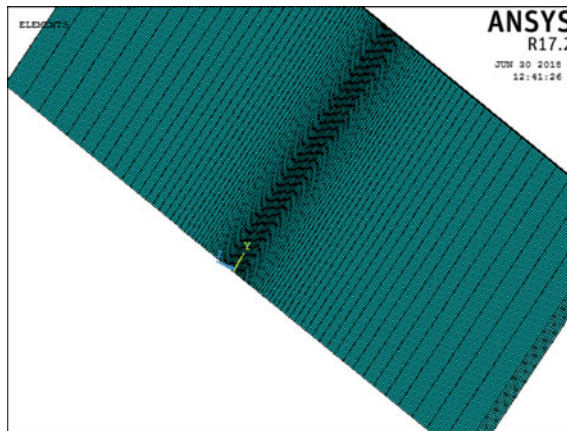


Fig. 64.1 Mesh of the geometry

Table 64.3 LBW process parameters incorporated

Sl. no.	Beam power (W)	Welding speed (mm/s)	Spot diameter (mm)
1.	225	5	0.75
2.	425	5	0.75
3.	625	5	0.75
4.	225	5	0.45
5.	425	5	0.45

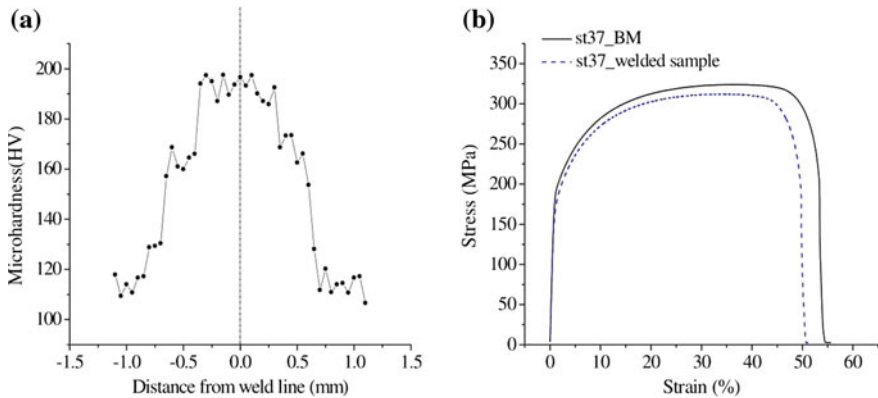


Fig. 64.2 Showing **a** microhardness distribution across the weld line and **b** stress–strain plot of welded specimen and carbon steel St37

64.4 Experimental Procedure and Mechanical Properties

The laser welding experiment has been carried to validate the numerically calculated temperature distribution and weld pool profile. The laser welding of St37 of 1.4-mm thickness has been done at beam power of 425 W, welding speed of 5 mm/s and spot diameter of 0.75 mm. Three K-type thermocouples (TC1, TC2 and TC3) were attached at a position (X) 3, 6 and 9 mm away from the weld line with probe penetration of 1.2 mm. Data logger along PC connected was used for recording temperatures measured by thermocouples.

Microhardness (HV) and UTS are mechanical properties of welded joints, measured at beam power of 425 W, scanning speed of 5 mm/s and spot size of 0.75 mm. At 0.98 N (load) of 20 s (dwell time), microhardness of the welded spec for transverse section was evaluated with Vickers microhardness machine. The microhardness of the welded specimen along both sides of the weld line is shown in Fig. 64.2a.

The specimens for tensile strength were made as per the ASTM E8 standards. Using Instron 1195, tensile test of the welded specimens was done with cross-head speed of 2 mm/min and load of 50 kN. The comparison of stress–strain curve of the welded joint and base metal is shown in Fig. 64.2b. The ductile fracture behavior for both the parent metal and the welded joints is observed from the stress strain curve.

64.5 Results and Discussion

The temperature distribution and temperature curve are valuated numerically computed using ANSYS APDL (FEM) for a different average beam power and laser spot size at constant welding speed. Many numerical models for different ranges of parameters for investigating the influence of LBW parameters on temperature distribution

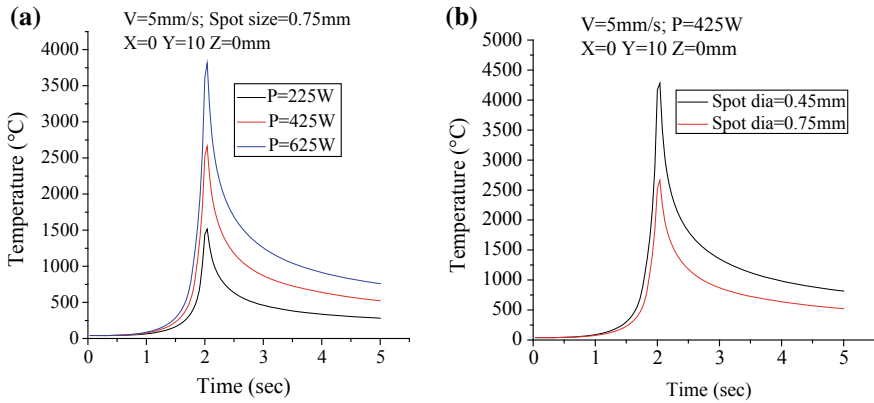


Fig. 64.3 **a** Transient temperature distribution for varying average beam power at constant scanning speed (5 mm/s) and laser spot size (0.75 mm). **b** Transient temperature distribution for varying laser spot diameter at constant scanning speed of 5 mm/s and average beam power (425 W)

and temperature profile are performed and mentioned in Table 64.3. Figure 64.3a shows the transient temperature distribution of laser welding of St37 for varying average beam power (225–625 W) at constant welding speed 5 mm/s and laser spot diameter of 0.75 mm. The influence of peak temperature was that it increases with increase in beam power when welding speed was constant. The highest peak temperature measured was nearly $3812\text{ }^\circ\text{C}$ at constant scanning speed of 5 mm/s and average beam power of 625 W, and lowest peak temperature was $1516\text{ }^\circ\text{C}$ at speed of 5 mm/s and average power of 225 W. Figure 64.3b shows the transient temperature distribution for varying laser spot diameter at constant scanning speed of 5 mm/s and average beam power of 425 W. It has been observed that the peak temperature increases with decreases in laser spot size at constant welding speed and average beam power. It has been found that the peak temperature decreases with increase in distance (x) far from the weld line for each case.

Numerically obtained weld profile has been compared with experimental results of temperature profile at scanning speed of 5 mm/s, average beam power of 425 W and laser spot size of 0.75 mm with good agreement, given in Fig. 64.4. Temperature distribution curve evaluated numerically has been validated with the experiment performed at beam power of 425 W, scanning speed of 5 mm/s and spot size of 0.75 mm with the help of three thermocouples (TC1, TC2 and TC3) fixed at position (X) 3, 6 and 9 mm distant from the weld line which are given in Fig. 64.5. The numerical results resemble in good agreement with those of experimentally obtained results.

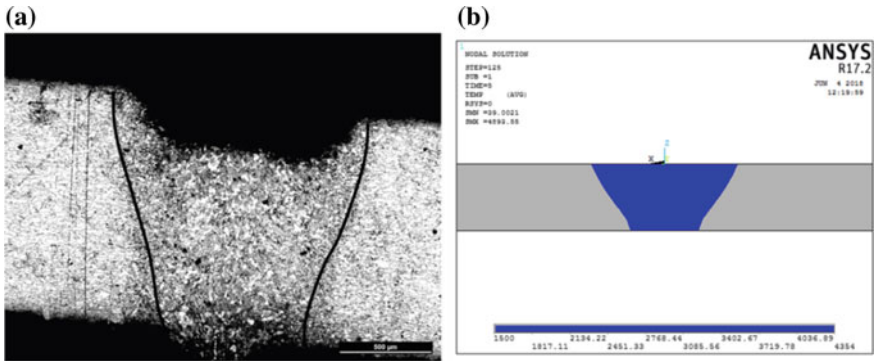


Fig. 64.4 Numerical weld pool profile compared with obtained experimental results at scanning speed of 5 mm/s, average beam power of 425 W and laser spot size of 0.75 mm; **a** experimental weld bead pool profile and **b** numerical weld pool profile

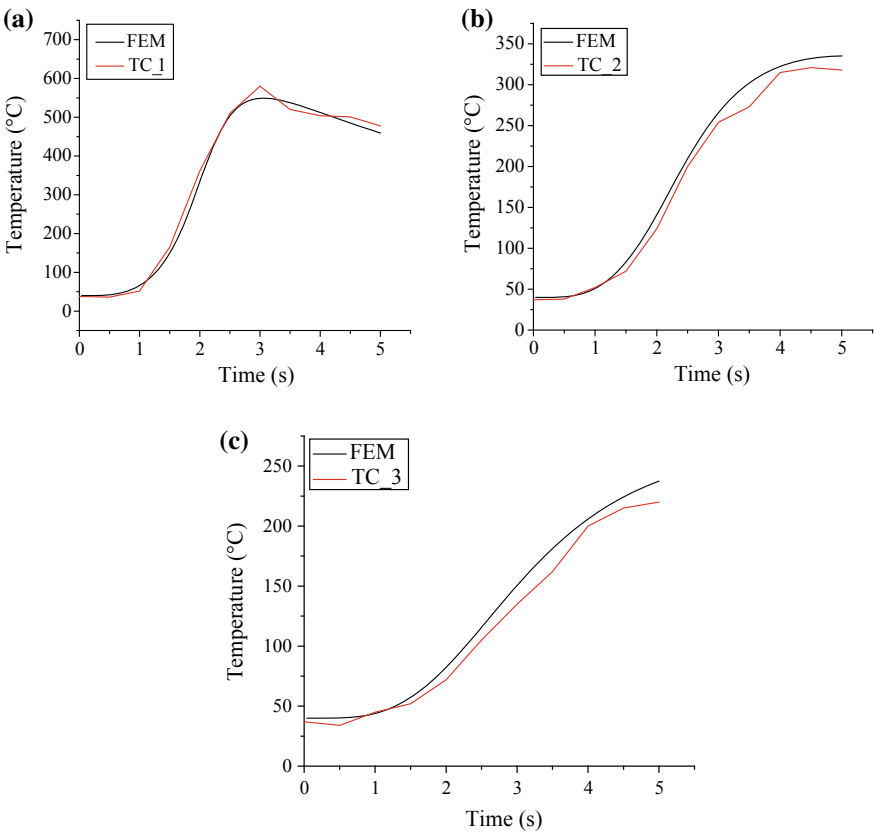


Fig. 64.5 Numerical results validated with experimental value with thermocouples **a** TC_1, **b** TC_2 and **c** TC_3

64.6 Conclusion

The following conclusions have been drawn in the present investigation.

- (a) The highest peak temperature measured is 3812 °C at scanning speed of 5 mm/s and average beam power of 625 W, and lowest peak temperature is 1516 °C at scanning speed of 5 mm/s and average power of 225 W.
- (b) The peak temperature decreases with increase in distance (x) far from the weld line at constant scanning speed and average beam power.
- (c) The numerical evaluated temperature distribution and weld profile are validated with experimental results with good agreement.
- (d) UTS of the welded specimen is only 3.7% less than base carbon steel St37.
- (e) Average microhardness of FZ, HAZ and parent carbon steel is 192HV, 167HV and 114HV, respectively.

Acknowledgements This work was supported by NIT Patna for financial support through TEQIP-II. The authors express special thanks to Central Mechanical Engineering Research Institute (CMERI), Durgapur, for laser welding facility which helped in validating the numerical results.

References

1. Chukkan, J.R., Vasudevan, M., Muthukumar, S., Kumar, R.R., Chandrasekhar, N.: Simulation of laser butt welding of AISI 316L stainless steel sheet using various heat sources and experimental validation. *J. Mater. Process. Technol.* **219**, 48–59 (2015)
2. Kumar, P., Sinha, A.N.: Studies of temperature distribution for laser welding of dissimilar thin sheets through finite element method. *J. Braz. Soc. Mech. Sci. Eng.* **40**(9), 455 (2018)
3. Tsirkas, S.A., Papanikos, P., Kermanidis, T.: Numerical simulation of the laser welding process in butt-joint specimens. *J. Mater. Process. Technol.* **134**(1), 59–69 (2003)
4. Frewin, M.R., Scott, D.: Finite element model of pulsed laser welding. *Weld. J. N Y* **78**, 15-s (1999)
5. Carmignani, C., Mares, R., Toselli, G.: Transient finite element analysis of deep penetration laser welding process in a single pass butt-welded thick steel plate. *Comput. Methods Appl. Mech. Eng.* **179**(3), 197–214 (1999)
6. Spina, R., Tricarico, L., Basile, G., Sibillano, T.: Thermo-mechanical modeling of laser welding of AA5083 sheets. *J. Mater. Process. Technol.* **191**(3), 215–219 (2007)
7. De, A., Walsh, C.A., Maiti, S.K., Bhadeshia, H.K.D.H.: Prediction of cooling rate and microstructure in laser spot welds. *Sci. Technol. Weld. Joining* **8**(6), 391–399 (2003)
8. Kumar, P., Sinha, A.N.: Studies on numerical simulation of temperature distribution in laser beam welding of 304L austenitic stainless steel. *Int. J. Manuf. Mater. Mech. Eng. (IJMMME)* **9**(1), 30–49 (2019)
9. Kumar, P., Sinha, A.N.: Microstructure and mechanical properties of pulsed Nd: YAG laser welding of st37 carbon steel. *Procedia Comput. Sci.* **133**, 733–739 (2018)
10. Attarha, M.J., Sattari-Far, I.: Study on welding temperature distribution in thin welded plates through experimental measurements and finite element simulation. *J. Mater. Process. Technol.* **211**(4), 688–694 (2011)

Chapter 65

Influence of Friction Pressure/Time on Mechanical and Microstructural Characteristics of Rotary Friction Welded LM25/10% SiC Aluminium Matrix Composites



M. Abdul Ghani Khan, S. Rajakumar and T. Pragatheswaran

Abstract The aluminium matrix composites have wide applications as structural components aerospace and automobile industries. Adding SiC to the aluminium matrix gives great value in terms of enhancing the mechanical properties of the material. Most of the materials used as structural components undergo not only forming processes but also joined by welding processes. Thus in this research work, the investigation is carried out on the rotary friction welded aluminium matrix composites, namely LM25 with added 10% SiC. The effect of the process parameter, i.e. friction pressure on the mechanical and microstructural characteristics, was analysed and studied. From the microstructural examination and mechanical property evaluation, it was found that increasing the friction pressure increases the mechanical properties and also aids in achieving finer microstructure.

Keywords Microstructure · Friction · Welding · Aluminium · Composite · Hardness

65.1 Introduction

Aluminium alloys are of important materials in many manufacturing industries, especially in structural applications. Thus, the research on improving the mechanical, electrical and thermal properties has increased tremendously in the past few decades. Over the years, the properties of the aluminium alloys are not sufficient and thus the emergence of metal matrix composites (MMCs) came into interest. The MMCs are

M. Abdul Ghani Khan

Department of Mechanical Engineering, School of Engineering & Technology, Ponnaiyah Ramajayam Institute of Science & Technology, Thanjavur, Tamil Nadu, India

S. Rajakumar (✉) · T. Pragatheswaran

Centre for Materials Joining and Research (CEMAJOR), Department of Manufacturing Engineering, Annamalai University, Annamalaiagar, Tamilnadu, India
e-mail: srkcemajor@yahoo.com

© Springer Nature Singapore Pte Ltd. 2020

M. S. Shunmugam and M. Kanthababu (eds.), *Advances in Additive Manufacturing and Joining*, Lecture Notes on Multidisciplinary Industrial Engineering,
https://doi.org/10.1007/978-981-32-9433-2_65

727

made by adding suitable reinforcement material into the metal matrix. The production of metal matrix can accomplish several techniques. One of the most common techniques is the stir casting. In this process, the aluminium metal is melted, and reinforcement material is added and stirred up to proper mixing. The MMCs undergo several processing such as forming and joining before turning into a usable product. Friction welding is used extensively in various industries. Heat in friction welding is generated by conversion of mechanical energy into thermal energy at the interface of workpieces during rotation under pressure. Friction welding is a solid-state welding process producing joints without melting the base materials. In friction welding process, the most important process parameters are friction pressure, forging pressure, friction time, forging time and rotational speed.

Achilles Vairis et al. [1] studied the three welding processes such as rotary friction welding, friction stir welding and linear friction welding processes. They compared temperature, stresses and strains, as well as strain rates developed in the early phases of the processes, which are essential in their successful development. The structure of welds formed by friction welding of sheets of aluminium alloys 1201 and AMg5 with a thickness of 2, 4, and 5 mm was studied by Silis et al. [2]. The mechanical properties of the welds were determined. The differences in the structure and properties of the welds were described. Friction welding was shown to be more advantageous than fusion welding. Kimura et al. [3] studied the characteristics of friction welding between a solid bar of 6061 Al alloy and a pipe of Al-Si12CuNi (AC8A) Al cast alloy. When the joint was made by a continuous drive friction welding machine (conventional method), the AC8A portion of the joint showed heavy deformation and the AA6061 showed minimal deformation. Srinivasan et al. [4] studied the feasibility of joining AZ31B magnesium nanocomposites by rotational friction welding. It was evident from the results that increase in friction pressure and forging pressure leads to the enhancement of joint efficiency. Also, as the friction time increased, the efficiency of the joint decreased. Sahin et al. [5] studied the interface properties of friction welded near-nanostructured Al 5083 alloys. Both fatigue and tensile strengths of friction welds were higher than the base material. However, the refining of grain size as shown from microstructures results in a significant increase in hardness and mechanical properties. Rafi et al. [6] studied the friction welding of AA7075-T6 rods of 13-mm diameter with an aim to understand the effects of process parameters on weld microstructure and tensile properties. Singh [7] highlighted the role of globular microstructure on the weldability of semi-solid processed aluminium alloys via high-temperature flow behaviour. The study was performed on welding thixocast A356 by friction welding. Many investigations were made on the friction welding of different aluminium alloys and aluminium metal matrix composites such as AlB2-reinforced aluminium matrix composites [8], AA6061 [9] and YSZ alumina matrix composite [10]. Also, there some works were performed to join the dissimilar combination of materials such as titanium alloys and steels [11, 12]. However, the present investigation concentrates on studying the effect of process parameter, i.e. friction pressure on the mechanical and microstructural characteristics of friction welded cast aluminium alloy LM25 with added 10% SiC.

65.2 Experimental Work

The base material used was the LM25 cast aluminium alloy with added 10% Si. This metal matrix composite was prepared by mixing the LM25 alloy with Si through stir casting process. The quantity of reinforcement added in the crucible was 10% volume fraction of SiC powder. After stir casting, the plates were turned to form cylindrical rods of 75-mm length and 12-mm diameter as base material for friction welding process. A hydraulic controlled continuous drive friction welding machine (20 kN capacity) was used to weld the joints. The chemical composition and mechanical properties of the base material are presented in Tables 65.1 and 65.2, respectively. The microstructure of the base material is shown in Fig. 65.1.

The machine used for the friction welding process was the hydraulic controlled continuous drive rotary friction welding machine with a 3T load capacity. The machine set-up and the process are depicted in Fig. 65.2. From the literature review, it was found that the major influencing process parameters in friction welding process are friction pressure, forging pressure and spindle rotational speed.

Table 65.1 Chemical composition of LM25 with added 10% SiC MMC

Element	Cu	Mg	Si	Fe	Mn	Ni	Zn	Pb	Sn	Ti	Al
% Wt	0.2	0.4	7.5	0.5	0.3	0.1	0.1	0.1	0.05	0.2	bal

Table 65.2 Mechanical properties of LM25 with added 10% SiC MMC

Ultimate tensile strength (MPa)	Yield strength (MPa)	Notch tensile strength (MPa)	% Elongation	Hardness (HV)
164	152	176	4	60

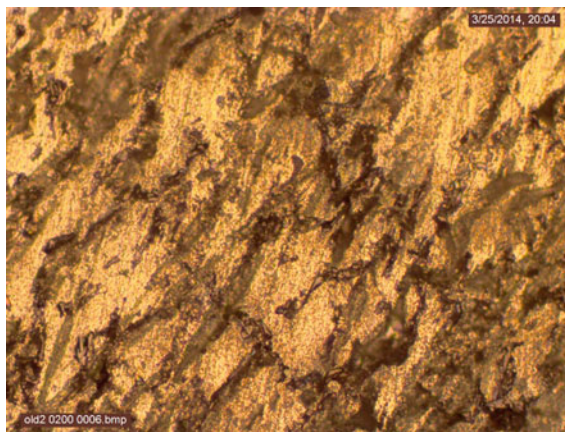


Fig. 65.1 Microstructure of the base material



Fig. 65.2 Friction welding machine set-up

Here in this research work, the forging time and friction time are calculated and represented as forging pressure per second and friction pressure per second, respectively. The effect study is conducted based on the experiments given in Table 65.3. The tensile test was conducted as per the ASTM E8 M standard. The tensile test was carried out in 100 kN, servo-controlled universal testing machine (make: FIE-Bluestar, India, and model: UNITEK 94100) with a cross-head speed of 0.5 mm/min at room temperature. Vickers microhardness testing machine (make: Shimadzu and model: HMV-2T) was employed for measuring the hardness of the weld nugget region with 0.05 kg load at 15 s of dwell time. The specimen surfaces were ground using 500, 800, 1200, 1500 and 2000 grit SiC paper, cleaned with acetone and distilled water and then dried by flowing air.

Table 65.3 Friction welding process parameters

Exp. No.	Forging pressure/time (MPa/s)	Friction pressure/time (MPa/s)	Rotational speed (rpm)
1.	0.9	0.07	2200
2.	0.9	0.08	2200
3.	0.9	0.09	2200
4.	0.9	0.1	2200
5.	0.9	0.11	2200

65.3 Results

65.3.1 Microstructure

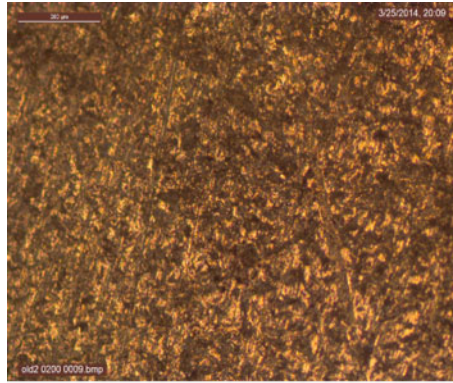
The microstructure of the friction welded joints usually consists of three important regions such as fully deformed zone (FDZ), partially deformed zone (PDZ) and heat-affected zone (HAZ). The microstructures of the friction welded joints at 0.11 MPa/s and 0.07 MPa/s with different zones are shown in Figs. 65.3 and 65.4. Comparing the microstructures of welds produced at 0.11 and 0.07 MPa/s friction pressures, 0.11 MPa/s joint has very finer grains in the FDZ and PDZ. By comparing the HAZs, the grains were very coarser in 0.07 MPa/s and it is finer in 0.11 MPa/s. The elemental distribution and the fractograph of friction welded reinforced LM25 alloy at different friction pressures are shown in Figs. 65.4 and 65.5. The elemental distribution and EDS analysis were conducted to quantify and visualize the distribution of major alloying elements such as Si, Mg, Zn and C and the base element Al. The distribution of elements is more uniform at the friction pressure per time of 0.11 MPa/s compared to the friction pressure per unit time of 0.07 MPa/s.

65.3.2 Mechanical Properties

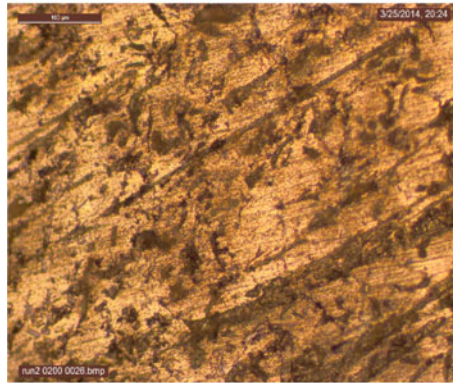
The mechanical properties of the joints such as tensile strength, yield strength and per cent elongation are shown in Table 65.4. The strength is higher in the joints welded at 0.11 MPa/s, and lowest values were recorded for the joints welded at 0.07 MPa/s. On the contrary, the highest value of the elongation was recorded for the joints welded at 0.07 MPa/s and lowest at 0.11 MPa/s. Hardness distribution was measured across the welded joints, and it is shown in Fig. 65.8. Highest value of the hardness was recorded at the FDZ of the joint produced at 0.11 MPa/s, and lowest was found at 0.07 MPa/s in the FDZ.

65.4 Discussion

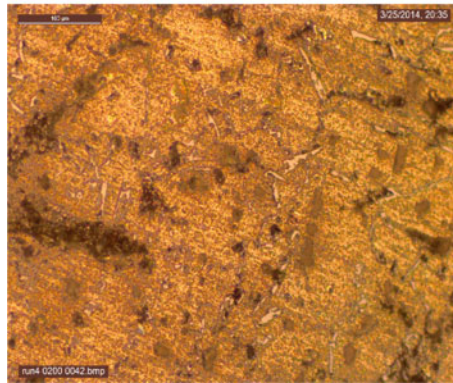
From the microstructural observations, it was found that when the spindle rotational speed is increased, the grains in the FDZ and PDZ get finer which leads to the increase in the strength of the joints. Coarser grain structure was found at the HAZ region which has the lower strength and becomes the very likely region for the failure to occur. But when comparing the HAZ of the joints welded at 0.11 and 0.07, 0.07 MPa/s joint has coarser grains which make the joints to attain premature failure. From Figs. 65.5 and 65.6, it was observed that the distribution of alloying elements in the matrix is highly uniform at high friction pressure. Uniform distribution attributes to the improvement in the mechanical properties such as tensile strength, elongation



(a) Fully deformed zone

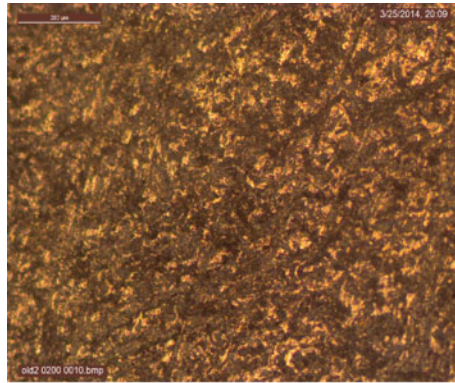


(b) Partially deformed zone

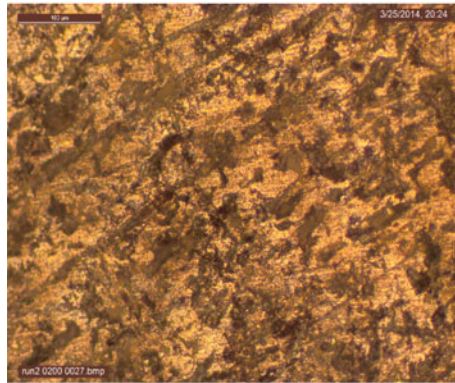


(c) Heat affected zone

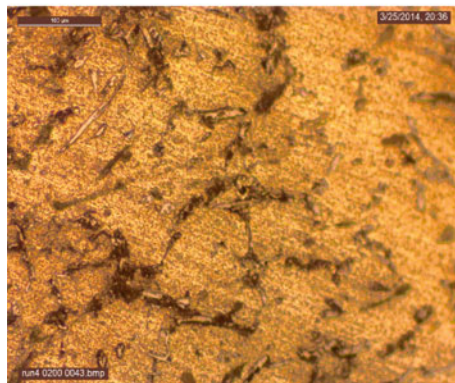
Fig. 65.3 Microstructures of the 0.11 MPa/s joints



(a) Fully deformed zone



(b) Partially deformed zone



(c) Heat affected zone

Fig. 65.4 Microstructures of the 0.07 MPa/s joints

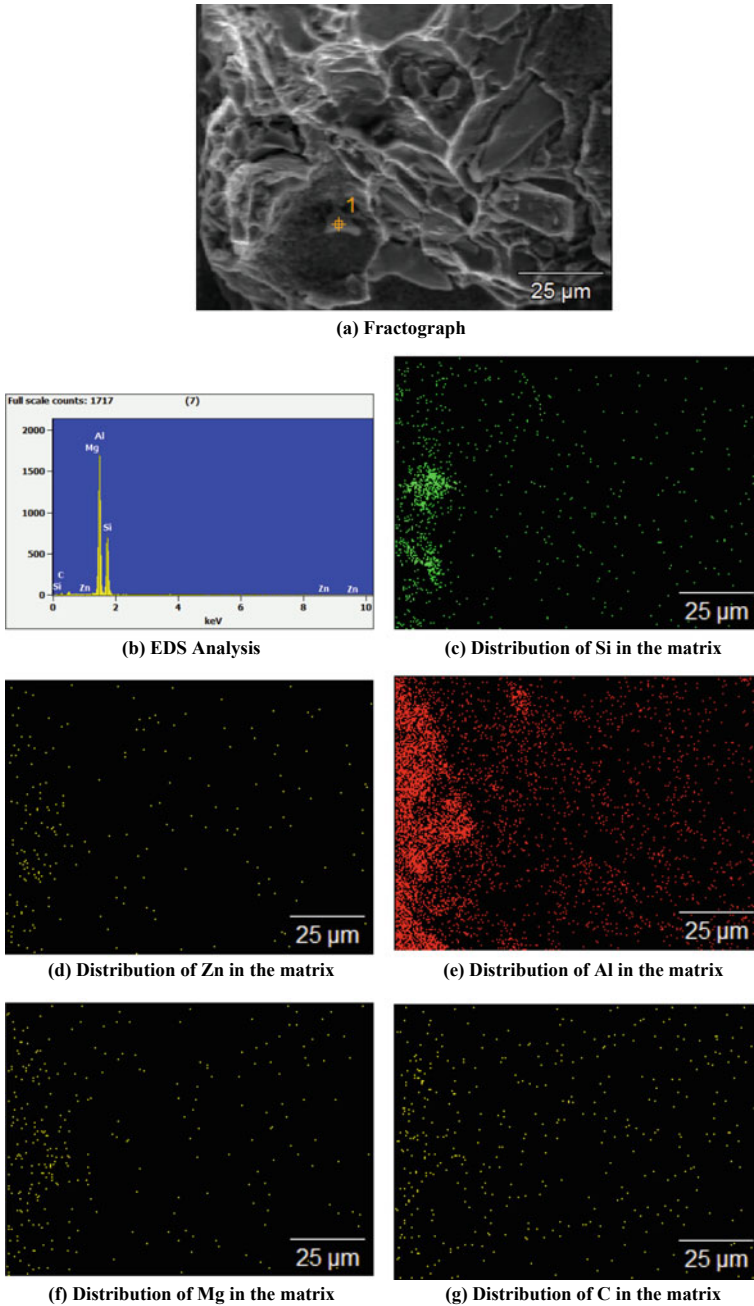


Fig. 65.5 Analysis of fractography and distribution of elements in the matrix of LM25 + 10% SiC friction welded at 0.7 MPa/s

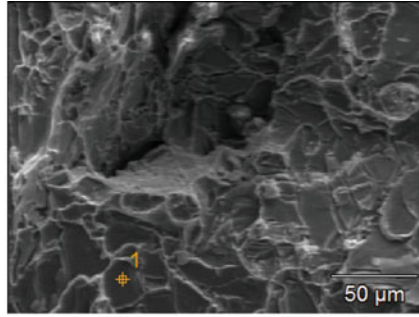
Table 65.4 Mechanical properties of the friction welded joints

Exp. No.	Friction pressure/time (MPa/s)	Yield strength (MPa)	Tensile strength (MPa)	% Elongation
1.	0.07	137	153	3.8
2.	0.08	145	162	3.4
3.	0.09	150	168	3.6
4.	0.1	160	175	2.5
5.	0.11	164	183	3.2

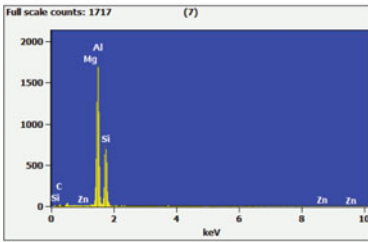
and hardness. The values of elongation are not following a linear trend due to the uneven distribution caused by the effect of process parameters. The matrix and the reinforcement are seemed to be mixed thoroughly throughout the matrix from the elemental distribution and EDS analysis. The mechanical behaviour of the composite aluminium friction welds welded at different friction pressures is shown in Fig. 65.7.

The trend of the graphs shows that the mechanical properties of the friction welds increase with increase in the friction pressure. The difference in the values of the mechanical properties is reducing over the increase in the friction pressure. This indicates that the mechanical properties will start to fall after a certain increment in the friction pressure. This is due to the fact that the high friction pressure causes more plastic deformation during welding which will lead to reduced strength and hardness (Fig. 65.8).

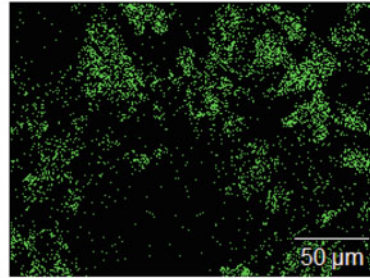
Thus when the friction pressure increases, the finer microstructure can be achieved. From the mechanical property evaluation, it was found that the results were in good agreement with the results obtained from the microstructure examinations. The highest tensile strength and yield strength recorded were 183 MPa and 164 MPa, respectively, in the 0.11 MPa/s joints. Due to the softening effect during the friction welding process, lowest hardness was recorded in the HAZ whereas the peak hardness was recorded in the FDZ for all the joints made at different friction pressures.



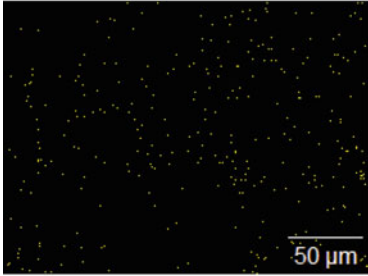
(a) Fractograph



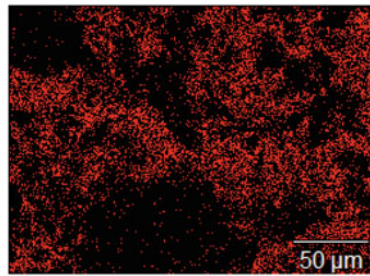
(b) EDS Analysis



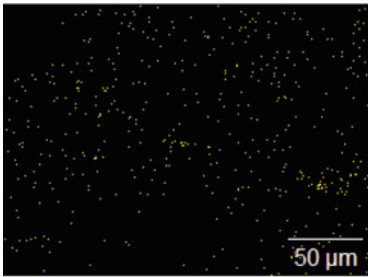
(c) Distribution of Si in the matrix



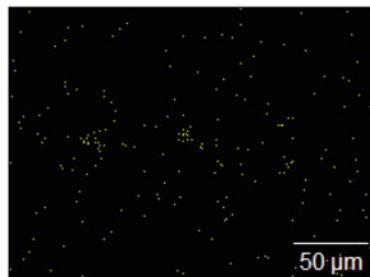
(d) Distribution of Zn in the matrix



(e) Distribution of Al in the matrix



(f) Distribution of Mg in the matrix



(g) Distribution of C in the matrix

Fig. 65.6 Analysis of fractography and distribution of elements in the matrix of LM25 + 10% SiC friction welded at 0.11 MPa/s

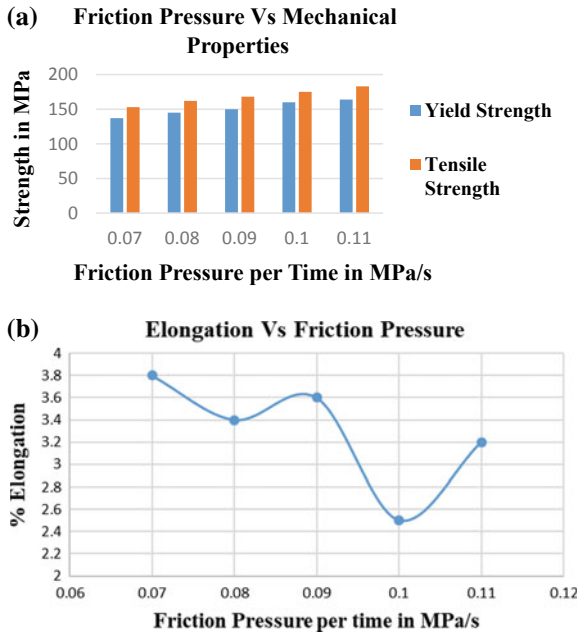


Fig. 65.7 Effect of friction pressure on mechanical properties of LM25 + 10% SiC friction welded joints

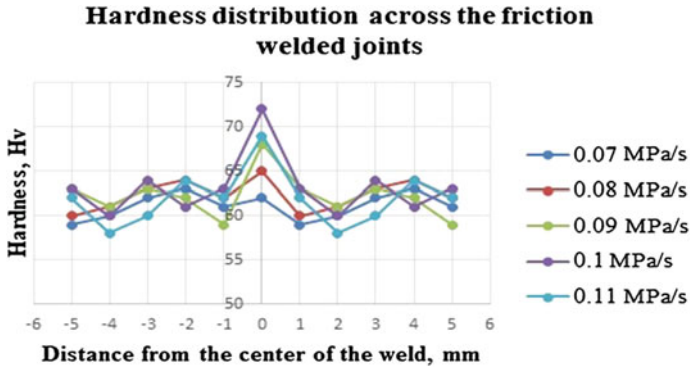


Fig. 65.8 Hardness distribution of the friction welded joints at different rotational speeds

65.5 Conclusions

- The effect of friction pressure per time on the mechanical and microstructural characteristics of the rotary friction welded composite cast aluminium alloy LM25 + 10% SiC was studied.
- From the microstructural examination, the finer grains can be achieved in the FDZ by increasing the friction pressure.
- The mechanical properties of the friction welded LM25 + 10% SiC joints such as tensile strength and yield strength were increased with increase in rotational speed, and the highest value achieved was 183 MPa and 164 MPa, respectively, at 0.11 MPa/s.
- The hardness plots show that the peak hardness was recorded at the FDZ in all the joints, and the highest hardness achieved was 72 Hv in the FDZ of 0.11 MPa/s joint.

References






1. Vairis, A., Papazafeiropoulos, G., Tsainis, A.: A comparison between friction stir welding, linear friction welding and rotary friction welding. *Adv Manuf.* (2016). <https://doi.org/10.1007/s40436-016-0163-4>
2. Silis, M.I., Eliseev, A.A., Silis, V.É., et al.: Special features of the structure of aluminum alloy welds formed by friction welding. *Met. Sci. Heat Treat.* **51**, 184 (2009). <https://doi.org/10.1007/s11041-009-9140-x>
3. Kimura, M., Sakaguchi, H., Kusaka, M., et al.: Characteristics of friction welding between solid bar of 6061 Al alloy and pipe of Al–Si12CuNi Al cast alloy. *J. Mater. Eng. Perform.* **24**, 4551–4560 (2015). <https://doi.org/10.1007/s11665-015-1735-3>
4. Srinivasan, M., Loganathan, C., Balasubramanian, V., et al.: Feasibility of joining AZ31B magnesium metal matrix composite by friction welding. *Mater. Des.* **32**, 1672–1676 (2011)
5. Sahin, M., Balasubramanian, N., Misirli, C., et al.: On properties at interfaces of friction welded near-nanostructured Al 5083 alloys. *Int. J. Adv. Manuf. Technol.* **61**, 935–943 (2012). <https://doi.org/10.1007/s00170-011-3775-7>
6. Rafi, H.K., Ram, G.D.J., Phanikumar, G., Rao, K.P.: Microstructure and tensile properties of friction welded aluminum alloy AA7075-T6. *Mater. Des.* **31**, 2375–2380 (2010). <https://doi.org/10.1016/j.matdes.2009.11.065>
7. Singh, S.K., Chattopadhyay, K., Phanikumar, G., Dutta, P.: Experimental and numerical studies on friction welding of thixocast A356 aluminum alloy. *Acta Mater.* **73**, 177–185 (2014). <https://doi.org/10.1016/j.actamat.2014.04.019>
8. P. PR, J. BR (2017) Investigations on Mechanical and Metallurgical Properties of Friction Welding of AlB2 Reinforced Aluminum Matrix Composites. *Silicon*. <https://doi.org/10.1007/s12633-017-9615-0>
9. Fauzi, M.N.A., Uday, M.B., Zuhailawati, H., Ismail, A.B.: Microstructure and mechanical properties of alumina-6061 aluminum alloy joined by friction welding. *Mater. Des.* **31**, 670–676 (2010). <https://doi.org/10.1016/j.matdes.2009.08.019>
10. Uday, M.B., Fauzi, M.N.A., Zuhailawati, H., Ismail, A.B.: Thermal analysis of friction welding process in relation to the welding of YSZ-alumina composite and 6061 aluminum alloy. *Appl. Surf. Sci.* **258**, 8264–8272 (2012). <https://doi.org/10.1016/j.apsusc.2012.05.035>

11. Pinheiro, G.A., Pankiewicz, C.G., Hort, N., et al.: Effects of welding conditions on microstructural transformations and mechanical properties in AE42-HP friction welded joints. *Weld World* **52**, 10–17 (2008). <https://doi.org/10.1007/BF03266678>
12. Li, X., Li, J., Liao, Z., et al.: Microstructure evolution and mechanical properties of rotary friction welded TC4/SUS321 joints at various rotation speeds. *Mater. Des.* **99**, 26–36 (2016). <https://doi.org/10.1016/j.matdes.2016.03.037>

Chapter 66

Effect of Holding Time on Microstructural Characteristics and Mechanical Properties of Ti64 Diffusion Bonds



T. Pragatheswaran , S. Rajakumar , V. Balasubramanian ,
Vijay Petley  and Shweta Verma 

Abstract The investigation was performed on rolled sheets (2 mm thick) of titanium alloy Ti6Al4V joints which are diffusion bonded. The objective of this investigation is to study and analyse the effect of holding time on the diffusion bond characteristics. The time for bonding was kept between 15 and 60 min. The pressure and bonding temperature were maintained constantly at 8 MPa and 900 °C, respectively. Metallurgical characteristics were analysed by optical and scanning electron microscopy. The mechanical properties of the Ti6Al4V alloy joints were evaluated. The strength of the bonds was correlated with the microstructures to study the effect of holding time. The microstructure reveals that the defect-free bond can be produced when holding time is increased to a certain limit. The maximum bonding strength and tensile shear fracture load (TSFL) were attained for a holding time of 60 min yields 138 MPa and 40 kN, respectively.

Keywords Diffusion · Time · Titanium · Microstructure · Tensile shear

66.1 Introduction

Titanium (Ti) and its alloys have become significant material nowadays in the aerospace engineering, chemical engineering and automobile engineering fields [1]. Ti is considered as a potential candidate for engineering applications not only because it is highly strong and tough but also it is lighter compared to other high-strength materials. Ti alloys are having mere equivalent strength and density slightly more than half of the important high-strength steels and nickel base super alloys. In addition, properties such as low density, bio compatibility and outstanding corrosion resistance

T. Pragatheswaran (✉) · S. Rajakumar · V. Balasubramanian
Centre for Materials Joining and Research (CEMAJOR), Department of Manufacturing
Engineering, Annamalai University, Annamalainagar, Tamil Nadu, India
e-mail: thirupragathesh@gmail.com

V. Petley · S. Verma
Materials Group, Gas Turbine Research Establishment (GTRE), Bengaluru, India

© Springer Nature Singapore Pte Ltd. 2020
M. S. Shunmugam and M. Kanthababu (eds.), *Advances in Additive Manufacturing
and Joining*, Lecture Notes on Multidisciplinary Industrial Engineering,
https://doi.org/10.1007/978-981-32-9433-2_66

are possessed by Ti alloys [2, 3]. Especially in gas turbine manufacturing industries, the components such as compressor discs, wide chord fan blade, hollow vanes and blades are made of Ti alloys [4]. Joining of Ti alloys was found to be difficult since it has poor and moderate weldability and machinability due to the complexities in its crystal structure. Thus, welding of Ti alloys requires a special technique capable of rectifying the complexities. One of the more sophisticated and reliable joining techniques for Ti alloys is the solid-state welding technique called vacuum diffusion bonding in order to achieve good quality joints. In this diffusion bonding process, the surfaces of the workpieces are joined to each other by applying pressure at elevated temperature for a certain period of time. The elevated temperature range must be between 0.5 and 0.8 T_m , the melting temperature of the workpiece material [5]. Since this process does not have melting criteria, the defects due to solidification can be eliminated. During dissimilar materials joining, there may be a requirement of an interlayer material usually a thin metal foil of beneficial properties at the joint interface to strengthen the bond interface and also avoid brittle intermetallics [6, 7]. But in the case of similar material joints, the quality of the joints is recognized by the complete disappearance of the interface line. The diffusion bonding process can be controlled by bonding temperature, bonding pressure and holding time [8–10]. Studying the influence of the process variables will give exploration on controlling the bond characteristics. Among all the diffusion bonding process parameters, time plays a predominant role in the completion of the diffusion phenomenon for joining the materials. Generally, there are three different stages such as heating cycle, holding cycle and the cooling cycle that play a significant role in the process of diffusion bonding. During the heating cycle, the surfaces to be bonded will be activated while in the cooling cycle the material attains a stable structure according to the requirements. But during the holding cycle, the diffusion of atoms across the interface will occur. Thus, in the process diffusion bonding, holding cycle and its period are considered significant while other stages are kept constant according to the standards. So, this present research work focused on studying an influential diffusion bonding process parameter, i.e. bonding time and its effect on the metallurgical characteristics and mechanical properties of the bonds such as bonding strength and shear strength.

66.2 Experimental Work

Diffusion bonding experiments were conducted by a high-temperature diffusion bonding equipment having a maximum operating temperature capacity of 1600 °C and equipped with a hydraulic pressurizing unit with a maximum axial pressure capacity of 10 tonnes. The heating chamber is equipped with a vacuum in order to prevent contamination at elevated temperatures. The diffusion bonding equipment setup is shown in Fig. 66.1. The base material used in this research work was Ti6Al4V alloy thin sheets of 2 mm thick. The diffusion bonded specimens were extracted from the rolled sheets of Ti6Al4V having dimensions of 50 × 50 × 2 mm³. The base material composition and its mechanical properties are shown in Tables 66.1 and 66.2, respectively.



Fig. 66.1 Diffusion bonding machine setup

Table 66.1 Chemical composition (wt%) of the base material Ti6Al4V

Element	Al	V	Fe	C	O	N	H	Ti
%Wt	6.2	4.15	0.01	0.03	0.15	0.01	0.003	Balance

Table 66.2 Mechanical properties of the base material Ti6Al4V

Material	Yield tensile strength (MPa) at 0.2% strain	Ultimate tensile strength (MPa)	Elongation (%) at 25 mm GL	Hardness (Hv) at 50 g load
Ti6Al4V	985	1068	18.5	338

The bonding specimens were polished finely through the SiC emery sheets (up to 2000 grit) to minimize the surface asperities in order to achieve successful void-free bonds. And they were cleansed with acetone in order to get rid of the surface contaminants. The diffusion bonding experiments were carried out inside a vacuum chamber at various holding time such as 15, 30, 45 and 60 min. Other parameters such as bonding pressure and bonding temperature were kept constant at 8 MPa and 900 °C, respectively. All the diffusion bonding experiments were conducted at a heating rate of 5 °C/min, and after the holding cycle the diffusion bonds were allowed to be furnace cooled.

The diffusion bonded specimens were machined into various profiles by wire-cut EDM process for lap shear test, ram tensile test and microstructural analysis through optical and scanning electron microscopy (SEM). The designs for the specimen preparation for various tests are shown in Fig. 66.2a, b. The fabricated specimens for tests are shown in Fig. 66.3a, b.

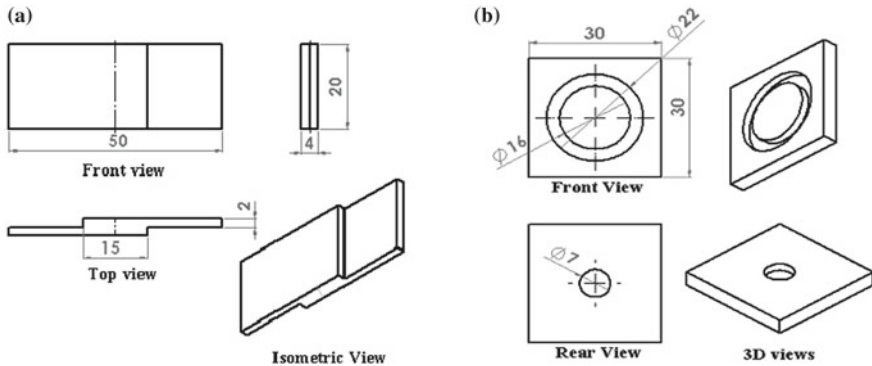


Fig. 66.2 Specimen design **a** lap shear test **b** Ram tensile tests

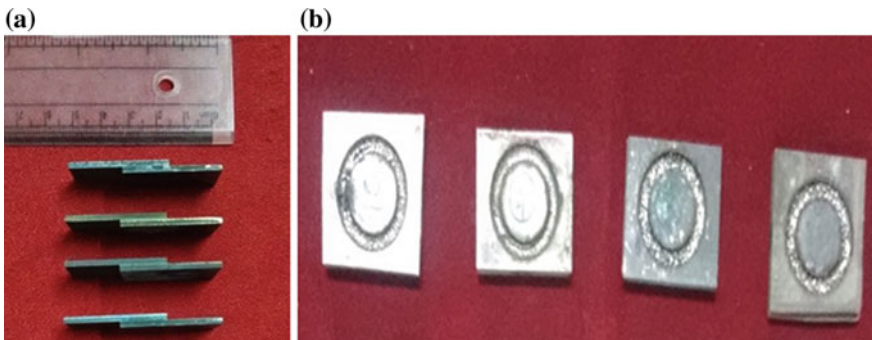


Fig. 66.3 Fabricated before test specimen **a** Lap shear **b** Ram tensile tests

66.3 Results and Discussion

66.3.1 Microstructural Characterization

The microstructure evolution of diffusion bonds is determined predominantly by the heating and cooling cycle of the bonding operation, i.e. the process variables “bonding temperature and holding time” contribute an important role since they are interdependent on each other. To attain a successful defect-free bond, the above-mentioned process parameters must be studied. The most usual defect that is encountered during diffusion bonding is the formation and presence of voids or gaps in the joint interface as it reduces the bond quality by affecting the strength. Figure 66.4 shows the microstructure of the diffusion bonds produced at different holding times. From Fig. 66.4a, the presence of a large number of voids and the grains are as fine as in the case of base materials, a little elongated and equiaxed throughout the Ti6Al4V alloy matrix.

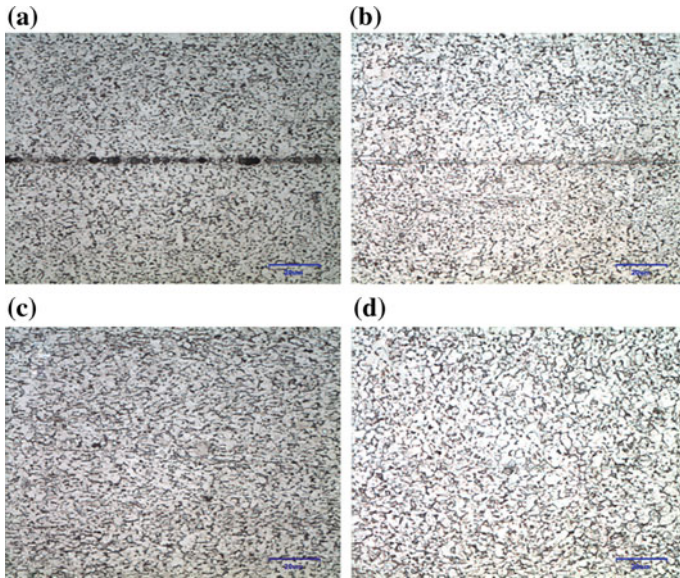


Fig. 66.4 Optical micrographs at different holding time **a** 15 min **b** 30 min **c** 45 min **d** 60 min

The formation and presence of voids might be due to the fact that the holding time of 15 min is insufficient to achieve void-free bond. Here, the bonding pressure promotes the plastic deformation of the surface asperities so that the two surfaces might have intimate contact. Though the void closure is influenced predominantly by the bonding pressure, the holding time also influences it considerably which can be seen from the microstructure comparison. At subsequent higher holding times of 30, 45 and 60 min, from Fig. 66.4b–d it was observed that the number and area of the voids in the interface get gradually decreased. Comparing Fig. 66.4c, d, the size of the grains becomes coarser in both cases but bond at 60 min shows more evenly distributed equiaxed coarser grains than the bond at 45 min. The high-resolution SEM examination shows the morphology of the voids present in the bond interface region evidently which is shown in Fig. 66.5. When bonding temperature is below 900 °C, the titanium alloy thin sheet specimen is heated to attain a region where α and β phase can coexist.

The diffusion rate is determined by the temperature and time of the process. In general, the time for bonding is set between the completion of the heating cycle and initiation of the cooling cycle, i.e. holding at the definite temperature. The diffusion of atoms completes when the temperature is sufficient for a certain period of time, and all the asperities of the surface are deformed. When the time increased, the diffusion process is allowed to complete the closure of voids and thus results in good integrity of the joint. When the holding time is increased gradually, the voids present in the joint interface slowly disappear. This happens due to the fact that this process involves time-dependent deformation and diffusion which facilitates the

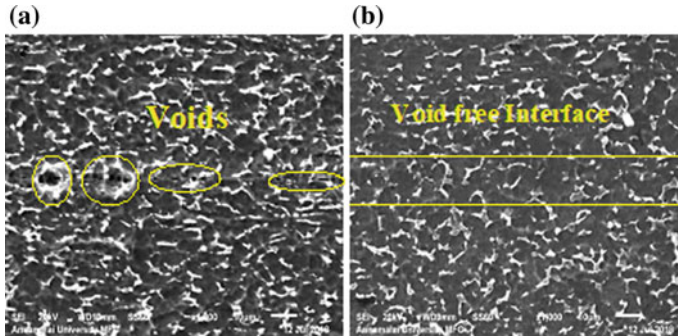


Fig. 66.5 SEM microstructures at different holding times: **a** 15 min **b** 60 min

deformation of the surface asperities over time. And the interdiffusion of the atoms is also increasing over the increase in the bonding time. A perfect joint in diffusion bonding is characterized by the disappearance of the interface. At 45 min and 60 min diffusion bonds, the interface was found to be completely disappeared; whereas, in the case of 15 and 30 min diffusion bonds, the voids are found and observed the complete presence of the interface and the number and area of the voids were found to be in a progressive decrement.

66.3.2 Mechanical Properties

The strength of the diffusion bonds was assessed by mechanical tests such as lap shear test and ram tensile test and are tabulated in Table 66.3.

The highest TSFL attained is 40 kN at a holding time of 60 min, and the minimum value is 18 kN at 15 min. The maximum bonding strength from ram tensile test attained is 138 MPa at 60 min holding time and minimum value of 66 MPa at 15 min. It is observed from the results that the strength of the diffusion bonds increases with increase in holding time initially but it gradually decreases afterwards which can be confirmed from the difference in the strength values which can be observed from

Table 66.3 Mechanical properties of the diffusion bonds at different temperatures

Exp. No.	Holding time, minutes	Bonding strength, MPa	TSFL, kN	Lap shear failure details
1.	15	66	18	Bond separated
2.	30	95	24	Bond separated
3.	45	135	38	Fractured at the base material
4.	60	138	40	Fractured at the base material

the plot shown in Fig. 66.6. The fractured specimen's ram tensile and lap shear tests were analysed, and it is shown in Fig. 66.7.

From the lap shear fractured specimen, it was observed that failure occurrence is different for different holding times. For a holding time of 15 and 30 min, the bond gets separated whereas for 45 and 60 min the bond stayed strong, failure occurred at the base material. The fracture morphology of the different conditions, i.e. the bond gets separated and the bond failed at the base material was examined through SEM, and it is shown in Fig. 66.8.

The fracture morphology shows that no significant dimples or any other fracture profiles for bonds produced at 15 min (bonds get separated during testing); whereas,

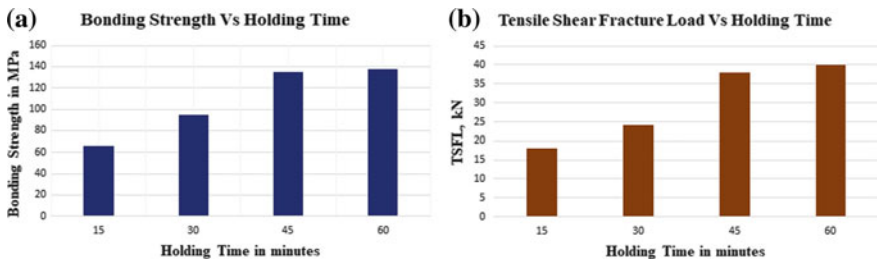


Fig. 66.6 Effect of holding time on mechanical properties of the diffusion bonded Ti6Al4V joint

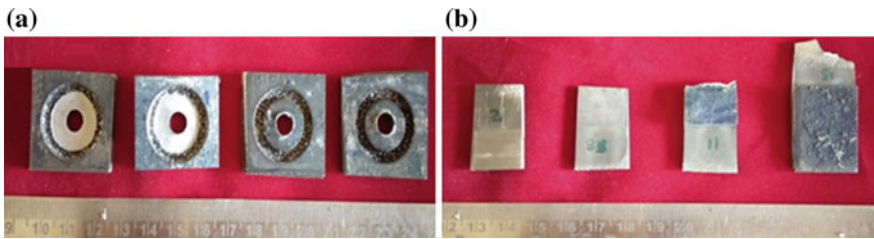


Fig. 66.7 After test specimens of a Ram tensile and b Lap shear tests

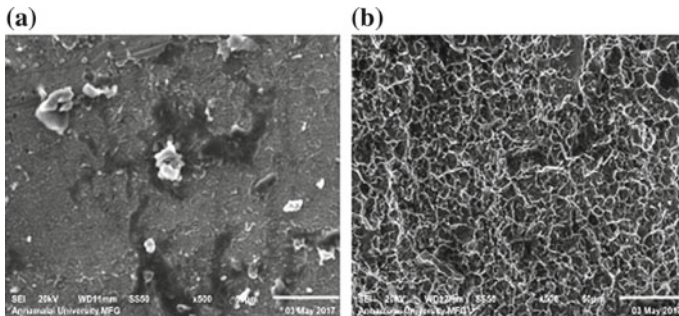


Fig. 66.8 Fracture morphology of diffusion bonded lap shear specimen a At 15 min b At 60 min

for the bonds produced at 60 min (bonds fractured at the base material), there were extensive domination of dimples found on the fractured surfaces, i.e. ductile fracture results when the holding time is higher than 15 min. The difference in time causes variations in strength that contributes the changes in the fracture phenomenon.

66.4 Conclusion

- The bonding time influences the strength of the bond such as bonding strength and shear strength of the Ti6Al4V bonds predominantly, but the proportionality of temperature and mechanical properties changes after a certain limit.
- The microstructures revealed that time contributes a vital role in producing the defect-free joints with good joint integrity.
- The highest bonding strength attained was 138 MPa and the lowest was 66 MPa for temperatures 15 and 60, respectively.
- The highest shear strength attained was 40 kN and the lowest was 18 kN for temperatures 15 and 60, respectively.

Acknowledgements The authors are very grateful to Gas Turbine Research Establishment (GTRE), Ministry of Defence for providing financial support under the Contract Acquisition Research Support (CARS) scheme (Grant No. GTRE/MMG/BMR1/1022/16/CARS/A/16).

References

1. ASM Handbook.: Properties and selection: nonferrous alloys and special purpose materials, 10th edn. ASM International Handbook Committee, vol. 2 (1990)
2. Kim, Y., Kim, E., Song, Y., Lee, S., Kwon, Y.: Microstructure and mechanical properties of hot isostatically pressed Ti–6Al–4V alloy. *J. Alloys Compd* **603**, 207–212 (2014)
3. Hamilton, B., Oppenheimer, S., Dunand, D., Lewis, D.: Diffusion bonding of Ti–6Al–4V sheet with Ti–6Al–4V foam for biomedical implant applications. *Metall. Mater. Trans. B* **44B**, 1554–1559 (2013)
4. Fitzpatrick, G.A., Broughton, T.: Diffusion bonding of aero engine components. *Defence Sci. J.* **38**(4), 477–486 (1988)
5. Lee, H., Yoona, J., Yi, Y.: Fabrication of titanium parts by massive diffusion bonding. *J. Mater. Process. Technol.* **201**, 280–284 (2008)
6. Rahman, A.: Cavalli MN Diffusion bonding of commercially pure Ni using Cu interlayer. *Mater. Charact.* **69**, 90–96 (2012)
7. Samavatian M, Halvae A, Amadeh A, Khodabandeh. A Transient liquid phase bonding of Al 2024 to Ti–6Al–4V alloy using Cu–Zn interlayer. *Trans. Nonferrous Metals Soc. China* **25**,770–775 (2015)

8. Mahendran, G., Balasubramanian, V., Senthilvelan, T.: Influences of diffusion bonding process parameters on bond characteristics of Mg-Cu dissimilar joints. *Trans. Nonferrous Metals Soc. China* **20**(6), 997–1005 (2010)
9. Joseph Fernandus, M., Senthilkumar, T., Balasubramanian, V., Rajakumar, S.: Optimizing diffusion bonding parameters to maximize the strength of AA6061 aluminium and AZ31B magnesium alloy joints. *Mater. Des.* **33**, 31–41 (2012)
10. Samavatian, M., Zakipour, S., Paidar, M.: Effect of bonding pressure on microstructure and mechanical properties of Ti–6Al–4V diffusion-bonded joint. *Welding World* **61**(1), 69–74 (2017)